Project: CPF#05-17 **COPY NO. ….**

R-Factors for Coupled Composite Plate Shear Walls / Concrete Filled (CC-PSW/CF)

Final Report

Prepared for

Charles Pankow Foundation & American Institute of Steel Construction

University at Buffalo
Department of Civil, Structural and Environmental Engineering
Buffalo, NY

Purdue University
Lyles School of Civil Engineering
West Lafayette, IN

Dr. Michel Bruneau
SUNY Distinguished Professor, University at Buffalo
Dr. Amit H. Varma
Karl H. Kettelhut Professor, Purdue University
Emre Kizilarslan
Graduate Research Assistant, University at Buffalo
Morgan Broberg
Graduate Research Assistant, Purdue University
Soheil Shafaei
Graduate Research Assistant, Purdue University
Dr. Jungil Seo
Research Engineer, Purdue University

July 19th, 2019

ACKNOWLEDMENTS

This research was conducted with support from the Charles Pankow Foundation (CPF) and the American Institute of Steel Construction (AISC), through CPF research grant #05-17 "R-Factors for Coupled Composite Plate Shear Walls—Concrete Filled (CC-PSW/CF)" awarded to co-PIs Michel Bruneau, from the University at Buffalo, and Amit Varma, from Purdue University.

The researchers are also grateful to members of the FEMA P695 Peer-Review Panel:

- Gregory G. Deierlein, *Professor,* Stanford University;
- Ron Klemencic, *Chairman & CEO,* Magnusson Klemencic Associates (MKA), and;
- Rafael Sabelli, *Principal and Director of Seismic Design,* Walter P.Moore;

and members of the Project Advisory Team:

- Larry Kruth, *Vice President,* American Institute of Steel Construction (AISC);
- John D. Hopper, *Senior Principal/Director of Earthquake Engineering,* MKA;
- Jim Malley, *Senior Principal,* Degenkolb Engineers;
- Bonnie Manley, *Regional Director of Construction Codes and Standards,* American Iron and Steel Institute (AISI), and;
- Tom Sabol, *Principal*, Englekirk Institutional;

for their technical guidance.

The researchers also thank all at Magnusson Klemencic Associates (MKA), Cives Steel Co., Supreme Group, J.F.Stearns Co., and Turner Construction, for their outstanding support, donation of steel, and fabrication of specimens in the experimental projects cross-references as part of this study, as well as Anne Ellis *Executive Director of* of the Charles Pankow Foundationm, Thomas J. Schlafly, *Chief of Engineering Staff*, AISC, Devin Huber, *Director of Research*, AISC, and Mike Gannon, *Senior Engineer*, AISC, for their valuable support.

TABLE OF CONTENTS

“This Page Intentionally Left Blank”

LIST OF FIGURES

“This Page Intentionally Left Blank”

LIST OF TABLES

“This Page Intentionally Left Blank”

Abstract

Composite Plate Shear Wall—Concrete Filled (C-PSW/CF) is an efficient seismic force-resisting system for buildings and is already addressed by ASCE-7 2016. Coupled Composite Plate Shear Walls—Concrete Filled (Coupled C-PSW/CF) are more ductile and have more redundancy than non-coupled composite plate shear walls, but ASCE currently does not assign them seismic design coefficients and factors. This FEMA P695 study was conducted to substantiate the design coefficients and factors that should be used for such CC-PSW/CF structures. Adding this as a separate category in ASCE-7 is important because modern high-rise buildings have core-wall systems; many of these core walls could utilize the CC-PSW/CF.

This report outlines the steps of the collapse assessment studies performed that have led to the proposed design provisions for this structural system, including a description of the design requirements prescribed for CC-PSW/CF, the 3-story, 8-story, 12-story, 18 story, and 22-story archetypes designed following these requirements, information on the non-linear models used and validated in that study, details of the non-linear time history dynamic analysis parameters, findings from the Incremental Dynamic Analyses (IDA) performed, and resulting Adjusted Collapse Margin Ratio values for all of the archetypes considered. Two different IDA were performed in parallel, using different non-linear models to assess sensitivity of the results, and non-linear finite element analyses were conducted for selected archetypes to provide greater insights into the ultimate behavior of the structural system upon increasing severity of ground motion excitation. This contributed to enhanced confidence in the results and provided a more robust validation of the proposed design provisions and seismic design coefficients and factors.

Results from this study indicate that an R factor of 8, Ω_o factor of 2.5, and C_d factor of 5.5 can be specified in ASCE-7 for CC-PSW/CF designed in accordance to the specific provisions, design philosophy, and limits of applicability developed here for this CC-PSW/CF system. It is anticipated that these detailed designed provisions will ultimately end up distributed in AISC 360 and AISC 341 (2022).

SECTION 1
INTRODUCTION

1.1 Objective and Scope of Work

Nonlinear time history analysis is required to predict the seismic response of a ductile structure more accurately. However, for simplicity, the most common approach in design is to perform (static or dynamic) elastic analysis considering lateral forces and displacement determined on the basis of an elastic design spectrum and modified to account for the ductile response of structures. More specifically, ASCE 7-16 (2016) defines three seismic performance factors to approximately predict the elastic-perfectly plastic response of a seismic resisting system. These factors are the response modification factor, R; deflection amplification factor, C_d; and the system over-strength factor, Ω_0. The design response spectrum in ASCE 7-16 (2016) is based on elastic SDOF system with 5% damping. Therefore, the base shear calculated from the spectrum is divided by the R-factor to obtain design seismic force. The second factor, C_d, was adopted to multiply the deflections from a static analysis using the reduced base shear in order to estimate the actual ultimate deflection of the structure. Also, to account for factors that increase lateral load resistance beyond the point of first yield point as lateral load increases, the reduced base shear is multiplied by another factor, namely the over-strength factor (Ω_0), to reach the yield mechanism at the strength level. ASCE 7-16 (2016) specifies values for these factors for specific seismic force-resisting systems.

The research presented here only investigates the value of the above factors for a special seismic-force resisting system defined as Coupled Composite Plate Shear Walls-Concrete Filled (CC-PSW/CF) (designation proposed here for future editions of ASCE-7 and AISC-341, as an extension of the name Composite Plate Shear Walls-Concrete Filled (C-PSW/CF) already used in those documents). C-PSW/CF consists of two steel plates with concrete infill in between them. The steel plates are connected to each other using tie bars that are embedded in the concrete infill and, in some instances, steel-headed stud anchors. The steel plates serve as the primary reinforcement for the concrete infill and provide stay-in-place formwork during construction. The concrete infill also prevents inward local buckling of the steel plates thus improving their stability (Alzeni and Bruneau 2014; Zhang et al. 2014).

The ASCE 7-16 (2016) and AISC 341-16 (2016) seismic provisions refer to more specific requirements for the use of planar composite steel plate shear walls in seismic regions. The ASCE-7 specifications do not differentiate between coupled and non-coupled walls.

The aim of this project is to determine what should be the R-factor (and other corresponding seismic response parameters, C_d and Ω_O) for CC-PSW/CF. The FEMA P695 procedure is used for this purpose (details on the FEMA P695 procedure are provided in Chapter 2). The FEMA P695 procedure is intended to ensure that an adequate margin against collapse exists for the maximum considered earthquake (MCE) hazard, as established by performing a large number of nonlinear earthquake analysis (i.e., incremental dynamic analysis) for a significant set of strong earthquakes records. Given that C-PSW/CF is a relatively new structural system, it was also decided in this study to perform the incremental dynamic analyses required by the FEMA P695 procedure using two different set of non-linear models, as a way to gage the sensitivity of response to changes in numerical models and enhance confidence in the final results.

The findings from this study are presented in this report. They are intended to substantiate proposed revised R-values in subsequent editions of ASCE 7. It is foreseen that a larger R factor would be logical for composite coupled walls; more specifically, the current R-value of 6.5 specified in ASCE-7-16 for composite walls could increase to a value as high as 8.

1.2 Outline

The section provides a general outline of this report. Section 2 provides a brief description of Coupled Composite Plate Shear wall/Concrete-Filled (CC-PSW/CF) as a lateral force resisting system, focusing on some of system's advantages in construction and in overall structural behavior. Also, a review of the collapse assessment methodology outlined in FEMA P695 is summarized in that section, as this methodology is used in Section 10 to investigate the seismic performance of CC-PSW/CF archetypes designed per different parameters.

Detailed design requirements for Coupled Composite Plate Shear Walls/Concrete-Filled (CC-PSW/CF) were presented in Section 3 and Section 4. On the basis of the design requirements presented in Section 3, the archetypes were designed as summarized in more details in Section 5.

In order to create models of the archetypes in a format compatible with the FEMA P695 methodology for collapse assessment, material models and element types were chosen from the OpenSees library and details on that information are summarized in Section 6.

A calibration process was also performed in order to validate the chosen material models and element types. Since two different types of non-linear models were used to analyze the archetypes (as part of the two parallel FEMA P695 analyses conducted on the same archetypes), each component of the CC-PSW/CF system was calibrated with various test data. The results of this calibration work are presented in Section 7 and in Section 8 for the two non-linear models, respectively.

The numerical behavior of models used to analyze the proposed system are examined in Section 9 for selected archetypes. This section (Section 9) also includes some trial IDA runs performed on an arbitrary structure in order to eliminate possible modeling and numerical errors issues. The behavior of these walls and their plastic hinges is scrutinized to determine additional adjustments needed to ensure credible analysis results.

Section 10 presents collapse assessment on the archetypes of CC-PSW/CF wall system designed as described in Section 5. The seismic performance factors that could be used for CC-PSW/CF are determined in this section. This is done using two different modeling approaches for two different configurations of CC-PSW/CF wall systems, namely planar shaped CC-PSW/CF wall systems; and C-shaped CC-PSW/CF wall systems (as defined in Section 5.1). The specific seismic performance factors (SPF) determined for these structural systems are the response modification coefficient (R), the system over-strength factor (Ω_o), and the deflection amplification factor (C_d). First, the collapse assessment is done for planar CC-PSW/CF wall system (Type I in Figure 5-1). Collapse assessment is also performed for the second configuration (Type II in Figure 5-1). SPF for both configurations of C-PSW/CF wall system are identified.

Finally, Section 11 provides a summary of the work accomplished, and conclusions for the implementation in codes and specifications.

SECTION 2
OVERVIEW OF STRUCTURAL SYSTEM AND FEMA P695 METHODOOGY

2.1 General

This section consists of two parts. First is a brief description of Coupled Composite Plate Shear wall/Concrete-Filled (CC-PSW/CF) as a lateral force resisting system, focusing on some of system's advantages in construction and in overall structural behavior. Extensive descriptions of the structural system have been provided elsewhere (e.g., (AISC 2019)) and, for expediency, are not repeated here. Second is a review of the collapse assessment methodology outlined in FEMA P695, as this methodology is used in Section 10 to investigate the seismic performance of CC-PSW/CF archetypes designed per different parameters.

2.2 Coupled Composite Plate Shear Wall/ Concrete-Filled as a Lateral Force Resisting System

2.2.1 Description of the Structural System

A Coupled Composite Plate Shear Wall-Concrete Filled (CC-PSW/CF) is a special lateral-force resisting system consisting of two major components, namely: (i) Composite Plate Shear Walls/Concrete Filled (C-PSW/CF) and composite coupling beams at each story level along the height of a structure (Figure 2-1a). The C-PSW/CF are composed of two steel plates with concrete infill between them. The steel plates are connected to each other using tie bars that are embedded in the concrete infill and, in some instances, steel-headed stud anchors. Examples of typical C-PSW/CF cross-sections are shown in Figure 2-1b. The coupling beams are typically steel built-up boxes filled with concrete.

The benefit of these systems is that the steel plates serve as the primary reinforcement for the concrete infill and provide stay-in-place formwork during construction. The concrete infill also prevents inward local buckling of the steel plates thus improving their stability (Alzeni and Bruneau 2014; Zhang et al. 2014). Hence, it is fast in construction, which is considered to be a major advantage as proven by recent construction (Post 2019). Moreover, from the point of behavior, both composite walls and coupling beams are designed to develop their inelastic flexural strength during severe earthquake excitations, and experiments have shown their ability to develop a displacement ductility of 3 or more. In coupled wall

systems, plastic hinging of the coupling beam occurs along the height of structure, not only base of the walls, which benefits the system's ductile response.

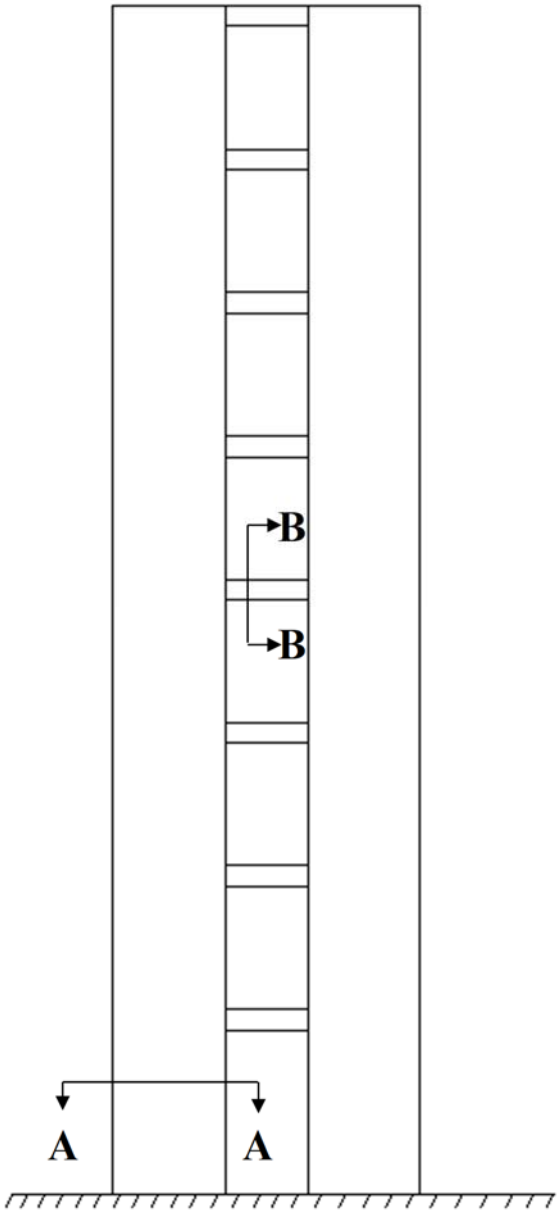

a)

Figure 2-1. CC-PSW/CF schematic description: a) Elevation, b) example wall cross-sections, and; c) beam cross-section

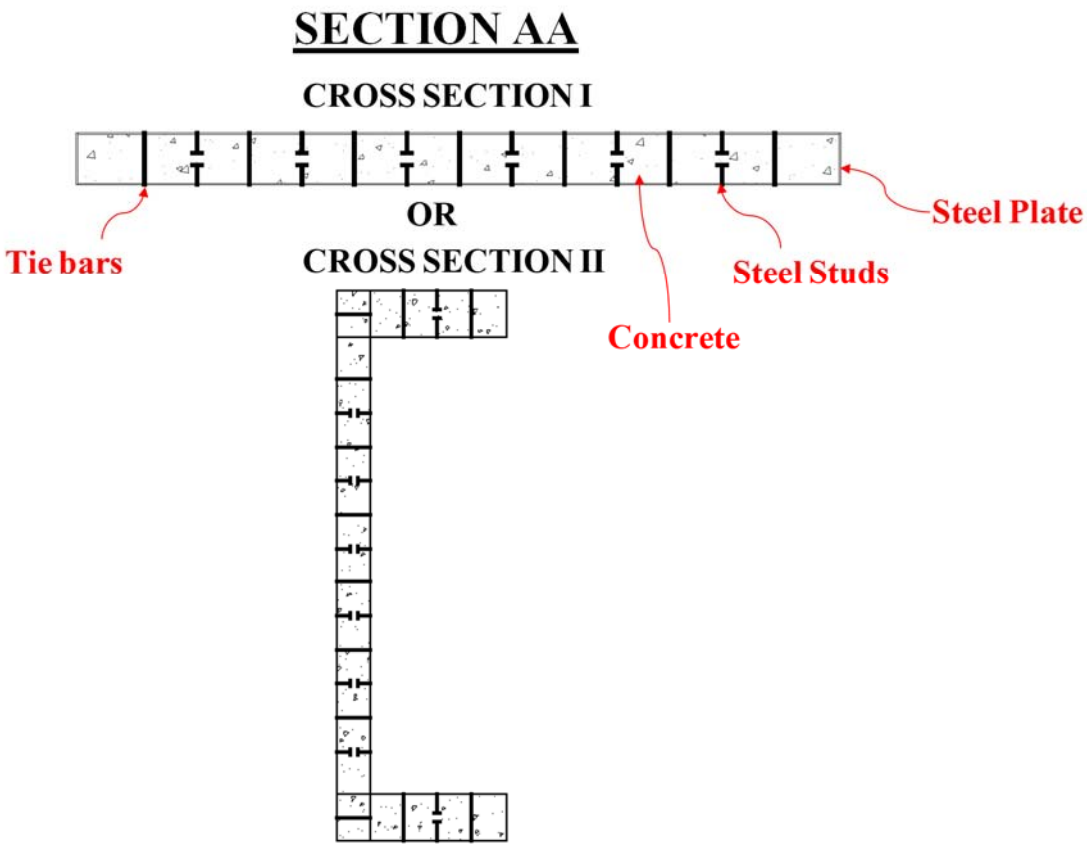

b)

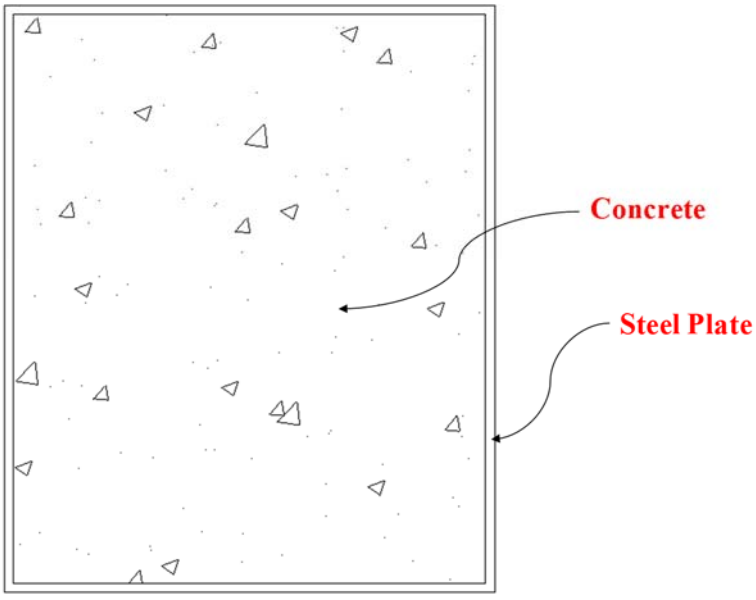

c)

Figure 2-1. (Continued)

2.2.2 Coupling Ratio

Lateral loads cause a global over-turning moment (OTM) at the base of the walls. The proportion of OTM resisted by the axial force couple (ΣV_{BEAM} with the lever arm L) developed from the accumulation of the shear in the beams is defined as the coupling ratio (CR) (Borello and Fahnestock 2012; El-Tawil et al. 2010). The calculation of CR is obtained at the base of the wall when the system has developed a plastic mechanism (Figure 2-2). In this case, it is assumed that the coupling beams sustain their plastic shear capacity as the walls yield. The CR is mathematically expressed as:

$$CR = \frac{L * \Sigma V_{CB}}{L * \Sigma V_{CB} + \Sigma m_i} = \frac{L * \Sigma V_{CB}}{OTM} \quad \textbf{(2.1)}$$

where $\sum V_{CB}$ =accumulation of coupling beam shears acting on each wall pier; L=lever arm between the centroids of the wall piers, and; m_i=OTM resisted by wall *i*.

This ratio ranges from zero to unity. Zero indicates that lateral forces are resisted by only walls and unity is for the case where the coupling beams alone would resist the lateral loads (which is an unlikely situation and more a theoretical limit). Using the flexural strength coming from the axial force couple, more economical design can be obtained with smaller wall dimensions.

Note that consulting engineers involved in the design of tall buildings have indicated that the coupling ratio, as presented above, is not a design parameter typically used in practice. However, it a useful as a measure to gage the extent to which coupling beams contribute to inelastic response, and will be used in that perspective here, together with a new and complementary parameter (somehow related to Eq. 2.1) introduced and described in Section 5.3, which is the stiffness based coupling ratio (CR_K).

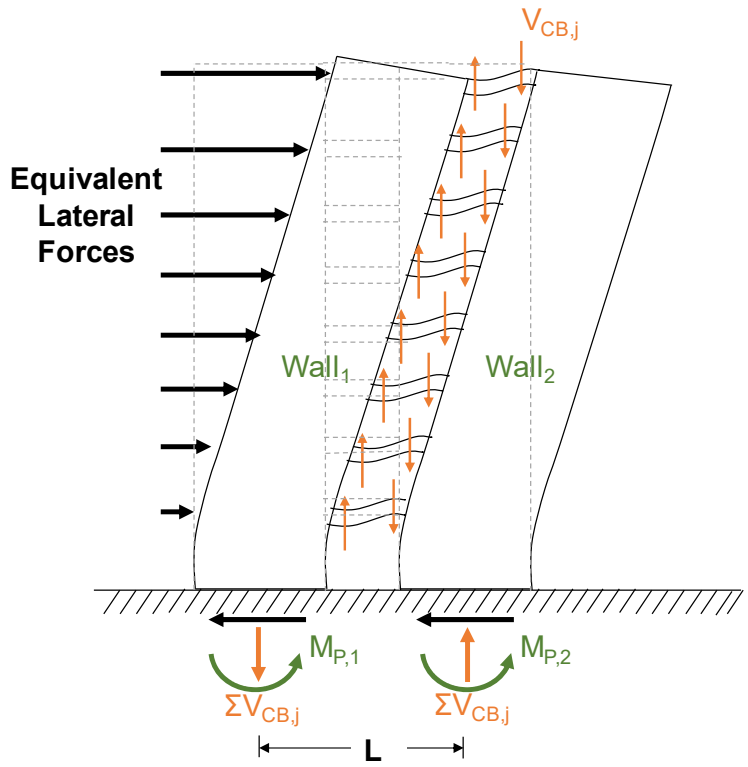

Figure 2-2. Coupled Wall behavior (not to scale)

2.3 Collapse Assessment Methodology: Overview of FEMA P695 Procedure

The FEMA P695 document, developed by the Applied Technology Council (ATC) under the ATC-63 project name, provides a suggested methodology to quantify global seismic performance factors (SPF) of new seismic-force-resisting systems for use in seismic design. This procedure is used in this study to examine the seismic performance of Coupled Composite Plate Shear Wall/Concrete-Filled (CC-PSW/CF), and is therefore briefly summarized here.

This FEMA P695 procedure relies on inelastic nonlinear time history analysis to determine response of structural system archetypes using Incremental Dynamic Analysis (IDA) for a suite of ground motions, comparison of their response with demand for Maximum Considered Earthquake (MCE), and probabilistic evaluation of their collapse risk. The methodology provides a rational basis to quantify seismic performance factors, namely: response modification coefficient (R factor), system over-strength factor (Ω_0 factor), and deflection amplification factor (C_d factor). Key steps of the methodology for establishing these factors include: 1) development of archetype buildings having the structural system under consideration; 2) development of nonlinear analytical models that appropriately captures the hysteretic behavior of the structural elements considered, including strength and stiffness degradation; 3) nonlinear static and dynamic

analyses (i.e., pushover and incremental dynamic analyses), and; 4) performance evaluation of the system under consideration in terms of probabilistic collapse assessment under MCE ground motions. Therefore, a brief overview of each of these key steps is summarized in the successive sub-sections.

2.3.1 Development of Archetypes

The FEMA P695 methodology describes an archetype as "a prototypical representation of a seismic-force-resisting system configuration that embodies key features and behaviors related to collapse performance when the system is subjected to earthquake ground motions". The methodology requires careful consideration of a series of archetypes that replicate a broad range of design parameters to make it possible to observe the key seismic behaviors of the proposed seismic-force resisting system. Design parameters that are considered in developing the archetypes are: 1) various elevation and plan configuration (e.g., frame span length, story height, number of stories, geometric variation of seismic-force resisting system); 2) type of structural components; 3) occupancy and building usage; 4) variations in gravity loads, and; 5) different seismic design category (SDC).

Archetypes with similar design criteria are put into performance groups (or bins). Archetypes in one performance group have similar gravity load level, basic structural configuration, period domain, seismic design category, and other design features that result in similar seismic behavior. Binning of archetypes into performance groups, also, enables a basis for statistical assessment of minimum and average collapse margin ratios (CMR) for seismic performance factors of the system. A minimum of three archetypes is required for each performance group. For example, assuming two seismic design categories (i.e., max and min SDC), high and low tributary seismic masses, two assumed basic structural configurations, and two period domains (short and long periods), 48 archetypes in 16 performance groups would be needed to perform the FEMA P695 for that structural system. However, the methodology allows performing FEMA P695 study on smaller number of archetypes with proper justifications and with no detrimental effect to the examination of key behaviors for the proposed seismic-force resisting system under consideration. Using this FEMA P695 procedure, development of archetypes of CC-PSW/CF for collapse assessment is presented in Section 5.

2.3.2 Nonlinear Model Development

The nonlinear models used in the FEMA P695 study must be able to simulate all main failure and deterioration modes that contribute to global structural collapse of the seismic-force resisting system under consideration. For that reasons, previous experimental data or observations from past earthquakes is used

to identify the failure modes of the system and of its structural elements. However, if failure modes can be prevented by enforcing principles outlined in the system design requirements, then they do not need to be accounted in the nonlinear model.

Component models must capture hysteretic strength and stiffness degradation under large deformations up to collapse. According to Ibarra et al. (2005), the nonlinear model should explicitly simulate the yielding condition, maximum strength (i.e., the capping point), post capping tangent stiffness (i.e., rate of degradation), and residual strength in order to define the backbone curve of a system. In addition, cyclic deterioration that decreases stiffness and reduces energy dissipation capacity per cycle should be included in order to capture the collapse response of a system under consideration during nonlinear dynamic analysis. Furthermore, nonlinear models should be calibrated against available experimental data to validate their ability to replicate the test results. At the global level, P-Δ effects due to gravity loads at large lateral deformations must be considered. Development of deteriorating material models used for collapse assessment of CC-PSW/CF system is presented in Section 6.

2.3.3 Nonlinear Static and Dynamic Analyses

Nonlinear static (pushover) and nonlinear dynamic (time history) analyses are conducted on the numerical models of each archetype developed in the previous step. Pushover analyses are performed to confirm that the numerical models behave as expected, and to quantify V_{max} and δ_u, which are then used to get the system overstrength, Ω_o, and period base ductility, μ_T, of each archetype. To quantify these values, the archetypes are pushed monotonically until the archetypes lose 20% of their base shear ($0.8V_{max}$) while the effective yield displacement is obtained as the roof displacement corresponding to an intersection point of the elastic stiffness and maximum base shear tangents. The system overstrength factor and period base ductility are defined as follows:

$$\Omega_o = \frac{V_{max}}{V_{design}} \quad \textbf{(2.2)}$$

$$\mu_T = \frac{\delta_u}{\delta_{y,eff}} \quad \textbf{(2.3)}$$

where V_{max} and V_{design} are the maximum and design base shear strength for a given archetype model; and δ_u and $\delta_{y,eff}$ are the ultimate and effective yield roof displacement of the archetype model. Figure 2-3 shows these parameters in a typical nonlinear static (pushover) analysis curve.

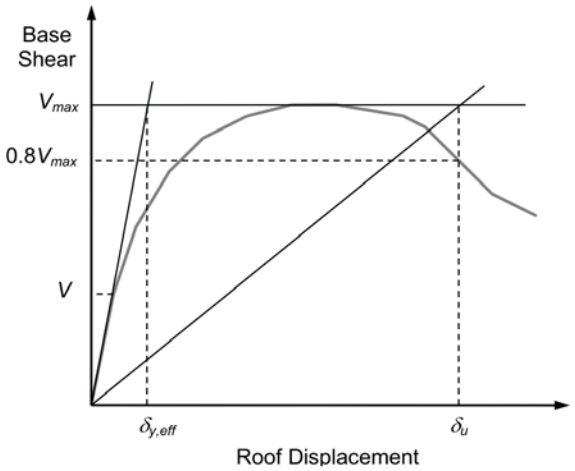

Figure 2-3. Typical nonlinear static (pushover) analysis (FEMA 2009).

Nonlinear dynamic analyses are conducted to measure the median collapse capacity, $\hat{S}_{CT}$, and collapse margin ratios, *CMR*. A suite of ground motions must be used for this purpose. For convenience, a set of 22 ground motion record pairs (44 individual components) of large magnitude (M > 6.5) from sites located at distances greater than or equal to 10 km from fault rupture (i.e., "Far-Field" record set) is recommended by FEMA 695, and these are available in the Pacific Earthquake Engineering Research Center (PEER) Next Generation Attenuation (NGA) database (PEER 2005). The far-field record sets are specified in Table A-4A of the FEMA P695 document (FEMA 2009). The median collapse capacity, $\hat{S}_{CT}$, is defined as the spectral intensity when half of the specified ground motions cause an archetype to collapse; and it is used to calculate the collapse margin ratio, which is defined as follows:

$$CMR = \frac{\hat{S}_{CT}}{S_{MT}} \tag{2.4}$$

where S_{MT} is the response spectrum of MCE ground motions at the fundamental period of a given archetype. Figure 2-4 illustrates how to define the value of these two parameters. Figure 2-4(a) shows nonlinear dynamic analysis results in terms of spectral acceleration versus maximum story drift obtained in each analysis for all considered ground motions. Each point is the maximum story drift from one nonlinear dynamic analysis of an archetype model that is run for one particular scaled ground motion. Thus, each curve is the results of one ground motion scaled to increasing intensity levels, until collapse is observed. The most common indicator of collapse is the nearly flat part of an IDA curve when excessive lateral displacement occurs for a relatively small increment of ground motion intensity. However, a semi-arbitrary practical drift limit is also used as a definition of collapse. In this example, the median collapse capacity,

$\hat{S}_{CT}$, is 2.8g. An appropriate way to determine $\hat{S}_{CT}$ is to generate a collapse fragility curve, as in Figure 2-4(b). This figure is constructed by a lognormal cumulative distribution function (CDF) of the collapse data points from IDA curves of an archetype for each ground motion, as shown in Figure 2-4(a). This helps to inform the probability of archetype collapse for a given spectral acceleration. The median collapse capacity corresponds to a 50% probability of collapse, which is 2.8g for the example in Figure 4-3. Using this number, and based on Equation 2.4, the CMR is calculated as 2.5 for a MCE intensity, S_{MT}, of 1.1g. Nonlinear monotonic pushover and incremental dynamic analyses conducted on a series of CC-PSW/CF archetypes for quantifying the seismic performance factors are presented in Section 10.

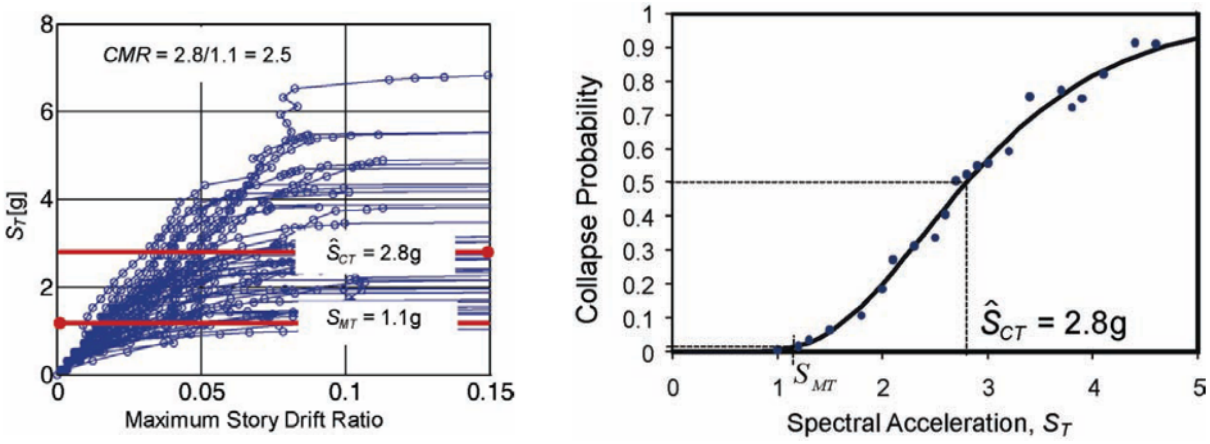

a) **b)**

Figure 2-4. Typical a) incremental dynamic analysis and b) collapse fragility curve (FEMA 2009).

2.3.4 Performance Evaluation

Performance evaluation of a proposed seismic-force-resisting system designed with a trial R factor is done by evaluating if the collapse margin ratios calculated from nonlinear time history analyses are bigger than a pre-established acceptable threshold value. For CMR values calculated for all considered archetypes, this evaluation procedure is as follows:

Step 1: Adjusting Collapse Margin Ratio

The calculated CMR (Section 2.3.3) is first multiplied by the spectral shape factor (SSF) to obtain an adjusted collapse margin ratio (ACMR), to account for the effects of spectral shape (i.e., frequency content of the specified ground motions):

$$ACMR = SSF(T, \mu_T) x CMR \quad \textbf{(2.5)}$$

where SSF value is a function of the fundamental period T of an archetype and period-based ductility, μ_T, obtained from pushover analysis (Equation 2.3). The SSF values are obtained from Tables 7-1a and 7-1b in the FEMA P695 document (FEMA 2009) for archetypes designed with different seismic design categories (SDC). CMRs of archetypes with larger ductility and longer fundamental periods are multiplied by larger SSF values to get ACMR. Further description on the background and development of SSF can be found in Appendix B of the FEMA P695 document.

Step 2: Estimation of Total System Collapse Uncertainty

Acceptable values of the ACMR (determined in Step 3) are obtained from total system collapse uncertainty and specified acceptable collapse probabilities. The total system collapse uncertainty (β_{TOT}) is calculated from combination of the effect of four sources of uncertainties, namely: (1) ground motion record-to-record uncertainty (β_{RTR}); (2) uncertainty related to the completeness and robustness of design requirements (β_{DR}); (3) uncertainty related to the completeness and robustness of test data (β_{TD}); and (4) uncertainty related to modeling (β_{MDL}) in terms of how well nonlinear models could capture the actual structural collapse behavior.

$$\beta_{total} = \sqrt{\beta_{RTR}^2 + \beta_{DR}^2 + \beta_{TD}^2 + \beta_{MDL}^2} \quad \textbf{(2.6)}$$

Based on the far-field ground motions selected, the FEMA P695 methodology gives a fixed value of β_{RTR} (= 0.4) for archetypes with period-based ductility larger than 3 ($\mu_T \geq 3$). Values of the other uncertainties factor are taken from Tables 2-1 to 2-3 for β_{DR}, β_{TD}, and β_{MDL}, respectively. The FEMA P695 methodology gives smaller uncertainty factors for seismic-force-resisting systems that have well-defined design requirements, comprehensive experimental data, and accurate nonlinear models that captures the actual collapse behavior. This suggest that there is less uncertainty in the expected seismic performance of such systems.

Table 2-1. Quality Rating of Design Requirements (FEMA 2009).

Completeness and Robustness	Confidence in Basis of Design Requirements		
	High	Medium	Low
High. Extensive safeguards against unanticipated failure modes. All important design and quality assurance issues are addressed.	(A) Superior $\beta_{DR} = 0.10$	(B) Good $\beta_{DR} = 0.20$	(C) Fair $\beta_{DR} = 0.35$
Medium. Reasonable safeguards against unanticipated failure modes. Most of the important design and quality assurance issues are addressed.	(B) Good $\beta_{DR} = 0.20$	(C) Fair $\beta_{DR} = 0.35$	(D) Poor $\beta_{DR} = 0.50$
Low. Questionable safeguards against unanticipated failure modes. Many important design and quality assurance issues are not addressed.	(C) Fair $\beta_{DR} = 0.35$	(D) Poor $\beta_{DR} = 0.50$	--

Table 2-2. Quality Rating of Test Data from an Experimental Investigation (FEMA 2009).

Completeness and Robustness	Confidence in Test Results		
	High	Medium	Low
High. Material, component, connection, assembly, and system behavior well understood and accounted for. All, or nearly all, important testing issues addressed.	(A) Superior $\beta_{TD} = 0.10$	(B) Good $\beta_{TD} = 0.20$	(C) Fair $\beta_{TD} = 0.35$
Medium. Material, component, connection, assembly, and system behavior generally understood and accounted for. Most important testing issues addressed.	(B) Good $\beta_{TD} = 0.20$	(C) Fair $\beta_{TD} = 0.35$	(D) Poor $\beta_{TD} = 0.50$
Low. Material, component, connection, assembly, and system behavior fairly understood and accounted for. Several important testing issues not addressed.	(C) Fair $\beta_{TD} = 0.35$	(D) Poor $\beta_{TD} = 0.50$	--

Table 2-3. Quality Rating of Index Archetype Models (FEMA 2009).

Representation of Collapse Characteristics	Accuracy and Robustness of Models		
	High	Medium	Low
High. Index models capture the full range of the archetype design space and structural behavioral effects that contribute to collapse.	(A) Superior $\beta_{MDL} = 0.10$	(B) Good $\beta_{MDL} = 0.20$	(C) Fair $\beta_{MDL} = 0.35$
Medium. Index models are generally comprehensive and representative of the design space and behavioral effects that contribute to collapse.	(B) Good $\beta_{MDL} = 0.20$	(C) Fair $\beta_{MDL} = 0.35$	(D) Poor $\beta_{MDL} = 0.50$
Low. Significant aspects of the design space and/or collapse behavior are not captured in the index models.	(C) Fair $\beta_{MDL} = 0.35$	(D) Poor $\beta_{MDL} = 0.50$	--

Step 3: Determination of Acceptable Value of Adjusted Collapse Margin Ratio

Once β_{TOT} is calculated and an acceptable collapse probability is determined, the acceptable value of ACMR can be obtained from Table 7-3 in the FEMA P695 document (FEMA 2009). A higher acceptable value of ACMR must be achieved by a seismic-force resisting system with higher total system collapse uncertainty.

Step 4: Evaluation of Response Modification Coefficient (R Factor)

The ACMR calculated in Step 1 is compared with the acceptable ACMR obtained in Step 3 in order to evaluate if the initial R factor used in the design of archetypes fulfills the performance criteria. The FEMA P695 methodology specifies two performance criteria be must satisfied, namely for individual archetype and performance groups, as follows:

1. The probability of collapse for MCE ground motions applied to an individual archetype is restricted to 20%. In other words, the ACMR calculated for each archetype should exceed an acceptable ACMR corresponding to a 20% collapse probability ($ACMR_{20\%}$):

$$ACMR \geq ACMR_{20\%} \quad \textbf{(2.7)}$$

2. The probability of collapse for MCE ground motions applied to a population of archetypes in one performance group is restricted to 10%. In other words, the average of the calculated ACMR within a performance group should exceed an acceptable ACMR corresponding to a 10% collapse probability ($ACMR_{10\%}$):

$$ACMR \geq ACMR_{10\%} \quad \textbf{(2.8)}$$

The initial value of R for which archetypes are designed is deemed acceptable if these two performance criteria are satisfied, which implies that the ACMRs are sufficient to enable an adequately small probability of collapse at the MCE level. If not, further iteration of the evaluation process is needed to reach acceptable seismic performance factors. This can be done by enhancing the design requirements and nonlinear archetype models to lower the total collapse uncertainty, or by redesigning the archetypes with a lower R factor.

Step 5: Estimation of System Overstrength (Ω_o) and Deflection Amplification (C_d) Factors

After having established an adequate R factor following the above steps, the system overstrength (Ω_o) and deflection amplification (C_d) factors can be estimated. The system overstrength, Ω_o, should be taken as the largest average value of the calculated archetype overstrength in all performance groups (see Section 2.3.3). However, Ω_o should not be more than 1.5 times the accepted R factor and be restricted to 3.0 to be consistent with the largest value provided in Table 12.2-1 of ASCE 7-05 for lateral-force resisting system overstrength. The deflection amplification factor, C_d, is as follows:

$$C_d = \frac{R}{B_I} \tag{2.9}$$

where R is the accepted value of the response modification factor (Step 4) and B_I is the constant specified in Table 18.7-1 of ASCE 7-16 (formerly Table 18.6-1 of ASCE 7-05 referenced by FEMA P695) for a given inherent effective damping β_I of the structure and the fundamental period, T. B_I equals 1.0 for critical inherent damping of 5%. Hence, in this case, the C_d factor is equal to the *R* factor. Performance evaluation to quantify seismic performance factors for CC-PSW/CF system is presented in Section 10.

“This Page Intentionally Left Blank”

SECTION 3
DESIGN REQUIREMENTS / CRITERIA FOR COUPLED COMPOSITE PLATE SHEAR WALLS – CONCRETE FILLED (CC-PSW/CF)

The FEMA P695 methodology requires that the design requirements used to proportion and detail the archetypes be well defined. This is important because these design requirements not only also set boundaries in the application of the system, but also impact the results from the non-linear inelastic responses used to confirm the behavior of a proposed system. The development of such design procedures for CC-PSW/CF was therefore an important part of this process.

Chapters 3 and 4 here present the design provisions formulated and used to design the archetypes presented in Chapter 5. They are the outcome of a process that benefited from extensive reviewed and input from members of the Project Advisory Group and the Peer Review Panel assembled for this FEMA P695 project (see Acknowledgment section), as well as from practicing engineers serving in committees of the Building Seismic Safety Council (BSSC).

The information presented in Chapter 3 and 4 reflects the design provisions and corresponding commentary as submitted to BSSC committees as an important step for consideration by ASCE-7. It is foreseeable that slight wordsmithing and clarifications to the text will occur as it proceeds through the review of various committees towards possible adoption in design specifications, but the design provisions that define the essence of the resulting designs' seismic response and behavior are expected to remain unaltered.

3.1 General

3.1.1 Scope

Coupled composite plate shear walls-concrete filled (CC-PSW/CF) shall be designed in accordance with this section. CC-PSW/CF consist of: (i) composite plate shear walls / concrete filled, and (ii) filled composite coupling beams.

The composite plate shear walls of CC-PSW/CF consist of planar, C-shaped, or I-shaped walls, where each wall element consists of two planar steel plates with concrete infill between them. Composite action between the plates and concrete infill is achieved using either tie bars or combination of tie bars and steel headed stud anchors. In each wall element, the two steel plates shall be of equal nominal thickness and connected using tie bars. A flange (or closure) plate shall be used at the open ends of the wall elements. No

additional boundary elements (besides the closure plate) are required to be used with the composite walls. The wall height-to-length, h_w/L_w, ratio of the composite walls shall be greater than or equal to 4.

Coupling beams shall consist of concrete-filled built-up box sections of uniform cross-section along their entire length, and with width equal to or greater than the wall thickness at the connection. The clear length-to-section depth, L/d, ratios of the coupling beams shall be greater than or equal to 3 for all stories of the building, and less than or equal to 5 for at least 90% of the stories of the building.

3.1.2 Notation

The symbols listed below are to be used in addition to or as replacements for those in AISC 360 and AISC 341.

A_c Area of concrete in the composite cross-section, in.^{2} (mm^2)

E_c Modulus of elasticity of concrete

E_s Modulus of elasticity of steel = 29,000 ksi (200,000 MPa)

F_y Specified minimum yield stress, ksi (MPa). As used in the Specification, AISC 360, "yield stress" denotes either the minimum specified yield point (for those steels that have a yield point) or the specified yield strength (for those steels that do not have a yield point).

R_c Factor to account for expected strength of concrete = 1.5

R_y Ratio of the expected yield stress to the specified minimum yield stress, F_y

f_c' Specified compressive strength of concrete, ksi (MPa)

3.1.3 Glossary

The terms listed below are to be used in addition to those in AISC 360 and AISC 341. Some commonly used terms are repeated here for convenience.

Applicable building code. Building code under which the structure is designed. [AISC 360-16]

Available strength. Design strength or allowable strength, as applicable. [AISC 341-16]

Capacity-limited seismic load. The capacity-limited horizontal seismic load effect, E_{cl}, determined in accordance with these Provisions, substituted for E_{mh}, and applied as prescribed by the load combinations in the applicable building code. [AISC 341-16]

Composite. Condition in which steel and concrete elements and members work as a unit in the distribution of internal forces. [AISC 360-16]

Flexural buckling. Buckling mode in which a compression member deflects laterally without twist or change in cross-sectional shape. [AISC 360-16]

Load effect. Forces, stresses and deformations produced in a structural component by the applied loads. [AISC 360-16]

Nominal strength. Strength of a structure or component (without the resistance factor or safety factor applied) to resist load effects, as determined in accordance with the Specification, AISC 360. [AISC 341-16]

Required strength. Forces, stresses and deformations acting on a structural component, determined by either structural analysis, for the LRFD or ASD load combinations, as applicable, or as specified by this Specification or Standard. [AISC 360-16]

Resistance factor, ϕ. Factor that accounts for unavoidable deviations of the nominal strength from the actual strength and for the manner and consequences of failure.[AISC 341-16]

Steel anchor. Headed stud or hot rolled channel welded to a steel member and embodied in concrete of a composite member to transmit shear, tension, or a combination of shear and tension at the interface of the two materials. [AISC 360-16]

Stiffness. Resistance to deformation of a member or structure, measured by the ratio of the applied force (or moment) to the corresponding displacement (or rotation). [AISC 360-16]

3.2 Basis of Design

CC-PSW/CF designed in accordance with these provisions shall provide significant inelastic deformation capacity through flexural plastic hinging in the composite coupling beams, and through flexural yielding at the base of the composite wall elements.

3.3 Analysis

3.3.1 Stiffness.

The effective flexural and axial stiffness of filled composite coupling beams shall be calculated in accordance with AISC 360, Section I1.5. The effective flexural and axial stiffnesses of composite walls shall be calculated using cracked-transformed section properties associated with the neutral axis location corresponding to 60% of the calculated nominal flexural capacity. The effective shear stiffness of the composite coupling beams and walls shall be calculated using the shear stiffness of the composite cross-section.

3.3.2 Required Strength for Coupling Beams

Analyses in conformance with the applicable building code shall be performed to calculate the required strengths for the coupling beams.

3.3.3 Required Strengths for Composite Walls

The required strengths for the composite walls shall be determined using the capacity-limited seismic load effect in accordance with Section *3.3.4*.

3.3.4 Capacity-Limited Seismic Load

The capacity-limited seismic load refers to the capacity-limited horizontal seismic load effect, E_{cl}, which shall be determined from an analysis in which all the coupling beams are assumed to develop plastic hinges at the both ends with expected flexural capacity of $1.2M_{p,exp}$, and the maximum overturning moment is amplified to account for the increase in lateral loading from the formation of the earliest plastic hinges to the formation of plastic hinges in all coupling beams over the full wall height. The earthquake-induced axial force in the walls for determining the required wall strength shall be calculated as the sum of the capacity-limited coupling beam shear forces, using Eq. 3-13, along the height of the structure. The portion of the maximum overturning moment resisted by coupling action shall be calculated as the couple caused by the wall axial forces associated with the coupling beam strengths. The remaining portion of the earthquake-induced overturning moment shall be distributed to the composite walls in accordance with their flexural stiffnesses, which shall be calculated using the section secant stiffness corresponding to 60% of the calculated nominal flexural capacity while accounting for the effects of simultaneous axial force. The required axial and flexural strengths for the composite walls shall be determined directly from this analysis, while the required wall shear strengths determined from this analysis shall be amplified by a factor of four.

3.4 Composite Wall Requirements

The composite wall shall be designed in accordance with the requirements of this section.

3.4.1 Minimum Area of Steel

The steel plates shall comprise at least 1% of the total composite cross-section area.

3.4.2 Steel Plate Slenderness Requirement for Composite Walls

In regions of flexural yielding (at the base), the steel plate slenderness ratio, b/t_p, shall be limited as follows.

$$\frac{b}{t_p} \leq 1.05\sqrt{\frac{E_s}{R_y F_y}} \tag{3.1}$$

where,

b = largest unsupported length of the plate between rows of steel anchors or ties, in. (mm)

t_p = thickness of plate, in. (mm)

3.4.3 Tie Spacing Requirement for Composite Walls

The tie spacing to plate thickness ratio, S/t_p, shall be limited as follows:

$$\frac{S}{t_p} \leq 1.00\sqrt{\frac{E_s}{2\alpha + 1}} \tag{3.2}$$

$$\alpha = 1.7\left[\frac{t_{sc}}{t_p} - 2\right]\left[\frac{t_p}{d_{tie}}\right]^4 \tag{3.3}$$

where,

S = largest clear spacing of the ties

t_p = thickness of the steel plate

t_{sc} = thickness of the composite wall

d_{tie} = effective diameter of the tie

3.4.4 Tie-to-Plate Connection

The tie bar to steel plate connection shall develop the full yield strength of the tie bar.

3.5 Composite Coupling Beam Requirements

The composite coupling beam shall be designed in accordance with the requirements of this section.

3.5.1 Minimum Area of Steel

The cross-sectional area of the steel section shall comprise at least 1% of the total composite cross-section of the coupling beam.

3.5.2 Slenderness Requirement for Coupling Beams

The slenderness ratios of the flanges and webs of the filled composite coupling beam, b_c/t_f and h_c/t_w, shall be limited as follows:

$$\frac{b_c}{t_f} \leq 2.37\sqrt{\frac{E_s}{R_y F_y}} \tag{3.4}$$

$$\frac{h_c}{t_w} \leq 2.66\sqrt{\frac{E_s}{R_y F_y}} \tag{3.5}$$

where,

b_c = clear unsupported width of the coupling beam flange plate

h_c = clear unsupported width of the coupling beam web plate

t_f = thickness of the coupling beam flange plate

t_w = thickness of the coupling beam web plates

3.5.3 Flexure-Critical Coupling Beams

The composite coupling beams shall be proportioned to be flexure critical with design shear strength, ϕV_n, as follows:

$$\phi V_n \geq \frac{2.4 M_{p,exp}}{L_{cb}} \tag{3.6}$$

where,

ϕV_n = design shear strength of composite coupling beam calculated in accordance with Section *3.7.2*

$M_{p,exp}$ = expected flexural capacity of composite coupling beam calculated in accordance with Section *3.7.1* while using the expected yield strength, $R_y F_y$, for steel and the expected compressive strength $R_c f'_c$ for concrete

L_{cb} = clear span length of the coupling beam

3.6 Composite Wall Strength

The nominal strengths of composite walls shall be calculated in accordance with this section. The available strengths shall be calculated using resistance factor (ϕ) equal to 0.90.

3.6.1 Tensile Strength

The nominal tensile strength, P_n, shall be determined for the limit state of yielding as:

$$P_n = A_s F_y \tag{3.7}$$

where, A_s = area of steel plates in the wall cross-section

3.6.2 Compressive Strength

The nominal compressive strength shall be determined for the limit state of flexural buckling in accordance with the AISC 360, Section I2.1b. The value of flexural stiffness from Section *3.3.1* shall be used along with the section axial load capacity, P_{no}, determined as follows:

$$P_{no} = A_s F_y + 0.85 f_c' A_c \tag{3.8}$$

3.6.3 Flexural Strength

The nominal flexural strength shall be determined as the moment corresponding to plastic stress distribution over the composite cross-section. Steel components shall be assumed to have reached a yield stress of F_y in either tension or compression, and concrete components in compression due to axial force and/or flexure shall be assumed to have reached a stress of $0.85f_c'$, where f_c' is the specified compressive strength of concrete, ksi.

3.6.4 Combined Axial Force and Flexure.

The nominal strength of composite walls subjected to combined axial force and flexure shall account for their interaction in accordance with the plastic stress distribution method of AISC 360, Section I1.2a or the effective stress-strain method of AISC 360, Section I1.2d.

3.6.5 Shear Strength

The nominal in-plane shear strength, V_n, shall be determined as follows:

$$V_n = \frac{K_s + K_{sc}}{\sqrt{3{K_s}^2 + {K_{sc}}^2}} \times A_{sw} \tag{3.9}$$

where,

$$K_s = G_s A_{sw} \tag{3.10}$$

$$K_{sc} = \frac{0.7(E_c A_c)(E_s A_{sw})}{4E_s A_{sw} + E_c A_c} \quad \textbf{(3.11)}$$

where,
A_{sw} = Area of the steel plates in the direction of in-plane shear

G = Shear modulus of steel, ksi (MPa)

3.7 Composite Coupling Beam Strength

The nominal strengths of composite coupling beams shall be calculated in accordance with this section. The available strengths shall be calculated using resistance factor (ϕ) equal to 0.90.

3.7.1 Flexural Strength

The nominal flexural strength of coupling beams shall be determined as the moment corresponding to plastic stress distribution over the composite cross-section. Steel components shall be assumed to have reached a yield stress of F_y in either tension or compression, and concrete components in compression due to axial force and/or flexure shall be assumed to have reached a stress of $0.85f_c'$.

3.7.2 Shear Strength

The nominal shear strength, V_n, of coupling beams shall account for the contributions of the steel webs and concrete infill and be determined as follows:

$$V_n = 0.6A_w F_y + 0.06A_c\sqrt{f_c'} \quad \textbf{(3.12)}$$

where,

A_w = Area of coupling beam steel web plates

3.8 Coupling Beam-to-Wall Connections

The coupling beam-to-wall connections shall be design in accordance with the requirements of this section.

3.8.1 Required Flexural Strength

The required flexural strength, M_u, for the coupling beam-to-wall connection shall be 120% of the expected flexural capacity of the coupling beam ($M_{p,exp}$).

3.8.2 Required Shear Strength

The required shear strength, V_u, for the coupling beam-to-wall connection shall be determined using capacity-limited seismic load effect as follows:

$$V_u = 2(1.2M_{p,exp})/L_{cb} \quad \textbf{(3.13)}$$

where,

$M_{p,exp}$ = expected flexural capacity of composite coupling beam calculated using expected yield strength, R_yF_y, for steel and the expected compressive strength $R_cf'_c$ for concrete

L_{cb} = clear span length of the coupling beam

3.8.3 Rotation Capacity

The coupling beam-to-wall connection shall be detailed to allow the coupling beam to develop a plastic hinge rotation capacity of 0.030 rad before flexural strength decreases to 80% of the flexural plastic strength of the beam. Connection details that have been previously demonstrated to have adequate plastic rotation capacity shall be approved for use. The available plastic rotation capacity of coupling beam using other connection details shall be verified through testing, advanced analysis, or combination thereof.

3.9 Composite Wall-to-Foundation Connections

Where the composite walls are connected directly to the foundation at the point of maximum moment in the walls, the composite wall-to-foundation connections shall be designed in accordance with the requirements of this section.

3.9.1 Required Strengths

The required strengths for the composite wall-to-foundation connections shall be determined using the capacity-limited seismic load effect. The coupling beams shall be assumed to have developed plastic hinges at both ends with the expected flexural capacity of $1.2M_{p,exp}$. The composite walls shall also be assumed to have developed plastic hinges at the base with expected flexural capacity of $1.2M_{p,exp}$, while accounting for the effects of simultaneous axial force. The required shear strength for the composite wall-to-foundation connections shall be equal to the required shear strength for the composite walls calculated in accordance with Section *3.3.4.*

3.10 Protected Zones

The requirements for protected zones shall be in accordance with AISC 341 Section D1.3 and Section I2.1. The following regions shall be designated as protected zones:

(a) The regions at ends of the coupling beams subject to inelastic straining.

(b) The regions at the base of the composite walls subject to inelastic straining

3.11 Demand Critical Welds in Connections

The requirements for demand critical welds shall be in accordance with AISC 341 Section A3.4b and Section I2.3. Unless demonstrated through testing, the welds connecting the coupling beam flanges and web plates to composite wall steel plates shall be demand critical and shall satisfy the applicable requirements.

Where located within the protected zones identified in Section 3.10, the following welds shall be demand critical and shall satisfy the applicable requirements:

(a) Welds connecting the composite wall flange (closure) plates to the web plates

(b) Welds connecting the coupling beam web plates to flange plates in built-up box sections

(c) Welds in the composite wall steel plate splices

(d) Welds at composite wall steel plate-to-base plate connections

SECTION 4 COMMENTARY FOR DESIGN REQUIREMENTS / CRITERIA FOR COUPLED COMPOSITE PLATE SHEAR WALLS – CONCRETE FILLED (CC-PSW/CF)

As mentioned in Section 3, Section 4 presents the commentary to the design provisions formulated and used to design the archetypes presented in Section 5. The material presented in Section 4 was generated at the end of the project, to document and summarize the findings from this FEMA P695 study in a commentary format suitable for consideration and possible adoption by code and specifications committees (i.e., documenting the rational for each clause indicated in Section 3, and including the list of references cited in this commentary). As such, it brings forth information and findings presented elsewhere in this report, which makes the presentation here somewhat "unorthodox" in relation to how information is sequentially presented in a technical report. However, since it was necessary to present above the requirements and provisions (Section 3) that drove the design of the archetypes (Section 5), it was deemed appropriate to insert this commentary material here rather than in an Appendix or later in the report.

4.1 Scope

A coupled composite plate shear walls - concrete-filled (CC-PSW/CF) is a coupled-wall system comprised of composite walls and composite coupling beams, for which both walls and beams consists of a concrete core sandwiched between two steel plates that serve as the primary reinforcement, replacing conventional rebars. These sandwich panels are depicted in Figure 4-1. Tie bars connect the two steel plates together and provide stability during transportation and construction activities. After casting, the tie bars become embedded in the concrete infill and provide composite action between the steel and concrete. The coupling beams are built-up steel box sections with concrete infill. Similar to the wall panels, the built-up steel section provides primary reinforcement to the coupling beam. The empty steel modules, including both the walls and coupling beam components, are typically fabricated in the shop, transported to the site, erected, and filled with concrete. The composite walls can be planar, C-shaped, or I-shaped, following the typical geometric configurations of conventional concrete core walls.

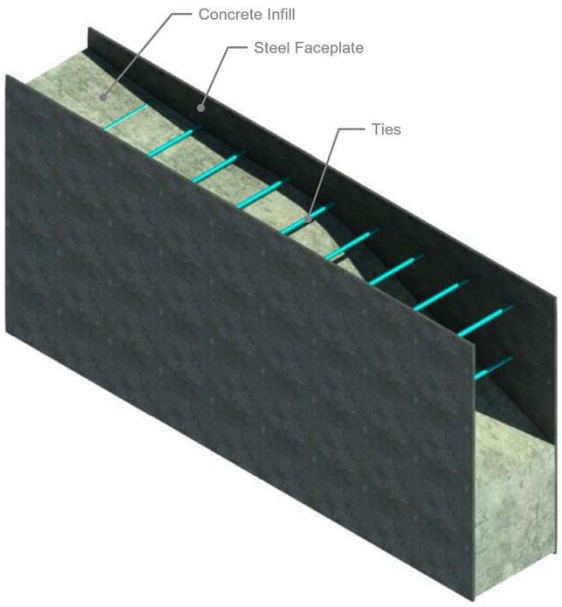

Figure 4-1. Composite Plate Shear Wall Section / Concrete-Filled

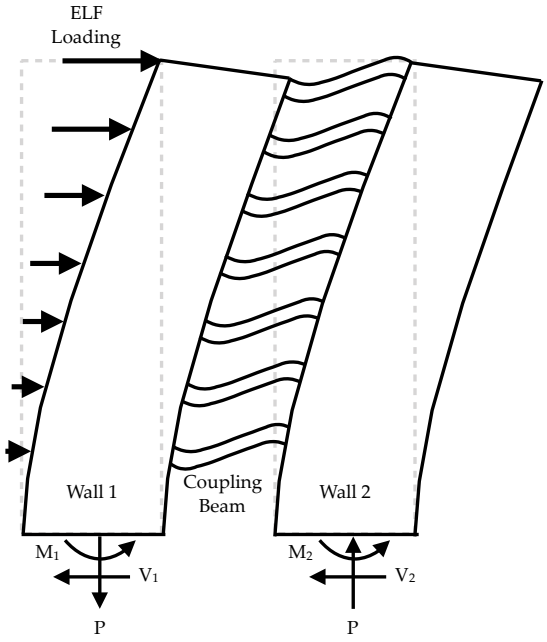

Figure 4-2. Deformed shape of Coupled Composite Plate Shear Wall under Lateral Loads

The requirement for composite walls to have height-to-length (h_w/L_w) ratio greater than or equal to 4.0 is specified to ensure that the walls are flexure critical, i.e., flexural yielding and failure governs behavior rather than shear failure. Calculations can also be performed to show that the wall is flexure-critical, i.e., plastic hinges (with flexural capacity equal to $1.2M_{p,exp}$) form at the base of the walls before shear failure occurs. The shortest archetype structure that was evaluated using the FEMA P695 approach for this system was three stories with two 45 feet tall composite walls of 10-foot length, corresponding to a height-to-length ratio equal to 4.5 for each wall that constituted the coupled wall.

The requirement for coupling beams to have length-to-depth ratios greater than or equal to 3 and less than or equal to 5 is based on: (i) the range of parameters included in the FEMA P695 studies conducted in order to establish the seismic factor (R) for the system, and (ii) the fact that coupling beams with length-to-depth ratios less than 3 tend to be shear critical, which is not recommended. Section 6.5.3 explicitly requires coupling beams to be flexure critical, i.e., flexural yielding and failure governs their behavior rather than shear failure.

4.2 Basis of Design

The CC-PSW/CF system uses coupled walls to resist lateral loads as shown in Figure 4-2. This system is expected to undergo significant inelastic deformation in large (design-basis and maximum considered)

seismic events. The inelastic deformation has two sources: (1) flexural plastic hinges at the ends of coupling beams, and (2) flexural yielding at the base of walls. The preferred inelastic (failure) mechanism consists of forming flexural plastic hinges at both ends of the coupling beams and at the base of the composite walls. The design implements a strong wall-weak coupling beam approach that must be followed for appropriately sizing the composite members. This design approach helps achieve development of extensive plastic hinging in most of the coupling beams before significant yielding of the walls.

4.3 Analysis

The design philosophy expressed in Section 6.3 leads to structures with the characteristic pushover behavior depicted in Figure 4-3. The initial branch represents the elastic behavior of the structure, and the slope of this branch represents the effective structural stiffness which is approximated by elastic models such as those used with the Equivalent Lateral Force procedure (ELF) defined by ASCE 7. On the base shear-roof displacement curve, Point A represents the lateral load level corresponding to the ELF distribution. The coupling beams are designed to reach their flexural capacity at this demand. As the lateral load (and base shear force) increases, the coupling beams along the height of the structure undergo flexural plastic hinging at both ends. The response reaches the next milestone, Point B, where all of the coupling beams have developed flexural hinges. The composite walls are designed to have a flexural capacity adequate to resist this demand level. The next milestone on the response, Point C, corresponds to the overall inelastic mechanism with flexural plastic hinging in all the coupling beams and the base of the composite walls. A final milestone, point D, represents fracture failure of the composite walls. The overstrength factor for this system, defined as the ratio of ultimate load capacity to capacity at ELF level loads, is approximately the ratio of base shear force at Point C to Point A.

The Seismic Response Modification Factor (R) is given in ASCE 7-16 for non-coupled composite plate shear walls to be equal to 6.5. A FEMA P695 (Quantification of Building Seismic Performance Factors) study was conducted to evaluate an appropriate R-Factor for CC-PSW/CF systems. This FEMA P695 study demonstrated that coupled composite plate shear walls considered here can be designed with a greater R-Factor of 8. This increase in the value of R for coupled walls is due to the spread of plastic hinging and inelastic deformations (energy dissipation) in the coupling beams along the height of the structure. This lateral load behavior is illustrated in Figure 4-4 and Figure 4-5 using finite element analysis for an 8-story archetype structure having coupling beams span-to-depth ratio of 5. The nonlinear static pushover behavior predicted by the finite element model (Figure 4-4) follows the expected behavior presented in Figure 4-3.

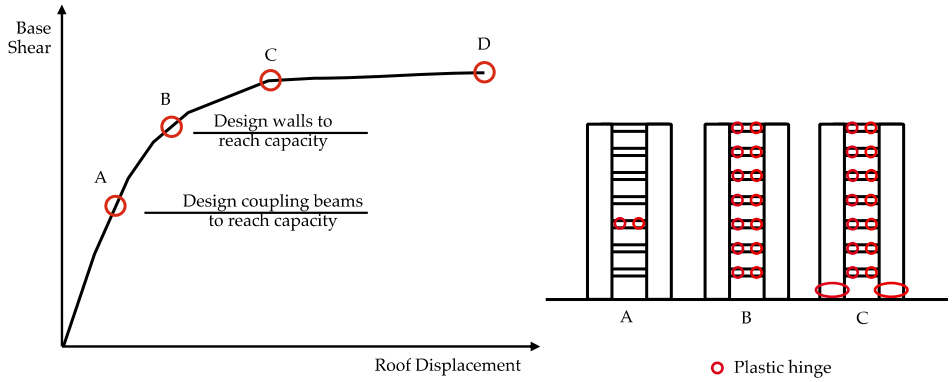

Figure 4-3. Characteristic Pushover (Base Shear-Roof Displacement) Behavior (Broberg et al. 2019)

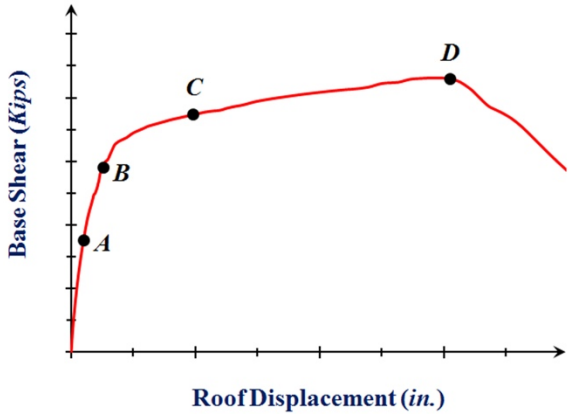

Figure 4-4. Pushover Behavior from 3D FEM Analysis (Broberg et al. 2019)

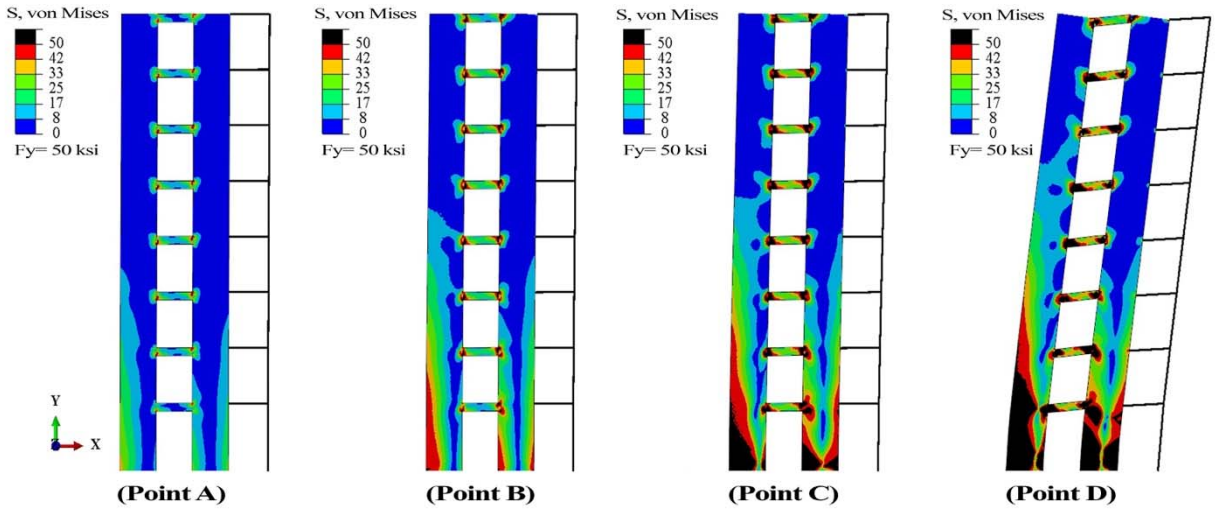

Figure 4-5. Extent of Steel Yielding for Different Points on Pushover Curve (From 3D FEM) (Bro berg et al. 2019)

In the FEMA P695 study, archetype structures having 3, 8, 12, 18, and 22 stories and coupling beam span-to-depth ratios of 3, 4, and 5 were designed. The archetypes were designed using an R value of 8 and C_d

value of 5.5. The 8 and 12-story archetype structures used planar composite walls, while the 18 and 22 story archetype structures used C-shaped walls. These archetype structures were doubly symmetric in plan, and the wall thickness was uniform along the height of the structure. For the 18 and 22 story archetype structures, the thickness of the steel plates for the composite walls and the coupling beams was reduced in the top half of the structure. The 22 story archetype had an overall height of 311 ft. These structures were designed to meet the composite member and system requirements outlined in Section 6. The coupling ratio for the archetype structures was about 50 - 80%, where the taller buildings had higher coupling ratios. In this context, coupling ratio is defined at point B on the characteristic pushover curve as the proportion of the total overturning moment resisted by coupling action.

Seismic demands followed standards set in ASCE 7 and the FEMA P695 procedure. The numerical models for the structures accounted for the various complexities of flexural behavior of the coupling beams and composite walls including the effects of concrete cracking, steel yielding, local buckling, concrete crushing, and steel inelastic behavior up to fracture due to cumulative plastic strains and low cycle fatigue. The numerical models were benchmarked using experimental data available in the literature.

Results from the FEMA P695 analyses indicated that all archetypes reached collapse at drifts greater than 5%, but all collapse margin ratios established in this study were conservatively calculated based on results obtained at 5% drift (i.e., at less than actual collapse points). Consequently, collector beams must be designed to be able to accommodate up to 5% drift – note that in wall systems, at a given roof drift, the rotation in collector beams varies along the height of the walls. Results of the FEMA P695 studies indicated that collapse margin ratios increased for the taller buildings, which is consistent with the fact that code-specified drift limits governed the design of the 18 and 22 stories archetypes.

4.3.1 Elastic Analysis

An elastic model of the structure is used to conduct structural analysis for design by the Equivalent Lateral Force procedure (ELF) defined by ASCE 7. The results of this analysis are used to determine the design demands for the coupling beams and the maximum elastic story drift ratio, which is amplified by C_d to estimate the inelastic story drift ratio for design. This analysis can be performed in accordance AISC Specification Section I1.5, which is based on the direct analysis method, and includes recommendations for the flexural (EI_{eff}) and axial stiffness of filled composite members (i.e., composite coupling beams). The flexural (EI_{eff}) and axial stiffnesses (EA_{eff}) of composite walls can be calculated using cracked-transformed section properties corresponding to 60% of the calculated nominal flexural capacity of the wall (without

accounting for axial force effects). It is important to use the reduced (cracked) axial stiffness of the walls as they have an influence on the structure lateral stiffness (and story drift) through the coupling frame action. The shear stiffness of the composite walls and coupling beams does not have a significant influence on the structure stiffness as flexure behavior dominates. As such, the uncracked composite shear stiffness can be used for both the coupling beams and composite walls.

4.3.2 Capacity-Limited Analysis

The design demands for the composite walls are estimated using a capacity-limited seismic load effect, E_{cl}, where all the coupling beams are assumed to develop plastic hinges at both ends with flexural capacity equal to $1.2M_{p,exp}$, i.e., at point *B* in Figure 4-3. The total overturning moment at B can be estimated using the total overturning moment at point A in Figure 4-3 amplified by the factor given below.

$$\gamma_1 = \frac{\sum_n 1.2M_{p,exp}^{cb}}{\sum_n M_u^{cb}} \quad \textbf{(4.1)}$$

where,

$\sum_n 1.2M_{p,exp}^{cb}$= sum of the expected flexural capacities of coupling beams along structure height

$\sum_n M_u^{cb}$ = sum of the flexural design demands for the coupling beams along structure height

n = number of coupling beams along structure height

The capacity-limited shear force in the coupling beams can be summed over the height of the structure to estimate the axial forces acting in the walls as shown below.

$$P_w = \sum_n \frac{2.4M_{p,exp}^{cb}}{L_{cb}} \quad \textbf{(4.2)}$$

The portion of the total overturning moment resisted by coupling action can be estimated by the equal and opposite axial forces at the base of the walls (P_w) multiplied by the distance between them. The remaining portion of the total overturning moment can be distributed to the individual walls based on their effective flexural stiffness (while accounting for the effects of tensile or compressive axial force). The shear force in the walls obtained from this analysis is amplified by a factor of four to conservatively account for: (i) effects of higher modes, and (ii) the overstrength in the walls resulting from the difference between their expected flexural capacity (at point C in Figure 4-3) and design demand (point B). For reinforced concrete walls, this amplification factor is about 2 - 3 (Wallace et al. 2019). A conservative value of 4 was used for composite walls in the absence of better information, and in recognition of their inherent (significant) shear strength.

The shear strength of these composite walls is very high due to the significant contribution of the steel plates and composite action.

4.4 Composite Wall Requirements

4.4.1 Minimum Area of Steel

The minimum area of steel requirement is based on the AISC Specification Section I2 requirements for composite columns.

4.4.2 Slenderness Requirement

The steel plates of composite walls are required to be nonslender, i.e., yielding in compression must occur before local buckling. When subjected to compressive stresses, the plate undergoes local buckling between the steel ties or anchors as shown below. The horizontal lines joining the steel anchors (or ties) act as fold lines, and local buckling occurs between them. The buckling mode indicates fixed-ends along the vertical lines with steel anchors, and partially fixity along the vertical lines between steel anchors.

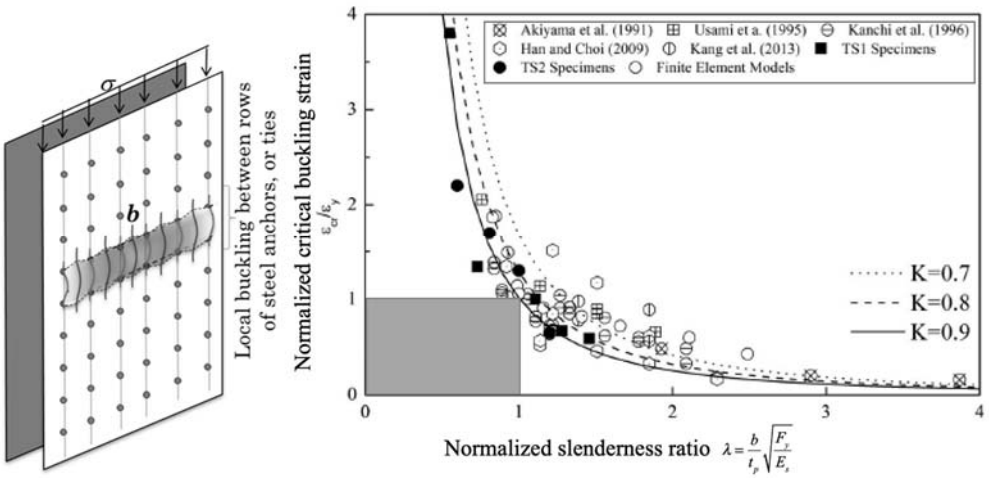

Figure 4-6. Local buckling of steel plates, and plot of normalized critical buckling strain vs. slenderness ratio (Zhang et al. 2014, 2019)

Experimental studies have been conducted to evaluate the effects of plate slenderness ratio, s/t_p, defined as the steel anchor spacing, s, divided by the plate thickness, t_p, on local buckling of plates. Zhang et al. (2014, 2019) have summarized these experimental studies, and conducted additional numerical analyses to confirm and expand the experimental database. Figure 4-6 from Zhang et al. (2014, 2019) shows the relationship

between the normalized critical buckling strain (buckling strain/steel yield strain, $\varepsilon_{cr}/\varepsilon_y$) and the normalized plate slenderness ratio ($s/t_p \times F_y/E$). As shown, ε_{cr} is reasonably consistent with Euler's curve with a partially fixed ($K = 0.8$) end condition. Also, no data point falls in the shaded area, implying yielding occurs before local buckling for a normalized plate slenderness ratio less than 1.0. Since ties may also act as anchors, the equation considers the largest unsupported length between rows of steel anchors or ties, b.

4.4.3 Tie Spacing Requirement for Composite Walls

The tie spacing requirement is based on the flexibility and shear buckling of empty steel modules before concrete placement, discussed in detail in Shafaei et al. (2018). The flexibility of the empty modules for transportation, shipping and handling activities is dominated by their effective shear stiffness GA_{eff}, which can be estimated accurately using numerical models as shown in Shafaei et al. or calculated conservatively (for a unit cell of the module) using Equation 4.3. In this equation, I_p and I_t represent the moments of inertia of the steel faceplates and tie bar. S and d_{tie} represent the tie spacing and bar diameter. Equation 4.4 defines α, which is the ratio of the flexural stiffness of the steel pate to the flexural stiffness of the tie bar, and simplifies to the form of Equation 4.3.

$$GA_{eff} = 24\left(\frac{EI_p}{S^2}\right)\frac{1}{(2\alpha+1)} \tag{4.3}$$

$$\alpha = \frac{\left(\frac{E_s I_p}{S}\right)}{\left(\frac{E_s I_t}{t_{sc}-2t_p}\right)} = \frac{\left(\frac{St_p^3}{12S}\right)}{\left(\frac{\pi d_{tie}^4}{12(t_{sc}-2t_p)}\right)} = 1.7\left[\frac{t_{sc}}{t_p}-2\right]\left[\frac{t_p}{d_{tie}}\right]^4 \tag{4.4}$$

After assembly, and before concrete casting, the empty modules provide structural support for construction activities, loads, and the steel framework connected to it. The buckling of the empty module subjected to compression loading is also governed by its effective shear stiffness GA_{eff}, and can be estimated conservatively using Equation 4.5. The requirements of Equations 3.2 and 3.3 will result in critical buckling stress greater than or equal to 1000 psi, which is equivalent to a distributed loading of 12,000 lbs per linear foot for walls with two 0.5 in. thick steel plates. The stresses and deflections induced by concrete casting hydrostatic pressure can also be estimated as shown in Shafaei et al. (2018). Research by Bhardwaj et al. (2018) indicates that modules that meet the plate slenderness requirement of Section 6.4.2 can be typically cast with concrete pour heights of up to 30 ft. without significant influence of induced deflections and stresses on the compressive strength and buckling of the steel plates.

$$\sigma_{cr} = \frac{E}{\left(\frac{S}{t_p}\right)^2} \times \frac{1}{(2\alpha + 1)} \quad \textbf{(4.5)}$$

4.4.4 Tie-to-Plate Connection

This requirement develops the yield strength of the tie bars, and enables yielding before failure of the tie-to-plate connection. Samples of tie-to-plate connection details are shown below in Figure 4-7 for round tie bars.

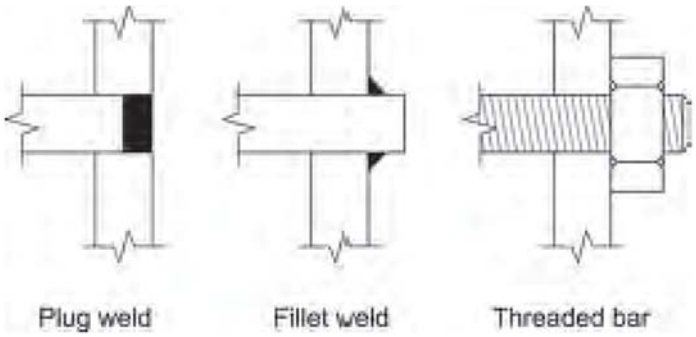

Figure 4-7. Tie bar-to-plate connection detail samples

4.5 Composite Coupling Beam Requirements

4.5.1 Minimum Area of Steel

The minimum area of steel requirement is based on the AISC Specification Section I2 requirements for composite columns.

4.5.2 Slenderness Requirement for Coupling Beams

The slenderness requirements are based on compact section requirements in the AISC Specification Section I1.4 for filled composite members. The web slenderness ratio requirement is based on developing the shear yield strength of the web plates before shear buckling as per AISC Specification Section G4. Figure 4-8 shows a schematic of the coupling beam cross-section along with the clear widths of the flange and web plates.

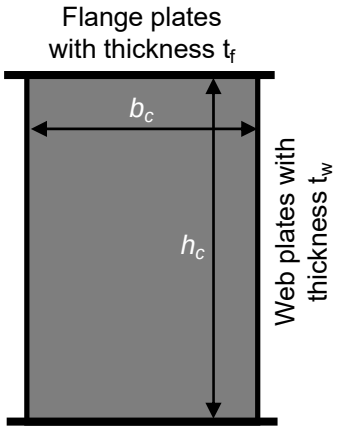

Figure 4-8. Coupling beam cross-section

4.5.3 Flexure Critical Coupling Beams

This requirement is based on achieving flexure critical behavior in composite beams. The requirement increases the capacity-limited shear force capacity ($2\ M_{p,exp}/L_{cb}$) by a factor of 1.2 to account for the effects of steel inelastic hardening in tension, concrete confinement, the biaxial (tensile) stress effect in the steel tension flange.

4.6 Composite Wall Strength

The requirements for axial tensile strength, compressive strength, flexural strength, and combined axial force and flexure are based on the recommendations for filled composite members in the AISC Specification Chapter I. The unsupported length for the flexural buckling of composite walls is typically equal to the story height. The requirements for flexural strength have been verified using experimental data by Kurt et al. (2016) and Alzeni and Bruneau (2017) and for combined axial force and flexure by Shafaei et al. (2019) and Bruneau et al. (2019) for C-shaped walls.

4.6.1 In-Plane Shear Strength

The in-plane shear behavior of composite walls is governed by the plane stress behavior of the plates and the orthotropic elastic behavior of concrete cracked in principal tension. Varma et al. (2014) and Seo et al. (2016) discuss the fundamental mechanics based model (MBM) for in-plane shear behavior of composite walls. The in-plane shear behavior can be estimated as the tri-linear shear force-strain curve shown in Figure

4-9. The first part of the curve is before the concrete cracks. The second part is after the concrete cracking but before the plate yielding. The third part of the curve corresponds to the onset of plate Von Mises yielding. The shear force corresponding to this onset of von Mises yielding is given by Equation 3.9. The corresponding principal compressive stress in the cracked (orthotropic) concrete is less than $0.7f'c$ for typical composite walls with reinforcement ratios ($2t_p/t_{sc}$) less than or equal to 10%. For walls with very high reinforcement ratios (i.e., walls with very thick steel plates compared to overall thickness), the concrete principal compressive stress can be the limiting failure criterion (Seo et al. 2016, Varma et al. 2014)

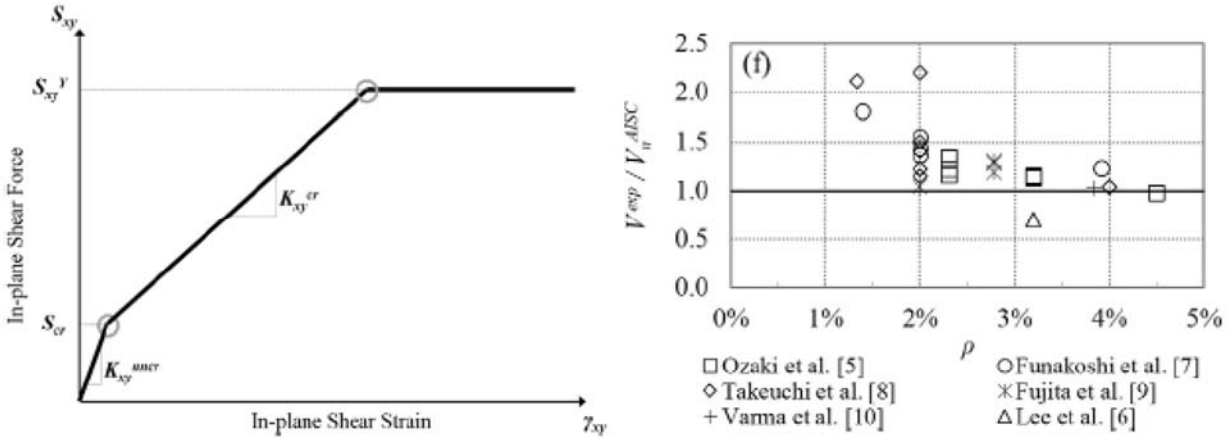

Figure 4-9. In-plane shear force-stain response of composite walls, and comparison of experimental results with shear strength calculated using Equation 3.9 **(Seo et al. 2016)**

4.6.2 Nominal vs. Expected Flexural Capacity

The flexural capacity of composite walls and coupling beams can be calculated using the plastic stress distribution method or the effective stress-strain method in AISC Specification I1.2. The nominal flexural capacity (with or without concurrent axial force) can be calculated using nominal steel (F_y) and concrete (f'_c) material strengths. The expected flexural capacity can be calculated using expected steel (R_yF_y) and concrete ($R_cf'_c$) material strengths. The expected flexural capacity is amplified by a factor of 1.2 to account for the effects of steel inelastic hardening in tension, concrete confinement, and the biaxial (tensile) stress effect in the steel tension flange.

4.7 Composite Coupling Beam Strength

The requirements for flexural strength are based on the recommendations for filled composite members in the AISC Specification Chapter I. The requirements for shear strength are based on recommendations for

filled composite members in AISC Specification Chapter I as modified to reflect the latest research (Lehman et al. 2018, Bruneau and Kenarangi 2018, Bruneau and Varma, 2019).

4.8 Coupling Beam-to-Wall Connections

The coupling beam-to-wall connections are designed to develop and transfer the expected flexural capacity (and corresponding capacity-limited shear force) of the associated coupling beams. Figure 4-10 shows the envelope of the inelastic moment-rotation response assumed in the FEMA P695 (analytical) studies for the flexural (plastic) hinges in the coupling beams. As shown, the plastic rotation before degradation of flexural capacity due to fracture failure was assumed to be equal to 0.025 rad.

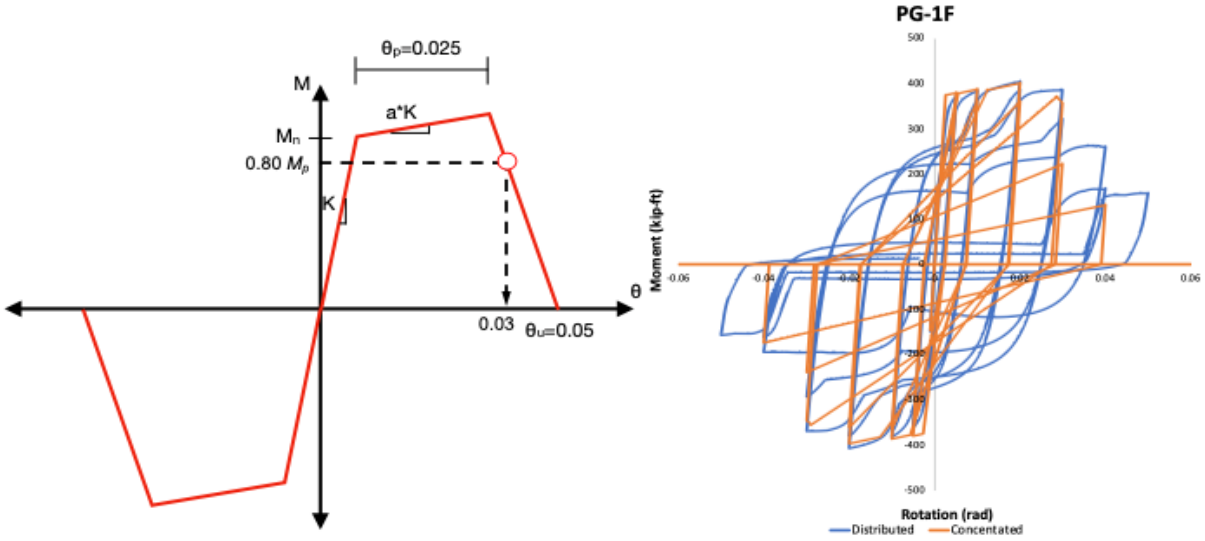

Figure 4-10. Envelop of cyclic moment-rotation response and hysteretic behavior of plastic hinges in composite coupling beams (Broberg et al. 2019)

Coupling beam-to-wall connections have been tested in the past, for example, Nie et al. (2014), and additional testing of coupling beam-to-wall connections are currently ongoing. Some details that may be demonstrated to be acceptable by testing include those shown in Figure 4-11 and Figure 4-12. If the wall flange plate is interrupted, design must account for the local discontinuity in the contribution of the flange plate to wall flexural and axial strength.

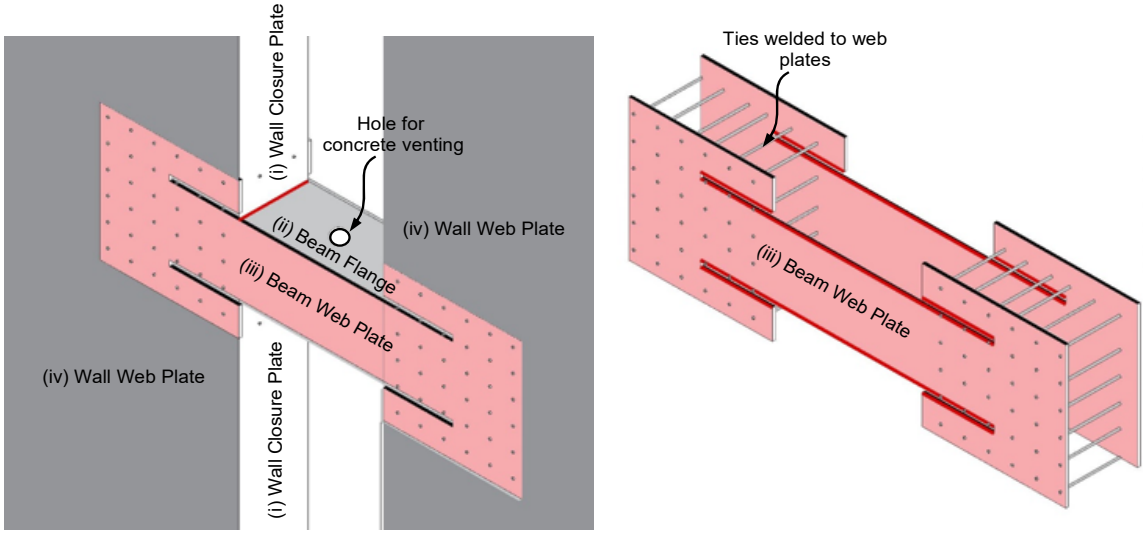

(i) Wall closure plate interrupted and welded to beam flange plate
(ii) Beam flange plate penetrates into wall, and welded to wall web plate
(iii) Beam web plate continuous with wall web plate
(iv) Wall web plate welded to continuous beam web plate away from connection

Figure 4-11. Coupling beam connection with continuous web plate and interrupted wall closure plate

Figure 4-11 shows a connection where: (i) the web plates are continuous between the coupling beam and the composite walls, (ii) the coupling beam flange plates are continued into the wall, and welded to the wall web plates to develop their expected tensile strength, and (iii) the wall closure plate is interrupted at the coupling beam.

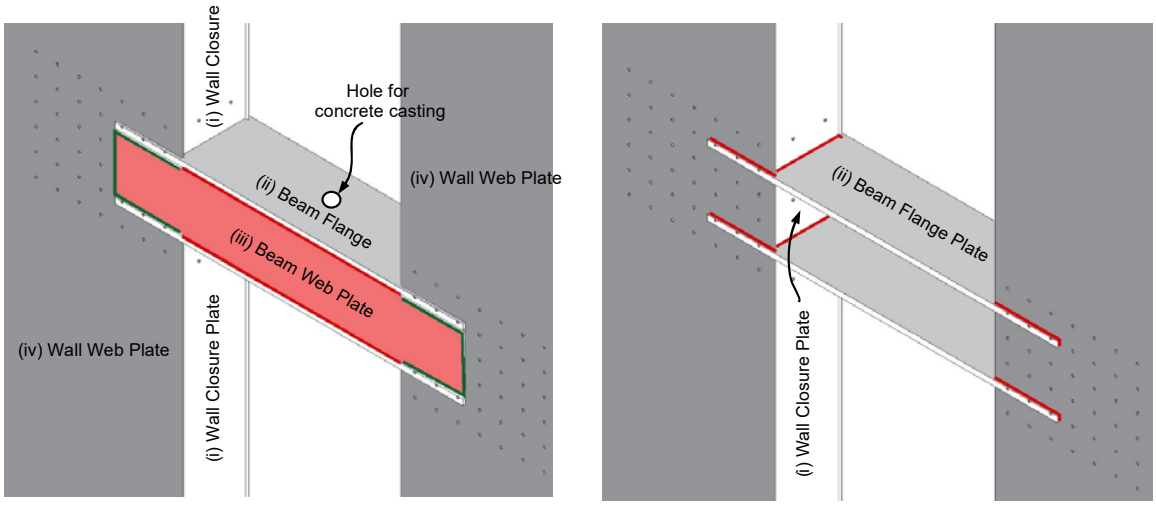

(i) Uninterrupted wall closure plate welded to beam flange plates
(ii) Beam flange plate penetrates into wall, and welded to wall web plate
(iii) Beam web plate lapped and welded to wall web plate from outside

Figure 4-12. Coupling beam connection with lapped web plate and continuous wall closure plate

Figure 4-12 shows a connection where: (i) coupling beam web plates are lapped and welded to the composite wall web plates, (ii) the coupling beam flange plates are continued into the wall, and welded to the wall web plates to develop their expected tensile strength, and (iii) the wall closure plate is not interrupted at the coupling beam.

4.9 Composite Wall-to-Foundation Connections

For structures with sub-grade basement stories, the maximum shear force and overturning moment in the composite walls at the grade level can be transferred gradually through the basement stories. For structures that are connected to the concrete basemat / foundation at the location of maximum shear force and overturning moment, the wall-to-basemat connections have to be designed for: (i) the expected flexural capacity of the composite walls (accounting for effects of axial force), (ii) the expected axial forces associated with capacity-limited shear forces in the coupling beams, and (iii) and the amplified shear force demand (amplification factor of 4) used for the design of the composite walls. Some connection details that have been used in the past include details with welded base plates and rebar couplers as shown in Figure 4-13. The base plate can be continuous or discontinuous across the wall thickness depending on the needs of the project and wall thickness. Another potential connection with the wall embedded in the concrete foundation is shown in Figure 4-14.

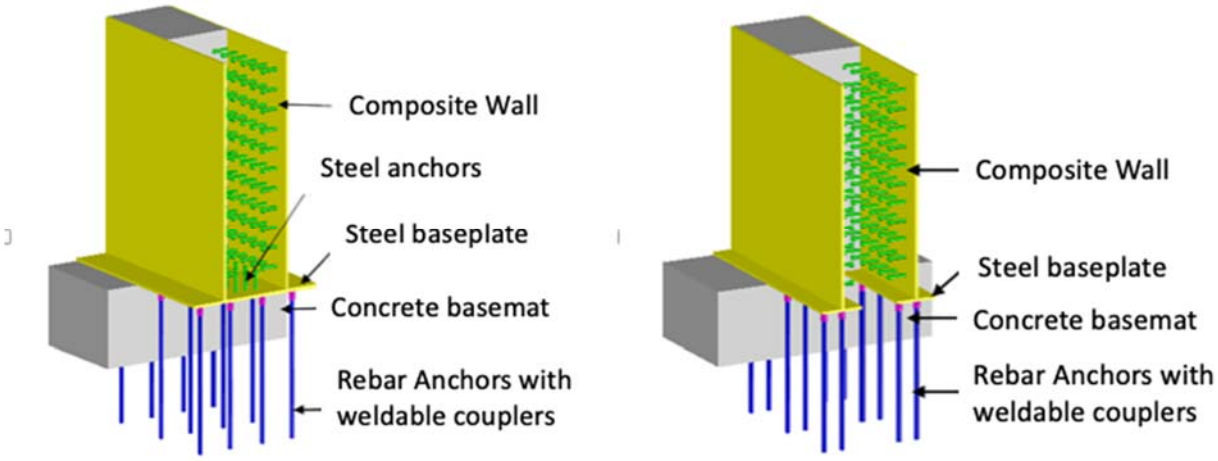

Figure 4-13. Composite wall-to-basemat connections with welded base plate and rebar couplers (concrete only shown partially to highlight rebars and couplers) (Bhardwaj and Varma, 2016)

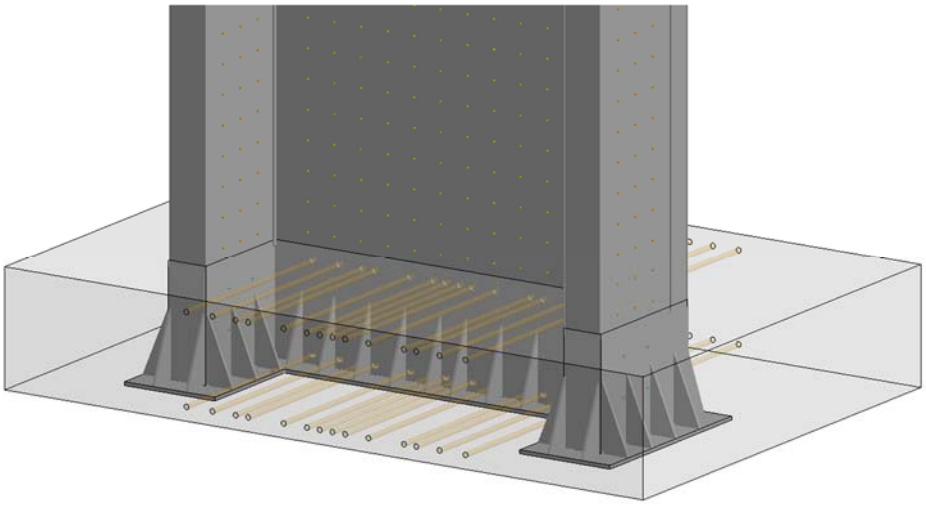

Figure 4-14. Composite wall-to-basemat connections with wall embedded into concrete foundation (Bruneau et al., 2019)

4.10 Protected Zones

Protected zones are defined in AISC 341 as regions of members or connections of members undergoing large inelastic strains or plastic hinging to provide significant inelastic deformation capacity and energy dissipation during design-basis or higher magnitude earthquakes. FEMA / SAC testing has demonstrated the sensitivity of these regions to discontinuities caused by fabrication or erection activities or from other attachments. For this reason, operations specified in AISC 341 Section I2.1 are prohibited in the protected zones.

For the CC-PSW/CF system, the protected zones are designated as the regions at the ends of coupling beams that will undergo significant inelastic straining and plastic hinging, and portions of the adjacent wall (if any) undergoing yielding at the connection. The typical length of the plastic hinge region will extend from the face of the composite wall to a distance equal to coupling beam depth. However, the extent of the plastic hinge (and the protected zone) can depend on the cross-section geometry, flange and web plate thicknesses, and the length-to-depth ratio of the coupling beam. The extent of the protected zone can be determined from analysis.

Additionally, the regions of the composite walls undergoing significant inelastic straining and plastic hinging are also designated as protected zone. The extent of the plastic hinge region undergoing significant inelastic strains (and the protected zone) can depend on wall cross-section geometry, web plate and flange

(closure) plate thickness and lengths, and the height-to-length ratios of the walls. The extent of the protected zone can be determined from analysis.

4.11 Demand Critical Welds

Demand critical welds are defined in AISC 341, and the requirements are specified in Section A3.4b and I2.3. These include requirements for the filler metals in terms of minimum levels of CVN toughness using two different test temperatures and specified test protocols, unless exempted from testing. Demand critical welds are generally complete-joint-penetration groove (CJP) welds because they are subjected to yield level or higher stress demand and located in joints where failure can result in significant degradation in strength or stiffness.

Welds used to connect the coupling beam flanges and web plates to the composite wall steel plates are designated as demand critical, and therefore required to meet the corresponding requirements.
Additionally, welds are used within the protected zones of coupling beams and composite walls are also designated as demand critical, and therefore required to meet the corresponding requirements. These include potential CJP welds connecting the composite wall flange (closure) plates to the web plates, potential CJP welds connecting the coupling beam web plates to flange plates in built-up box sections, potential CJP welds used in composite wall steel plate splices, and potential CJP welds used in composite wall steel plate-to-base plate connections.

4.12 References

Alzeni, Y., Bruneau, M., (2017). "In-Plane Cyclic Testing of Concrete Filled Sandwich Steel Panel Walls with and without Boundary Elements", ASCE Journal of Structural Engineering, Vol.143, No.9, DOI: 10.1061/(ASCE)ST.1943-541X.0001791

Bhardwaj, S., and Varma, A.H. (2016). *AISC Design Guide 32: Design of Modular Steel Plate Composite (SC) Walls for Safety Related Nuclear Facilities*. AISC, Chicago, IL.

Bhardwaj, S., Wang, A.Y., and Varma, A.H. (2018). "Slenderness Requirements for CF-CPSW: The Effects of Concrete Casting." *Proceedings of the Eighth International Conference on Thin-Walled Structures*, ICTWS 2018, Lisbon, Portugal, July 24-27. ISBN: 978-989-20-8665-1

Broberg M., Kizilarslan, E., Shafaei, S., Varma, A.H., Bruneau, M., (2019). "Non-linear Inelastic Behavior of Coupled Composite Plate Shear Walls—Concrete Filled (Coupled-C-PSW/CF)." *Engineering Journal*, AISC, In Preparation

Bruneau, M., and Kenarangi, H. (2018). "Investigation of Cyclic Shear Behavior of Circular Reinforced Concrete Filled Steel Tubes." *Journal of Structural Engineering*, Under Review.

Bruneau, M., and Varma, A.H. (2019). "Shear Strength of Filled Composite Members." *Engineering Journal*, AISC, In Preparation.

Bruneau, M., Kizilarslan, E., Kenarangi, H. (2019) "Cyclic Behavior of C-Shaped Composite Plate Shear Walls – Concrete Filled." *Journal of Structural Engineering*, ASCE, In Preparation

Booth, P., Varma, A.H., and Seo, J. (2015). "Lateral Load Capacity of Steel Plate Composite Wall Structures." Transactions of SMiRT 23 in Manchester, UK, Paper ID 791, IASMIRT, North Carolina State University, Raleigh, NC, pp. 1-10, http://smirt23.uk/attachments/SMiRT-23_Paper_791.pdf

Kurt, E.G., Varma, A.H., Booth, P.N., and Whittaker, A., (2016). "In-plane Behavior and Design of Rectangular SC Wall Piers Without Boundary Elements." ASCE *Journal of Structural Engineering*, Vol. 142, No. 6, http://dx.doi.org/10.1061/(ASCE)ST.1943-541X.0001481

Lehman, D., Roeder, C., Heid, A., Maki, T., and Khalegi, B., (2018). "Shear Response of Concrete Filled Tubes. Part 1: Experiments." *Journal of Constructional Steel Research*, Volume 150, November 2018, Pages 528-540, https://doi.org/10.1016/j.jcsr.2018.08.027

Nie, J.-G., Hu, H.-S., and Eatherton, M. R. (2014). "Concrete filled steel plate composite coupling beams: Experimental study." *Journal of Constructional Steel Research*, Elsevier, 94 49-63.

Seo, J., Varma, A.H., Sener, K., and Ayhan, D. (2016). "Steel-Plate Composite (SC) Walls: In-Plane Shear Behavior, Database, and Design." *Journal of Constructional Steel Research*, Elsevier Science, Volume 119, Pages 202-215, http://dx.doi.org/10.1016/j.jcsr.2015.12.013

Shafaei, S., Seo, J., and Varma, A.H. (2019). "Cyclic Behavior of Planar Composite Plate Shear Walls – Concrete Filled." *Journal of Structural Engineering*, ASCE, In Preparation.

Shafaei. S., Wang, A., Varma, A.H., and Morgen, B. (2018). "Stability of Steel Modules During Construction." *Proceedings of the Annual Stability Conference*, Baltimore, MD, April 10-13, 2018.

Varma, A.H., Malushte, S., Sener, K., and Lai, Z., (2014). "Steel-Plate Composite (SC) Walls for Safety Related Nuclear Facilities: Design for In-Plane Force and Out-of-Plane Moments." *Nuclear Engineering and Design*, Special Issue on SMiRT-21 Conference, Vol. 269, pp. 240-249, Elsevier Science, http://dx.doi.org/10.1016/j.nucengdes.2013.09.019

Wallace, J. et al. (2019). *R-Factor for Coupled Concrete Core Wall System.* Report to the Charles Pankow Foundation.

Zhang, K., Varma, A.H., Malushte, S., and Gallocher, S. (2014). "Effects of Shear Connectors on the Local Buckling and Composite Action in Steel Concrete Composite Walls." *Nuclear Engineering and Design*, Special Issue on SMiRT-21 Conference, Vol. 269, pp. 231-239, Elsevier Science, http://dx.doi.org/10.1016/j.nucengdes.2013.08.035

Zhang, K., Varma, A.H. and Seo, J. (2019). "Steel-Plate Composite (SC) Walls: Behavior and Design and Behavior for Axial Compressive Loading." *Journal of Structural Engineering*, ASCE, submitted for review.

SECTION 5 DETAILED DESIGN PROCESS FOR ARCHETYPE STRUCTURES

This section presents a detailed design process for archetype structures that will be used in Task 4 (FEMA P695 analyses). The design focuses on low to mid-rise office buildings (8 – 22 stories). Based on FEMA P695 recommendations, only the lateral load resisting system (core wall) is designed in this task. A set of initial parameters and a design procedure was developed prior to designing these structures. The initial parameters were developed in consultation with the review panel as the team desired to create archetype structures using a similar approach to industry professionals. For example, the length of the walls was considered a fixed parameter as the review panel indicated this dimension would typically be set by architectural considerations. The design procedure focused on current applicable code provisions paired with these recommended parameters.

Initial archetype structures were designed by sizing walls and coupling beams based on the initial design parameters discussed above. These initial designs were then revised based on the results from design checks including maximum inter-story drift ratio, shear and flexural capacities, and plate slenderness ratio. In this report, the archetype structures for low to mid rise (8, 12, 18, and 22 story) office buildings are presented. Details of designing of these structures are presented in the following sections.

5.1 Archetype Design Space

The design space for this study is the core walls of low to mid-rise (8-22 story) commercial buildings. The core walls are concrete-filled composite plate shear walls (CF-CPSWs), and they are coupled using filled composite members (also known as concrete filled tubes). This design space is broken down into performance groups for the FEMA P-695 study. Basic configuration, design load level, and structure period differentiate these performance groups. In this study, two structural configurations, under two seismic load levels will be evaluated. These parameters correspond to 4 performance groups (PG) with up to 16 archetypes designed and analyzed. A summary of the performance groups is presented in Table 5-1.

The two structural configurations are coupled and uncoupled planar walls (Type I) and two coupled C-shaped walls (Type II). A plan view depiction of these different configurations is shown in Figure 5-1. The maximum considered seismic demand for this system is seismic design category D. Both the maximum (D_{max}) and minimum (D_{min}) seismic design parameters should be evaluated per the FEMA P-695 procedure.

The procedure provides spectral acceleration values corresponding to these load levels; these values are reproduced in Table 5-2. The height of the structure influences both the period and the wall configuration.

Table 5-1. Archetype performance group summary table.

Performance Group Summary				
Group No.	**Grouping Criterial**			**Number of Archetypes**
	Basic Configuration	**Design Load Level**		
		Gravity	**Seismic**	
PG-1	Type I	Typical	SDC D_{max}	6 (8 & 12 Story)
PG-2			SDC D_{min}	2 (8 & 12 Story)
PG-3	Type II	Typical	SDC D_{max}	6 (18 & 22 story)
PG-4			SDC D_{min}	2 (18 & 22 story)

Table 5-2. Spectral Acceleration for seismic design category D.

Seismic Design Category (SDC)	Spectral Acceleration (g)
D_{max}	S_{DS} = 1.0
	S_{D1} = 0.6
D_{min}	S_{DS} = 0.5
	S_{D1} = 0.2

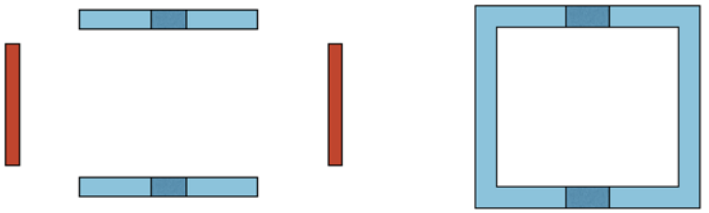

Type I
Coupled and uncoupled Walls

Type II
CC-shaped coupled walls

Figure 5-1. Basic configuration Type I and II.

5.2 Initial Core Wall Parameters

As only a limited number of archetype structures within the archetype design space are designed and evaluated under the FEMA P-695 procedure, a special emphasis was placed on detailing archetype structures that closely followed industry standard design and construction practices. For example, varying the wall core wall thickness while keeping the geometry fixed. Recommended initial parameters were selected after discussions with the review panel. These initial core wall parameters are detailed below in Table 5-3.

Table 5-3. Archetype Structure Initial Parameters.

Parameter	Value	Reasoning
Coupling beam aspect ratio (*L*/*d*)	3, 4, or 5	ACI318-14 allows ratios of 2.0 to 5.0. In practice, most work uses an L/d of 3 as the lower bound ratio.
Story Height	First story: 17ft Typical story: 14ft	Review panel recommendation for typical story heights
Seismic Weight	Floor load of 120psf	Estimated from components: Steel framing (12 psf) 2.5" Normal Weight Concrete on 3" Steel Deck (50 psf) Curtain Wall (15 psf on facade area) Superimposed Dead Load (15 psf) Partitions (15 psf)
Coupled wall length	30ft	Typical bay is 30ft long, the wall would typically run the length of the bay with the wall thickness being the parameter adjusted in design
Floor Dimensions	120ft x 200ft	Review panel recommendation for typical floor geometry
Base Shear Amplification Factor	4	Review panel recommendation

5.3 Design Procedure

As this system is relatively new in its use as a seismic force resisting system, limited design procedures had been developed; therefore, a detailed design procedure was written. Establishing this design methodology ensured consistent archetype designs that met relevant code provisions and outlined design checks performed outside of currently existing code provisions. This procedure can be generalized in 5 steps: (1) Obtain predefined floor and core wall dimensions from architect (in this case industry recommendations); (2) Perform Equivalent Lateral Force analysis using ASCE7 defined loads; (3) Choose preliminary dimensions for walls and coupling beams; (4) Perform a structural analysis, (5) Perform design checks including for strength, drift, slenderness, and tie reinforcement; (6) Redesign as necessary. This procedure is detailed below. An example archetype designed explicitly using this procedure is provided in Appendix C.

Step 1: Predetermined floor and core wall geometry

As previously discussed in section 5.1, structural wall layout is largely determined by architects. Additionally, material parameters were held constant for all archetype designs. For the design of these archetypes, the following were predetermined:

- Floor plan including bay width wall lengths
- Floor loading
- Core wall configuration (Type I or II)
- Number of stories and story height
- Material properties (f'_c and f_y)
- L/d ratio (3, 4, or 5)

Step 2: Equivalent Lateral Force Analysis

The Equivalent Lateral Force (ELF) Analysis follows the procedure laid out in ASCE 7-16. These steps are detailed below.

Step 2-1: Develop response spectra

The design response spectra are built based on provided S_{DS} and S_{D1} values. ASCE7 outlines a procedure based on site class, importance factor, and soil conditions to find these parameters but FEMA directly

provides representative S_{Ds} and S_{D1} values. The design response spectra for SDC D_{max} and D_{min} are plotted below in Figure 5-2.

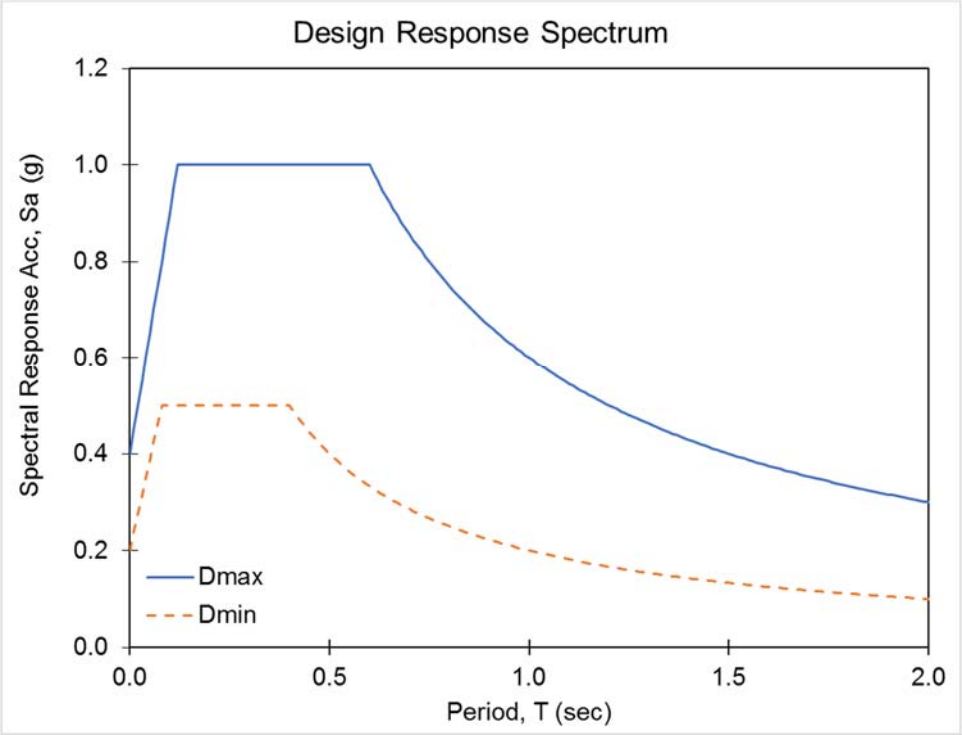

Figure 5-2. Design Response Spectra for Seismic Loads corresponding to D_{max} and D_{min}.

Step 2-2: Estimate Fundamental Period

Initially, the fundamental period was estimated using Equation (**5.1** (ASCE7 Eq. 12.8-7) with the default period parameters C_t and x of 0.02 and 0.75 respectively. After developing initial section sizes, this analysis was improved by using the fundamental period from modal analysis. Per ASCE7 Section 12.8.2, the fundamental period can be adjusted to the minimum of Equation 5.2 and the fundamental period from modal analysis. The upper limit coefficient is based on S_{D1} and taken as 1.4 for D_{max} and 1.5 for D_{min} per ASCE 7 Table 12.8-1.

Additional finite element analyses were conducted to confirm the validity of Equation (**5.1**. The analysis results suggested that the analytically predicted fundamental period is significantly longer than from the one approximated using Equation 5.2. Therefore, the upper limit period is used for the design.

$$T_a = C_t h_n^{\,x} \tag{5.1}$$

$$T_{\max} = C_u T_a \tag{5.2}$$

Step 2-3: Compute Seismic response coefficient, C_s

The seismic response coefficient is then calculated using ASCE Eq. 12.8-2 and the associated limits presented in Eqs. 12.8-3 - 12.8-6. These equations are presented in Equations. 5.3 - 5.7. The importance factor, I_e, was taken as 1.0, consistent with risk category II. An expected response modification factor, R, of 8 was used. T_L, the long period transition period, was taken as 8s.

$$C_s = \frac{S_{DS}}{\left(\frac{R}{I_e}\right)} \tag{5.3}$$

$$C_{s,\max} = \frac{S_{D1}}{T\left(\frac{R}{I_e}\right)} \text{ for } T \le T_L \tag{5.4}$$

$$C_{s,\max} = \frac{S_{D1}T_L}{T^2\left(\frac{R}{I_e}\right)} \text{ for } T > T_L \tag{5.5}$$

$$C_{s,\min} = 0.044 S_{DS} I_e \text{ for} \ge 0.01 \tag{5.6}$$

$$\text{If } S_1 \ge 0.6\text{g } C_{s,\min} = \frac{0.5S_1}{\left(\frac{R}{I_e}\right)} \tag{5.7}$$

Step 2-4: Distribute seismic forces vertically

Distribution of the seismic forces along the height follows the procedure laid out in ASCE7 Section 12.8.3. First base shear is calculated per ACSE7 Eq. 12.8-1 using the seismic weight, W and the C_s factor determined in Step 2-3 as shown in Equation 5.8. Next, the vertical distribution factor (ASCE7 Eq. 12.8-12) is found using the story weight, w_x or w_i and the height from the base to the i or x level as found in Equation 5.9. Finally, the story shear is calculated using Equation 5.10 (ASCE7 Eq. 12.8-12).

$$V = C_s W \tag{5.8}$$

$$C_{vx} = \frac{w_x h_x^k}{\sum_{i=1}^{n} w_i h_i^k} \tag{5.9}$$

$$F_x = C_{vx} V \tag{5.10}$$

Step 2-5: Compute base shear force and apply amplification factor

The base shear is adjusted to four times the value found in Equation 5.8 to account for base shear amplification found in higher modes of tall structures. This value becomes the shear design demand value but is not used to determine the overturning moment.

Step 2-6: Compute overturning moment at base

The overturning moment is computed from the distribution of seismic forces.

Step 2-7: Compute sum of coupling beam forces

The total coupling beam forces are computed using Equation 5.11. In the equation, *CR* is the assumed coupling ratio and *OTM* is the overturning moment at the base. The value of CR_K is initially assumed to be 60%. The level of coupling action (*CR*) is not a design parameter, and it is used only to initiate the process. The initial design done through Steps 2-1 ~ 2-3 should be most likely revised in Step 2-5 since most of design parameters are predetermined and based on assumptions such as 60% coupling ratio.

$$\sum_{i=1}^{n} V_{beam,i} = \frac{CR \cdot OTM}{L} \tag{5.11}$$

Step 2-8: Compute shear force on coupling beam

After determining the total shear force taken by the coupling beams, the individual coupling beam shear force is estimated by assuming the coupling beam shear distribution is uniform. This expression is shown below in Equation 5.12.

$$V_{beam} = \frac{\sum_{i=1}^{n} V_{beam,i}}{N} \quad \textbf{(5.12)}$$

Step 3: Preliminary Design

Preliminary Design consists of selecting total wall thickness, steel plate thickness, and sizing the coupling beams. No discrete recommendations for the sizes are provided in the design procedure but experience aids in selecting initial sizes.

Step 4: Perform a structural analysis

A structural analysis is conducted in this step. The preliminary sized composite walls and coupling beams in Step 4 are modeled in the analysis in accordance with Section 4.3. The required strengths (shear and flexure) for both C-PSWs/CF and coupling beams are accurately recomputed. The lateral deflection at the roof is also computed in this step.

Step 5: Design Checks

The design checks include steel plate slenderness, empty module requirements, couple beam width-to-thickness ratio, inter-story drift, shear and flexural strength, and tie reinforcement.

Step 5-1: Wall steel plate slenderness

The wall steel plate slenderness checks are performed for the tie spacing, *s*, before and after concrete placement using the equations provided in Section 4.4.2.

Step 5-2: Corner box steel plate slenderness (structures with Type II configuration only)

Corner box steel plate slenderness limits are based on AISC 360-16 Table I1.1a. This limit applies to corner box sections which are found in C-shaped walls. The limit on spacing of ties ensures that the section remains compact. This limit is reproduced below in Equation 5.13.

$$\frac{b}{t_p} or \frac{s}{t_p} \leq 2.37\sqrt{\frac{E_s}{R_y F_y}} \quad \textbf{(5.13)}$$

Step 5-3: Coupling Beam width-to-thickness ratio

The coupling beam steel plate slenderness checks are performed using the equations provided in Section 4.5.2.

Step 5-4: Inter-story Drift Ratio

The story displacement is analytically estimated from the structural analysis in Step 4. This story displacement is then converted to the inter-story drift ratio by taking the story displacement difference of two adjacent stories over the corresponding story height. The maximum inter-story drift ratio is then checked against the limit of $0.02h_{sx}$ per ASCE7-16 Table 12.12-1.

Step 5-5: Coupling beam shear strength

The required shear strength of coupling beams is determined from the structural analysis in Step 4. The available shear strength of coupling beams is determined according to Section 4.7.

Step 5-6: Coupling Beam Flexural Strength

The required flexural strength of coupling beams is determined from the structural analysis in Step 4. The available flexural strength of coupling beams is determined according to Section 4.7.

Step 5-7: Wall Shear Strength

The required in-plane shear strength of each individual wall is the base shear (V_{base}) computed from Step 2. V_{base} is then divided by two (two individual walls) and amplified by 4 (shear amplification factor) to calculate the required in-plane shear strength. The available in-plane shear strength of walls is determined according to Section 4.6.1.

Step 5-8: Wall Flexural Strength

For calculating the required flexural strength of walls, the overturning moment (OTM) computed from Step 2 is increased by the 1st overstrength factor (γ_1). It is increased to ensure that the two walls form plastic hinges at the bottom after all coupling beams form plastic hinges at their both ends. The 1st overstrength factor (γ_1) is calculated using Equation 5.14. In Equation 5.14, $\Sigma(1.2M_{p,CB,exp})$ is the sum of the expected flexural strength of coupling beams and $\Sigma M_{u,CB}$ is the required flexural strength for coupling beams.

The increased OTM is then multiplied by (1-CR_s) to compute the total required wall flexural strength. CR_s is the strength-based coupling ratio that can be computed using Equation 5.15. The total required wall flexural strength is further proportioned based on the ratio of individual wall flexural stiffness. That is, only the steel flexural stiffness ($E_sI_s = EI_{wall,T}$) is considered for the individual wall under tension force induced by the coupling action. On the other hand, the whole composite flexural stiffness ($EI_{wall} = EI_{wall,C}$) is considered for the individual wall under compression force. The required wall flexural strength for the tension wall is computed using Equation 5.16 and the required wall flexural strength for the compression wall is computed using Equation 5.17.

The available wall flexural strength is calculated using Section 4.6. During this calculation, the influence of the axial force (P) induced by the coupling action on the wall flexural strength is considered. That is, the flexural strength of individual wall subjected to either axial tension or compression force is directly calculated.

$$\gamma_1 = \frac{\sum(1.2M_{p,CB,\exp})}{\sum M_{u.CB}} \tag{5.14}$$

$$CR_S = \frac{\sum V_{1.2M_{p,CB,\exp}} L}{OTM\gamma_1} \tag{5.15}$$

$$M_{u,T} = \left(\frac{EI_{wall,T}}{EI_{wall,T} + EI_{wall,C}}\right)(\gamma_1 OTM)(1 - CR_s) \tag{5.16}$$

$$M_{u,C} = \left(\frac{EI_{wall,C}}{EI_{wall,T} + EI_{wall,C}}\right)(\gamma_1 OTM)(1 - CR_s) \tag{5.17}$$

When the design procedure (being described in this document) is implemented for coupled concrete-filled composite plate shear walls (CF-CPSWs), the coupled wall system will form plastic hinges in the coupling beams and it will be followed by plastic hinges formed in the walls as illustrated in Figure 5-3. The 1st overstrength factor (γ_1) corresponds to this mechanism. The additional strength before forming hinges in the walls is quantified as the 2nd overstrength factor (γ_2) and it can be estimated using Equation 5.18. In Equation 5.18, $\Sigma(1.2M_{p,wall,exp})$ is the sum of the expected flexural strength of the walls and $\Sigma M_{u,wall}$ is the sum of the required flexural strength for the wall. The overall overstrength factor (Ω) is then simply calculated as $\Omega = \gamma_1 \times \gamma_2$.

$$\gamma_2 = \frac{\sum(1.2M_{p,wall,\exp})}{\sum M_{u.wall}} \qquad \textbf{(5.18)}$$

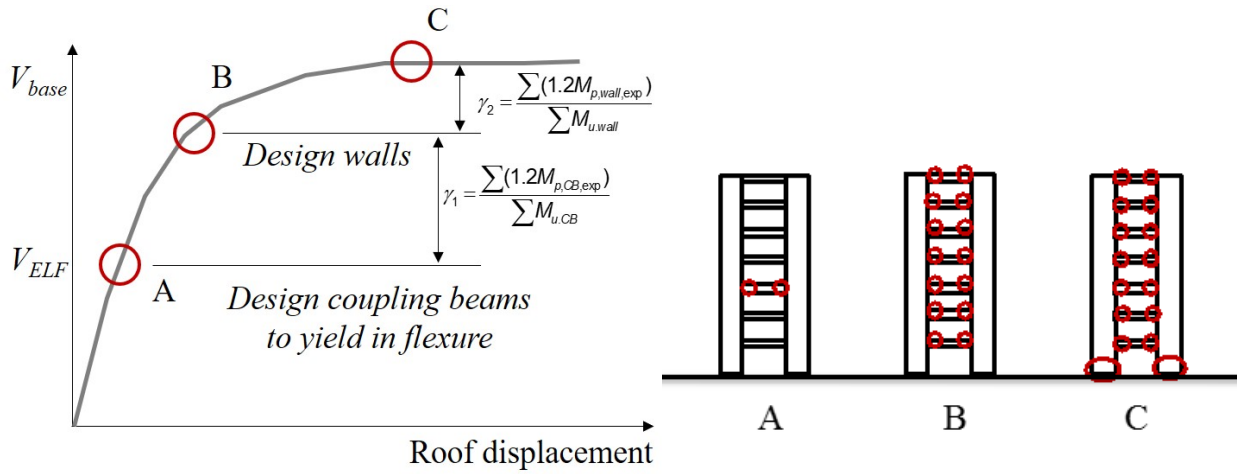

Figure 5-3. Failure mechanism of coupled CF-CPSW system.

Step 6: Redesign

After completing all the design checks, redesign may be necessary. The preliminary design choices, namely the wall thickness, plate thickness, and coupling beam dimensions, are adjusted and the design checks repeated as needed until a system that passes all checks is established.

5.4 Designed Archetype Structures

Table 5-4 and Table 5-5 presents 8 story archetype structures and 12 story archetype structures, respectively, as discussed in Section 3.3. Table 5-6 and Table 5-7 presents 18 story archetype structures and 22 story archetype structures, respectively. Note that PG-1 structures are structures with wall type I subjected to S_{DS} and S_{D1} values corresponding to D_{max} and PG-2 structures are structures with wall type I subjected to S_{DS} and S_{D1} values corresponding to D_{min}. PG-3 structures are structures with wall type II subjected to S_{DS} and S_{D1} values corresponding to D_{max} and PG-4 structures are structures with wall type II subjected to S_{DS} and S_{D1} values corresponding to D_{min}. Table 5-8 details 3 story structures; these structures were designed to investigate the appropriateness of the R factor recommendations for shorter structures and structures with high and low coupling ratios.

Table 5-9 presents additional information of the designed archetype structures. This table includes the strength based coupling ratio (CR_s), strength margin of individual wall and coupling beam of each of the designed archetype structures. The table also presents the maximum inter-story drift ratio estimated using the FE models.

Appendix C of this report presents the detailed calculations of an example case (PG-1B). The example case looks at the design of an 8-story archetype structure in performance group 1 (PG-1). This structure is subjected to seismic loads corresponding to D_{max}. First the initial parameters are laid out then ELF analysis is performed. After selected preliminary sizes the design checks are performed as laid out in the design procedure.

Table 5-4. 8-story archetype structures.

Case	No. Stories	L/d	Cs	Coupled Wall Length, in	Wall Thickness, t_{sc}, in	Plate Thickness, t_p, in	CB Length, in	CB Section, in	Uncoupled Wall Length, in	Performance Group
PG-1A	8	3	0.076	144	20	9/16	72	20x24x 3/8(f), 3/8(w)	252	1
PG-1B		4		132	24	9/16	96	24x24x 1/2(f), 3/8(w)	240	1
PG-1C		5		120	24	5/8	120	24x24x 1/2(f), 3/8(w)	240	1
PG-2B	8	4	0.024	144	10	3/16	72	10x18x 3/16(f), 1/4(w)	240	2

Table 5-5. 12-story archetype structures.

Case	No. Stories	L/d	Cs	Coupled Wall Length, in	Wall Thickness, t_{sc}, in	Plate Thickness, t_p, in	CB Length, in	CB Section, in	Uncoupled Wall Length, in	Performance Group
PG-1D	12	3	0.057	204	18	9/16	72	18x24x 5/16(f), 3/8(w)	348	1
PG-1E		4		192	22	9/16	96	22x24x 7/16(f), 3/8(w)	336	1
PG-1F		5		180	24	9/16	120	24x24x 1/2(f), 3/8(w)	324	1
PG-2E	12	4	0.017	204	8	3/16	72	8x18x 3/16(f), 1/4(w)	336	2

Table 5-6. 18-story archetype structures.

Case	No. Stories	L/d	Cs	C wall depth, in (c-c)	C wall width, in (c-e)	$t_{sc.f}$, in	$t_{sc.w}$, in	$t_{p.bot}$, in	$t_{p.top}$, in	CB Length, in	CB Section, in	Performance Group
PG-3A	18	3	0.042	360	180	18	14	1/2	5/16	72	18x24x 5/16(f), 3/8(w)	3
PG-3B		4		360	168	24	14	1/2	5/16	96	24x24x 7/16(f), 3/8(w)	3
PG-3C		5		360	156	26	16	9/16	5/16	120	26x24x 1/2(f), 3/8(w)	3
PG-4B	18	4	0.014	360	162	12	12	3/16	3/16	72	12x18x 1/4(f), 1/4(w)	4

Table 5-7. 22-story archetype structures.

Case	No. Stories	L/d	Cs	C wall depth, in (c-c)	C wall width, in (c-e)	$t_{sc.f}$, in	$t_{sc.w}$, in	$t_{p.bot}$, in	$t_{p.top}$, in	CB Length, in	CB Section, in	Performance Group
PG-3D	22	3	0.036	360	204	20	14	1/2	3/8	72	20x24x 3/8(f), 3/8(w)	3
PG-3E		4		360	192	24	14	1/2	3/8	96	24x24x 7/16(f), 3/8(w)	3
PG-3F		5		360	180	28	16	9/16	3/8	120	28x24x 9/16(f), 3/8(w)	3
PG-4E	22	4	0.012	360	162	14	10	3/16	3/16	72	14x18x 1/4(f), 1/4(w)	4

Table 5-8. 3-story archetype structures.

Case	No. Stories	Coupled Wall Length, in.	Wall Thickness, t_{sc}, in	Plate Thickness, t_p, in	CB Length, in	CB Section, in	Design CR, %	Performance Group
1	3	120	12	1/8	120	12x24x 1/2(f), 3/8(w)	63.1	5
2		120	12	3/16	120	12x24 3/8(f), 3/8(w)	47.6	5
3		108	14	1/4	84	14x24 3/8(f), 3/8(w)	54.1	5
4		108	12	5/16	84	12x24 5/16(f), 3/8(w)	48.5	5
5		216	10	3/32	120	10x24 3/16(f), 3/8(w)	32.1	5

Table 5-9. Archetype structures - coupling ratio, strength, and inter-story drift ratio.

Case	No. Stories	Wall Strength Margin		Coupling Beam Strength Margin		Max. Inter-story Drift Ratio (%)
		$\phi M_{n,wall}/M_{u,wall}$	$\phi V_{n,wall}/V_{u,wall}$	$\phi M_{n,CB}/M_{u,CB}$	$\phi V_{n,CB}/V_{u,CB}$	
PG-1A	8	0.98	6.30	1.42	1.19	1.35
PG-1B		1.17	6.00	1.30	1.39	1.52
PG-1C		1.88	5.93	1.03	1.74	1.92
PG-2B	8	1.43	7.26	1.29	1.31	1.39
PG-1D	12	1.09	7.81	1.44	1.15	1.32
PG-1E		1.14	7.70	1.42	1.45	1.39
PG-1F		1.33	7.34	1.28	1.74	1.65
PG-2E	12	1.35	8.91	1.40	1.10	1.24
PG-3A	18	1.02	2.84	1.12	1.14	1.77
PG-3B		1.10	2.79	1.09	1.04	1.90
PG-3C		1.29	2.90	1.05	1.09	2.10
PG-4B	18	1.07	3.14	1.20	1.40	1.96
PG-3D	22	0.95	3.12	1.21	1.06	1.89
PG-3E		1.21	3.03	1.07	1.02	2.01
PG-3F		1.25	3.22	1.12	1.03	1.99
PG-4E	22	0.90	2.98	1.06	1.14	1.92

“This Page Intentionally Left Blank”

SECTION 6
MATERIAL MODELS FOR FEMA P695 NON-LINEAR ANALYSES

6.1 General

This section presents information on the nonlinear materials models chosen for the steel and concrete components of the CC-PSW/CF, taken from the element library available in the software OpenSees (McKenna et al. 2016) that will be used in some of the incremental dynamic analyses (IDA) as part of this project (as mentioned earlier, two different sets of models are considered in this study, and information on inputs to the material models used is introduced later). This is followed by a description of the analyses to validate and calibrate the model using the available test data from the study of composite wall by Alzeni and Bruneau (2014).

As indicated earlier, the FEMA P695 procedure (FEMA 2009) has been developed and proposed for the purpose of establishing R-factor for a structural system. It requires the use of incremental dynamic analysis (IDA), which relies on nonlinear time history analysis. The credibility of the result obtained by this procedure depend on appropriately capturing the hysteretic behavior of the structural elements in the system considered. The FEMA P695 approach requires to run twenty-two earthquakes (44 individual components whose event magnitudes ranges from M6.5 to M7.6) from sites located at distances greater than or equal to 10 km from fault rupture (far-field record from Pacific Earthquake Engineering Research Center (PEER) 2017). It also requires performing IDA for each of these earthquake records. This implies increasing the severity of each earthquake component from analysis to analysis, until collapse is reached, which may require up to 100 separate analyses for the same earthquake. Furthermore, this procedure must be repeated for a large number of archetypes (i.e., example structures). This results in intense computation. For this reason, the software OpenSees has been selected as it allows to model nonlinear behavior using macro fiber models with relatively rapid execution time compared to other approaches, such as 2-D or 3-D finite element approaches based on continuum mechanics available in other software platforms. Moreover, OpenSees provides a wide range of constitutive models, elements and solution algorithms. Hence, many researchers have been using OpenSees for IDA, e.g., (Kanvinde 2003; Lignos 2008; Rodgers and Mahin 2006), particularly within the framework of FEMA P695 studies.

In Section 6.2, the steel material models retained for this study are described in details. The backbone curve that the steel material uses is presented in Section 6.2.1. The effect of buckling on the shape of the backbone

curve is addressed in Section 6.2.2. Moreover, the calculation of accumulated plastic strain and how the steel model account for fracture of steel is covered in Section 6.2.3. Then, parameters related to the Menegotto Pinto model, isotropic hardening, and stress overshooting are described in Sections 6.2.4, to 6.2.6, respectively. Then, information related to the concrete model is presented in Section 6.3, where the required parameters to define the concrete model are described in Section 6.3.1, and the nonlinear displacement-based and force-based element types available in OpenSees are introduced in Section 6.4, discussing the performance of these element types with an example.

6.2 Steel Model

The material called *Reinforcing Steel Material* in OpenSees was selected here to model the steel fibers of the cross-section. This model was developed by Kunnath et al. (2009). The advantage of this particular material model is that its constitutive equations allow simulating both buckling and fracturing. This material model was preferred as the ability to model steel fracture and ensuing loss of strength is primordial given that past experiments have shown that it is fracture (and not local buckling) that leads to strength degradation in composite walls. The "Reinforced Steel Material" is currently the only OpenSees material model capable of accounting for steel fracture. It is based on the Chang and Mander (1994) uniaxial material, available in OpenSees, but with the added benefit of being able to model fracture by eliminating the strength and stiffness of a fiber once it has reached specified cumulative plastic strains. Even though the material was originally calibrated to model reinforcing steels, input parameters can be set to represent the behavior of construction steel in a general sense. Some of the key aspects of this model are described below. More detailed information on how this model is defined is provided in Appendix A.

6.2.1 Backbone Curve

As frequently done in the definition of various constitutive models used in fiber analysis or finite element models, the steel material model uses true stress and true strain, rather than engineering stress and strain. This corrects for the fact that engineering stresses underestimate the tensile backbone curve, and overestimate the compression one. The natural (true) stress-strain curve in the *Reinforcing Steel Material* model, however, only requires inputting the engineering stress-strain tensile backbone curve parameters to automatically define the characteristics of both the tensile and compressive true stress curves. The conversion is based on the principle of conservation of steel volume (Restrepo-Posada et al. 1994). More details as to how the curve is constructed are presented in Appendix A.

In order to define the backbone curve in OpenSees, the yield strength (f_y), ultimate strength (f_u), initial Young's modulus (E_s), Modulus at strain hardening (E_{sh}), strain at initial strain hardening (ε_{sh}) and ultimate strain at which stress is maximum (ε_u) are the input parameters to be provided. For example, for an A572 Grade 50 steel having yield strength of 50 ksi, the inputs in Table 6-1 are entered, and the resulting backbone is shown in Figure 6-1, compared to the corresponding engineering stress one. Note that for the *Reinforcing Steel Material* model, the generated true stress curves in compression and tension are symmetric, as explained by Kunnath et al. (2009). Most importantly, the difference between true strain and engineering strain is of little significance for strain less than 0.05 in./in. (as indicated in Section 7), as most C-PSW/CF failed in fracture at cyclic stresses less than that. However, note that when buckling is considered (see Figure 7-6), this symmetry will be lost.

Table 6-1. Inputs for Grade 50 steel.

f_y (ksi)	f_u (ksi)	E_s (ksi)	E_{sh} (ksi)	ε_{sh}	ε_u
50	**65**	**29000**	**967 (Es/30)**	**10*ε_y**	**0.15**

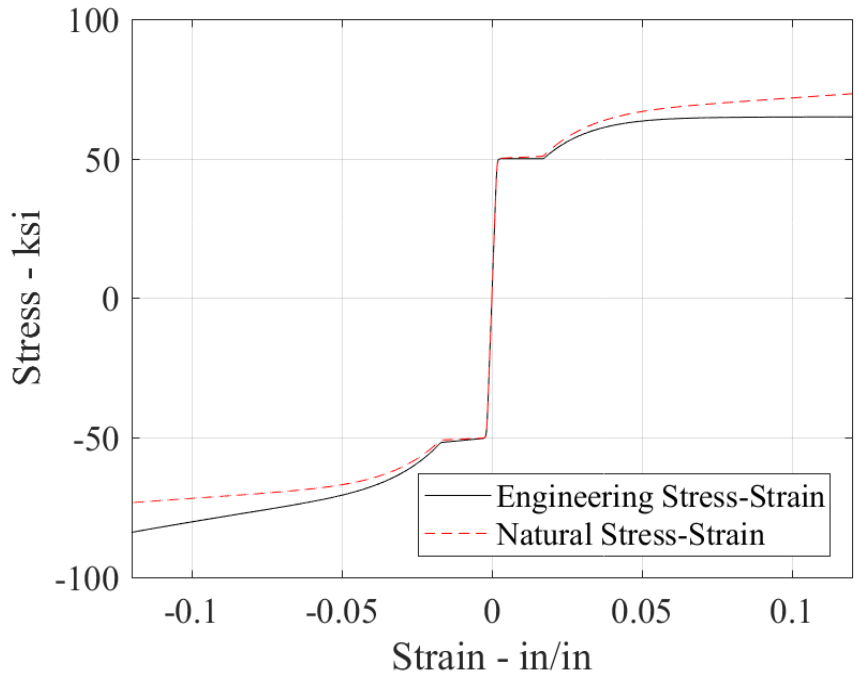

Figure 6-1. Steel backbone curve.

6.2.2 Buckling Model

Buckling is generally modeled either by equations derived from rigorous modeling of the physical geometric instability (which can be complex to capture for cyclic inelastic deformations), or by empirical relationships that capture the hysteretic expression of buckling behavior. Even though less rigorous than the physical approach, the empirical approach is commonly used as an effective way to model buckling during cyclic inelastic response. The *Reinforcing Steel Material* model in OpenSees considers two types of buckling models, namely; (1) a buckling model based on Gomes and Appleton (1997), and: (2) a buckling model based on Dhakal and Maekawa (2002). The first of the two is the one that was used here; the latter is described briefly at the end of this section.

The buckling model of Gomes and Appleton (1997) is defined in the steel material model by four constant parameters, namely, the slenderness ratio (l_{SR}), the amplification factor for buckled stress strain curve (β), the buckling reduction factor (r), and the buckling constant (γ) (which are the required input parameters in OpenSees for that model). Recalling that the model was developed for steel re-bars, the slenderness ratio (l_{SR}) is used to define buckling of the re-bars (which are equivalent to fibers in the cross-sections considered here). This ratio is defined as the unsupported length (L_u) divided by the diameter of the re-bars (d_b), as shown in Equation 6.1.

$$l_{SR} = \frac{L_u}{d_b} \tag{6.1}$$

For the composite walls considered here, the unsupported length was taken to be the length between the tie bars of the wall, and the rebar diameter was set to be equal to the effective bar diameter ($d_{b,eff}$), which can be determined by equating the radius of gyration of a bar having $d_{b,eff}$ to the radius of gyration of the rectangular steel plate of composite walls.

Definition of the remaining parameters is graphically shown is Figure 3.2. The amplification factor (β) is used to adjust the location of the bifurcation point where buckling initiates. The buckling reduction coefficient (r) is introduced to adjust the shape of the post-buckling curve, using a value ranging between 0 and 1.0. The initiation of buckling is introduced by the gamma factor, meaning that stresses are reduced after γf_{su}. The way each of these parameters affect, the shape of the hysteretic curve has been investigated and results are presented in Appendix A.1.2.1. The buckled stress is defined by Equations 6.2 and 6.3 in the *Reinforcing Steel Material* model.

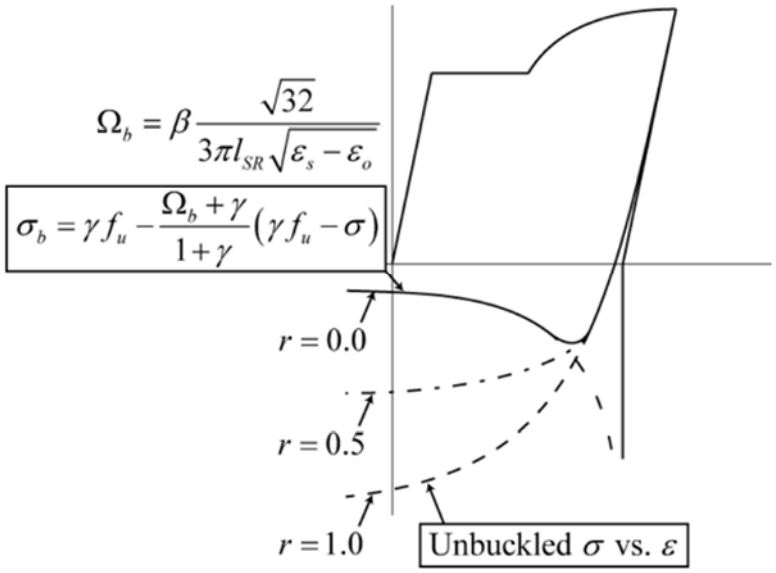

Figure 6-2. Buckled stress-strain curve (McKenna et al. 2016).

$$\Omega_b = \beta * \frac{\sqrt{32}}{3 * \pi * l_{SR} * \sqrt{\varepsilon_s - \varepsilon_o}} \quad \textbf{(6.2)}$$

$$\sigma_b = \gamma * f_u - \frac{\Omega_b + \gamma}{1 + \gamma} * (\gamma * f_u - \sigma) \quad \textbf{(6.3)}$$

Communications with the co-developer of the material model (Personal communication, Professor Sashi Kunnath, University of California, Davis, September 2017) confirmed that an exact relationship cannot be established between the parameters in Equations 6.2 and 6.3 for the Gomes and Appleton buckling material model as implemented in OpenSees (i.e., in the *Reinforced Steel Material*) and the equations presented by Gomes and Appleton (1997). Therefore, parametric studies to investigate the effect of the parameters on the shape of the hysteretic curve were conducted, to help understand how to make the model capture the desired behavior. Such studies are presented in Appendix A.1.2.1. However, for the composite wall used in calibration of the model, values selected for the defining parameter are presented in Section 7.

Compared to the Gomes and Appleton Model (Gomes and Appleton 1997), Dhakal and Maekawa buckling model (Dhakal and Maekawa 2002) requires only two constants, slenderness ratio (l_{SR}) and single response modifier (α_B) to model post-buckling response, which provided less flexibility to capture the experimentally observed stiffness and strength behavior of the composite walls (Appendix A.1.2.2). Hence, this buckling model was not considered in this research.

6.2.3 Low-Cycle Fatigue

As mentioned earlier, the objective of using a low cycle fatigue model in this study is to capture fracture of the steel, given that experiments have shown this to be the limit state that leads to strength degradation of composite walls (i.e., as fracture progresses across the wall cross-section). For this purpose, the *Reinforcing Steel Material* model in OpenSees uses the Coffin-Manson fatigue life equations (Coffin 1954; Coffin 1971; Manson 1965), given by Equation 6.4.

$$\Delta\varepsilon_P = \varepsilon'_f * (2 * N_f)^{\alpha} \quad \textbf{(6.4)}$$

where $\Delta\varepsilon_p$ is the plastic strain amplitude; $2*N_f$ is the number of half cycles to failure (one cycle is equal to two reversals, N_f); ε'_f is the fatigue ductility coefficient (denoted C_f in the *Reinforcing Steel Material* model); α (denoted alpha in the *Reinforcing Steel Material* model) is the fatigue ductility exponent. The constants in that equation were obtained from analyses considering engineering stresses and strains. Therefore, the low-cycle fatigue calculations in the *Reinforcing Steel Material* model implemented in OpenSees are performed using engineering values.

The peak plastic strain amplitudes in tension and compression are measured for each loading branches during analysis and the number of half cycles to failure is calculated by Equations 6.5 and 6.6. Then, cumulative damage is calculated using the Palmgren-Miner rule (Miner 1945). Per that procedure, a steel fiber prior to the application of strains starts with a cumulative damage of zero, D_f. Once the cumulative damage reaches 1.0, as calculated by Equations 6.7 and 6.8, the steel area fractures and the stress that can be resisted by that fiber rapidly reduces to zero.

$$\Delta\varepsilon_P = \varepsilon_t - \frac{\sigma_t}{E_S} \quad \textbf{(6.5)}$$

$$2N_f = \left(\frac{\Delta\varepsilon_P}{\varepsilon'_f}\right)^{-\frac{1}{\alpha}} \quad \textbf{(6.6)}$$

$$D_i = \left(\frac{1}{2 * N_f}\right) \quad \textbf{(6.7)}$$

$$D_f = \Sigma D_i \quad \textbf{(6.8)}$$

where ε_p is the plastic strain amplitude; ε_t and σ_t are the total strain and stress amplitudes per cycle; C_f and α are the material constants; D_i is the fatigue damage per cycle; and D_f is the cumulative fatigue damage.

A strength degradation model linked to fatigue damage was also implemented in the *Reinforcing Steel Material* (Figure 6-3). The model assumes a linear relationship between cumulative strength degradation (which is defined by summation of the strength loss factor per cycle, f_{SR}), and cumulative fatigue damage, D_f, per Equation 6.9. In support of this assumption, Brown and Kunnath (2000) conducted a constant amplitude cyclic test and calibrated the material constants, β, C_d and α and C_f separately using the method of least squares (Figure 6-4) and came up with Equation 6.10. On that basis, the strength degradation characteristic implemented in the model are related to the fatigue damage of material properties of steel.

$$\sum_{i=1}^{n} (f_{SR})_i = Z_d * D_f \quad \textbf{(6.9)}$$

$$Z_d = \left(\frac{C_f}{C_d}\right)^{1/\alpha} \quad \textbf{(6.10)}$$

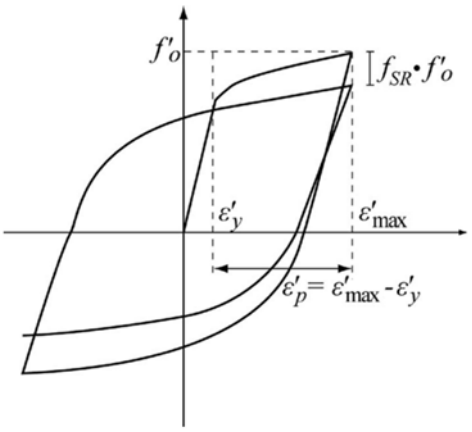

Figure 6-3. Cyclic degradation (Kunnath et al. 2009).

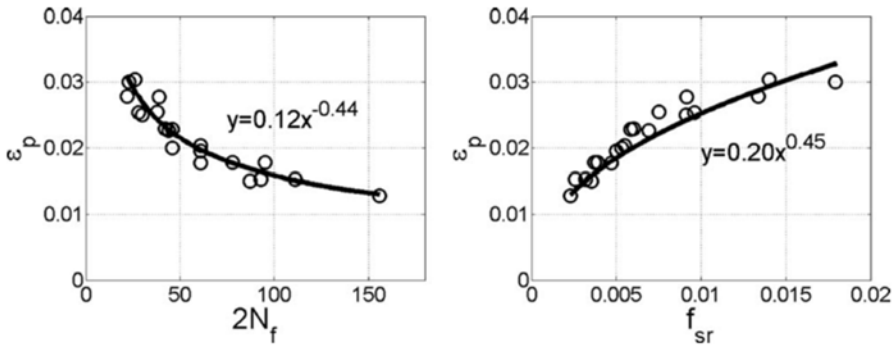

Figure 6-4. Calibration of material coefficients: β, C_d and α and C_f (Kunnath et al. 2009).

The above Coffin-Manson equations have been derived from tests at constant strain amplitudes. Given that structural response to earthquake excitations leads to variable strain histories in structural members, the rainflow method (Downing and Socie 1982) is integrated in the *Reinforcing Steel Material* model to count equivalent cycles.

6.2.4 Menegotto-Pinto Curve Parameters

The Menegotto-Pinto equation (Menegotto 1973) is useful for defining a curve tangentially connecting two points, and having a variable radius of curvature at the two intersection points (as shown in Figure 6-5). This radius of curvature is defined by Equation (6.11), as a function of the three constants, R1, R2 and R3, which are also input parameters for the *Reinforcing Steel Material* model.

$$R = \mathrm{R2} * \left(\frac{f_y}{E_s}\right)^{R1} * (1 - \mathrm{R3} * \Delta\varepsilon_a) \qquad \textbf{(6.11)}$$

The recommended default values for the three constants are 0.333, 18.0, and 4.0, which were obtained by curve fitting of test results on reinforcing bars based on the study of Panthaki (1992). Even though different constants can be input, default values were found to be sufficient to describe the steel hysteretic curve for composite walls. Details on derivation of the Menegotto-Pinto equation are provided in Appendix A.1.4.

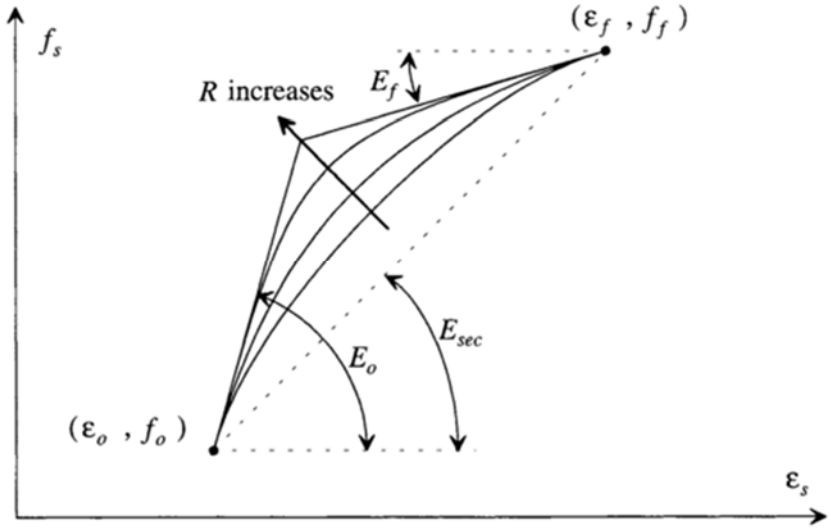

Figure 6-5. Different curves having the same starting point (Chang and Mander 1994).

6.2.5 Isotropic Hardening / Diminishing Yield Plateau

The *Reinforcing Steel Material* model also has the ability to account for both the diminishing yield plateau and isotropic hardening. Two parameters are needed to define the isotropic hardening and yield plateau diminishing, namely: (1) a hardening constant, a1, and (2) a hardening limit, HL, to quantify the reduction of the yield plateau. With these parameters, the model calculates a hardening factor, HF (Equation 6.12), and uses this factor for calculation of strain and stress in the strain-hardening region (Equations 6.13 and 6.14).

$$HF = 1.0 - a1 * \Delta\varepsilon_p \quad \textbf{(6.12a)}$$

$$if\ HF < HL\ \ then\ \ HF = HL \quad \textbf{(6.12b)}$$

$$if\ HF > 1.0\ \ then\ \ HF = 1.0 \quad \textbf{(6.12c)}$$

$$\varepsilon_{sh\_location} = \varepsilon_y + HF * (\varepsilon_{sh} + \varepsilon_y) \quad \textbf{(6.13a)}$$

$$\varepsilon_{sh} = log(1.0 + \varepsilon_{sh\_location}) \quad \textbf{(6.13b)}$$

$$f_{shp} = f_y * (1.0 + \varepsilon_{sh\_location}) \quad \textbf{(6.14)}$$

6.2.6 Overshooting/Undershooting

Events producing random vibrations involve local unloading and reloading of structural elements. However, in many of the materials in OpenSees such as *Steel01*, *Steel02*, etc., true responses are over-predicted or under-predicted upon unloading and reloading to the same yielding level (without yielding reversal) over short instants of the earthquake response because of inadequate allocated storage capacity in the models; this is called overshooting (or undershooting). This overshooting (or undershooting) effect is due to numerical shortcomings in some models due to an artificial hardening developing in the stress–strain behavior upon reloading from the partial unloading loop. To resolve this issue, the original unloading path parameters must be stored in memory so that reloading behavior after partial unloading does not overshoot the previous loading loop in the cyclic stress-strain behavior.

The accuracy of how this behavior is modeled is also enhanced when more information on more "loading branches" is kept in memory (where a loading branch is defined as an unloading/reloading rule (i.e., flow, rule) for partial reversal sequences accounting for the values of stress and strain-hardening rate of the point of elastic reversal). For example, at any point during the time-history, the Chang-Mander model implemented in OpenSees (*Steel02*) stores information on the 10 previous loading branches in the bounding curves (backbone curves) and significant improvement in eliminating overshooting/undershooting has been reported when 16 loading branches were used instead (Figure 6-6) (Kunnath et al. 2009). Figure 6-6 shows the noticeable effect of overshooting or undershooting when inadequate branch memory locations are used for *Steel02* model. The *Reinforcing Steel Material* model used here keeps track of 20 memory branches of loading of the steel material.

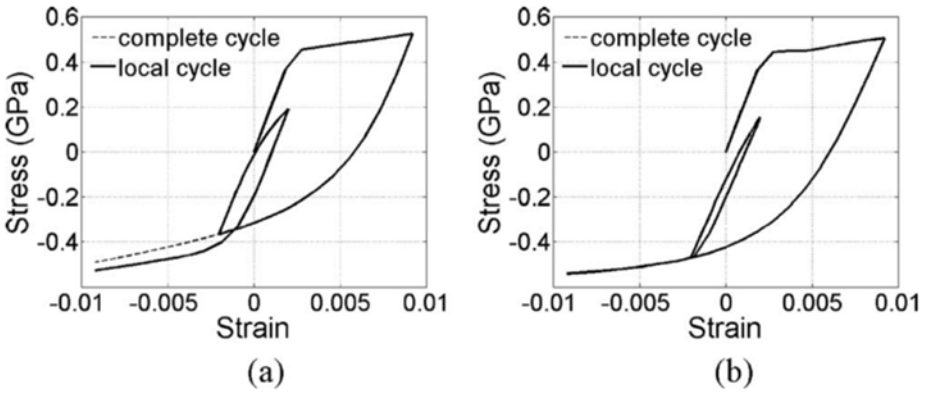

Figure 6-6. Stress overshooting due to (a) 10 memory branches (b) 16 memory branches (Kunnath et al. 2009).

6.3 Concrete Model

The *Concrete02* material model in OpenSees was used here. The model is based on the work of Yassin and Hisham (1994) and uses Modified Kent-Park model equations (see Appendix A.2). The benefits of the *Concrete02* material model is that it can account for:

- The effect of confinement, which is specified by defining a monotonic-loading stress-strain curve that serves as the compression backbone curve for cyclic response;
- The degradation of stiffness in both the unloading and reloading curves at increasing compressive strain;
- Tension stiffening;
- Hysteretic response under cyclic loading;
- Concrete crushing.

The model simulates concrete damage by stiffness degradation when unloading/reloading excursions occur at increasing strain. However, the model does not capture the possible reduction of concrete strength in subsequent excursions at a given strain. The model allows accounting for tension stiffening, which is the ability of concrete to resist tensile stress between cracks, providing additional flexural stiffness. As magnitude of tension stresses increases, more cracks form, reducing the ability to provide tensile stiffness to the concrete. The *Concrete02* model accounts for this phenomena using a linear reduction of tensile strength after fracture strength of concrete is reached.

Additionally, it requires less memory from past stress-strain history than other concrete models, such as the *ConcreteCM* that was also tried but proved to be excessively computationally demanding and did not allow to model the ductile compressive behavior expected for composite sections. The *Concrete02* model only tracks: (1) the stress and strain at the point corresponding to the last model state; (2) the strain at the last unloading point on the compressive monotonic envelope, and (3) the strain difference between maximum previous tensile strain and cracking strain. Further details on the compression and tension behavior of the *Concrete02* model are provided in Appendix A.2.

As shown in Figure 6-7, seven parameters are required to define the *Concrete02* model in OpenSees, namely: the concrete compressive strength, f_{pc}; concrete strain at maximum strength, ε_0; concrete crushing strength, f_{pcU}; concrete strain at crushing strength, ε_u; ratio between unloading slope at ε_U and initial slope, lambda; tensile strength, f_t; and tension stiffening stiffness, E_{ts}.

To illustrate the backbone curve for an unconfined and a confined concrete, the concrete parameters in Table 6-2 were assigned to the concrete model and the curve is shown in Figure 6-8.

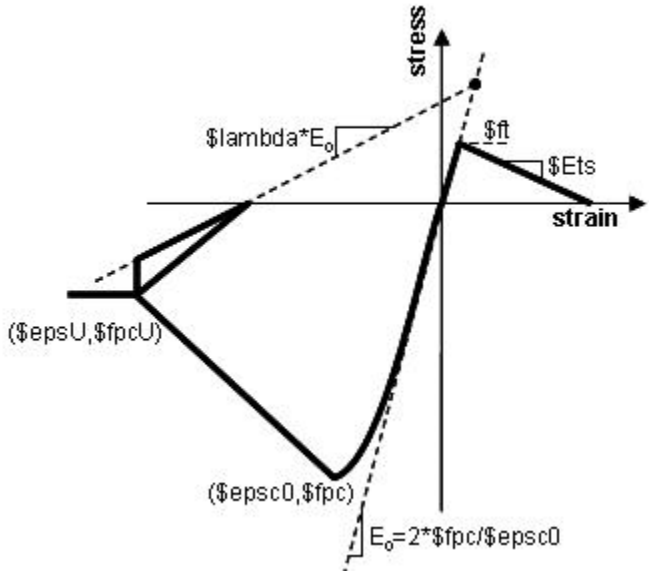

Figure 6-7. *Concrete02* model in OpenSees (McKenna et al. 2016).

Table 6-2. Inputs for unconfined and confined concrete.

Concrete	f'_c (ksi)	E_C (ksi)	ε_0	f_u (ksi)	ε_u	lambda	f_t (ksi)	E_t (ksi)
Unconfined	-7.0	4840	-0.002	-0.8	-0.003	0.1	0.4	200
Confined	-10.21	4840	-0.0042	-10.21	-0.025	0.1	0.4	200

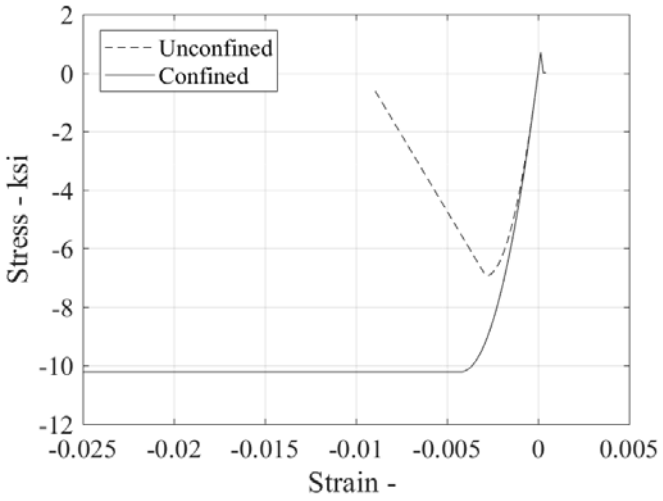

Figure 6-8. Backbone curve for unconfined and confined concrete.

6.3.1 Confined Concrete Model and Properties

The concrete inside composite walls is confined to some degree by the steel plates – particularly the concrete in the half-HSS part of Specimen C-PSW/CF-NB1 wall. The uniaxial stress-strain model for confined concrete in steel tubes developed by Susantha et al. (2001) was used here to determine the values for the parameters of the *Concrete02* material model in OpenSees. The Susantha et al. model was developed analytically and verified against existing experimental results for concrete-filled steel tube columns. Then, a concrete-steel interaction was used to predict the lateral pressure between the steel tube and the concrete (which are both expanding laterally under longitudinal compressive axial stresses), to use in the following empirical formula to calculate the strength of confined concrete:

$$f'_{cc} = f'_c + m * f_{rp} \quad \textbf{(6.15)}$$

where f_{rp} is the maximum radial pressure on concrete depending on the shape of tube as shown in Figure 6-9 and *m* is an empirical coefficient. Also, it was suggested to apply a 0.85 reduction factor for f'_c in this

calculation for f'_{cc}. Based on experiments, the *m* value was found to be in the range of 4-6, but the authors recommended using a value of 4.0 for this parameter. Finally, the Susantha et al. equations recognize that the shape of the cross-section affects the confinement properties of the concrete (Figure 6-9), and alternative confinement equations were provided depending on the shape of the bounding steel (further information on that model is presented Appendix A.3.1). Even though the Susantha et al. model was developed for columns, the model can be applicable to the boundaries of C-PSW/CF walls to locally predict the confined concrete properties of the concrete there.

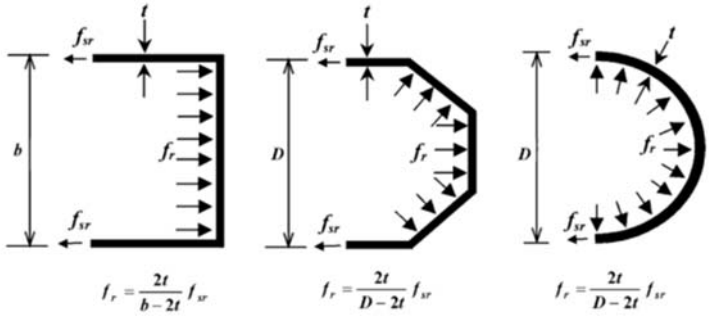

Figure 6-9. Lateral pressure in various sections (Susantha et al. 2001).

6.4 Element Type

As stated before, OpenSees models will be used to run Incremental Dynamic Analysis (IDA) for multiple story coupled composite walls. The material elements described before are used in cross-sections that themselves are part of element of given length for which plastic hinge rotations can be obtained. Building model with 3D element might give more accurate results in terms of global and local responses but it would be substantially more computationally expensive to perform IDA, even for one archetype. Therefore, 2D beam element types are selected here to describe the hysteretic behavior while achieving manageable computational times. For that purpose, for the walls considered here, plastic hinge locations and lengths will be determined, nonlinear elements will be only assigned to these locations, and the rest of the wall will be modeled using elastic beam column elements.

There are two types of nonlinear elements in OpenSees, namely force-based and displacement-based elements. Example of two options for force-based elements are “beamWithHinge” and “nonlinearBeamColumn” elements; and the “dispBeamColumn” is the only displacement-based elements.

Both type of elements allows spread of plasticity along elements. The modelling of these two types of elements, however, is performed differently to obtain a comparable level of accuracy. The theory underlying these two type of elements summarized (and presented in more details in Appendix A.4.1), and the example application described below, were taken from the study of Neuenhofer and Filippou (1997).

Fundamentally, both types of elements require an iteration process for a solution and the main difference is that displacement based methods (a.k.a. stiffness-based methods) iterates from an initial displacements of nodes, while the force based method starts iterations with initial set of nodal forces. Numerical integration is used over a number of integration points inside of the element to determine the physical parameters of interest (e.g., stiffness, force, displacement, and/or others, depending on the type of element). Moreover, to serve a broad range of possible intended applications, OpenSees offers different types of numerical integrations schemes (such as Legendre (default), Lobotto, Radau, NewtonCotes, and Trapezoidal integration rules, to name a few), for both nonlinear element types.

To illustrate the above, Neuenhofer and Filippou (1997) examined a steel beam (Figure 6-10) having 210 GPa elastic modulus and a 21 GPa strain-hardening modulus. The beam was subjected to compressive force of 20 MN and uniformly distributed load in y- and z- directions.

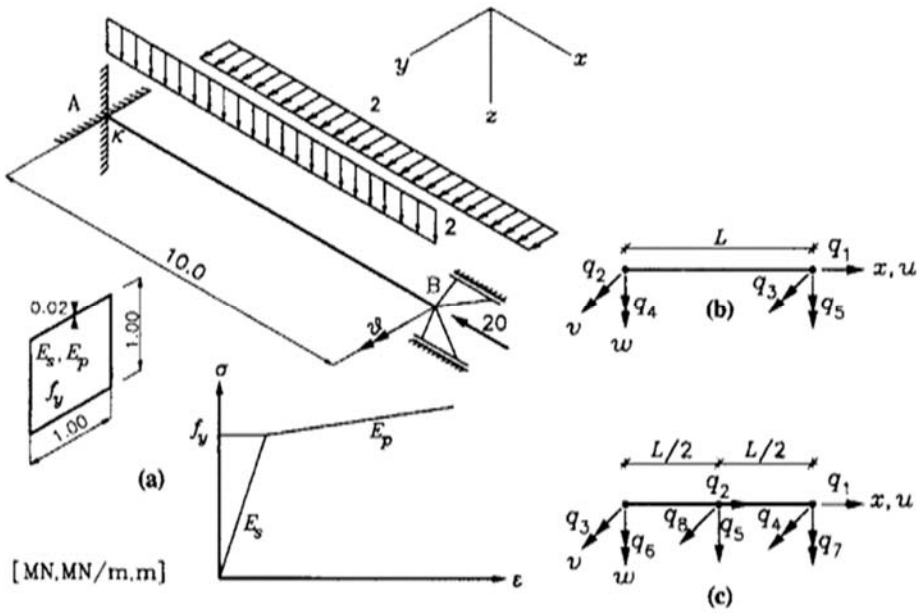

Figure 6-10. a) Sample steel beam b) conventional element c) higher-order element (Neuenhofer and Filippou 1997).

To illustrate the error in the displacement-based elements (stiffness method), the same beam was modeled with conventional force-based (or flexibility-based) beam elements (Figure 6-10b), conventional displacement-based (or stiffness-based) beam elements (Figure 6-10b) and higher-order displacement-based (stiffness-based) beam elements (meaning that there is an additional node in the middle of element in Figure 6-10c) with 3, 5, and 7 Gauss-Lobatto integration points. The error compared with exact solution to governing differential equations in the calculated deflections in z-direction, *v*, and rotation in the same direction, *κ*, are calculated from equations 6.16 and 6.17, respectively.

$$E_v = 100 * \left| \frac{v}{v_{exact}} - 1 \right| \quad \textbf{(6.16)}$$

$$E_\kappa = 100 * \left| \frac{\kappa}{\kappa_{exact}} - 1 \right| \quad \textbf{(6.17)}$$

where E_v and E_κ are the errors in the deflection and rotation in z-direction, respectively; v is the deflection in z-direction and κ is the rotation in z-direction.

The errors observed for the three different situations are shown in Figure 6-11. The two plots on the top row in these figures are for the case of beam with conventional force-based (or flexibility-based) beam elements; the plots on the second row is for beam with conventional displacement-based (or stiffness-based) beam elements; and figures on the bottom are the result of beam with higher-order displacement-based (or stiffness-based) beam elements.

Figure 3-11 shows that, for force-based elements, increasing the number of integration points or number of elements helped to achieve less error in deflection and rotation results. For conventional displacement-based (or stiffness-based) beam elements, the error is not sensitive to the number of integration points, but reduces with the number of elements used, especially for curvature. The higher-order displacement-based (or stiffness-based) beam elements got good agreement with exact result with fewer elements compared to conventional ones.

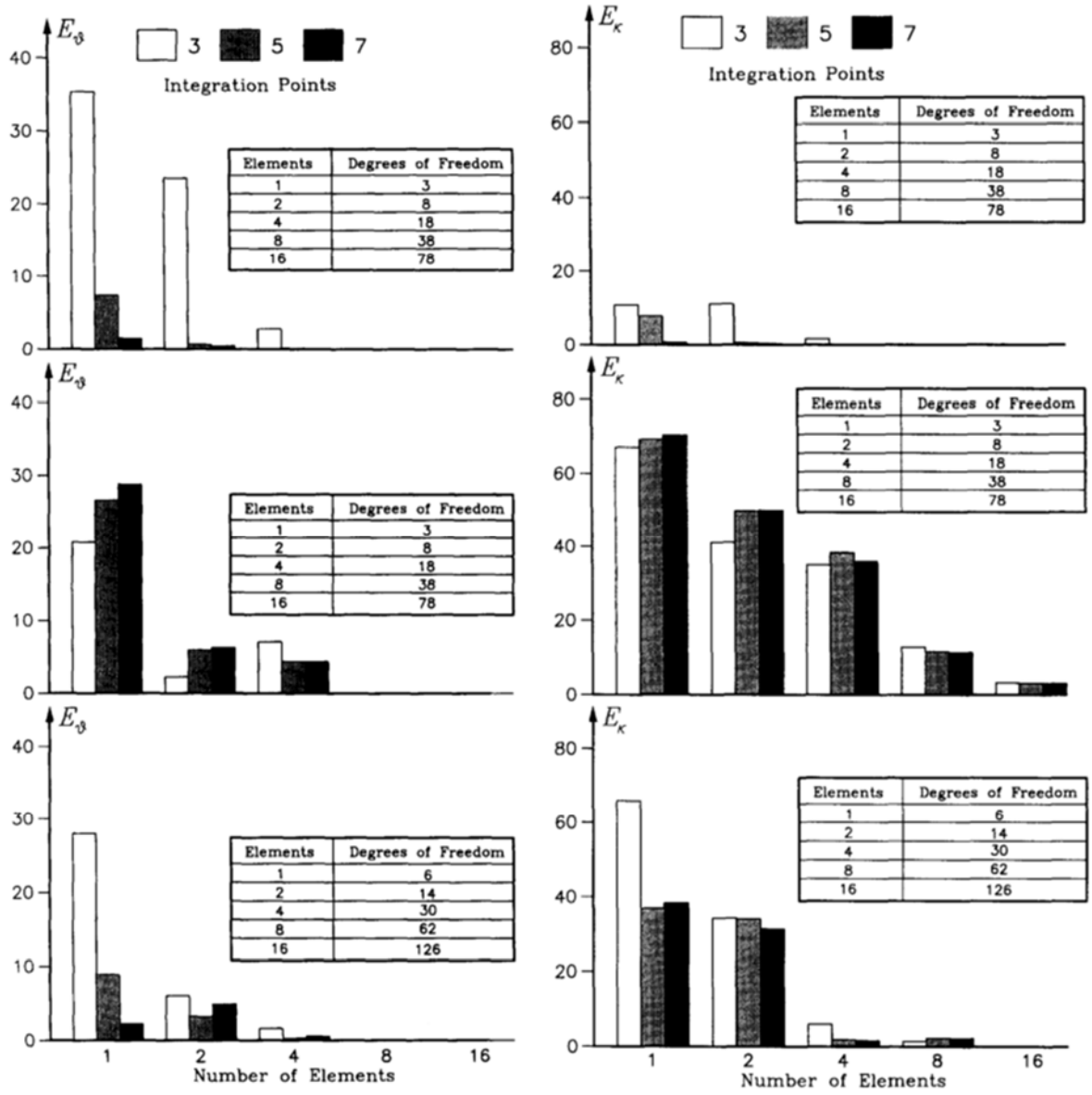

Figure 6-11. Errors for different types of elements: a) Error in displacement in z-direction and b) Error in curvature (Neuenhofer and Filippou 1997).

Neuenhofer and Filippou indicated that since force-based (flexibility-based) elements depend on exact force shape (interpolation) functions, the solution only involves a numerical integration error that can be reduced by increasing the number of integration points (and/or increasing the number of element over a given plastic hinge length). It was also reported that because the displacement interpolation functions of displacement-based (stiffness-based) elements diverge from the exact solution, finer discretization and consequently higher computational effort are required to achieve comparable accuracy.

“This Page Intentionally Left Blank”

SECTION 7
VERIFICATION

7.1 General

The material models described in Section 6 include a number of parameters that must be calibrated based on experimental results. In addition, a number of analyses must be conducted to verify that the composite section and each of its parts behave as expected when using the selected fiber models in OpenSees (McKenna et al. 2016). To do this, in Section 7.2, trial cross-sections are subjected to cyclic loading to observe and verify the expected behavior. Then, in Section 7.3, after a brief review of experimental results obtained by Alzeni and Bruneau (2014), calibration is accomplished for base shear versus tip displacement (Section 7.3.4.4), moment curvature relationship (Section 7.3.4.5), and stresses in cross-section (Section 7.3.4.6) for those results.

Then, calibration was performed for the two different modeling approaches adopted for the parallel IDA analyses to be conducted as part of this study. In the first approach, walls and coupling beams were modelled using a fiber-hinge elements (i.e., distributed plasticity model) with properties obtained from coupon test results and unconfined concrete strength. In the second approach, the walls were modelled with fiber-hinge elements having effective stress-strain curve obtained from Abaqus models, and the coupling beams were modelled with concentrated plastic hinges at their ends using a Modified Ibarra-Medina-Krawinkler Deterioration Model with Pinched Hysteretic Response (MIMKD Model). The calibration work performed with the distributed plasticity model is presented in this section. Similar work performed with the concentrated plasticity models (CPM) is provided in Section 8.

As mentioned in Section 5, the archetypes have two components; walls and coupling beams, and the designed archetypes have two wall configurations. Therefore, three different set of test results were used for verification of the two different element models used to analyze the archetypes. In Section 7.4, the calibration of planar C-PSW/CF wall models is accomplished. Then, calibration of coupling beams are achieved and shown in Section 7.5. Finally, the DPM models is calibrated with test data on C-shaped C-PSW/CF walls in Sections 7.6.

7.2 Analysis on Arbitrary Cross-sections

Before verifying the Alzeni and Bruneau (2014) test data with the OpenSees *Reinforcing Steel Material* model, trial analyses using arbitrary cross-sections were conducted to verify that steel fractures as expected in accordance with the fracture model presented in Section 6.2.3, and that fracture propagates through the cross-section in a logical manner. For that purpose, a 20 in. x 20 in. square cross-section was analyzed (at the base of a 10 ft. cantilever column square cross-sections). First, a solid steel cross-section was considered (Figure 7-1a); then, a composite cross-section was analyzed (Figure 7-1b). A total of one-hundred-and-eighteen layers were used for steel cross section: thirty-eight layers were used along the web of the cross-sections and forty were used through the thickness of top and bottom steel for composite cross section (each flange layer was full width).

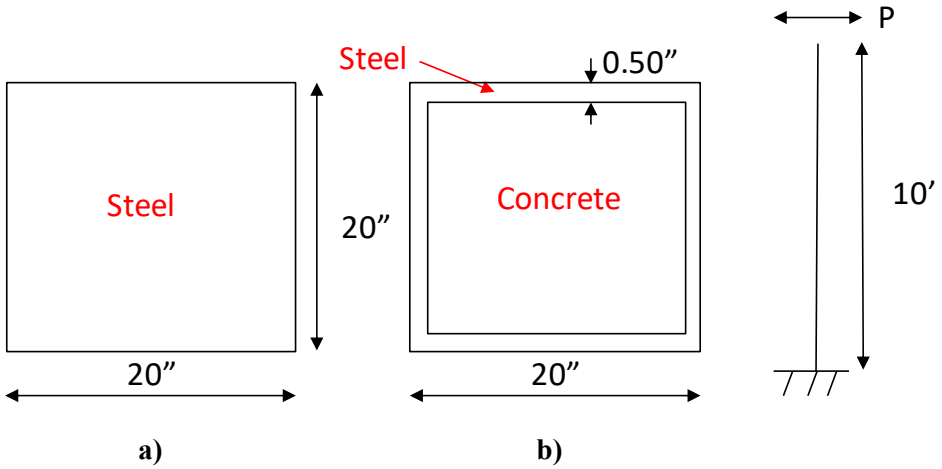

Figure 7-1. Trial cross-sections: a) All-steel; b) Composite concrete-filled square steel tube

The main steel material parameters were defined by the stress-strain curve shown in Figure 6-1 and the parameters in Table 6-1. The fatigue parameters used for these analyses were adopted from Kaufmann et al. (2001) (C_f = 0.21; α = 0.47; C_d = 0.0). The buckling parameters were, however, chosen randomly following the guidance presented in Section 6.2.2 (l_{SR} = 16.0 /; β=1.0; r = 0.4; γ = 0.5). Furthermore, default values were used for the Menegotto-Pinto equation (Menegotto 1973) (RC1 = 0.33; RC2 = 18.0; RC3 = 4.0) and isotropic hardening parameters (a1 = 4.3; limit = 0.01). For simplicity, elastic-perfectly plastic material with 4 ksi compressive strength and no tensile strength were assigned to concrete for the composite cross-section.

For comparison purpose, the same displacement protocol was applied at the top of the column for both the all-steel and the composite cross-sections. It was decided to use the yield displacement, δ_y, of the composite

cross-section for this purpose (recognizing that the yield displacement for the all-steel section would be greater). For the column with composite cross-section, maximum strength was reached at a displacement of 15.8 inches, after which fracture initiated and strength dropped rapidly (analysis stopped with a convergence error at 18 in.) Then, an elastic-plastic bilinear curve was drawn on top of the actual lateral load versus top deflection curve to identify an equivalent yield displacement. The horizontal line was located by visually attempting to make the area between the pushover curve and the bilinear curve the same above and below the line. The resulting equivalent yield displacement was then used to construct a cyclic loading protocol for the trial columns, starting with displacement cycles at an amplitude with $\delta_y/3$, $2\delta_y/3$, and δ_y; and continuing by increment of δ_y, until $10\delta_y$, as shown in Figure 7-6a. Points 1 to 11 shown at the peak of each cycle in Figure 7-2 are used to identify the stress diagrams plotted in the next section. The same loading protocol was applied to both the all-steel and the composite cross-sections. Results for these two cross-sections are respectively shown in Sections 7.2.1 and 7.2.2.

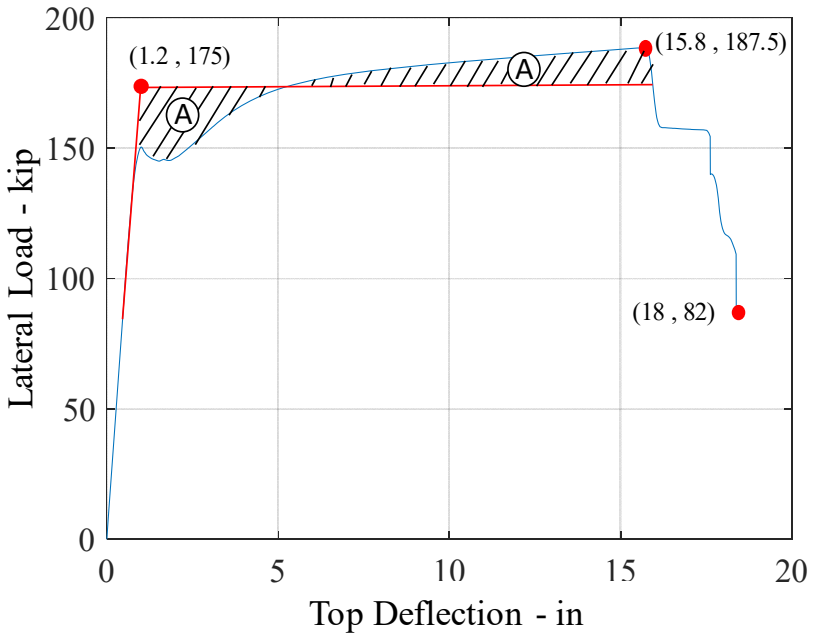

Figure 7-2. Pushover result of trial wall

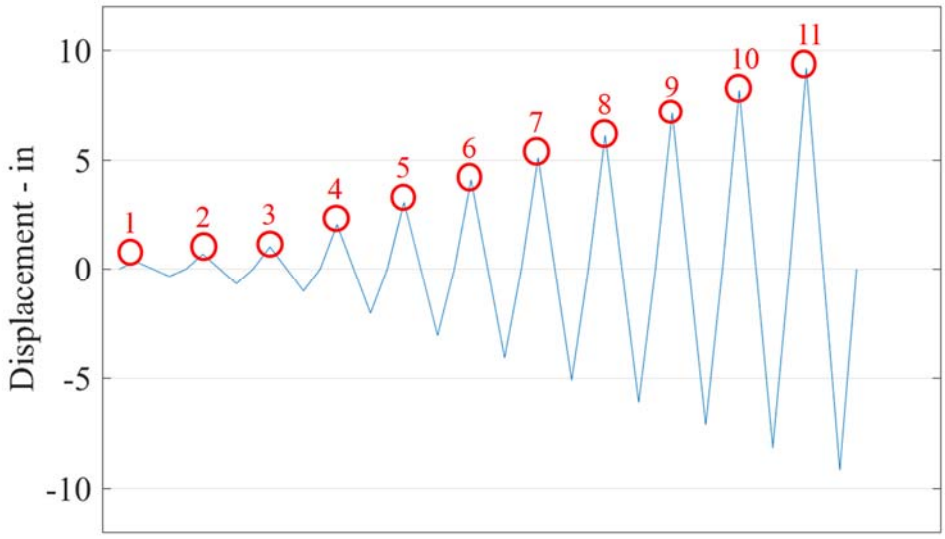

Figure 7-3. Loading Protocol for trial walls

7.2.1 Steel Cross-section

The main reason for analyzing this cross-section is to ensure that the *Reinforcing Steel Material* model in OpenSees behaves as intended and that the neutral axis and the center of gravity continue to coincide through the cyclic loading when only fracture is included in the models (Figure 7-4). Even though the engineering compressive and tensile backbone curves are not symmetric (see Section 6.2.1), the neutral axis should remain close to the center of gravity because the difference is not significant for most of the strain range. Note that outputs of all stresses and strains presented below are in engineering stresses and strains. In addition, analyses are also conducted to verify that the neutral axis shifts when the modeling of buckling is added to the steel material due to the significant loss of symmetry introduced in the stress-strain behavior after bucking.

The stress-strain of the outer most fiber was recorded for the case including fracture-only; the resulting curve is shown in Figure 7-5. It is observed that the tensile and compressive strains in a given cycle are the same for both true and engineering strain except for a small difference observed in the last cycle before fracture. True and engineering stresses are also close to each other with insignificant differences observed at larger strains. The reason for that small difference is that the maximum engineering stresses in compression and tension in large strains are not the same for the *Reinforcing Steel Material* model. Overall,

Figure 4-5 suggests that engineering stresses are not significantly different from true stresses up to fracture for the range of inelastic action of interest here.

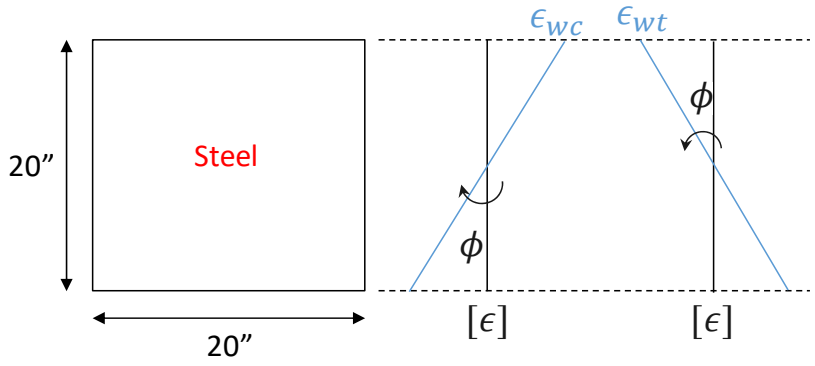

Figure 7-4. Expected behavior of steel cross-section

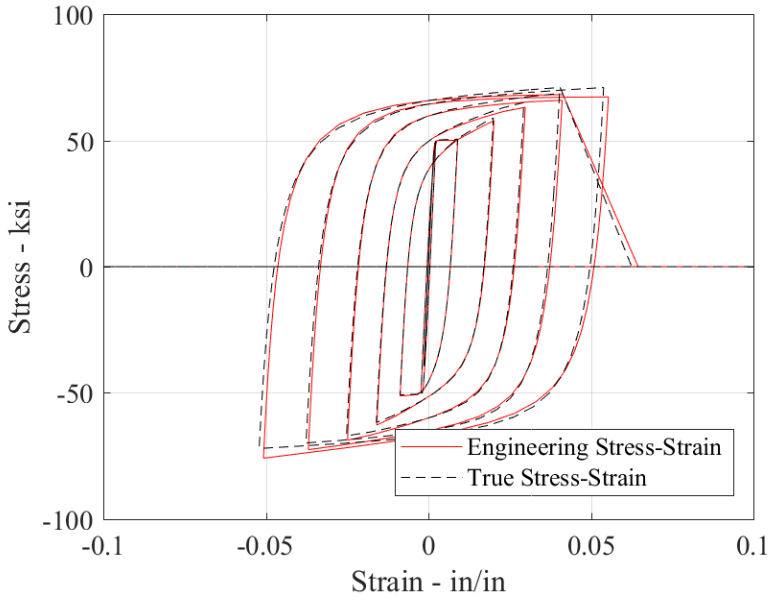

Figure 7-5. Stress-strain curve of outer most fiber in steel section for fracture-only case

The results of cyclic analysis for the column having a steel cross-section are shown in Figure 7-6a for the case considering fracture, and in Figure 7-6b for the case considering both fracture and buckling included. Since the loading protocol is the one derived for the composite cross-section, behavior remained elastic up to the displacement of $2\delta_y$ defined above. Then, in the fifth cycle, the section in both cases started to yield. In the next (sixth) cycle, the compressive steel stress in the buckling-included case reduced due to buckling and stress in the fracture-only case strain-hardened. The stresses in the buckling-included case started to

strain harden in the seventh cycle; and fracture initiated in the ninth cycle. On the other hand, in the fracture-only case, strain hardening started in the 8th cycle and fracture started in the next cycle.

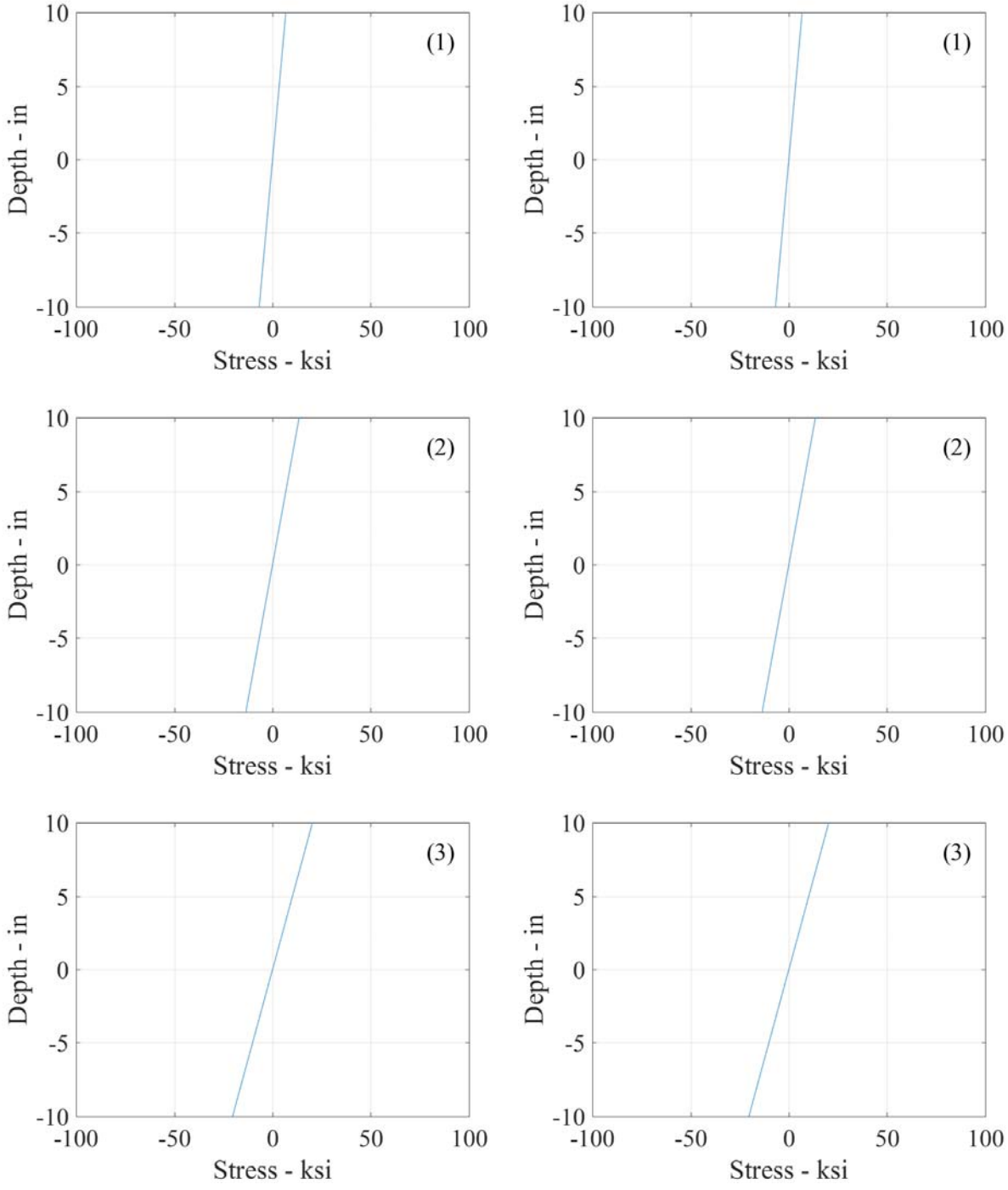

Figure 7-6. Steel stresses in the cross-section at each peak displacement, considering: a) fracture-only b) fracture and buckling

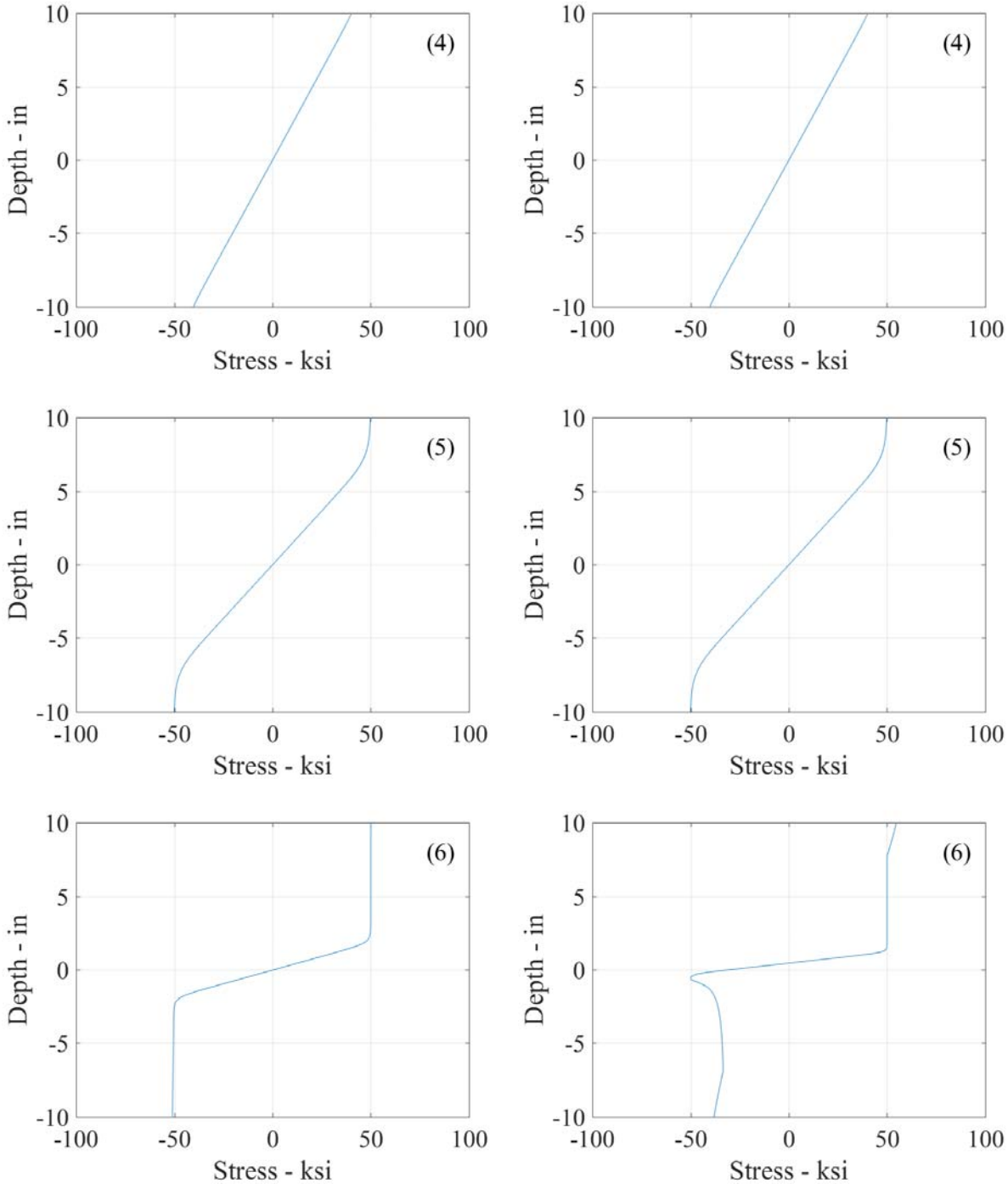

Figure 7-6. (Continued)

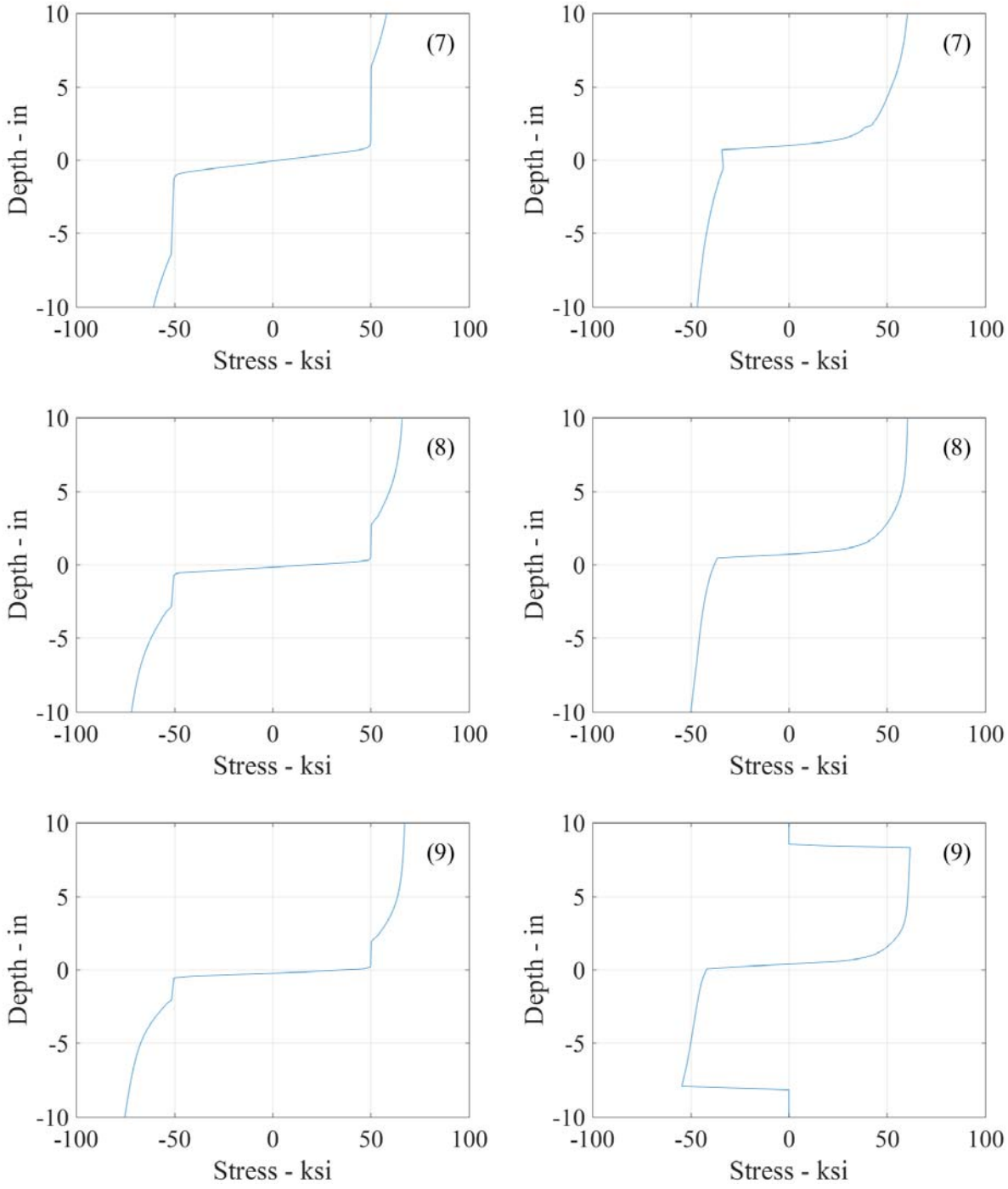

Figure 7-6. (Continued)

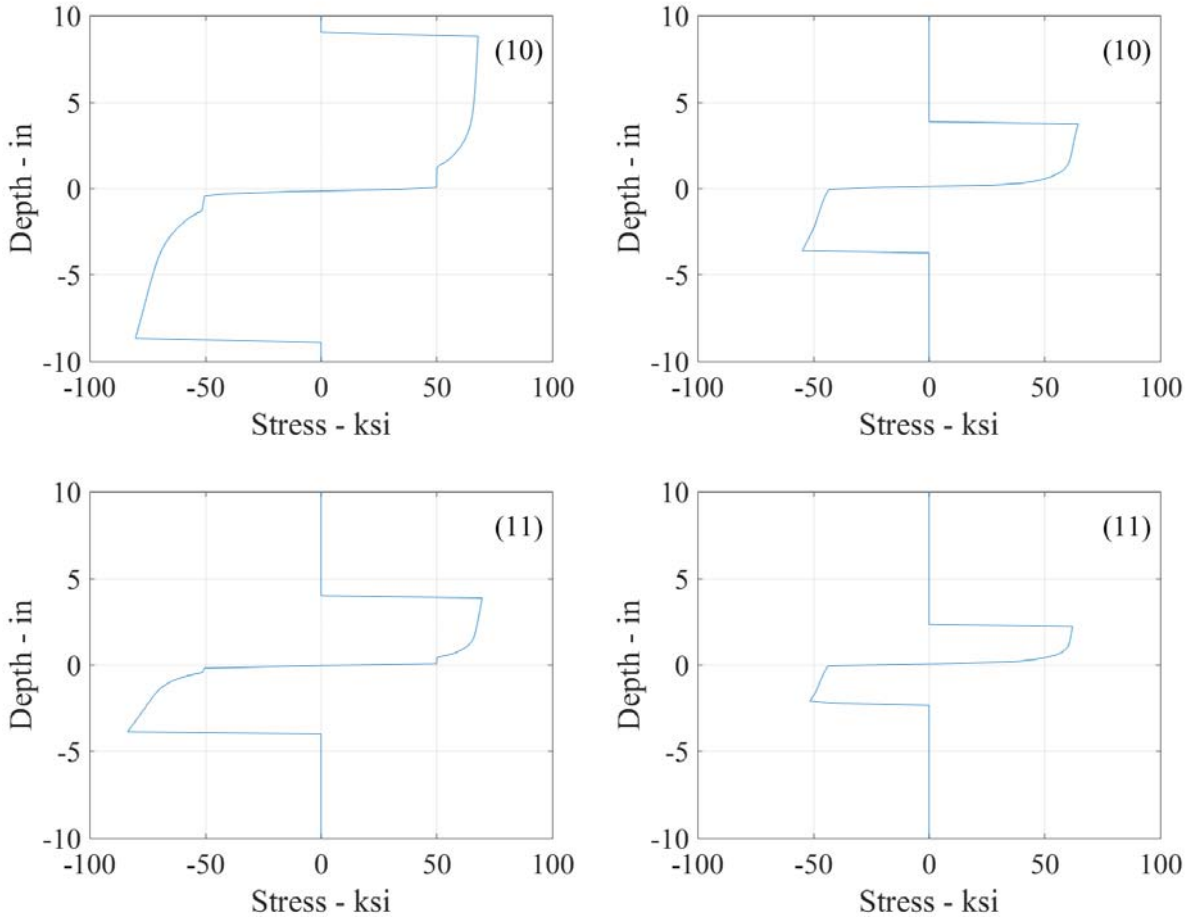

a) **b)**

Figure 7-6. (Continued)

7.2.2 Composite Cross-section

The stress strain behavior of the composite cross-section shown in Figure 4-1b was also investigated. The purpose of this study was: (i) to verify that the *Reinforcing Steel Material* model still behaves as expected when part of the composite section fractures (focusing also on crack propagation along the cross-section after the initiation of fracture; (ii) to verify that the cyclic stress-strain behavior of the concrete material behaved as expected, and; (iii) to confirm that the concrete and steel shared the same neutral axis on strain diagram throughout the range of response, as expected when full composite action is assumed.

The composite section is made of concrete and steel. Even though they have different strength and stiffness, the condition of composite behavior requires they share the same strain diagram and neutral axis along the entire cross-section. However, due to the fact that concrete has a fundamentally different response in

compression and tension, the neutral axis changes position along the height of member – more significantly so upon load reversal – with larger tension strain than compressive strain for a given curvature (Figure 7-7).

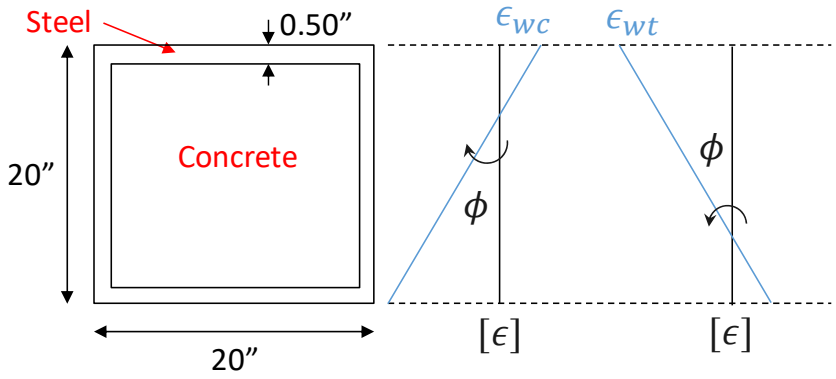

Figure 7-7. Expected behavior of composite cross-section

Here, to verify cyclic behavior of the composite cross-section, the same loading protocol used previously (Figure 7-3) was applied to the composite section (having the cross-section shown in both Figures 7-1b and 7-7). For simplicity, the *Concrete02* material model with elastic-perfectly plastic strength in compression and 10% of compressive strength for cracking strength with linear tension stiffening in tension (increase in strength due to steel confinement was not considered in this study) was assigned to concrete layers in the cross-section.

Figures 7-8a and 7-8b show the results from cyclic loading of the composite section for the cases of fracture-only and fracture-and-buckling, respectively. Since the loading protocol was derived from this cross-section, it stayed elastic up to the δ_y cycle. Then, in the fourth cycle, stresses in the fracture-only case strain-hardened; in comparison, the steel stress in the buckling-included case reduced due to buckling. The stresses in the buckling-included case started to strain hardened in the next excursions until fracture initiated in the seventh cycle. The extent of fracture in the cross-section increased in each cycle, until the last cyclic loading case considered at a displacement of $9\delta_y$ (point 11 in the loading protocol). In the fracture-only case, however, the initiation of fracture was at the eighth step. Then, it continued fracturing until the analysis stopped. In order to completely understand how fibers are eliminated from analysis using the low cycle fatigue model, the strains and stresses of the outermost fiber in the cross-section were tracked for the fracture-only case, and cumulative damage was calculated as explained in Appendix A.1.3; results are shown in Table 7-1. The cumulative damage for the first two cycles is zero as the cross-section was elastic. Starting from the 3rd cycle, damage started to accumulate until the cumulative damage exceeded “1” during the cycle 8, and fracture initiated as observed at the top edge of the cross-section in part 8 of Figure 7-8a.

Table 7-1. Low cycle fatigue calculation for fracture-only case

Cycle No	Δε	Δσ	$\Delta\varepsilon_p$	Damage	Cumulative damage
1	1.30E-03	37.72	-2.91E-06	0.00	0.00
2	2.66E-03	75.98	4.25E-05	0.00	0.00
3	5.68E-03	100.29	2.22E-03	0.0001	0.0001
4	2.90E-02	114.94	2.50E-02	0.02	0.0201
5	5.36E-02	131.02	4.91E-02	0.09	0.11
6	8.45E-02	136.94	7.97E-02	0.25	0.37
7	1.11E-01	140.48	1.06E-01	0.47	0.83
8	8.9E-02	27.00	8.81E-02	0.16*	1.0*

* Fractured before completion of this cycle, which is why damage is smaller than during previous cycle.

In addition to stress diagrams in Figure 7-8, the stress-strain of the outer most fiber was recorded for the fracture-only and both fracture-and-buckling included cases. The resulting curves are shown in Figure 7-9. As expected, the compressive strains are smaller than tensile strain and fracture occurred in tension after repeated cycles in Figure 7-9a. The same phenomenon is observed for both fracture-and-buckling included case as shown in Figure 7-9b.

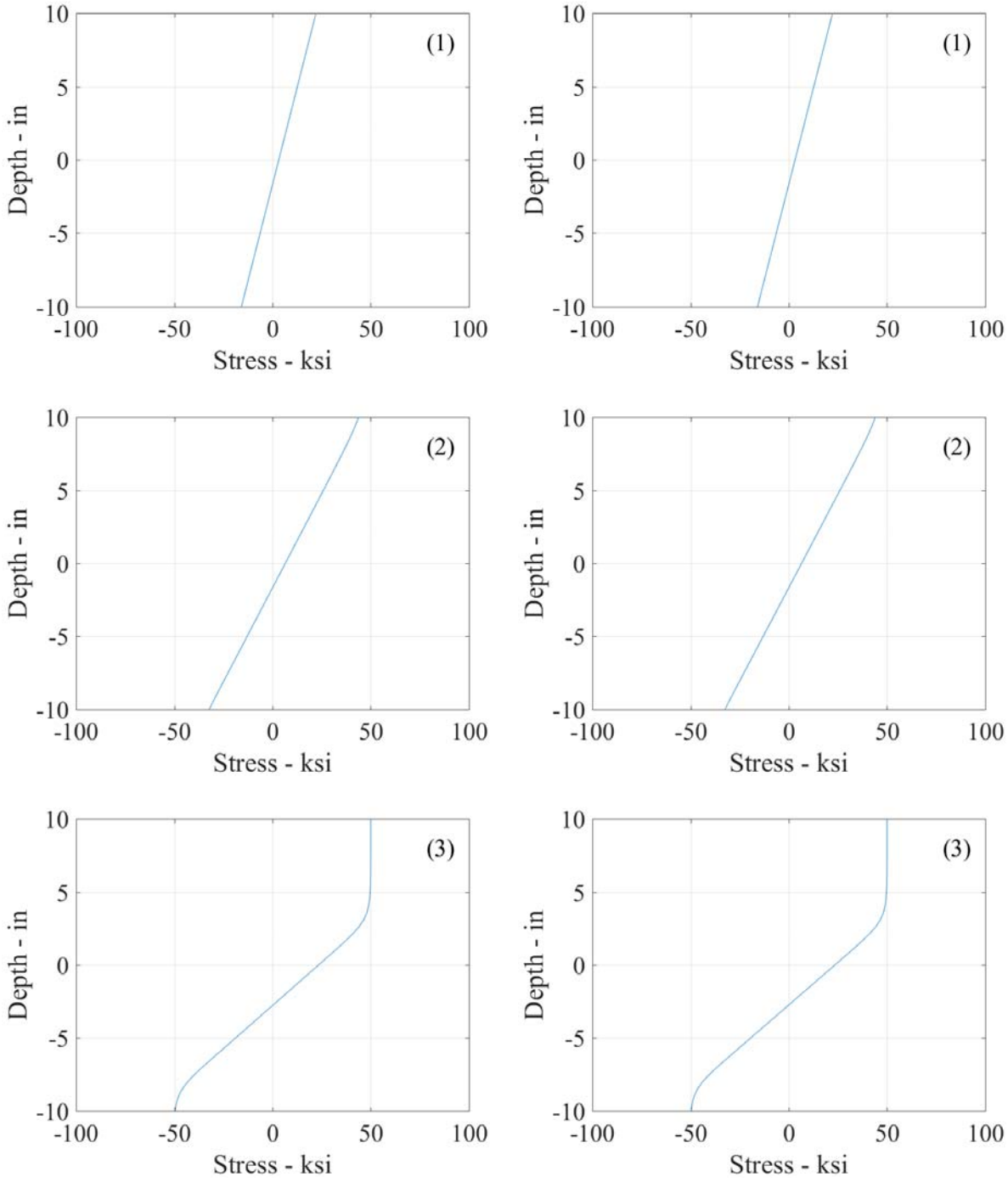

Figure 7-8. Steel stresses in the cross-section: a) fracture-only included; b) both fracture-and- buckling included cases

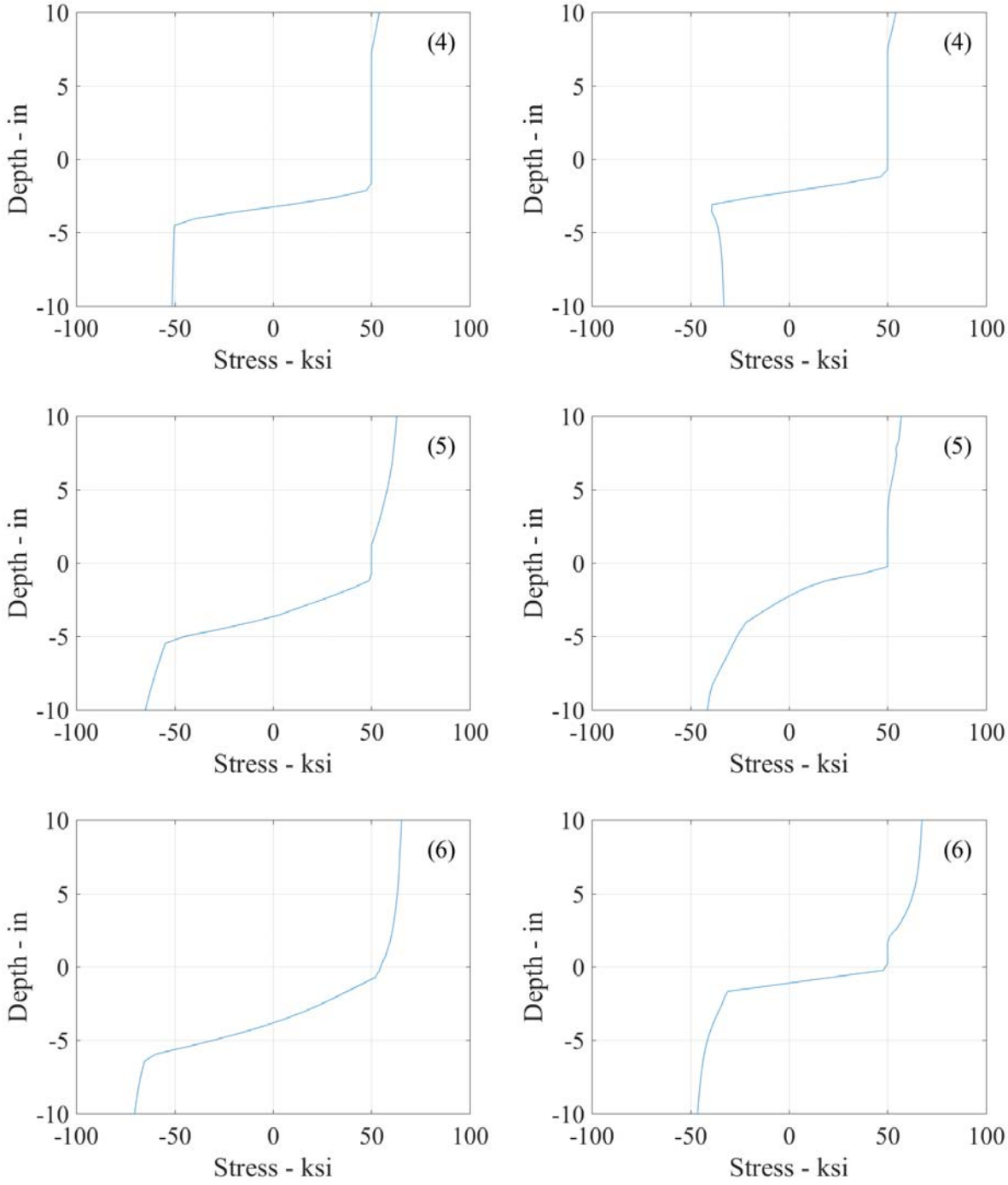

Figure 7-8. (Continued)

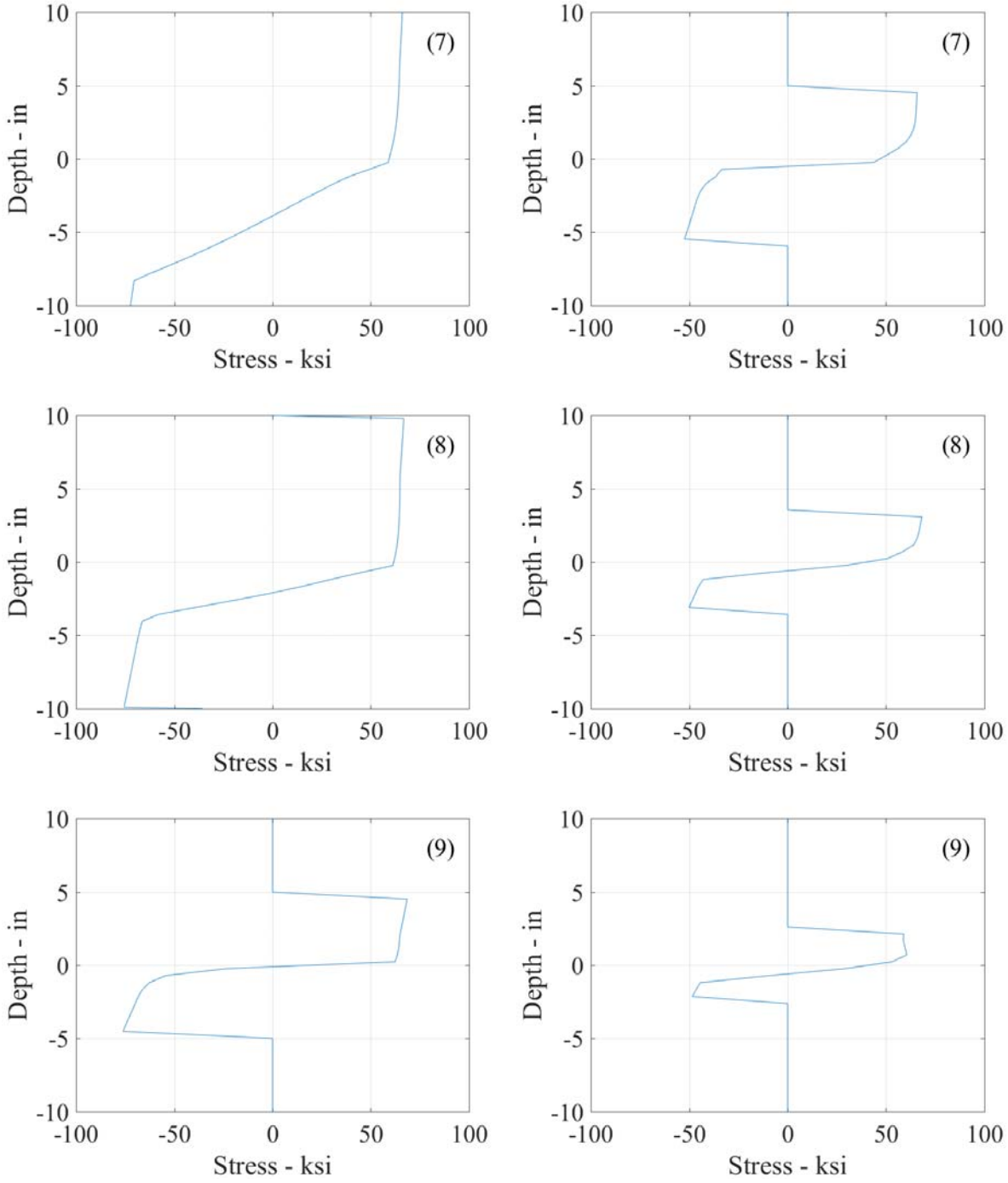

Figure 7-8. (Continued)

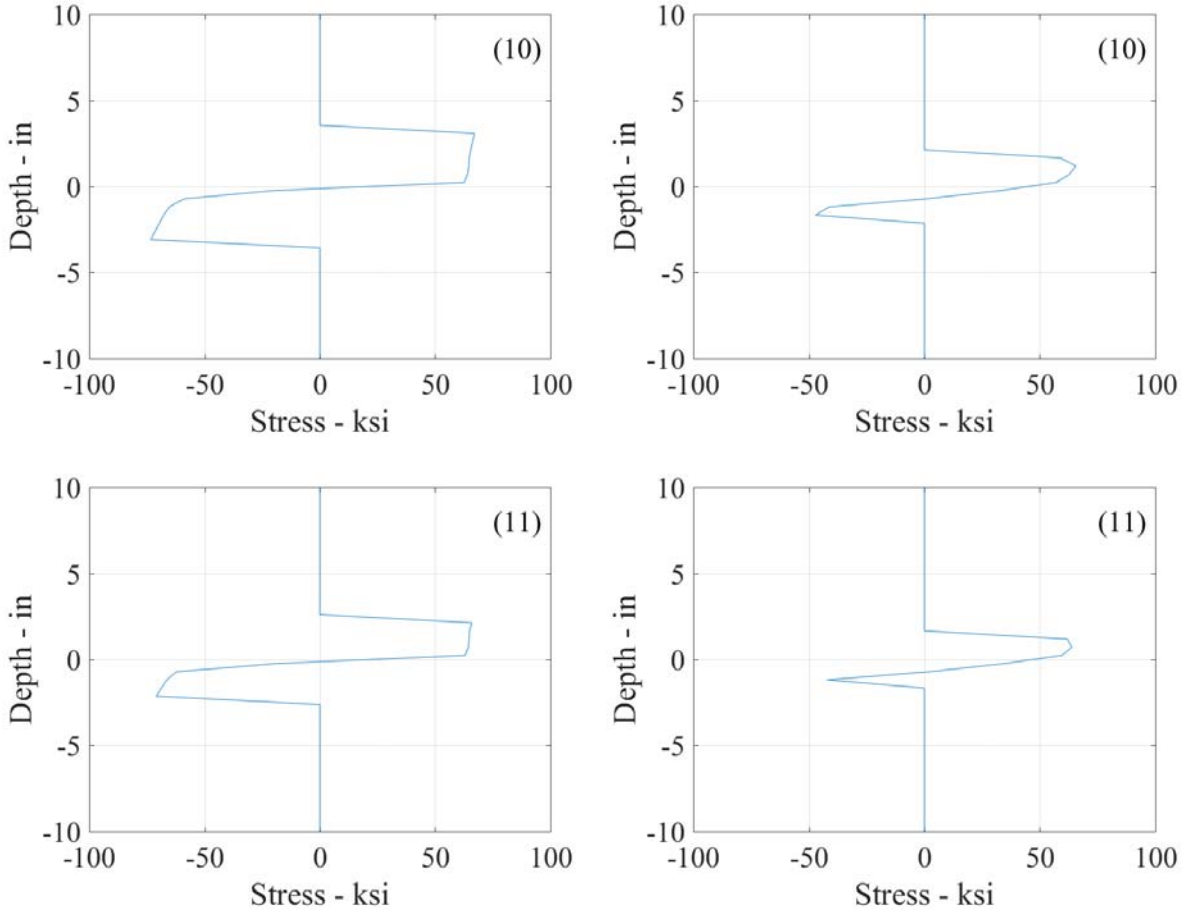

a) b)

Figure 7-8. (Continued)

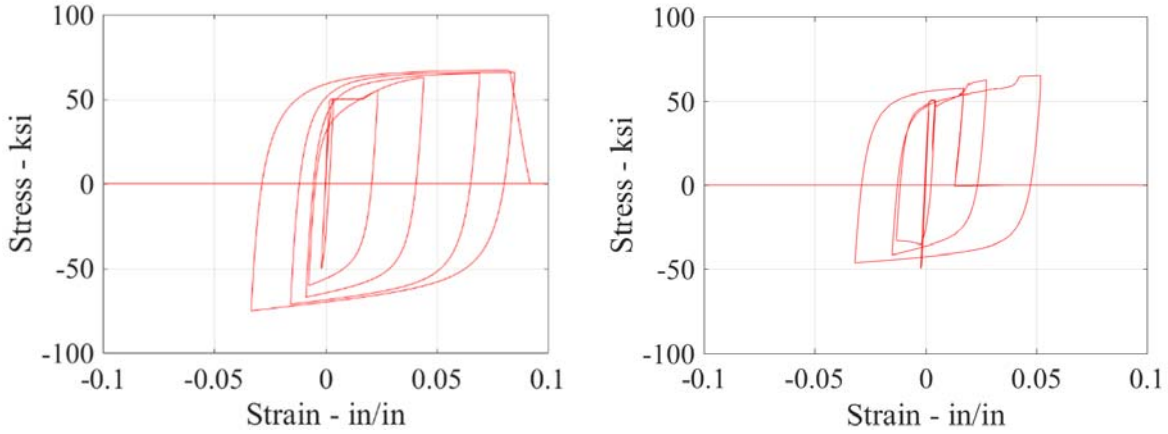

a) b)

Figure 7-9. Stress-strain curve of outer most fiber in the composite section for a) fracture-only included and b) both fracture-and-buckling included cases

Comparison of steel and concrete stress distributions along the cross-section throughout the cyclic loading is shown in Figures 7-10 and 7-11, respectively. Results are shown for the fracture-only case. Figure 7-10 shows the strains diagram along the cross-section through the cyclic loading history; it is observed that both steel and concrete share the same neutral axis (strain diagrams at each peak displacements are superposed for both steel and concrete) and that full composite action is maintained throughout response. However, the stress diagrams in Figure 7-11, after multiple cycles, could inadvertently lead to a different conclusion and require additional explanations.

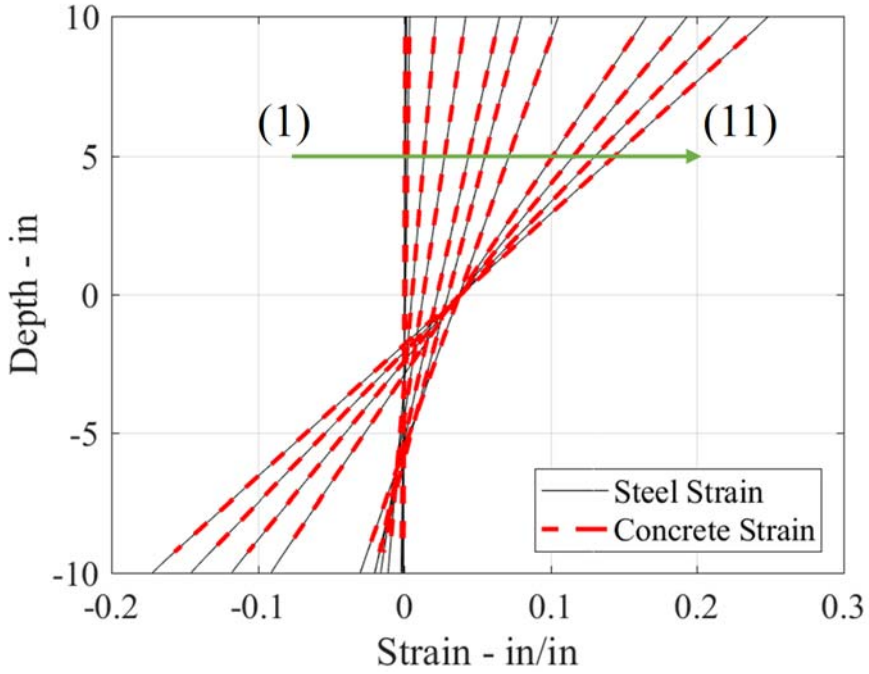

Figure 7-10. Strain diagram for all peak cycles

In the plastic range or response, residual stresses are introduced in the cross section when unloading from a previous inelastic excursion; these add to the steel stresses developing in each peak cycle. Keeping in mind that, in accordance with the concrete model presented earlier (Section 6.3), concrete reloads from where it unloaded in a previous cycle, after some large inelastic excursion, not all concrete is necessarily in compression under compressive strains. This is why concrete stresses in a given layer are sometimes shown as zero at the peak of a cycle even though the steel at that same layer is in compression, as observed in the latter part of Figure 7-11. Moreover, it is observed that before the fracture of steel, the effective area of concrete constantly decreases. Once steel fractures, the neutral axis moves closer to the center of the cross-section, engaging more concrete in compression to resist the cyclic loading.

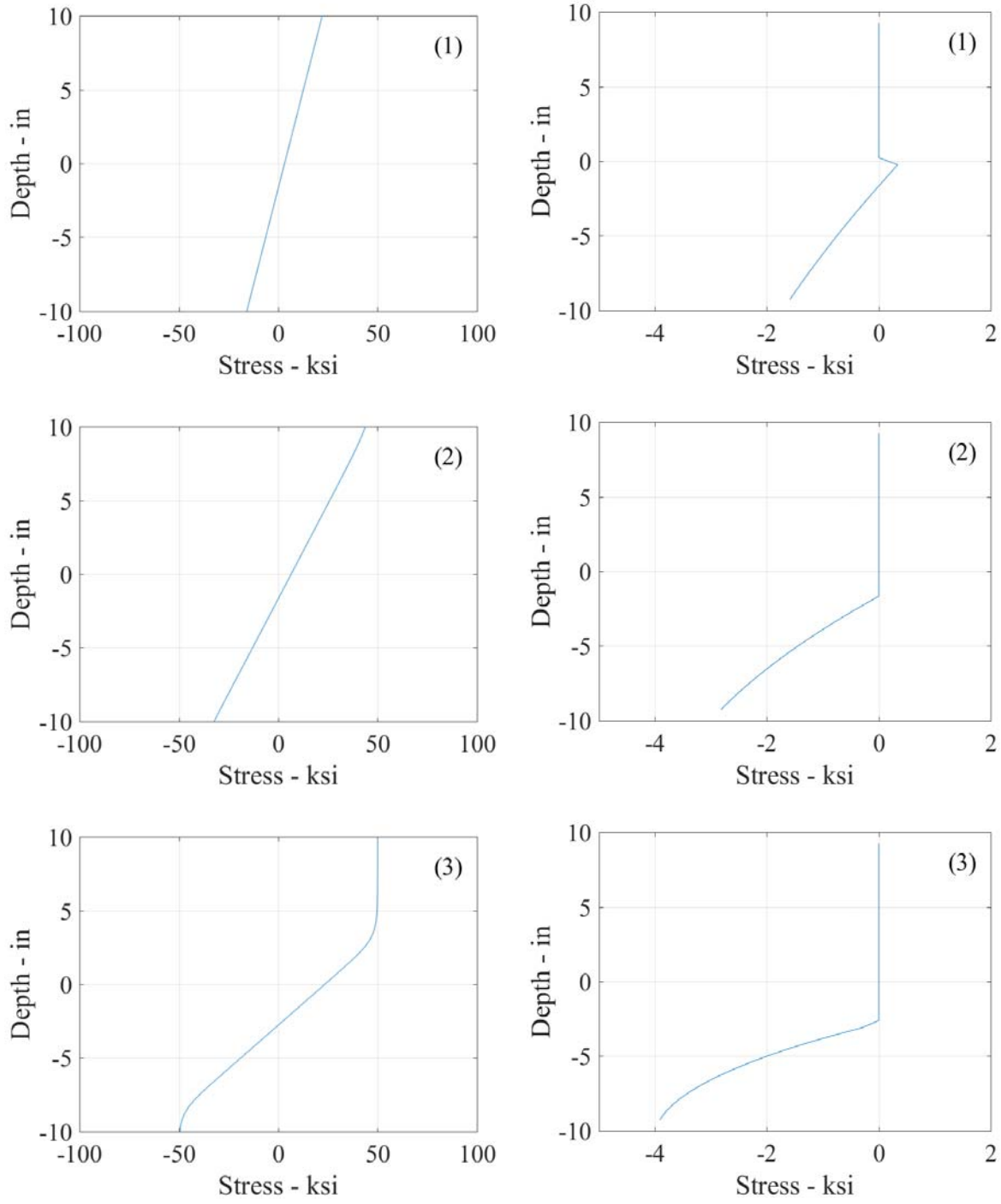

Figure 7-11. Stresses of a) steel; and b) concrete fracture-only cases in the composite cross-section

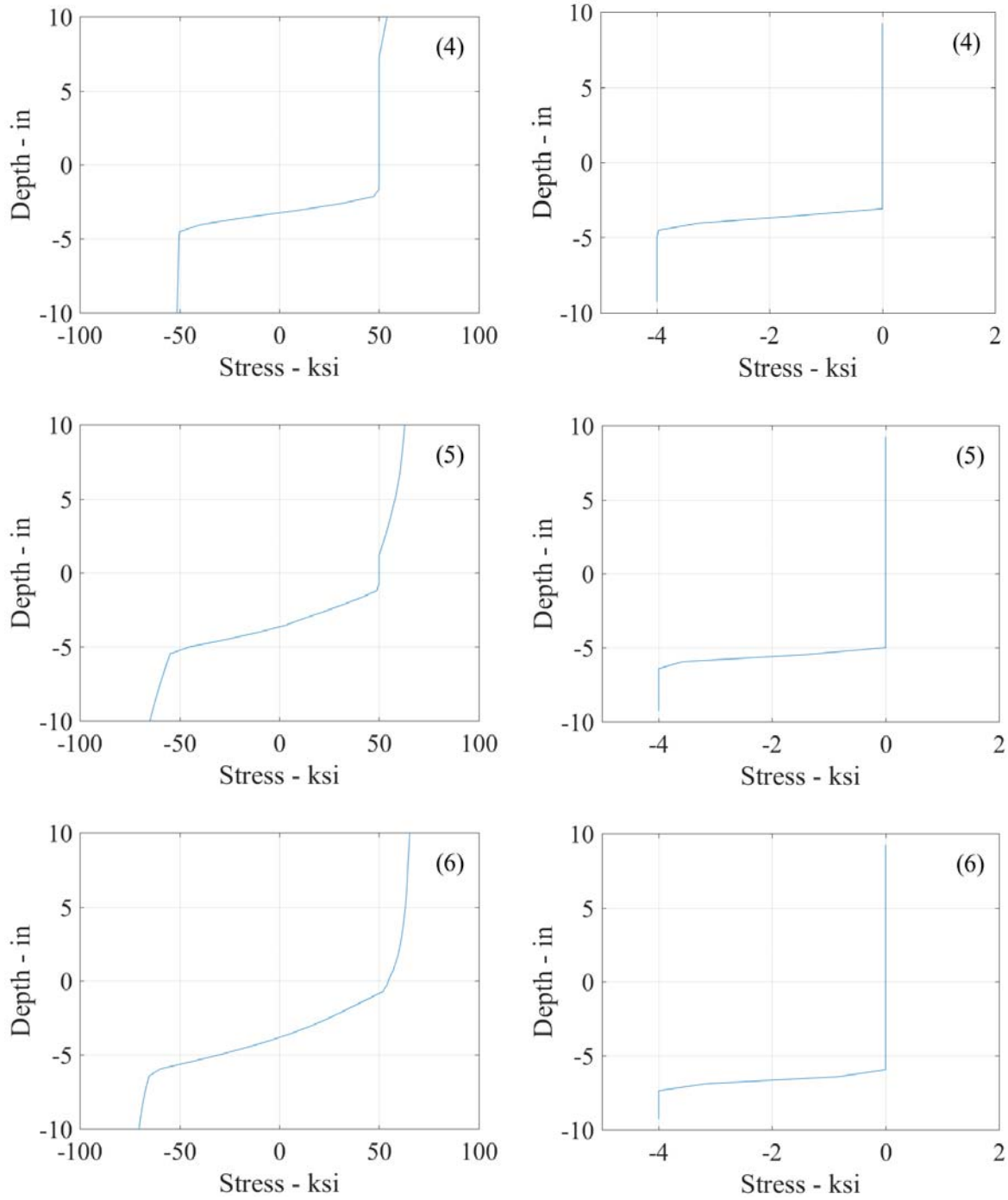

Figure 7-11. (Continued)

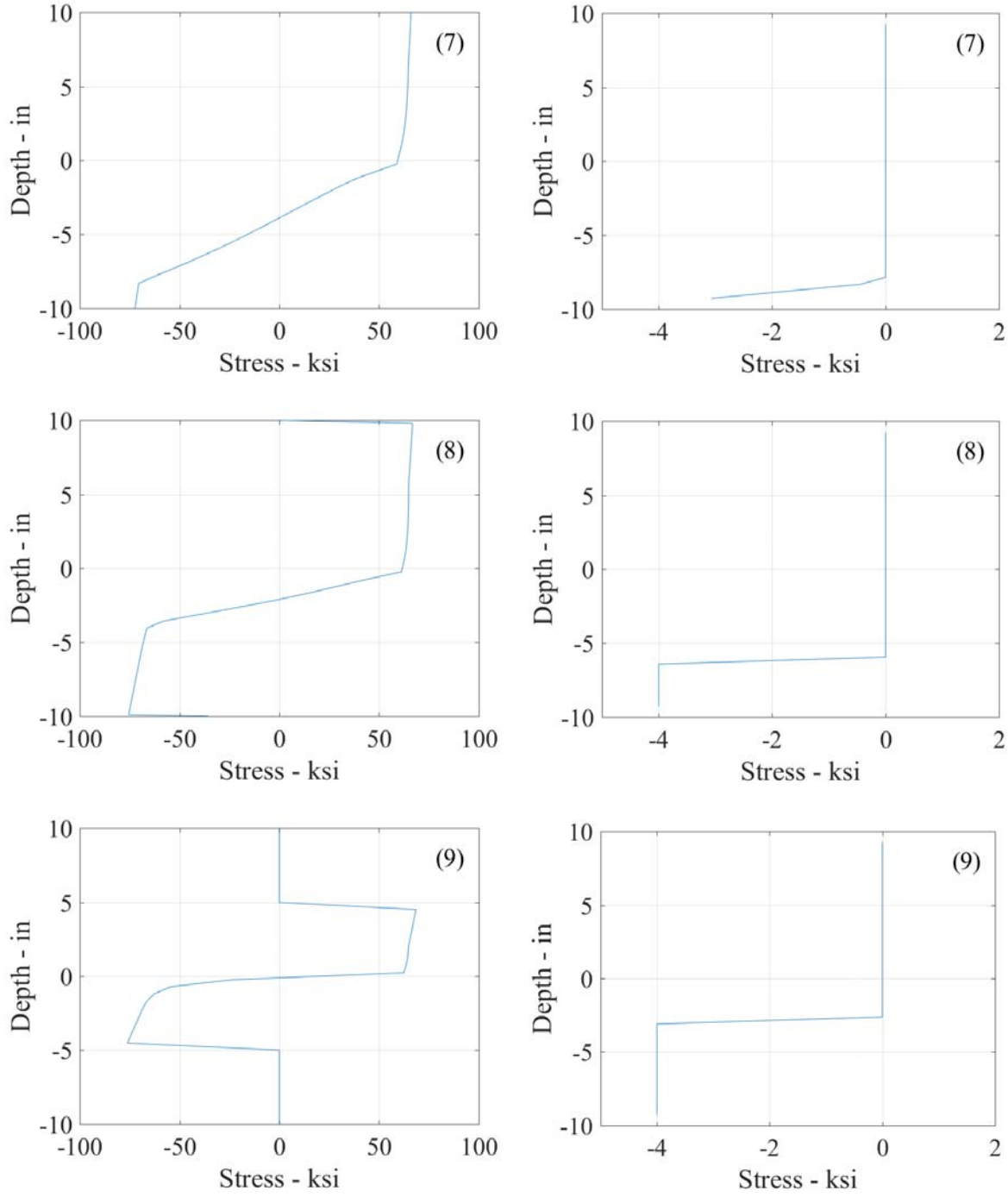

Figure 7-11. (Continued)

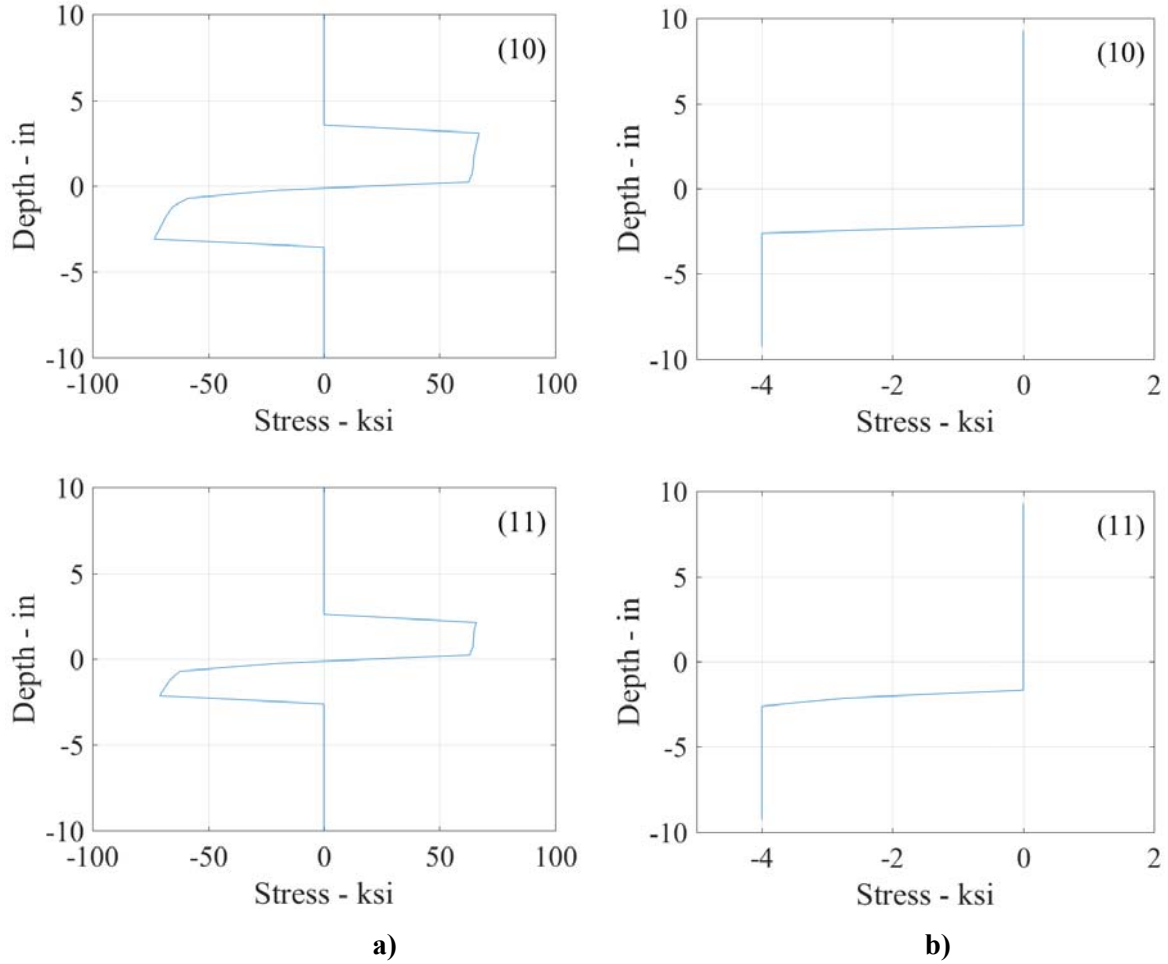

Figure 7-11. (Continued)

7.3 Test of Planar C-PSW/CF Walls With Round Ends (Alzeni and Bruneau 2014)

Alzeni and Bruneau (2014) have tested four large scale C-PSW/CF-Wall in the Structural Engineering and Seismic Simulation Laboratory (SEESL) at the University at Buffalo. Two specimens were defined as C-PSW/CF walls having no boundary elements (Group NB), and two as C-PSW/CF walls having boundary (Group B). In that later case, two large concrete-filled HSS of diameter greater than the thickness of the rest of the wall were used as the boundary elements. The C-PSW/CF-NB specimens were used here for calibration of the material model, as they are closer in cross-section to the wall specimens of interest here. Validation of the OPENSEES models was done with one of the two C-PSW/CF-NB specimens, identified as Specimen C-PSW/CF-NB1, due to the similarities in expected behavior and tie spacing with the types of walls that will be used to conduct IDA.

The cross-section of C-PSW/CF-NB1 specimen is shown in Figure 7-12. The C-PSW/CF-NB specimens were composed of double web skin plates having thickness, t, 5/16" and width, w, of 40", connected by circular tie bars spaced equally in both horizontal and vertical directions at a spacing, S, equal to 8" and 12" for Specimens C-PSW/CF-NB1 and C-PSW/CF-NB2, respectively. The ends of the specimens were made of half HSS 8.625x0.322 sections (of diameter equal to the thickness of the rest of the wall) to avoid the premature failure of the cross-section's corner welds due to concentration of stresses that has been observed in prior research for rectangular sections (e.g., Alzeni and Bruneau, 2014; El-Bahey and Bruneau, 2010 and others). The C-PSW/CF-NB walls had a total width, W, of 48.625" (40" deep web plus two half-HSS 8.625×0.325 of 8.625" diameter) and total thickness, b, of 8-5/8". Also, the height of both specimens was 10 ft. above the top of foundation, resulting in a wall aspect ratio (height to total cross-section depth), H/W, of 2.56.

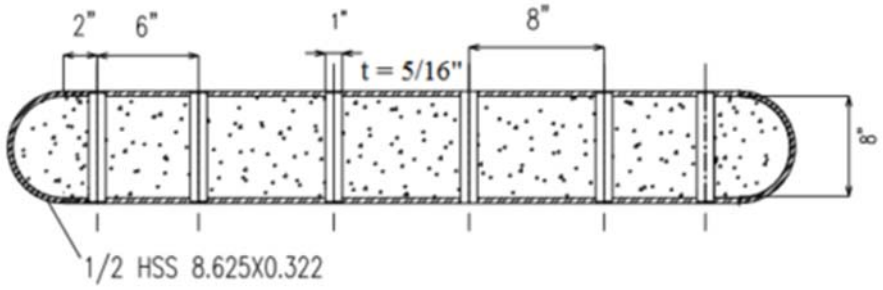

Figure 7-12. Cross-section of C-PSW/CF-NB1 Wall (Alzeni and Bruneau 2014).

In addition, as part of the test setup, each wall specimen was continuous into a reinforced concrete foundation designed to transfer forces from the specimens to the strong floor of the laboratory. This foundation was connected to the strong floor by sixteen DYWIDAG bars pre-tensioned to prevent uplift of the concrete base and develop friction resistance to resist lateral loads. The thickness of the 60"x144" concrete base was 24".

7.3.1 Material Properties

7.3.1.1 Concrete Material

Self-consolidating concrete (SCC), with a prescribed strength of 4 ksi, was used in all specimens (for the wall composite cross-section as well as for the wall's foundation). Also, three standard cylinders, 6" in diameter and 12" in. height, were taken. After at least 14 days of curing, the cylinders were tested on the same day as testing of the specimens. The maximum strengths from cylinder test taken from the concrete

batch of C-PSW/CF-NB1 specimen were measured to be 6780, 7140, and 6900 psi and their average strength of 6940 psi was considered in OpenSees models.

7.3.1.2 Steel Material

For each specimen tested by Alzeni and Bruneau, two coupons were taken both from the steel plates of the web of the wall and from the HSS. All coupon tested exhibited similar stress-strain curve and maximum elongation, and one representative coupon test result is shown in Figures 7-13a and 7-13b for the web steel and HSS steel in the C-PSW/CF-NB1 specimen, respectively. The average yield strength of two coupons taken from web steel was 62.5 ksi and the average tensile strength was 73.75 ksi (for coupon results of 64 and 61 ksi yield strengths and 77 and 71.50 ksi tensile strengths) with maximum elongation of 23%. The average yield strength measured for the HSS steel was 43.75 ksi, with 62.13 ksi tensile strength (for coupon results of 46 ksi and 42 ksi for yield strength and 65 and 62 ksi for tensile strength), with maximum elongation of 21%. However, the HSS steel did not show a yield plateau.

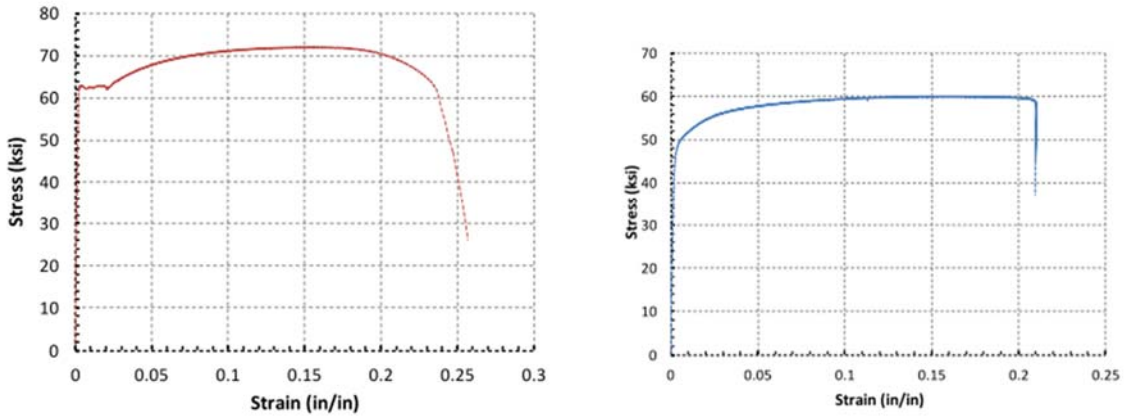

a) **b)**

Figure 7-13. Stress-strain average coupon results for specimen C-PSW/CF-NB1 a) web steel and b) HSS steel Coupon test results (Alzeni and Bruneau 2014).

7.3.2 Instrumentation

The C-PSW/CF walls were instrumented with strain gauges to measure the propagation of yielding along the widths of the walls, displacement (linear) potentiometers to measure rotations near the base to obtain moment-curvature relationships, and string potentiometers to measure the wall displacements along the height of the wall.

Strain gauges were placed in the second tie row and in between second and third tie rows, as shown in Figure 7-14. Also, a half dozen displacement potentiometers were mounted up to 2 feet on both the west and east side of the boundary elements of the walls as shown in Figure 7-15. Although not shown in Figure 7-15, two string potentiometers were also used to measure average rotation over a height of 30" at the base of the wall. Moreover, five string potentiometers were placed horizontally to measure the lateral deflected shape of the walls at various places along the height.

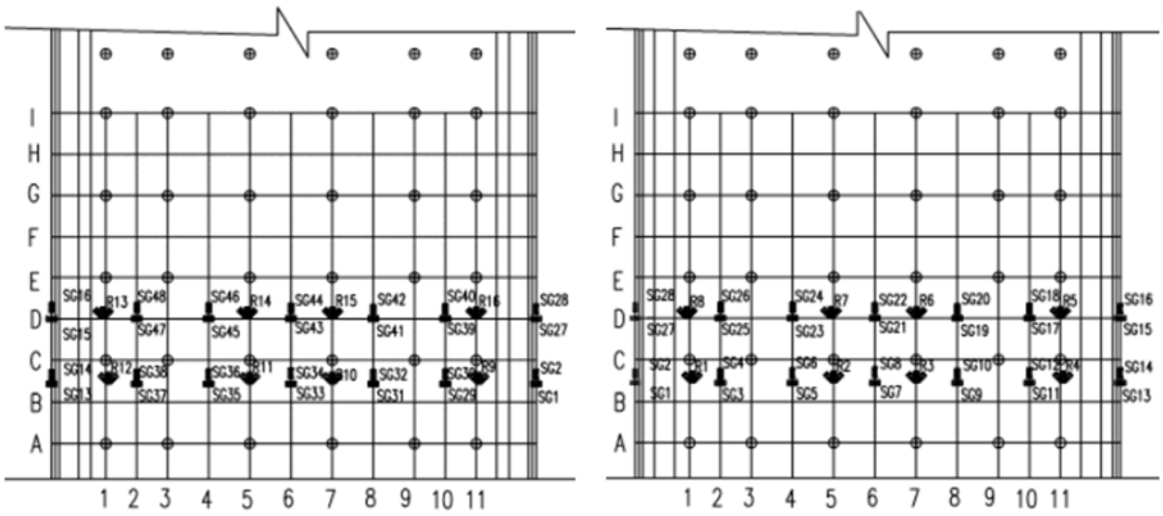

a) **b)**

Figure 7-14. Strain gauge configuration: a) South-North view, b) North-South view (Alzeni and Bruneau 2014).

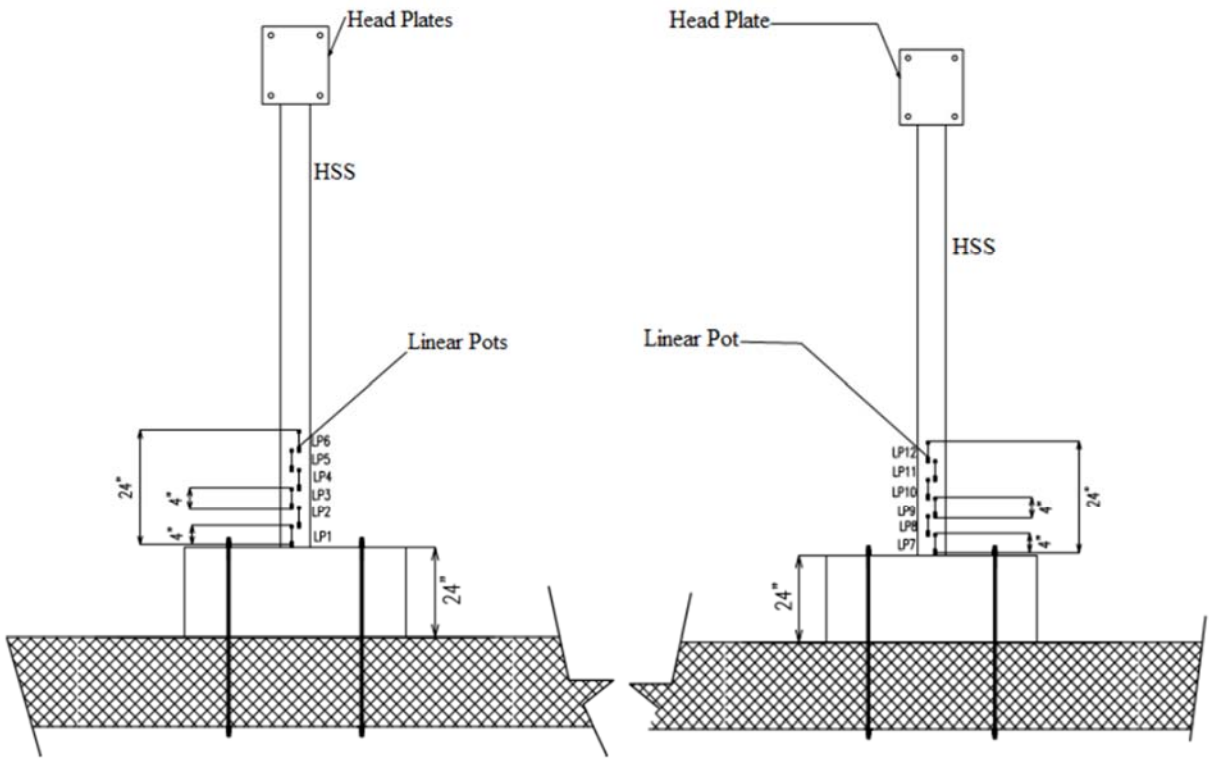

a) b)

Figure 7-15. Linear potentiometer configuration: a) east direction b) west direction (Alzeni and Bruneau 2014).

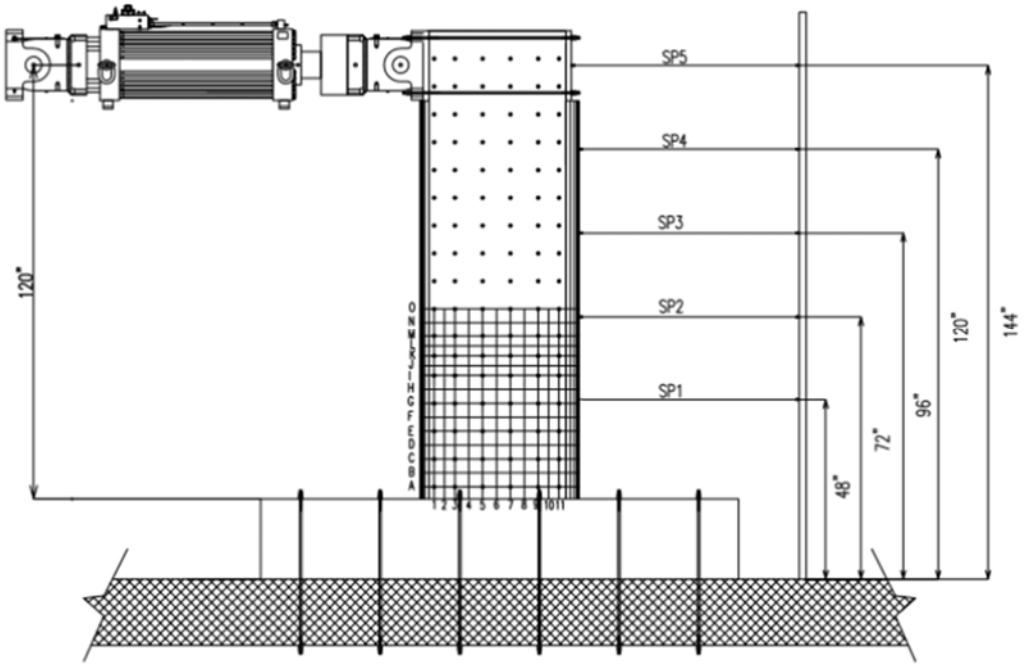

Figure 7-16. String potentiometer configuration (Alzeni and Bruneau 2014).

7.3.3 Loading Protocol

Cyclic loading of all specimens tested by Alzeni and Bruneau was done in accordance with the ATC 24 protocol (ATC 1992). However, an additional displacement cycle at $1.5\delta_y$ was added during test to capture the drift at attainment of the plastic moment (M_p), assuming a yield displacement of 0.72". Table 7-2 and Figure 7-17 show the loading protocol used. Points 1 to 10 shown at the peak of end excursion of each cycle and at the end of test in Figure 7-17 are used to identify the stress diagrams plotted in the Section 7.3.4.6.

Table 7-2. Loading protocol for Group NB (Alzeni and Bruneau 2014).

Order	Total Number of Cycles	Displacement factor of Δy	Drift (%)
1	3	Δy/3	0.2
2	3	2Δy/3	0.402
3	3	Δy	0.6
4	3	1.5Δy	0.9
5	3	2Δy	1.2
6	3	3Δy	1.8
7	2	4Δy	2.4
8	2	5Δy	3.0
9	2	6Δy	3.6
10	2	7Δy	4.2
11	2	8Δy	4.8

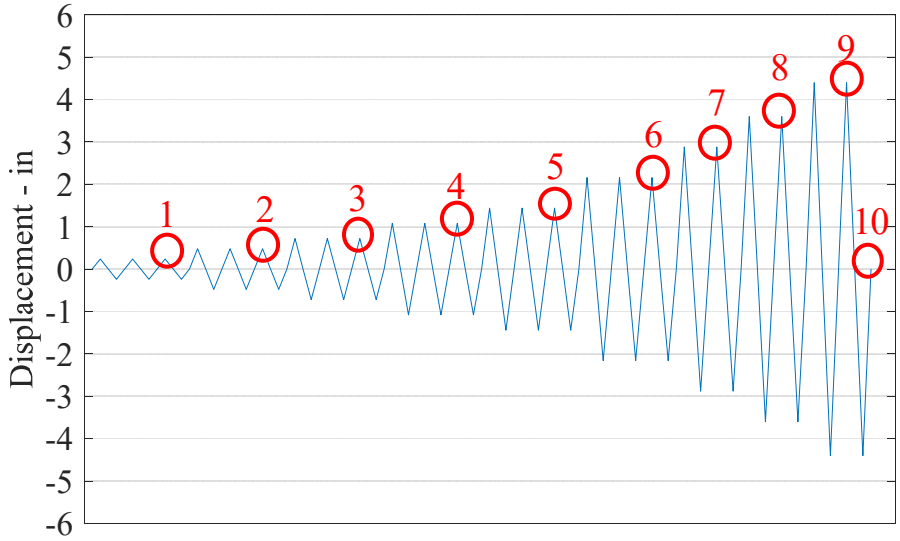

Figure 7-17. Loading Protocol for the specimens.

7.3.4 Numerical Calibration

7.3.4.1 Cross Section Analysis for Elasto-Plastic Material

OpenSees does not have a graphic interface to present results. Therefore, a cross section analysis using elastic-perfectly-plastic material behavior was first conducted to compare results with hand calculations (from simple plastic theory) and make sure that correct information was entered to define the cross section of the Alzeni and Bruneau wall in OpenSees. Steel was defined as an elastic perfectly plastic material having 63 ksi and 44 ksi yield strengths for web steel and HSS steel, respectively, and concrete was defined as an elastic-perfectly plastic material with no tensile strength and a 6.94 ksi compressive strength. The cross section was patched with quadrilateral elements for the web steel and concrete; and circular quadrilateral elements for the HSS steel and concrete enclosed by the HSS; this meshing was used by OpenSees to generate layers.

Two nodes having the exact same coordinates were connected by a zero length element for the cross sectional analysis. One of nodes was fixed in all direction, and the other one was only fixed in the vertical direction (y-direction). Moreover, no axial was applied to the cross-section of the wall. Then, a lateral displacement was applied at the top of the wall until it developed a maximum curvature of 0.01 rad/in. at its base. For the measurement of plastic neutral axis, concrete and steel strains at both ends and at the quarters depth of the cross- section were measured and the plastic neutral axis was obtained by a straight line through the points where strains were measured and the point where it crosses the zero strain axis was

taken as plastic neutral axis. The resulting moment versus curvature and plastic neutral axis was drawn using MATLAB (Mathworks 1992) as shown in Figures 7-18 and 7-19, respectively. According to these plots, the plastic moment of the cross section is 2718 k-ft. (32616 kip-in) and the plastic neutral axis is located at 9.598" from the tip of the cross-section on the compression side.

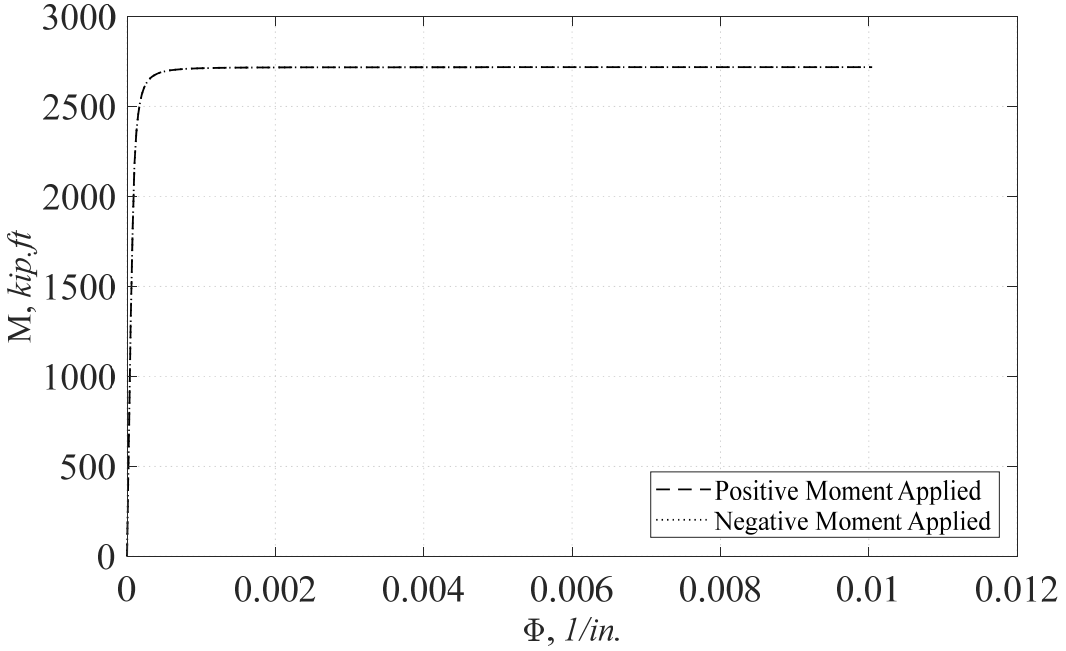

Figure 7-18. Moment Curvature for the cross-section of C-PSW/CF-NB1 Wall using Elasto- Perfectly Plastic Materials.

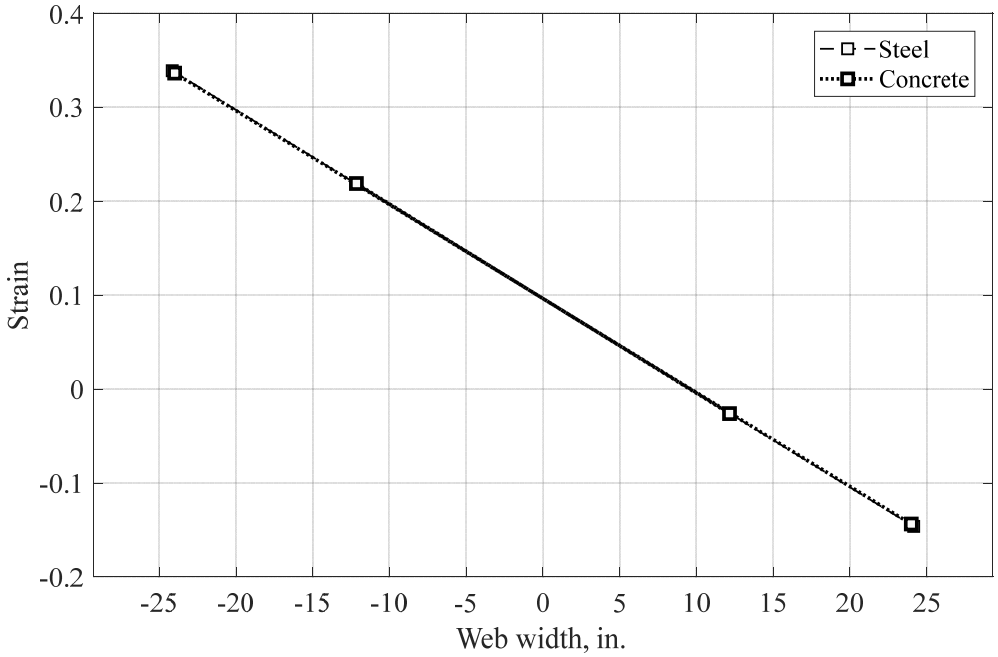

Figure 7-19. Plastic neutral axis from cross sectional analysis in OpenSees.

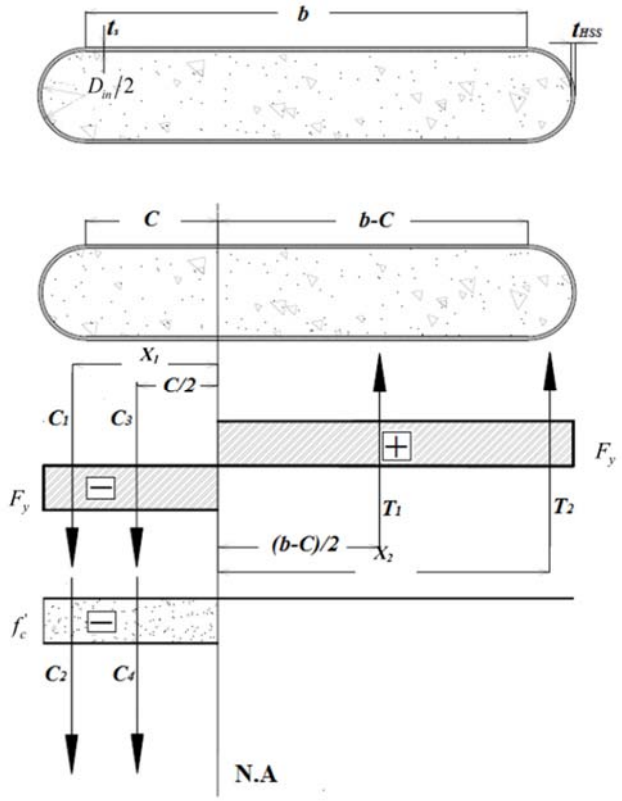

Figure 7-20. Stress Distribution for CFSSP-NB cross section (Alzeni and Bruneau 2014).

To compare with hand calculation results from simple plastic theory, the same elasto-perfectly-plastic material properties were used. Also, the reduction in concrete stress block (i.e., the value of 0.85 typically used) was not considered in the calculation. The equilibrium equations used for this purpose considered the following forces in compression:

$$C_1 = 0.5 * A_{HSS} * F_{y,HSS} \quad \textbf{(7.1)}$$

$$C_2 = \left(\frac{\pi d_{in}^2}{8}\right) f_c' \quad \textbf{(7.2)}$$

$$C_3 = 2 * t_s * c * F_{y,WEB} \quad \textbf{(7.3)}$$

$$C_4 = t_c * c * f_c' \quad \textbf{(7.4)}$$

where c is the web part of the plastic neutral axis, shown in Figure 7-20, and the forces in tension:

$$T_1 = 0.5 * A_{HSS} * F_{y,HSS} \quad \textbf{(7.5)}$$

$$T_2 = 2 * (b - c) * t_s * F_{y,WEB} \quad \textbf{(7.6)}$$

By equating compressive forces to tensile force, the length of the web under compression (c) can be calculated:

$$C_1 + C_2 + C_3 + C_4 = T_1 + T_2 \quad \textbf{(7.7)}$$

$$c = \frac{2 * t_s * b * F_{y,WEB} - 0.125 * \left(\pi d_{in}^2\right) * f_c'}{4 * t_s * F_{y,WEB} + t_c * f_c'} \quad \textbf{(7.8)}$$

The resulting plastic moment capacity is given by following formula:

$$M_p = 0.5 * A_{HSS} * F_{y,HSS} * \left(\frac{2 * d_{HSS}}{\pi} + b\right) + (b^2 + 2 * c^2 - 2 * c * b) * t_s * F_{y,WEB} + \left(\frac{2 * d_{in}^3 + 3 * \pi * d_{in}^2 * c}{24} + \frac{c^2 * t_c}{2}\right) * f_c' \quad \textbf{(7.9)}$$

Using Equations 7.8 and 7.9, the plastic moment, M_p, was calculated to be 32622 kip-in and the neutral axis was located at 9.569 in. The difference in plastic moment between the values obtained from hand calculations and from OpenSees is 0.018%, while the error in plastic neutral axis location is 0.06%. The error in that later case comes from ignoring the elastic part of the stress-strain curve in hand calculations, and is considered negligible. This confirmed that the correct cross section was created for this wall in the OpenSees model.

7.3.4.2 Material Inputs

Calibration of the OpenSees model then proceeded using the cross-section defined above and the material models described in Section 3, but using the material properties obtained for Specimen C-PSW/CF-NB1. The *Reinforcing Steel Material* model and *Concrete02* model for concrete have been described in Sections 6.2 and 6.3. The work presented in this section is about selection of the values for the inputs parameters that define the steel and concrete material used in modeling Specimen C-PSW/CF-NB1 (Alzeni and Bruneau 2014). The parameters were selected to replicate the behavior observed during the test of that wall.

The steel grade of HSS and web steel were ASTM A252 Gr3 and ASTM A572 Gr 50, respectively. However, for the lack of better information in light of all other uncertainties, the same buckling and fatigue properties were assumed for both steel grades. Moreover, confined concrete parameters based on Susantha et al (2001) were used for the concrete enclosed by the HSS, while the between two web steel plates was assigned the strength of unconfined concrete but the same ductile behavior as for the HSS-enclosed concrete.

The first step taken was to create the stress-strain backbone curves for the HSS steel and web steel, based on data from coupon tests (Figure 7-13) performed prior to the test. The backbones are different because these were of different grades of steel. The backbone curves are defined by the parameters, f_y, E_s, ε_y, f_u, E_{sh}, ε_{sh}, and ε_u (see Section 6.2.1). For these parameters, using 63 ksi, 29800 ksi, 0.0021, 72.5 ksi, 215 ksi, 0.021 and 0.15 for the web steel; and 44 ksi, 27500 ksi, 0.0016, 61 ksi, 1721.5 ksi, 0.0017 and 0.15 for the HSS steel (Figure 7-13), respectively provided good agreement with the coupon test results for the corresponding steels.

Then the buckling parameters were assigned such that buckling in the material model would start to occur approximately at the same drift when local buckling was visually observed to occur the test. From visual observations, slight evidence of local buckling was reported to initiate between first and second row of ties

during the first cycle at 1.8% drift, after the peak flexural strength was reached. When the specimen was cycled during the third excursion at the same drift, it was observed that the white paint flaked on the perimeter of the first and second row, indicating yielding of the cross section. Then, buckling of the HSS steel was observed at 2.4% drift. When using the above material model in OpenSees analyses, the steel was observed to start locally buckling when the yield strength was reached, which was much sooner than what had been observed during test. To correct this, the buckling curve was adjusted in order to match the test data for Specimen C-PSW/CF-NB1. For the slenderness ratio, l_{SR}, of 25.6 (that is set by the given tie spacing divided by equivalent steel thickness), it was found that good results were empirically obtained by using a buckling curve reduction factor, r, of 0.4; an amplification factor, β, of 1.0; and a buckling constant, γ, of 1.0.

After selecting the above buckling parameters, the fracture model parameters were determined to replicate how fracture affected behavior during test. During test, minor cracks were first observed around tie bars at 2.4% lateral drift and started to propagate toward the HSS steel ends at 3% lateral drift. More significantly, a crack occurred in the HSS part of cross section during the first excursion at 3.6% lateral drift; this crack developed in the middle of the buckled wave on the HSS; loss of flexural strength became more noticeable from that point onward. During the third reversal at the same drift, cracks around the tie bars propagated across the first tie bar row. During the second excursion at that drift, the steel was fractured over 28 in. of the total cross section depth through the centerline of first tie bar row. In addition, the crack in the HSS was 5" in length. At that point, the test stopped due to safety concerns as only 20" of the web of the specimen remained unfractured.

One of the complication that arises in using a fracture model to replicate the above behavior is that, in the specimens, fracture occurred as a consequence of low-cycle fatigue where local buckling created large localized strains. In other words, local buckling introduce additional local flexural strains that superpose to the plane-strain condition that exists through the cross-section, which reduces the number of cycle to failure. Given that the OpenSees models are based on the assumption that "plane sections remain plane in bending", the additional strains due to local buckling cannot be modelled in OpenSees. Therefore, even though the material model accounts for low-cycle fatigue, it remains that the defining fatigue parameters must be empirically determined from experiments where local buckling affects the fatigue results (which is not accounted by the model). In other words, even though the *Reinforcing Steel Material* model has the ability to account for both buckling and fatigue, the fatigue properties and buckling properties are modeled independently. On the basis of that empirical calibration, the fatigue ductility coefficient, C_f, typically equal to 0.21 for the type of steel used in the experiments, was adjusted to 0.3 to match the shorter fatigue life

resulting from local buckling. Likewise, the fatigue ductility exponent, α, was set to 0.45, and to replicate the softening observed in the base shear in repeated excursions at the same drift, the cyclic strength reduction constant, C_d, was set to 0.5 to improve the hysteretic behavior.

Finally, for simplicity, default values for the Menegotto-Pinto curve parameters and hardening constant were used. All the parameters used to capture the steel behavior in the C-PSW/CF-NB1 Specimen are summarized in Table 7-3. Note that while the above is presented as a linear process, multiple trial-and-error were required to converge on the final set of model parameters reported here.

Table 7-3. Steel inputs.

	HSS Steel	**Web Steel**
f_y (ksi)	44.0	63.0
E_s (ksi)	27500	29800
ε_y	0.0016	0.0021
f_u (ksi)	61.0	72.5
E_{sh} (ksi)	0.0626*E_s	0.0072*E_s
ε_{sh}	0.0017	0.021
ε_u	0.15	0.15
l_{SR}	25.6	25.6
β	1.0	1.0
r	0.4	0.4
γ	1.0	1.0
C_f	0.3	0.3
α	0.45	0.45
C_d	0.5	0.5
R1,R2.R3	0.333; 18.0; 4.0	0.333; 18.0; 4.0
a1, limit	4.3; 0.01	4.3; 0.01

Note that parameters for the confined concrete were taken as set value and not iterated upon to improve the match with experimental results, given that the behavior of steel is recognized to have greater impact the on behavior of such composite walls. Values to define the confinement model of the concrete enclosed by the HSS steel were obtained by inputting the reported average strength obtained from cylinder tests into the Susantha et al. (2001) equations for circular composite cross-section (see Appendix A.3.1.1); these are listed in Table 7-4. However, the *Concrete02* material model (a,k.a. the Modified Kent-Park model, as mentioned earlier in Section 6.3) does not have the same equations (Appendix A.2) as Susantha et al (2001)

to construct the backbone curve for confined concrete. Therefore, the strain at maximum peak strength in the *Concrete02* model was altered (ε_{cc}) from 0.0093 to 0.0042 in order to match the stiffness as in elastic range of concrete (shown as the "Adjusted Modified Kent-Park" results in Figure 7-21). Also, as shown in that figure, as a result of the adjusted material properties, the model used will reach maximum concrete strength sooner than predicted from the Susantha et al. model, but the largest difference in stress between the two curves is on the order of 10%, and of no significant effect on the ultimate response of the system. Note that the same ductile behavior was assigned to the concrete located between the web steel, but using the average unconfined concrete strength obtained from cylinder tests, based on observations from tests results.

Table 7-4. Concrete inputs.

	Concrete in HSS	**Concrete in Between Web Steel**
f'_{cc} (ksi)	10.21	6.94
E_c (ksi)	4840	4840
ε_{cc}	0.0093 / 0.0042	0.00287
ε_{cu}	0.025	0.025
Z	0	0
α	1.0	1.0
f_t (ksi)	$0.1*f'_c$	$0.1*f'_c$
E_t (ksi)	E_s	E_s
Lambda (λ)	0.1	0.1

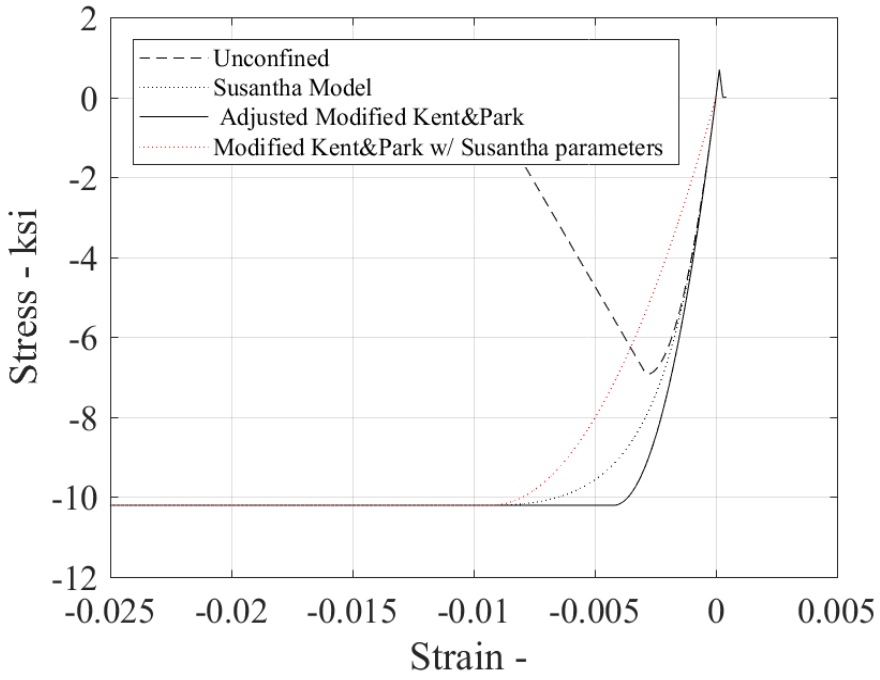

Figure 7-21. Confined concrete models for concrete in HSS steel.

7.3.4.3 Element Type

Nonlinear element types available in OpenSees have been presented in Section 6.4. In this section, the specific element type used for C-PSW/CF-NB1 wall is addressed from a calibration perspective.

Plasticity is spread over some length of a structural member, called plastic hinge length. To save from computation time, nonlinear elements are only assigned to the plastic hinge regions, and the rest of the structural members (such as walls or coupling beams) are modeled using elastic beam column elements having the elastic stiffness of the given cross section (Figure 7-18). Selection of plastic hinge length has an impact on results; for example, in wall, the large curvatures that develop over the plastic hinge length significantly contribute to a wall's top displacement (likewise, curvature demands at a given drift also depend on plastic hinge length).

The C-PSW/CF-NB1 specimen used for calibration here (Alzeni and Bruneau 2014) was a cantilever wall subjected to a lateral load at its top. Its plastic hinge length was determined as the vertical distance between the yield and plastic moments long the linear moment diagram. The yield and plastic moments of the wall were taken from the fiber cross section analysis results shown in Figure 7-18, which are 2353 k-ft. and 2718 k-ft., respectively, resulting in a plastic hinge length of 16.11 in. However, to account for strain

hardening that developed at the base of the wall, it was increased up to 24". The moment curvature curve experimentally obtained from linear potentiometers located 24" above the base of the wall confirms the development limited nonlinearity there, as shown in Figure 7-22.

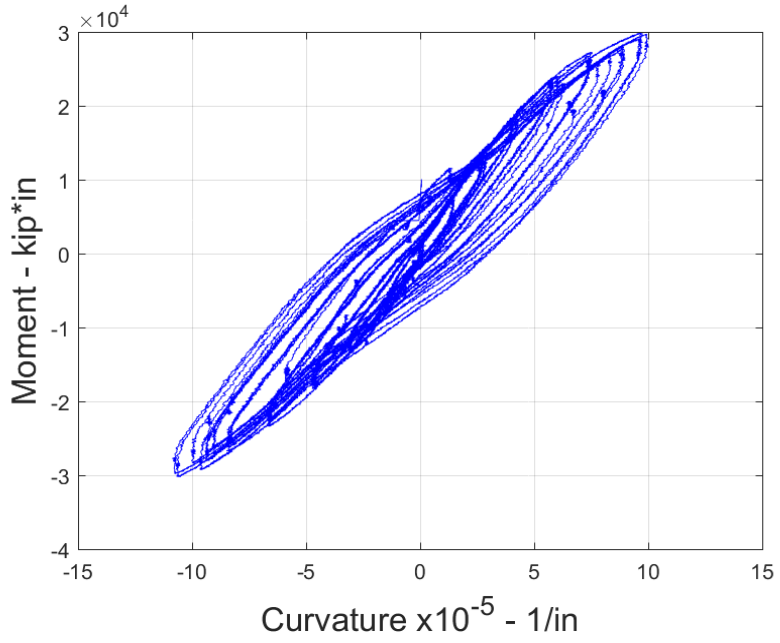

Figure 7-22. Moment Curvature curve at 24 inches from the base of the wall.

As indicated in Section 6.4, even though force based (flexibility method) nonlinear beam column elements are generally preferred because they use exact force interpolation functions, it could not be used here for the specific material model selected. Generally, with force-based elements, accuracy of the solution can only be improved by increasing the number of integration points (preferred from computational point of view) or increasing number of elements as they only involve numerical error (not discretization error). However, in the *Reinforcing Steel Material* model, increasing the number of integration points causes higher local curvature that influences the fatigue life and buckling behavior, and increasing the number of force based nonlinear elements caused convergence problems in OpenSees (Kunnath et al. 2009). Analyses with force-based nonlinear beam column elements were nonetheless attempted but were not successful. This is because the program ran when only one force based nonlinear element was assigned over the plastic hinge length, which led to unrealistic fatigue parameters. Moreover, in a trial earthquake runs, analysis using that model did not converge in spite of multiple attempts considering various time steps, algorithm types, tolerance, and combinations of these. Therefore, displacement base elements were tried instead.

The only way to achieve accuracy in displacement based nonlinear elements is to increase the number of elements over hinge length (Section 6.4). Increasing the number of integration point is not helpful for accuracy. To illustrate this, the OpenSees model of Specimen C-PSW/CF-NB1 having three 8" displacement based elements over a plastic hinge length of 24" was modeled with different number of integration points (NIP) and subjected to the loading protocol in Figure 7-17. The maximum top wall displacement reached in each cycle is shown in Figure 7-23 (the small drops in the curve are due to the lower strength reached during the second excursion at a given drift). In that figure, all curves plotted fall on top of each other, indicating that increasing number of integration points did not affect the results. Hence, in all subsequent analyses, three NIPs were given to the elements.

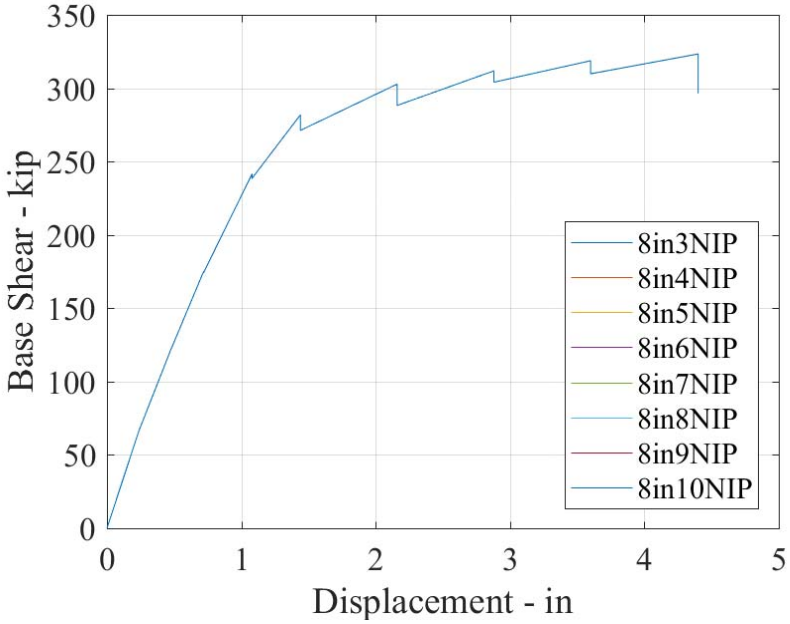

Figure 7-23. Number of integration study (all curves line on top of each other).

The *Reinforcing Steel Material* model is also sensitive to the number and size of elements in the plastic hinge region. To investigate what number of elements should be used across the plastic hinge regions in this study, the same model was analyzed using various number of elements while the number of integration points (i.e., three NIPs) and other material parameters were kept the same**.** Figure 7-24 **s**hows that for the same steel material parameter, response is changing with different element sizes. Results converged to a replicable strength-displacement curve when elements 6" in size or larger were used. Given that curvature data for Specimen C-PSW/CF-NB1 was reported at 4" spacing, 8" element length with three NIPs (i.e. spaced at 4" from each other) was selected to facilitate comparison with test data. Usually, in finite element analysis, more elements are better for convergence. Here, it is not the case as shown in Figure 7-24. The

degradation due to buckling will be localized with many elements with 3 NIPs over given plastic hinge length and fracture will happen sooner (Kunnath et al. 2009).

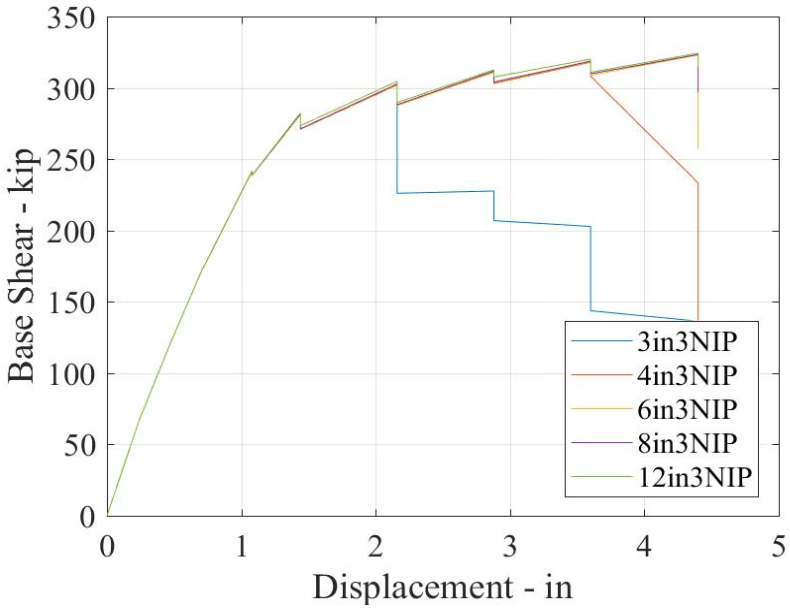

Figure 7-24. Number of element study.

7.3.4.4 Base Shear versus Top Displacement Comparison

The plot of the base shear-displacement hysteretic relationship obtained for Specimen C-PSW/CF-NB1 is shown in Figure 7-25 (base shear in that figure is effectively equal to the lateral load that was applied at the top of the specimen). Firstly, a model of the wall having a rigid fixed base was compared with the data. However, in the elastic range, stiffness of the model was greater than that measured experimentally, as shown in Figure 7-25, because the flexibility of the specimen foundation was not captured. Therefore, a rotational spring with 8,400,000 kip-in stiffness was inserted in the model at the base of the wall to replicate the foundation flexibility observed in the test. This foundation stiffness was determined by trial-and-error until the elastic stiffness matched.

After including the above rotational spring to account for foundation flexibility, the OpenSees models agreed well with the test data. In particular, the maximum force of 305 kips was matched within 3.93 %. Then, as parameters for the low-cycle fatigue were calibrated from this specimen, fracture initiated during the same cycle as what was observed during the test, namely during the first cycle at 3.6% drift (i.e. 4.32 in displacement). However, the sudden reduction in strength observed during the first excursion in the

negative direction and the second excursion in the positive direction at that drift were not replicated well. Even though the OpenSees model cannot replicate this behavior exactly, on the last negative excursion the strength degradation for OpenSees was close to the experimental values. Note that additional minor fractures initiated earlier during cyclic loading. While these small cracks did not degrade the strength significantly, the strength loss was more sudden when these cracks propagated significantly, simultaneously with cracks that developed in the middle of the buckled HSS. Note that the OpenSees model does not have the capability to model the fracture mechanics phenomena that initiates cracks around ties, and that the cracking model in element *Reinforcing Steel Material* is used in a phenomenological manner in relation to the hysteretic response.

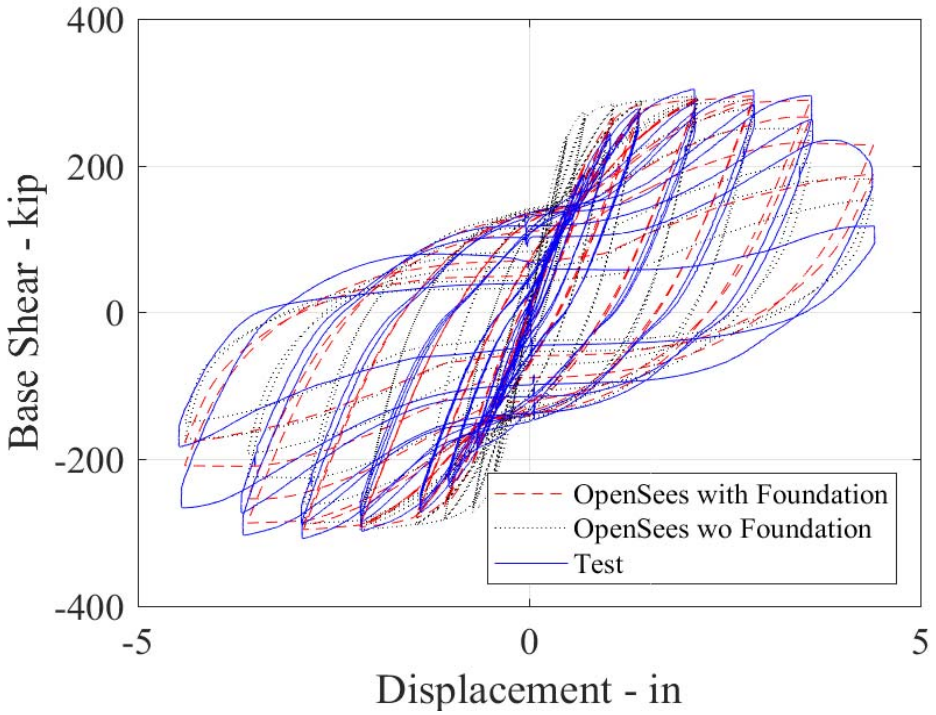

Figure 7-25. The comparison of base shear versus tip displacement for C-PSW/CF-NB1 specimen

7.3.4.5 Moment Curvature Relations

Moment-curvature relationships at various heights of the wall were calculated using the results from six pairs of linear potentiometers used at both ends of the wall at a spacing of 4", as shown in Figure 7-15. In addition, two string potentiometers were used to calculate average curvatures over the height of 30" spanned

by these linear potentiometers at the base of the wall, and compared to the results extracted from the individual pairs of linear potentiometers.

The results are shown in Figures 7-26 to 7-32, using different horizontal scale for clarity in showing the hysteretic curves. Note that, during the experiment, some linear potentiometers were dislodged from their original positions at higher drifts because of either local buckling of the steel of the specimen or slipping of the mounting magnets at either end of the potentiometers. However, for the string potentiometers, this error due to slippage is averaged over a greater distance (i.e., 30" instead of 4") and the magnitude of the errors should be less significant.

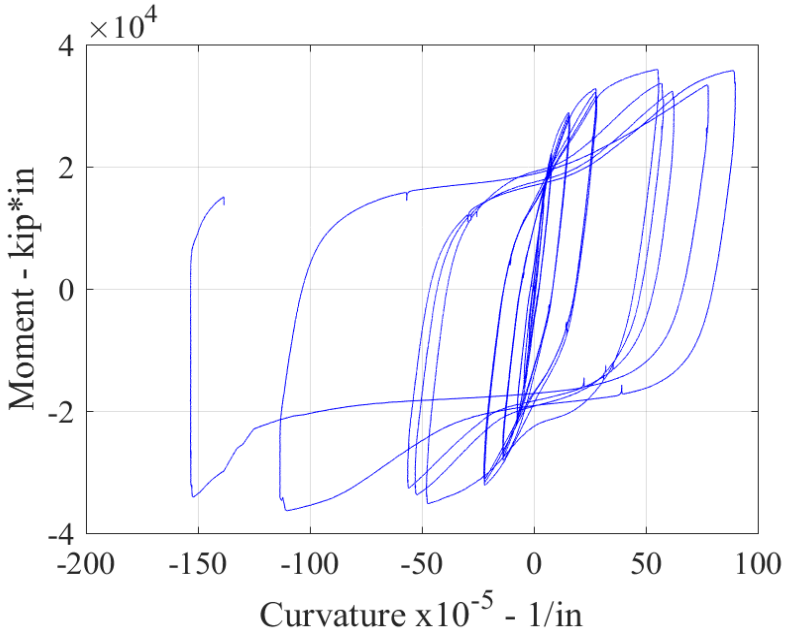

Figure 7-26. Moment curvature relationship for C-PSW/CF-NB1 at 2" from base.

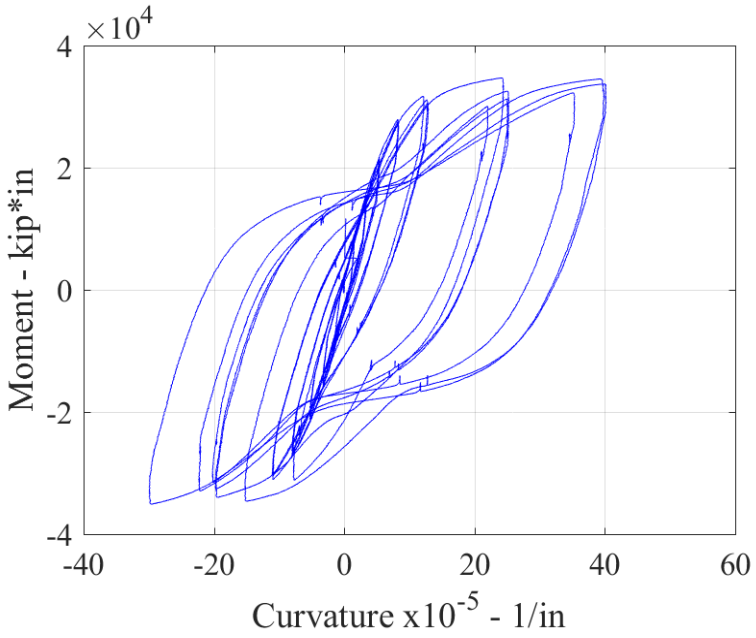

Figure 7-27. Moment curvature relationship for C-PSW/CF-NB1 at 6” from base.

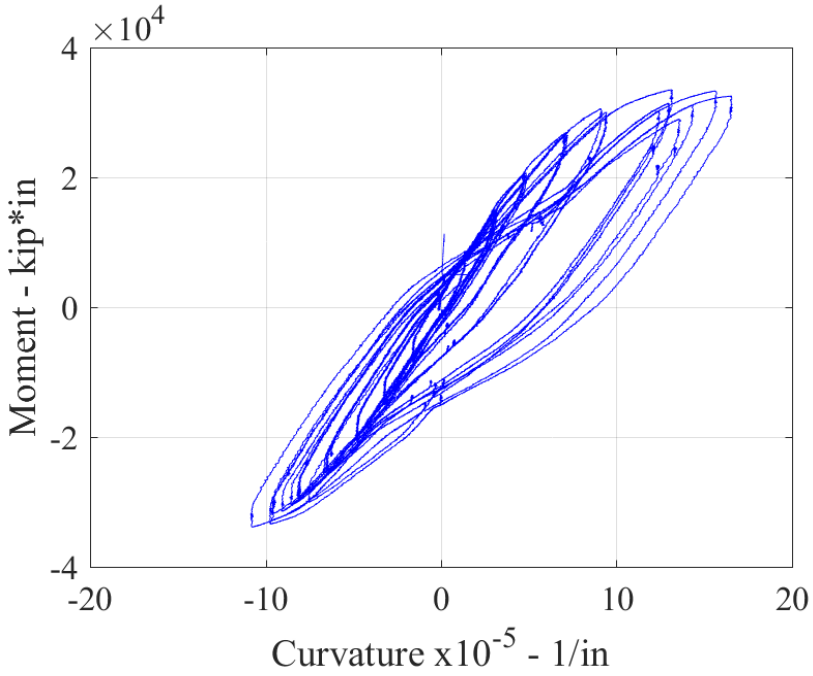

Figure 7-28. Moment curvature relationship for C-PSW/CF-NB1 at 10” from base.

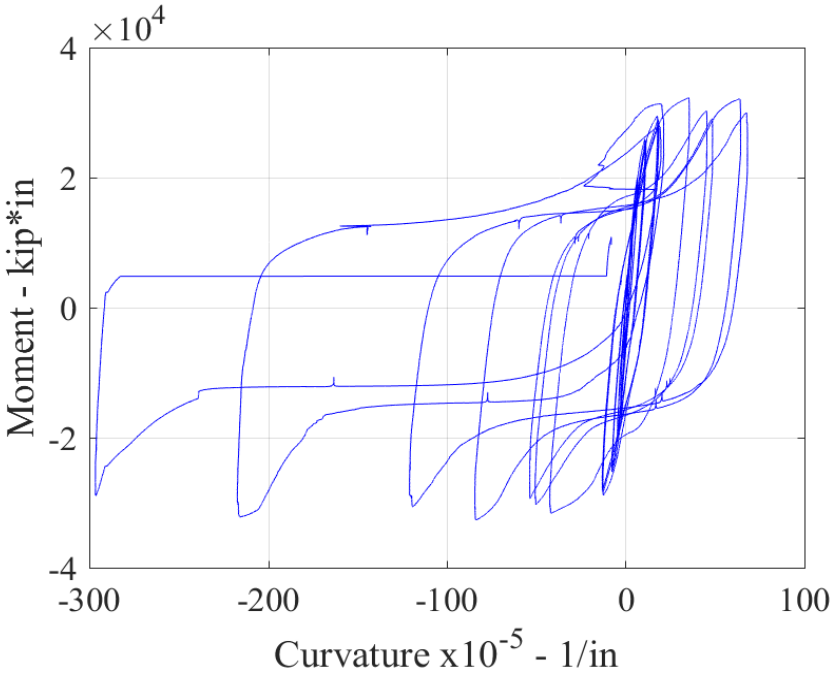

Figure 7-29. Moment curvature relationship for C-PSW/CF-NB1 at 14" from base.

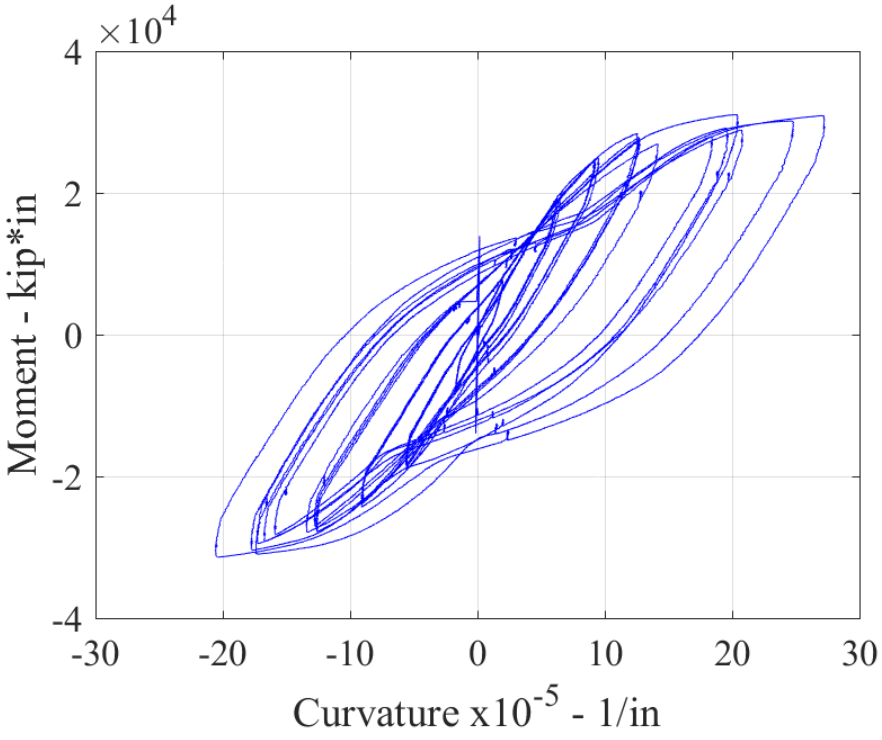

Figure 7-30. Moment curvature relationship for C-PSW/CF-NB1 at 18" from base.

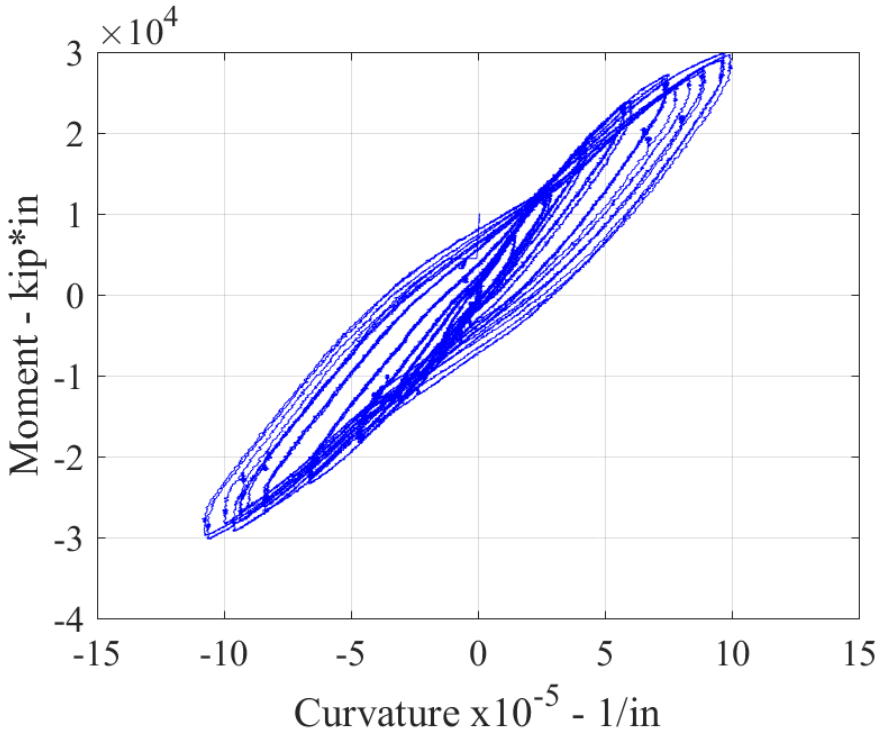

Figure 7-31. Moment curvature relationship for C-PSW/CF-NB1 at 22” from base.

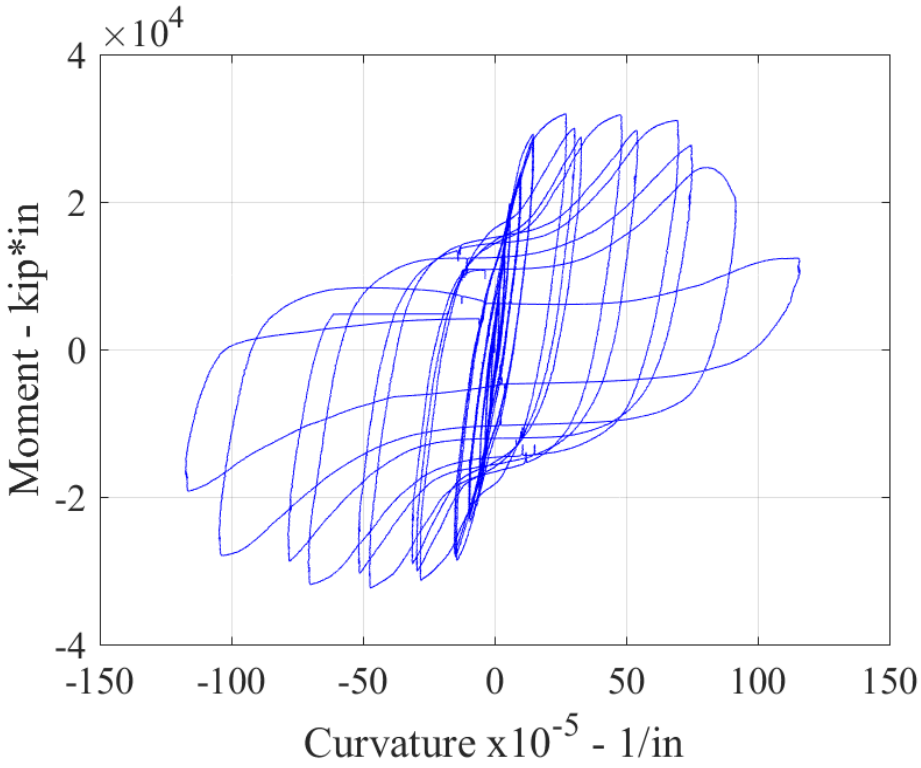

Figure 7-32. Moment curvature relationship for C-PSW/CF-NB1 at 15” from base.

Slipping of the linear potentiometers led to inaccurate data at large drifts so the lateral drift of 1.8% (which is the point at which local buckling started to occur and M_{max} was reached) is considered here to be the limit for which relatively reliable data could be obtained from all the linear potentiometers. Therefore, the maximum curvatures reached along the lower 30" height of the specimen (i.e., the height instrumented by potentiometers), in each cycle up to 1.8% lateral drift in both the positive and negative directions, are taken and compared with the OpenSees results, as shown in Figure 7-33. In addition, the theoretical curvature calculated from the elastic-perfectly-plastic material model shown in Figure 7-18 was also plotted in the figures to check if the curvature values where within a reasonable range. Figure 7-33 shows that in the elastic range of response, both the test and OpenSees results are aligned with the theoretical curve. As the specimen is laterally displaced to higher drift, close to the wall base, the experimentally measured curvature started to diverge from OpenSees curvature value. However, some of the values of large drifts are questionable because of repeated slip described earlier. Recognizing this, Alzeni and Bruneau (2014) plotted the curvature readings of linear potentiometers over the instrumented length of specimen, and the values achieved from the string potentiometers over that height (as an average curvature). Curvature values are shown Figure 7-34 at drift values of 0.6% and 1.8%, which are the values at which M_y and M_p are attained, respectively; these are labeled "yield curvature" and "maximum curvature" in Figure 7-34. Figure 7-34 shows that results fluctuates significantly at large drifts and that the average curvature is a better measure in that perspective. Therefore, the moment curvature relation from OpenSees results averaged over 30" length was compared with the data from the string potentiometers.

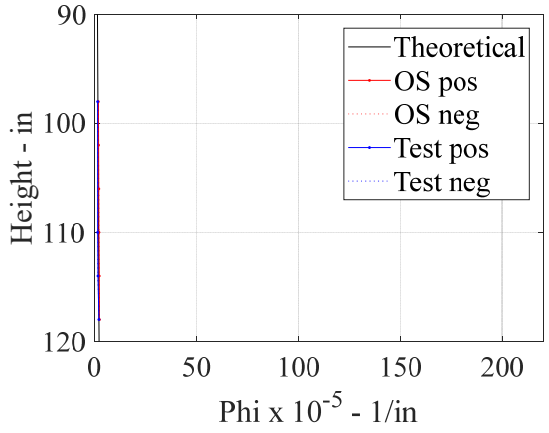

Δ = 0.24 in (0.2%)

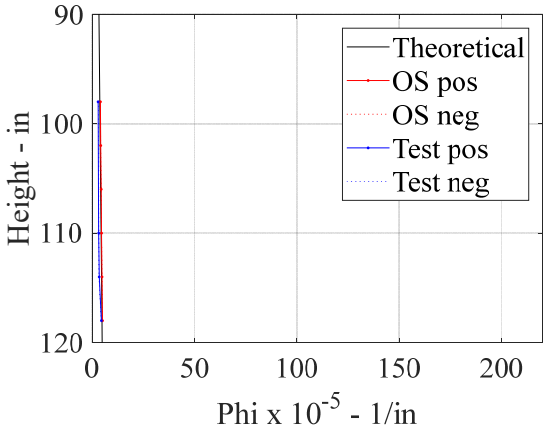

Δ = 0.48 in (0.4%)

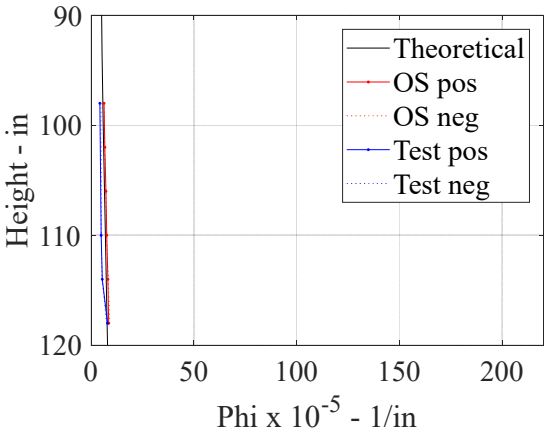

Δ = 0.72 in (0.6%)

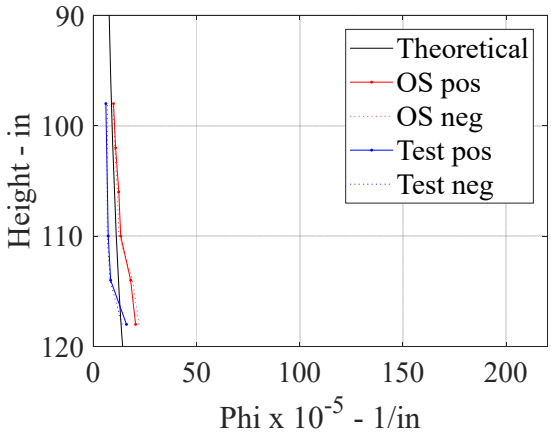

Δ = 1.08 in (0.9%)

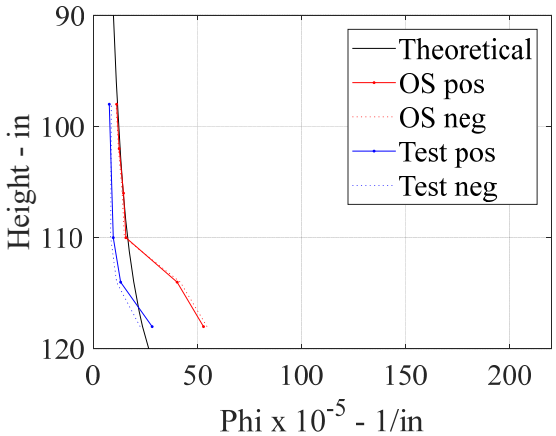

Δ = 1.44 in (1.2%)

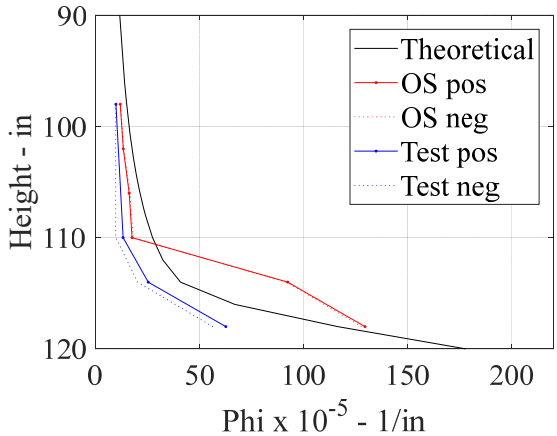

Δ = 2.16 in (1.8%)

Figure 7-33. Moment curvature comparison for each linear potentiometer in Alzeni wall (Note that OpenSees results are on top of each other).

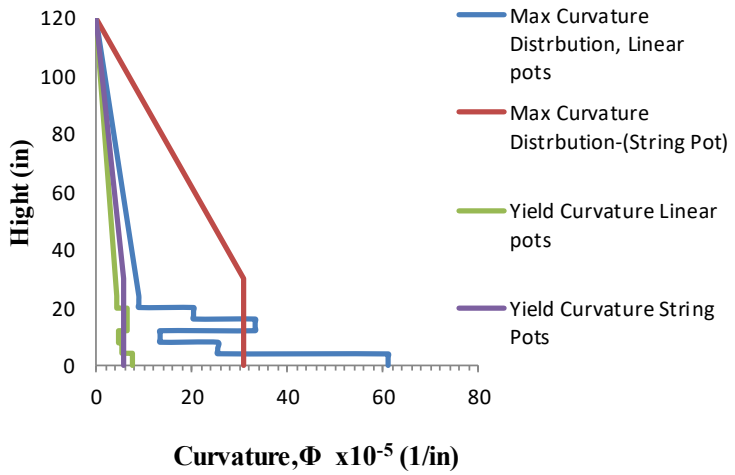

Figure 7-34. Curvature distribution along C-PSW/CF-NB1 at 0.6% and 1.8% Drift (Alzeni and Bruneau 2014).

The string potentiometer readings are average curvatures over the plastic hinge length of the wall and these values include the contribution of local buckling and fracture. The average curvature from the OpenSees model of the wall is calculated and compared with the data from string potentiometers in Figure 7-35. Except for last cycle, the OpenSees models agreed well with test data as the maximum error in curvature is 13% and the moment values are almost the same as test data. The experimental curve shows a more severe strength degradation in the last cycle, even though, the curvature matched with test data. However, it was reported that the magnet at the end of the string potentiometers had slipped during the last cycle of the test, which may partly explain this difference.

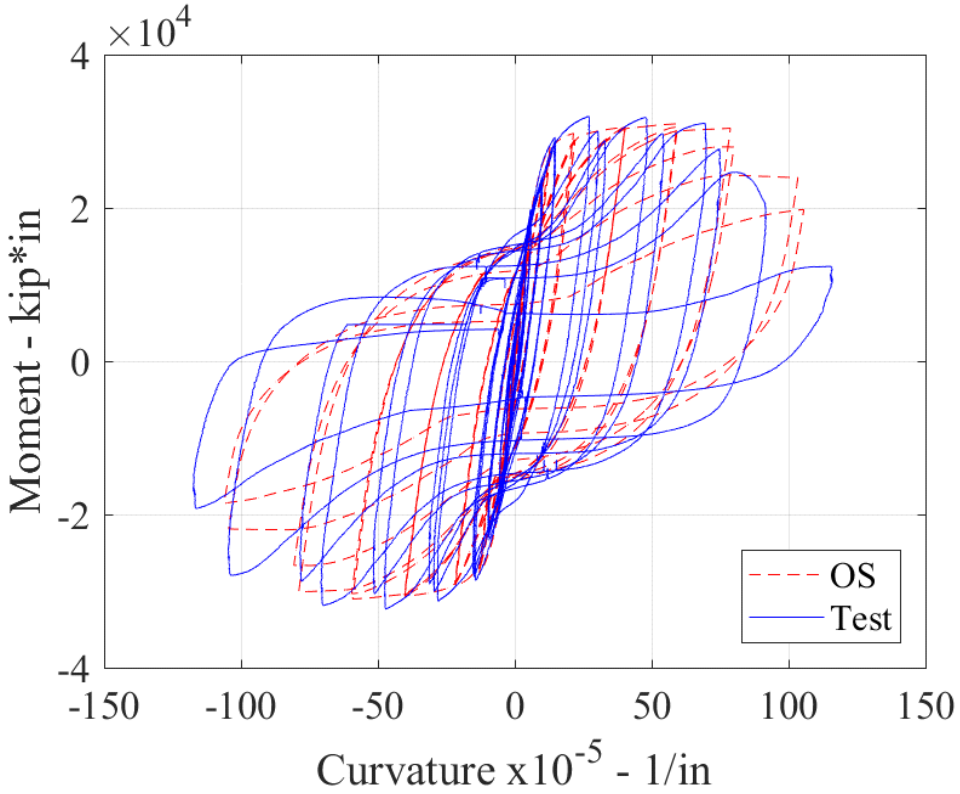

Figure 7-35. Moment curvature comparison for string potentiometers.

7.3.4.6 Stresses in the Cross-Section

Following loading protocol in Figure 7-17, the steel and concrete stress diagrams from the analysis of the model of C- PSW/CF-NB1 wall are shown in Figure 7-36. Although the strain gauge data from the experiments are not available for direct comparison, the following general behavior of the steel in the cross section of the wall was described by Alzeni and Bruneau (2014):

- The first yield of steel observed in the HSS steel occurred at the estimated yield displacement, δ_y (0.6% drift).
- At 0.9% drift, 30% of the entire steel section was reported to have yielded
- At 1.2% drift, 52% of the cross section had yielded.
- After full cycle at drift of 1.8%, all of the plate between ties buckled at some point during cycle. Since for designed specimen, buckling happen after yielding can infer that most of cross-section had yielded

Therefore, the steel stresses in the Figure 7-36 are compared with the above observations. On that basis, the OpenSees model of C-PSW/CF-NB1 wall correctly estimated first yield of the HSS steel (third point). However, the stresses are reduced as the *Reinforcing Steel Material* model was defined to buckle when a

fiber reaches the yield stress. Therefore, 30% and 52% yielding of cross-section at 0.9% (Cyclic 4) and 1.2% (Cyclic 5) drift did not match with OpenSees results, which shows 60.9% and 78.4% yielding instead. The model was however able to simulate nearly full yielding of the cross-section (86.3%) during the third excursion at 1.8% drift (Cyclic 6). Finally, point 10 in Figure 7-36 shows the residual stresses after the end of the last cycle upon unloading.

When the test was stopped, 18 in. on the east side of the wall and 10 in. on the west of the wall was cracked, leaving only about 20" total of specimen unfractured. Results from the OpenSees model shows that approximately 23 in. of the web steel remained.

However, it should be noted that a lot of the above discrepancies are due to the lack of quantitative strain data from the experiment beyond the aforementioned descriptions.

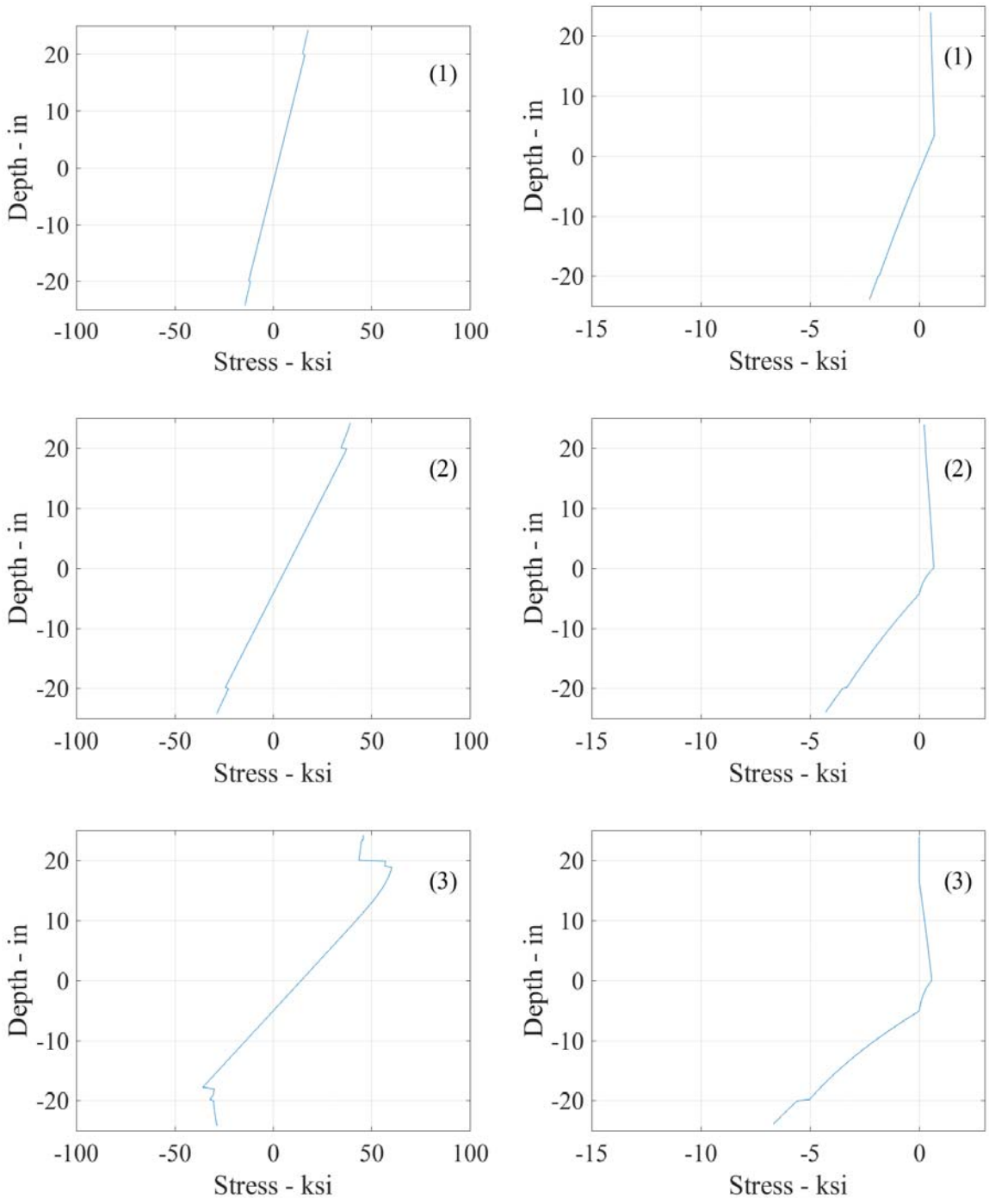

Figure 7-36. Stresses of a) steel and b) concrete in the cross-section from OpenSees model

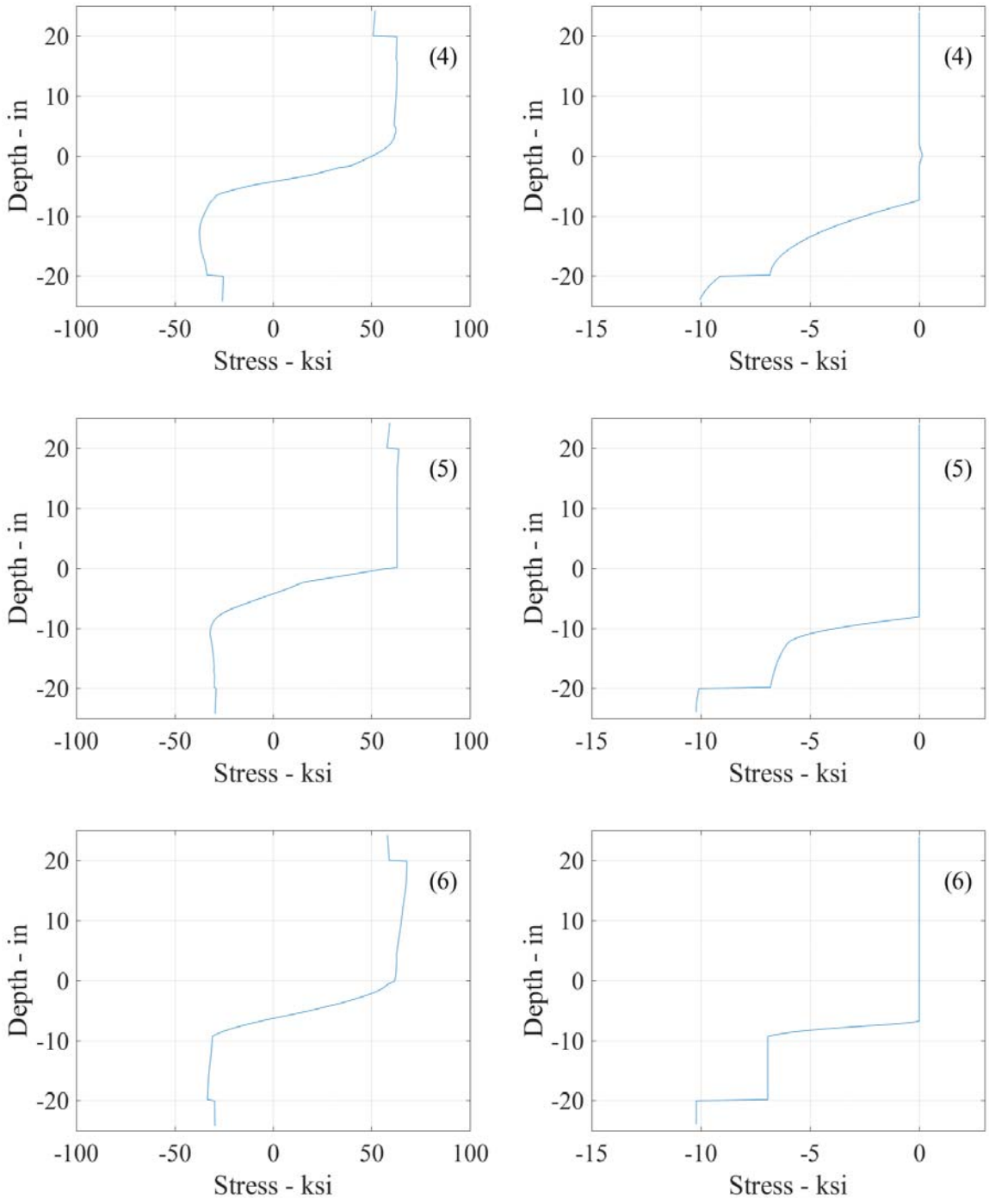

Figure 7-36. (Continued)

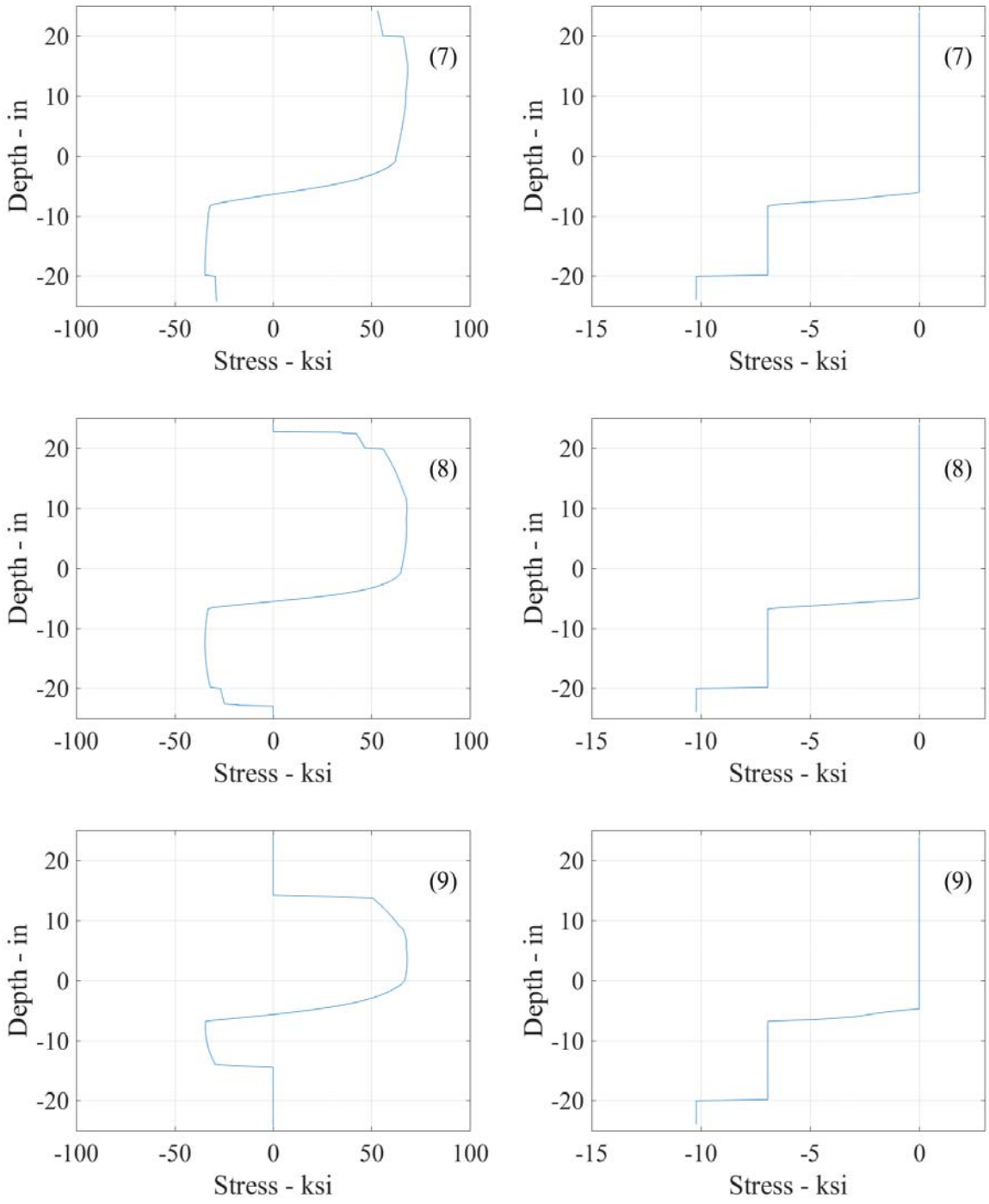

Figure 7-36. (Continued)

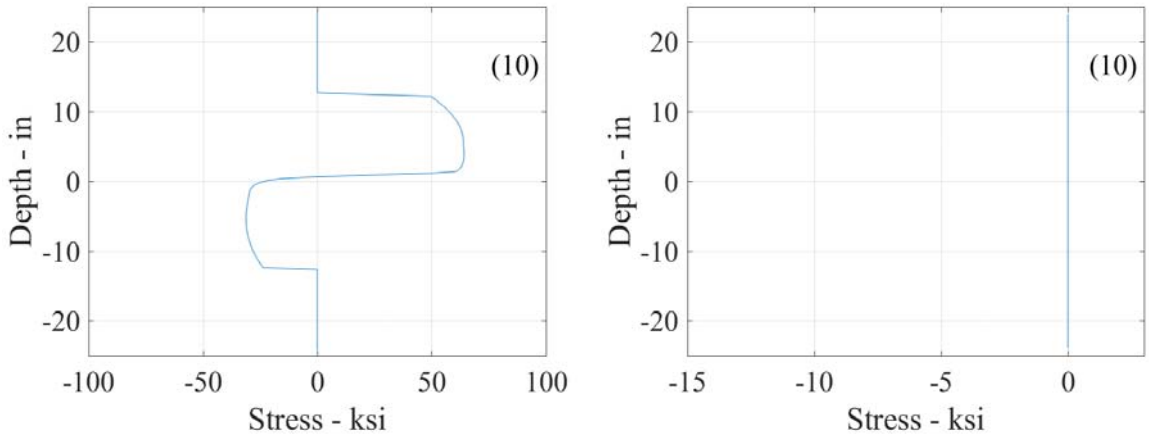

a) **b)**

Figure 7-36. (Continued)

7.4 Tests of Planar C-PSW/CF Walls (Shafaei et al. 2019)

Five planar C-PSW/CF walls tested by Shafaei et al. (2019) are then used for calibrating the models on walls having boundary elements representative of the details used on CC-PSW/CF walls. In this test series, both axial and cyclic loading were applied at the top of the specimens with a 500-ton actuator connected through a loading frame pinned at its base; lateral load was applied to the specimen using horizontal actuators. This test set-up is shown in Figure 7-37.

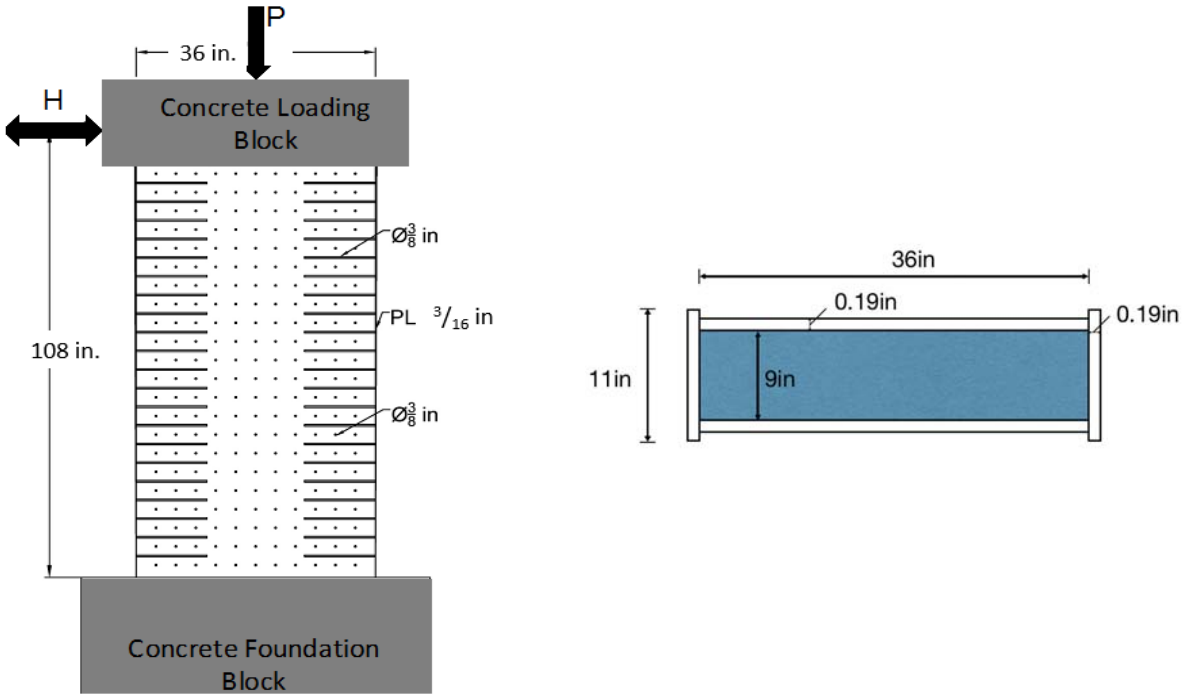

a) **b)**

Figure 7-37. C-PSW/CF walls in a) elevation view and b) plan view

The details of each specimen are shown in Table 7-6. The information provided includes: names of the specimens; their height (H) and width (L); magnitude of axial load applied to the walls as a percentage of the strength of the concrete cross-section area; thickness of the concrete (t_{sc}) and steel faceplate thickness (t_p); stud/tie spacing (s_{tie}) and diameter (d_{tie}); slenderness ratio (s_{tie}/t_p) and tie reinforcement ratio (ρ_t) of the web; flange plate width (t_{p_f}), and; thickness (w_f) of the flanges. The height-to-length ratio (H/L) of the specimens is 3.0 and the specimens were subjected to constant axial forces equal to either 10%, 20%, or 30% of the strength of the concrete area (i.e., $A_g f'_c$)). Specimens also one of three different tie reinforcement ratios (namely, 0.14%, 0.24%, and 0.55%).

Table 7-5. Details of planar C-PSW/CF walls.

Specimen	General				Web									Flange	
	H (in)	L (in)	P (%$A_g f'_c$)	t_{sc} (in)	t_p (in)	ρ (%)	s_{stud} (in)	d_{stud} (in)	s_{stud}/t_p	s_{tie} (in)	d_{tie} (in)	s_{tie}/t_p	ρ_t (%)	$t_{p\ f}$ (in)	w_f (in)
CW-42-55-10-T	108	36	10	9	3/16	4.2	-	-	-	4.5	0.375	24.0	0.55	3/16	11
CW-42-55-20-T	108	36	20	9	3/16	4.2	-	-	-	4.5	0.375	24.0	0.55	3/16	11
CW-42-55-30-T	108	36	30	9	3/16	4.2	-	-	-	4.5	0.375	24.0	0.55	3/16	11
CW-42-14-20-T	108	36	20	9	3/16	4.2	-	-	-	9	0.375	48.0	0.14	3/16	11
CW-42-14-20-TS	108	36	20	9	3/16	4.2	4.5	0.375	24	9	0.375	48.0	0.14	3/16	11

7.4.1 Material Properties

Concrete strength of the each specimens on day of testing was obtained from three standard cylinders, 6" in diameter and 12" in. height; results are presented in Table 7-6 and are the values used in the OpenSees models.

Table 7-6. Material properties of planar C-PSW/CF walls.

Names of Specimens	Concrete Strength (psi)	F_y (ksi)	F_u (ksi)	P (kip)
CW-42-55-10-T	6508.0	61.2	68.6	210
CW-42-55-20-T	7789.0	61.2	68.6	505
CW-42-14-20-T	8741.0	61.2	68.6	560
CW-42-14-20-TS	8408.0	61.2	68.6	540
CW-42-55-30-T	7386.0	61.2	68.6	710

The specimens were built from the same steel material (i.e., from the same steel heat), therefore, only three coupon tests were conducted total, as representative of all specimens; the resulting average stress-strain curve is presented in Figure 7-38 and was used to define the steel property of all specimens in the numerical analyses.

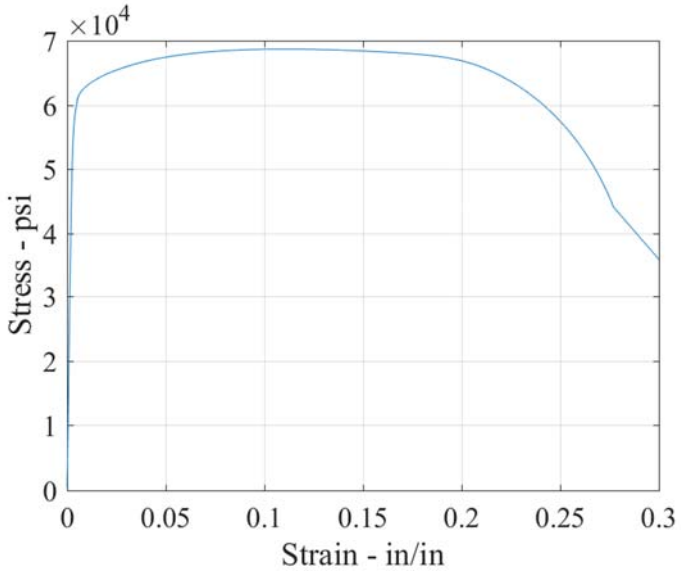

Figure 7-38. Stress-Strain relation of steel used in specimens.

7.4.2 Instrumentation

All of the planar C-PSW/CF wall specimens were instrumented with string potentiometers, inclinometers, linear variable differential transformer (LVDT), and strain gauges. String potentiometers were used to obtain in-plane displacements along the height and rotations at the base. LVDTs were mounted to measure the vertical and horizontal displacement of the concrete foundation (Figure 7-39).

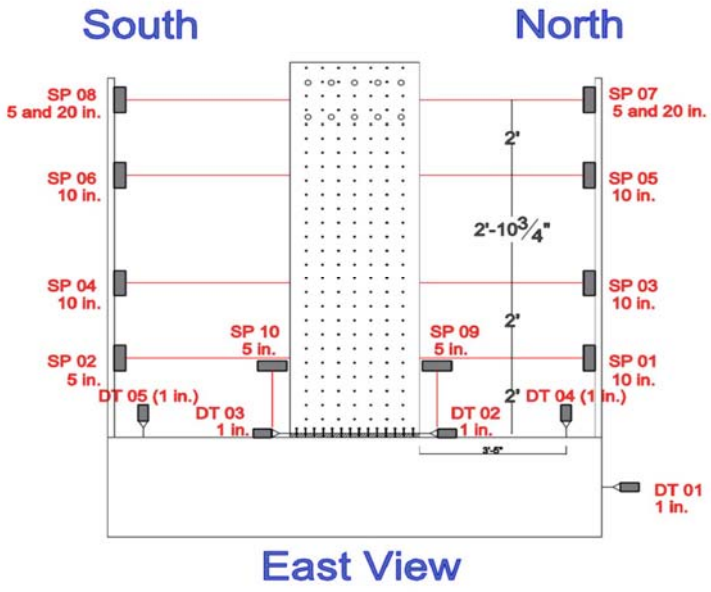

Figure 7-39. In-plane instrumentation of string potentiometers and LVDTs.

In order to measure the global rotation at set locations, inclinometers were put on the concrete foundation, the base plate, clevises, and load beams as shown in Figure 7-40.

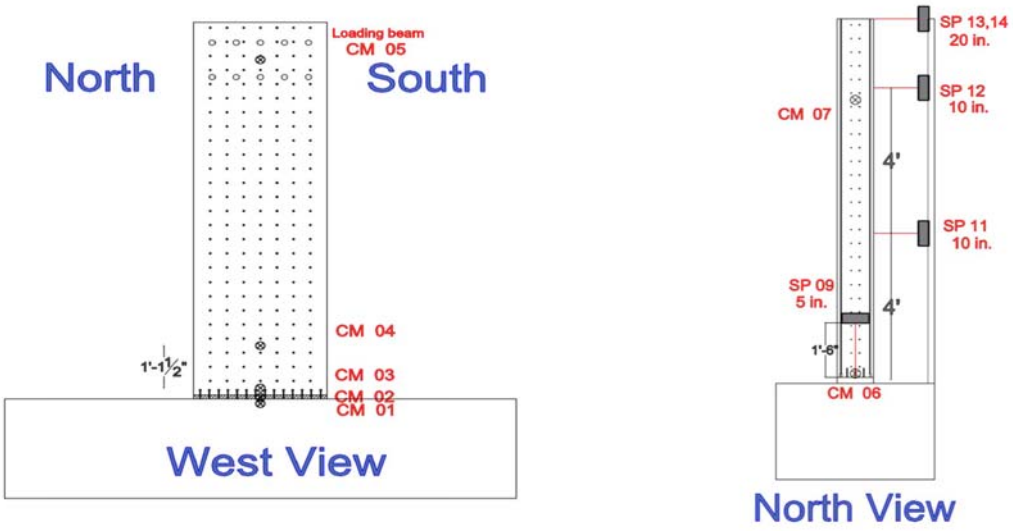

a) **b)**

Figure 7-40. The location of inclinometers in a) West view and b) North view.

7.4.3 Loading Protocol

The walls were tested using three force-controlled cycles up to 75% of yield force, and then with displacement-controlled cycles with three cycles at each target displacement amplitudes up to $3\Delta_y$ and two cycles thereafter until the test was stopped. The corresponding loading protocol is schematically shown in Figure 7-41.

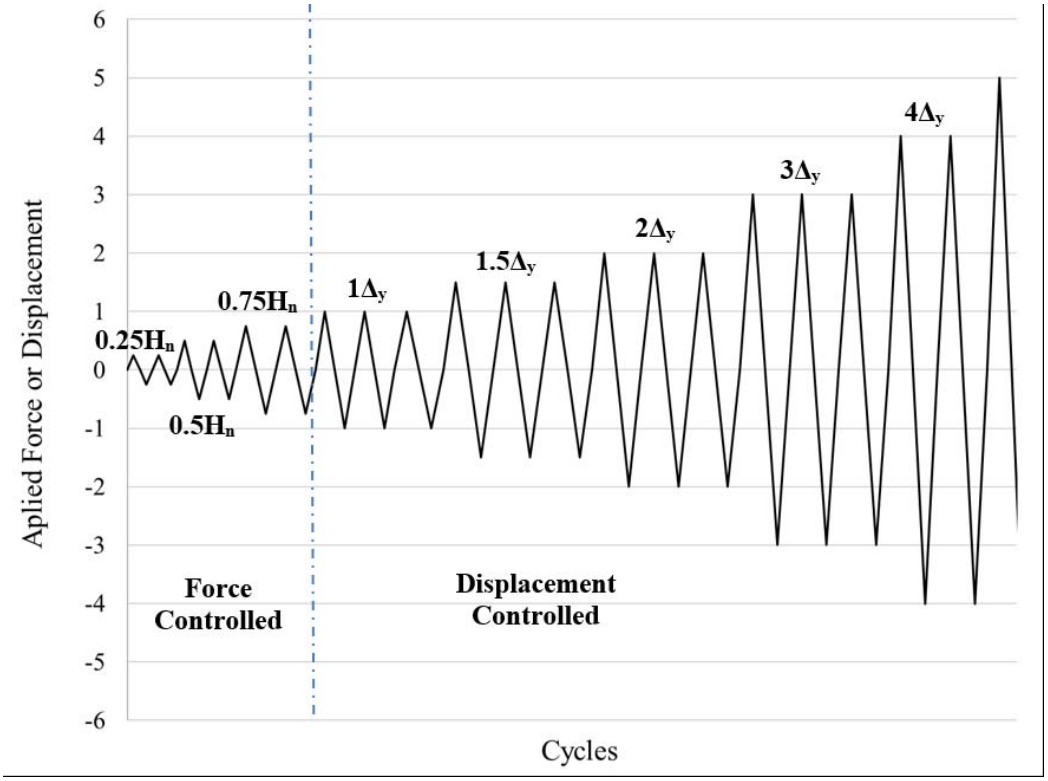

Figure 7-41. Loading protocol of the specimens.

7.4.4 Numerical Calibration for Distributed Plasticity Models

7.4.4.1 Cross Sectional Analysis of Planar C-PSW/CF Walls for Elasto-Plastic Material

To eliminate risk of errors due to lack of a graphic interface, a cross-sectional analysis using elastic-perfectly-plastic material behavior was first performed to compare the OpenSees results for the planar C-PSW/CF walls with those from hand calculations assuming simple plastic theory. Steel was defined as an elastic perfectly plastic material having 50 ksi strength in both compression and in tension; and concrete was 6 ksi strength in compression but no tensile strength. The same fiber analysis code mentioned in Section 7.3.4.1 was used to obtain the moment-curvature relation of the cross-section shown in Figure 7-42. Results show the plastic moment of the cross section to be 1115 k-ft. (13,380 kip-in) and the plastic neutral axis is located at 7.68” from the tip of the cross-section on the compression side.

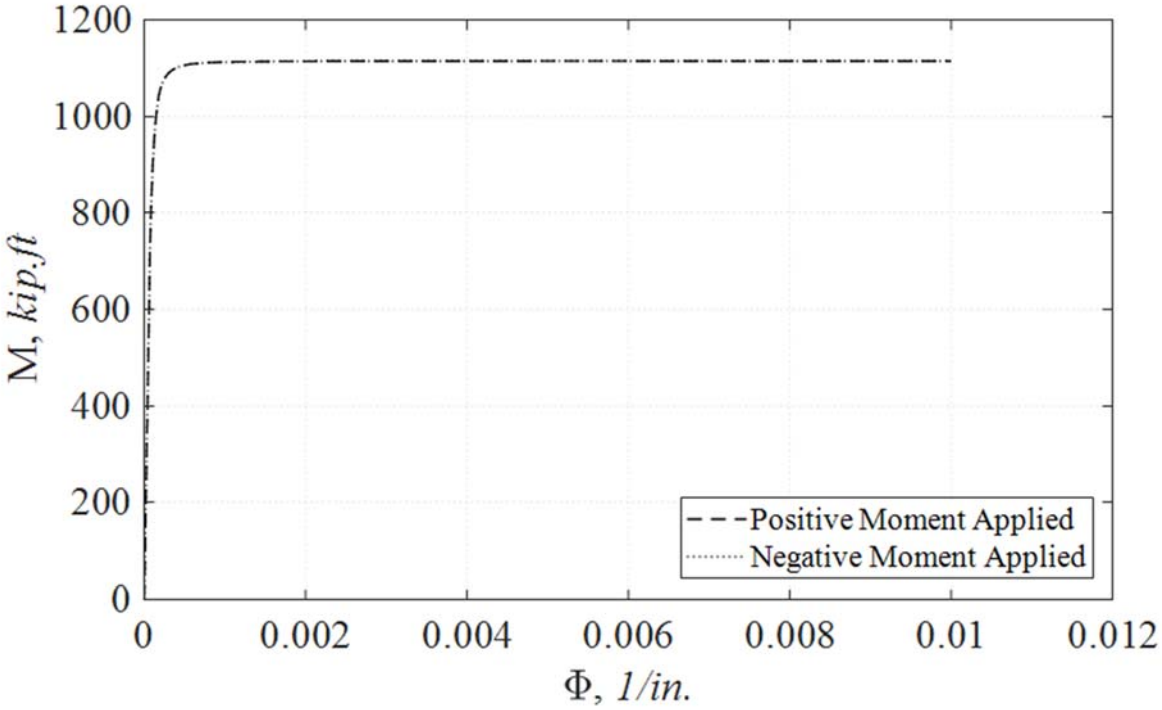

Figure 7-42. Moment Curvature relation for the cross-section of planar C-PSW/CF walls using Elasto-Perfectly Plastic Materials.

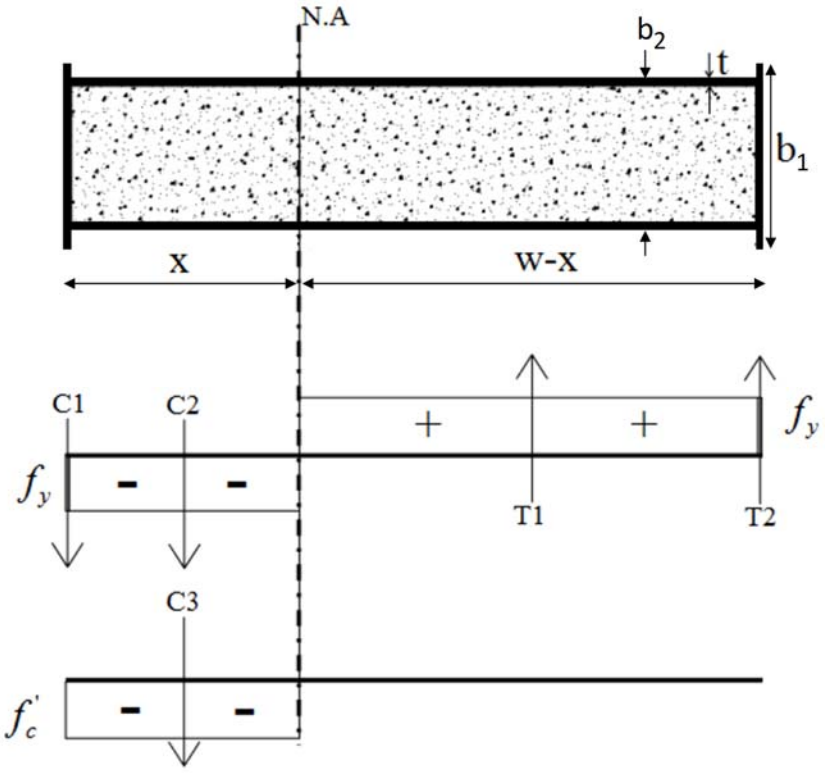

Figure 7-43. Stress distribution for planar C-PSW/CF walls.

Using the cross-section and stress distribution shown in Figure 7-43, results from cross-section analysis using simple plastic theory were obtained as follows:

The compression forces are:

$$C_1 = b_1 * t * F_y \quad \textbf{(7.10)}$$

$$C_2 = 2 * t * (x - t) * F_y \quad \textbf{(7.11)}$$

$$C_3 = (b_2 - 2 * t) * (x - t) * f'_c \quad \textbf{(7.12)}$$

where *x* is the distance from plastic neutral axis (PNA) to top of flange, and the tensile forces are:

$$T_1 = 2 * t * (w - t - x) * F_y \quad \textbf{(7.13)}$$

$$T_2 = b_1 * t * F_y \quad \textbf{(7.14)}$$

By equating compressive forces to tensile forces, *x* can be calculated as:

$$C_1 + C_2 + C_3 = T_1 + T_2 \quad \textbf{(7.15)}$$

$$x = \frac{2 * t * w * F_y + (-2 * t + b_2) * t * f'_c}{4 * t_s * F_y + (b_2 - 2 * t) * f'_c} \quad \textbf{(7.16)}$$

The resulting plastic moment capacity is given by:

$$M_p = C_1 * \left(x - \frac{t}{2}\right) + (C_2 + C_3) * \frac{(x - t)}{2} + T_1 * \frac{(w - t - x)}{2} + T_2 * (w - x - \frac{t}{2}) \quad \textbf{(7.17)}$$

Using Equations 7.16 and 7.17, the plastic moment, M_p, was calculated to be 1116 kip-in and the neutral axis was determined to be at 7.6 in. The difference in the plastic moments obtained from hand calculations and from the fiber-analysis code developed in OpenSees is 0.09%, while the error in the plastic neutral axis location is 0.22% (the difference coming from neglecting the short elastic part of the stress-strain curve,

which is considered negligible). This confirmed that the correct cross section was created for the walls in the OpenSees models.

7.4.4.2 Material Models Parameters

For the above verified cross-sections of the walls, calibration of the OpenSees models were performed with the material models in Section 6 using material properties measured from coupon and cylinder tests. This section documents how the material model parameters were selected in order to replicate the hysteretic planar C-PSW/CF wall specimens.

The same steel grade was used for web and flanges, which is ASTM A572 Gr 50. Therefore, the same buckling and low-fatigue parameters were assigned to the *Reinforcing Steel Material* used for the flanges and web. Also, the concrete confinement model by Susantha et al. (2001) was used to determine the concrete strength and ductility at both ends of the cross-section over a length equal to half the width of the cross-section, while rest of the concrete cross-section was assigned a concrete model having unconfined concrete strength (corresponding to the value measured on the day of the testing) but the same ductility as that of the confined concrete.

The backbone curves of the steel material was defined by the parameters, f_y, E_s, ε_y, f_u, E_{sh}, ε_{sh}, and ε_u (see Section 6.2.1) to replicate the data from coupon test, using values of 61.2 ksi, 22500 ksi, 0.00211, 68.6 ksi, 1125 ksi, 0.00221 and 0.15 to obtain good agreement with coupon test, as shown in Figure 7-44.

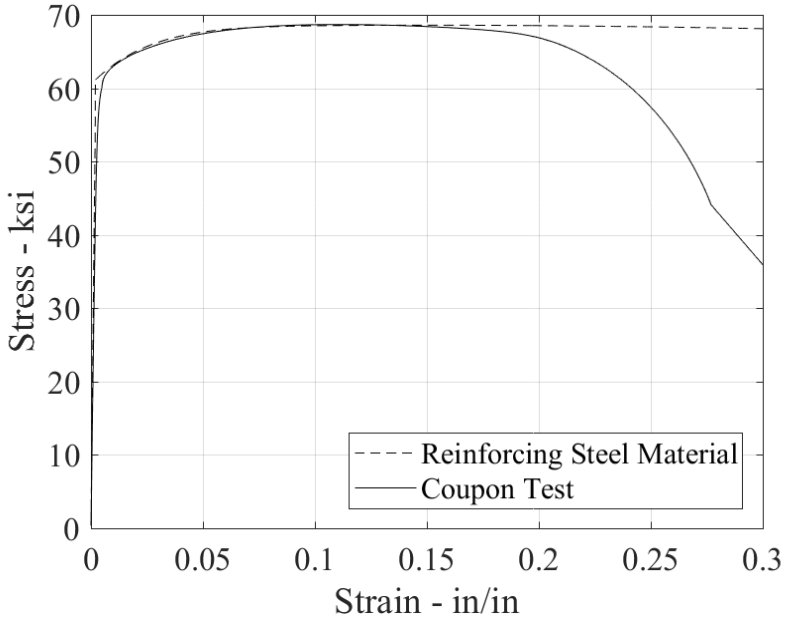

Figure 7-44. Steel backbone curve comparison between RSM parameter and coupon test.

For the five planar C-PSW/CF walls tested used for calibration of the hysteretic steel model, different axial loads and tie spacing were used, and, correspondingly, buckling and fracture occurred at various points during the hysteretic response, but at similar locations. However, the calibration objective was to replicate as closely as possible all of the test results with a single set of buckling and fracture parameters to be used in the IDA. After many trials, good results were empirically obtained for the buckling parameters using a buckling curve reduction factor, r, of 0.4; an amplification factor, β, of 1.0; and a buckling constant, γ, of 1.0 for buckling, which are the same parameters used for C-PSW/CF-NB1 wall (Alzeni and Bruneau 2014) (see Section 7.3.4.2). However, note that since the slenderness ratio in this model is a physical parameter, different slenderness ratios were input to walls having 4.5" tie spacing (20.8) and to walls having 9" tie spacing (41.6). As for the low-cycle fatigue parameters, new values were determined to fit the results for the planar walls having rectangular ends. Following the on empirical calibration approach described in Section 7.3.4.2, using a fatigue ductility coefficient, C_f, of 0.21, a fatigue ductility exponent, α, of 0.515, and a cyclic strength reduction constant, C_d, of 0.3 allowed to replicate closely the observed hysteretic behavior of the tested specimens, including the strength and stiffness degradation observed in repeated excursions at the same drift. Default values for the Menegotto-Pinto curve parameters and hardening constant were used.

The values for the confined concrete parameters (Table 7-7) were obtained by entering measured average concrete strength from cylinder tests into the Susantha et al. (2001) equations for rectangular composite cross-section (see Appendix A.3.1.2) at the ends of the concrete cross-section (i.e., the region labeled as "1" in Figure 7-45). In addition, the same ductile behavior was given to the concrete located between these ends (i.e., the region labeled "2" in Figure 7-45), but using the average unconfined concrete strength from cylinder tests. Figure 7-46 illustrates the resulting backbone curve for the concrete used in both regions, using the values for Specimen *CW-42-55-10-T.*

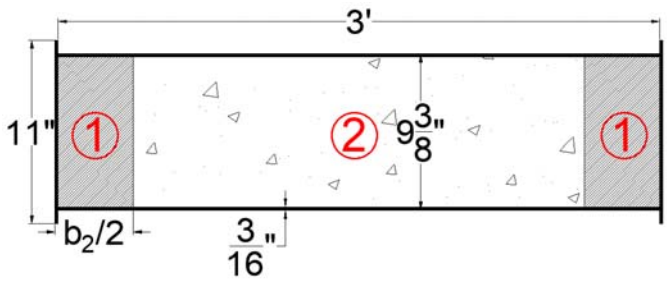

Figure 7-45. Two different concrete regions where different properties were assigned to the cross-section.

Table 7-7. Concrete inputs for planar C-PSW/CF walls.

Specimens	f_{PC}, ksi (Region2/ Region1)	E_C, ksi	ε_{CO} (Region2/ Region1)	f_{CU}, ksi (Region2/ Region1)	ε_{CU}	Lambda	Z, ksi	α
CW-42-55-10-T	6.508/ 8.61	4598	2.831E-3/3.754E-3	5.88/ 7.79	0.04	0.7	25	0.903
CW-42-55-20-T	7.789/ 9.752	5031	3.096E-3/3.877E-3	6.924/ 8.67	0.04	0.1	33	0.889
CW-42-14-20-T	8.7411/ 10.77	5329	3.28E-3/ 4.04E-3	7.7/ 9.495	0.04	0.7	38	0.881
CW-42-14-20-TS	8.408/ 10.42	5227	3.22E-3/ 3.98E-3	7.43/ 9.21	0.04	0.7	36	0.884
CW-42-55-30-T	7.386/ 9.31	4899	3.02E-3/ 3.8E-3	6.59/ 8.305	0.04	0.05	30	0.892

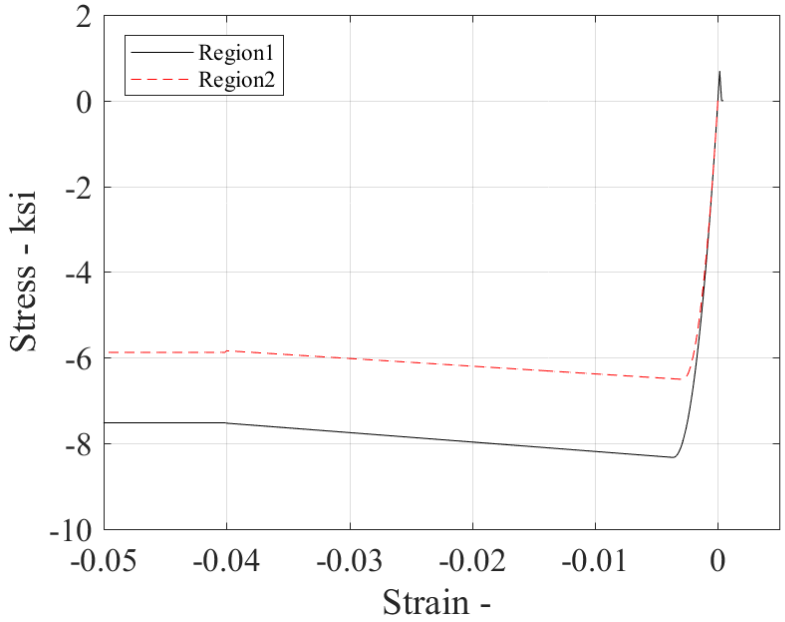

Figure 7-46. Concrete backbone curves for both Region 1 and Region 2.

7.4.4.3 Element Type

In this section, the specific element type used for the planar C-PSW/CF walls is addressed in calibration point of view.

As was previously done for wall C-PSW/CF-NB1 (as described in Section 7.3.4.3), displacement-based nonlinear elements were only assigned to the plastic hinge region of the walls and elastic elements were used for the rest of the wall specimens (Figure 7-47). The plastic hinge length was again determined from the vertical distance between the yield (1063 kip-ft) and plastic (1115 kip-ft) moments of the cross-section (Figure 7-42). This resulted in 5.04 in. plastic hinge length, but this length was increased to 18 in., to include two more 6 in. elements to account for the fact that the maximum moment developed at the base is greater than the plastic moment value.

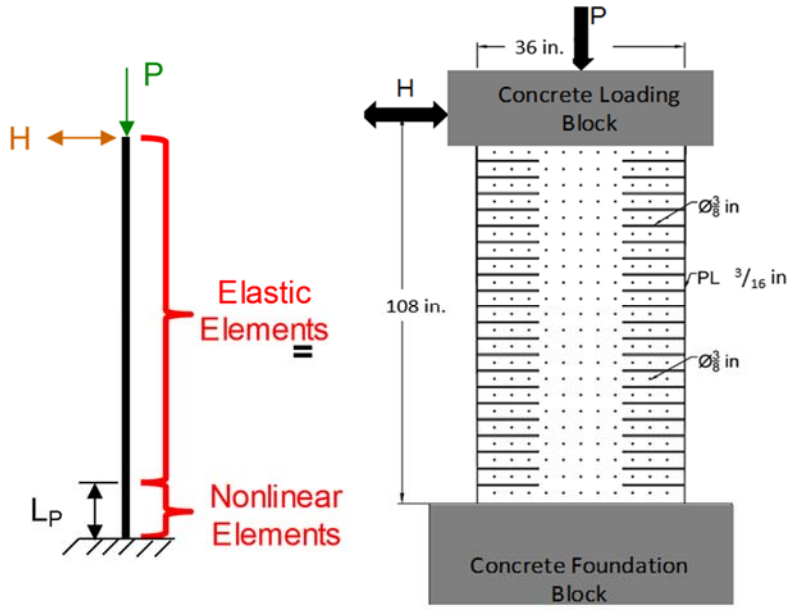

Figure 7-47. Representation of OpenSees models for the wall specimens.

Analyses were conducted to determine the appropriate number and size of elements to use in plastic hinge region for the *Reinforcing Steel Material* model. For this purpose, the test results of specimen *CW-42-55-10-T* were used and compared with analysis results obtained with various number of elements having three integration points (NIPs) using the same material parameters. As seen in Figure 7-48, there was no convergence in results as a function of the element sizes considered, unlike what was observed for the walls having round-end C-PSW/CF-NB1 (Alzeni and Bruneau 2014) in Figure 7-24. To investigate this further, the models were re-analyzed without accounting for material degradation (i.e., not accounting for fracture and buckling) and the largest element size for which convergence was observed at high local curvature values was chosen for the wall specimens. Figure 7-49 shows that using 6" long elements was adequate for

the specimen, and that results diverged for longer elements. Therefore, 6 in. elements were used over plastic hinge length.

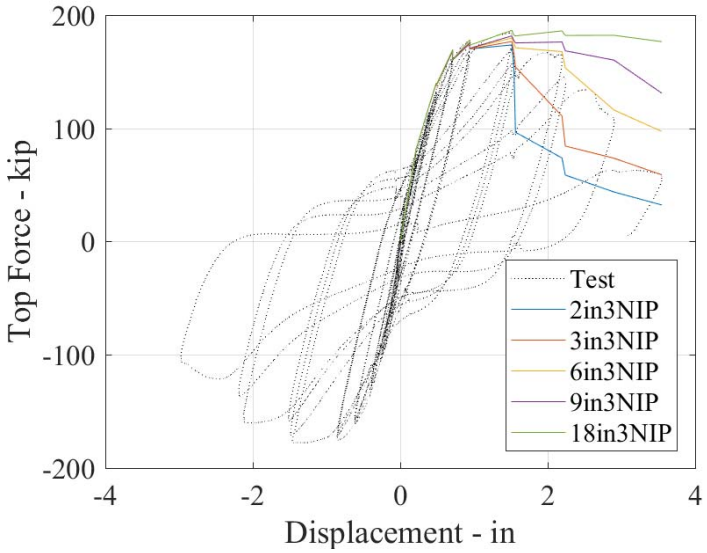

Figure 7-48. Element size study for specimen CW-42-55-10-T.

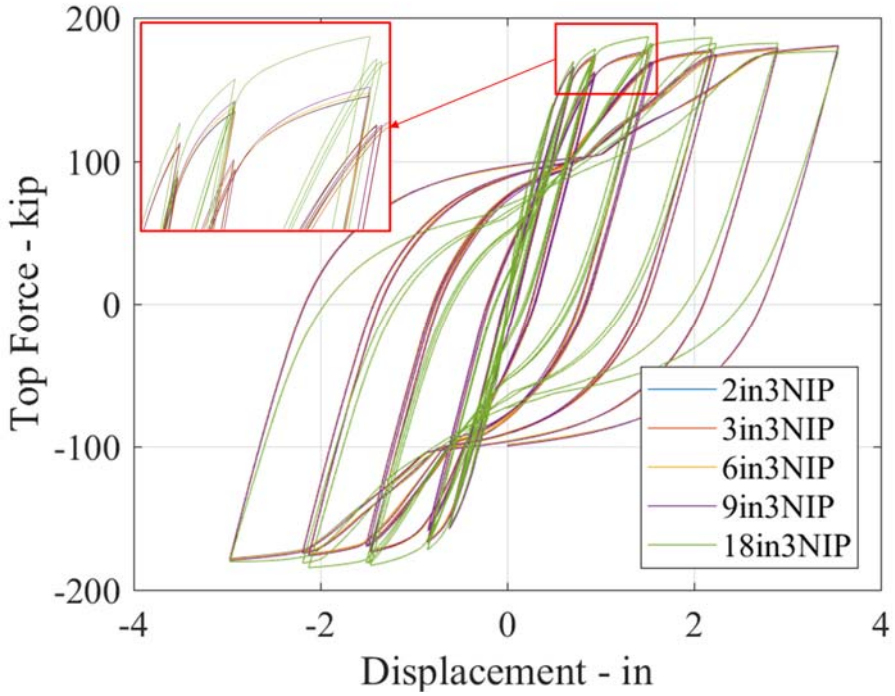

Figure 7-49. Element size study with no degradation models for specimen CW-42-55-10-T.

Moreover, the sensitivity of results to two additional parameters was assessed. First, the effect of mesh size for the fibers used in the cross-section was investigated. Results in Figure 7-50 indicate that using different

mesh sizes did not affect the response. Nonetheless, 1 in. thick fibers were used to avoid possible convergence errors (due to abrupt shifts in location of the plastic neutral) axis during earthquake analysis. This was done while also balancing the fact that using more fibers can cause premature termination of the analysis due to the high memory requirement of the *Reinforcing Steel Material* model used for the steel fibers. Second, a comparison of results obtained with displacement-based and force-based elements was performed. The two element types have different iteration procedures (see Section A.4). Since the iteration of force-based elements starts with initial force at the nodes, the local curvature becomes high with smaller elements, such as with 6 in. elements. Hence, fibers fractured quicker and OpenSees (McKenna et al. 2016) gave "large trial strain" errors. In order to have the same response when fracture and buckling are considered, the curvatures along the plastic hinge length should be close to each other when obtained with each type of elements. Therefore, one force-based element with four NIPs (including the integration points at the element ends) was used to replicate three displacement-based elements (with three NIPs, including the element ends) over the plastic hinge length, with the same steel and concrete parameters as in Figure 7-51. The results are shown in Figure 7-52. Before fracture, both element types have the same response. After fracture, there is a slight observable difference in the response obtained from the two element types but it is negligible for all practical purposes.

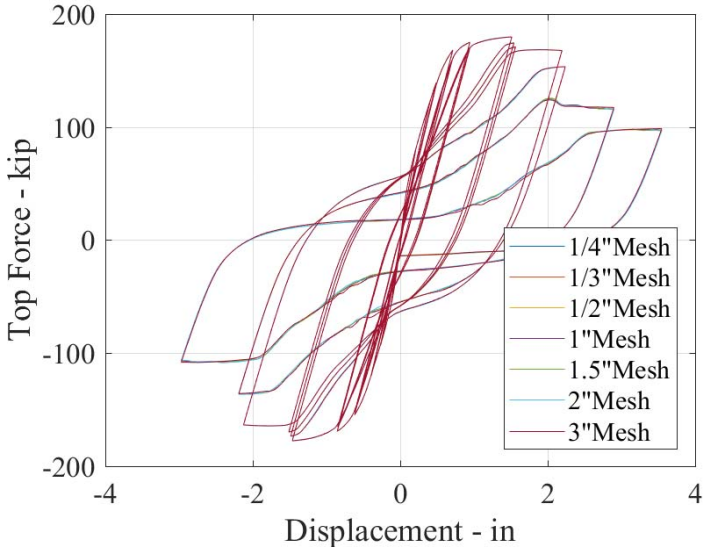

Figure 7-50. Mesh size study for specimen CW-42-55-10-T.

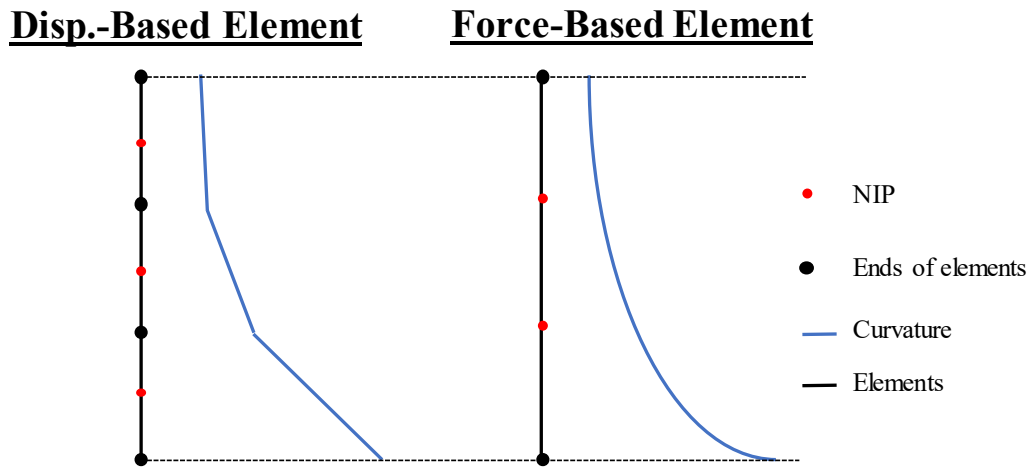

Figure 7-51. Curvature representation at the base for displacement-based and force-based element types for the element study of specimen CW-42-55-10-T.

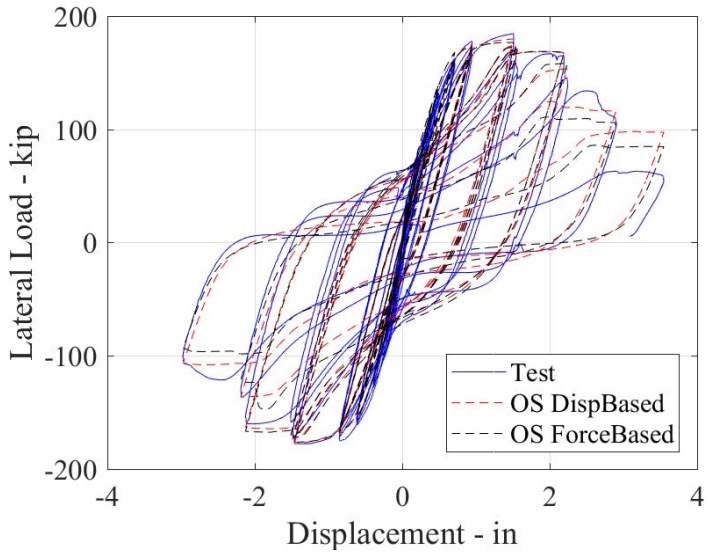

Figure 7-52. Two different nonlinear element type study for specimen CW-42-55-10-T.

7.4.4.4 Comparison of OpenSees Models with Test Data

The base shear-displacement and moment-rotation hysteretic relationships for all of the tested planar C-PSW/CF walls are presented in Figures 7-53a to 7-53e, comparing the experimental results with those obtained using OpenSees. Note that the experimental data was corrected to remove the contribution of the

flexibility of the specimen's footing; correspondingly, the base of the walls was fixed in all of the OpenSees models.

At this time of writing, results for five specimens were reported, namely CW-42-55-10-T, CW-42-55-20-T, CW-42-14-20-T, CW-42-55-30-T and CW-42-14-20-TS. Note that all comparisons are made with the same set of fracture and buckling parameters that will be used for incremental dynamic analysis (IDA). It is understood that if each test were investigated separately, better match between the curves can be obtained by calibrating the set of parameters to each individual specimen. Base shear versus displacement (or lateral load-displacement) are plotted on the left side of Figures 7-53a to 7-53e; corresponding moment-rotation hysteretic curves are plotted on the right side of these figures. Moments were obtained by multiplying the values of the lateral load at the top of the wall (equal to base shear values) by the distance from the top of wall to the location where the inclinometers (107.25 in.) were placed for calculating rotation. CM2 and CM4 (Figure 7-40) were used for analyzing the plastic rotation capacity of CW-42-55-10-T and CW-42-55-20-T, and CM 2 and CM 6 (Figure 7-40) were used for the rest of specimen. However, the location of CM6 was changed to the location of CM4 for the others.

A detailed description of all observations made throughout each test is provided by Shafaei et al. (2019). Therefore, focus here is on presenting the difference between the experimental data obtained by Shafaei et al. (2019) and the results obtained from OpenSees models described above.

Results obtained from the OpenSees model of the *CW-42-55-10-T* specimen closely matched the experimental data, with small errors, as shown in Figure 7-53a. The maximum force of 185 kips (hence maximum moment of 1523 kip-ft.) was matched within 2.7%. In addition, the rotation at maximum force (0.00982 rad), corresponding to when the specimen was displaced 1.50 in., matched with a maximum difference of 13%. The difference in maximum lateral load increased to 7% for the *CW-42-55-20-T* specimen. However, in the first excursion at 2.5 in. displacement in the negative direction, the discrepancy in lateral load increased to 19%, even though a relatively good match (8% difference) was obtained for the same excursion in the positive direction. For the moment-rotation curve comparison, the rotation at maximum moment of 0.0079 rad, reached when the drift was 1.33 in. matched with a maximum difference of 18%. By comparison, the maximum lateral load capacity and moment capacity obtained with OpenSees were only within 1.8% of the experimental results for Specimen *CW-42-14-20-T*. Also, the rotation at maximum force matched within 5%. However, the sudden drop in strength that occurred during the last excursion was not captured by the analytical model. The difference in the maximum lateral load (or moment) and rotation are 1.4% and 8% for Specimen *CW-42-14-20-TS*, respectively. However, the last two

excursions did not match as closely as for the other specimens, with maximum differences of 30% in lateral load capacity. For the Specimen *CW-42-55-30-T*, the lateral load capacity matched within 10%. For this particular specimen, the initial stiffness did not match closely experimental curve for the lateral load versus displacement curve, but the same initial stiffness matched better for the moment-curvature curve. In addition, in this case, the OpenSees models started fracturing before the test data. Therefore, there is a mismatch for maximum rotation (70% difference), with the OpenSees results being on the conservative side.

Recall that the objective of the above calibration exercise was to determine one a single of fatigue and buckling parameters that allows matching as best as possible all of the test data of planar C-PSW/CF walls, and that could consequently be used in the FEMA P695 analyses. Evidently, if the objective instead was to find individual sets of buckling and fatigue parameters to match each of the test data individually, a better match for all the specimens would be possible, and magnitude of the above discrepancies could have been reduced.

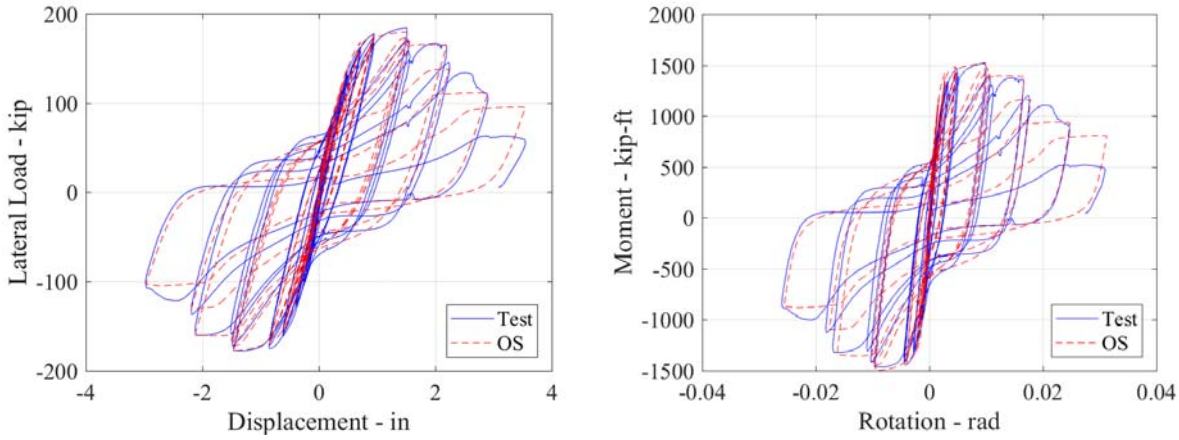

a)

Figure 7-53. Base shear-displacement (left) and moment-rotation (right) comparisons of OpenSees models with test data for a) CW-42-55-10-T; b) CW-42-55-20-T; c) CW-42-14-20-T; d) CW-42-14-20-TS; and e) CW-42-55-30-T.

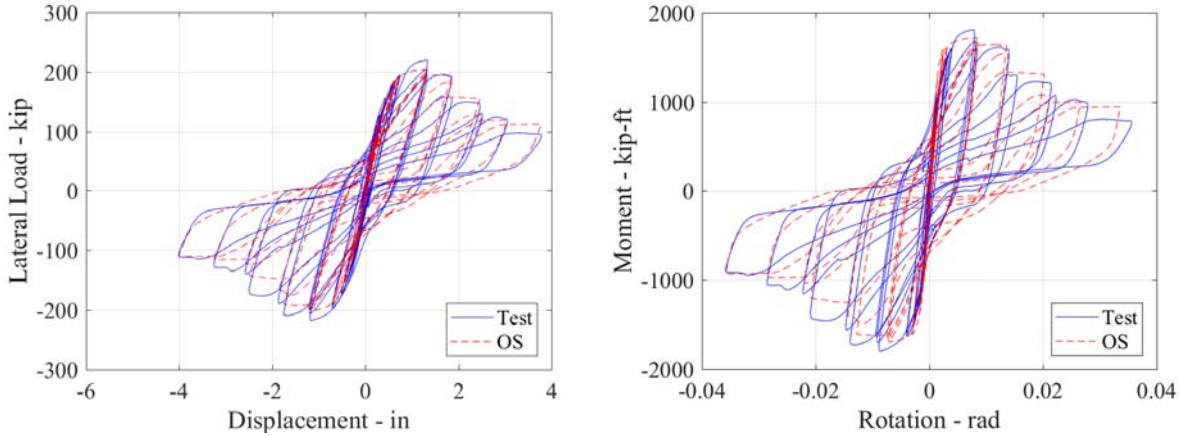

b)

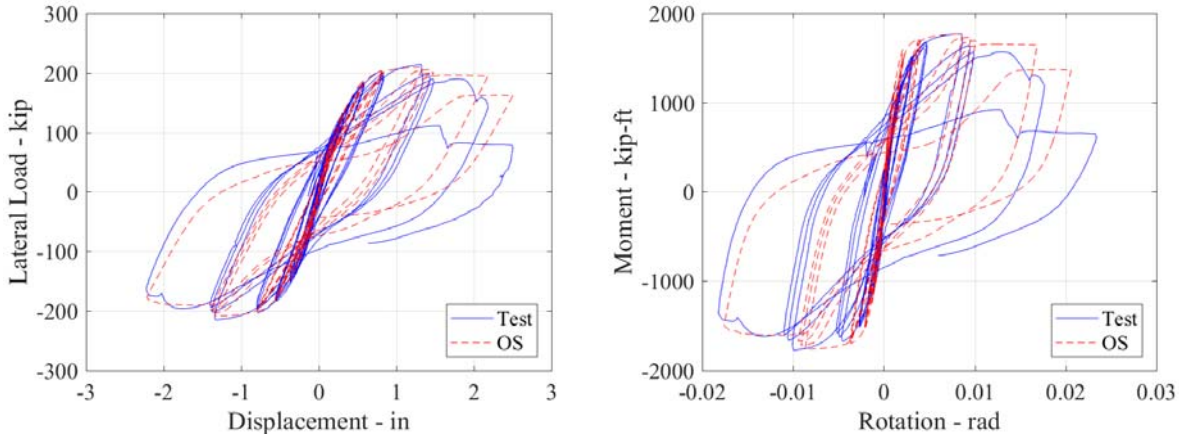

c)

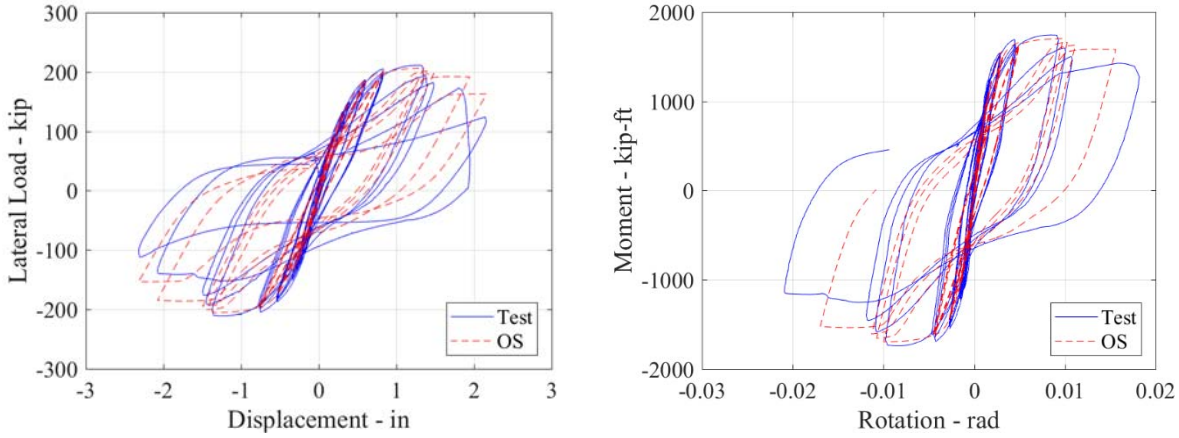

d)

Figure 7-53. (Continued)

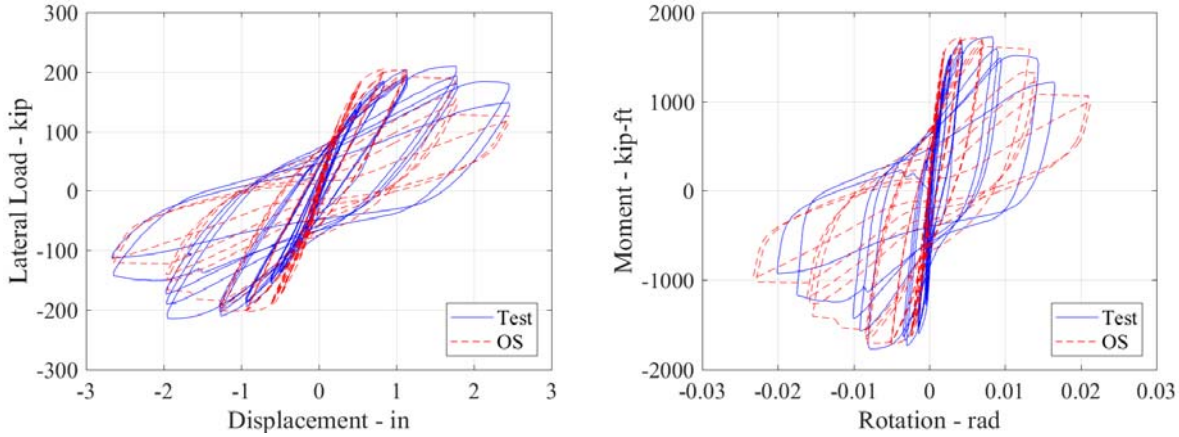

e)

Figure 7-53. (Continued)

7.5 Tests of Coupling Beams by Nie et al. (2014)

The calibration of the OpenSees models used for the coupling beams was done using experimental results from the study conducted by Nie et al. (2014) on six coupling beam specimens connected to two shear wall piers and subjected to cyclic loading. The coupling beam width and height were 5.91 in. (150 mm.) and 11.81 in. (300 mm.), respectively, as shown in Figure 7-54. The thickness (t) and the length of the specimen (l_b) varied from one specimen to the other.

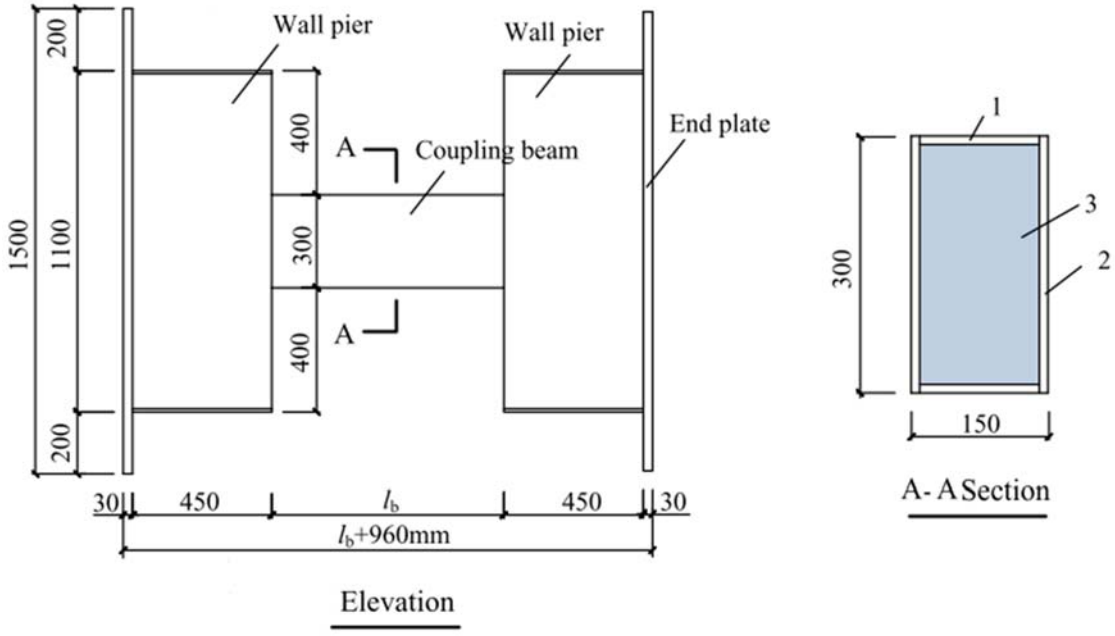

Figure 7-54. The details of tested specimens (dimensions are in mm.) (Nie et al. 2014).

Table 7-8 shows the span and thickness of the flange and web for each specimen. Nie et al. (2014) calculated the shear forces associated with flexural capacity and associated with the nominal shear capacity of specimens, and concluded that the Specimens *CFSCB-1* to *-3* coupling beams had a flexure-governed behavior and failure mode, but that those of Specimens CFSCB-4 to *-6* were shear-governed. The coupling beams in the archetype of the C-PSW/CF system considered for the current FEMA P695 study (these archetypes will be described in Section 5) will be purposely designed to fail in a flexure-governed mode. In addition, these archetypes will be designed with coupling beams having span-to-depth ratio of three, four and five. Therefore, the results of *CFSCB-1* to *-3* were considered more representative and used here to calibrate the coupling beam models in OpenSees (McKenna et al. 2016). Among those three coupling beam specimens tested by Nie et al. (2014), *CFSCB-1* and *CFSCB-3* were retained for calibration, because they provided a good range of different steel plate sizes and thickness for flange and web.

Table 7-8. Parameters of coupling beam specimens (Nie et al. 2014).

Specimen Name	***Span, l_b (in.)***	***Coupling Beam Thickness, t (in.)***		***Span-to-height ratio***
		Flange	**Web**	
CFSCB-1	29.53	0.196	0.196	2.5
CFSCB-2	29.53	0.118	0.118	2.5
CFSCB-3	29.53	0.315	0.118	2.5
CFSCB-4	15.75	0.196	0.196	1.33
CFSCB-5	15.75	0.118	0.315	1.33
CFSCB-6	15.75	0.196	0.196	1.33

Figure 7-55 schematically shows the setup used for testing the coupling beam specimens (commonly known as a pantograph). The specimens (indicated as 1 in Figure 7-55) were rotated 90º and attached with high-strength bolts to a foundation girder (number 4 in Figure 7-55) and an L-shape loading girder (2 in Figure 7-55). In this test set-up, a four bar mechanism (3 in Figure 7-55) is used to prevent the rotation of the L-shape loading girder. Such pantograph devices have commonly been used by many researchers to perform shear tests in the past. The specimens were cycled with a 225-kip (1000-kN) servo-hydraulic actuator whose center of loading passed through the inflection points (i.e. the center of specimens). This enables equal rotations at the two ends of the beams.

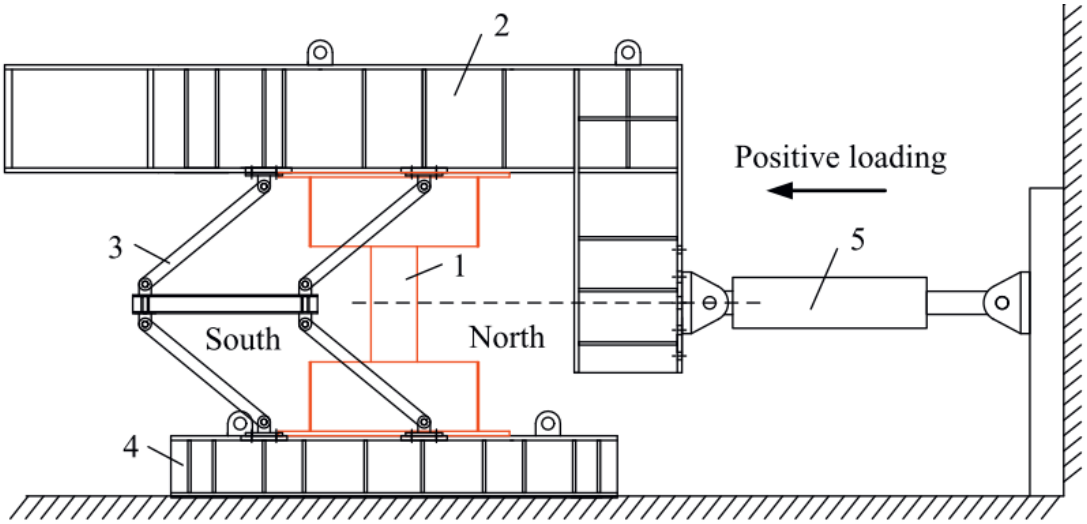

1- Specimen; 2- L-shape loading girder; 3- Four-bar mechanism;
4- Foundation girder; 5- Actuator.

Figure 7-55. Test setup of coupling beams (Nie et al. 2014).

7.5.1 Material Properties

Table 7-9 shows the Young's Modulus (E_s), the yield strength (f_y) and the ultimate strength (f_u) for each type of steel plates used for the beam specimens. The average concrete strength was measured with three 6 in. x 6 in. cubes for each specimen. However, the concrete strength in U.S. practice are from 6 in. x 12 in. cylinder tests. Therefore, the relationship (equation 7.18) by Mindess et al. (1981) was used to convert the cubic strength, f_{cu}, into the corresponding 28 day compressive strength of a 6″ diameter by 12″ high cylinder, f'_c. Hence, instead of 7.38 ksi and 8.25 ksi cubic strengths (f_{cu}), 5.904 ksi and 6.6 ksi concrete strength was used for *CFSCB-1* and *CFSCB-3*, respectively.

$$f_c' = 0.8 * \mathrm{f_{cu}} \quad \textbf{(7.18)}$$

where f_{cu} is the concrete strength from cubic specimens, and f'_c is the concrete strength from cylinder specimens.

Table 7-9. Material properties of steel plates in coupling beam specimens (Nie et al. 2014).

Steel Plates	E_s (ksi)	f_y (ksi)	f_u (ksi)
0.118 in.	29878	48.88	70.49
0.196 in.	29733	42.35	66.43
0.315 in.	29733	42.64	67.44

7.5.2 Instrumentation

The specimens were instrumented with linear variable differential transformer (LVDT) and strain gauges (Figure 7-56). Five of the LVDTs were mounted horizontally in order to measure the lateral displacement. The deformation components of the coupling beam were measured by two pairs of diagonal LVDTs and four pairs of LVDTs. The vertical LVDTs were attached to the specimen to provide data for calculation of rotations. Finally, strain-gauge rosettes were mounted on steel flange and web at critical locations.

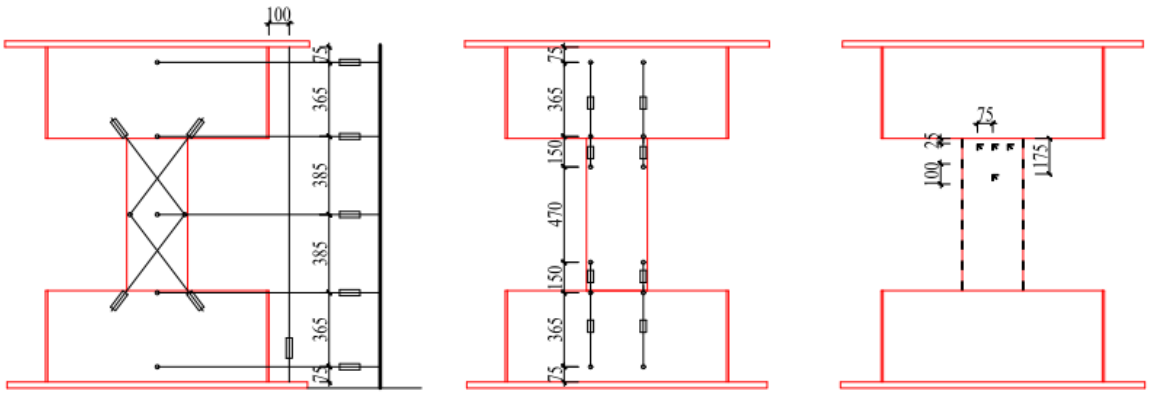

Figure 7-56. Instrumentation of coupling beams (dimensions are in mm.) (Nie et al. 2014).

7.5.3 Loading Protocol

The loading protocol for the beam specimens is shown in Figure 7-57. For cycles having lateral displacement amplitude less than the value of Δ_{inc} shown in that figure (referred to as the "prescribed displacement increment"), the loading was force-controlled, or which a single cycle at each displacement magnitude was applied at corresponding applied force levels equal to 25%, 50% and 75% of the nominal shear capacity of the cross-section. After Δ_{inc}, the test proceeded in a displacement-control regime, with the specimens subjected to two cycles at each displacement level. For *CFSCB-1*, the Δ_{inc} was chosen as 0.3 in.

(7.5 mm), corresponding to chord rotation (defined by the equation 7.19) of 1/100 rad. However, during the test of *CFSCB-1*, steel fracture propagated quickly. Therefore, for the other specimens, Δ_{inc} was taken as 0.2 in. (5 mm), corresponding to the chord rotation of 1/150 rad.

$$\theta = \frac{\Delta_{upp} - \Delta_{low}}{l_b} \tag{7.19}$$

where Δ_{upp} is the top displacement of the beam, Δ_{low} is the displacement of the beam at the base and l_b is the length of the specimens.

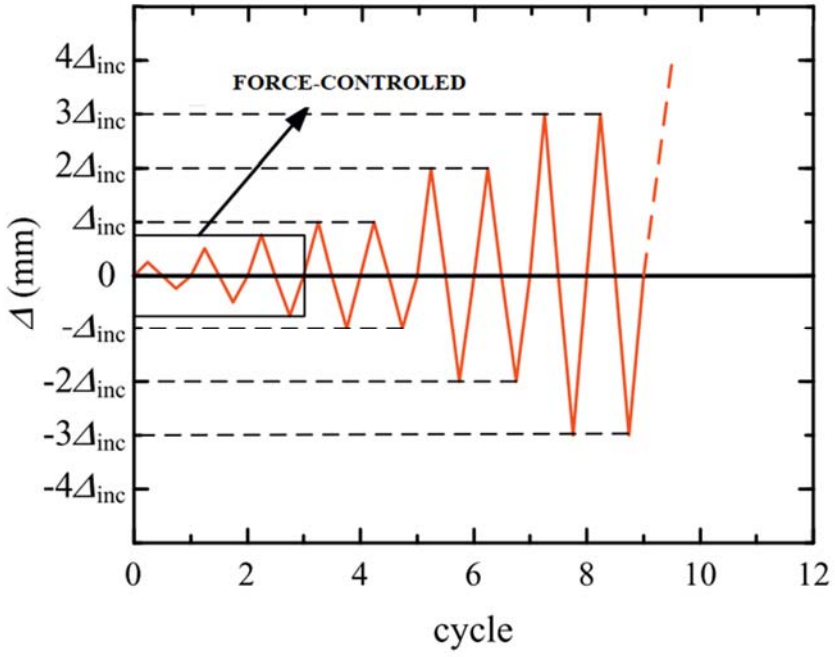

Figure 7-57. Loading protocol of coupling beams (Nie et al. 2014).

7.5.4 Numerical Calibration for Distributed Plasticity Models

7.5.4.1 Cross Sectional Analysis of Coupling Beam Specimen for Elasto-Plastic Material

A cross-sectional analysis using elastic-perfectly-plastic material behavior was first made to relate the OpenSees results for the coupling beam cross-section with those from hand calculations assuming simple plastic theory in order to remove the risk of errors due to lack of a graphic interface. The coordinates of the cross-section in OpenSees function was defined with variables so that the same coordinates can be used for coupling beams that have different dimensions. Therefore, the cross-section analysis was only done for one specimen (*CFSCB-1*) and after satisfactory verification; the variables were changed to define the other specimen.

Steel was defined as an elastic perfectly plastic material having 50 ksi strength in both compression and in tension; and concrete was 6 ksi strength in compression but no tensile strength. The same fiber analysis code mentioned in Section 7.3.4.1 was used to obtain the moment-curvature relation of the cross-section of the coupling beams as shown in Figure 7-58. The plastic moment of the cross section is 134 k-ft. (1608 kip-in) and the plastic neutral axis is located at 2.55 in. from the tip of the cross-section on the compression side.

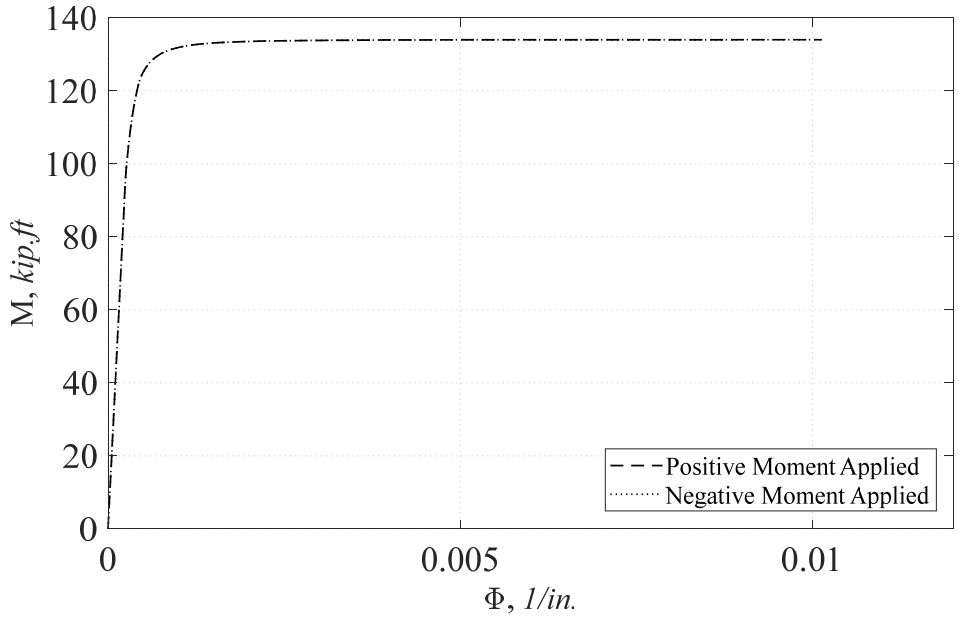

Figure 7-58. **Moment Curvature relation for the cross-section of coupling beams using Elasto-Perfectly Plastic Materials.**

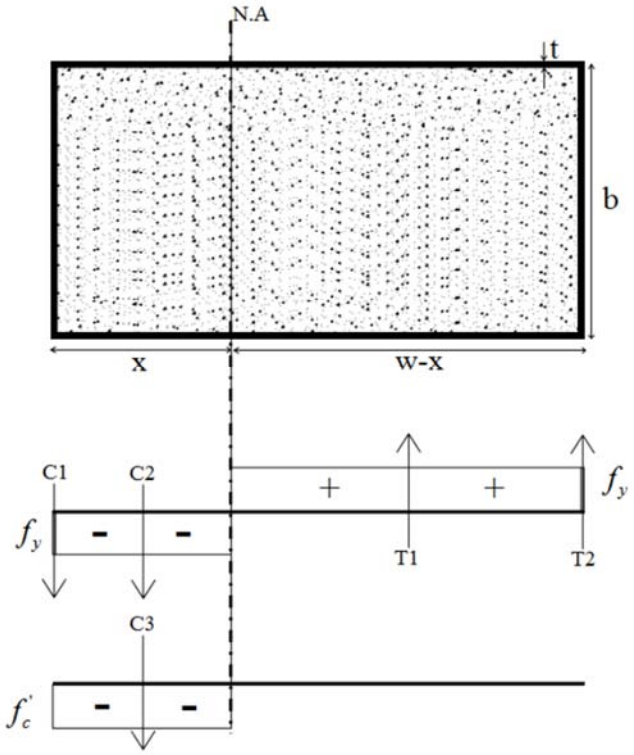

Figure 7-59. Stress distribution for coupling beam.

Using the cross-section and stress distribution shown in Figure 7-59, results from cross-section analysis using simple plastic theory were obtained as follows:

The compression forces are:

$$C_1 = b * t * F_y \quad \textbf{(7.20)}$$

$$C_2 = 2 * t * (x - t) * F_y \quad \textbf{(7.21)}$$

$$C_3 = (b - 2 * t) * (x - t) * f_c' \quad \textbf{(7.22)}$$

where *x* is the distance from plastic neutral axis (PNA) to top of flange, and the tensile forces are:

$$T_1 = 2 * t * (w - t - x) * F_y \quad \textbf{(7.23)}$$

$$T_2 = b * t * F_y \quad \textbf{(7.24)}$$

By equating compressive forces to tensile forces, *x* can be calculated as:

$$C_1 + C_2 + C_3 = T_1 + T_2 \quad \textbf{(7.25)}$$

$$x = \frac{2 * t * w * F_y + (-2 * t + b) * t * f'_c}{4 * t * F_y + (b - 2 * t) * f'_c} \quad \textbf{(7.26)}$$

The resulting plastic moment capacity is given by:

$$M_p = C_1 * \left(x - \frac{t}{2}\right) + (C_2 + C_3) * \frac{(x - t)}{2} + T_1 * \frac{(w - t - x)}{2} + T_2 * (w - x - \frac{t}{2}) \quad \textbf{(7.27)}$$

Using Equations 7.26 and 7.27, the plastic moment, M_p, was calculated to be 134.12 kip-ft and the neutral axis was determined to be at 2.61 in. The difference in the plastic moments obtained from hand calculations and from the fiber-analysis code developed in OpenSees is 0.1%, while the error in the plastic neutral axis location is 0.51%. This confirmed that the correct cross section was created for the walls in the OpenSees models.

7.5.4.2 Material Inputs

After validating that cross-section of the walls was correctly defined (per previous section), calibration of OpenSees models was performed with the material models in Section 6 using material properties measured from coupon and cylinder tests. This section indicates how the material model parameters were selected in order to replicate the coupling beam tests by Nie et al. (2014).

The same steel grade, and therefore the same buckling and low-fatigue parameter values, were assigned to the *Reinforcing Steel Material* model of the web and flanges. However, different backbone curve parameters (f_y, E_s, ε_y, f_u, E_{sh}, ε_{sh}, and ε_u) were assigned for each different type of steel plate as described in Table 7-9. Also, the equations of Susantha et al. (2001) was used to specify the values of the parameters for the confined concrete.

Only three backbone parameters were reported by Nie et al. (2014), which are yield strength (f_y), Young's Modulus (E_s) and ultimate strength (f_u) for each different size of plates, are shown in Table 7-9 (references with complementary information could not be found). The yield strain was calculated by dividing the yield strength to Young's Modulus. However, strain and modulus at the onset of strain-hardening (ε_{sh}, and E_{sh})

and ultimate strain (ε_u) were guessed by trial-and-error. Yield plateau was not considered in the backbone curve, by effectively setting the strain-hardening strain (ε_{sh}) as 0.0001 greater than yield strain (ε_y). Also, the strain-hardening Modulus (E_{sh}) was assumed to be 0.03 times the Young's Modulus (E_s). The ultimate strain was presumed to be 0.15.

Since there were no ties in the coupling beam specimens, the slenderness ratio was calculated by dividing the length of plastic hinges (Figure 7-60) (where steel buckled after yielding) at the ends of the specimens by the average equivalent depth of steel plates. An average value of slenderness ratio was used for *CFSCB-3* specimen, as the thickness of flange and web is different. The resulting slenderness ratios were 10 and 12 for *CFSCB-1* and *CFSCB-3*, respectively.

After many trials, good results were empirically obtained for the buckling parameters using a buckling curve reduction factor, r, of 0.4; an amplification factor, β, of 1.0; and a buckling constant, γ, of 1.0 for buckling. As for the low-cycle fatigue parameters, using a fatigue ductility coefficient, C_f, of 0.21, a fatigue ductility exponent, α, of 0.56, and a cyclic strength reduction constant, C_d, of 0.25 gave good correlation for the observed hysteretic behavior of the tested specimens, even for the strength and stiffness degradation observed in repeated excursions at the same drift. Default values for the Menegotto-Pinto curve parameters and hardening constant were used.

Only confined concrete properties were used for the concrete in coupling beams and values used for the parameters of that model (Table 7-10) were obtained by inputing measured average concrete strength (corrected from cubes by equation 7.18) into the Susantha et al. (2001) equations for rectangular composite cross-section (see Appendix A.3.1.2).

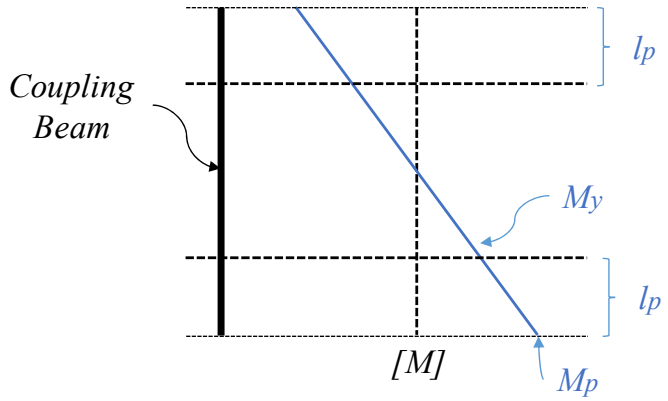

Figure 7-60. Representation of moment diagram for coupling beam specimens.

Table 7-10. Concrete inputs for coupling beams.

Specimens	f_{PC}, ksi	E_C, ksi	ε_{CO}	f_{CU}, ksi	ε_{CU}	Lambda	Z, ksi	α
CFSCB-1	6.52	4380	2.98e-3	5.23	0.04	0.05	37	0.801
CFSCB-3	7.25	4631	2.85e-3	5.24	0.04	0.05	42.6	0.794

7.5.4.3 Element Type

As was done for previous walls, displacement-based nonlinear elements were assigned to the coupling beam specimens. However, fracture and buckling were included only in the elements located at the ends of the coupling beams. Moreover, the wall piers to which the coupling beams were attached had some flexibility that resulted in some additional rotations at the specimens ends as they were cycled. To account for that effect, two rotational spring, whose stiffness was determined by trial-and-error, were added to the ends of the beams (Figure 7-61). After many trials, the resulting stiffness of the rotational springs were assigned to the OpenSees models were 250000 kip-in. and 210000 kip-in. for *CFSCB-1* and *CFSCB-3*, respectively.

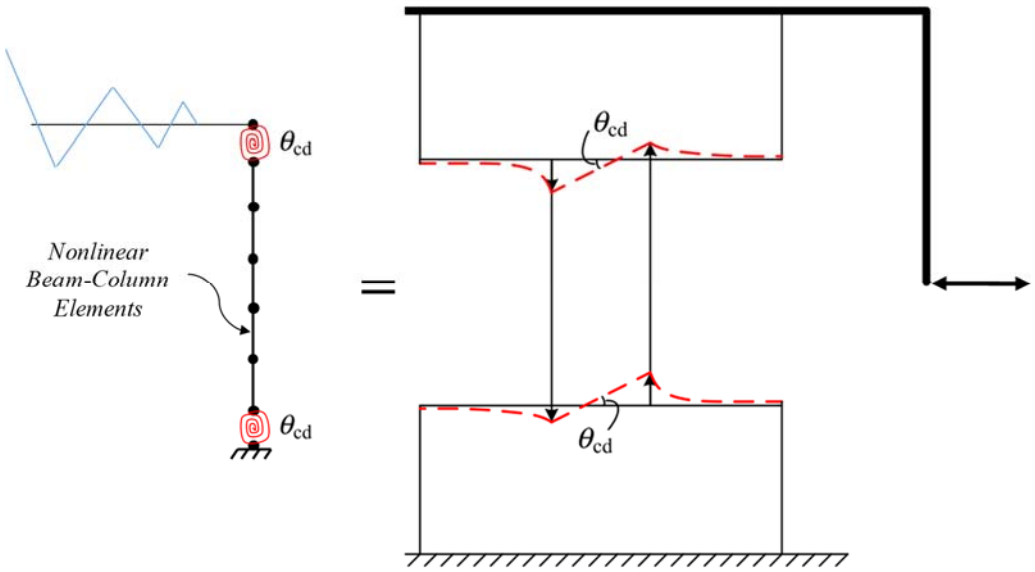

Figure 7-61. Representation of OpenSees models for coupling beam specimens.

As previously shown in Figure 7-48 for planar wall results for the *CW-42-55-10-T* specimen, results vary when different number and size of elements are used with *Reinforcing Steel Material* model. Recall that it was due to high local curvature effect. To investigate this further at that time, the models were re-analyzed without accounting for material degradation (i.e., not accounting for fracture and buckling) and the largest element size for which results superposed with other lines was chosen for the wall specimens. Therefore,

the same strategy was applied here for the coupling beam specimens. The model for Specimen *CFSCB-1* was run with various element sizes having three NIPs and the largest element for which convergence was achieved was chosen for calibration of *Reinforcing Steel Material* model parameters to match the coupling beam experimental results. Figure 7-62 shows that using 6 in. long elements reduced the error between analyses significantly and that results diverged for longer elements. Therefore, 6 in. elements were used along coupling beam specimens.

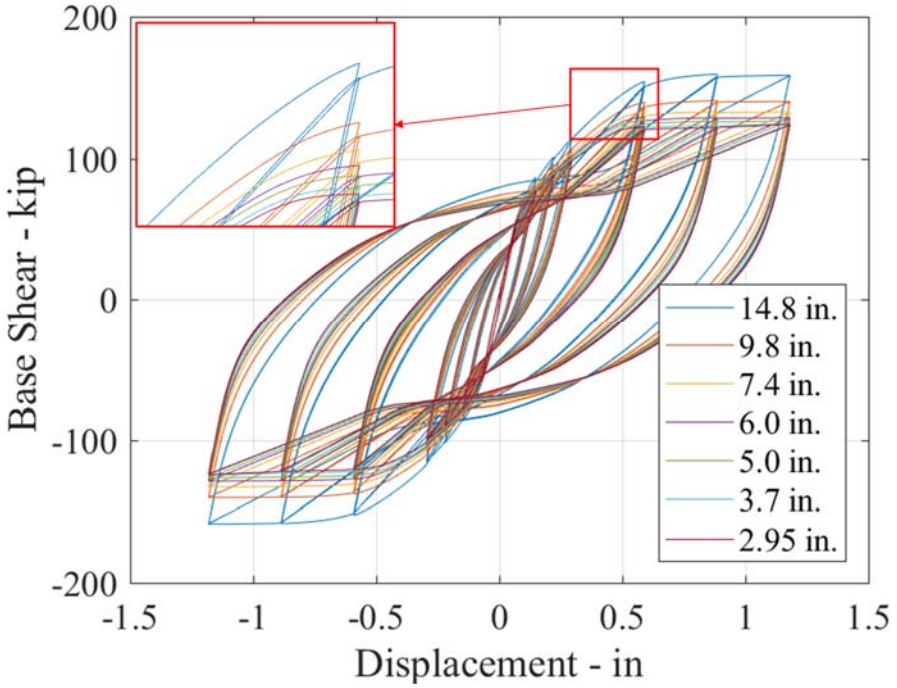

Figure 7-62. Element size study with no degradation models for specimen CFSCB-1.

7.5.4.4 Comparison OpenSees Models with Test Data

The shear force (in kN) versus chord rotation hysteretic relationship for the *CFSCB-1* and *CFSCB-3* coupling beams are presented in Figure 7-63a and 7-63b, comparing the experimental results with those obtained using OpenSees. The chord rotation was calculated by dividing the relative displacements between two ends of coupling beam of the specimens by the length of the coupling beam part of the specimen (Equation 7.19).

CFSCB-1 reached a maximum shear force of 564 kN at a positive rotation of 0.0281 rad and -526 kN at negative rotation of 0.0295 rad. The OpenSees model maximum shear force results matched the experimental ones within 11.3 % in positive direction and 4.8 % the negative direction. However, the

difference increased to 16% in the positive direction and 19% in the negative direction for the first excursion of the subsequent cycle. At the peak displacements in the last cycles, the shear force capacity obtained in the positive and negative directions were 30% and 2% of the experimental value. For the *CFSCB-3* specimen, the maximum shear force observed was 522 kN at 0.0235 rad in the positive direction and -500 kN at 0.0252 rad in the negative direction. The OpenSees models agreed quite well. The difference in rotation at maximum force is 6.7% in positive and 12% in negative directions, respectively. Moreover, the same difference was observed in many of the excursion prior to that point. The reason for the difference might be due to the behavior of this specimen, as it was reported that the specimen underwent some shear yielding along the web. However, the last two cycles of the test results agreed with OpenSees model within acceptable tolerance.

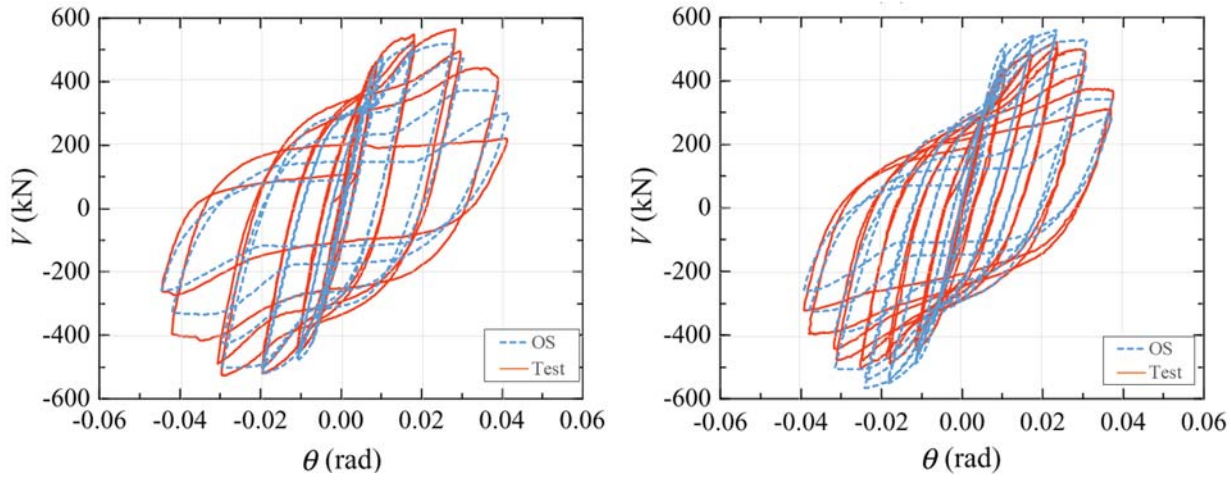

Figure 7-63. The comparison between OpenSees and Test results for a) CFSCB-1 specimen and b) *CFSCB-3* specimen.

7.6 Tests of C-Shaped C-PSW/CF Walls (Kizilarslan et al. 2019)

The calibration of the OpenSees model of the C-shaped composite core walls was done using experimental results from the study conducted by Kizilarslan et al. (2019) at the University at Buffalo on two C-shaped C-PSW/CF subjected to both axial and cyclic loadings. Figures 7-64a to 7-64d show the test setup details of the C-shaped wall specimens. The vertical actuators, each with a nominal capacity of 450kips in tension, were used to apply the axial load on the specimen. The cyclic loading was applied by two horizontal actuators, each having a nominal capacity of 220kips. The specimens were ¼ scale of a prototype core wall model. The tested cross-section was decided from 15,000 possible cross sections considering desired values of flange (α), web (β), and cross section (γ) aspect ratios (defined in Figure 7-65b) within ±35% of those from the prototype model, reinforcement ratio (ρ, less than 4.5%), SEESL laboratory constraints, target

axial compression forces (equal to 15%, and 20% of the axial loading capacity of the infill concrete, defined as $A_g f'_c$), and disposal cost. The dimensions and cyclic loading protocol were the same for both C-Shaped wall specimens, except that different axial loads were applied as indicated above (i.e., 20% and 15% of axial loading capacity). The final selected C-shaped walls cross section had a flange length of 97.5in., web length of 30in., and flange thickness of 6in., as shown in Figure 7-65b. For both specimens, the walls were built of 3/16in. thick steel plates, and were 168in. tall. Detailed dimensions, properties of the prototype wall, and properties of the tested specimens are presented in Table 7-11.

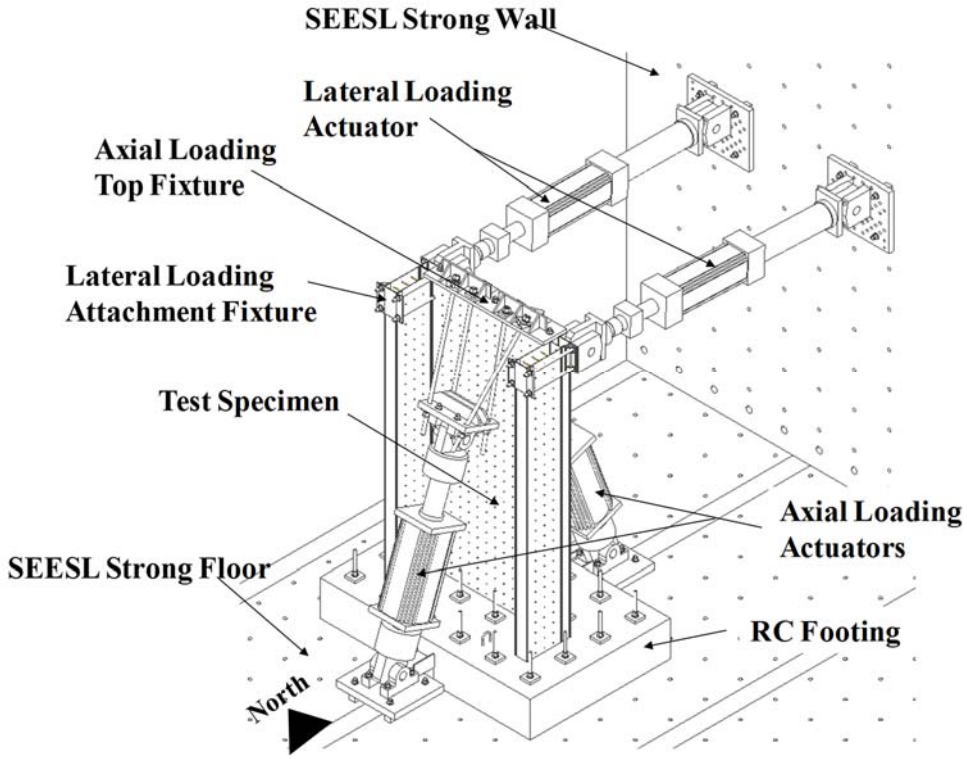

a)

Figure 7-64. Details of test setup of the C-shaped wall specimens: a) isometric view; b) West elevation view; c) South elevation view, and; d) top view

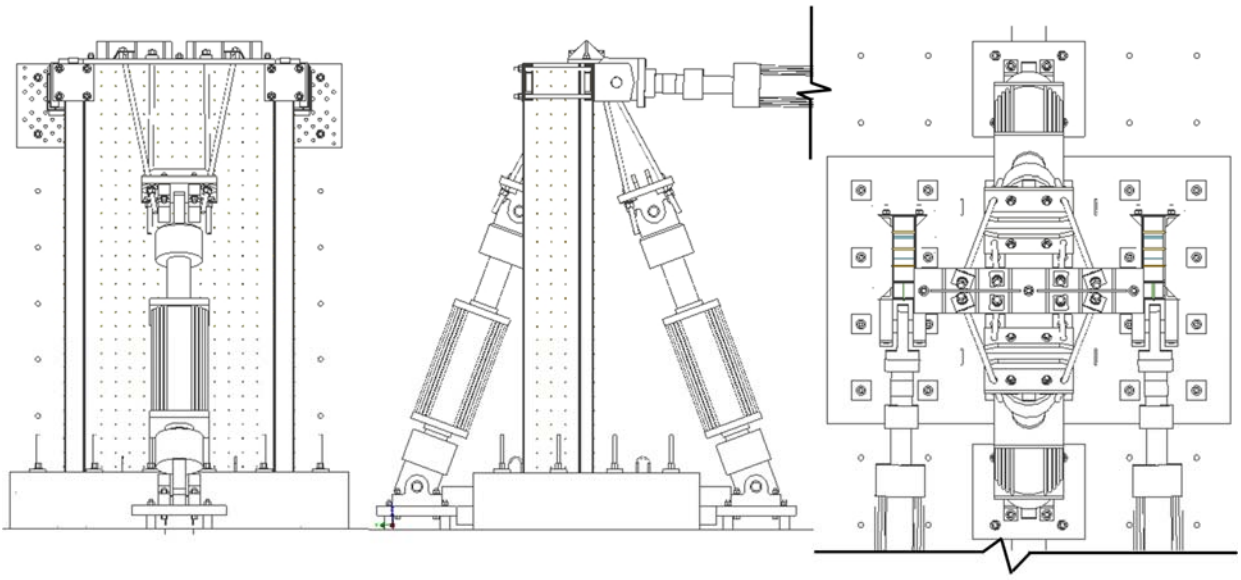

b) c) d)

Figure 7-64. (Continued)

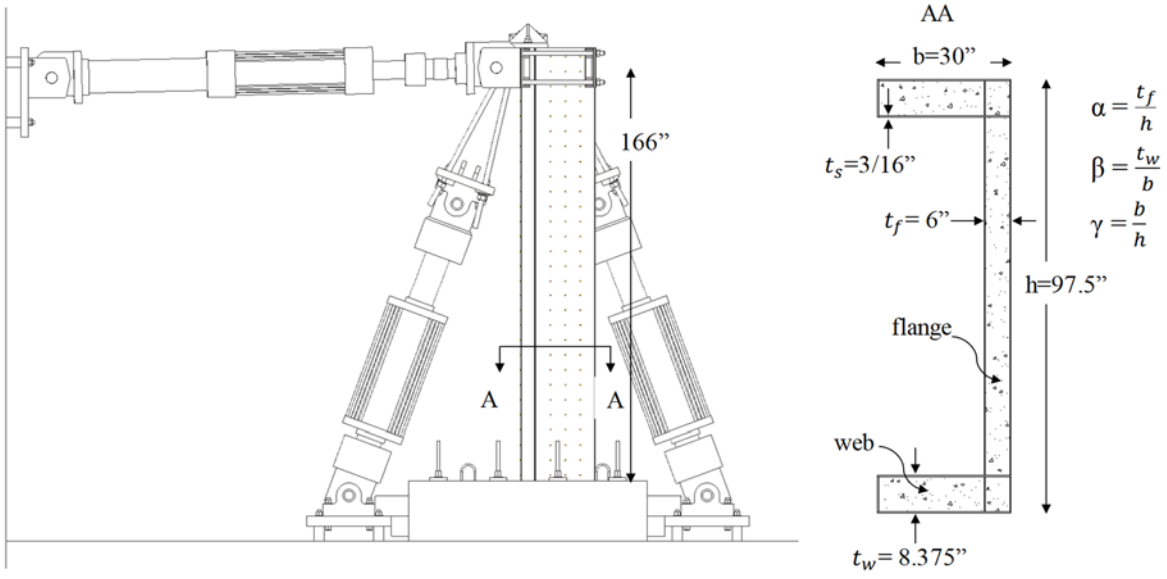

a) b)

Figure 7-65. Tested specimens: a) height, and; b) cross-section

Table 7-11. Details of C-Shaped C-PSW/CF walls

Wall Parameters	Units	Prototype	C1	C2
Wall Height, H	*in.*	N/A	166	166
Flange length, h	*in.*	360.0	97.5	97.5
Web length, b	*in.*	120.0	30.0	30.0
Steel plate thickness, t_s	*in.*	1/2	3/16	3/16
Flange thickness, d	*in.*	25.0	6.0	6.0
Web thickness, c	*in.*	25.0	8.375	8.375
Tie spacing (vertical and horizontal)	*in.*	12	6	6
Tie diameter	*in.*	1	7/16	7/16
Wall aspect ratio (height to web), H/b	N/A	N/A	5.53	5.53
Cross-section aspect ratio, $\gamma=b/h$	N/A	0.33	0.31 (=γ_p)	0.31 (=γ_p)
Flange aspect ratio, $\alpha=d/h$	N/A	0.07	0.06 (=α_p)	0.06 (=α_p)
Web aspect ratio, $\beta=c/b$	N/A	0.21	0.28 (=t_w)	0.28 (=t_w)
Steel area, A_s	$in.^2$	622	61.8	61.8
Concrete area, A_c	$in.^2$	13128	925.2	925.2
Gross area, A_g	$in.^2$	13750	987	987
Reinforcement ratio of web, ρ_{web}	%	4.2	4.5	4.5
Reinforcement ratio of flange, ρ_{flange}	%	4.2	6.3	6.3
Reinforcement ratio, ρ_s	%	4.5	6.3	6.3
Yield strength, F_y	*ksi*	50	55.4	55.2
Young's Modulus	*ksi*	29000	27925	28400
Concrete strength, f_c'	*ksi*	6	4.5	5.1
Crushing load of concrete, $A_c f_c'$	*kips*	78770	4163	4719
Target axial load ratio	%	N/A	20	15

7.6.1 Material Properties

Three coupons for the steel used in the web and flange of the specimens (respectively identified as p261 and p307 in Figure 7-66) were tested under uniaxial tension for each specimen. Results of coupon tests are presented in Figures 7-66a and 7-66b. A572Gr50 steel was used in construction of the flange and web plates. However, no definite yield plateau was observed in the stress-strain behavior of the tested coupons. Using the 0.2% offset method, the average yield strength of all plates was 55.4ksi (average of 56.2ksi for flange plates and 54.6ksi for the web plates) and 55.2ksi (the average of 57.8ksi for flange plates and 52.65ksi for the web plates) for the C1 and C2 specimens, respectively.

For concrete, 3in.x6in. and 6in.x12in. cylinders were taken for each specimen on the day of concrete pouring. Different cylinders were taken from the concrete batches used for the footing and the infill of the wall. The average strength of infill concrete obtained from cylinders were 4.5ksi and 5.1ksi for Specimen

C1 and C2, respectively. The average concrete strength of the concrete used in the footings were 4.7ksi and 4.3ksi for C1 and C2 specimens, respectively.

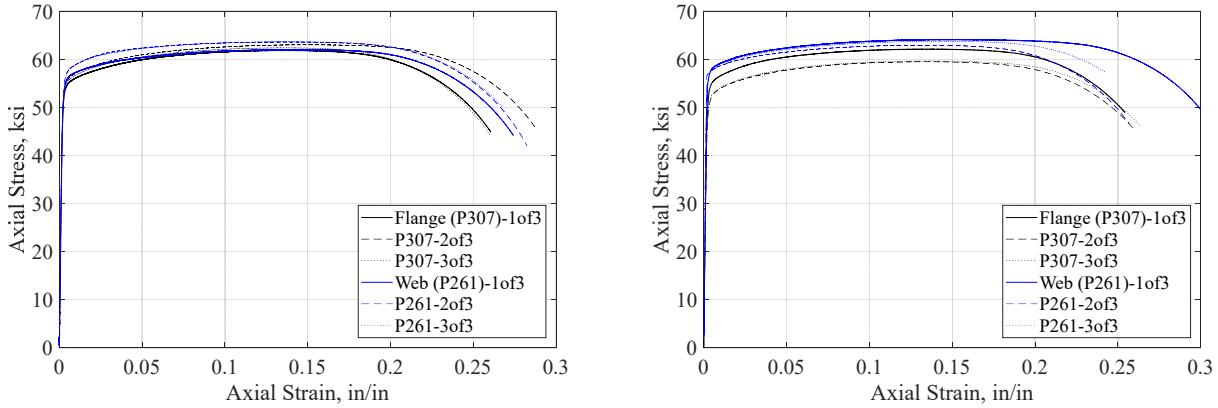

Figure 7-66. Coupon tests of steel plates at web (p261) and flange (p307) for a) C1 and b) C2 Specimens

7.6.2 Instrumentation

All of the C-Shaped C-PSW/CF core wall specimens were instrumented with strain gauges, string potentiometers, and linear variable differential transformer (LVDT). Strain gauges (Figure 7-67) were placed on the surface of the specimen at three different locations along the height of the wall in order to measure the curvatures and strains of the cross-sections during the test. The same gages were also used to verify that the vertical loading applied uniform stresses throughout the cross-section at the base of the wall specimens before applying cyclic loading. String potentiometers (Figures 7-68 and 7-69) were used to obtain rotations at the base (vertical string potentiometers) and in-plane displacements along the height (horizontal string potentiometers). LVDTs (Figure 7-68) were also mounted to measure the vertical displacement of the concrete foundation.

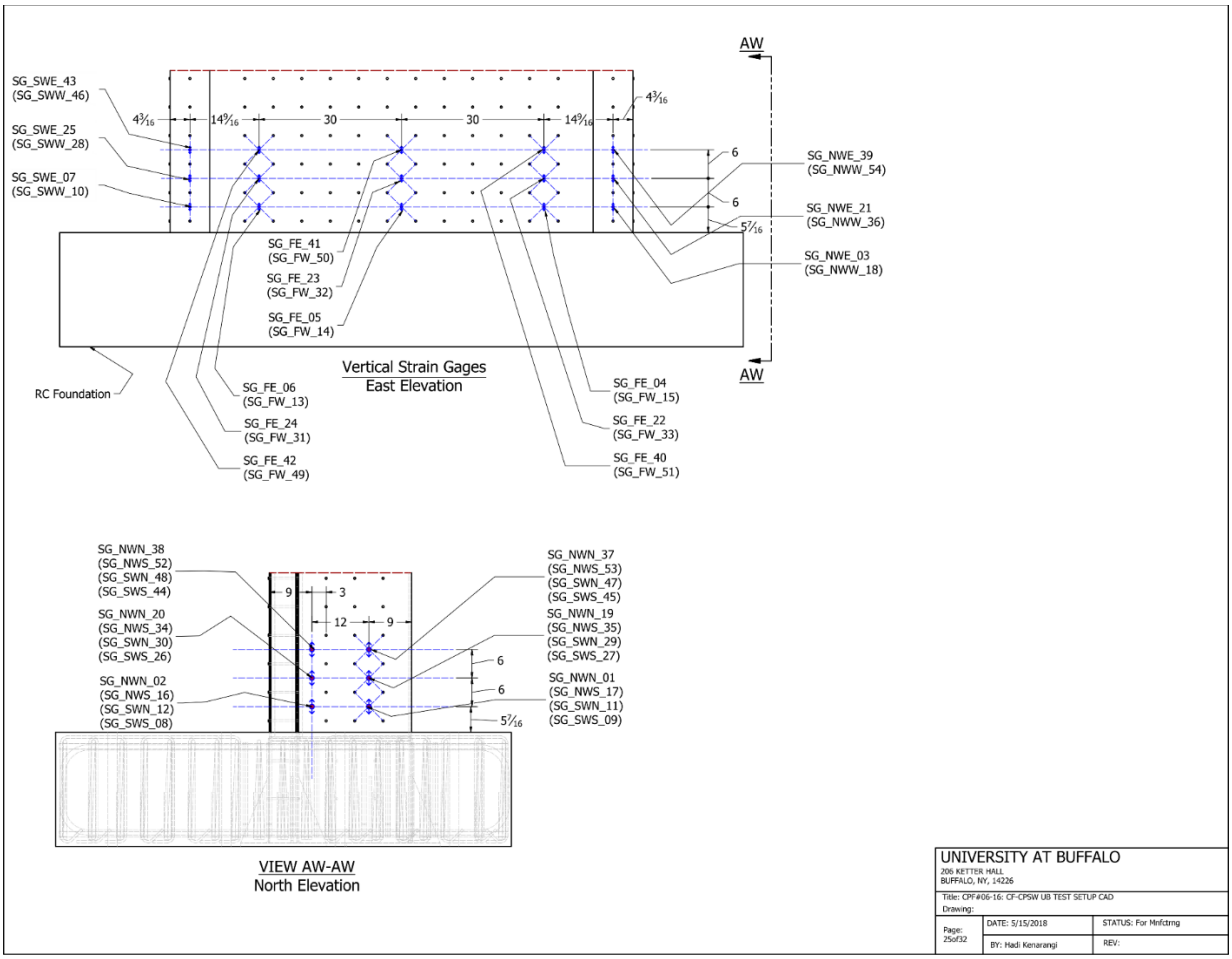

Figure 7-67. Strain gauge instrumentation plan

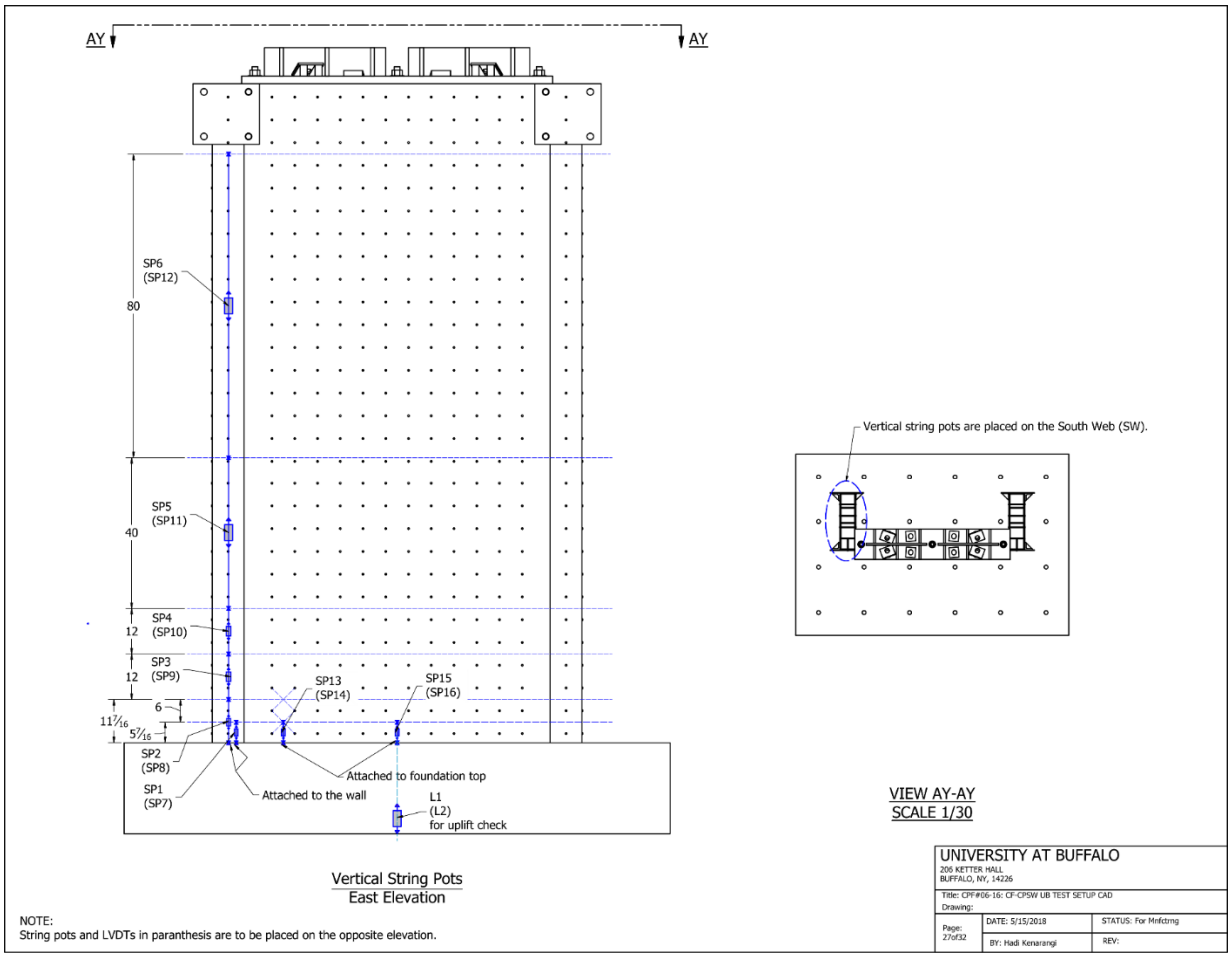

Figure 7-68. Vertical string potentiometer plan

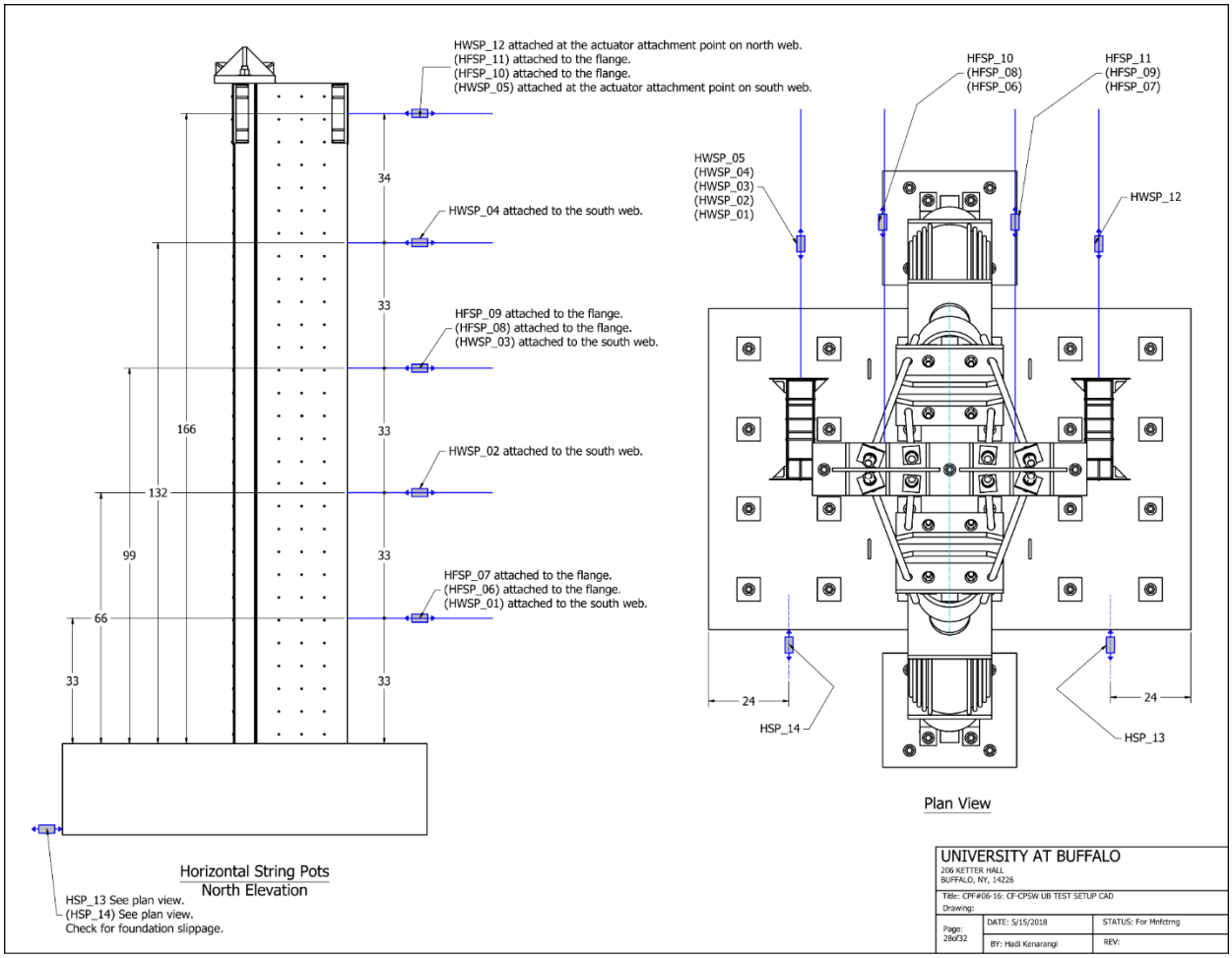

Figure 7-69. Horizontal string potentiometer plan

7.6.3 Loading Protocol

The cyclic testing protocol was designed based on the yield displacements obtained from the Finite Element Analysis (FEA) of Specimen C1. The model was run based on the expected material behavior of the steel and concrete. The result of the average of steel coupon tests (with Fy equal to 55.4 ksi) was directly input into the model and the concrete strength was assumed to be 4 ksi as the true strength of the concrete had not been measured by then. Figure 7-70 shows the resulting pushover curve in both the positive and negative directions and the corresponding bi-linear curve estimate for the pushover curves. The yield displacements (Δy) in the positive and negative directions are 1in. and 0.5in., respectively. However, the loading protocol was mainly created based on yield displacements obtained from the estimated bi-linear curve for both directions ($\Delta y'$), which are 1.75in. in the positive direction and 1.5in. in the negative direction, as shown in Figure 7-70. To facilitate the comparison, both C-Shaped specimens were subjected to the same cyclic displacement loading protocol that was created for Specimen C1.

Up to the equivalent yield displacements (+1.75in./-1.5in.) obtained from the bi-linear simplification of the pushover curves, specimens were cycled in force-controlled mode for the first 10 cycles. Beyond that, the specimens were tested in displacement-controlled mode. The resulting loading protocol is shown in Figure 7-71. Initially, only two cycles per drift amplitude were applied in the force-controlled cycles. However, three cycles per drift amplitude were applied in the displacement-controlled cycles, up to when maximum capacity of specimens was reached (at +5.25 in./-4.50 in.), after which two cycles per drift amplitude were applied. The original protocol planned for only two cycles at 6% drift, but, as will be shown later, specimens were cycled repeatedly at that drift, as needed to observe the further progression of fracture. Drifts were limited to 6% for safety reasons and to keep the specimen stable upon substantial strength degradation.

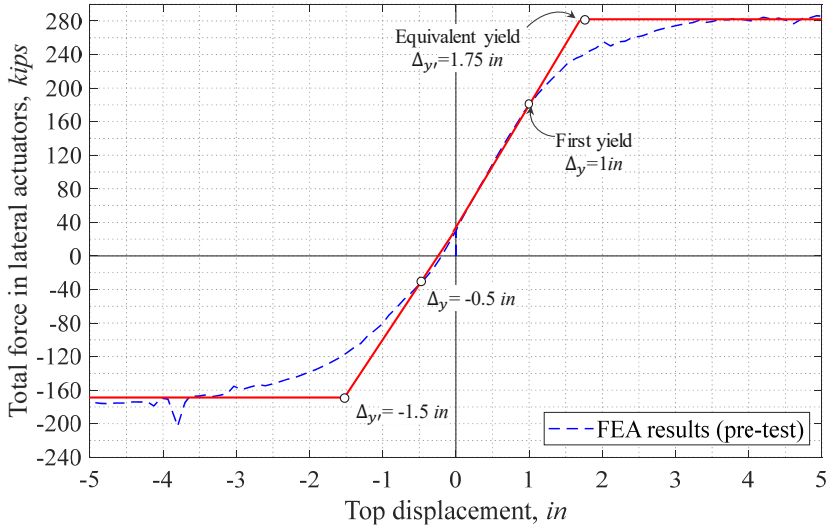

Figure 7-70. Pushover result of the FEA model of Specimen C1 and bi-linear approximation of the curves in positive and negative directions

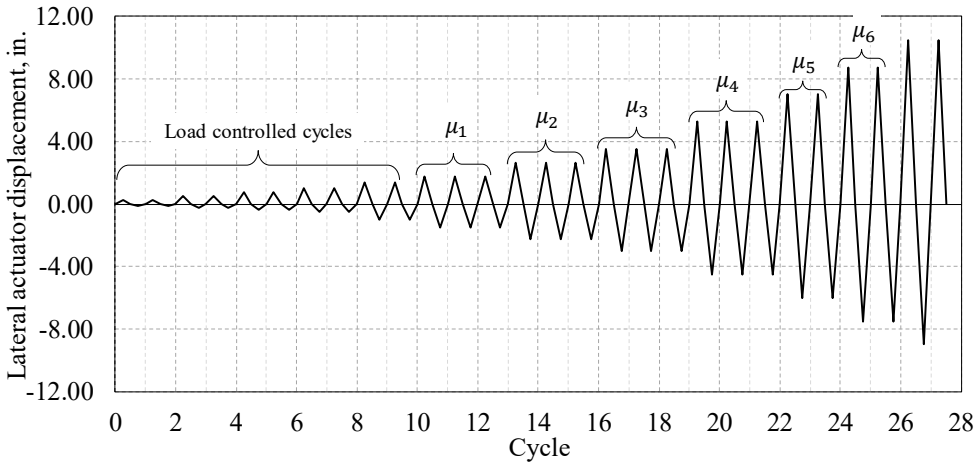

Figure 7-71: Loading protocol for C-Shaped specimens

7.6.4 Numerical Calibration for Distributed Plasticity Models

7.6.4.1 Cross Sectional Analysis of C-Shaped C-PSW/CF Walls for Elasto-Plastic Material

To eliminate risk of errors due to lack of a graphic interface in OpenSees, a cross-sectional analysis using elastic-perfectly-plastic material behavior was first done to match the OpenSees results for the C-Shaped C-PSW/CF core walls with those from hand calculations assuming simple plastic theory. Steel was defined as an elastic perfectly plastic material having 50 ksi strength in both compression and in tension; and concrete was set as having a 6 ksi strength in compression but no tensile strength. The same fiber analysis code mentioned in Section 7.3.4.1 was used to obtain the moment-curvature plot for the cross-section, as shown in Figure 7-72. Results show the plastic moment of the cross section to be 3566 kip-ft. (42,792 kip-in.) in the positive moment direction (i.e., when the web of the cross-section is in compression) and 2098 kip-ft. (25,176 kip-in.) in the negative moment direction (i.e., when the flange of the cross-section is in compression). Also, in those two cases, the plastic neutral axis is located at 13.44 in. and 2.2 in., respectively, from the top of flange of the cross-section.

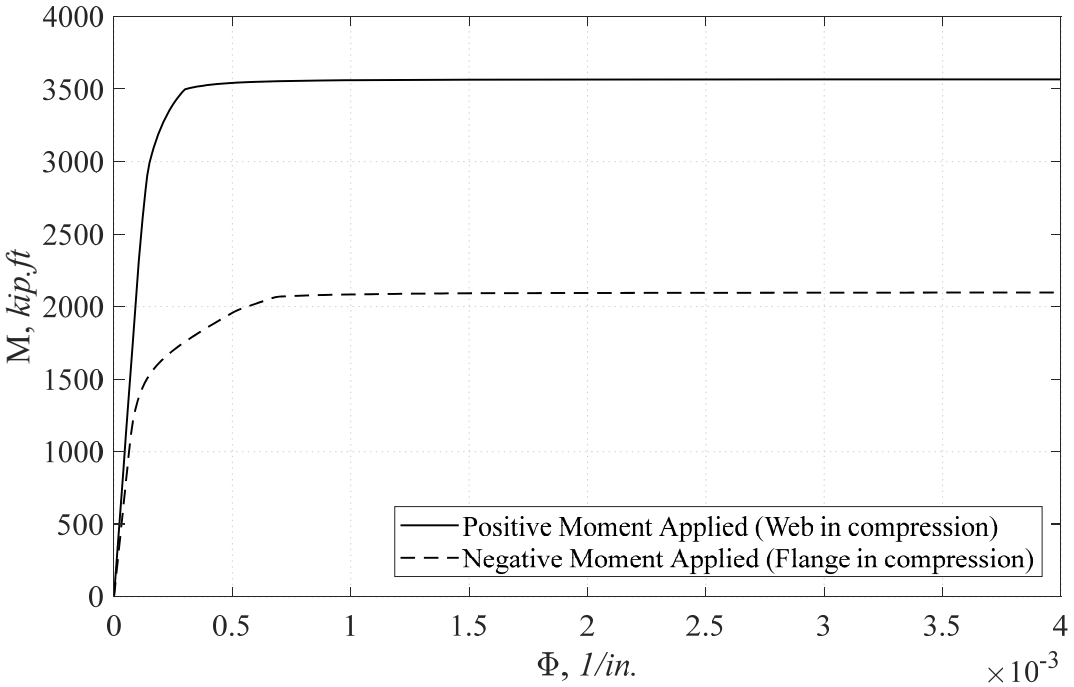

Figure 7-72. Moment Curvature for positive and negative moment directions for the C-Shaped C-PSW/CF walls using Elasto-Perfectly Plastic Materials

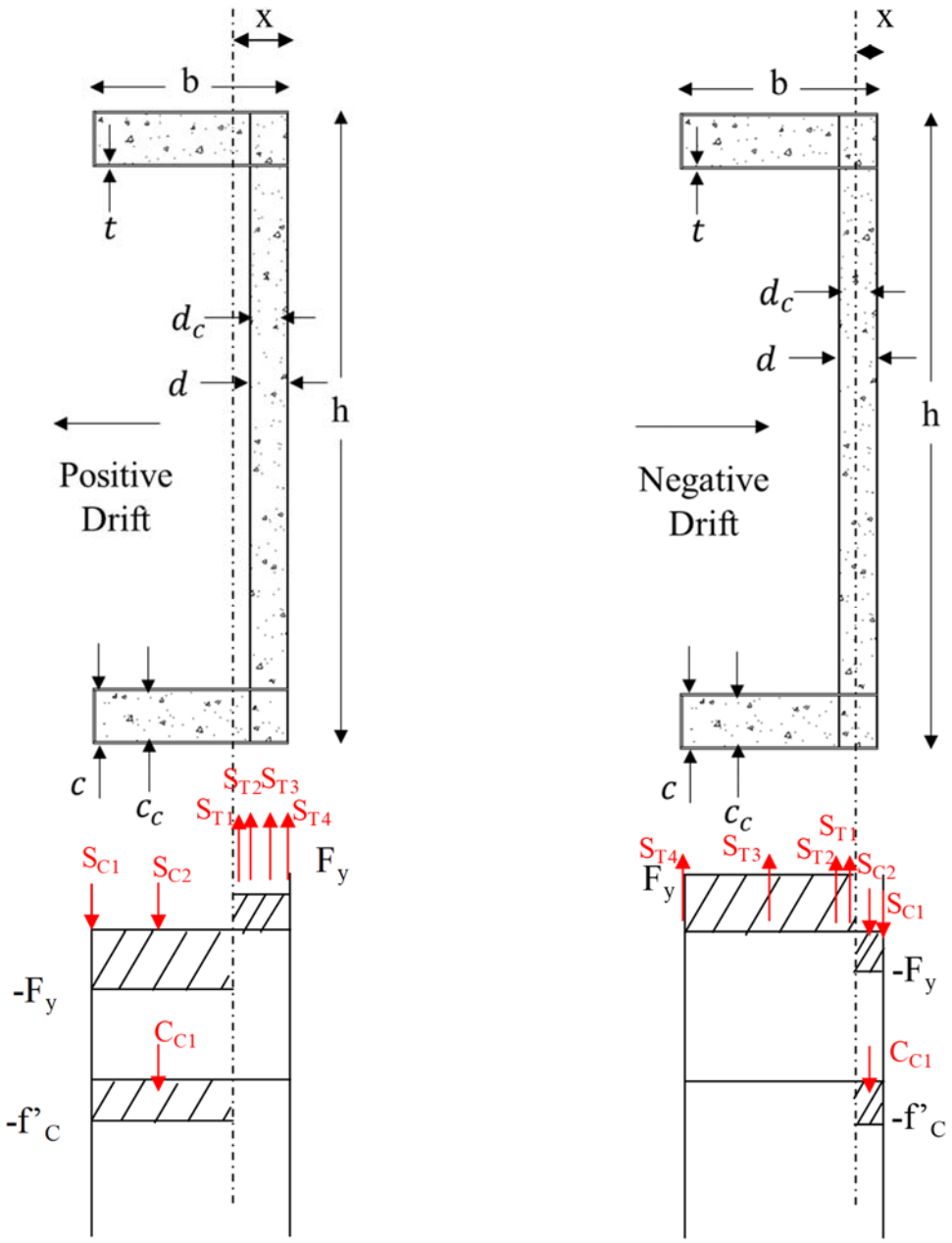

Figure 7-73. Stress distribution for C-Shaped C-PSW/CF walls in: a) the positive direction, and; b) the negative direction

Using the cross-section and stress distribution shown in Figures 7-73a and 7-73b, results from cross-section analysis using simple plastic theory were obtained for both positive and negative directions as follows:

For Positive Direction:

The compression forces are:

$$S_{C1} = 2 * c * t * F_y \quad \textbf{(7.28)}$$

$$S_{C2} = 4 * t * (b - x - t) * F_y \quad \textbf{(7.29)}$$

$$C_{C1} = 2 * c_c * (b - x - t) * f'_c \quad \textbf{(7.30)}$$

where *x* is the distance from plastic neutral axis (PNA) to top of flange, and the tensile forces are:

$$S_{T1} = 4 * t * (x - d) * F_y \quad \textbf{(7.31)}$$

$$S_{T2} = h * t * F_y \quad \textbf{(7.32)}$$

$$S_{T3} = 4 * t * d_c * F_y \quad \textbf{(7.33)}$$

$$S_{T4} = h * t * F_y \quad \textbf{(7.34)}$$

By equating compressive forces to tensile forces, *x* can be calculated as:

$$C_1 + C_2 + C_3 = T_1 + T_2 + T_3 + T_4 \quad \textbf{(7.35)}$$

$$x = \frac{(2 * c * t + 4 * t * b + 4t^2 + 4 * t * d - 2 * h * t - 4 * t * d_c) * F_y + (2 * c_c * b - 2 * c_c * t) * f'_c}{8 * t * F_y + 2 * c_c * f'_c} \quad \textbf{(7.36)}$$

The resulting plastic moment capacity is given by:

$$M_p = S_{C1} * \left(b - x - \frac{t}{2}\right) + (S_{C2} + C_{C1}) * \frac{(b - x - t)}{2} + S_{T1} * \frac{(x - d)}{2} + S_{T2} * (x - d + \frac{t}{2}) + S_{T3} * (x - t + \frac{d_c}{2}) + S_{T4} * (x - \frac{t}{2}) \quad \textbf{(7.37)}$$

For Negative Direction:

The compression forces are:

$$S_{C1} = h * t * F_y \quad \textbf{(7.38)}$$

$$S_{C2} = 4 * t * (x - t) * F_y \quad \textbf{(7.39)}$$

$$C_{C1} = (h - 4 * t) * (x - t) * f'_c \quad \textbf{(7.40)}$$

where *x* is the distance from plastic neutral axis (PNA) to top of flange, and the tensile forces are:

$$S_{T1} = 4 * t * (d - t - x) * F_y \quad \textbf{(7.41)}$$

$$S_{T2} = h * t * F_y \quad \textbf{(7.42)}$$

$$S_{T3} = 4 * t * (b - d - t) * F_y \quad \textbf{(7.43)}$$

$$S_{T4} = 2 * c * t * F_y \quad \textbf{(7.44)}$$

By equating compressive forces to tensile forces, *x* can be calculated as:

$$C_1 + C_2 + C_3 = T_1 + T_2 + T_3 + T_4 \quad \textbf{(7.45)}$$

$$x = \frac{(-4 * t^2 + 4 * t * b + 2 * c * t) * F_y - 4 * t^2 * f'_c}{8 * t * F_y + (h - 4 * t) * f'_c} \quad \textbf{(7.46)}$$

The resulting plastic moment capacity is given by:

$$M_p = S_{C1} * \left(x - \frac{t}{2}\right) + (S_{C2} + C_{C1}) * \frac{(x - t)}{2} + S_{T1} * \frac{(d - t - x)}{2} + S_{T2} * (d - x - \frac{t}{2}) + S_{T3} * (d - x + \frac{b - d - t}{2}) + S_{T4} * (b - x - \frac{t}{2}) \quad \textbf{(7.47)}$$

Using Equations 7.36, 7.37, 7.46, and 7.47, the plastic moment, M_p, was calculated to be 3,567 kip-ft. and 2,099 kip-ft. for the positive and negative directions, and the neutral axes were determined to be at 13.58 in. and 2.11 in. for the positive and negative directions, respectively. The difference in the plastic moments obtained from hand calculations and from the fiber-analysis code developed in OpenSees is 0.0245% and 0.0257% for the positive and negative directions, while the error in the plastic neutral axis location is 0.5% and 0.7% for positive and negative directions (the difference comes from neglecting the short elastic part of the stress-strain curve, which is considered negligible). This confirmed that the correct cross section was created for the walls in the OpenSees models.

7.6.4.2 Material Inputs

After verifying that the cross-section of the C-shaped walls was correctly defined (per previous section), calibration of the OpenSees models of the C-Shaped core walls was done using the material models presented in Sections 6.2 and 6.3 and material properties measured from coupon and cylinder tests. This section indicates how the material model parameters were selected in order to replicate the experimental results for the C-Shaped core walls tested by Kizilarslan et al. (2019).

Even though different plates were provided by the steel supplier to take coupons for the flanges and webs of the C-Shaped specimens, this steel was of the same steel grade (and from the same steel batch), the flanges and webs were assigned the same values for each of the *Reinforcing Steel Material* model parameters, including the buckling and low-fatigue parameter values. However, the stress-strain steel material parameters (f_y, E_s, ε_y, f_u, E_{sh}, ε_{sh}, and ε_u) were assigned, as described in Table 7-11. Also, the equations of Susantha et al. (2001) were used to specify the values of the parameters for the confined concrete.

The yield strength (f_y), and Young's Modulus (E_s) were taken from coupon tests, with values reported in Table 7-11. The yield strain (ε_y) was calculated by dividing the yield strength by Young's Modulus. The ultimate strain (ε_u) and ultimate strength (f_u) were taken from coupon tests results shown in Figures 7-66a and 7-66b (namely, ε_u equal to 0.15 for both specimens and f_u equal to 62.73ksi. and 62.50ksi for the C1 and C2 specimens, respectively). This defines similar stress-strain curves for all practical purpose). Since a yield plateau was not observed in the stress-strain curves, in defining the computational model, the strain at the onset of the strain-hardening strain (ε_{sh}) was set to be 0.0001 greater than the yield strain (ε_y). Also, the strain-hardening Modulus (E_{sh}) was assumed to be 0.01 times the Young's Modulus (E_s). With these parameters, as shown in Figures 7-74a and 7-74b, a good agreement was observed between the coupon tests (blue and black lines) and OpenSees results (red lines).

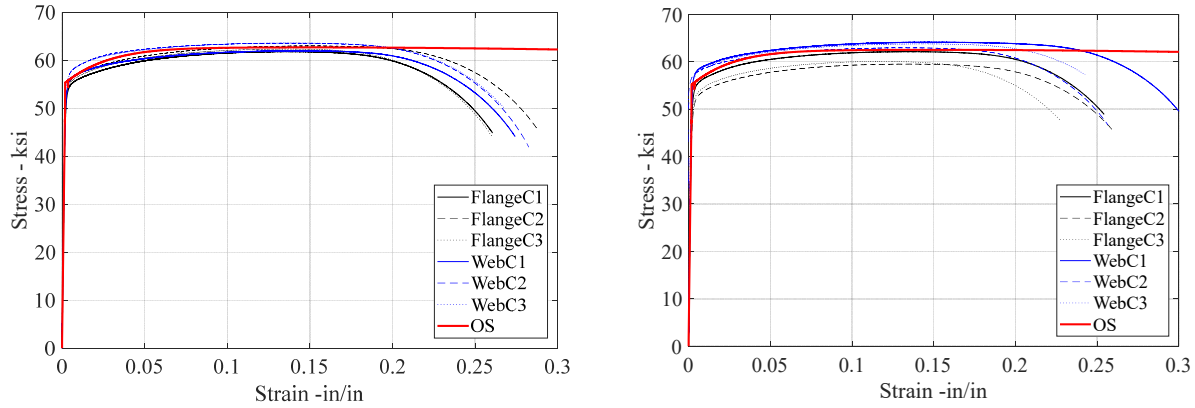

Figure 7-74. Steel backbone curve comparison between RSM parameters and coupon tests of: a) C1, and; b) C2 Specimens

After many trials, good results were empirically obtained for the buckling parameters using a buckling curve reduction factor, r, of 0.9; an amplification factor, β, of 1.0; and a buckling constant, γ, of 1.0 for buckling. The slenderness ratio, l_{SR}, was calculated by dividing the tie spacing (6in.) by the equivalent steel plate thickness (as described in Section 6.2.2), which is 20.8. As for the low-cycle fatigue parameters, new values were determined to fit the results for the C-Shaped core walls. Following the empirical calibration approach described in Section 7.3.4.2, using a fatigue ductility coefficient, C_f, of 0.21, a fatigue ductility exponent, α, of 0.575, and a cyclic strength reduction constant, C_d, of 0.4 gave good correlation for the observed hysteretic behavior of the tested specimens, even replicating well the strength and stiffness degradation observed in repeated excursions at the same drift. Default values for the Menegotto-Pinto curve parameters and hardening constant were used.

The values for the confined concrete parameters (Table 7-12) were obtained by entering measured average concrete strength from cylinder tests into the Susantha et al. (2001) equations for rectangular composite cross-section (see Appendix A.3.1.2) at the ends of the webs, and the corners of flange and webs in the cross-section (i.e., the regions labeled as "1" in Figure 7-75). In addition, the same ductile behavior was given to the concrete located between the end of webs and corners (i.e., the regions labeled "2" in Figure 7-75), but using the average unconfined concrete strength from cylinder tests. Figure 7-76 illustrates the resulting backbone curve for the concrete used in both regions, using the values for the Specimen C2. Note that Young's modulus of the wall's infill concrete for the Specimen C1 was measured from linear potentiometers that were attached to the cylinders during the concrete compression tests. This is because the test for Specimen C1 was conducted only five days after the wall's infill concrete was poured (for reasons presented in Kizilarslan et al. (2019)). Since concrete was not cured for 28 days, the equation in Section 19.2.2 of ACI-318-14 was deemed to be not applicable. However, this was not the case for Specimen C2, and the Young's Modulus in that case was calculated using the equation from ACI-318-14.

Table 7-12. Values of concrete parameters for planar C-PSW/CF walls models

Specimens	f_{PC}, ksi (Region2/ Region1)	E_C, ksi	ε_{CO} (Region2/ Region1)	f_{CU}, ksi (Region2/ Region1)	ε_{CU}	Lambda	Z, ksi	α
C1	4.5/5.21	1819	4.95E-3/5.73E-3	4.02/4.66	0.04	0.1	16	0.893
C2	5.1/5.88	4071	2.51E-3/2.89E-3	4.5/5.13	0.04	0.1	20	0.883

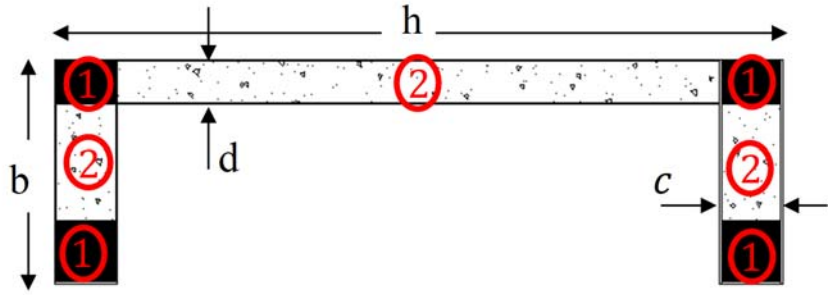

Figure 7-75. Regions of the cross-section where different concrete properties were used to model the C-Shaped wall

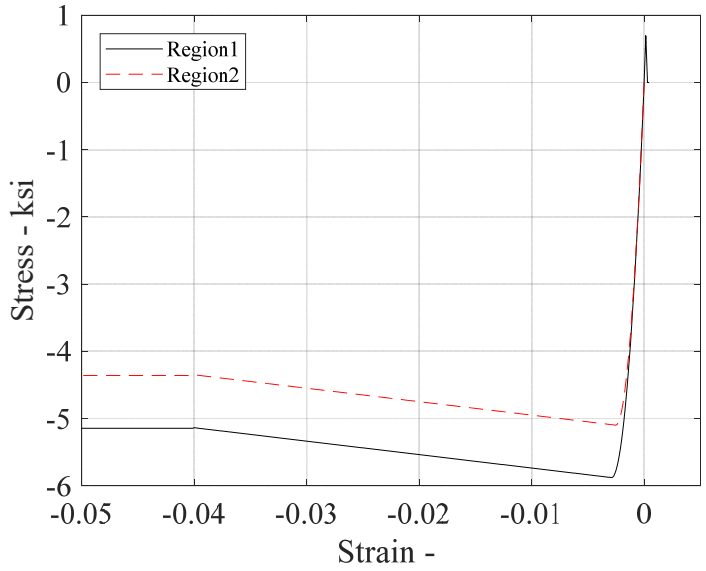

Figure 7-76. Concrete backbone curves for both regions 1 and 2 for C2 Specimen

7.6.4.3 Element Type

In this section, the effect of choosing different element type and element size for the C-Shaped C-PSW/CF walls, is investigated, in terms of its impact on calibration of the inelastic models against experimental results. As was previously done for the C-PSW/CF-NB1 wall in Section 7.3.4.3, for the Specimen CW-42-55-10-T in Section 7.4.4.3, and for coupling beams in Section 7.5.4.3, displacement-based nonlinear elements were only assigned to the plastic hinge region of the walls and elastic elements were used for the rest of the wall specimens. The plastic hinge length was determined to be the vertical distance between the yield and plastic moments of the cross-section (Figure 7-72). Since the yield and plastic moments differ in the positive and negative directions, the maximum of the two was taken as the plastic hinge length for modeling purposes, which resulted in a 68 in. plastic hinge length. However, this length was arbitrarily increased to 84 in., to account for the fact that the plastic hinge length will be longer when considering strain hardening (note that the elements used were 12 in. long).

Analyses were conducted to determine the suitable number and size of elements to use in the plastic hinge region for the *Reinforcing Steel Material* model. For this purpose, the test results of Specimen C1 were used and compared with analysis results obtained using various number of elements having three integration points (NIPs) using the same material parameters. As seen in Figure 7-77, after crack initiation started in the wall, there was no convergence in the results as a function of the element sizes considered, unlike what has been previously observed in Figure 7-24 for the walls having round-end C-PSW/CF-NB1 (Alzeni and Bruneau 2014). To investigate this further, the models were re-analyzed without accounting for material

degradation (i.e., not accounting for fracture and buckling) and the largest element size for which convergence was observed at high local curvature values was chosen for the wall specimens. Figure 7-78 shows that using 12" long elements was adequate for the specimen, and that results diverged for longer elements. Therefore, 12 in. elements were used over the plastic hinge length in the models. Note that results in Figure 7-50 indicate that using different mesh sizes did not affect the response of Specimen CW-42-55-10-T for planar wall. Therefore, a mesh size study was not conducted for the C-Shaped walls and 1 in. thick fibers were used to avoid possible convergence errors (due to abrupt shifts in location of the plastic neutral) axis during the earthquake time history analysis to be conducted as part of the IDA, and to prevent premature termination of these analyses due to the high memory requirement of the *Reinforcing Steel Material* model used for the steel fibers.

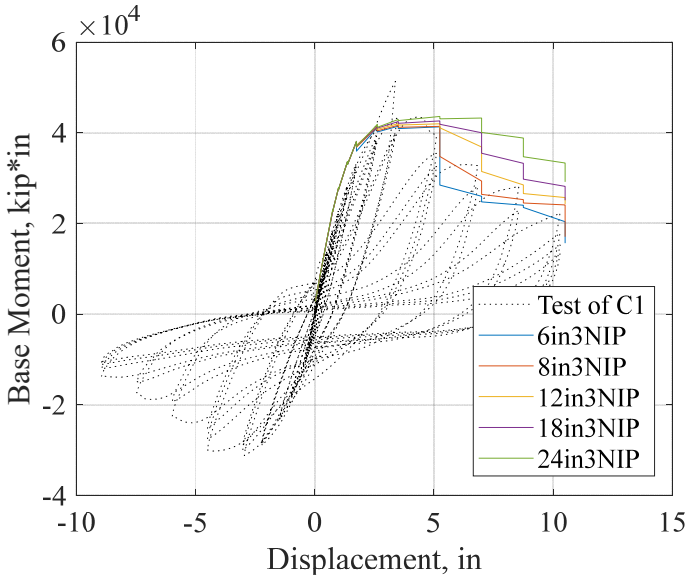

Figure 7-77. Element size study for Specimen C1

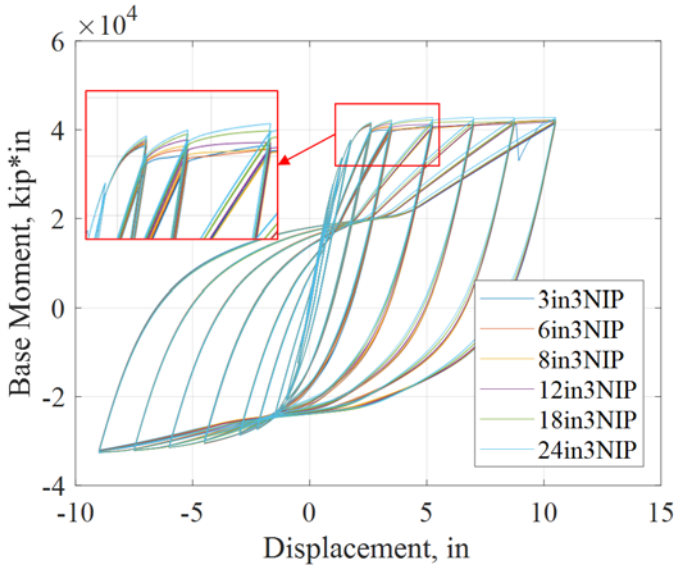

Figure 7-78. Element size study with no degradation models for Specimen C1

7.6.4.4 Modeling of the Test Setup

As mentioned in Section 7.6.4.3, the plastic hinge region of the C-Shaped walls was modeled with displacement based nonlinear elements. The nonlinear elements were placed at the centroid of the cross-sections, which is 9.11 in. from the face of the flange, as shown in Figure 7-79. However, for practical reasons, in these tests, the axial loading was only applied to the flange rather than at the centroid of the cross-section. This resulted in a moment due to the eccentricity of the axial load. To account for this additional moment, at the point of axial load application, a rigid link was included in the model between that point and the centroid of the wall, as shown in Figure 7-80. In addition, during execution of the test, because of the moment caused by this eccentricity of the axial loading, the horizontal actuators were locked at the initial point of zero horizontal displacement until the full axial load was applied. Then, while keeping the axial loading constant, the cyclic loading was applied to the specimens. Here, to simulate the same test procedure, the horizontal movement of the node at the top of the wall where lateral cyclic loading was to be applied, was restrained (locked) during application of the axial loading, and then, released before applying lateral cyclic loading.

As Figure 7-80 shows, the initial angle between the inclined actuators and the strong floor was 70º. This angle changed by about ±5º during the test as the top of the wall drifted back and forth. To account for the change of angle, and therefore change in the direction of axial loading, the vertical actuators were simulated as elastic beam-column elements, and the values of axial loading recorded from test were directly applied as an element loading along the elastic elements (i.e., local coordinate of the elements) using the “single

point (sp) constraint" command in OpenSees at the centroid of the flange at the top of the wall. Small area and moment of inertia were assigned to elastic beam-column elements, because double spherical washers (Figure 7-81) were used at the threaded bar joints to eliminate rotational constraints there and, thus, to avoid the development of moments in the actuators to accidental eccentricities.

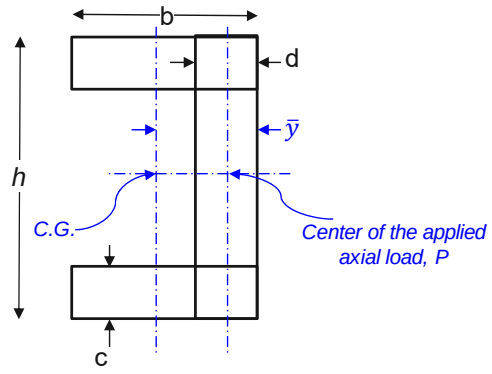

Figure 7-79. Location of centroid and centerline of axial load for C-Shaped wall specimens

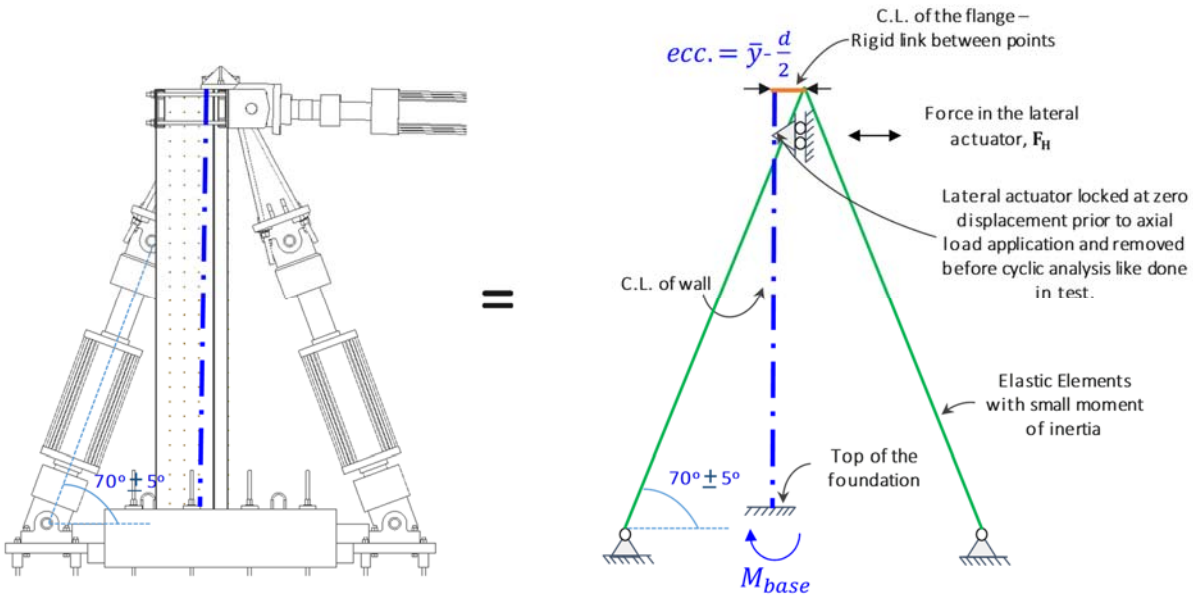

Figure 7-80. Modeling of C-Shaped wall specimens

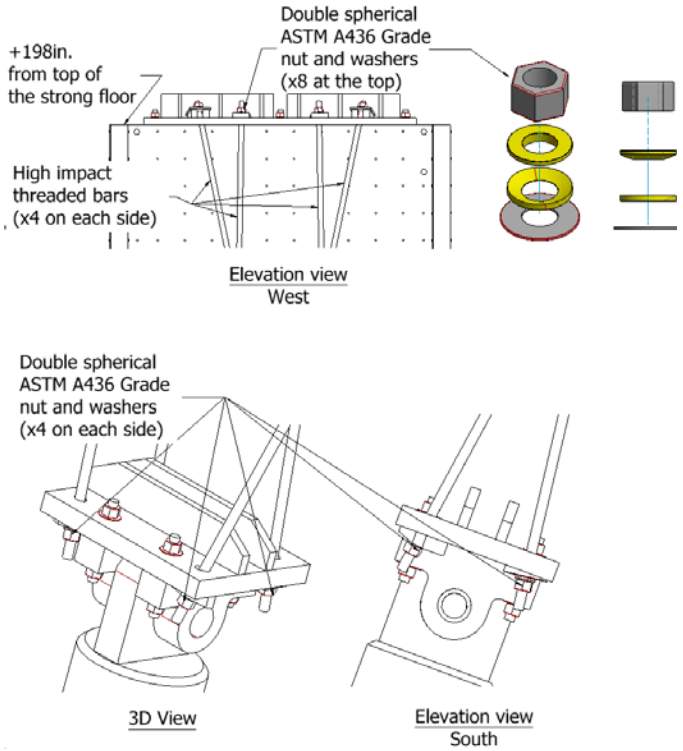

Figure 7-81. Threaded bars connection details in the vertical loading system

7.6.4.5 Comparison of OpenSees Models with Test Data

The base moment-displacement and base moment-rotation hysteretic relationships for all of the tested C-Shaped C-PSW/CF walls are presented in Figures 7-82a and 7-82b, comparing the experimental results with those obtained with OpenSees. Note that the experimental data was corrected to remove the contribution of the flexibility of the specimen's footing; correspondingly, the base of the walls was fixed in all of the OpenSees models.

Note that all comparisons were made with the same set of fracture and buckling parameters that will be used for incremental dynamic analysis (IDA). It is understood that if each test were investigated separately, better match between the curves can be obtained by calibrating the set of parameters to each individual specimen (but this was not done here). Base moment versus displacement are plotted on the left side of 7-82a and 7-82b; corresponding moment-rotation hysteretic curves are plotted on the right side of these figures. The moment resisted by the wall at its base was calculated by correcting for the horizontal components of the force of the two vertical actuators that applied axial load on the wall. As it was mentioned before, the actuators used for the axial load application were placed with an inclination angle of 70 degrees from the strong floor and toward the wall (see Figure 7-83a). The trajectories of the axes of these actuators

intersect above the centerline of the flange of the wall. At the point of zero horizontal displacement at the top of the wall, the horizontal components of the forces in the two vertical actuators are equal and in opposite directions. At non-zero displacements of the top of the wall, as the inclination angles of the vertical actuators change, the summation of the horizontal components of the forces in these actuators develops an extra force that has to be carried by the horizontal actuators. The free-body diagram of the forces (at zero displacement) is shown in Figure 7-83b. The moment resisted by the wall at its base was calculated according to the free-body diagram shown in Figure 7-83b by Equation (7.48).

$$\overrightarrow{M_{base}} = \overrightarrow{r_{act}} \times \overrightarrow{F_H} + \overrightarrow{r_{top}} \times \left(\overrightarrow{F_{v1}} + \overrightarrow{F_{v2}}\right) \quad \textbf{(7.48)}$$

The rotations of the wall at the base where the plastic hinge was developed was calculated using the recorded horizontal movements of the wall for the string pot attached to the wall closest to the foundation, and then dividing its readings by its distance to the top of the foundation (33in.), which resulted in total rotations at the wall base (i.e., θ_{wt} as in Figure 7-84). Recognizing that this calculated rotation also included the rotations of the wall-foundation connection (i.e., θ_{wf}), these rotations at the wall-foundation connection (θ_{wf}) were subtracted from the total rotations (θ_{wt}) to obtain the wall rotations at the base (i.e., θ_{wb}). Figure 7-84 shows the composition of the rotations at the base of the wall. Note that there was no slippage between the footing and the strong floor during the test and therefore the lateral displacements of the footing was considered zero in calculation of the rotation.

A detailed description of all observations made throughout each test is provided by Kizilarslan et al. (2019). Therefore, focus here is on presenting the difference between the experimental data obtained by Kizilarslan et al. (2019) and the results obtained from the OpenSees model described above.

Results obtained from the OpenSees model of the Specimen C1 closely match the experimental data, with small errors, as shown in Figure 7-82a. Note that a peak base moment (4278 kip-ft.) at 2% horizontal drift of the wall was recorded for the test results of the Specimen C1, which is believed to be an outlier due to a glitch during the test, as the force readings in the horizontal actuators at that point were observed to be abnormally high when compared to prior and subsequent cycles. Therefore, the base moment in the next excursion (i.e., at 3% drift) was taken to be the maximum positive base moment. With that, the maximum positive base moment of 3619 kip-ft. was matched within 3.84% when comparing test result with those from analysis using the OpenSees model. In addition, the rotation at maximum positive base moment (0.0216 rad), corresponding to when the specimen was displaced to 3% drift, matched with a maximum difference of 5.47%. The maximum negative base moment (2504 kip-ft.) was reached at 2.7% drift and the

OpenSees result at that point matched within 2.76%. The rotation corresponding to the maximum negative base moment (-0.0141 rad) also had a good agreement, with differences remaining within 9%. A relatively good match was also obtained at the maximum rotation, with differences of 18% and 6% in the positive and negative moment values at the maximum rotations in their corresponding directions, and of 2.15% and 2.11% for the maximum positive and negative rotations, respectively.

For Specimen C2, the difference between the experimental and OpenSees results in maximum positive and negative base moments increased to 10.5% and 5.02% (Figure 7-82b), respectively. For the rotations at the maximum positive (0.01129 rad) and negative moments (-0.014 rad), the difference was greater than for the Specimen C1, but still good, at 19% and 15%, respectively. However, a relatively better match was obtained for the maximum rotations, with differences of 1.1% and 0.54% in the positive and negative directions, respectively.

Recall that the objective of the above calibration exercise was to select a single set of fatigue and buckling parameters that allowed matching as best as possible all of the test data of C-Shaped C-PSW/CF walls, and that could consequently be used in the FEMA P695 analyses. Evidently, as mentioned earlier, if the objective instead was to find individual sets of buckling and fatigue parameters to match each of the test data individually, a better match for all the specimens would be possible, and magnitude of the above discrepancies could have been reduced.

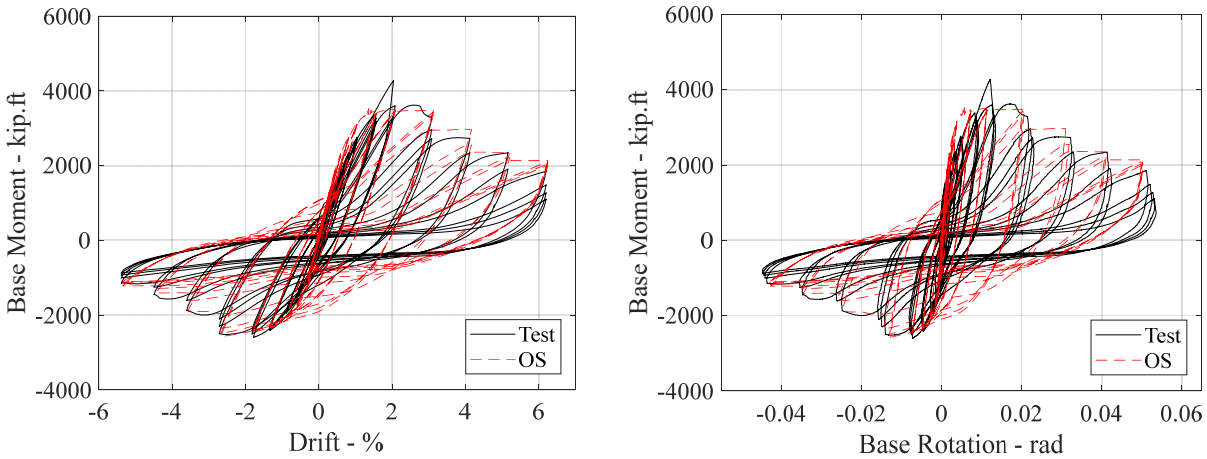

a)

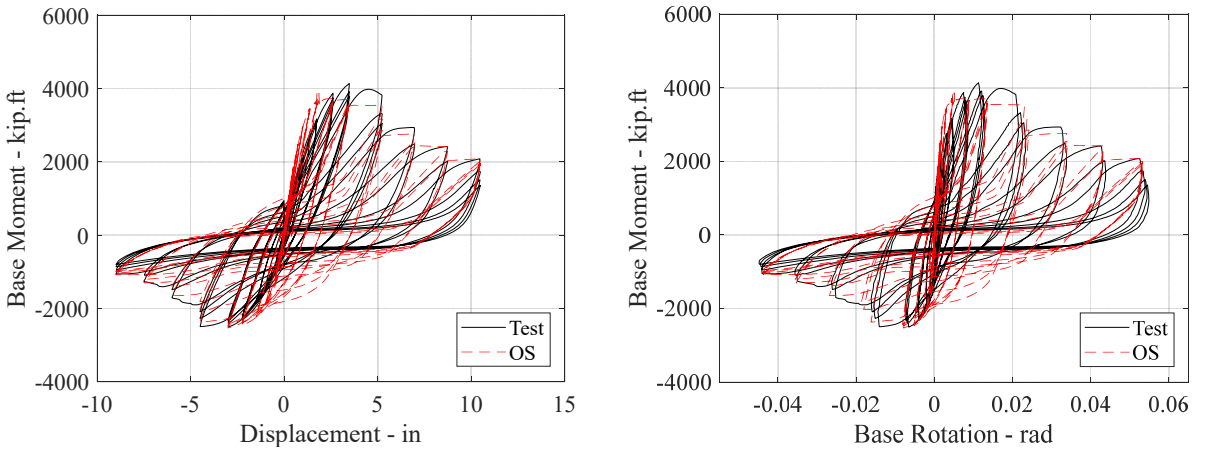

b)

Figure 7-82. Base moment-displacement (left) and base moment-rotation (right) comparisons of OpenSees models with test data for a) C1, and; b) C2 Specimens

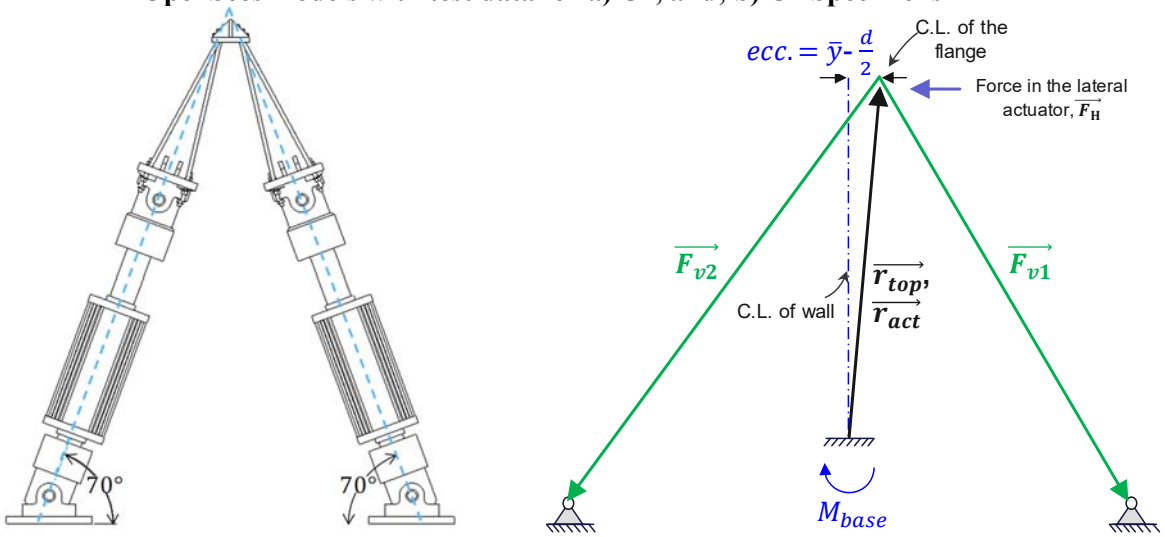

(a) (b)

Figure 7-83. Figures for (a) the inclination angle of vertical actuators at zero displacement, and; (b) the free body diagram of the specimen wall at zero displacement

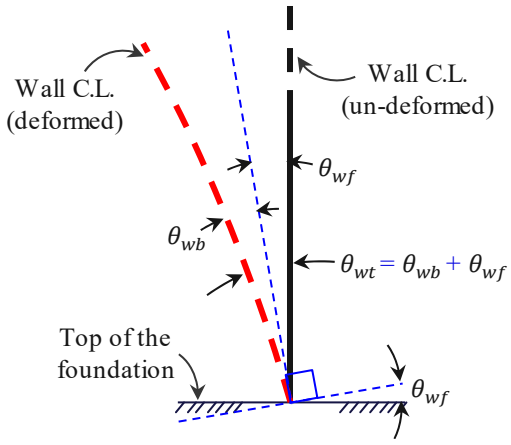

Figure 7-84. Composition of wall rotations at the base of the wall

In addition to the base moment versus drift and base moment versus rotation, selected results from the steel stresses recorded in the cross-section were also reviewed, to investigate the fracture propagation in C-Shaped walls and to compare with what was observed during the test of these walls. Figure 7-85 illustrates an example strain profile for a given curvature value, but for that value in the two different applied loading directions, throughout the cross-section of a C-Shaped wall (Specimen C1). It indicates that for the same curvature in the positive (where web is in compression) and negative (where flange is in compression) directions, the strains in the web are larger than the ones in the flange, regardless of the direction of the curvature. Therefore, throughout the entire loading protocol, the accumulation of cumulative plastic strains is more significant in the web than in the flange, which implies that the initiation of a fracture is expected to first start at the outermost steel fiber of the web, and propagate from there towards the flange; this is indeed what was observed during the C-Shaped wall tests. Figure 7-86 shows the steel stresses in the cross-section at the cycle amplitudes indicated in Figure 7-86part of that figure. Figures 7-86b and 7-86c shows these steel stresses corresponding to the positive and negative amplitude of selected cycles, respectively. In Figures 7-86b and 7-86c, the zero position on the vertical axis corresponds to the centroid of the cross-section (9.11 in. from face of the flange) and the cross-section is oriented such that the flange is at the bottom of the vertical axis. As observed in the test, Figure 6-114 indicates that first yield occurs in the web. The OpenSees model also simulated the fracture propagation correctly (from points (9) to (16) in Figure 7-86). Lastly, point 17 in Figure 7-86 shows the residual steel stresses in the cross-section after analysis was completed, and 80% of the web (19 in. out of 24 in. web) was fractured, which corresponds to the length of fracture reported by Kizilarslan et al. (2019) at the end of test for the C1 and C2 specimens.

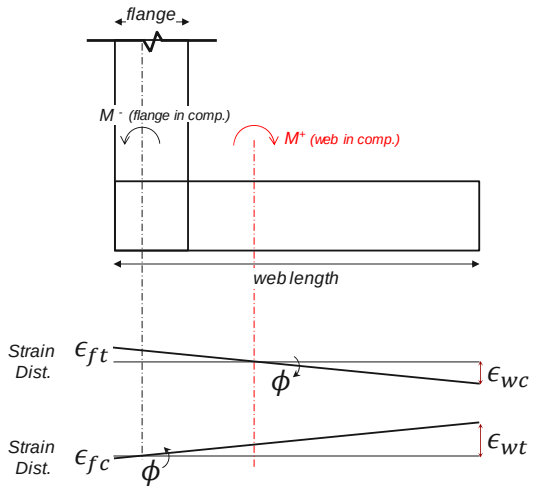

Figure 7-85. Strains in the web and flange due to the same curvature in both directions

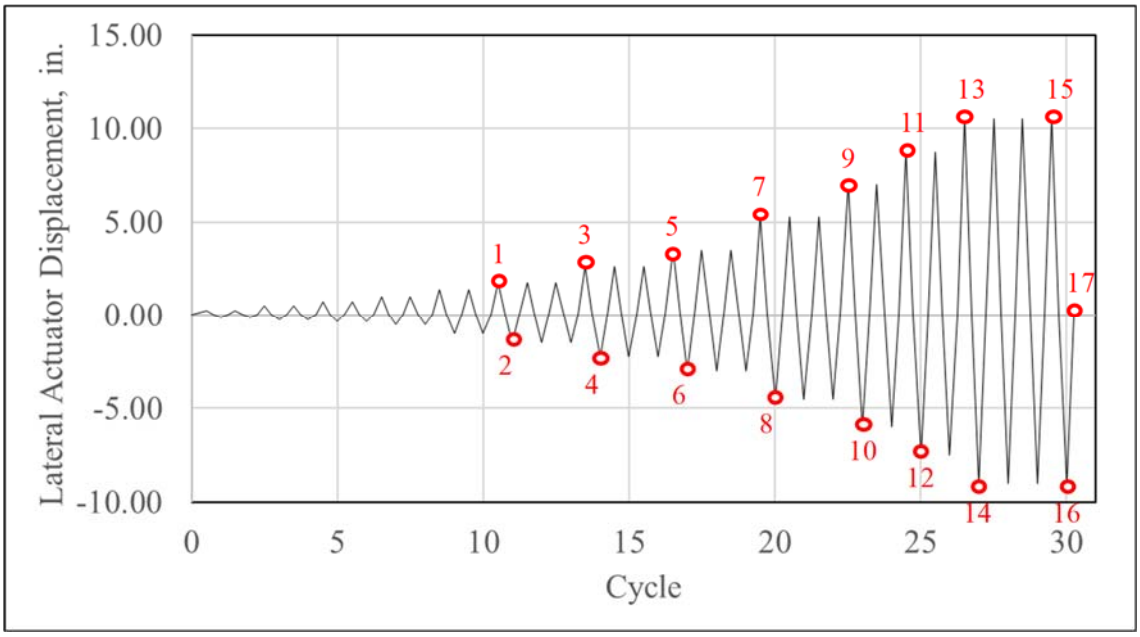

a)

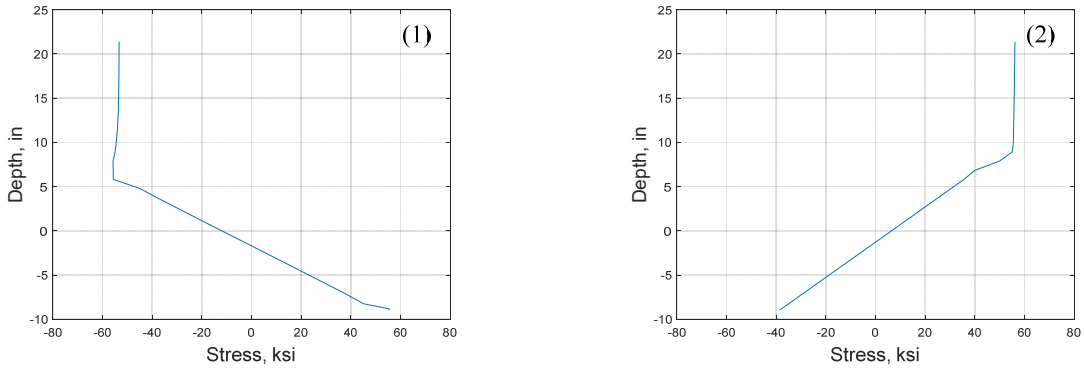

Figure 7-86. Figure of a) the loading protocol with number for which stresses of steel fibers at b) positive drift and at c) negative drift in the cross-section from OpenSees model are shown

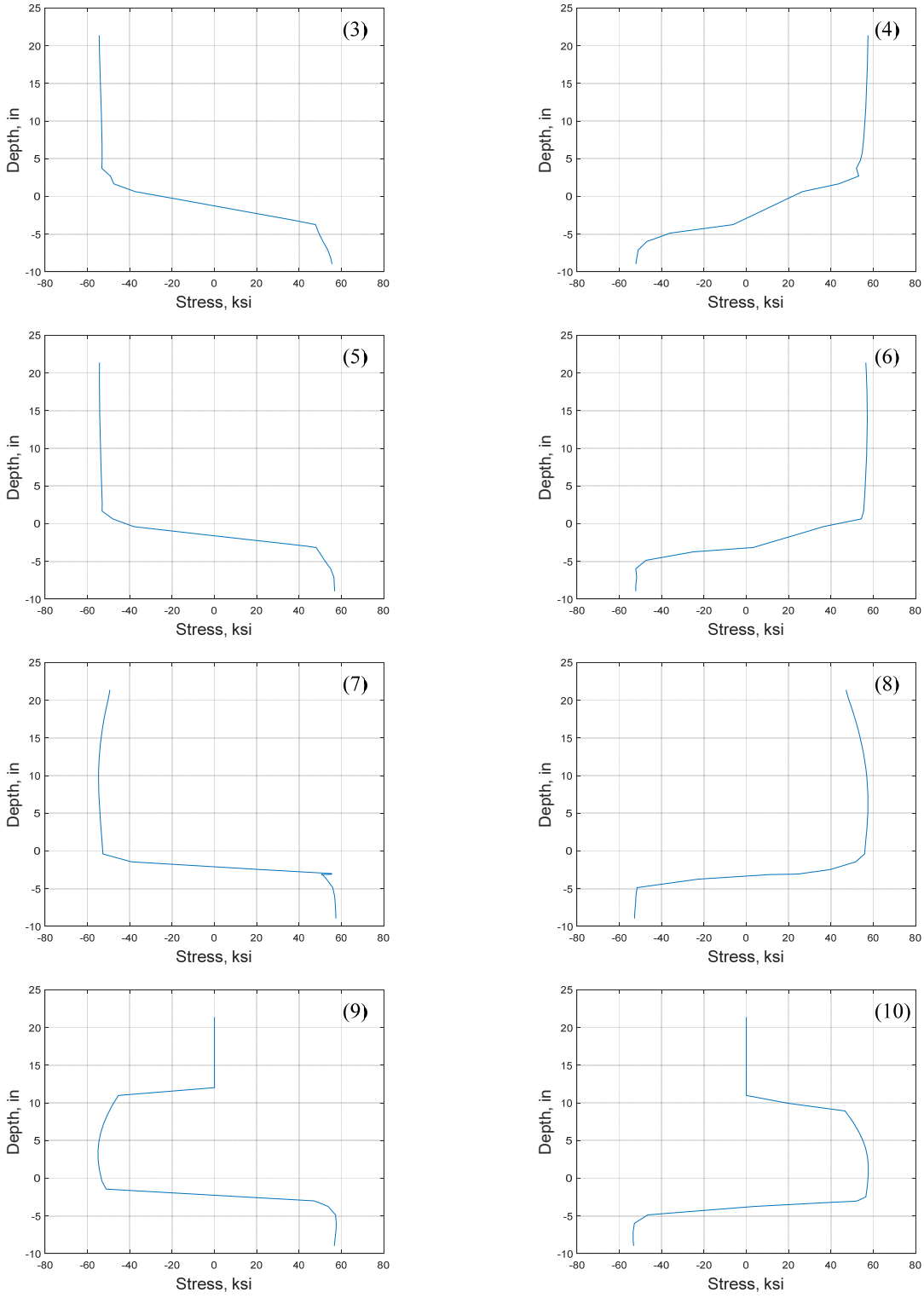

Figure 7-86. (Continued)

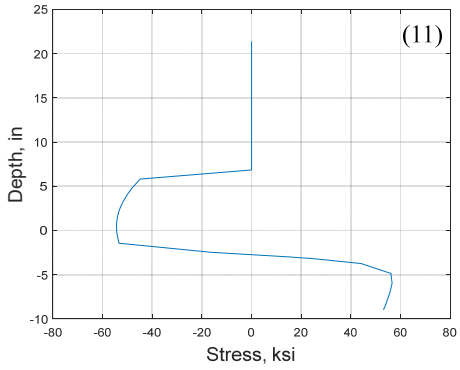

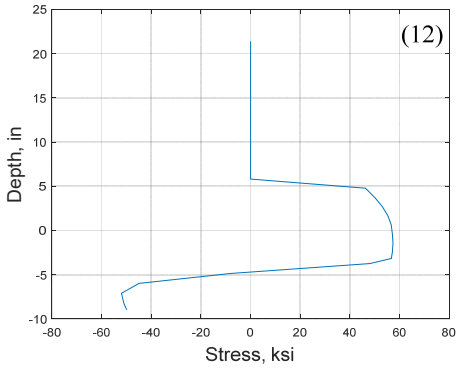

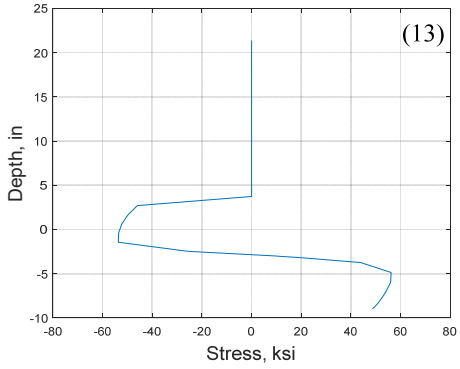

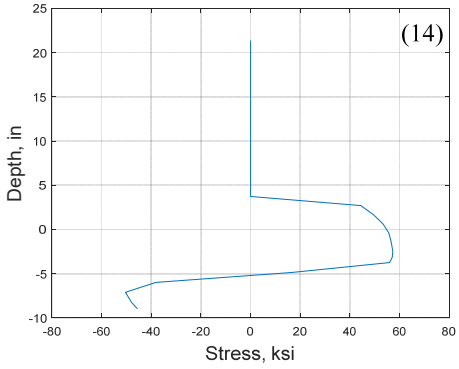

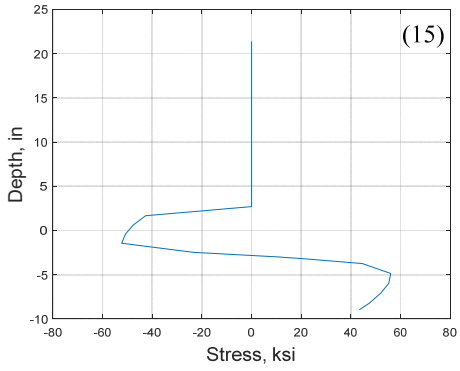

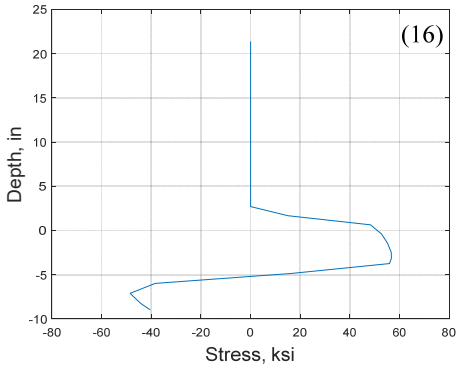

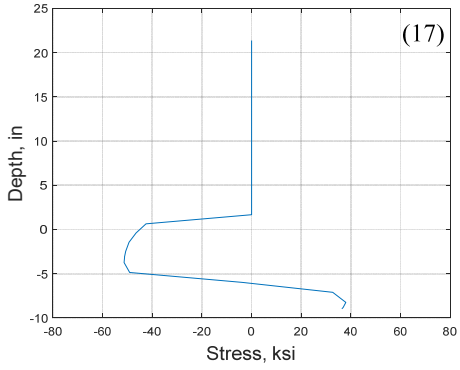

b) **c)**

Figure 7-86. (Continued)

“This Page Intentionally Left Blank”

SECTION 8 NUMERICAL CALIBRATION OF PLASTICITY MODELS USING EFFECTIVE STRESS STRAIN CURVES

Numercial calibration was also performed for a second non-linear model. This model serves as a complement to the distributed plasticity model presented in the previous section. This model used effective stress strain curves, developed from results of 3D finite element analyses, to define the material parameters presented Section 6. The walls were modeled with fiber-hinge elements having effective stress-strain curves, derived from results of 3D finite element analyses, and the coupling beams were modelled with concentrated plastic hinges at their ends using a calibrated "Modified Ibarra-Medina-Krawinkler Deterioration Model with Pinched Hysteretic Response" (MIMKD Model). The calibration for planar walls, composite coupling beams, and C-shaped walls are detailed in Section 8.2, 8.4, and 8.5, respectively.

8.1 Numerical Calibration of Planar C-PSW/CF Wall Model

The planar wall behavior was modeled using distributed plasticity elements. As detailed below, 3D finite element models were developed and analyzed using Abaqus to consider 3D effects necessary to account for the difference between the moment capacity calculated from elastic-plastic models and seen in the test. From these models, effective-stress strain curves for steel and concrete materials were developed for 2D models. These models correlate well to the experimental results.

8.1.1 Cross Sectional Analysis of Planar C-PSW/CF Walls

As shown in the prior cross-sectional analysis (Section 7.3.4.1) the moment capacity considering elasto-plastic behavior is 1116 k-in (93 k-ft) and can be mirrored in OpenSees elasto-plastic analysis. However, the experimental results, when considering the applied axial loads as well, reached a higher capacity than predicted by plastic stress distribution methods. As shown in Table 8-1 and Figure 8-1, the maximum lateral applied load found through plastic analysis or fiber analysis underestimates the capacity of the specimen. Different material models were developed to account for the additional capacity. A 3D Abaqus model of the specimens was developed to look into appropriate material models.

Table 8-1. Comparison of Experimental Lateral Load Capacity and Analytical Results.

Specimen	Experimental				Plastic Stress Distribution (AISC Method)	
	Axial Force (kips)	f'_c (psi)	H_{max} (Push) (kips)	H_{max} (Pull) (kips)	M (kip-ft)	Hn (kips)
CW-42-55-10-T	-210	6508	184.6	-177.6	1396.4	169.3
CW-42-55-20-T	-505	7789	219.6	-218.4	1553.8	188.3
CW-42-55-30-T	-710	7386	209.4	-214.5	1623.9	196.8
CW-42-14-20-T	-560	8741	214.2	-215.0	1606.1	194.7
CW-42-14-20-TS	-540	8408	211.3	-210.9	1587.6	192.4

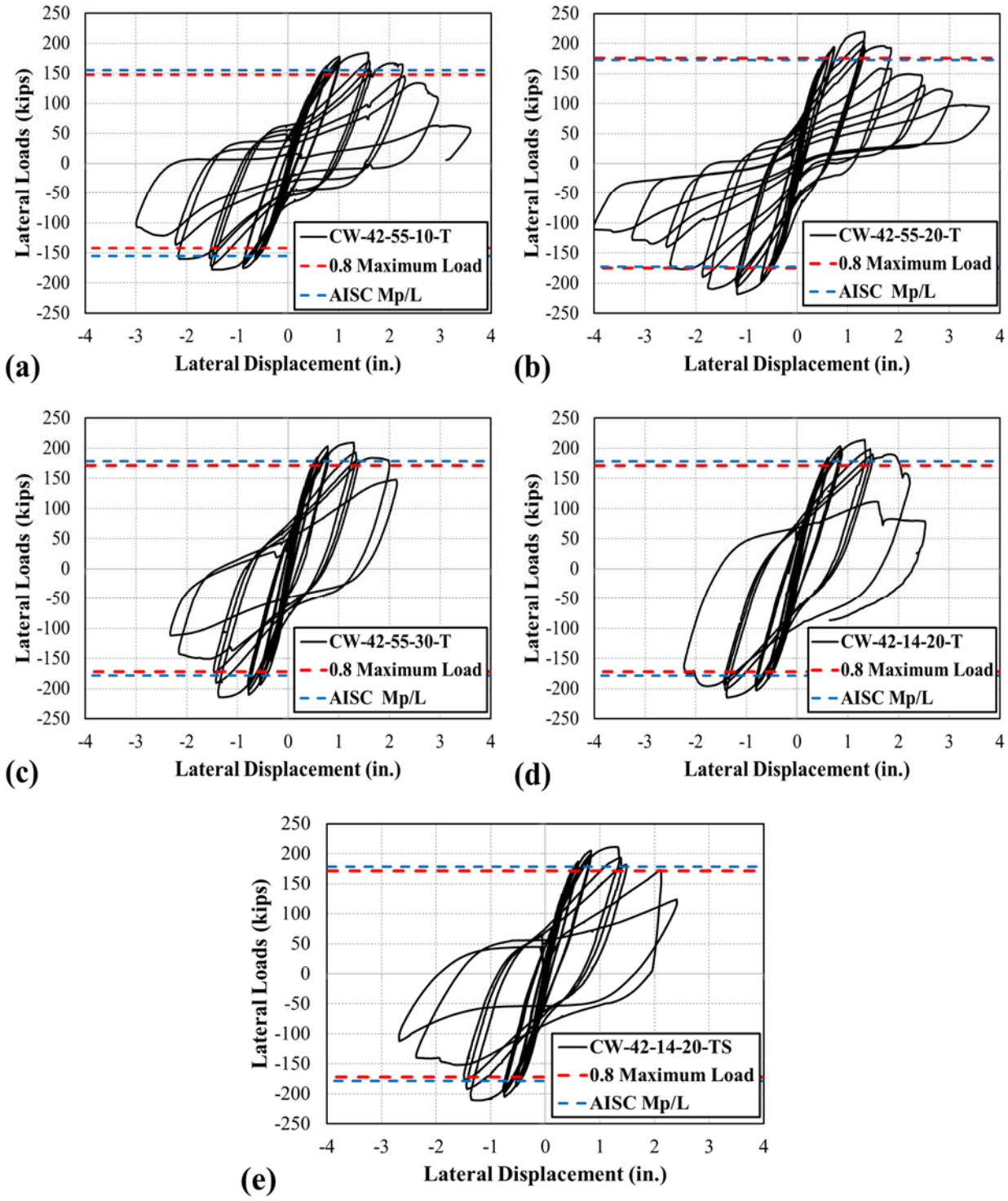

Figure 8-1. Lateral Force-Displacement Curve for (a) CW-42-55-10-T; (b) CW-42-55-20-T; (c) CW-42-55-30-T; (d) CW-42-14-20-T; (e) CW-42-14-20-TS.

8.1.2 Detailed 3D Finite Element Model of C-PSW/CF

Detailed three-dimensional finite element models were developed using Abaqus to investigate the behavior of CF-CPSW, as shown in Figure 8-2. The steel face plates were modeled using four-node shell elements with reduced integration (S4R). The concrete infill was modeled using eight-node solid elements with reduced integration (C3D8R). The tie bars were modeled using two-node beam elements (B31).
Shear connector elements (CONN3D2) were defined at the connection between the steel faceplates and tie bars to consider the axial and interfacial shear response of the connection. The shear response of tie bars was specified using the model proposed by Ollgaard et al. (1971). Initial geometric imperfections were defined in the steel faceplates to trigger the initiation of local buckling.

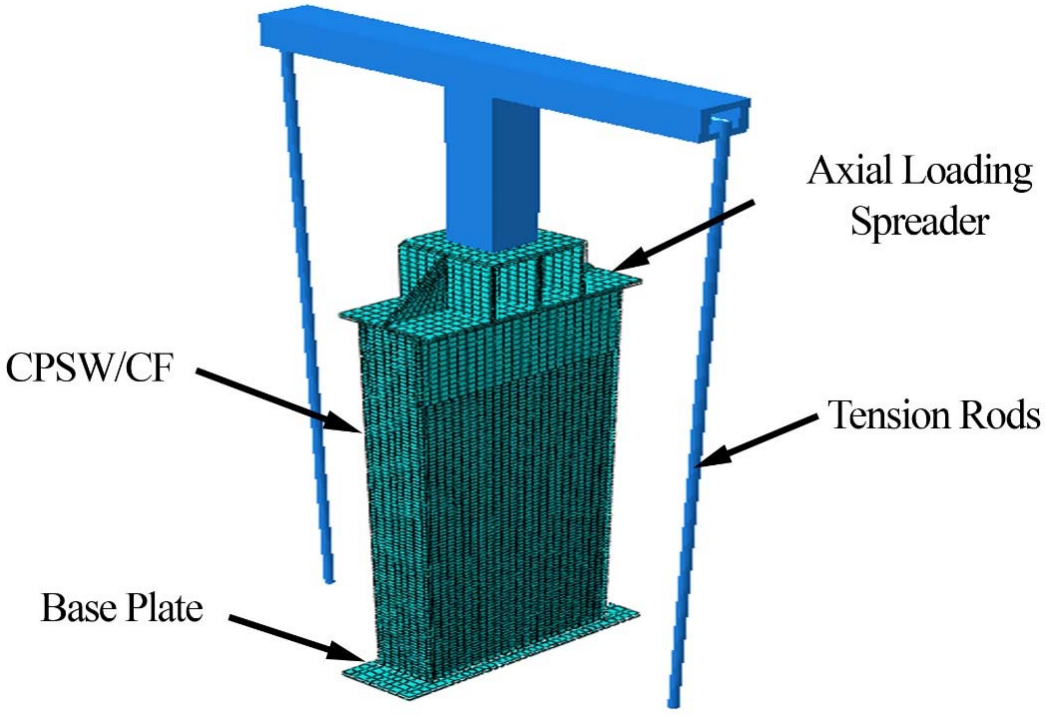

Figure 8-2. Finite element model of the C-PSW/CF specimen.

A nonlinear elastic-plastic material model, according to the results of tested steel coupons of the specimen, was considered for the steel faceplates, as shown in Figure 8-3(a). The fracture failure of the steel material was defined using the ductile damage option of the Abaqus software. In the ductile damage model: (i) damage initiated at 18% equivalent plastic strain, (ii) damage evolution was linear, and (iii) fracture (element deletion) occurred at 25% equivalent plastic strain. The concrete damage plasticity (CDP) model was used for the infill concrete core. The uniaxial compression behavior of concrete was developed using

a confined concrete model proposed by Tao et al. (2013), as shown in Figure 8-3(b). The CEB-FIP model (2010) was also used to specify the uniaxial tension behavior of concrete.

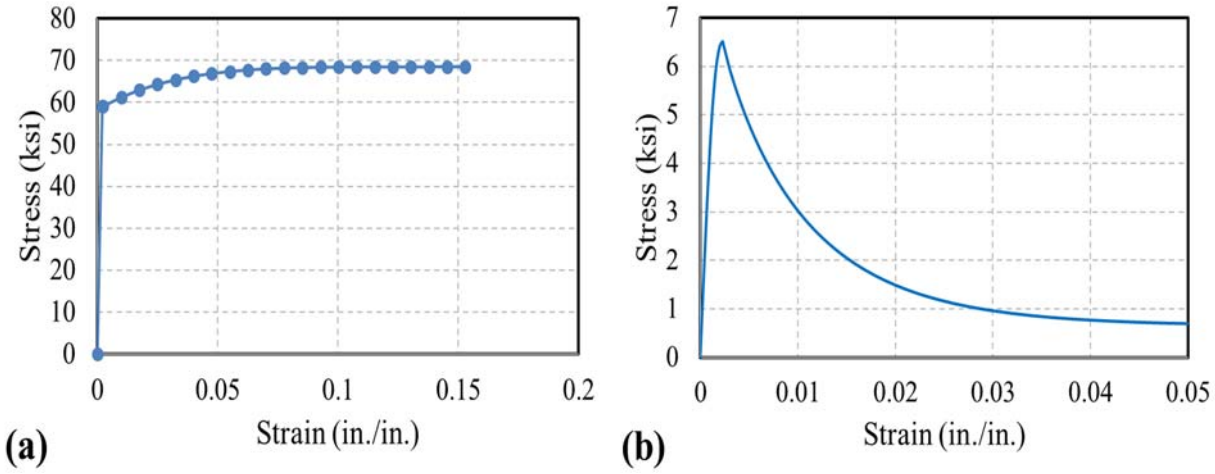

Figure 8-3. Material properties (a) steel stress-strain curve (b) Concrete stress-strain curve for compression.

Figure 8-4(a) shows the comparison of the experimental results of CW-42-55-10-T with the finite element model. The numerical and experimental results are in good agreement, which indicates that the complex behavior of C-PSW/CF can be reasonably and accurately predicted by finite element model. In the finite element model, the local buckling of the flange plates occurred between the first and second row of the flange shear studs from the bottom of the specimen, as shown in Figure 8-4(b). The locations of local buckling of steel flange plates in both the finite element model and experiment were the same.

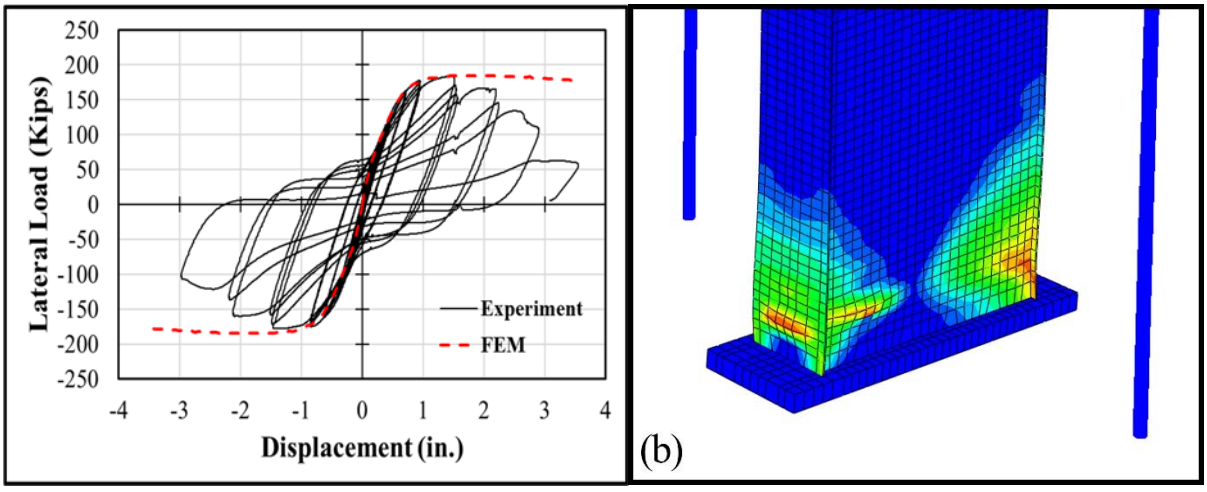

Figure 8-4. Finite element results: (a) Comparison of finite element model with experimental results (b) Local buckling of steel flange plates.

8.1.3 Effective stress-strain developed for C-PSW/CF

The 3D finite element model of CW-42-55-10-T was used to develop the effective stress-strain curves of the steel and concrete materials. Figure 8-5 represents the procedure used to develop the effective stress-strain curves in the steel flanges. In both the compression and tension flanges, a row of elements at 18 in. above the base plate (above the plastic hinge) was selected and the effective stress and the effective strain were calculated, as shown in Figure 8-5.

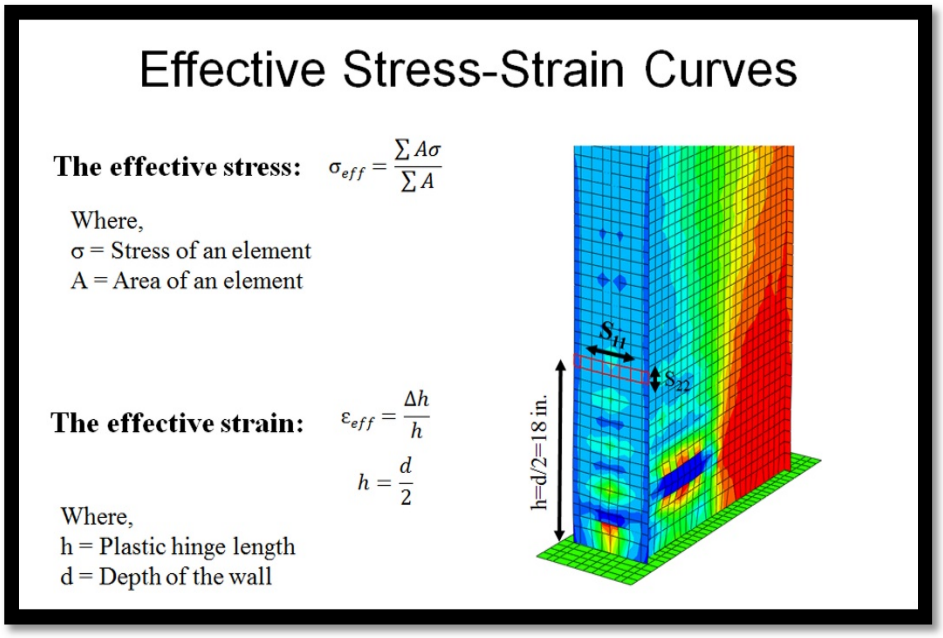

Figure 8-5. The procedure used to develop the effective stress-strain curves.

Figure 8-6 illustrates the effective stress-strain curves developed for steel flanges in compression and tension flanges. In accordance with the figure, the tension flange undergoes a biaxial stress state, which results in higher longitudinal stress (σ_{11}). The tension flange response follows plastic hardening behavior after yielding; however, the compression flange response is affected by the buckling and does not provide any strain hardening.

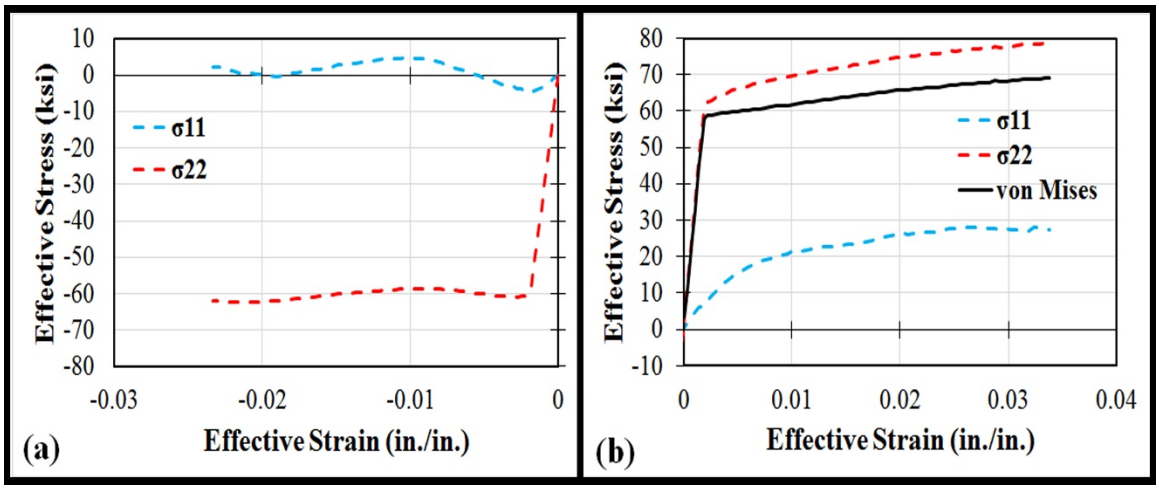

Figure 8-6. Effective stress-strain curves: (a) Compression flange (b) Tension flange.

Different sections of concrete at the plastic hinge location were considered to understand the compression response of the infill concrete. Figure 8-7 shows the locations of the selected layers in the compression concrete for development of the effective stress-strain curves. Figure 8-8 depicts the comparison of results of the effective stress-strain curves of selected concrete sections with the input confined concrete behavior in the program, Abaqus.

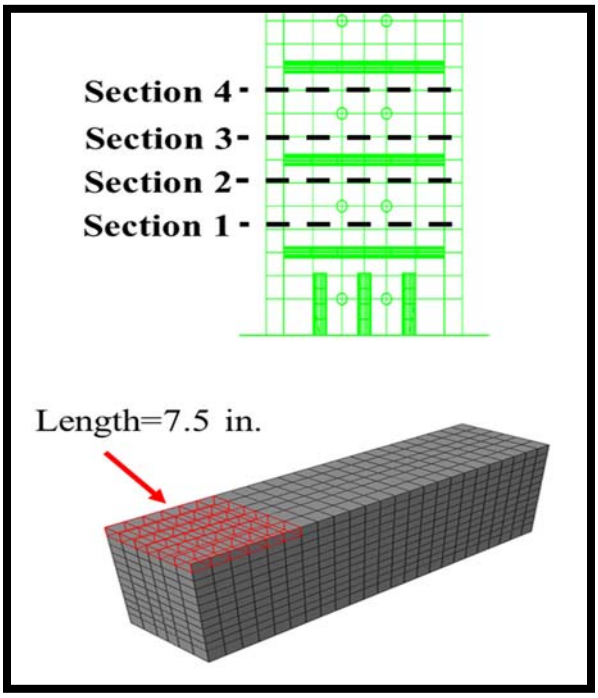

Figure 8-7. The location of selected sections in the compression concrete block.

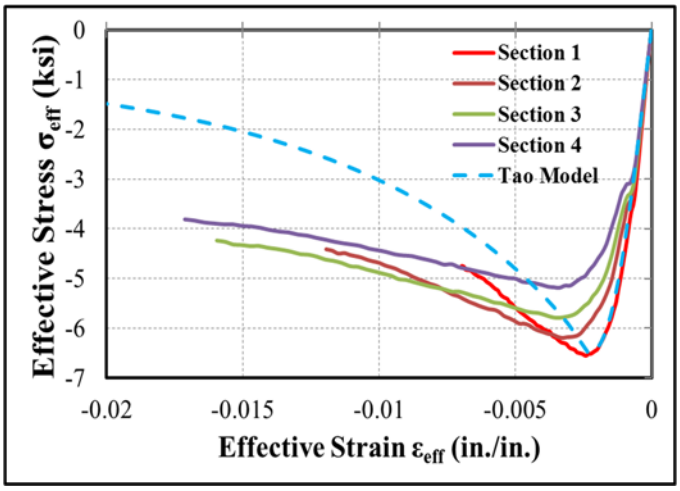

Figure 8-8. Comparison of the effective stress-strain curves of selected sections with the input confined concrete.

In accordance with the results, proposed effective stress-strain curves for steel and concrete are recommended. Figure 8-9 shows the phenomenological effective stress-strain curves for the tension and compression steel flanges and the compression infill concrete of C-PSW/CF. The behavior of compression flange is defined using an elastic-plastic response due to local buckling of the compression flange. The tension flange behavior is considered as an elastic-plastic with strain hardening. In addition, the yield strength is increased 10% in order to consider biaxial stress state of the tension flange. The uniaxial effective stress-strain curve for the compression concrete is developed using the ascending and descending branches of the concrete model by Tao et al. (2013). Additionally, the descending branch becomes constant at 60% of f'c to consider the effect of additional confinement due to steel faceplates.

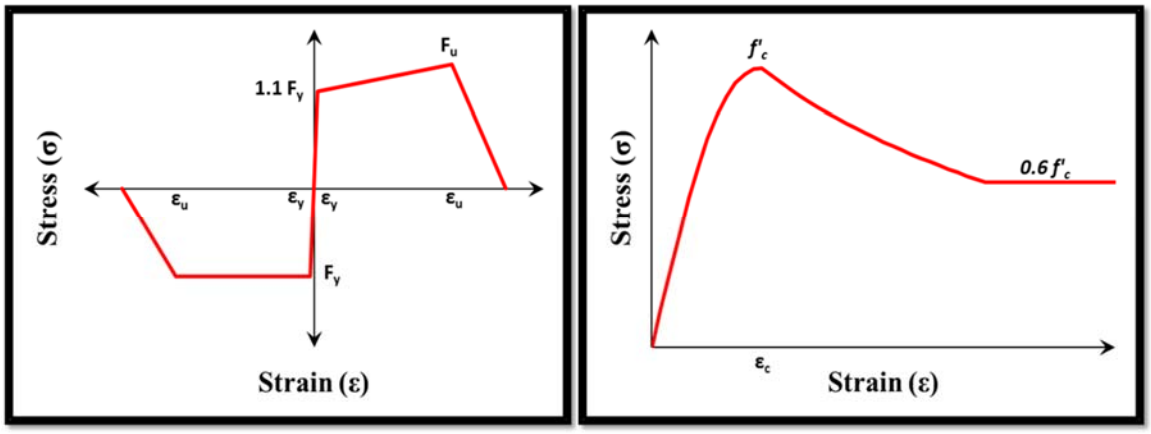

Figure 8-9. Proposed effective stress-strain curves for C-PSW/CF.

8.2 Implementation of effective stress-strain curves in planar C-PSW/CF

The proposed effective stress-strain relationships for the steel flange plates and the compression infill concrete were implemented in a 2D finite element model and fiber-based model.

8.2.1 Application in 2D finite element model (Abaqus)

The effective stress-strain curves developed for the steel flange plates and compression concrete core were implemented in a 2D finite element model of the tested C-PSW/CF specimen (CW-42-55-10-T). The infill concrete core and steel web plates were modeled using four-node composite shell section with reduced integration (S4R) and the steel flange plates were simulated using three-dimensional two-node truss elements (T3D2), as shown in Figure 8-10.

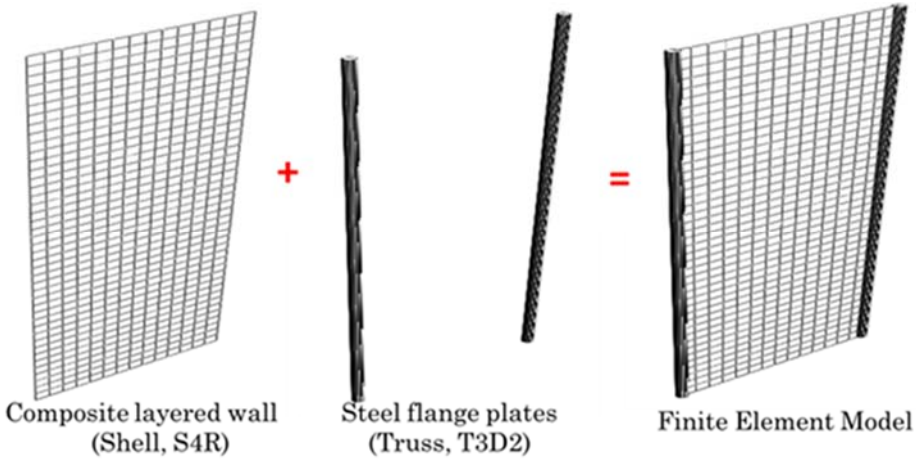

Figure 8-10. 2D finite element model of C-PSW/CF.

The 2D finite element model had a height of 9 ft. and a width of 3 ft. The area of the truss element was equal to the area of the steel flange plate, and truss elements were tied to the composite shell elements. The composite shell section included 3 layers; 2 layers of steel web faceplates with 3 integration points and a layer of infill concrete in the middle with 7 integration points.

A comparison of 2D finite element model with the 3D model and experimental results are illustrated in Figure 8-11. Additionally, a comparison of the von Mises stress distribution on steel faceplates in 3D finite element model with 2D model is shown in Figure 8-12. The comparison demonstrates the proposed idealized effective stress-strain curves for C-PSW/CF are conservative and valid for estimating the behavior.

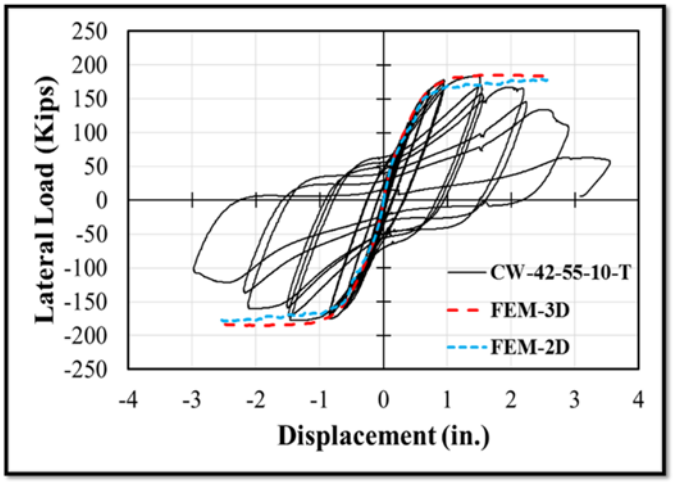

Figure 8-11. A comparison of finite element results of 3D model with 2D model.

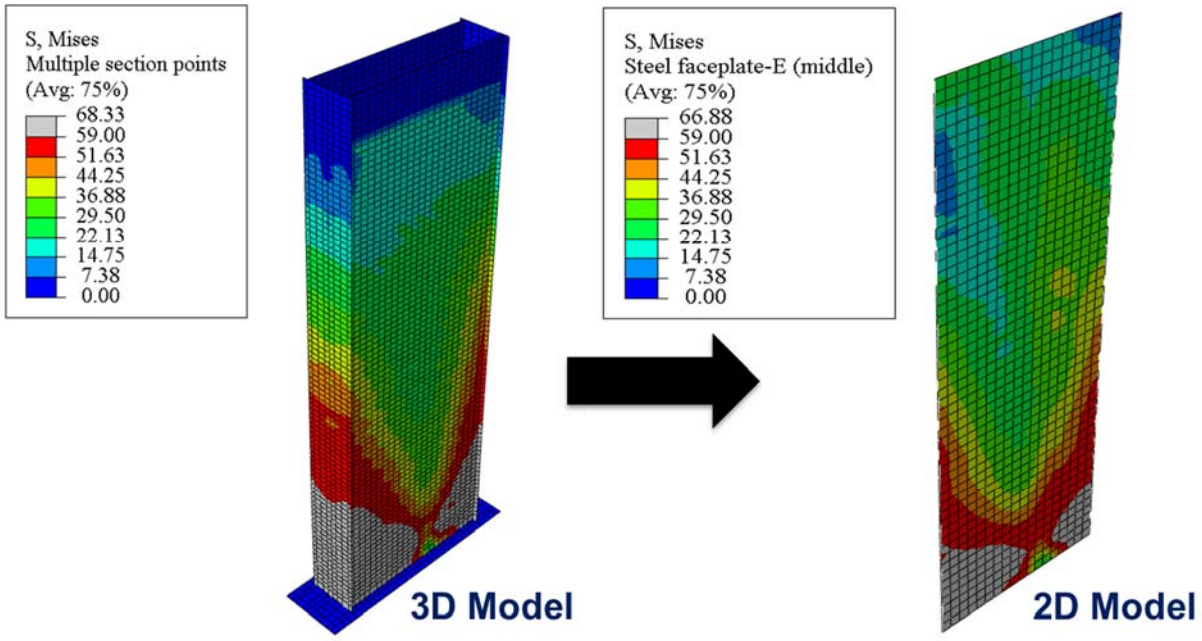

Figure 8-12. A comparison of the von Mises stress distribution in 3D model with 2D model.

8.2.2 OpenSees Material Model Parameters

OpenSees materials were developed to model the effective stress-strain relationships determined from Abaqus 3D models. The OpenSees material models presented before, Reinforcing Steel and Concrete 02, were used to model this behavior. Steel and concrete parameters used to model the effective stress-strain relationships are presented in Table 8-2 and Table 8-3 for concrete and steel, respectively. For further detail

on the material model, refer to Section 6.2 and 6.3. A comparison of the OpenSees stress-strain behavior and those from Abaqus models are shown in Figure 8-13 & Figure 8-14 for concrete and steel, respectively.

Table 8-2. Concrete material parameters for Abaqus effective stress-strain curves.

	Specimen 1	Specimen 2	Specimen 3	Specimen 4	Specimen 5
F_{pc} (ksi)	6.51	7.79	8.74	8.41	7.39
e_{psc0}	0.0023	0.00247	0.00259	0.00255	0.00242
F_{pcu} (ksi)	3.9	4.67	5.25	5.05	4.43
e_{psu}	0.0071	0.0071	0.0071	0.0071	0.0071
E_{ts}	4566	4996	5292	5190	4865

Table 8-3. Steel material parameters for Abaqus effective stress-strain curves.

Parameter	Value		Parameter	Value
E (ksi)	29000		L_{sr}	20.8
b	0.025		beta	1
E_{sh} (ksi)	725.0		r	0.8
F_y (ksi)	60.0		gamma	0.5
F_u (ksi)	71.0		C_f	0.3
e_{sh}	0.003		alpha	0.52
e_{ult}	0.153		C_d	0.32

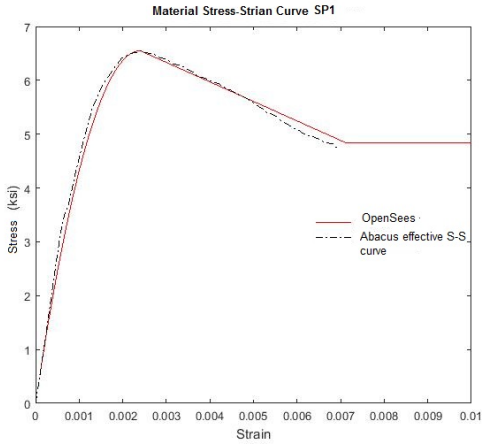

(a)

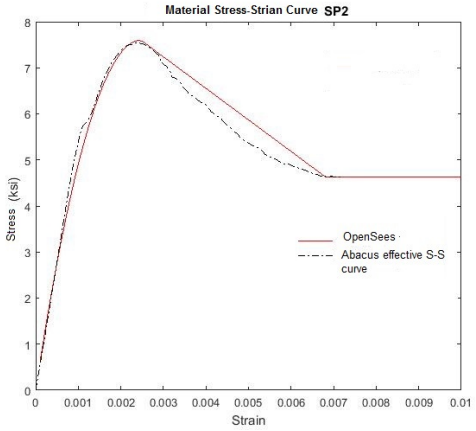

(b)

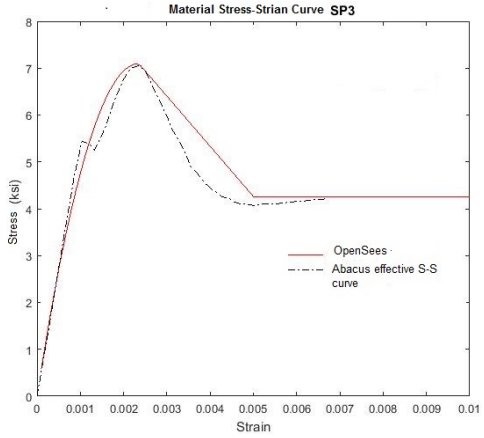

(c)

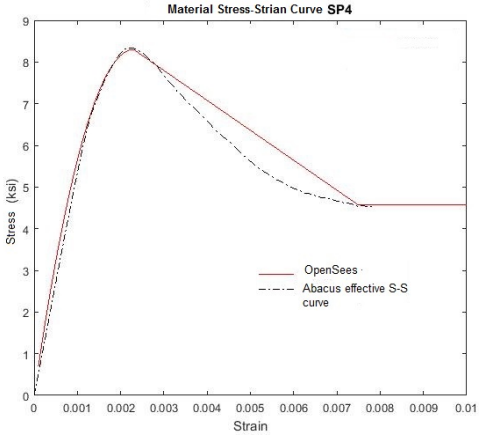

(d)

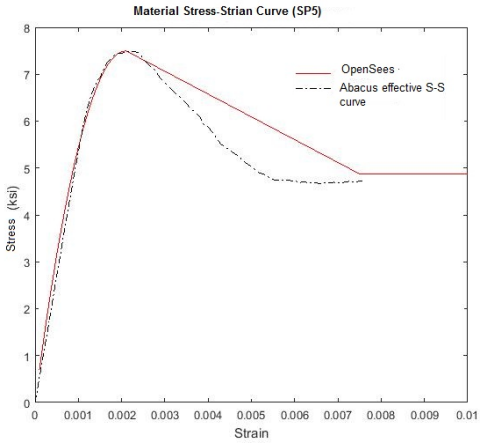

(e)

Figure 8-13. Comparison between concrete effective stress-strain curves developed in Abaqus to material models used in OpenSees to match these models. (a) CW-42-55-10-T; (b) CW-42-55-20-T; (c) CW-42-14-20-T; (d) CW-42-14-20-TS; and (e) CW-42-55-30-T.

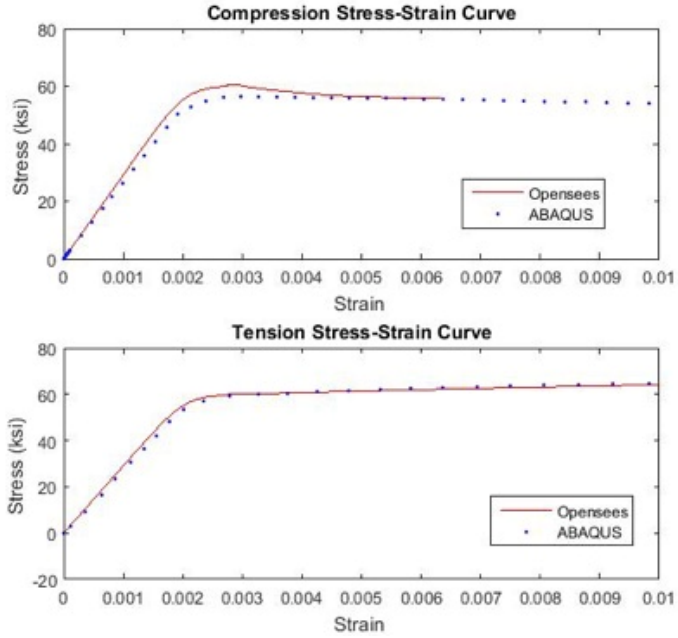

Figure 8-14. Comparison between steel effective stress-strain curves developed in Abaqus to material models used in OpenSees to match these models.

From the behavior seen in the effective stress-strain curves from Abaqus, general stress-strain material behavior curves were developed. These curves are shown in Figure 8-15 and Figure 8-16 for concrete and steel, respectively. The concrete model uses the model defined by Tao et al. (2013). The ascending and descending branch of the generalized concrete model are defined by the Tao concrete model, but the residual capacity is adjusted to $0.6f'_c$. This adjustment follows the Abaqus stress-strain curves developed. Steel and concrete parameters used to model the effective stress-strain relationships are presented in Table 8-4 and Table 8-5 for concrete and steel, respectively

Table 8-4. Concrete material parameters for assumed stress-strain curves.

	Specimen 1	Specimen 2	Specimen 3	Specimen 4	Specimen 5
F_{pc} (ksi)	6.51	7.79	8.74	8.41	7.39
e_{psc0}	0.0023	0.00247	0.00259	0.00255	0.00242
F_{pcu} (ksi)	$0.6*f'_c$	$0.6*f'_c$	$0.6*f'_c$	$0.6*f'_c$	$0.6*f'_c$
e_{psu}	0.0071	0.0071	0.0071	0.0071	0.006
E_{ts}	4566	4996	5292	5190	4865

Table 8-5. Steel material parameters for assumed stress-strain curves.

Parameter	Value		Parameter	Value
E (ksi)	29000		L_{sr}	10.0
b	0.015		beta	1.0
E_{sh} (ksi)	E*b		r	0.60
F_y (ksi)	59.1		gamma	0.50
F_u (ksi)	68.5		C_f	0.60
e_{sh}	$2*F_y/E$		alpha	0.50
e_{ult}	0.045		C_d	0.35

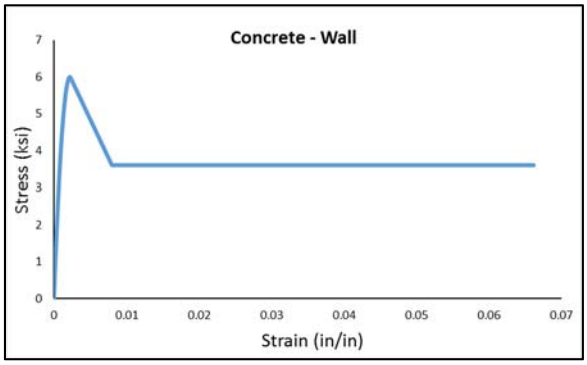

Figure 8-15. Generalized concrete material models for wall concrete.

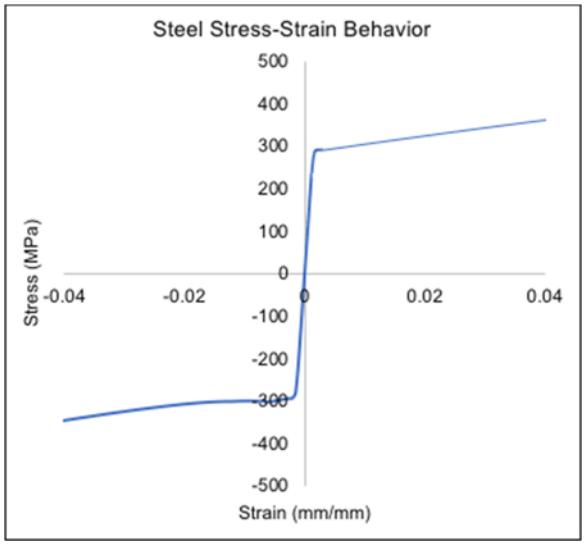

Figure 8-16. Generalized steel material behavior for wall steel.

Two sets of parameters were used to model the wall behavior: (1) OpenSees models following exact stress-strain curves developed for the tested specimens; (2) OpenSees materials following generalized stress-strain curves. The first set more closely follows the actual behavior, but this level of detail and calibration is impractical for the archetype walls. The second set of parameters will be used for the archetype structures as, although conservative, this set well models the behavior and can be easily implemented.

8.2.3 Element Distribution

Element distribution was evaluated to determine a scheme that would well address the wall behavior and be as coarse as possible to decrease the computation time. As seen in the testing performed at Purdue, inelastic behavior was confined to a height of half the wall width; therefore, non-linear elements were limited to this region. Above this region, the wall was assumed to be elastic. The steel material model in particular is sensitive to element distribution as the cumulative plastic strain tracked varies based on the number of elements. A comparison of various elements in the plastic hinge zone is shown in Figure 8-17. These results follow previously presented evaluation of the effect of element distribution in the nonlinear zone of the wall. Three elements in the plastic hinge zone (6" elements) were used after reviewing this curve and envelope cyclic curves like Figure 7-23.

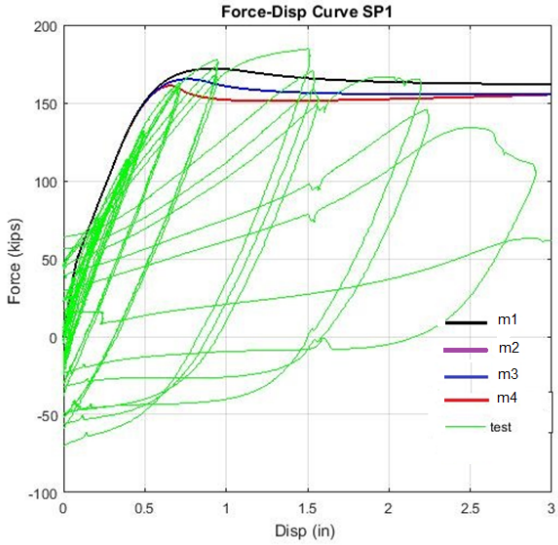

Figure 8-17. Envelope response of PG-1A for various element distributions.

8.2.4 Comparison of OpenSees Models with Test Data

From the material models and element distribution, OpenSees wall models were built. These models were run for both the material model matching the Abaqus effective stress-strain curves and material model matching the assumed stress-strain curve. As shown in Figure 8-18(a) for specimen 1 (CW-42-55-10-T), matching the effective stress-strain curves closely follows the actual response with both the peak load and the cycle at failure, following the experimentally observed response. The assumed stress-strain curves shown in Figure 8-18(b) also follows the behavior but is more conservative regarding strength. Although this model does not fit the experimental results as well as directly matching the effective stress-strain curves, this model can be replicated for the archetype structure models and is conservative with respect to wall capacity. The results for the remaining models using the generalized stress-strain curves are shown in Figure 8-19.

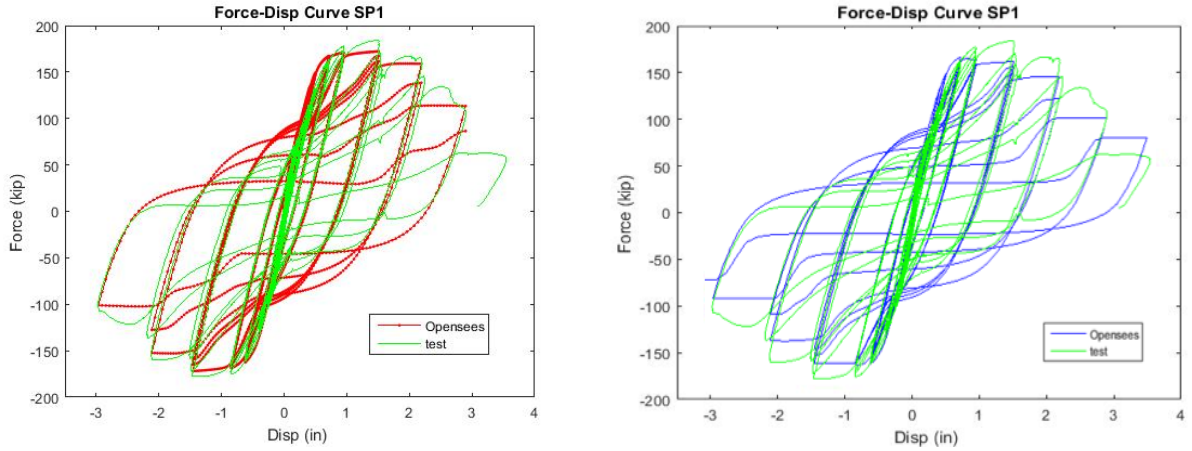

(a) (b)

Figure 8-18. Force versus displacement curves for CW-42-55-10-T. (a) Matching effective stress-strain curves; (b) Matching assumed stress-strain curves.

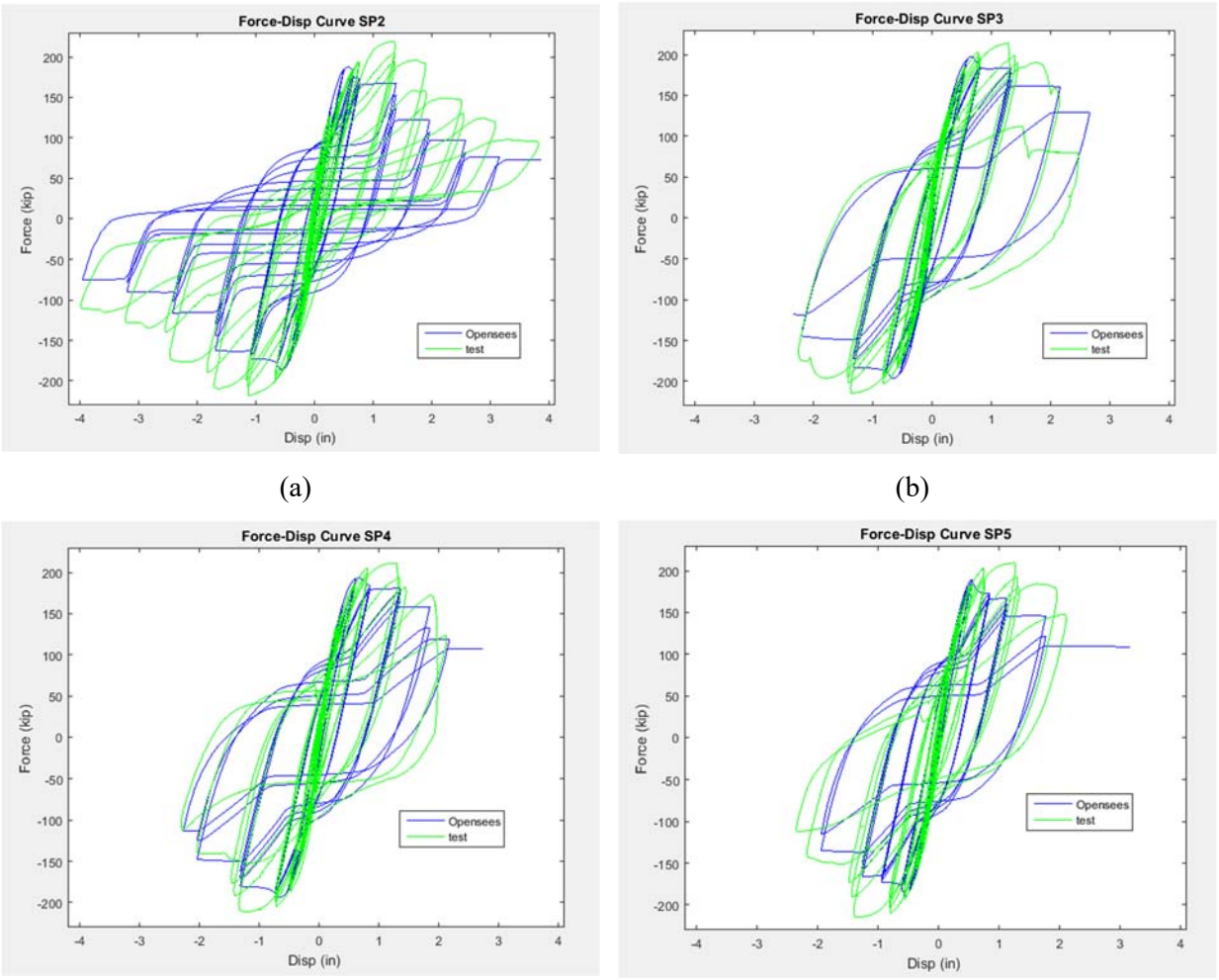

Figure 8-19. Force-Displacement comparison using assumed effective stress-strain curves for (a) CW-42-55-20-T; (b) CW-42-55-30-T; (c) CW-42-14-20-T; (d) CW-42-14-20-TS.

8.3 Numerical Calibration of Composite Coupling Beams Models

This model involves representing the coupling beam behavior with rotational spring elements. Modeling the coupling behavior is a two-step process first involving developing a fiber-based model similar to the one described in Section 7.5.4. From this model, concentrated plasticity elements are calibrated to the fiber-based response. Similar to modeling the wall as described in Section 8.1, this process involved developing material effective stress-strain curves. These material models were implemented in OpenSees. After running a distributed plasticity simulation, a second model using concentrated plasticity elements was created to match the results.

8.3.1 Cross Sectional Analysis of Composite Coupling Beams

Similar to the wall models, the experimental results showed a higher capacity then predicted by the plastic stress distribution. This difference in the plastic moment capacity and the experimental test results is reflected in Table 8-1. This additional capacity can be captured in 3D Abaqus models but not in traditional 2D models without developing effective material models.

8.3.2 Detailed 3D Finite Element Models of Composite Coupling Beams

A detailed three-dimensional finite element model of the composite coupling beams was developed using a commercial software program (Abaqus), as shown in Figure 8-20. The steel faceplates were modeled using four-node shell elements with reduced integration (S4R). The concrete infill was modeled using eight-node solid elements with reduced integration (C3D8R). The composite coupling beams were tested by Nie et al, as discussed in section 7.5.

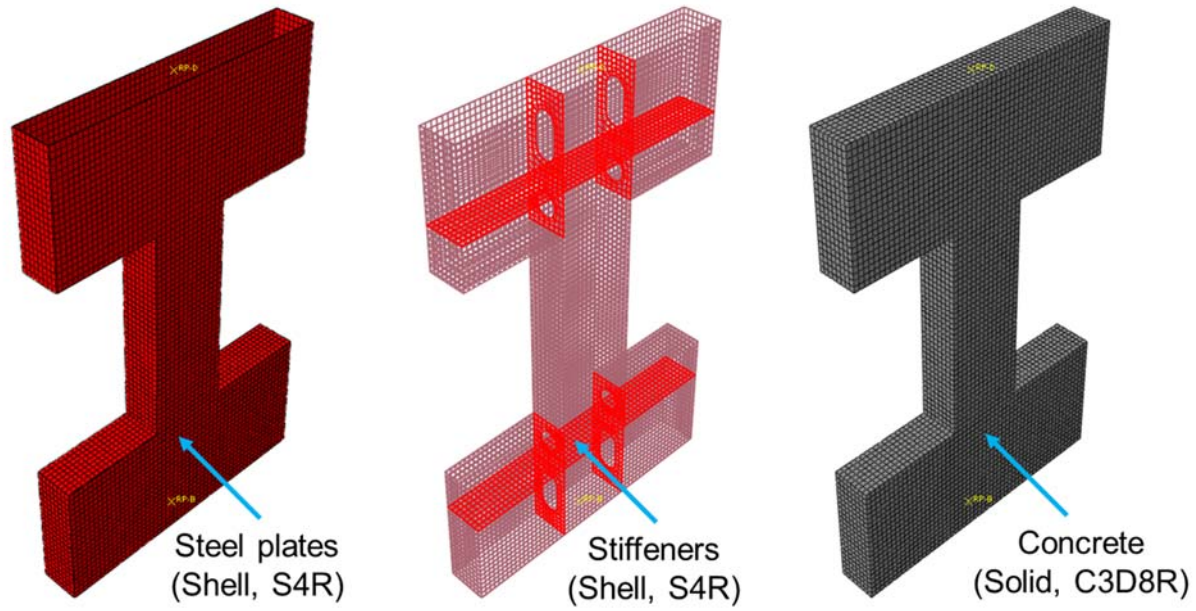

Figure 8-20. 3D finite element model of composite coupling beam.

The bottom of the 3D finite element model for the composite coupling beams was fixed, and lateral displacement was applied to the top, as shown in Figure 8-21.

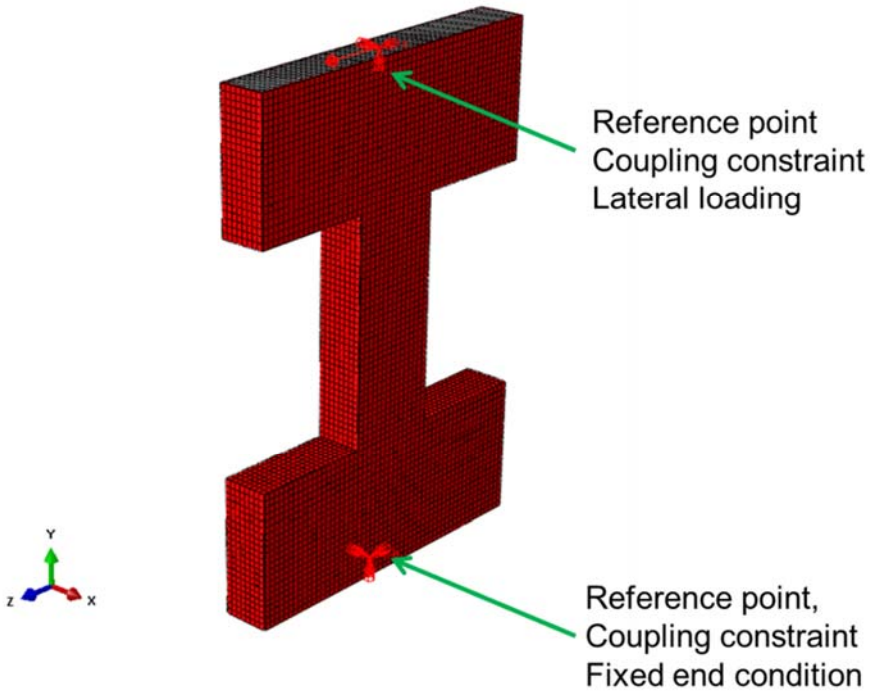

Figure 8-21. Loading and boundary conditions.

The comparisons of finite element model with experimental results are shown in Figure 8-22 and Figure 8-23. As shown, the finite element model is able to predict the behavior of composite coupling beams accurately. However, the 3D finite element model is not able to capture the pinching in cyclic analysis. This pinching is missing because the concrete damage plasticity model of Abaqus cannot accurately consider concrete crack opening and closure in tension behavior.

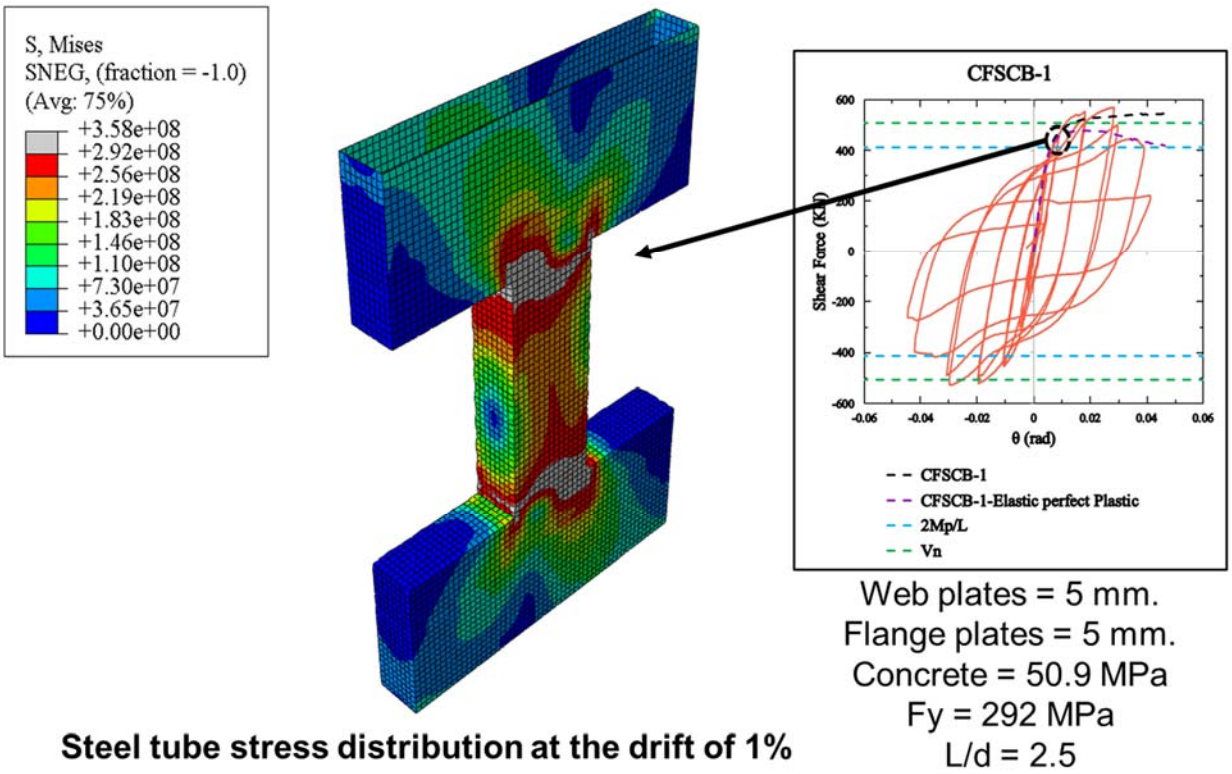

Figure 8-22. Comparison of monotonic response of finite element models with the experiment.

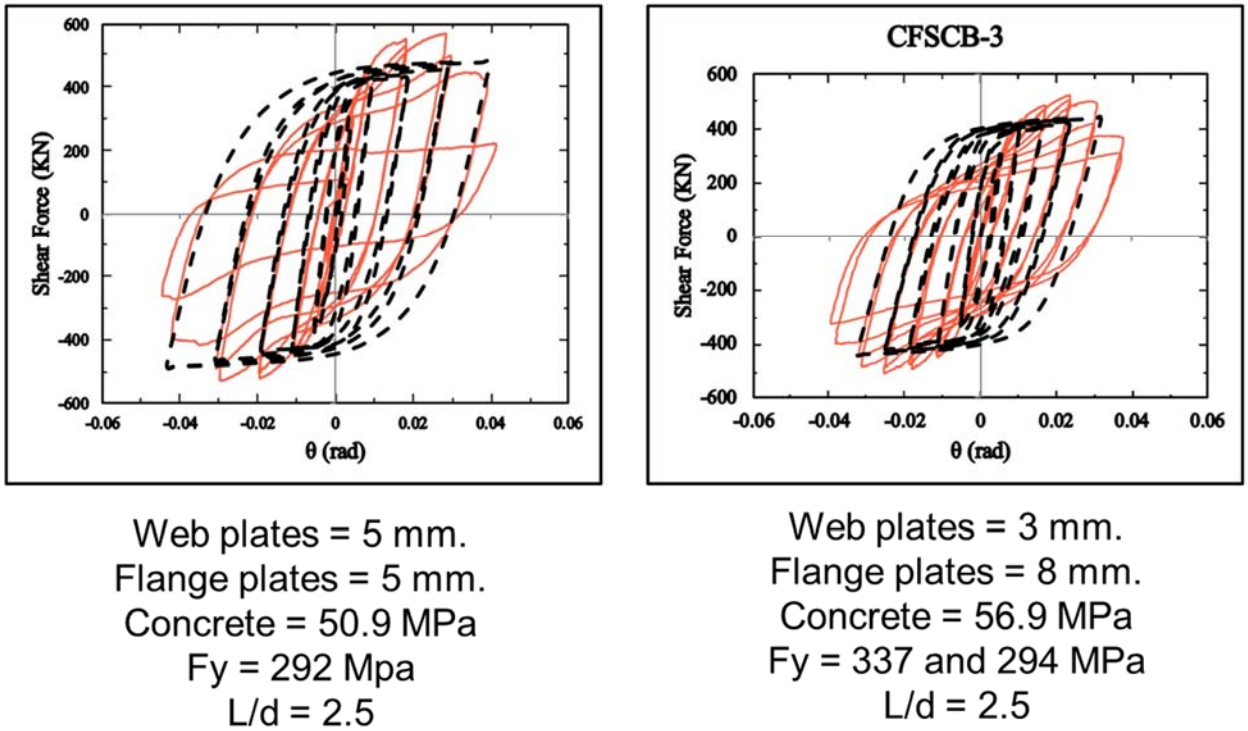

Figure 8-23.. Comparison of cyclic response of finite element models with the experiment.

8.3.3 Effective Stress-Strain developed for Composite Coupling beams

The 3D finite element model of composite coupling beam was benchmarked to develop the effective stress-strain curves for steel and concrete materials. Figure 8-24 shows the procedure used to develop the effective stress-strain curves in the steel flanges.

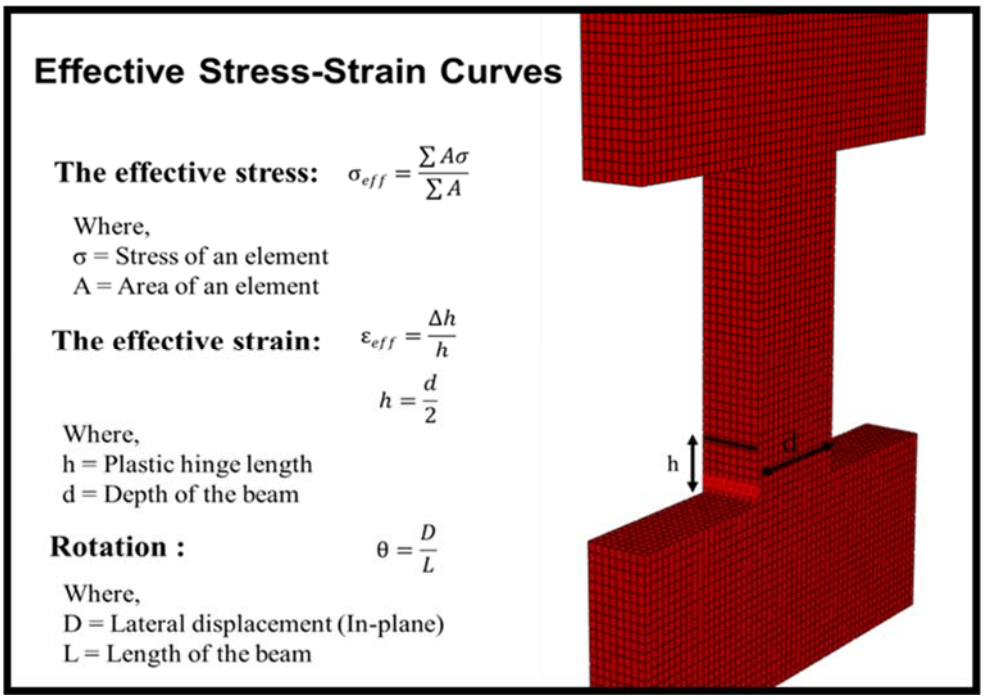

Figure 8-24. The procedure used to develop the effective stress-strain curves.

Figure 8-25 illustrates the effective stress-strain curves developed for the tension steel flange. The effect of biaxial stress state is seen in the tension flange; therefore, the composite coupling beams provide a higher flexural capacity.

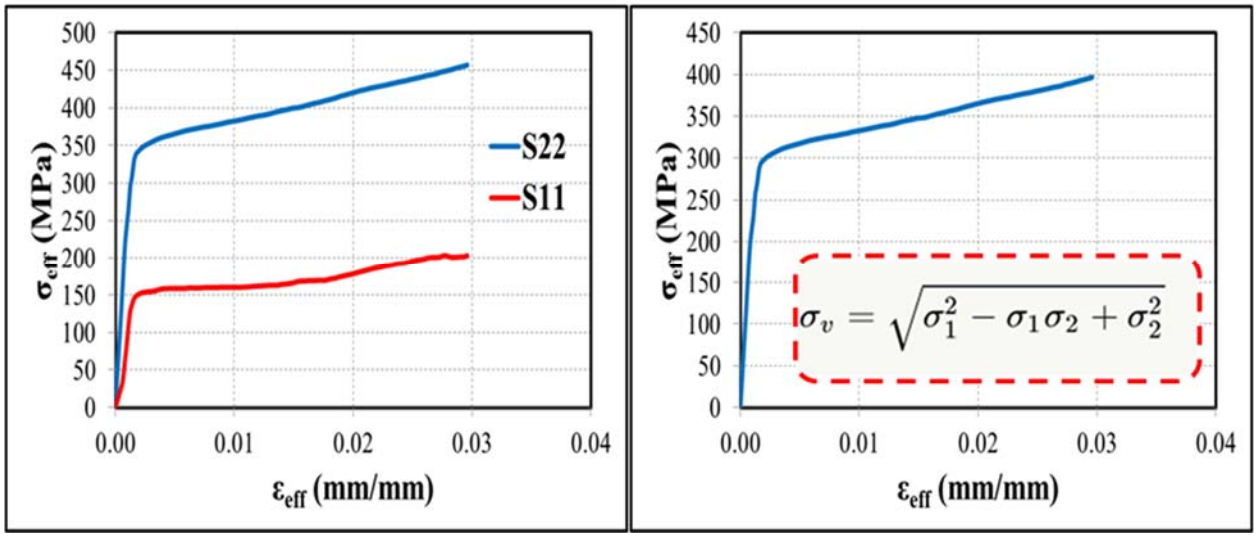

Figure 8-25. Effective stress-strain curves in the tension flange: (a) Principle stresses (b) The von Mises criterion.

The effective stress-strain curves developed for the compression steel flange are shown in Figure 8-26. In accordance with the figure, the compression flange response is affected by the buckling and does not provide plastic strain hardening.

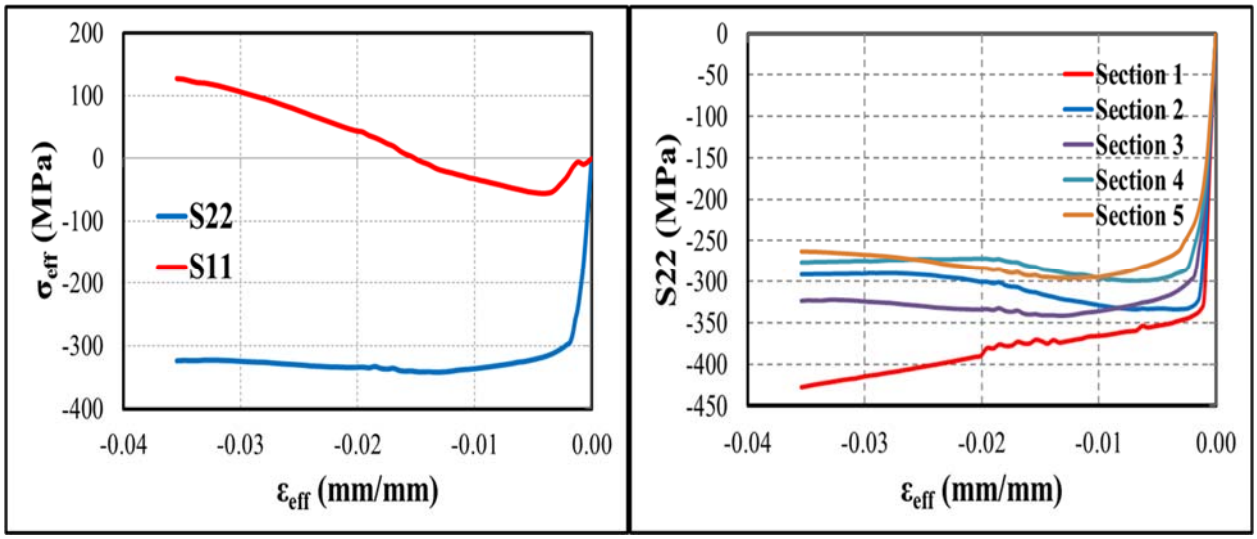

Figure 8-26. Effective stress-strain curves in the compression flange: (a) Principle stresses (b) Different sections.

Different sections of concrete at the plastic hinge location were considered to understand the compression response of the infill concrete. Figure 8-27 shows the locations of the selected sections in the compression

concrete for development of the effective stress-strain curves. Figure 8-28 depicts the comparison of results of the effective stress-strain curves of selected concrete sections with the input confined concrete behavior in the program, Abaqus.

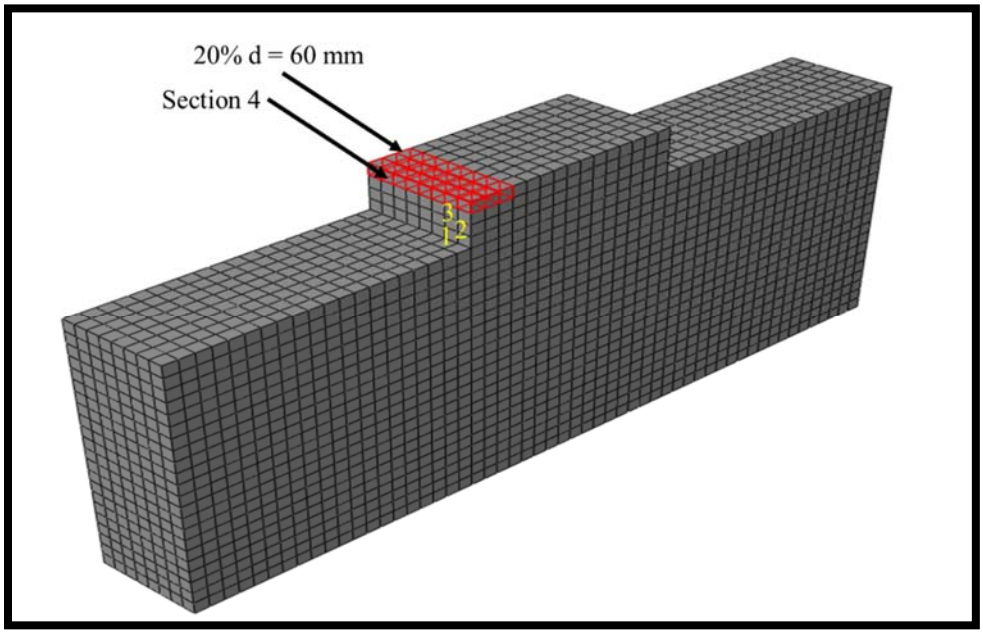

Figure 8-27. The location of selected sections in the compression concrete block.

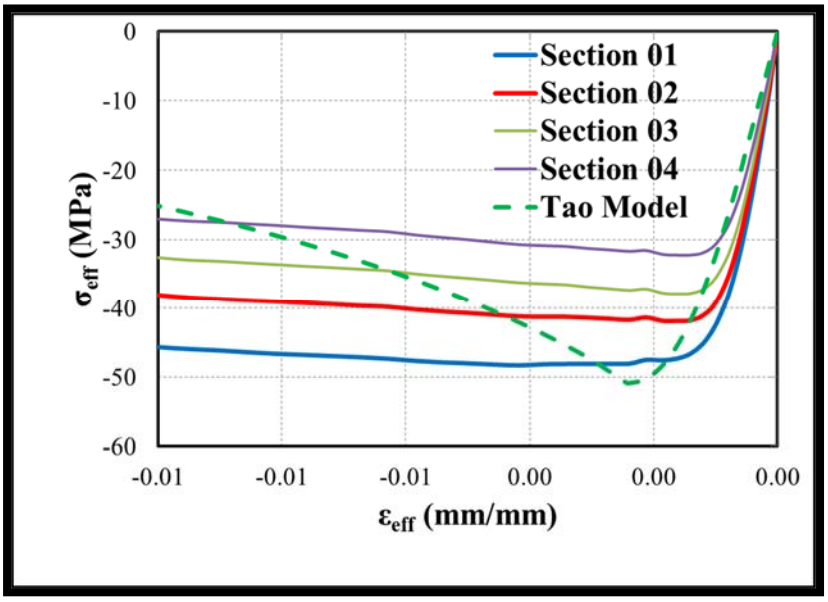

Figure 8-28. Comparison of the effective stress-strain curves of selected sections with the input confined concrete.

Figure 8-29 shows the phenomenological effective stress-strain curves for the tension and compression steel flanges and the compression infill concrete of composite coupling beams. The behavior of compression flange is defined using an elastic-plastic response due to inelastic local buckling of the compression flange. The tension flange behavior is considered as an elastic-plastic with strain hardening. In addition, the yield strength is increased 10% in order to consider biaxial stress state of the tension flange. The uniaxial effective stress-strain curve for the compression concrete is developed using only the ascending branch of concrete model and plastic behavior.

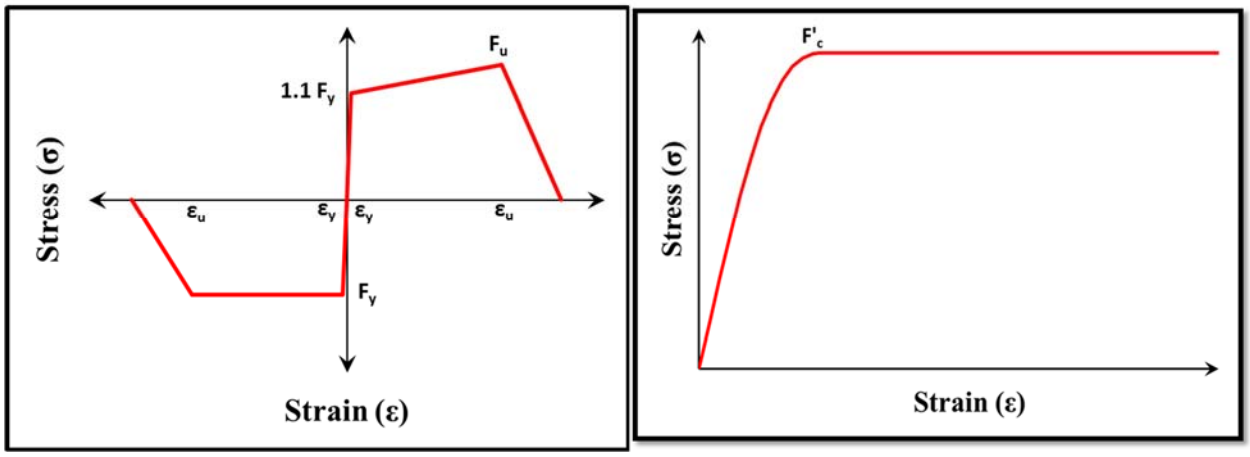

Figure 8-29. the proposed phenomenological effective stress-strain curves for the steel flanges and the compression infill concrete.

8.4 Implementation of Effective Stress-Strain Curves in Coupling Beams

The proposed effective stress-strain relationships for the steel flange plates and the compression infill concrete were implemented in a 2D finite element model and fiber-based model.

8.4.1 Application in 2D Finite Element Model (Abaqus)

A 2D finite element model of composite coupling beams was developed using the proposed effective stress-strain curves. The infill concrete core and steel web plates were modeled using four-node composite shell section with reduced integration (S4R) and the steel flange plates were modeled using three-dimensional two-node truss elements (T3D2), as shown in Figure 8-30.

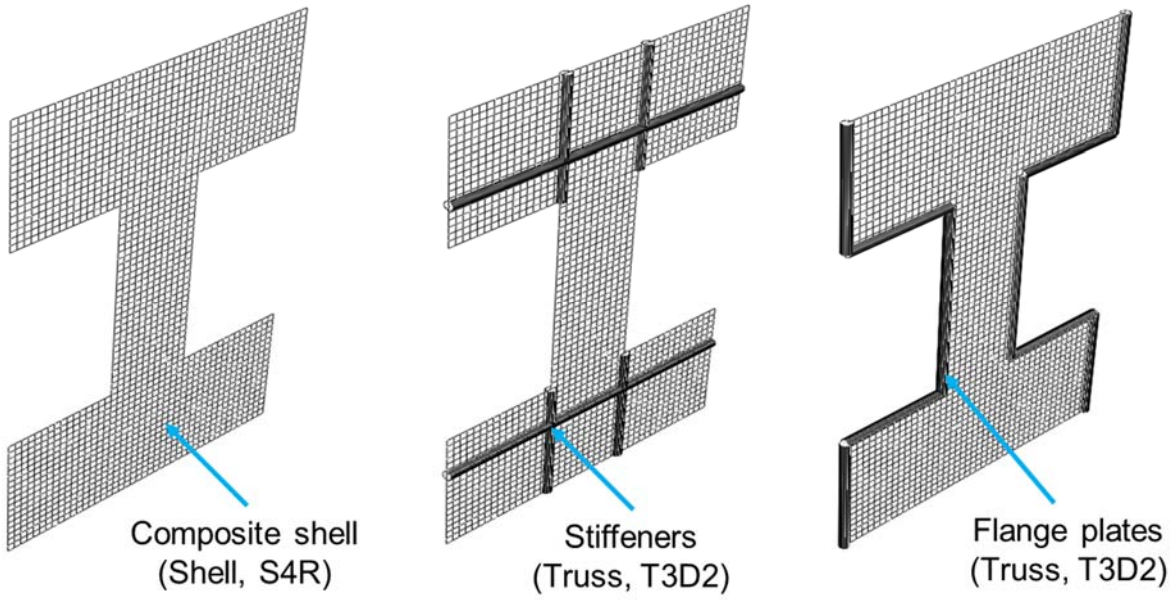

Figure 8-30. 2D finite element model of composite coupling beams.

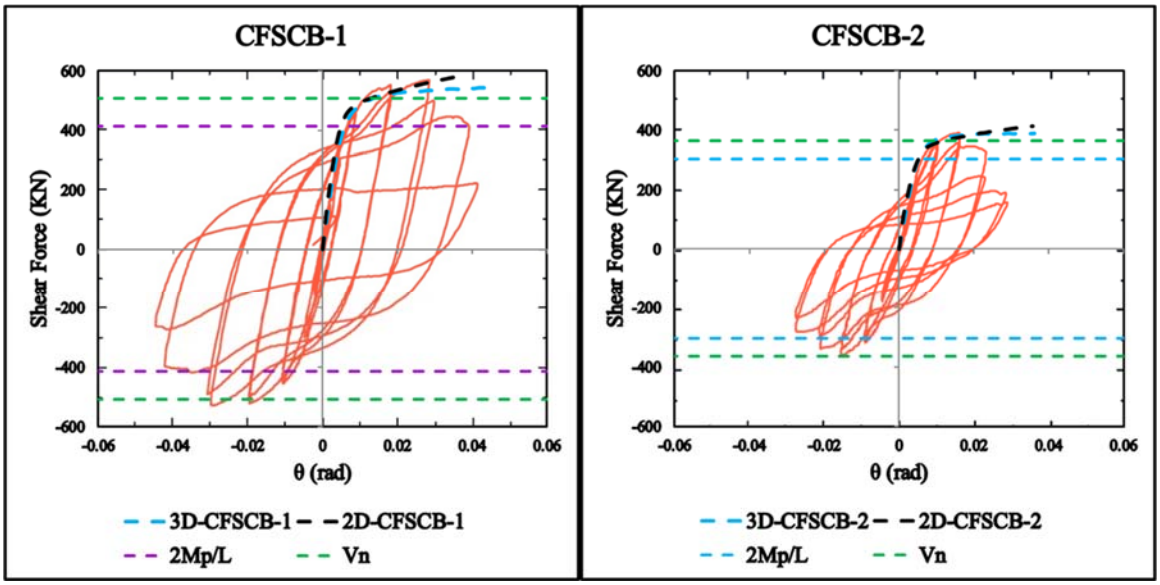

Figure 8-31. Pushover results of 3D and 2D models

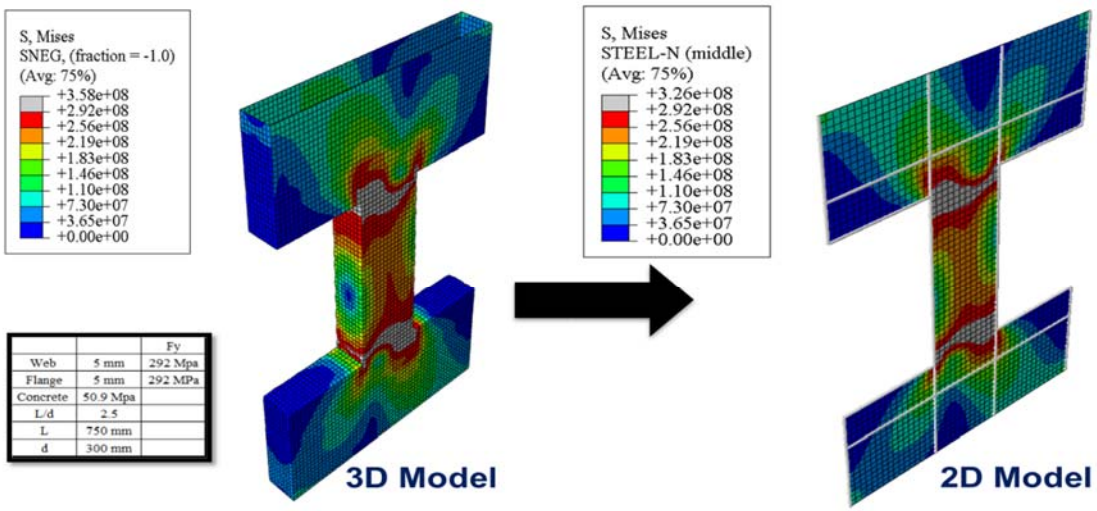

Figure 8-32. Comparison of the von mises stress distribution in 3D finite element model with 2D model

8.4.2 OpenSees Material Model Parameters

From the Abaqus effective stress-strain curves, generalized stress-strain curves were developed. Similar to using the generalized adjusted material models in Section 7.5.4, the generalized curves were used to model the material behavior as this procedure could be replicated for the archetype structures. These curves are shown in Figure 8-33 and Figure 8-34. The steel behavior follows the same curve developed for the wall model. The concrete behavior is adjusted to reach a peak stress of $0.85f'_c$ and maintain this stress. As the section is smaller, confinement has a larger effect as reflected in the Abaqus results.

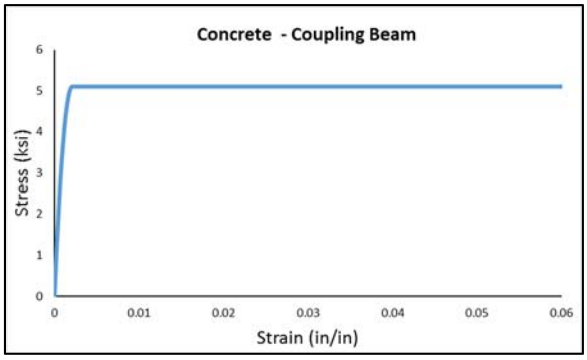

Figure 8-33. Assumed concrete stress-strain behavior for the coupling beams. Note: the peak stress is $0.85f'_c$

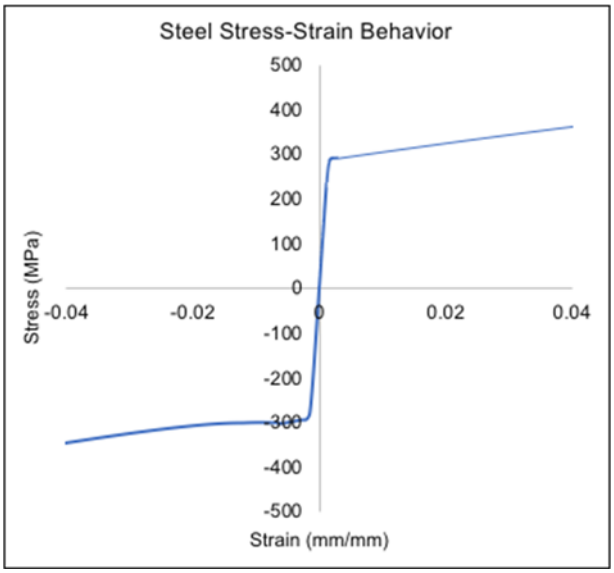

Figure 8-34. Assumed steel stress-strain behavior.

8.4.3 Element Distribution

For the initial distributed plasticity model, an element distribution study was conducted to determine appropriate element distributions. Results of this study are shown in Figure 8-35. Four elements in the hinge region (D away from the wall) were chosen for the archetype coupling beams.

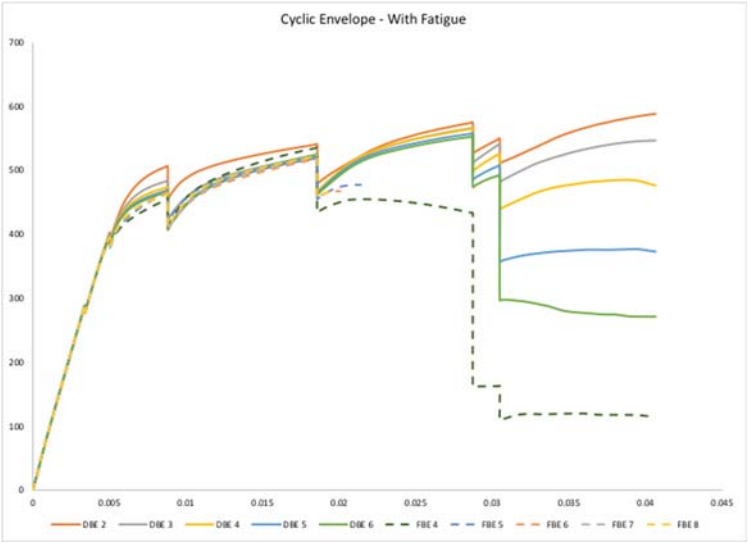

Figure 8-35. Cyclic envelope curve for coupling beam 1. Note - DBE stands for displacement-based elements while FBE stands for forced based elements. DBEs were used as they consistently converged.

Additionally, as described previously in Section 7.5.4.3, the rotation in the wall is also included in the test results. This rotation is accounted for by adding an elastic spring to match the initial elastic stiffness. A representation of this model is shown in Figure 8-36.

Figure 8-36. Graphical representation of coupling beam distributed plasticity model.

The concentrated plasticity model is presented in Figure 8-37. This model involves elastic elements as well as two concentrated plasticity elements. The concentrated plasticity elements or plastic hinge elements are modelled using zero length elements. For this element, a "Modified Ibarra-Medina-Krawinkler Deterioration Model with Pinched Hysteretic Response" (MIMKD Model) model was used. A figure from OpenSees documentation is replicated in Figure 8-38. The variables defining this element and a description are listed in Table 8-6. Although the material model allows different positive and negative definitions, the coupling beam hysteretic behavior was considered symmetric. Additionally, the hysteretic behavior is modified until the performance closely matches the fiber-based coupling beam model without respect to geometry or material parameters.

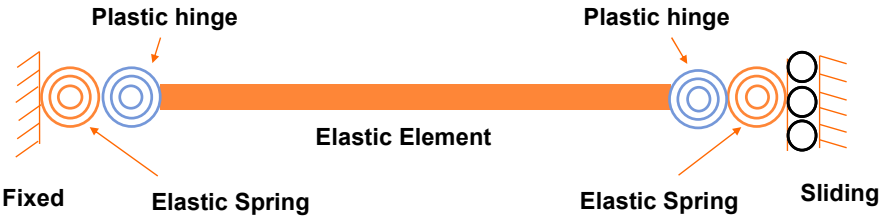

Figure 8-37. Graphical representation of coupling beam concentrated plasticity model.

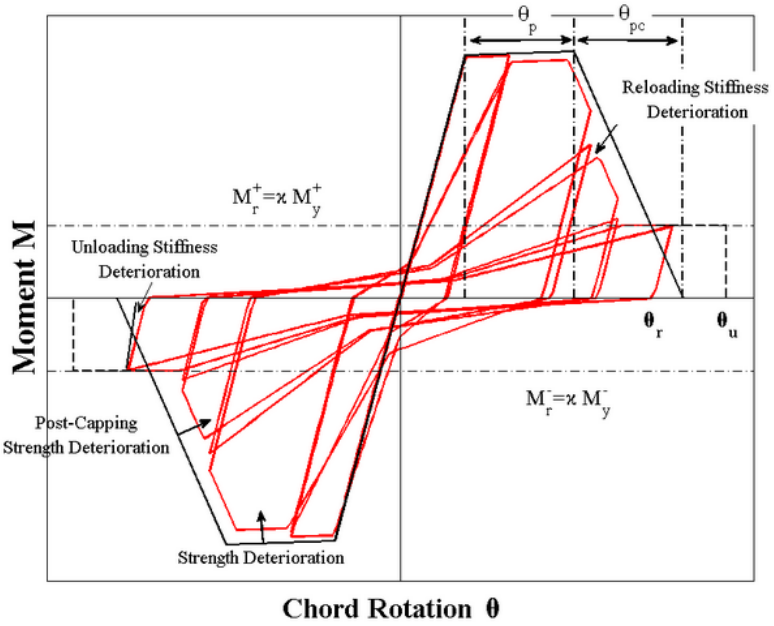

Figure 8-38. Modified Ibarra-Medina-Krawinkler Deterioration Model with Pinched Hysteretic Response (OpenSees).

Table 8-6. Parameters for Modified Ibarra-Medina-Krawinkler Deterioration Model with Pinched Hysteretic Response (OpenSees).

Parameter	Description		Parameter	Description
K_0	Elastic stiffness		λ_S	Cyclic deterioration parameter for strength deterioration
a_s	Strain hardening ratio		λ_C	Cyclic deterioration parameter for post-capping strength deterioration
M_y	Yield Moment		λ_A	Cyclic deterioration parameter for accelerated reloading stiffness deterioration
F_{pr}	Ratio of the force where reloading begins to the force at the maximum historic deformation		λ_K	Cyclic deterioration parameter for unloading stiffness deterioration
A_{Pinch}	Ratio of reloading stiffness		c_S	Rate of strength deterioration
θ_p	Pre-capping rotation		c_C	Rate of post-capping strength deterioration
θ_{pc}	Post-capping rotation		c_A	Rate of accelerated reloading deterioration
θ_u	Ultimate rotation capacity		c_K	Rate of unloading stiffness deterioration
Res	Residual strength ratio		**D**	Rate of cyclic deterioration

8.4.4 Comparison of OpenSees Models with Test Data

OpenSees coupling beam distributed plasticity models were built from the material models and element distribution. As shown in Figure 8-39 for CFSCB-1, the assumed stress-strain curves followed the experimental behavior well. From this model, or the experimental results, a concentrated plasticity model can be developed. Multiple sets of parameters can be used to fit the curve as this model is not directly connected to the physical geometry or material behavior. A concentrated plasticity model and the parameters used to build it are presented in Figure 8-40 and Table 8-7, respectively.

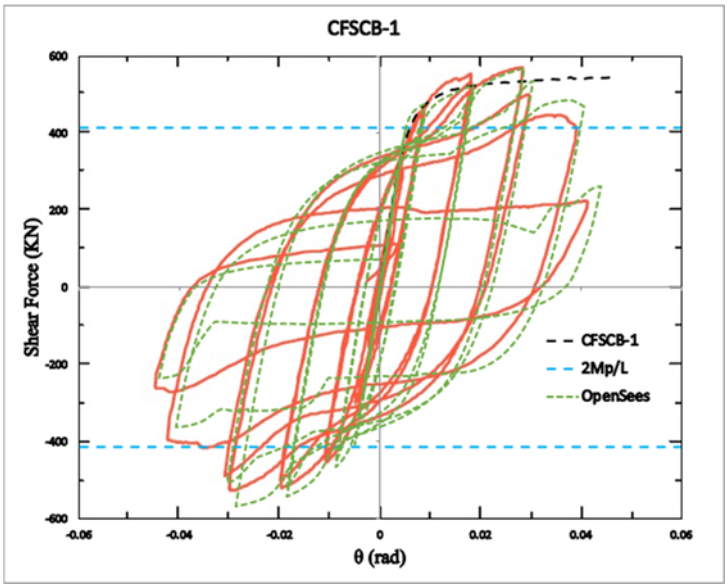

Figure 8-39. Comparison of OpenSees distributed plasticity model, Abaqus pushover, and experimental testing data.

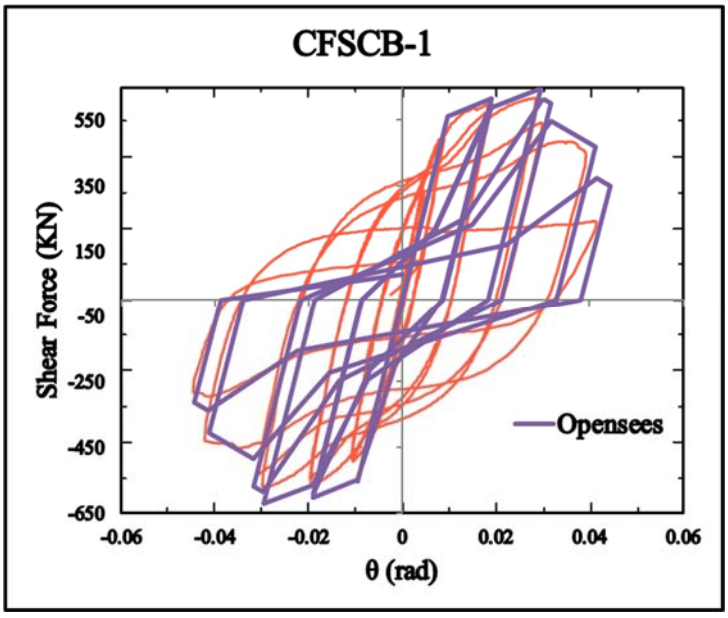

Figure 8-40. Comparison of concentrated plasticity model and experimental results

Table 8-7. Parameters used for CFSCB-1 concentrated plasticity elements.

Parameter	Value	Parameter	Value	Parameter	Value
Stiffness, K_0	4.0e5	**λ_S**	0.33	**c_S**	1.0
Post yield stiffness coefficient, a_s	0.06	**λ_C**	0.33	**c_C**	1.0
Yield Moment, My	1680	**λ_A**	1.0	**c_A**	1.0
Rotation at peak, Θ_p	0.02	**λ_K**	1.0	**c_K**	1.0
Rotation at post capping, Θ_{pc}	0.08	**Residual capacity ratio**	0.0	**F_{pr}**	0.6
Ultimate Rotation, Θ_u	0.4	**D**	1.0	**A_{Pinch}**	0.6

8.5 Numerical Calibration for C-Shaped C-PSW/CF Walls

Calibration of the concentrated plasticity model C-Shaped walls closely followed the parameters already established for the planar walls. The section geometry followed the University at Buffalo test specimen geometry as presented in Table 7-11. The material models and element distribution generally followed the same recommendations as the planar walls. These components are further detailed in section 8.5.1 and section 8.5.2, respectively.

8.5.1 Material Parameters

The effective stress strain curves previously developed (Sections 8.1.3 and 8.3.3) were also employed for the C-shaped wall models. Additionally, a confined concrete model was included to fit the behavior of the corners of the c-shape section as shown in Figure 8-41. This confined concrete used the material model (Concrete02) and used the same loading branch but maintained a higher residual capacity. The properties of the corner section confined concrete are presented in Table 8-8. The remainder of the concrete and steel material properties follow in Table 8-9 and Table 8-10, respectively.

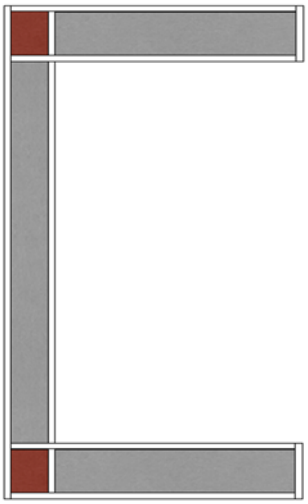

Figure 8-41. C-shape wall section. Red shading indicates where confined concrete material properties were applied

Table 8-8. Concrete material parameters for corner box section

	Specimen 1	Specimen 2
F_{pc} (ksi)	4.5	5.1
e_{psc0}	0.0020	0.0021
F_{pcu} (ksi)	1.0*f'$_c$	1.0*f'$_c$
e_{psu}	0.009	0.008
E_{ts}	3820	4070

Table 8-9. Concrete material parameters

	Specimen 1	Specimen 2
F_{pc} (ksi)	4.5	5.1
e_{psc0}	0.0020	0.0021
F_{pcu} (ksi)	0.6*f'$_c$	0.6*f'$_c$
e_{psu}	0.009	0.008
E_{ts}	4566	4996

Table 8-10. Steel material parameters for assumed stress-strain curves

Parameter	Value		Parameter	Value
E (ksi)	29000		L_{sr}	10.0
b	0.015		beta	1.0
E_{sh} (ksi)	E*b		r	0.60
F_y (ksi)	1.1*55.4		gamma	0.50
F_u (ksi)	1.1*65		C_f	0.60
e_{sh}	$2*F_y/E$		alpha	0.50
e_{ult}	0.05		C_d	0.35

8.5.2 Element Distribution

The element distribution followed the distribution developed for the planar walls. Three elements were located in the plastic hinge zone. Plasticization in the experiment was limited to the depth of the wall; therefore, this dimension was adopted as the length of the plastic hinge. Three nonlinear elements were located in this region.

8.5.3 Comparison of OpenSees Models with Test Data

From the material models and element distribution, OpenSees wall models were built. These models were run for the material model matching the assumed stress-strain curve. As shown in Figure 8-42 for specimen 1, the model well captures the degradation and rotation capacity but underestimates the initial strength in the positive direction. The initial stiffness and unloading stiffness also follow the observed experimental results. The comparison for specimen 2 is shown in Figure 8-43. Due to extensive model convergence issues, the concrete model used in this comparison for the OpenSees line uses the concrete properties of specimen 1. This approach is conservative as first specimen has a lower concrete strength than the second specimen.

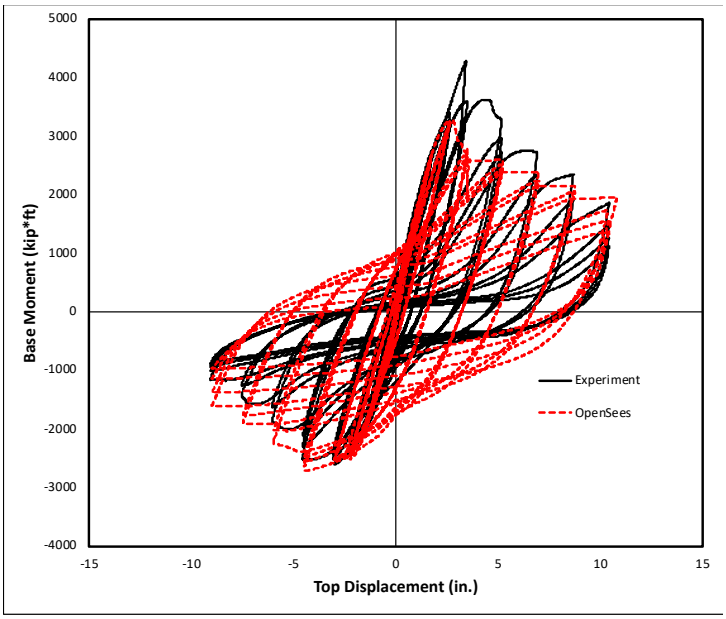

Figure 8-42. Base Moment vs. top displacement comparison between experimental results and OpenSees model for C-Shape Specimen 1.

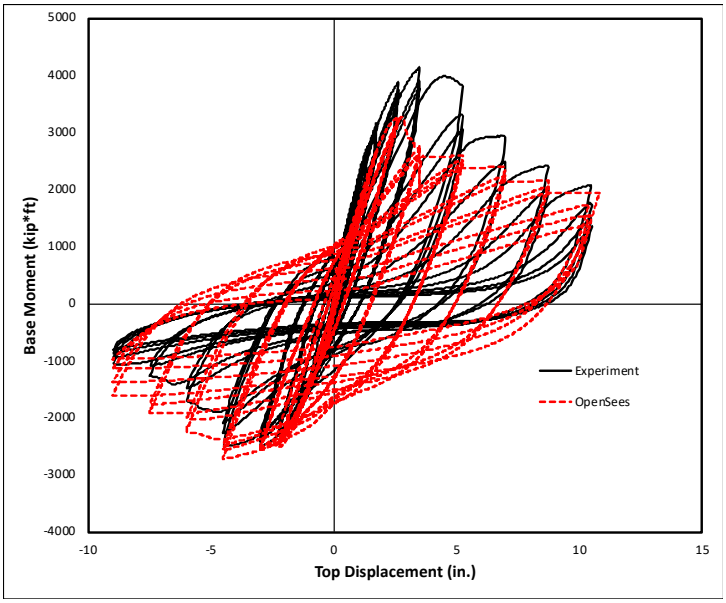

Figure 8-43. Base Moment vs. top displacement comparison between experimental results and OpenSees model for C-Shape Specimen 2.

“This Page Intentionally Left Blank”

SECTION 9
VERIFICATIONS AND TRIAL INCREMENTAL DYNAMIC ANALYSIS OF COUPLED WALLS

9.1 General

This section presents results from one chosen archetype subjected to a chosen earthquake from the set of 44 far-field ground motions given in FEMA P695 document, and results from Incremental Dynamic Analysis (IDA) conducted on trial Coupled Composite Plate Shear Walls-Concrete Filled (CC-PSW/CF) using OpenSees. These analyses were conducted (1) to verify the stability of OpenSees analysis for the structural configurations and material model used; (2) to ensure that important behaviors and failure modes can be captured throughout response, and; (3) to identify and resolve potential problems by scrutinizing results in greater depth before subjecting multiple archetypes to IDA from which only a few response values will be tracked. It was deemed important to perform such trial analyses before conducting the complete IDA program to ensure credible results, given that intensive computational time is required to analyze all the archetypes and that mistakes found later would require costly re-analysis and delays in the IDA study.

The trial IDA were performed on two arbitrarily chosen coupled composite wall systems, namely, a three-story composite walls coupled with I-shape steel beams and an eight-story composite walls with composite beams. Section 9.2 presents a brief description of the coupled walls used for the trial IDA. Then, the results and observations on response of the trial coupled walls are presented in Sections 9.3 and 9.4.

9.2 System Descriptions

This section provides a description of both the 3-story and 8-story coupled walls used for the trial IDA. In particular, the number of layers used in the cross-sections of the walls and the plastic hinge length calculations are presented.

9.2.1 Properties of Coupled Walls

One of the coupled walls used for trial IDA is a three story composite walls having I-shape steel link beams. This cross section was arbitrarily chosen as a time when the archetypes being developed as part of this study were not yet available. Although a three-story coupled-wall of that type is unlikely, this was done to keep the problem at a manageable size in case unexpected complications arose during the trial analyses. For the purpose of meeting the objectives described in Section 9.1, this was deemed acceptable as a first approach.

The arbitrarily chosen wall geometry and cross-sections are shown in Figure 9-1. The 3-story CC-PSW/CF wall was taken as 50" deep and 10" thick, with 0.3125" thick steel plates, and W18x86 steel coupling beams were used. For these cross-sections, a 30% coupling ratio (CR) is achieved, meaning that 30% of the base moment is resisted by the coupling beams.

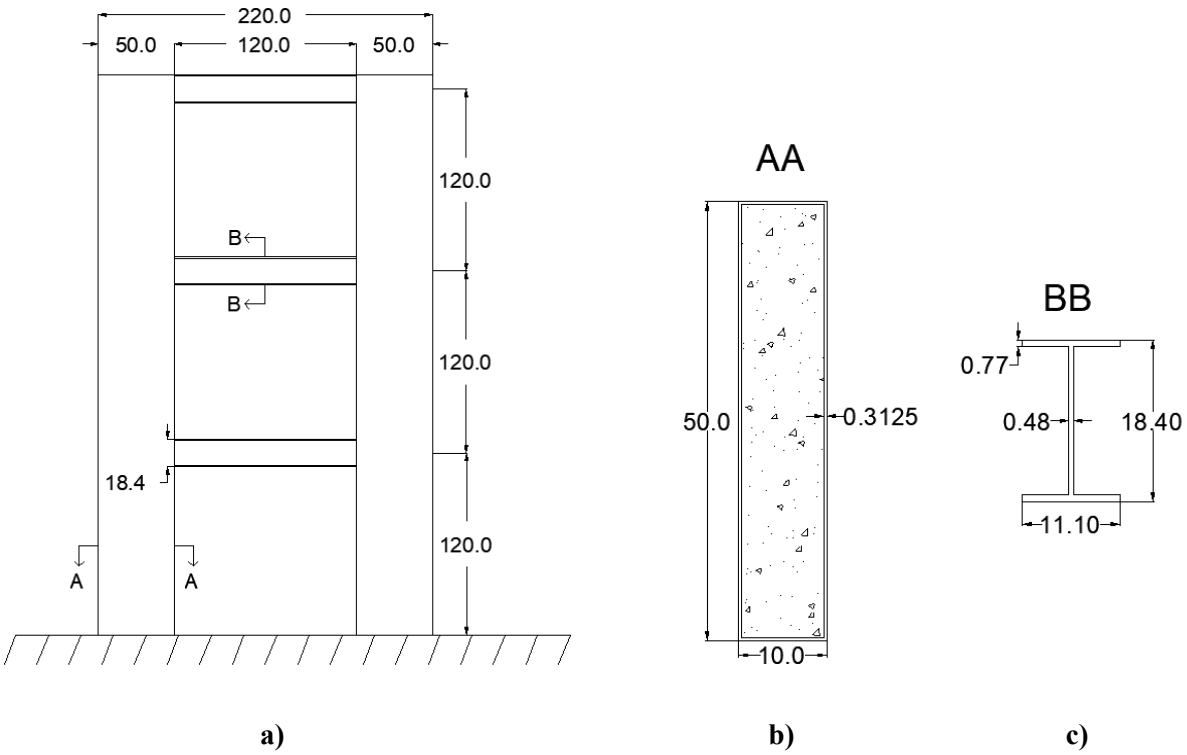

Figure 9-1. Three story coupled wall used for IDA: (a) Elevation (b) Composite wall cross-section (c) Steel beam cross-section (dimensions are in inches).

The other trial IDA was conducted on an eight story coupled wall having composite walls and composite coupling beams. This coupled wall was considered to correspond to an 80%-completed design for that archetype (some archetype optimization remained to be performed at the time this analysis was conducted). Results obtained for this archetype are believed to be close to those expected with the final archetype. The coupled composite walls and cross-sections are shown in Figure 9-2. The eight-story C-PSW/CF wall cross-section was 180" deep and 18" thick, with ½" steel plates, with beams providing a 60% coupling ratio (CR), meaning that 60% of the base moment is resisted by the coupling beams.

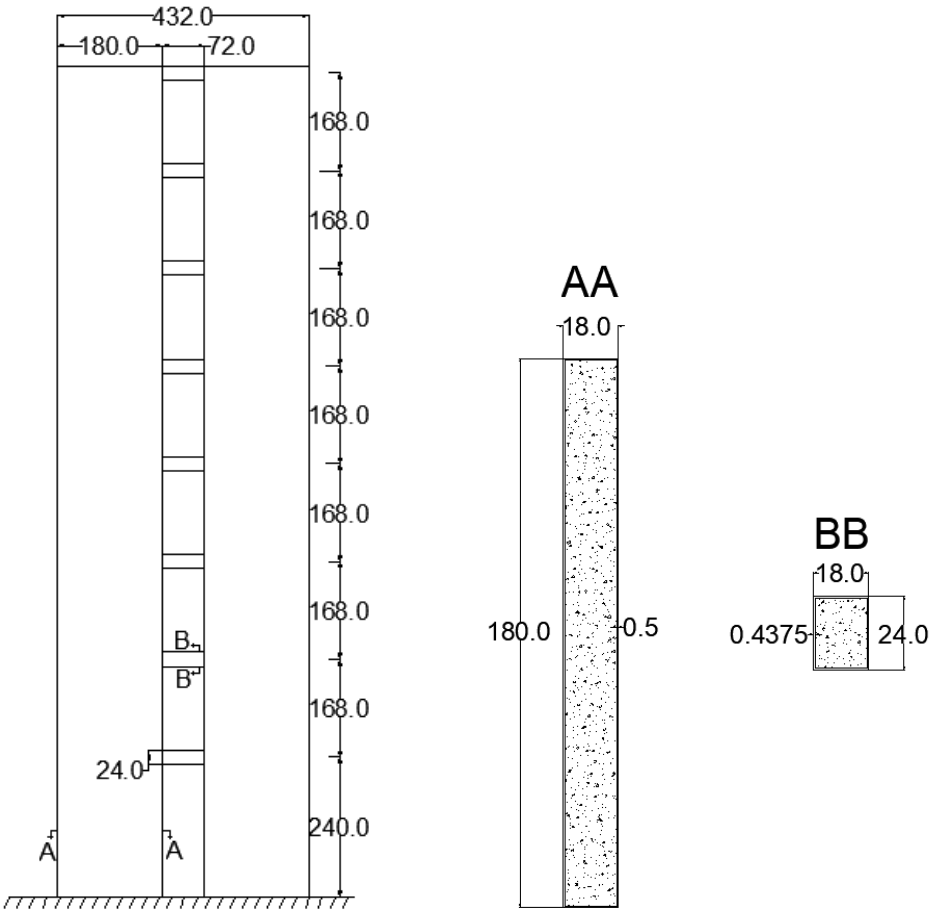

Figure 9-2. Eight story coupled wall used for IDA: (a) Elevation (b) Composite wall cross-section (c) Steel beam cross-section (dimensions are in inches).

As stated before, performing IDA is computationally demanding. Therefore, to expedite analysis, nonlinear elements were only used over the plastic hinge length of the walls and coupling beams. More specifically, *dispBeamColumn* elements having the *Reinforcing Steel Material* model for steel and the *Concrete02* for concrete defined by the calibrated parameters presented in Section 6 were assigned to these inelastic elements over the plastic hinge length. The rest of the wall and coupling beam elements were assigned with elastic beam column (*elasticBeamColumn*) elements. Figure 9-3 shows how the three and eight story coupled walls were modeled in OpenSees. The rectangles represent the plastic hinge length at the base of the walls and the ends of coupling beams. Also, the numbers at the plastic hinges located will be used to identify moment-curvature in Sections 9.3 and 9.4 (and the nomenclature for these numbers is: the first number is for the member identification (1 for left wall, 2 for right wall, and 3 for coupling beams); the second number is for floor level; and the last one or two numbers identify the element along each given member that can fracture and buckle).

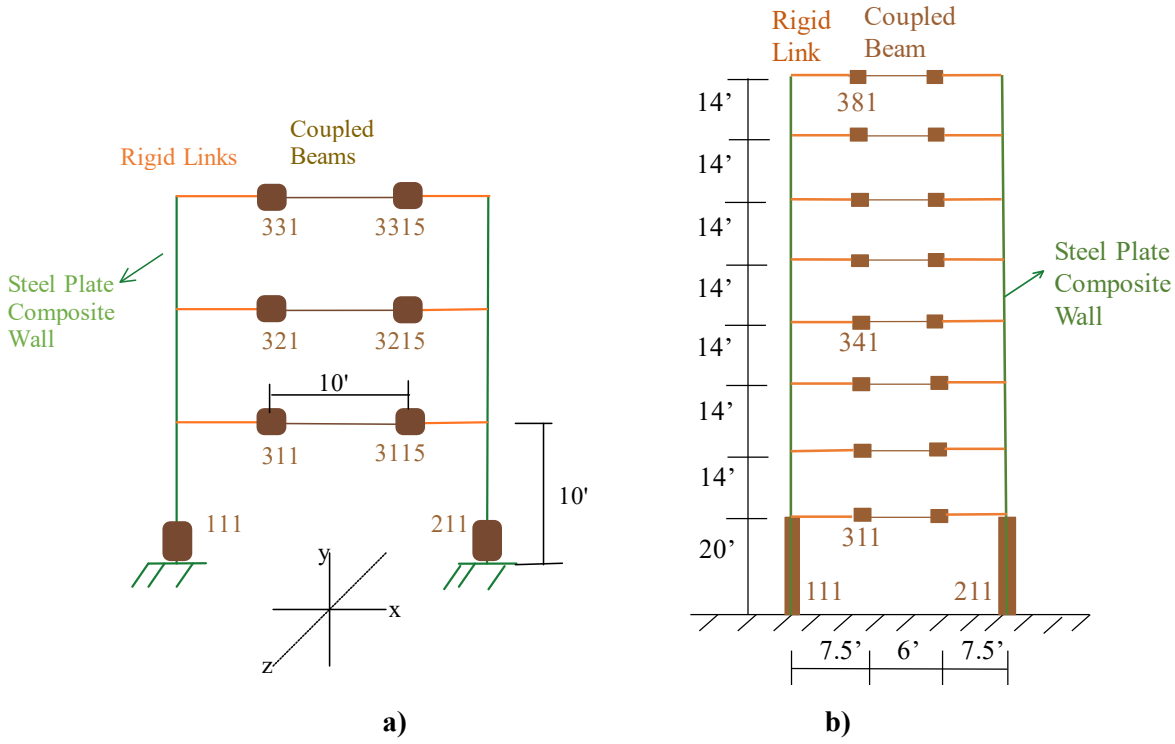

Figure 9-3. OpenSees models: (a) Three story coupled wall; (b) eight story coupled wall.

The equivalent Lateral Force (ELF) method was used to define the plastic hinge length for the composite walls, composite beams and steel I-shape beams. For expediency, the moment diagrams resulting from elastic analysis for the applied lateral forces calculated by the ELF method was scaled a first time to match the plastic moments at the base of the walls, and as needed (with different scaling factors) to make the moments at the end of the coupling beams equal to their plastic strength. Then, in each case, the distance from the plastic moment, M_p, to the yield moment, M_y, was considered to be the plastic hinge length of the members. The calculations used to determine the story forces for the ELF calculations for three story and eight story are presented in Appendix B.

As a first step, to ensure that proper cross-sections were duly defined in OpenSees (given the absence of graphic post-processing), the same cross-sectional analysis performed for the C-PSW/CF-NB1 wall in Section 7.3.4.1was done here for the cross-sections of the composite walls and composite beams of each coupled wall considered. To be able to compare with theoretical plastic moment values, elasto-perfectly plastic property with 50 ksi compressive and tensile strength was assigned to the steel layers and 6 ksi compressive strength with no tensile strength was given to the concrete layers. To be consistent with the

proportional number of layers used in the calibrated studies, 158 layers were used along the web of the cross-sections, and 20 were used through the thickness of the top, and bottom steel in the three story coupled composite walls (each flange layer was full width). In addition, 16 layers and 36 layers were used in the flange and web steel of I-shape steel beams, respectively. For the eight story coupled composite walls, the number of layers increased; 42 layers were used through the thickness of the top and bottom steel and 358 along the web of the composite wall; 42 layers were used through the thickness of top and bottom steel plates and 52 layers along web steel in the composite coupling beam. Results from the resulting moment-curvature analysis are shown in Figures 9-4 to 9-6. Based on Figure 9-4, three story coupled wall, the yield and plastic moments are 2761 k-ft. and 2985 k-ft. for the composite wall, respectively; the corresponding theoretical plastic moment obtained from hand calculation for the wall cross section is 2986 k-ft., which is within 0.034 percent of the value obtained by OpenSees. Using values from the AISC Steel Construction Manual (AISC 2013), the yield moment of W18x86 cross-section is 692 k-ft., and the plastic moment is 775 k-ft. Likewise, for the eight story coupled wall, Figure 9-5 and 5.6 shows that the yield and plastic moment of the composite wall are 51510 k-ft. and 56950 k-ft., respectively, and the corresponding theoretical plastic moment obtained from hand calculation for the composite wall cross section is 56960 k-ft.(0.018 percent of the value obtained by OpenSees). The yield and plastic moments from the cross-sectional analysis for the composite beams are 1312 k-ft. and 1522 kip-ft., respectively. Hand calculation of theoretical plastic moment for the coupling beam cross section is 1524 k-ft., which is within 0.13 percent of the value obtained by OpenSees. Therefore, this confirmed that the correct cross section was created for composite walls in three story coupled composite wall and for both composite walls and coupling beams in eight story coupled composite wall in the OpenSees model.

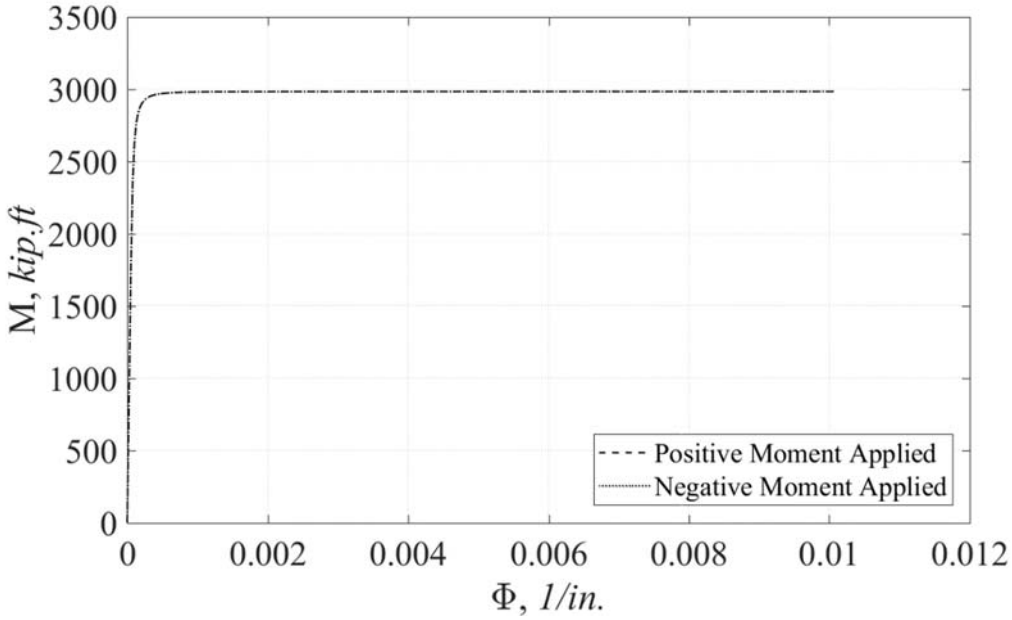

Figure 9-4. Cross-sectional analysis for composite wall cross-section in three story coupled composite wall.

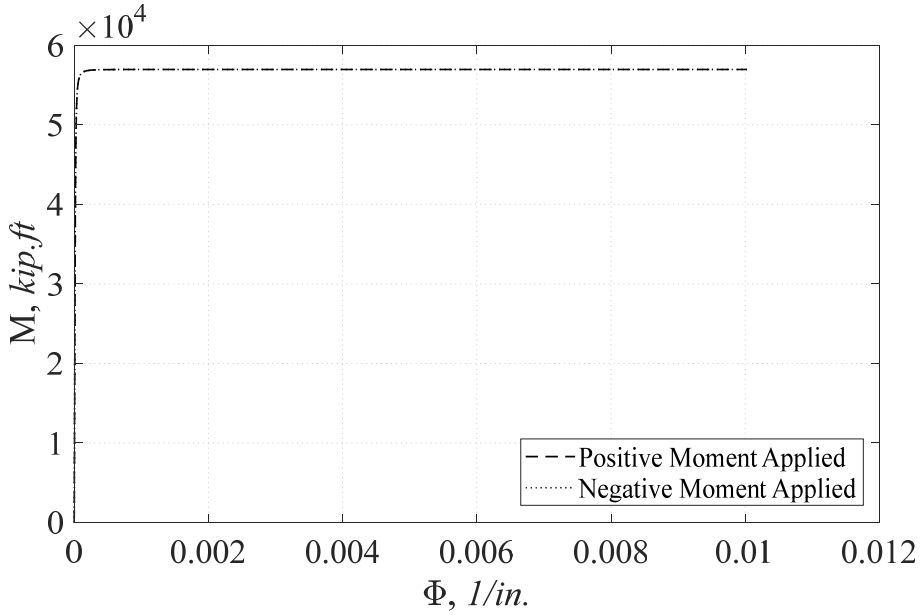

Figure 9-5. Cross-sectional analysis for composite wall cross-section in eight story coupled composite wall.

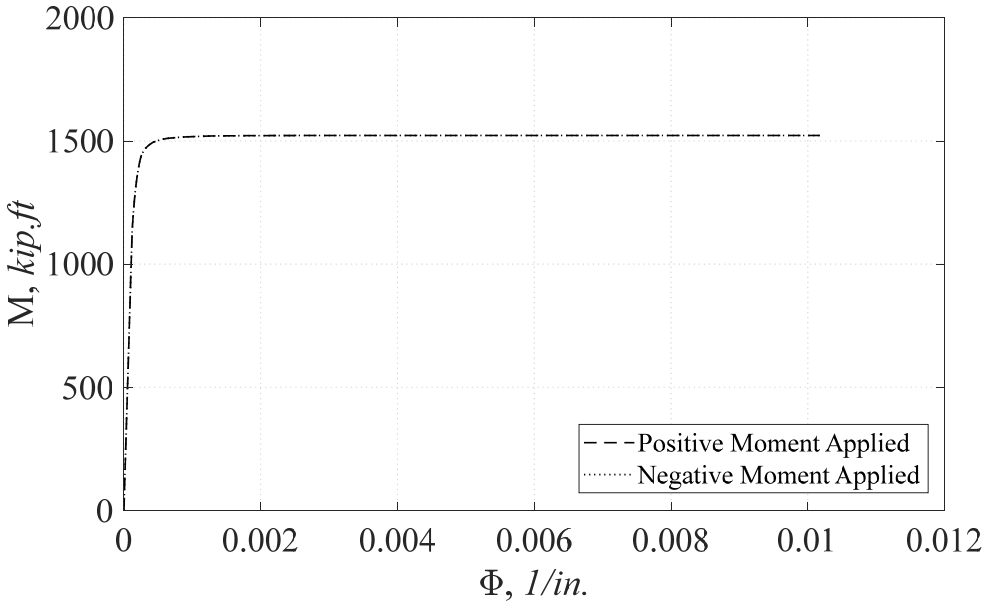

Figure 9-6. Cross-sectional analysis for composite beam cross-section in eight story coupled composite wall.

Again, because OpenSees does not have a graphic interface to present results, the forces from the ELF method were applied to a similar coupled wall modeled in SAP2000 (CIS 2017) and the results are shown in Figure 9-7. The base moment in the composite wall was 3,334 kip-ft. Once scaled to match the plastic moment of the wall cross-section, the plastic hinge length (i.e. distance between yield and plastic moments) was determined to be 13". To account for the fact that strain hardening is to be included in the subsequent IDA of the archetype, the plastic hinge length was assigned to be 24" (modeled by three elements each having 3 NIPs, as described in Section 7.3.4.3). Likewise, the end moments in the coupling beams obtained from the analysis under the applied ELF loads were 1,059 kip-ft. When this moment was scaled to the plastic moment of the coupling beam, the plastic length was calculated to be 5.0", and increased to 16" so that two 8" long elements could be used over that distance (as done consistently throughout due to calibration requirements – see Section 7.3.4.3).

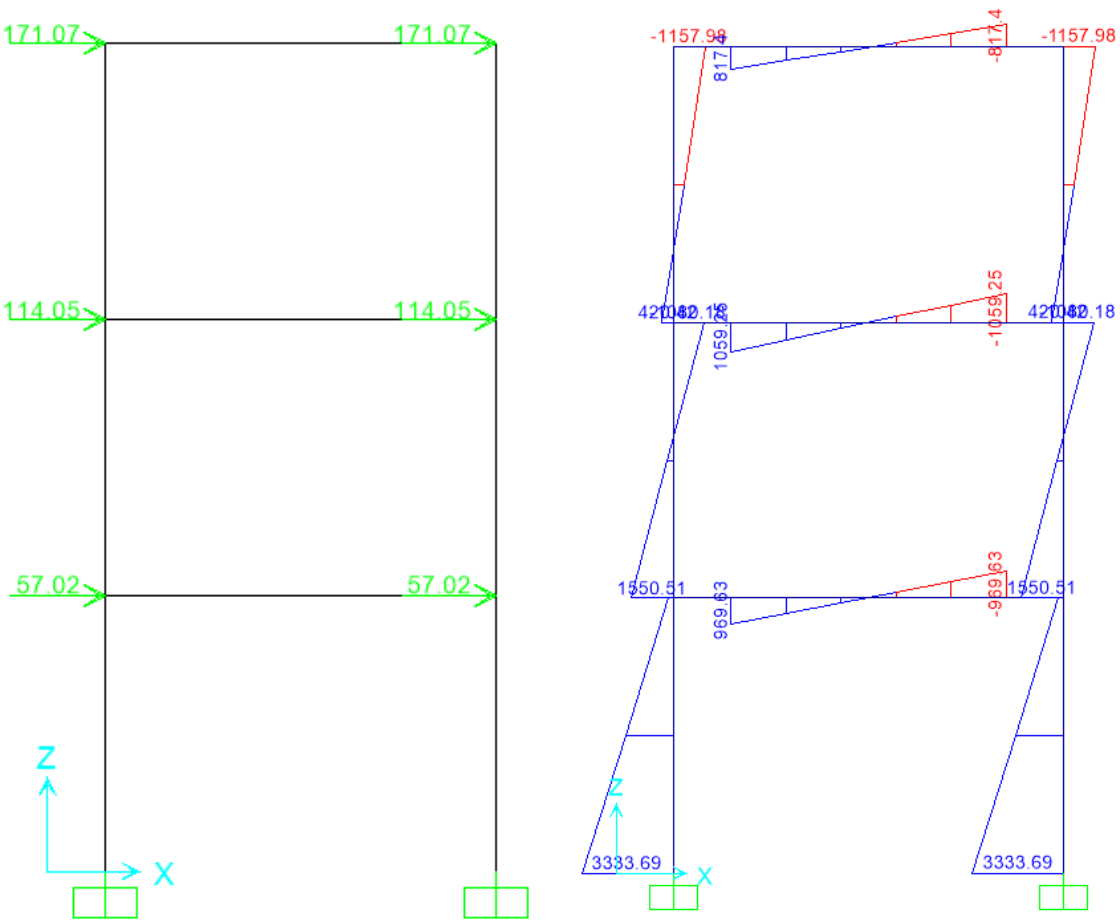

a) **b)**

Figure 9-7. ELF SAP200 Analysis for three story coupled composite wall: (a) Applied forces; (b) Moment Diagrams.

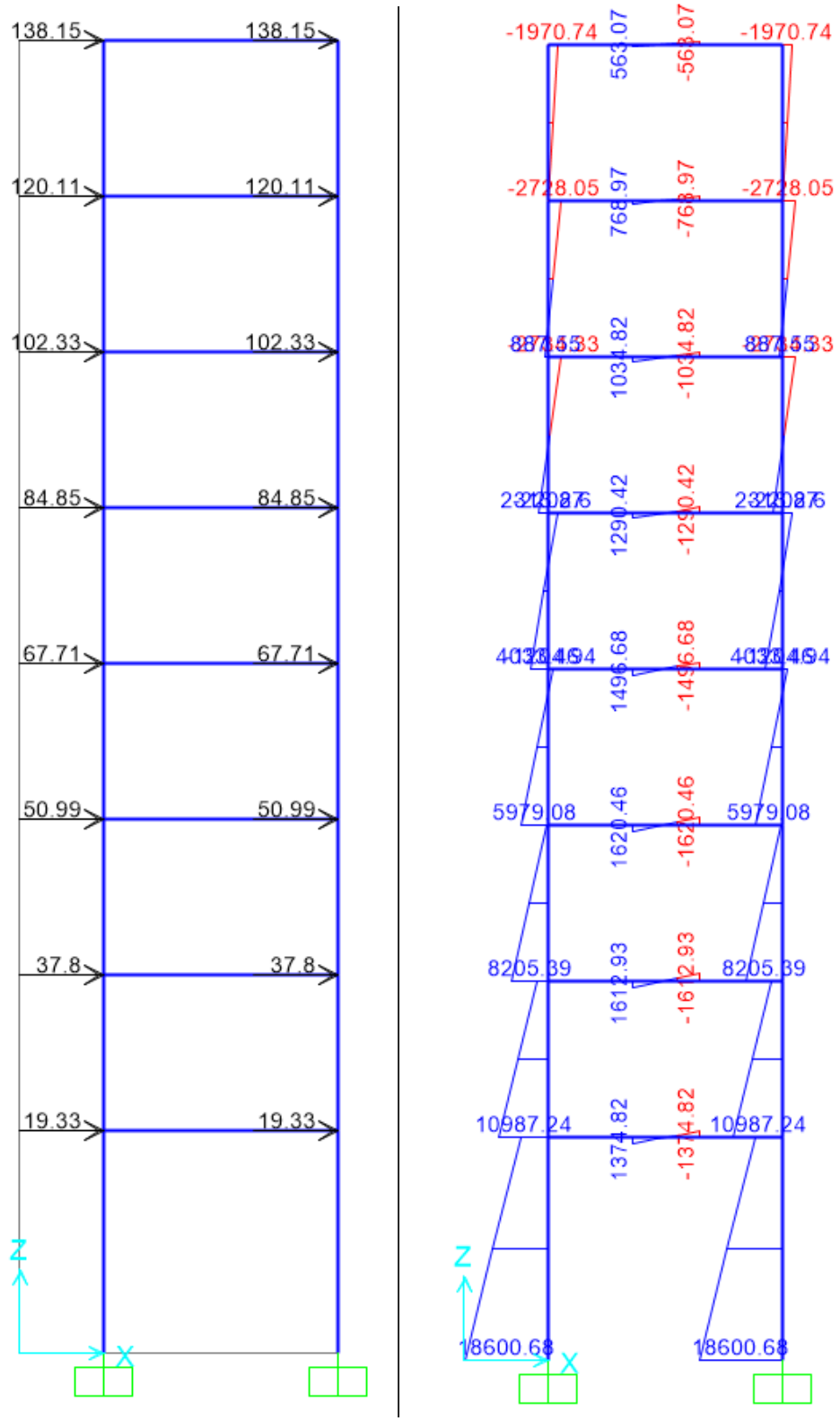

a) **b)**

Figure 9-8. ELF SAP200 Analysis for eight story coupled composite wall: (a) Applied forces; (b) Moment Diagrams.

The same procedure was followed for the eight story coupled composite walls. The results from the SAP2000 models are shown in Figure 9-8. The base moment in the composite wall was 18,600 kip-ft. Once scaled to the plastic moment, the plastic hinge length was calculated to be 112" – increased to 120" (using fifteen 8" long elements with three nodal interpolation points each) to account for strain hardening. Likewise, the coupling beam 1620 kip-ft. end moment in the coupling beams, when scaled to the plastic moment, gave a plastic hinge length of 32" in the coupling beam – increased to five 8" elements (plastic hinge length of 40") in order to account for strain hardening.

9.3 Results of Three Story Coupled Wall System

For the trial IDA, one of the most severe earthquakes among the 22 (44 considering two components of the same earthquake) that the FEMA P695 procedure (ATC 1992) provides was used; namely the Duzce earthquake in East-West direction. The main reason it was selected was because the ground acceleration record of this earthquake exhibits multiple pulses and is of significant duration. For example, between the times of 12.79 second and 14.34 second in this record, the area under the ground acceleration record is large, indicating a large velocity pulse for the earthquake. It was believed that using an earthquake with large pulses would more severely challenge the numerical calculations, which is aligned with the objectives outlined in Section 9.1.

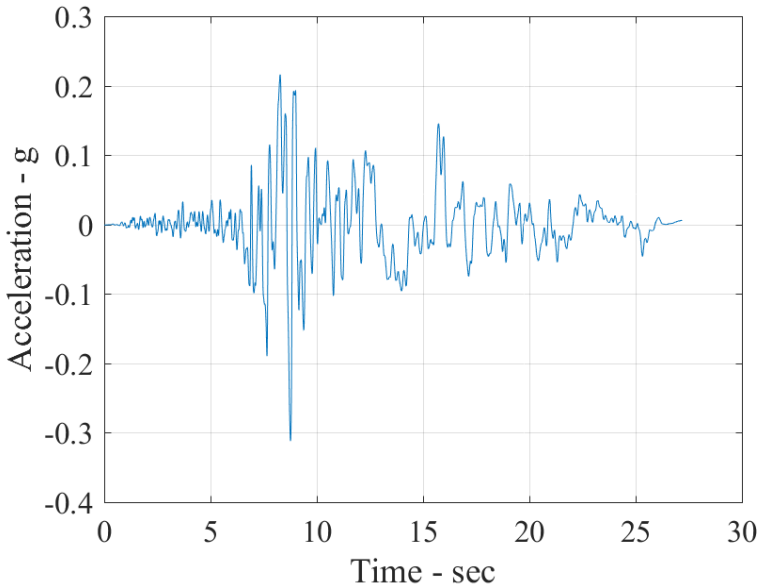

Figure 9-9. Acceleration history of Duzce earthquake in East-West direction.

To execute non-linear time-history analyses (NLTHA), the three story coupled composite wall was assumed to be part of a building having 150'x150' plan dimensions. The tributary mass was determined by assuming that in each of the building's principal axis, a coupled wall was used on each side of the building. For simplicity, weight of 1125 kips/coupled-wall (0.1 ksf over tributary area of 75'x150') was considered as a point load on each composite wall (562.5 kips per wall), and eigenvalue analysis indicated that the structure has a fundamental period of vibration of 0.53 sec.

The Duzce earthquake ground motion was used for the IDA, scaled by factors starting from 0.5 with increments of 0.145 until collapse is reached (note that the scale factors in this Chapter are only in reference to the unscaled ground, and not with respect to the design spectra, as the analyses here are not to determine collapse margin ratios, which will be the subject of the later analyses related to application of the FEMA P695 procedure). The 37 NLTHA analyses (scale factor of 6.982) were executed successfully, except for one (at a scaling factor of 7.127) for which the analysis stopped at what appeared to be an arbitrary time without OpenSees providing an error message. After investigating this issue, although the exact cause for the interruption of analysis could not be determined, it was speculated that this interruption might have been due to numerical errors introduced by the sudden drop in structural strength and stiffness at the plastic hinges when the coupling beams fractured through their cross section. Note that in the OpenSees code, no warning is produced when an entire cross-section defined by the *Reinforcing Steel Material* model is fractured. In an attempt to resolve this issue, *elasticBeamColumn* elements with low stiffness were used on top of the *dispBeamColumn* that used *Reinforcing Steel Material* with steel layers, as a measure to ensure a minimum strength and stiffness at the plastic hinge locations, and thus integrity of the structural models, after fracture. Analyses executed with this added small elastic stiffness and strength at the connections all ran to completion. Such elastic supplementary elements were therefore used in all subsequent analyses throughout this study. Note that, to ensure that the added strength and stiffness were marginal and did not otherwise influence response, analysis was performed by connecting the beams with only elastic members (i.e., removing the *dispBeamColumn* elements), and doing the same at the base of the walls; by comparing the periods of the two structures, results showed that the added elastic elements only account for 0.5% of overall stiffness of the whole coupled composite walls.

Results from the IDA (with the models modified as indicated above) are presented in Figure 9-10, both for the cases with and without P-Δ effects. Note that for the case without P-Δ effect, the IDA curve significantly changes slope at approximately 6% drift, collapse of the system was not observed in the IDA curve itself (where collapse is typically expressed by a nearly horizontal line due to excessively large increase in drift

at a subsequent analysis step corresponding to a small increase in ground motion scaling). In comparison, an easily identifiable point of collapse became visible when P-Δ effect were included by introducing a gravity column (a.k.a. leaning column) in the model. Here the floor gravity load (assumed to be 0.1 ksf) acting on half of the total floor plan area was applied to an arbitrary gravity column that does not contribute in resisting the earthquake loads.

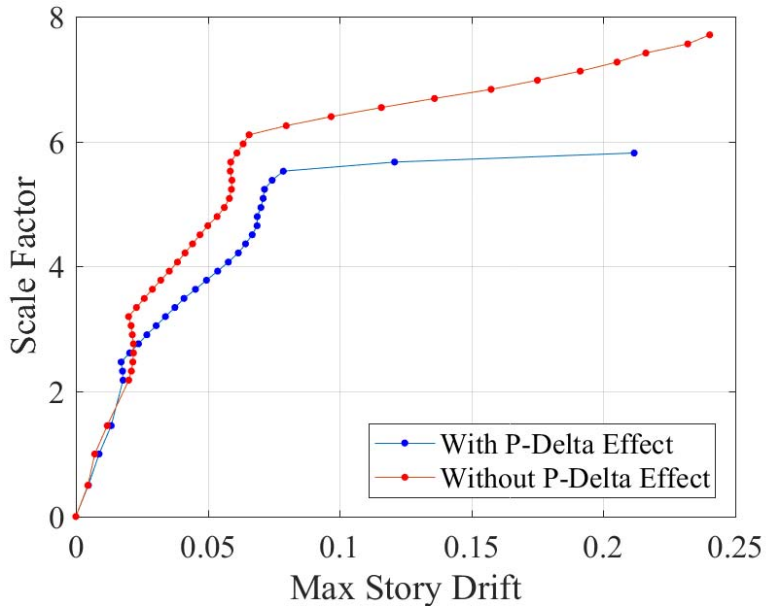

Figure 9-10. IDA for three story coupled composite walls

To illustrate the behavior of the coupled-wall, the results obtained at a scaling factor of 5.67 for which drift reached 12% (second-to-last point analyzed for case with P-Δ effect in Figure 9-10) were chosen; and the moment curvature relationship of the hinges throughout that specific time history is shown in Figure 9-11. In that case, all steel I-shape beams fractured through their entire cross-section, as seen for elements 311, 3115, 321, 3215, 331, and 3315 in Figure 5-11 (numbers in the upper corner of each plot refer to the plastic hinge designations in Figure 9-11) when flexural strength on the hysteretic curves dropped to zero; note that approximately half of the moment capacity of the composite left and right walls remained at the end of the analysis. Note that results are not presented for the point at 21% drift because the analysis stopped prior to completion of the earthquake due to excessive drifts (and OpenSees cannot provide all the results needed to plot the full moment curvature diagrams in that case).

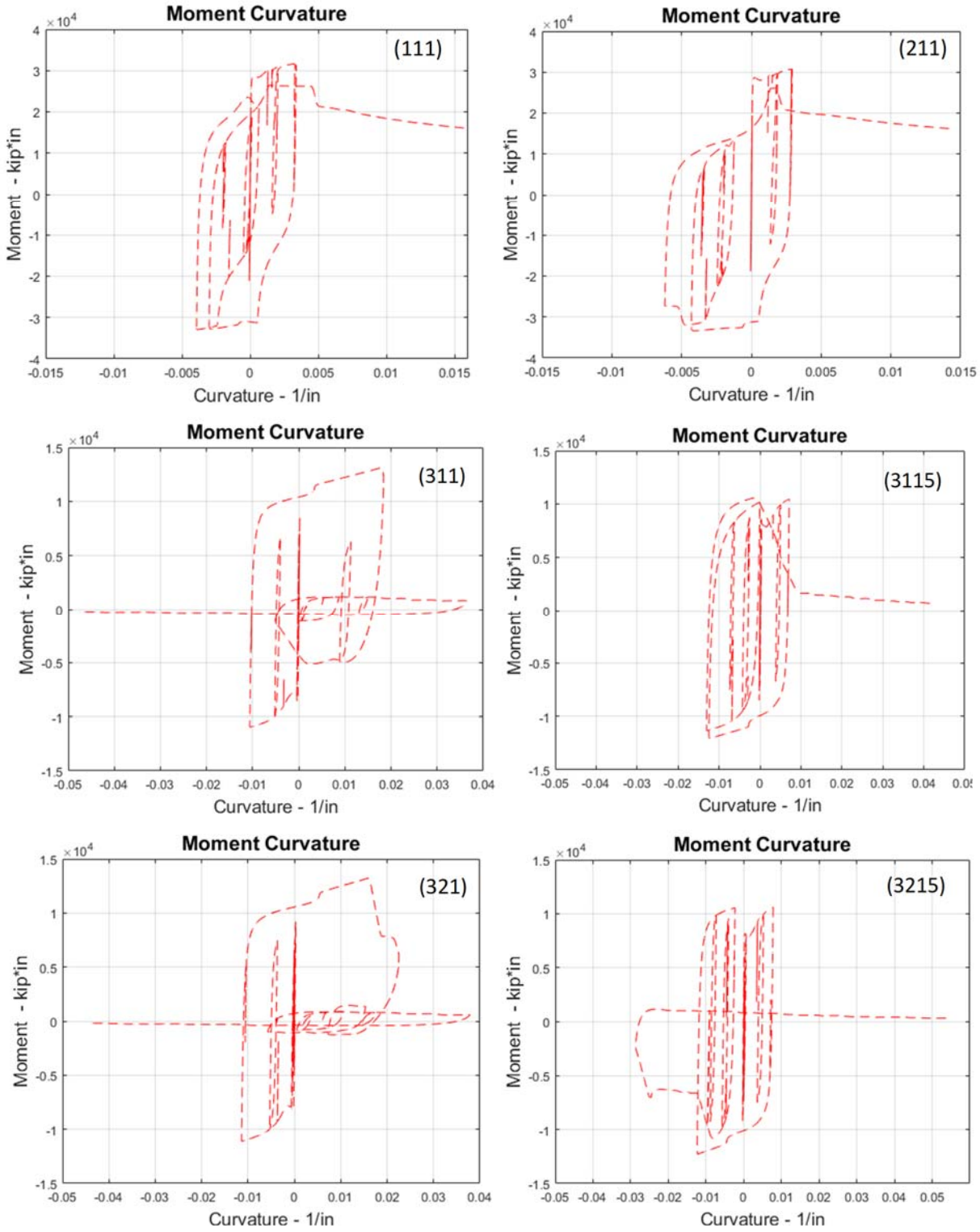

Figure 9-11. Moment Curvature relationship in hinges

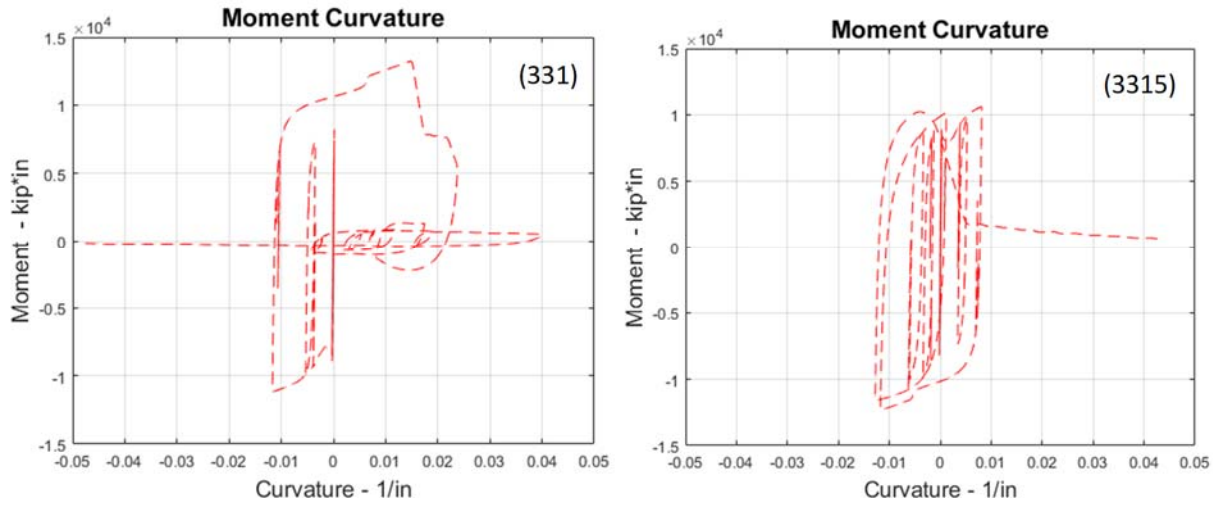

Figure 9-11. (Continued)

9.4 Results of Eight Story Coupled Wall System

Analyses for the eight story coupled walls used the same Duzce earthquake (in the same E-W direction) as for the three-story coupled walls analyses, for the same reasons. Also, as indicated above, *elasticBeamColumn* elements having low stiffness were assigned in parallel to the nonlinear plastic hinge elements to improve numerical stability, and P-Δ effects were considered by including a gravity column in the model as part of the IDA.

For this specific archetype, floor plan dimension is 120'x200' with 0.12 ksf floor loading. However, in many cases, the analysis stopped without giving an error message. Investigating this issue, it was judged that the modeling requirements for this structure due to the specific characteristics of the *Reinforcing Steel Material* model might have caused the problem. This is because for this eight story coupled composite wall, a total of 36,000 layers were used for the plastic hinges of the two walls (400 layers per cross section, times 3 NIPs per element, times 15 elements, times 2 hinges) and a total of 22,560 layers were used in the plastic hinges of the sixteen coupling beams (94 layers per cross section, times 3 NIPs per element, times 5 elements, times 16 hinges). Recall that the *Reinforcing Steel Material* model requires a large amount of memory to track buckling, low cycle fatigue, and unloading/loading branches (see Section 6.2). Tracking of all information for 58,560 layers might has been excessive. To simplify this requirement, the walls and coupling beams were remodeled with only three elements assigned with the *Reinforcing Steel Material* (as done for calibration for the Alzeni and Bruneau specimen (Section 7.3.4.3) and the rest of the nonlinear region of the plastic hinges was modeled using the *Steel02* steel material model. To make sure that *Steel02* model has a behavior close of that of the *Reinforcing Steel Material* model (as *Steel02* model is a bilinear

elasto-plastic material with strain hardening), a cross section analysis (as described in Section 7.3.4.1) was done for the coupling beams. Since the previous IDA results indicated that the coupled walls could develop significant curvatures before fractures develop, the strain-hardening factor (which is 0.0025) for the Steel02 material was selected such that the moment obtained or the cross-section analyzed using both materials would match at a curvature of 0.04 radians. The resulting moment curvature relationship for coupling beams analyzed with both material are compared in Figure 9-12.

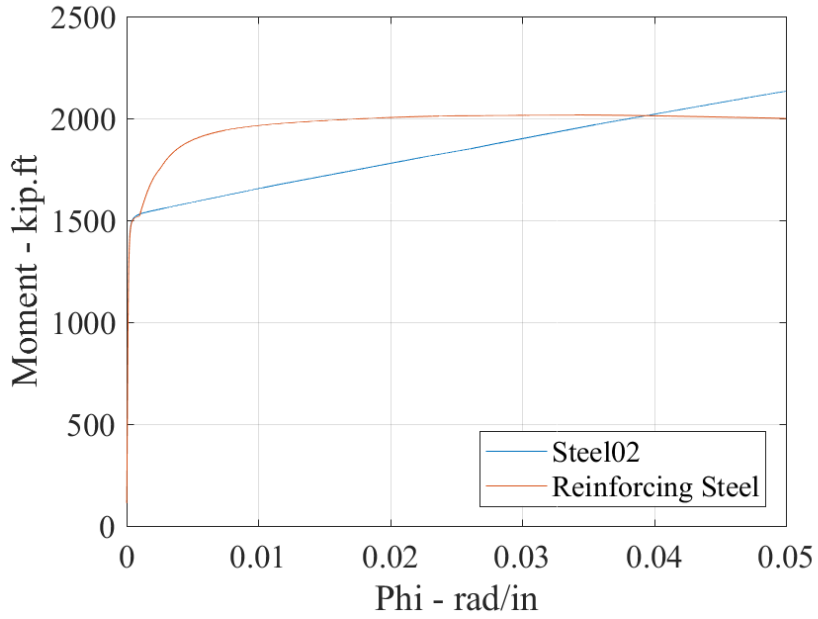

Figure 9-12. The backbone curve for Steel02 and Reinforcing Steel Material models

Results for the trial IDA (after the above adjustment was implemented) are shown in Figure 9-13. It is observed that the coupled composite walls reached collapse at approximately 15% and subsequent analyses did not converge. The fact that collapse was not reached prior to such an excessive drift suggests that the FEMA P695 study may need to define "collapse" instead as a drift, arbitrarily defined as possibly 5% or 10% drift. Irrespectively, to verify the correctness of models, additional analyses were conducted with additional gravity loads on the leaning columns, arbitrarily increased to 2 times, 4 times and 6 times of the gravity weight used in the above analyses. The results presented in Figure 9-14 confirm that the greater gravity load caused the structure to fail at lesser scale factors, which provides added confidence that in the analyses.

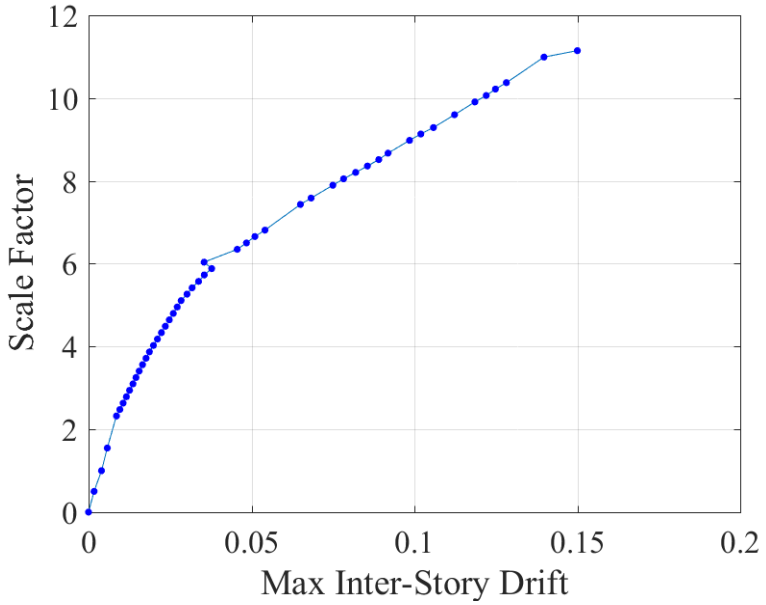

Figure 9-13. Trial incremental dynamic analysis for eight story coupled composite walls

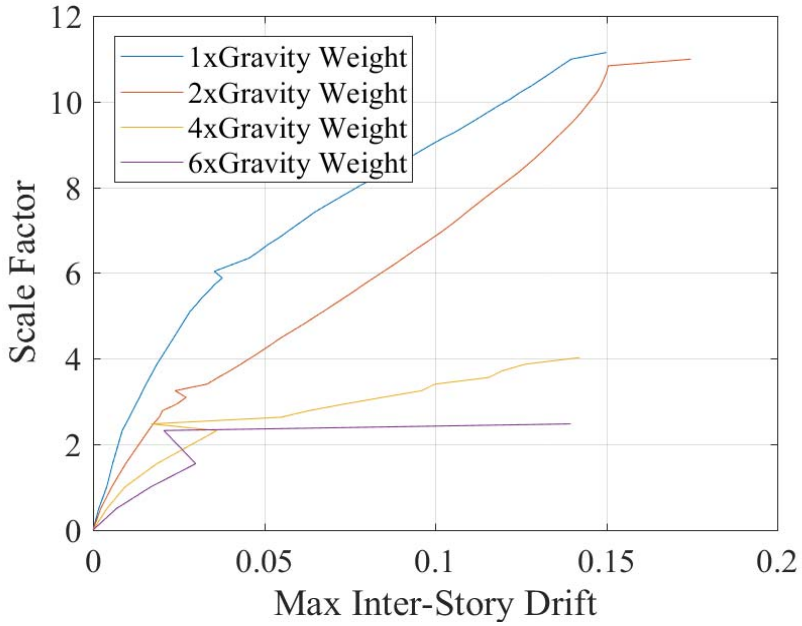

Figure 9-14. Trial study of IDA for eight story coupled composite walls with greater gravity load

The moment curvature hysteretic relationships in representative plastic hinges for which cross-sections were observed to experience fracture and buckling are plotted in Figures 9-15 to 9-17 for the non-linear time history analyses corresponding to 3%, 7% and 10% inter-story drifts (again, numbers in the upper corner of each plot refer to the plastic hinge designations in Figure 9-3). Here, since the coupling ratio for

this archetype is 60%, most of the earthquake energy is dissipated by the coupling beams. At 3% drift, all of the coupling beam cross-sections are cracked through and the walls started to develop fracture at their tip fibers a few seconds before the end of the earthquake. At 7% drift, all of the coupling beams are fractured through and the walls fractured 10” in the left wall and 2” in the right wall. At 10% drift, the left wall is almost completely fractured (116” of its cross-section is fractured, which is 65% of its cross section), and the fracture in the right wall is 46.74” of its cross-section (26% of the whole cross-section) and there is no coupling beams flexural strength left at the end of the earthquake excitation.

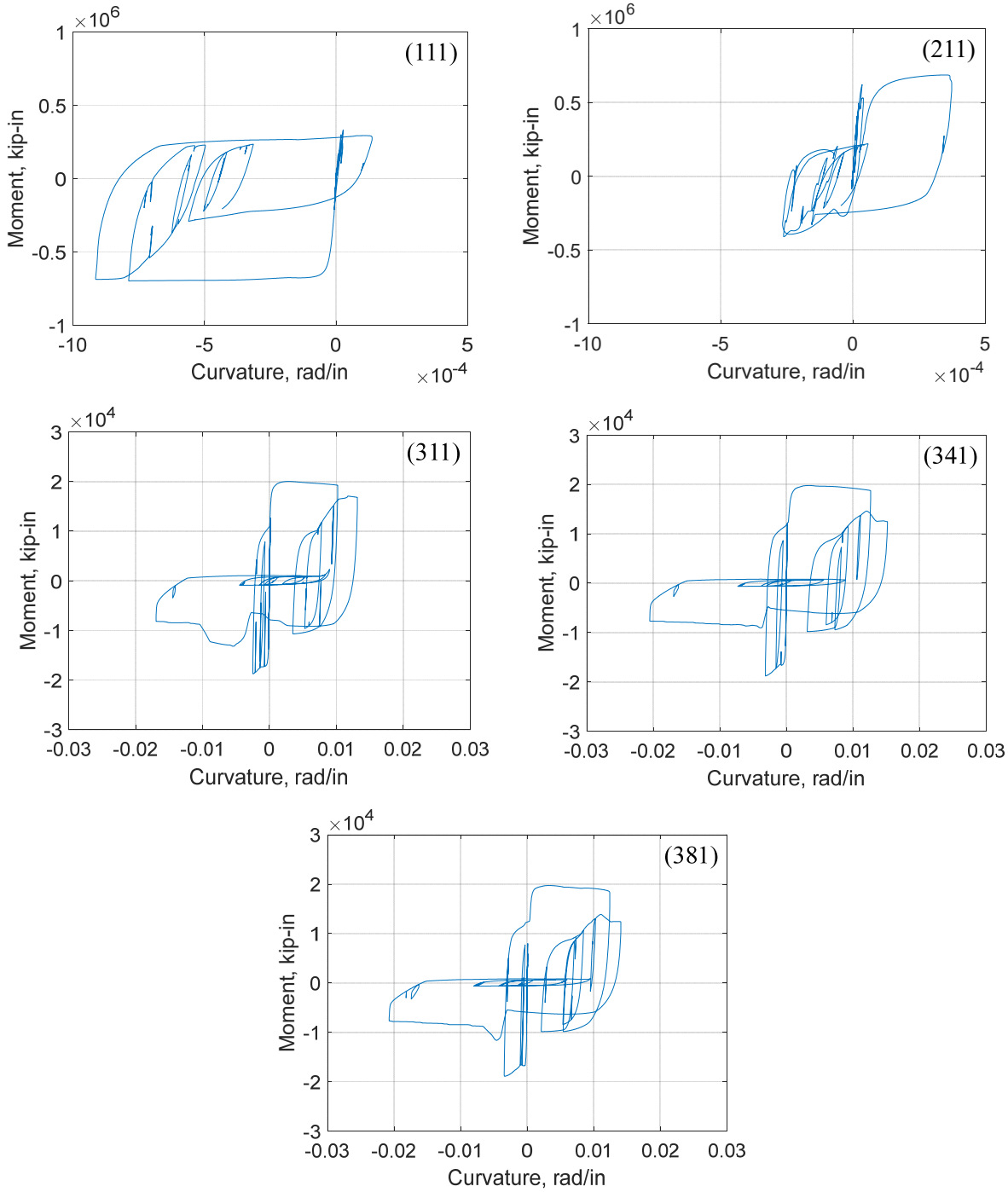

Figure 9-15. Hinge results for eight-story at 3% maximum story drift

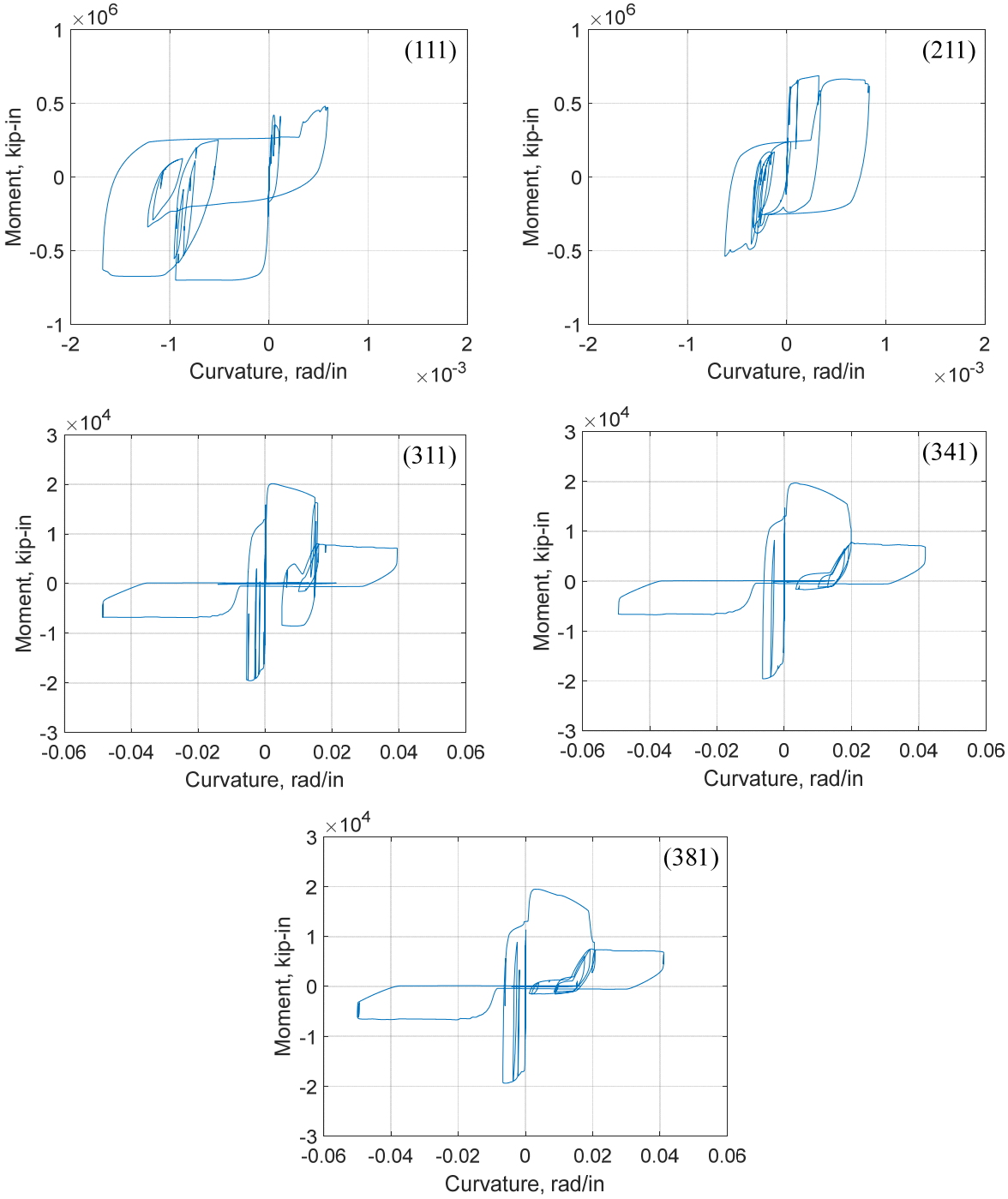

Figure 9-16. Hinge results for eight-story at 7% maximum story drift

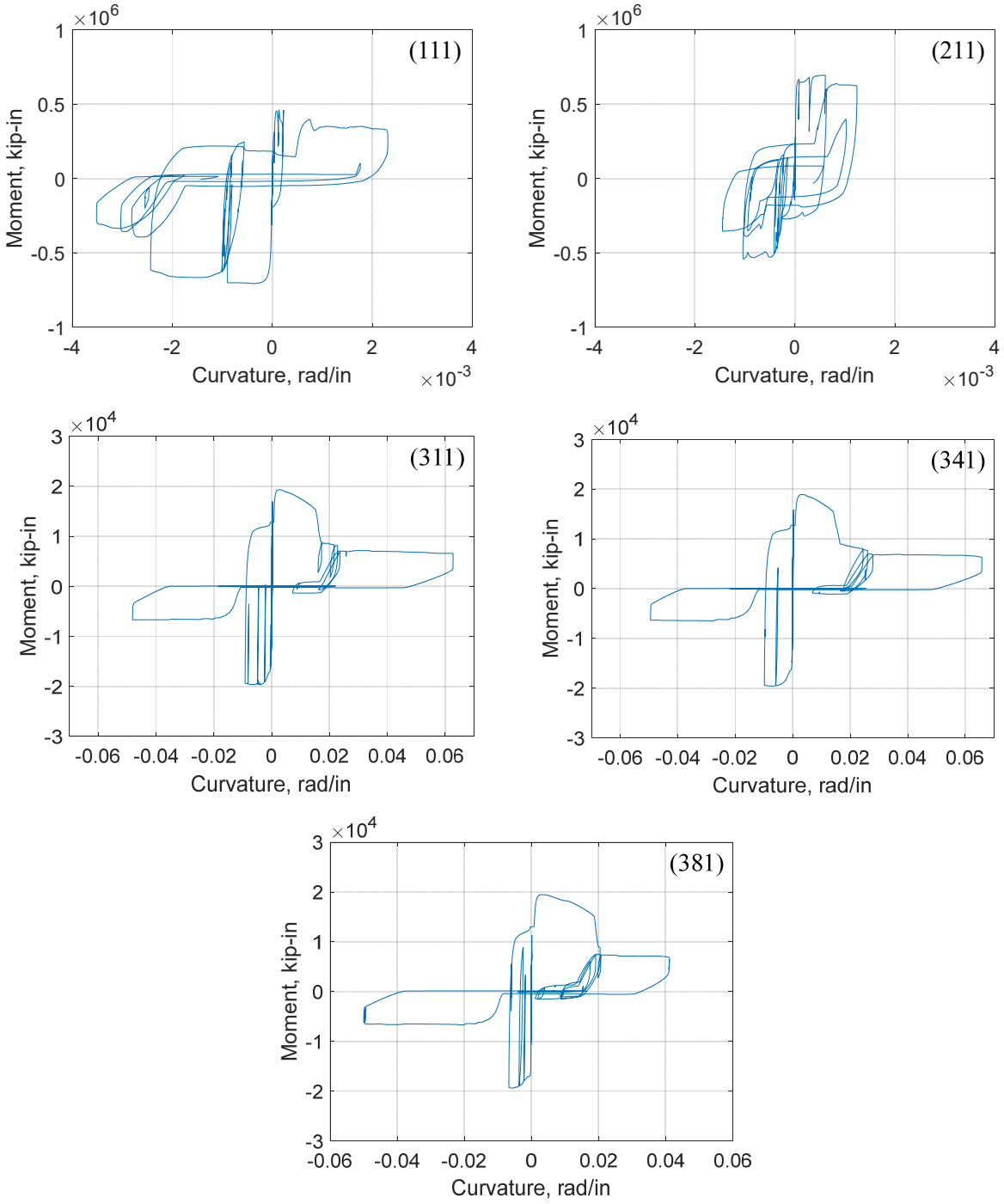

Figure 9-17. Hinge results for eight-story at 10% maximum story drift

Roof displacement histories for the above analyses that produced maximum 3%, 7% and 10% inter-story drifts are shown in Figure 9-18. The number added along these displacement histories indicate points where yielding, fracture initiation, and complete fracture occurred in various members.

Results for the 3% drift case show that yielding of the coupling beams first occurred (for the various beams) between 6.21 and 7.41 seconds (point 1 in Figure 9-18 a). Then, yielding of the right and left walls started at 7.70 and 8.40 seconds, respectively (points 2 and 3 in Figure 9-18 a). First crack initiation was observed in coupling beams between 11.53 and 13.73 seconds (point 4) and fracture of the entire cross-section completed for the various coupling beams between 15.28 and 16.28 seconds. By 22.77 seconds, the left wall started to fracture, followed by the right wall triggered at 23.1 seconds.

The above observed behavior occurred in the same order for the 7% drift case, except that each event occurred sooner (as expected due to the increased earthquake excitation). The coupling beams first yielded between 6.28 and 7.28 seconds (point 1 in Figure 9-18b); yielding of the right and left walls occurred at 7.1 and 7.67 seconds, respectively (points 2 and 3); fracture initiation happened between 7.63 and 9.83 seconds (point 4); complete fracture occurred between 14.70 and 15.50 seconds (point 5), and; the left and right walls started to fracture at 16.51 and 20.84 seconds, respectively (points 6 and 7).

At 10% drift, yielding of the coupling beams initiated between 4.38 and 8.38 seconds (point 1) and right and left walls subsequently yielded at 6.83 and 7.060 seconds, respectively (points 2 and 3). Then, fracture triggered in the coupling beams between 8.24 and 9.04 seconds (point 4). However, differently than for the other drift cases, the left wall began to fracture (at time 14.26 sec (point 5)) before complete fracture of the coupling beams between 14.9 and 15.0 seconds (point 6). It is speculated that this difference may be attributable to a progressively more dominant second mode of vibration slowing the accumulation of strains in the coupling beams, until the large velocity pulse between 12.79 and 14.34 seconds of Duzce earthquake as in Figure 9-9. Then, fracture initiated in the right wall at 16.31 seconds (point 7).

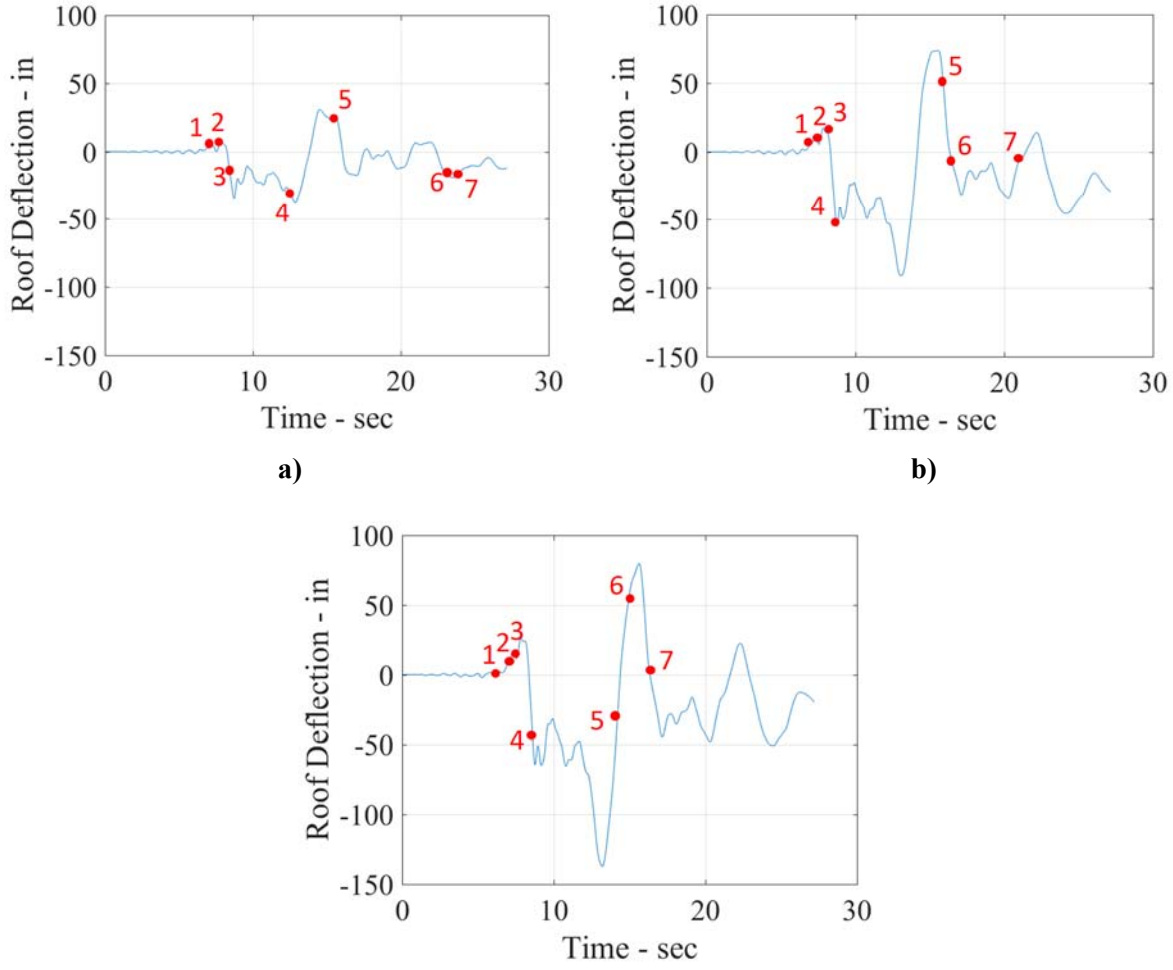

Figure 9-18. Roof Deflections at (a) 3%, (b) 7% and (c) 10% maximum inter-story drift in IDA curve.

“This Page Intentionally Left Blank”

SECTION 10
INCREMENTAL DYNAMIC ANALYSIS OF ARCHETYPES

10.1 General

The previous sections described key components required to perform collapse assessment of Coupled Composite Plate Shear Walls/Concrete-Filled (CC-PSW/CF) wall system. Using material models calibrated on test data in Section 6, Section 7, and Section 8, respectively for two different OpenSees models for CC-PSW/CF wall system, Section 10 presents collapse assessment on the archetypes of CC-PSW/CF wall system designed as described in Section 5. The objective here (i.e., in Section 10) is to determine the seismic performance factors that could be used for CC-PSW/CF. This is done using two different modeling approaches for two different configurations of CC-PSW/CF wall systems, namely planar shaped CC-PSW/CF wall systems; and C-shaped CC-PSW/CF wall systems (as defined in Section 5.1). The specific seismic performance factors (SPF) to be determined for these structural systems are the response modification coefficient (R), the system over-strength factor (Ω_o), and the deflection amplification factor (C_d). First, the collapse assessment is done for planar CC-PSW/CF wall system (Type I in Figure 5-1). Collapse assessment is also performed for the second configuration (Type II in Figure 5-1). SPF for both configurations of C-PSW/CF wall system are identified.

As indicated throughout this report, the FEMA P695 methodology is followed for the above purpose. This methodology for quantifying SPF (e.g., step-by-step procedures, required nonlinear analyses, performance criteria, and other relevant information) was summarized in Section 2. Chosen rating on beta factors are presented in Section 10.2. Key to this methodology is conducting nonlinear incremental dynamic analysis (IDA) for an ensemble of ground motions until global collapse of the archetypes is reached for each ground motion. Thus, the definition of collapse used in the IDA conducted here is first discussed in Section 10.3. Following this, results from the nonlinear static (pushover) analysis and from the IDA of distributed plasticity models, and the correspondingly obtained collapse margin ratios for the two groups of archetypes are reported in Section 10.4. The results from the concentrated plasticity models are then presented in Section 10.6.

10.2 The Beta Factor Study

This section summarizes findings from a review of the existing literature on past FEMA P695 studies that was carried out by Rahul Raman and Sai Chowdeswara Rao Korlapati to determine if a correlation exists between the number of test data available and the choice of the uncertainty factors related to test data, β_{TD},

and modeling, β_{MDL}, as well as to assess if there exists a trend in the choice of beta factors for new structural systems. An abbreviated version of the report by Raman and Korlapati can be found in Appendix D.

As it was mentioned in Section 2.3, the FEMA P695 methodology requires creating nonlinear models to represent the actual behavior of the system being studied over a range of time period and explicitly consider uncertainties in ground motions, modeling, design, and test data. To determine the seismic performance factors for the design of new seismic force resisting systems, these uncertainties should be evaluated. Understanding the variations of these uncertainty factors can help in achieving better estimates of the ACMR and hence of the seismic performance factors of the lateral load resisting system. Further, finding a correlation between the uncertainty factors selected in past FEMA P695 projects and the number of experimental studies conducted on the system can help minimize the number of tests required for a new system to determine appropriate performance factors. Therefore, the existing literature was reviewed to determine if a correlation exists between the number of test data available and the choice of the uncertainty factors related to test data and modeling, as well as to assess if a trend exists in the choice of beta factors for new structural systems.

The prior studies conducted by researchers who used the FEMA P695 methodology with various lateral load-resisting systems were reviewed in order to find a correlation between the choice of uncertainty factors and the number of test data used to validate the model used in each respective study. The initial list of 123 research publications related to FEMA P695 methodology were reviewed and the list was curtailed down to 31 publications based on (1) the availability of full text for the study, and (2) whether the study specifically provided a justification for the choice of uncertainty factors. These 31 studies were then further reviewed to single out those that referred to a total number of tests used to validate the models used in the study. This reduced the data set to only 11 studies out of the earlier 31 studies**.** Based on this data set, a correlation was established between the choice of uncertainty factor and the number of tests used to validate the model. This review found that studies with higher number of test data sometimes (but not always) had a better uncertainty factor, but no strong correlation could be established given the limited number of data in the set. A similar observation was made in case of the correlation between the number of tests and the modelling uncertainty. It was also observed, based on the 31 studies, that the uncertainty factor associated with test data and modeling were typically less for steel structural systems compared to the other building materials. In these 31 studies, “good” or better rating was selected ten times for β_{TD} and fourteen times for β_{MDL} out of sixteen structural systems with steel. Therefore, since the ultimate behavior of the composite structural system under investigation is effectively driven by the steel, and mostly because the modeling and analytical efforts invested here were deemed to be of a “good” quality and deserving of this rating (in

its own sake, but also by comparing with prior FEMA P695 studies on steel systems), a "good" rating was chosen for β_{TD} and β_{MDL} uncertainty factors in this study.

10.3 Collapse Definition for Incremental Dynamic Analysis

Incremental dynamic analysis (IDA) is a procedure that consists of performing successive time history analyses for a given structural model, for which the intensity of given ground motions is progressively scaled up from low to high magnitude until the structure reaches collapse. According to Vamvatsikos and Cornell (2002), spectral acceleration and peak ground acceleration (PGA) are the two most common intensity measures (IM) considered in such analyses; and top story drift, inter-story drift, cross-section plastic rotation, or base shear are commonly selected as corresponding damage measures (DM). Here, in compliance with the FEMA P695 methodology, IDA results are plotted in terms of spectral acceleration for the IM and maximum inter-story drift for the DM. In all cases, IDA are conducted until each archetype is deemed to have reached collapse.

In a typical IDA curve, when the IM vs DM curves becomes a nearly flat line upon increasing values of IM, it is an indication of structural collapse (or dynamic instability), because in this case, a slight increase in ground motion intensity from that in the previous IDA step causes extreme increases in lateral deformations of the structure under consideration. However, in most cases, for the types of structure considered here, collapse by this definition was often observed to occur at extreme drifts of nearly 10% (or even 15% in some cases). As such, other considerations must be taken into account to defining "collapse" from a practical perspective. Therefore, in addition to the "actual collapse" observed from the IDA, a semi-arbitrary practical drift limit is also used here as a definition of collapse. Recognizing that real buildings would suffer an extensive amount of non-structural damage if developing 5% drift during seismic response, even if not experiencing global collapse proper, for the IDA conducted here as part of this FEMA P695 study, when actual collapse occurred at drifts larger than 5%, the Collapse Margin Ratio (CMR) is calculated based on response values obtained at 5% drift for each archetype. Here, actual collapse obtained from IDA was defined in one of three possible ways, namely: (i) collapse at infinity (capped at 20% drift); (ii) collapse at a point obtained for an observed excessive increase in drift for a small increase in ground motion intensity; (iii) collapse based on a significant change of slope of the IDA curve – these are further defined below. In addition, a few words on the phenomenon of "weaving" in the IDA curves are also provided. Figure 10-1 shows an example for each collapse definition and for the weaving phenomenon. In all these analyses, a trigger was inserted to terminate the analysis if a drift equal to 20% or greater was

reached; any time history that completes without reaching this arbitrary drift limit is defined as being "stable" in the text below.

As an example of the first actual collapse definition, Figure 10-1a illustrates the collapse of the PG-1A archetype under the BOL090 earthquake. After the last point for which a full analysis is completed and a drift value is obtained (i.e., $S_a = 5.17g$, $\Delta_{max}/h = 9.4\%$, where Δ_{max} is the maximum inter-story drift and h is the story height), before, in the subsequent analysis step, the DM goes to 'infinity' (i.e., Δ_{max}/h is greater than 100%) for an increase of only 0.07g in the IM. Therefore, in such a case, the collapse IM is taken as equal to 5.17g. Note that in this case, there is a trigger specifically inserted in OpenSees instructing the analysis to stop if the calculated drifts at any time in the response are greater than 20%. In this case, the collapse point is at this 20% drift.

As an example of the second collapse definition, in some cases, a collapse point could be perceived as an excessive increase in DM from the previous step, without necessary having the DM go to infinity. In such cases, the collapse point could be considered as the first point for which this excessive increase in drift is observed, before DM goes to 'infinity'. To illustrate this case, the result of the PG-1A archetype under the BOL000 earthquake is shown in Figure 10-1b, where increase of 0.07g from the point (i.e., S_a of 4.05g and Δ_{max}/h of 7.65%) produced an increase of the maximum inter-story drift of over 100%, resulting in a value of 15.66% at 4.12g spectral acceleration.

As an example of the third collapse definition, note that in some cases, analysis results continued to be stable upon further increase in IM, but a significant change in the IM-DM slope between two points, where the slope in a subsequent step was substantially smaller than the slope over several previous IDA steps. Figure 10-1c (result of the PG-1A archetype under the LOS270 earthquake) illustrates such a case. After the point where S_a is 9.15g with a 10.96% maximum inter-story drift, there is a visible slope change, but the change of slope is not as large as the ones in Figures 10-1a and 10-1b.

Vamvatsikos and Cornell (2002) described that weaving can sometimes be observed in IDA curves. Weaving is a phenomenon where an increase in the IM (e.g., spectral acceleration) is not followed by a larger DM (e.g., inter-story drift). That phenomenon is illustrated in Figure 10-1d. Occurrence of weaving did not affect how actual collapse was determined by any of the above three procedures. Note that an event of weaving, by itself, is not a collapse point.

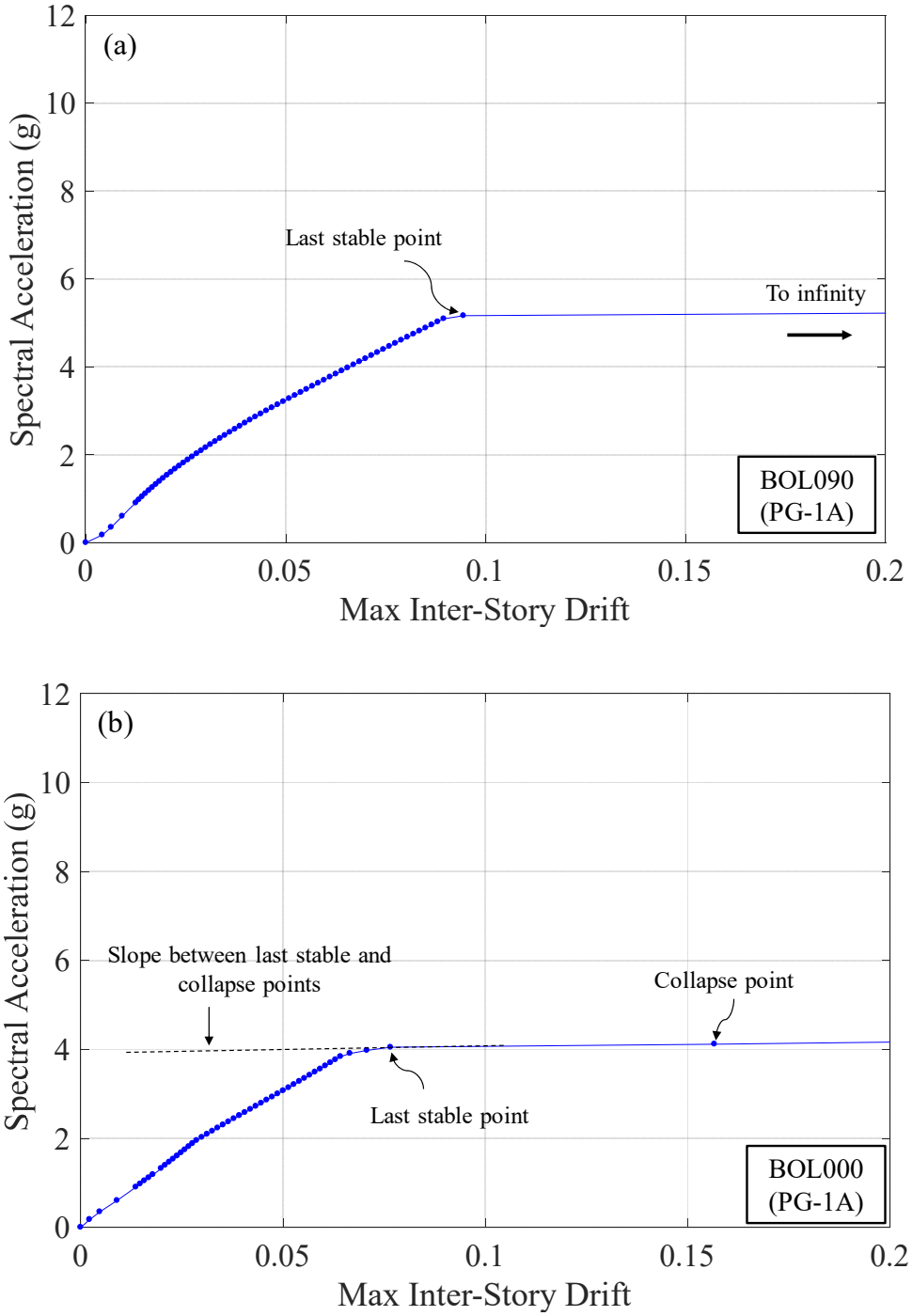

Figure 10-1. Collapse Definition for Incremental Dynamic Analysis: (a) Collapse occurred at infinity (capped at 20% drift); (b) Collapse at a point for an excessive increase in drift for a small increase in ground motion intensity; (c) Collapse based on a significant change of slope of the IDA curve; (d) Example of IDA curve with "Weaving".

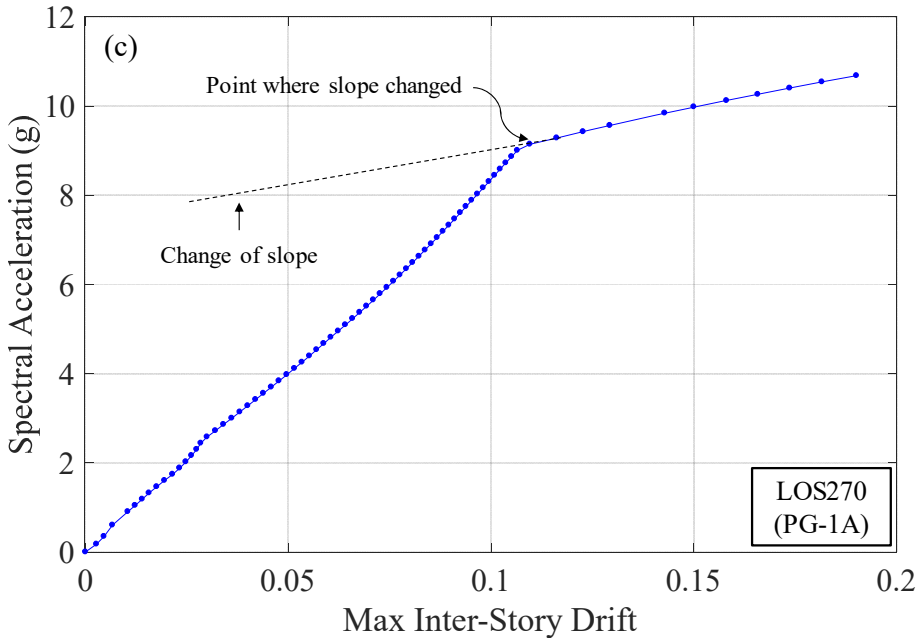

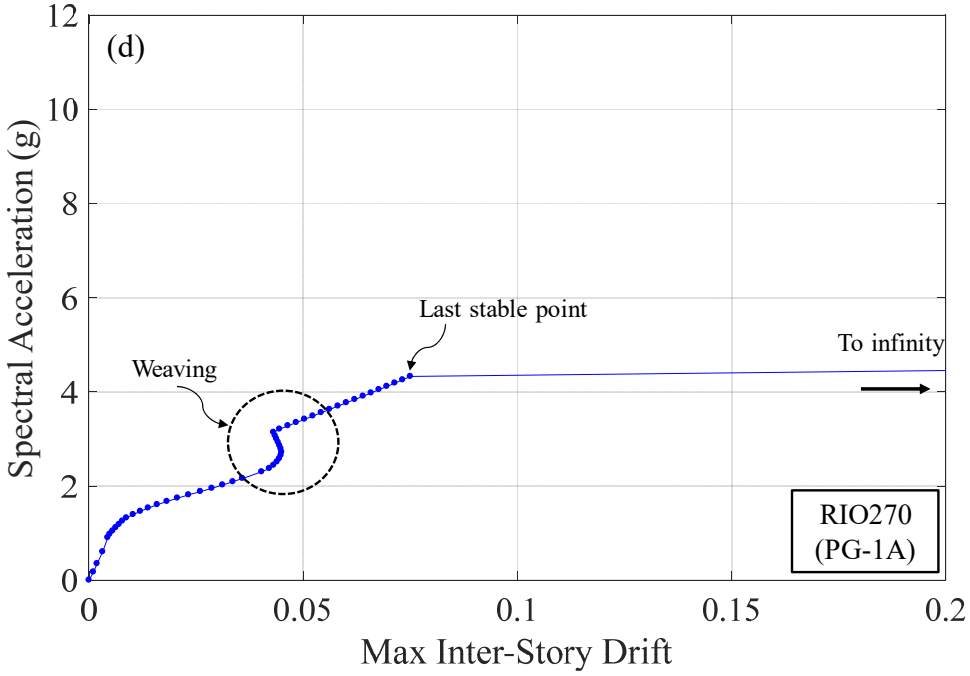

Figure 10-1. (Continued)

10.4 Nonlinear Static and Dynamic Analyses with Distributed Plasticity Models

Nonlinear static (pushover) and dynamic (response history) analyses were performed for the models built using OpenSees (as described in prior sections). Dynamic analyses were conducted for the 44 ground motions specified by the FEMA P695 procedure using supercomputers at the University at Buffalo. Procedures and results of both analyses are presented in the following subsections.

10.4.1 Nonlinear Models of the Archetypes

10.4.1.1 Archetype Model Geometry and General Characteristics

Figures 10-2a and 10-2b show two-dimensional nonlinear models for the collapse simulation of coupled planar C-PSW/CF and coupled C-Shaped C-PSW/CF archetypes. All deterioration material models, element types, and size for each component of the CC-PSW/CF system, as well as their calibration to test data, are presented in Section 7. For walls, the nonlinear beam-column elements were only assigned to the first floor of the walls and the rest of the floors were modeled using elastic beam-column elements having effective stiffness per AISC Equation I2-12, whereas the coupling beams are modeled using only nonlinear beam-column elements. The nonlinear elements were assigned to the centroid of the cross-section of composite walls as they were calibrated. Note that only half of C-Shaped walls were modelled for coupled C-Shaped C-PSW/CF archetypes in order to account for half of the lateral loading system. Leaning columns were also added to the structural model to capture the P-Δ effects in each given story due to gravity loads that are not located on the CC-PSW/CF system itself (1440 kips). They were modeled using elastic beam-column elements. Moment of inertia and cross section area of the elastic beam-column elements should be multiplied by the number of leaning column assumed to exist in the archetype structure. Since there is no definitive information on the number of leaning columns in the archetype design, their values were arbitrarily chosen to provide insignificant flexural stiffness. Tributary loads coming to the C-PSW/CF walls (72 kips per floor for planar walls and 144 kips for C-Shaped walls) are applied in each floor. Rigid links were assigned between the C-PSW/CF wall center of gravity and the point where the coupling beams frame into the walls, and rigid beams were used to connect the leaning column and C-PSW/CF wall at every floor (these rigid beams were modeled using truss elements with a cross section area increased arbitrarily to 100 times the elastic area of the coupling beams. No seismic mass was assigned to the leaning column; seismic masses were applied to the C-PSW/CF walls and distributed equally to its left and right joints at every story.

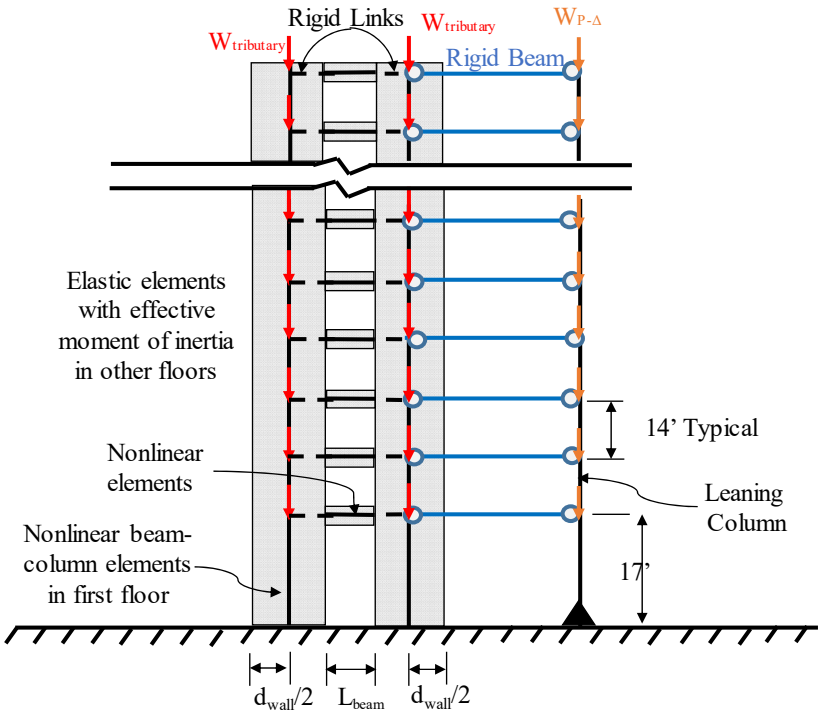

a)

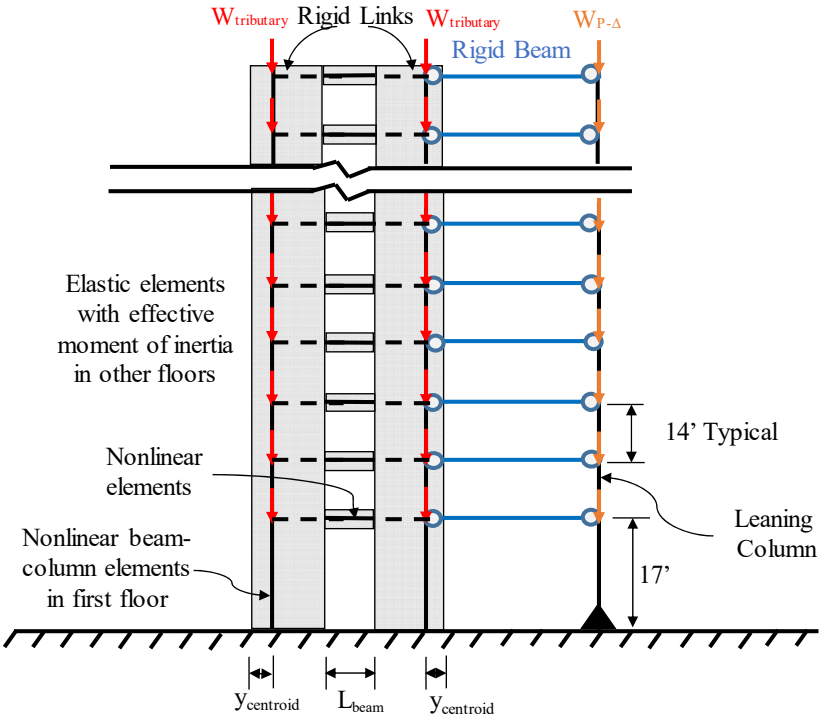

b)

Figure 10-2. Nonlinear model for collapse simulation for a) coupled planar C-PSW/CF wall system and b) coupled C-shaped C-PSW/CF wall system

10.4.1.2 Damping Ratio

In the nonlinear time history analyses of the archetypes, Rayleigh damping was used, with a value of 5% damping specified for the first and second periods of vibration.

10.4.2 Nonlinear Static Pushover Analysis of Archetypes

Nonlinear pushover analysis was also conducted, in compliance with the approach prescribed by the FEMA P695 methodology as described in Section 2.3.3 in order to estimate the overstrength (Ω_o) and period-based ductility (μ_T) factors for all archetypes. The results of pushover analysis for 8-, 12-, 18- and 22- story archetypes are shown in Figures 10-3 to 10-6. The overstrength (Ω_o) factor were obtained by dividing the maximum base shear obtained from the static pushover curve by the base shear for which archetypes were designed, as indicated in Equation 2.2. In order to determine the period-based ductility (μ_T) factor, effective yield and ultimate top floor displacements are required. The effective yield displacement ($\delta_{y,eff}$) was taken as the displacement corresponding to the intersection of a line tangent to the initial slope of the resulting pushover curve and a horizontal line set at the level of the maximum base shear obtained from this nonlinear pushover analysis, V_{max}. The displacement obtained at $0.8V_{max}$ on the descending branch (i.e., post-peak) of the pushover curve was taken for the ultimate top floor displacement (δ_u). The nonlinear pushover results of all archetypes are presented in Tables 10-1 and 10-2.

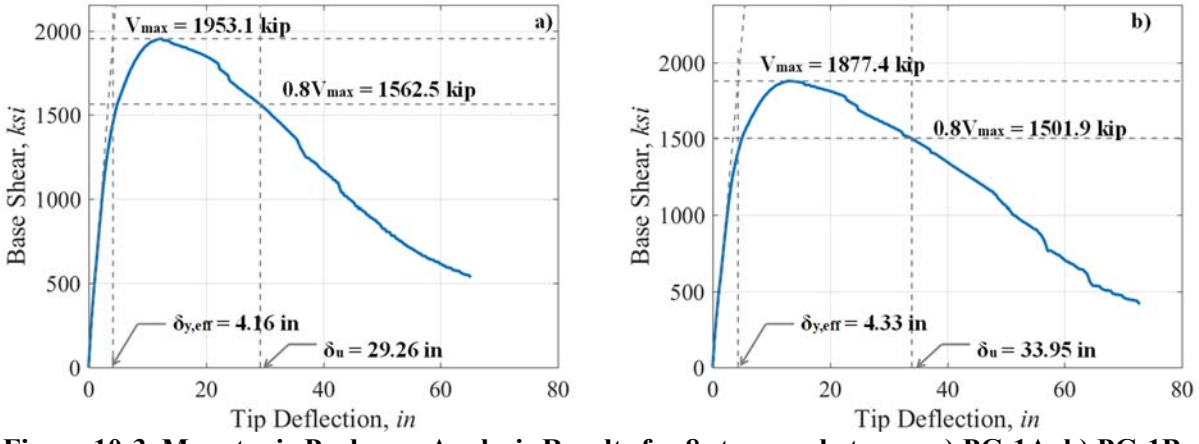

Figure 10-3. Monotonic Pushover Analysis Results for 8 story archetypes: a) PG-1A, b) PG-1B, c) PG-1C, and; d) PG-2B

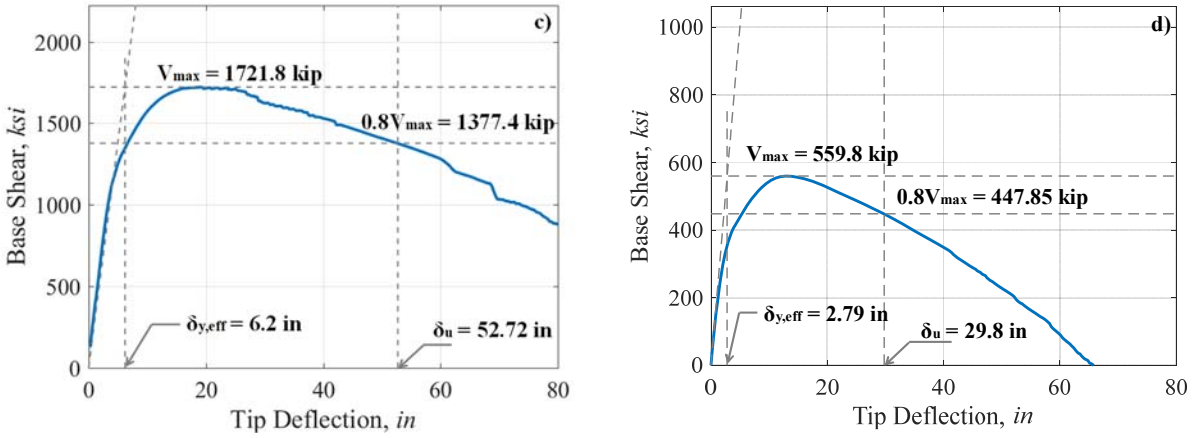

Figure 10-3. (Continued)

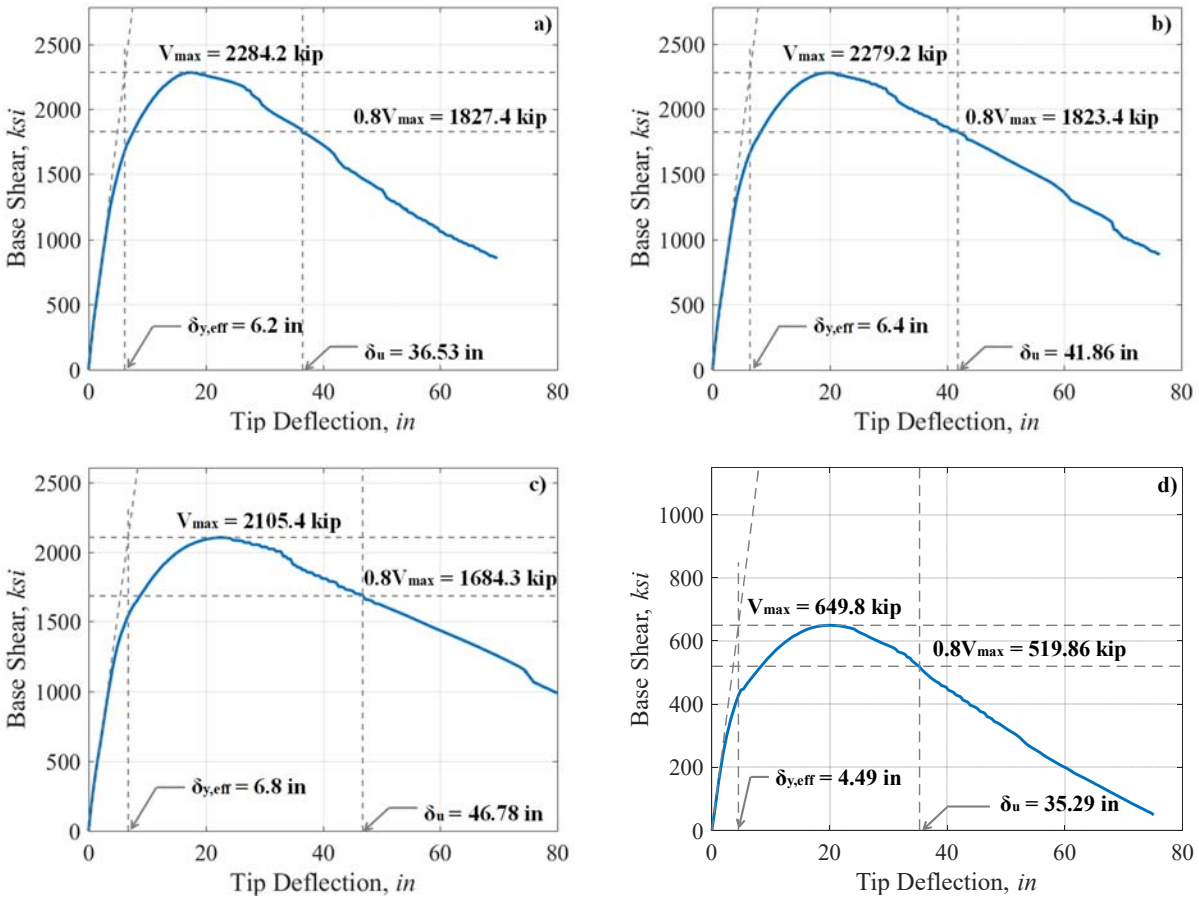

Figure 10-4. Monotonic Pushover Analysis Results for 12 story archetypes: a) PG-1D, b) PG-1E, c) PG-1F, and; d) PG-2E

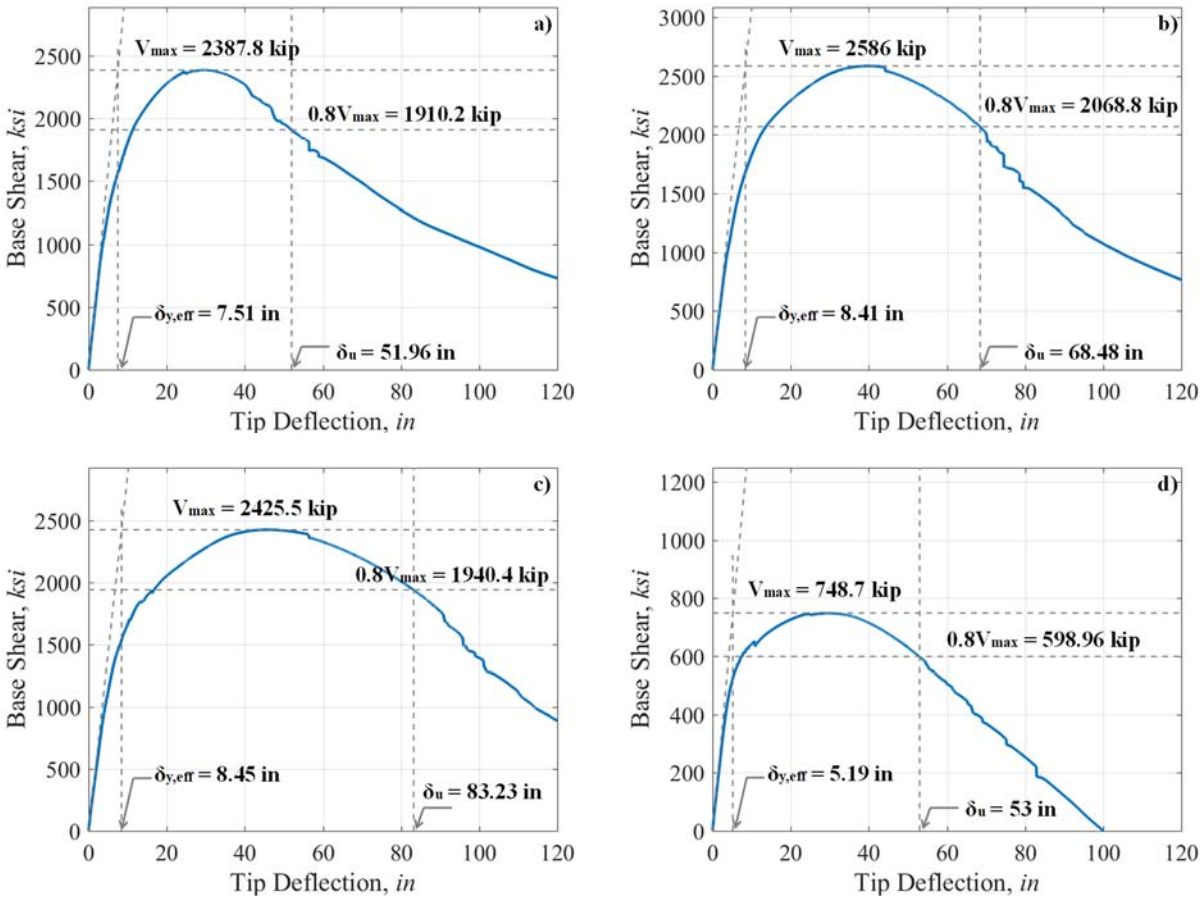

Figure 10-5. Monotonic Pushover Analysis Results for 18 story archetypes: a) PG-3A, b) PG-3B, c) PG-3C, and; d) PG-4B

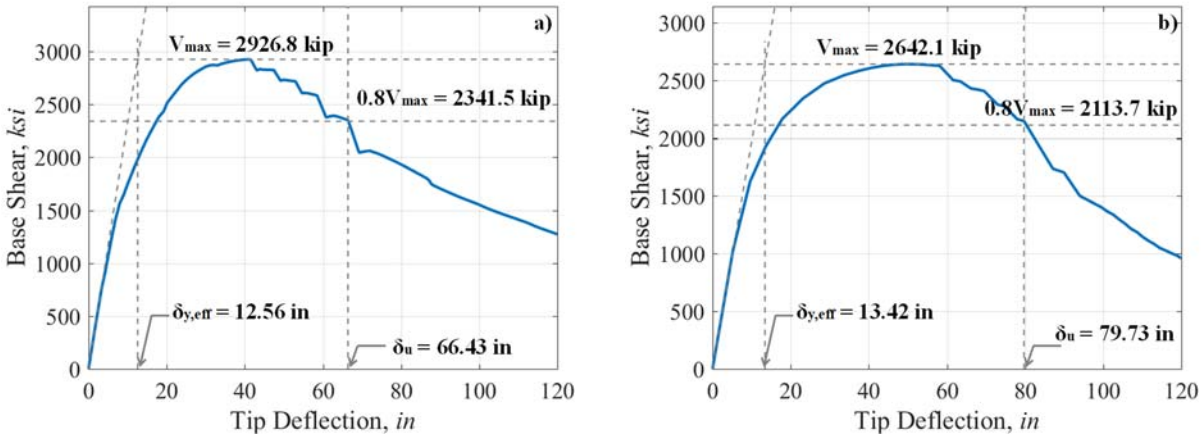

Figure 10-6. Monotonic Pushover Analysis Results for 22 story archetypes: a) PG-3D, b) PG-3E, c) PG-3F, and; d) PG-4E

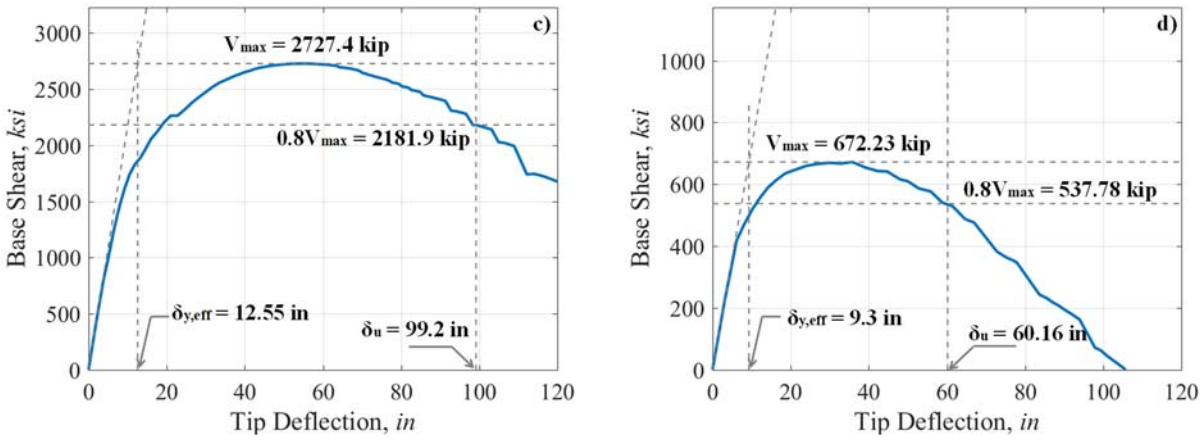

Figure 10-6. (Continued)

Table 10-1. Pushover Analysis results of 8- and 12-Story archetypes.
(Units: kips, in, sec., g)

Parameter	PG-1A	PG-1B	PG-1C	PG-2B	PG-1D	PG-1E	PG-1F	PG-2E
V_{max}	1953.1	1877.4	1721.8	559.8	2284.2	2279.2	2105.4	649.83
V_{design}	879	879	879	273	979	979	979	305
$\Omega = V_{max}/V_{design}$	2.22	2.14	1.96	2.05	2.33	2.33	2.15	2.13
$\delta_{y,eff}$	4.16	4.33	6.2	2.79	6.2	6.4	6.8	4.49
δ_u	29.26	33.95	52.72	29.81	36.53	41.86	46.78	35.3
$\mu_T = \delta_u/\delta_{y,eff}$	7.03	7.84	8.5	10.68	5.89	6.54	6.88	7.86

Table 10-2. Pushover Analysis results of 18- and 22-Story archetypes.
(Units: kips, in, sec., g)

Parameter	PG-3A	PG-3B	PG-3C	PG-4B	PG-3D	PG-3E	PG-3F	PG-4E
V_{max}	2387.8	2586	2425.5	748.7	2926.8	2642.1	2727.4	672.2
V_{design}	1088	1088	1088	338	1146	1146	1146	356
$\Omega = V_{max}/V_{design}$	2.19	2.38	2.23	2.22	2.55	2.31	2.38	1.89
$\delta_{y,eff}$	7.51	8.41	8.45	5.19	12.56	13.42	12.55	9.3
δ_u	51.96	68.48	83.23	53	66.43	79.73	99.2	60.16
$\mu_T = \delta_u/\delta_{y,eff}$	6.92	8.14	9.85	10.21	5.29	5.94	7.9	6.47

10.4.3 Nonlinear Dynamic Analysis

To investigate the numerically obtained behavior of the Coupled Composite Plate Shear Wall/Concrete-Filled (CC-PSW/CF) system and ensure that the nonlinear inelastic models considered led to a progression of damage that was rational, "spot checks" of selected IDA results were performed. For this purpose, one of the archetypes described in Section 5.4 was chosen, namely PG-1A. Then, one of the most severe ground motions among the 44 that the FEMA P695 procedure provides was used for this study, namely the N-S component of the Superstition Hills (BICC090) earthquake. This record was selected because it exhibits multiple pulses and is of significant duration. For example, between the times of 30.78 second and 33.39 second in this record (Figure 10-7a), the area under the ground acceleration record is large, indicating a large velocity pulse for the earthquake. It was believed that using an earthquake with large pulses would more severely challenge the numerical calculations, which is aligned with the objectives outlined in Section 9.1. This ground motion was also selected because the shape of its response spectra is such that the spectral acceleration demand at the period of the archetype is large, and remains large at adjacent larger periods (and slightly larger for that matter, as seen in Figure 10-7b), which will keep seismic demand intense as the archetype undergoes nonlinear inelastic response and its period elongates, thus making the archetype more prone to collapse.

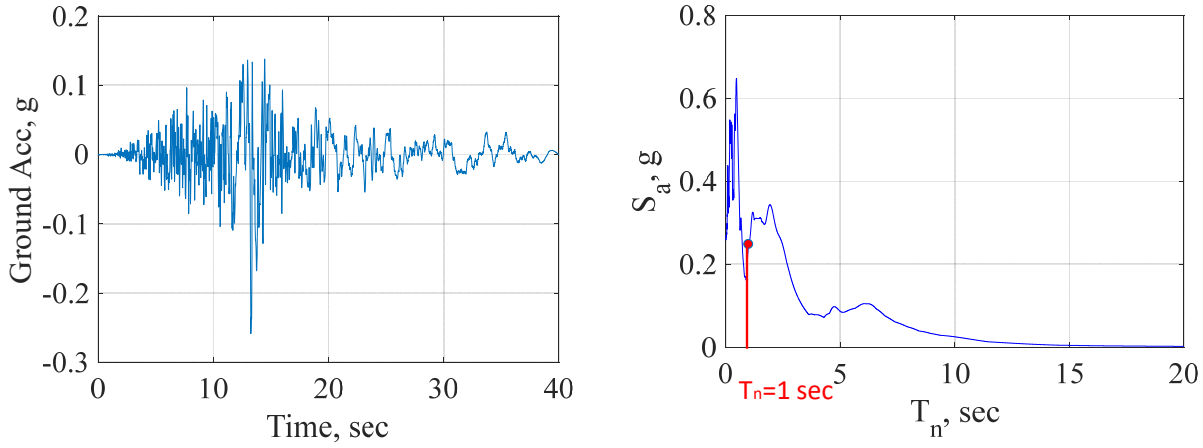

a) **b)**

Figure 10-7. Chosen a) ground acceleration history of BICC090 earthquake and b) spectral acceleration of the earthquake.

For comparison, roof displacement histories from the earthquake time history analyses of the PG-1A archetype, considering the two different non-linear inelastic models presented earlier, under the N-S BICC090 ground motion with scale factors 3, 6, and 9 are shown in Figures 10-8 to 10-10. In these figures, these points are identified on the full IDA curve for this archetype. Note that the vertical axis here

corresponds to the scale factors used for the BICC090 earthquake, not the spectral acceleration typically used for presentation of IDA results. The number added along the roof displacement histories in these figures indicate the points where yielding, fracture initiation, and complete fracture occurred in various members.

Results for the scale factor of "3" case show that first yielding of the coupling beams occurred (for the various beams) between 6.04 and 6.44 seconds (point 1 in Figure 10-8). Then, yielding of the right and left walls started at 6.89 and 11.96 seconds, respectively (points 2 and 3 in Figure 10-8). First crack initiation was observed in the coupling beams between 15.0 and 15.6 seconds (point 4 in Figure 10-8). No fracture initiation of in the walls, and no through-fracture of the coupling beams, were observed at this scale factor of the earthquake.

The above observed behavior occurred in the same order for the scale factor of "6" case, except that each event occurred sooner (as expected due to the increased severity of earthquake excitation). The coupling beams first yielded between 4.23 and 5.83 seconds (point 1 in Figure 10-9); yielding of the right and left walls occurred at 6.09 and 6.14 seconds, respectively (points 2 and 3 in Figure 10-9); fracture initiation of the coupling beams happened between 12.97 and 14.17 seconds (point 4 in Figure 10-9). Again, no wall fracture occurred, and no through-fracture of the coupling beams were observed.

At Scale factor of 9, yielding of the coupling beams initiated between 3.67 and 4.27 seconds (point 1 in Figure 10-10) and right and left walls subsequently yielded at 4.17 and 6.09 seconds, respectively (points 2 and 3 in Figure 10-10). Then, fracture triggered in the coupling beams between 12.36 and 13.16 seconds (point 4 in Figure 10-10). However, differently than what was observed at the other drift cases considered above, some of the coupling beams fractured through at 26.11 and 26.81 seconds (point 5 in Figure 10-10), and then the left and right walls began to fracture at 32.26 and 32.91 seconds (point 6 in Figure 10-10), respectively. However, full fracture of the walls were not observed at this scale factor.

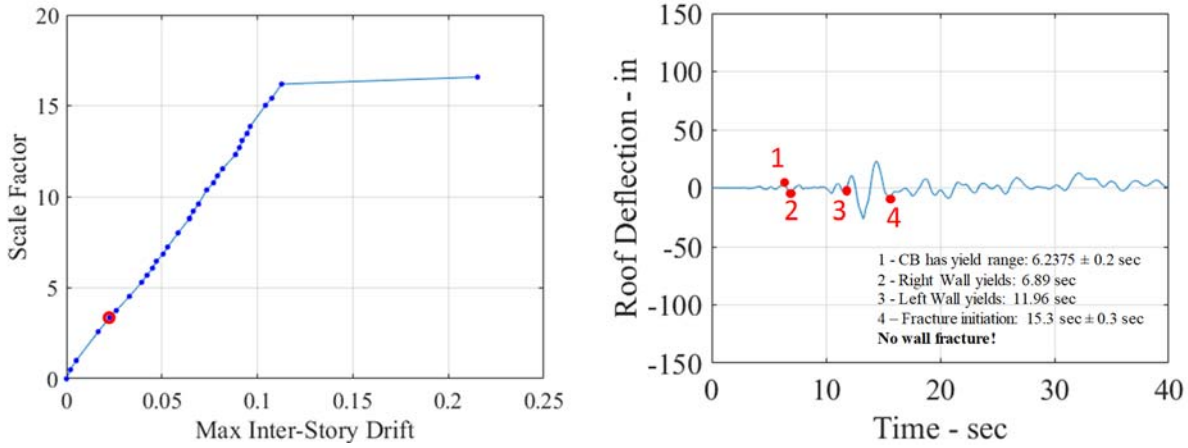

Figure 10-8. Response of PG-1A archetype under BICC090 earthquake at scale factor of "3".

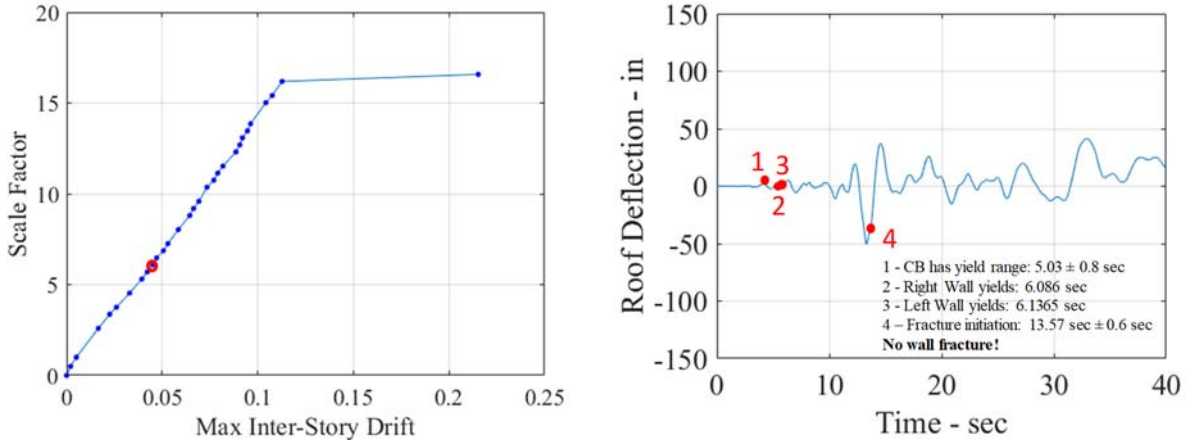

Figure 10-9. Response of PG-1A archetype under BICC090 earthquake at scale factor of "6".

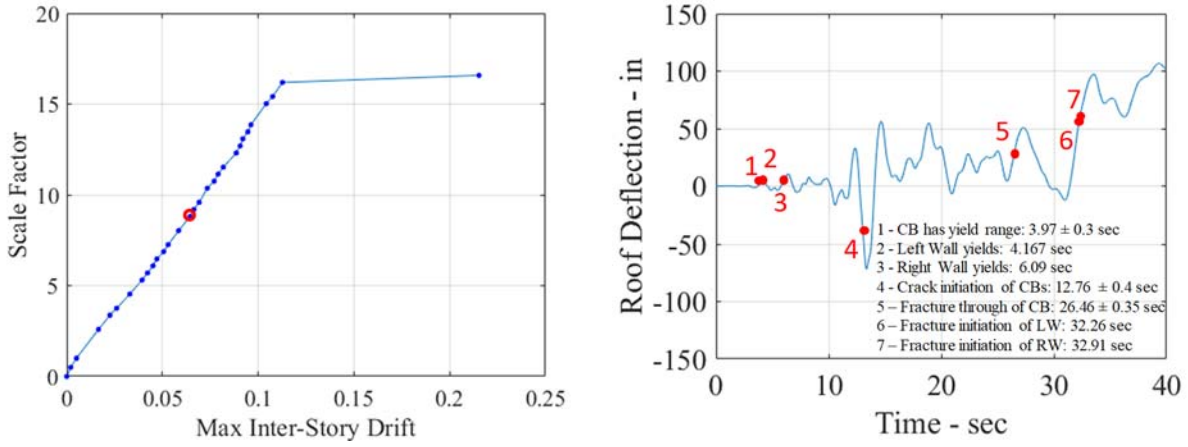

Figure 10-10. Response of PG-1A archetype under BICC090 earthquake at scale factor of "9".

10.4.4 Incremental Dynamic Analysis of Archetypes

Incremental dynamic analysis (IDA) consists of a series of successive time history analyses performed for a given structural model, for which the intensity of ground motions specified is gradually scaled up from low to high magnitude until collapse is observed in the structure. Theoretically, there is no unique rule for choosing intensity increments for IDA. In other words, any arbitrary incremental scheme of ground motion intensity can be selected. In this research project that considers the 44 far-field ground motions specified in the FEMA P695, the IDA started with an analysis using half of the actual un-scaled recorded ground motions, followed by one using the actual un-scaled record itself. The subsequent increments for which all ground motions were scaled such that the median spectral acceleration of the 44 ground motions (at the fundamental period of a given archetype being analyzed) matched that at the Design Basis Earthquake (DBE) and at the Maximum Considered Earthquake (MCE) spectral acceleration levels, respectively. Then, from there, each motion was gradually scaled up in steps equal to four-tenth, six-tenth, one , and one-and-half of the MCE level (i.e., $0.4S_{a\text{-}MCE}$, $0.6S_{a\text{-}MCE}$, $1.0S_{a\text{-}MCE}$, and $1.5S_{a\text{-}MCE}$) for the 8-, 12-, 18- and 22-story archetypes, respectively, up to the intensity that caused structural collapse for each individual ground motion. The balance sought was to limit the number of analysis to a manageable limit while maintaining sufficient accuracy in determining the collapse intensity level. Using increments equal instead to one-tenth of the median spectra beyond the MCE level was attempted with selected ground motions, but while the obtained resulted were found to be comparable, it required more than a hundred nonlinear analysis before reaching collapse intensity which was deemed to be too computationally intensive for a relatively small accuracy gain in the determination of the intensity at collapse. Such increased accuracy also became a moot point once it was realized that calculation of the collapse margin ratio would be performed in all cases at 5% drift (i.e., much smaller drifts than at the points of actual collapse).

Figures 10-11 to 10-14 present IDA results obtained for all the 8-, 12-, 18- and 22-story archetypes considered and their corresponding fragility curves developed based on the spectral accelerations close to 5% maximum inter-story drifts. For each archetype, the median collapse spectral acceleration intensity at 5% maximum inter-story drift (defined to be the limiting collapse definition, in Section 10.3), $\hat{S}_{CT}$, was taken from its corresponding collapse fragility curve as the spectral acceleration intensities that corresponded to a 50% probability of collapse at 5% maximum inter-story drift. These curves were obtained by fitting a lognormal distribution through the "collapse" data points. Note that this kind of data is lognormal distribution (Ang and Tang 2007); consequently, the median value of the collapse data points as $\hat{S}_{CT}$ is used here instead of the average (arithmetic mean).

The median collapse spectral acceleration intensity, $\hat{S}_{CT}$ and the median spectral acceleration, S_{MT} are also compiled in Tables 10-3 and 10-4. From these IDA results, the collapse margin ratio (CMR) was calculated as the ratio between $\hat{S}_{CT}$ and S_{MT}, per Equation 2.4.

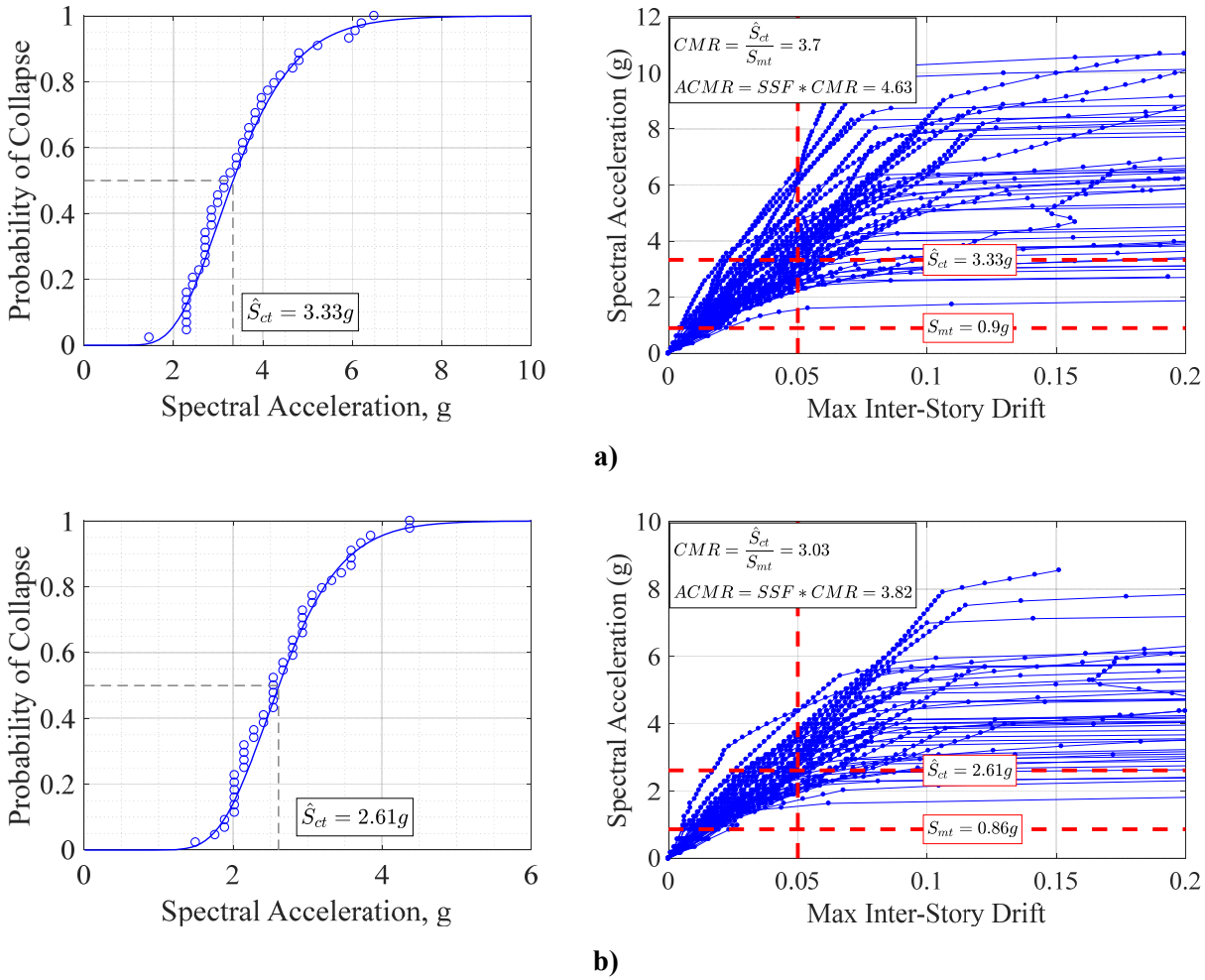

Figure 10-11. Fragility Curve (left) and Incremental Dynamic Analysis (IDA) (right) results for a) PG-1A, b) PG-1B, c) PG-1C, and; d) PG-2B

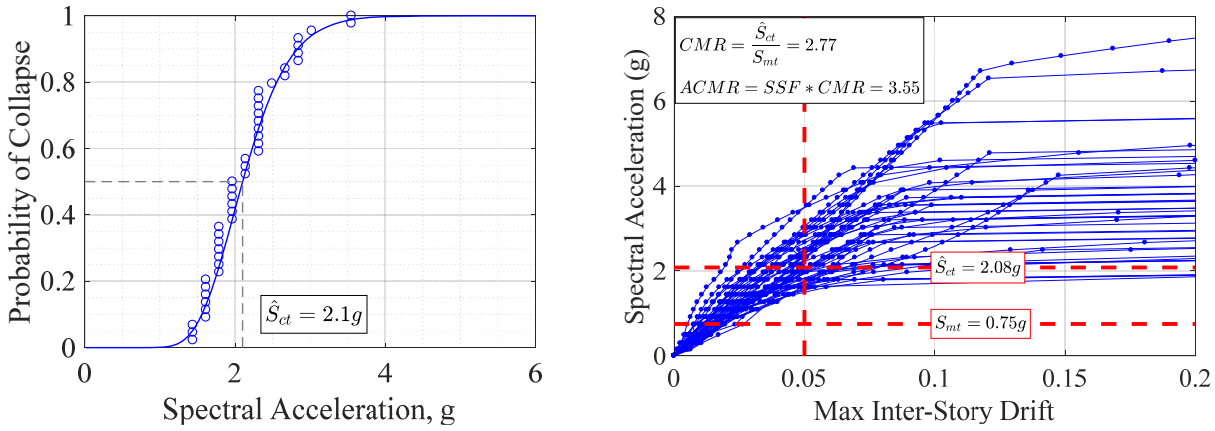

c)

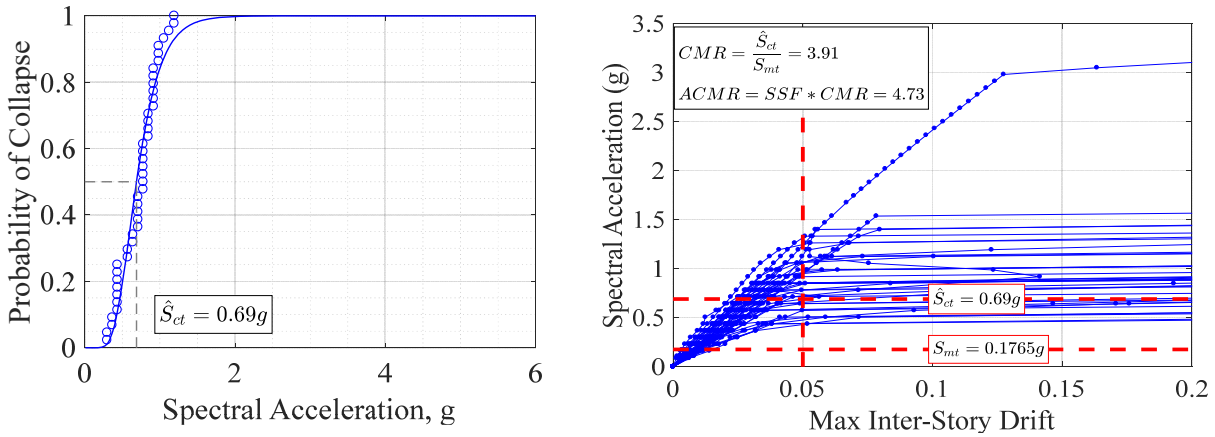

d)

Figure 10-11. (Continued)

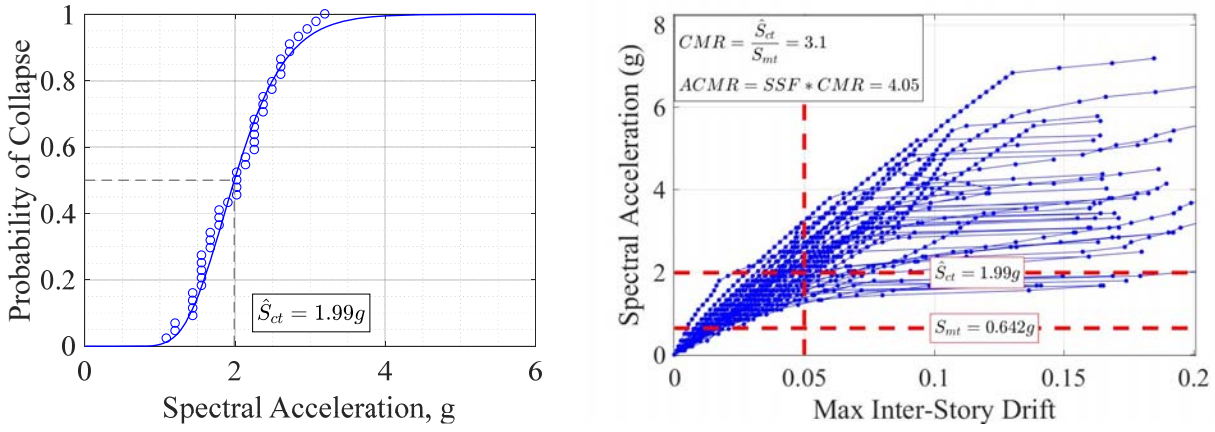

a)

Figure 10-12. Fragility Curve (left) and Incremental Dynamic Analysis (IDA) (right) results for a) PG-1D, b) PG-1E, c) PG-1F, and; d) PG-2E

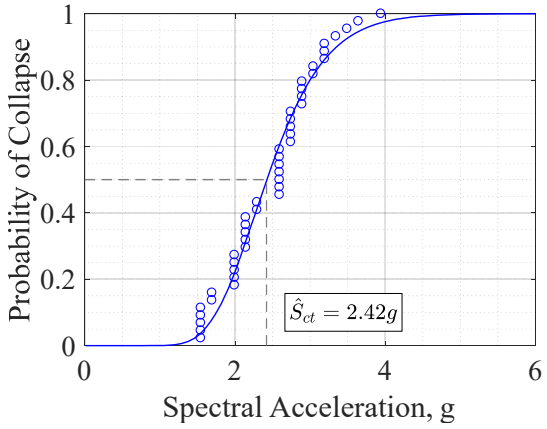

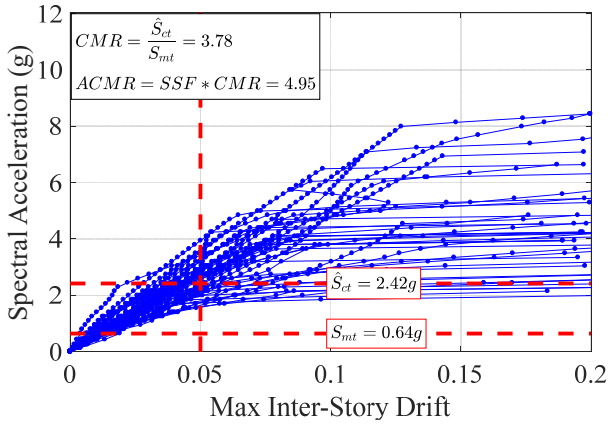

b)

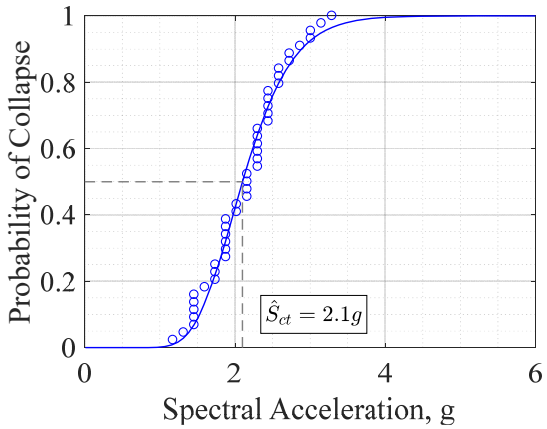

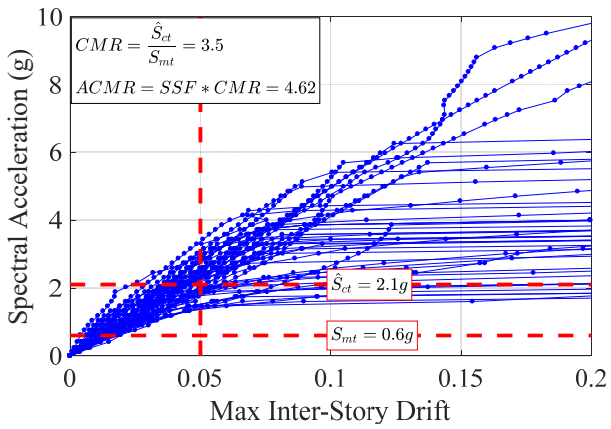

c)

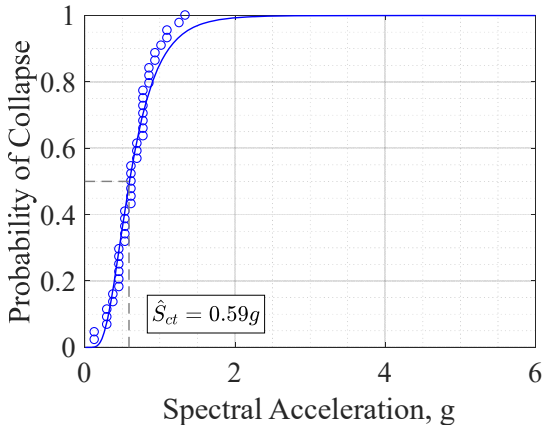

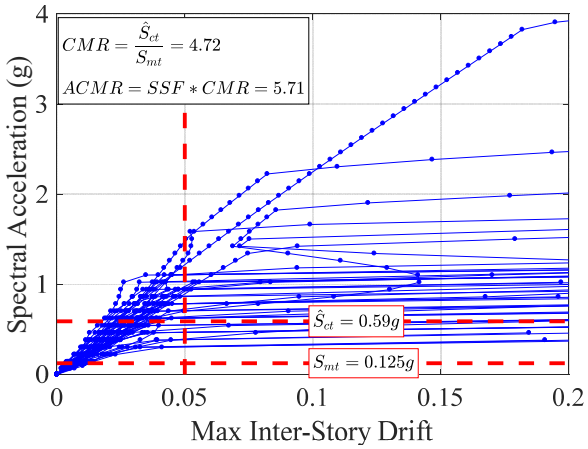

d)

Figure 10-12. (Continued)

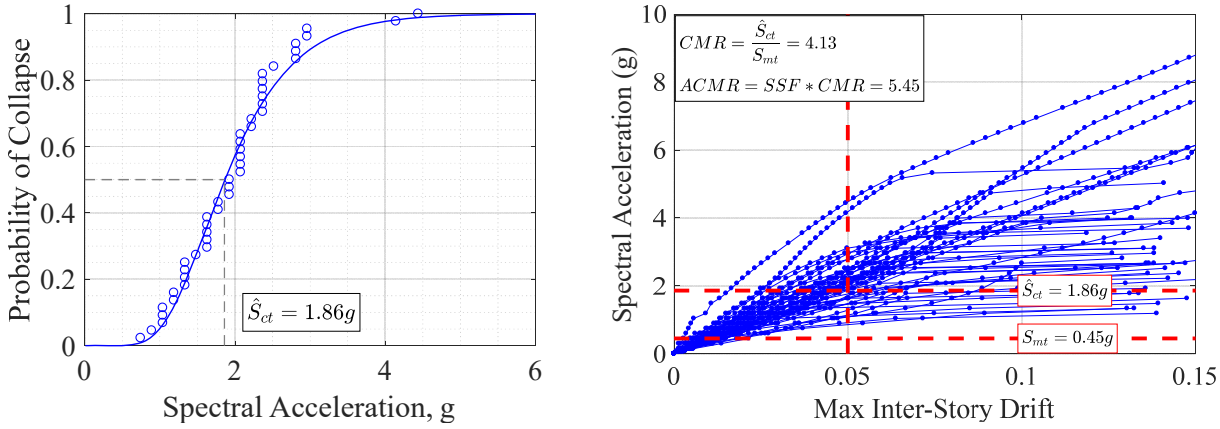

a)

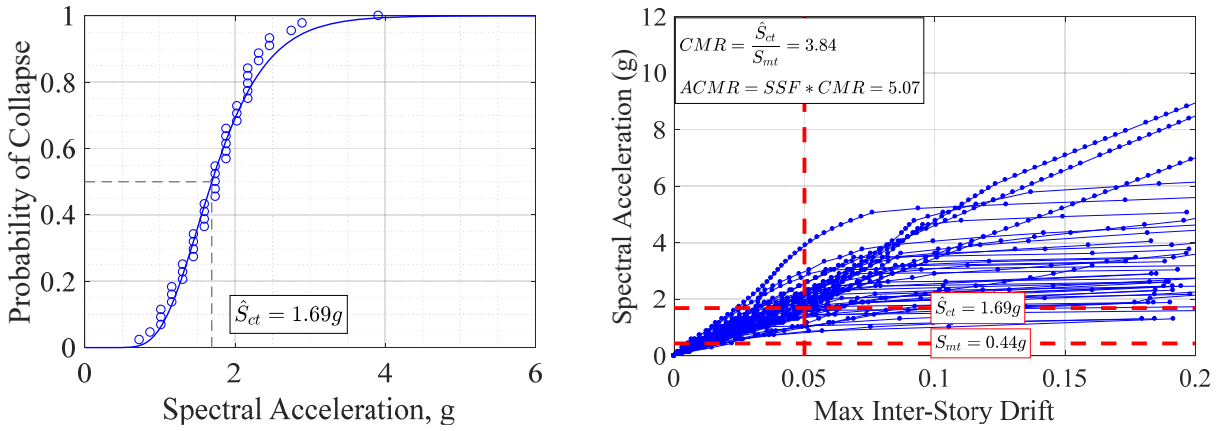

b)

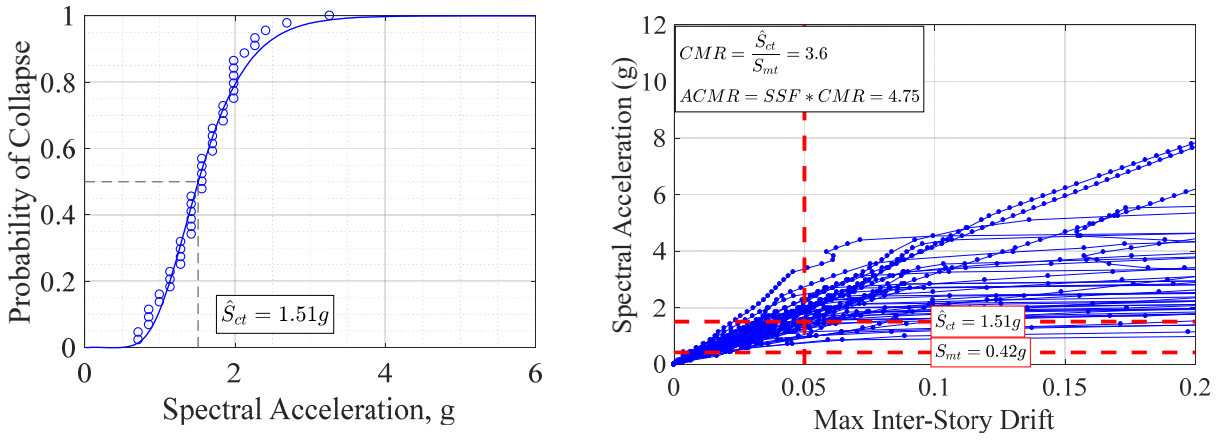

c)

Figure 10-13. Fragility Curve (left) and Incremental Dynamic Analysis (IDA) (right) results for a) PG-3A, b) PG-3B, c) PG-3C, and; d) PG-4B

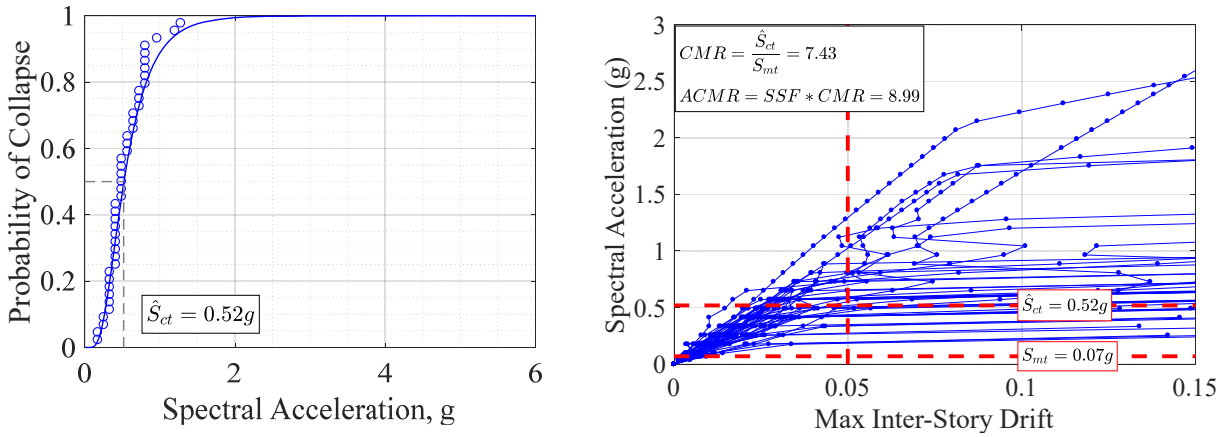

d)

Figure 10-13. (Continued)

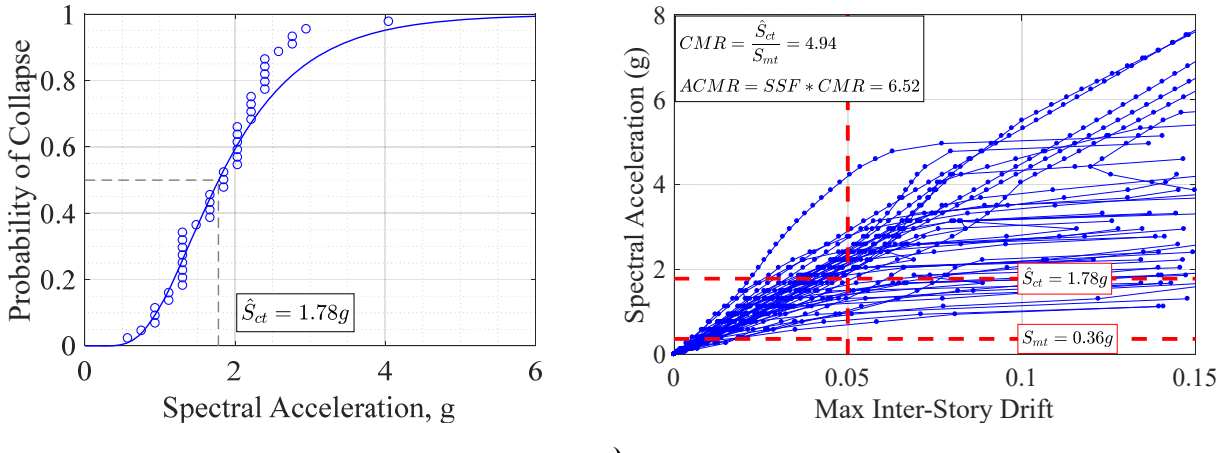

a)

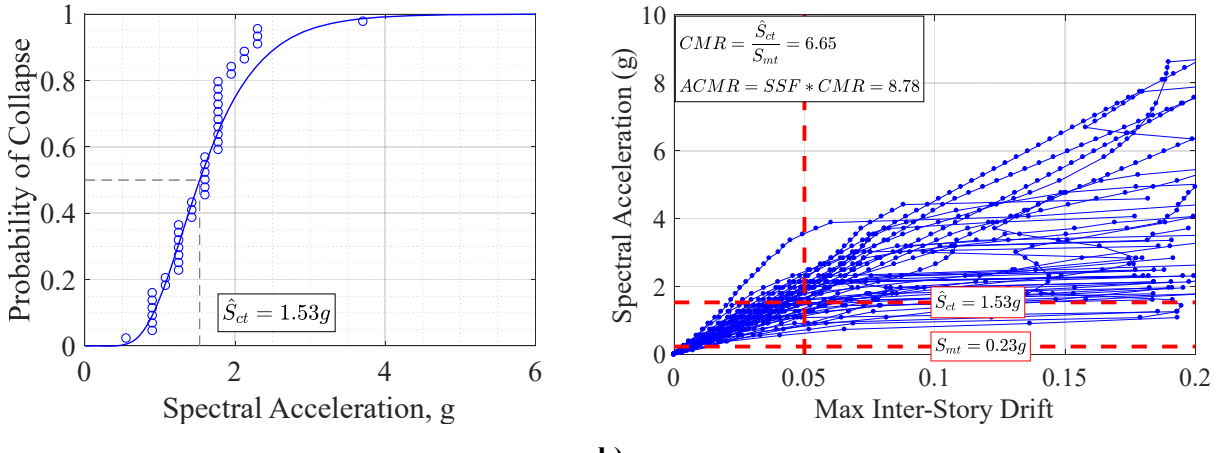

b)

Figure 10-14. Fragility Curve (left) and Incremental Dynamic Analysis (IDA) (right) results for a) PG-3D, b) PG-3E, c) PG-3F, and; d) PG-4E

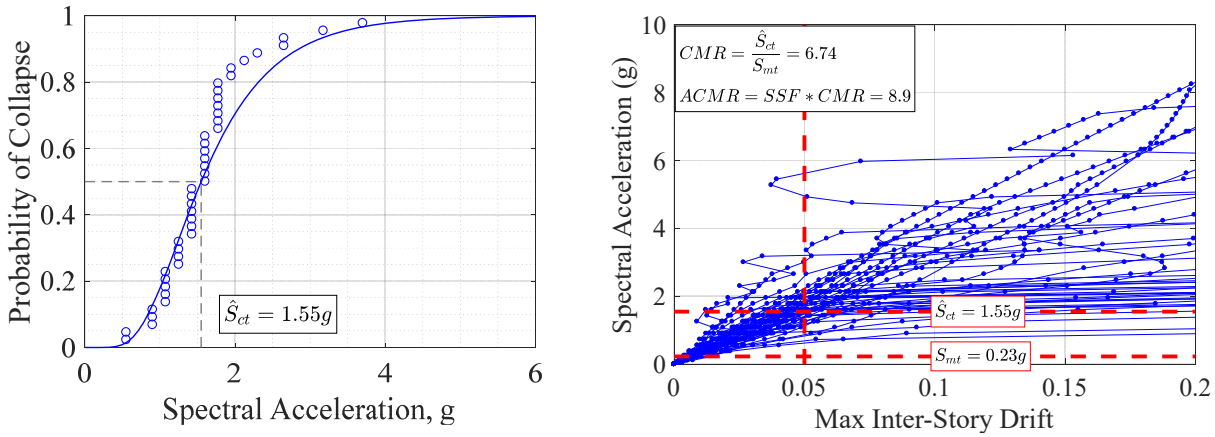

c)

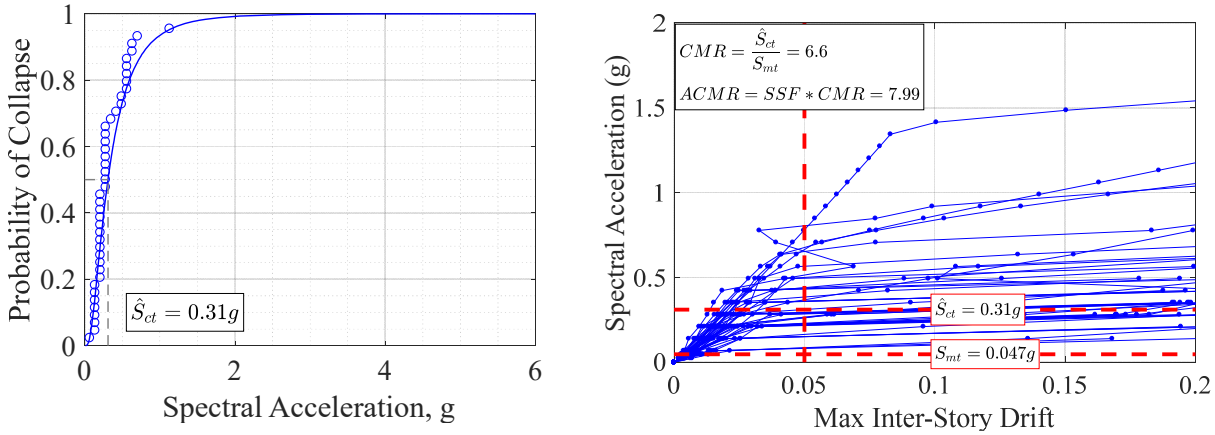

d)

Figure 10-14. (Continued)

Table 10-3. Incremental dynamic analysis (IDA) results of 8- and 12-Story archetypes (Units: kips, in, sec., g)

Parameter	PG-1A	PG-1B	PG-1C	PG-2B	PG-1D	PG-1E	PG-1F	PG-2E
S_{CT}	3.33	2.61	2.08	0.69	1.99	2.42	2.1	0.59
S_{MT}	0.9	0.86	0.75	0.1765	0.642	0.64	0.6	0.125
$CMR = S_{CT}/S_{MT}$	3.7	3.03	2.77	3.91	3.1	3.78	3.5	4.72

Table 10-4. Incremental dynamic analysis (IDA) results of 18- and 22-Story archetypes (Units: kips, in, sec., g)

Parameter	PG-3A	PG-3B	PG-3C	PG-4B	PG-3D	PG-3E	PG-3F	PG-4E
S_{CT}	1.86	1.69	1.51	0.52	1.78	1.53	1.55	0.31
S_{MT}	0.45	0.44	0.42	0.07	0.36	0.23	0.23	0.047
$CMR = S_{CT}/S_{MT}$	4.13	3.84	3.6	7.43	4.94	6.65	6.74	6.6

10.4.5 Collapse Performance Evaluation

Tables 10-5 to 10-8 compare collapse performance evaluation for the 8-, 12-, 18- and 22-Story archetypes, by summarizing design information, nonlinear static and dynamic analyses results, and evaluation of the seismic performance factors used for the original design. The initial step of the performance evaluation is to adjust the CMR value obtained from the IDA to take into account the frequency content of the selected ground motion records (i.e., the effect of spectral shape). The spectral shape factor (SSF) values that are used to modify the CMR to the adjusted collapse margin ratio (ACMR) are a function of the archetype fundamental period, the applicable Seismic Design Category (SDC) and period-based ductility (μ_T) attained from nonlinear pushover analysis. The fundamental period (T) of the archetypes were used instead of the maximum period for which archetypes are designed (note that this does not make a significant difference on the results). The period-based ductility (μ_T) was conservatively taken as 3 for all archetypes, based on observed behavior in experimentally obtained cyclic hysteretic curves, even though the nonlinear pushover analysis of archetypes proved that the ductility is more than 3 for all archetypes. The value of SSF are obtained from Tables 7-1a and 7-1b (depending on SDC) in the FEMA P695 document for both archetypes. Accordingly, the ACMR are obtained by multiplying the CMR by the SSF value. In Section 10.4.6, these values are compared to acceptable ACMR values to verify if the initial R factor used to design these archetypes satisfies the FEMA P695 requirements.

As such, total system collapse uncertainty (β_{TOT}) is required in order to calculate the acceptable ACMR value. The value of β_{TOT} is obtained by combining uncertainty factors related to record- to-record (β_{RTR}), design requirements (β_{DR}), test data (β_{TD}), and nonlinear modeling (β_{MDL}). For the selected ground motions used in the FEMA P695 methodology, a constant value of β_{RTR} equal to 0.4 is used, given that period-based ductility is larger than or equal to 3 ($\mu_T \geq 3$). With respect to the other three uncertainty factors (β_{DR}, β_{TD}, and β_{MDL}), based on information presented in Section 10.2, these values were taken as equal to 0.2, corresponding to the "good" rating (i.e., β_{DR}, β_{TD}, and β_{MDL} = 0.2). The corresponding total system uncertainty calculated using Equation 2.5 is 0.529. The acceptable ACMR for 10% and 20% collapse probability under MCE ground motions (i.e., $ACMR_{10\%}$ and $ACMR_{20\%}$) for β_{TOT} of 0.529 are 1.96 and 1.56 from Table 7-3 in FEMA P695 document, respectively.

The FEMA P695 methodology specifies that $ACMR_{20\%}$ and $ACMR_{10\%}$ are the acceptable threshold values to evaluate performance of individual archetype and average performance of several archetypes in one performance group, respectively. Hence, all archetypes passed the performance requirement. Here, results in Tables 10-5 to 10-8 show that for β_{TOT} of 0.529 and "good" rating, all individual 8-, 12-, 18- and 22-

story archetypes are considerably above the $ACMR_{20\%}$ threshold. Likewise, average of ACMR values in a performance group also passed $ACMR_{10\%}$ threshold.

Note that even if all these values of uncertainties were actually be taken as “poor” here, rather than “good”, with β_{DR}, β_{TD}, and β_{MDL} = 0.5), the corresponding ACMR values (i.e., $ACMR_{10\%}$ and $ACMR_{20\%}$) calculated for the resulting β_{TOT} of 0.954 with “poor” rating would be 3.38 and 2.22, and the ACMR of the archetypes considered would still have been found to be satisfactory.

Table 10-5. Summary of ATC-63 Methodology on 8-Story archetypes for: PG-1A, PG-1B, PG-1C and; PG-2B (Units: kips, in, sec., g)

Parameter	PG-1A	PG-1B	PG-1C	PG-2B	Note and Reference
1. Design Stage					
R	8	8	8	8	ASCE 7-10 (Table 12.2-1)
V_{design}	879	879	879	273	From ELF Method
2. Nonlinear Static (Pushover) Analysis					
V_{max}	1953.1	1877.4	1721.8	559.8	Figure 10-4
$\Omega = V_{max}/V_{design}$	2.22	2.14	1.96	2.05	Eq. 2.2
$\delta_{y,eff}$	4.16	4.33	6.2	2.79	Figure 10-4
δ_u	29.26	33.95	52.72	29.81	
$\mu_T = \delta_u/\delta_{y,eff}$	7.03	7.84	8.5	10.68	Eq. 2.3
3. Incremental Dynamic Analysis (IDA)					
S_{CT}	3.33	2.61	2.08	0.69	Figure 10-12
S_{MT}	0.9	0.86	0.75	0.1765	
$CMR = S_{CT}/S_{MT}$	3.7	3.03	2.77	3.91	Eq. 2.4
4. Performance Evaluation					
T	1.00	1.05	1.19	1.69	From OpenSees
SDC	D_{max}	D_{max}	D_{max}	D_{min}	FEMA P695 (Table 5-1)
$SSF(T,\mu_T,SDC)$	1.25	1.26	1.28	1.21	FEMA P695 (Table 7.1)
ACMR	4.63	3.82	3.55	4.73	Eq. 2.5
β_{RTR}	0.4	0.4	0.4	0.4	Section 10.2 (good)
$\beta_{DR}, \beta_{TD}, \beta_{MDL}$	0.2	0.2	0.2	0.2	Section 10.2 (good)
β_{tot}	0.529	0.529	0.529	0.529	Eq. 2.6
$ACMR_{20\%}$ (β_{tot})	1.56	1.56	1.56	1.56	FEMA P695 (Table 7-3)
$ACMR_{10\%}$ (β_{tot})	1.96	1.96	1.96	1.96	
$Status_i$	**Pass**	**Pass**	**Pass**	**Pass**	Pass if $ACMR_{20\%} <$ AMCR
$AMCR_{ave}$		4.0		4.73	Average in a performance group
$Status_{PG}$		**Pass**		**Pass**	Pass if $ACMR_{10\%} <$ $AMCR_{ave}$
5. Final Results					
R	8	8	8	8	
Ω	2.22	2.14	1.96	2.28	
μ_T	7.03	7.84	8.5	7.06	
C_d	5.5	5.5	5.5	5.5	

Table 10-6. Summary of ATC-63 Methodology on 12-Story archetypes for: PG-1D, PG-1E, PG-1F and; PG-2E (Units: kips, in, sec., g)

Parameter	PG-1D	PG-1E	PG-1F	PG-2E	Note and Reference
1. Design Stage					
R	8	8	8	8	ASCE 7-10 (Table 12.2-1)
V_{design}	979	979	979	305	From ELF Method
2. Nonlinear Static (Pushover) Analysis					
V_{max}	2284.2	2279.2	2105.4	649.83	Figure 10-4
$\Omega = V_{max}/V_{design}$	2.33	2.33	2.15	2.13	Eq. 2.2
$\delta_{y,eff}$	6.2	6.4	6.8	4.49	Figure 10-4
δ_u	36.53	41.86	46.78	35.3	
$\mu_T = \delta_u/\ \delta_{y,eff}$	5.89	6.54	6.88	7.86	Eq. 2.3
3. Incremental Dynamic Analysis (IDA)					
S_{CT}	1.99	2.42	2.1	0.59	Figure 10-12
S_{MT}	0.642	0.64	0.6	0.125	
$CMR = S_{CT}/S_{MT}$	3.1	3.78	3.5	5.85	Eq. 2.4
4. Performance Evaluation					
T	1.38	1.4	1.5	2.38	From OpenSees
SDC	D_{max}	D_{max}	D_{max}	D_{min}	FEMA P695 (Table 5-1)
SSF(T,μ_T,SDC)	1.306	1.31	1.32	1.21	FEMA P695 (Table 7.1)
ACMR	4.05	4.95	4.62	5.71	Eq. 2.5
β_{RTR}	0.4	0.4	0.4	0.4	Section 10.2 (good)
β_{DR}, β_{TD}, β_{MDL}	0.2	0.2	0.2	0.2	Section 10.2 (good)
β_{tot}	0.529	0.529	0.529	0.529	Eq. 2.6
$ACMR_{20\%}$ (β_{tot})	1.56	1.56	1.56	1.56	FEMA P695 (Table 7-3)
$ACMR_{10\%}$ (β_{tot})	1.96	1.96	1.96	1.96	
$Status_i$	**Pass**	**Pass**	**Pass**	**Pass**	Pass if $ACMR_{20\%} <$ AMCR
$AMCR_{ave}$		4.54		5.71	Average in PG
$Status_{PG}$		**Pass**		**Pass**	Pass if $ACMR_{10\%} <$ $AMCR_{ave}$
5. Final Results					
R	8	8	8	8	
Ω	2.33	2.33	2.15	2.24	
μ_T	5.89	6.54	6.88	5.84	
C_d	5.5	5.5	5.5	5.5	

Table 10-7. Summary of ATC-63 Methodology on 18-Story archetypes for PG-3A, PG-3B, PG-3C and PG-4B (Units: kips, in, sec., g)

Parameter	PG-3A	PG-3B	PG-3C	PG-4B	Note and Reference
1. Design Stage					
R	8	8	8	8	ASCE 7-10 (Table 12.2-1)
V_{design}	1088	1088	1088	338	From ELF Method
2. Nonlinear Static (Pushover) Analysis					
V_{max}	2387.8	2586	2425.5	748.7	Figure 10-4
$\Omega = V_{max}/V_{design}$	2.19	2.38	2.23	2.22	Eq. 2.2
$\delta_{y,eff}$	7.51	8.41	8.45	5.19	Figure 10-4
δ_u	51.96	68.48	83.23	53	
$\mu_T = \delta_u / \delta_{y,eff}$	6.92	8.14	9.85	10.21	Eq. 2.3
3. Incremental Dynamic Analysis (IDA)					
S_{CT}	1.86	1.69	1.51	0.52	Figure 10-12
S_{MT}	0.45	0.44	0.42	0.07	
$CMR = S_{CT}/S_{MT}$	4.13	3.84	3.6	7.43	Eq. 2.4
4. Performance Evaluation					
T	1.96	2.05	2.14	2.96	From OpenSees
SDC	D_{max}	D_{max}	D_{max}	D_{min}	FEMA P695 (Table 5-1)
SSF(T,μ_T,SDC)	1.32	1.32	1.32	1.21	FEMA P695 (Table 7.1)
ACMR	5.45	5.07	4.75	8.99	Eq. 2.5
β_{RTR}	0.4	0.4	0.4	0.4	Section 10.2 (good)
β_{DR}, β_{TD}, β_{MDL}	0.2	0.2	0.2	0.2	Section 10.2 (good)
β_{tot}	0.529	0.529	0.529	0.529	Eq. 2.6
$ACMR_{20\%}$ (β_{tot})	1.56	1.56	1.56	1.56	FEMA P695 (Table 7-3)
$ACMR_{10\%}$ (β_{tot})	1.96	1.96	1.96	1.96	
$Status_i$	**Pass**	**Pass**	**Pass**	**Pass**	Pass if $ACMR_{20\%} <$ AMCR
$AMCR_{ave}$		5.09		8.99	Average in a performance group
$Status_{PG}$		**Pass**		**Pass**	Pass if $ACMR_{10\%} <$ $AMCR_{ave}$
5. Final Results					
R	8	8	8	8	
Ω	2.19	2.38	2.23	2.22	
μ_T	6.92	8.14	9.85	10.21	
C_d	5.5	5.5	5.5	5.5	

Table 10-8. Summary of ATC-63 Methodology on 22-Story archetypes for PG-3D, PG-3E, PG-3F and PG-4E (Units: kips, in, sec., g)

Parameter	PG-3D	PG-3E	PG-3F	PG-4E	Note and Reference
1. Design Stage					
R	8	8	8	8	ASCE 7-10 (Table 12.2-1)
V_{design}	1146	1146	1146	356	From ELF Method
2. Nonlinear Static (Pushover) Analysis					
V_{max}	2926.8	2642.1	2727.4	672.2	Figure 10-4
$\Omega = V_{max}/V_{design}$	2.55	2.31	2.38	1.89	Eq. 2.2
$\delta_{y,eff}$	12.56	13.42	12.55	9.3	Figure 10-4
δ_u	66.43	79.73	99.2	60.16	
$\mu_T = \delta_u/\ \delta_{y,eff}$	5.29	5.94	7.9	6.47	Eq. 2.3
3. Incremental Dynamic Analysis (IDA)					
S_{CT}	1.78	1.53	1.55	0.31	Figure 10-12
S_{MT}	0.36	0.23	0.23	0.047	
$CMR = S_{CT}/S_{MT}$	4.94	6.65	6.74	6.6	Eq. 2.4
4. Performance Evaluation					
T	2.49	2.56	2.57	4.22	From OpenSees
SDC	D_{max}	D_{max}	D_{max}	D_{min}	FEMA P695 (Table 5-1)
SSF(T,μ_T,SDC)	1.32	1.32	1.32	1.21	FEMA P695 (Table 7.1)
ACMR	6.52	8.78	8.9	7.99	Eq. 2.5
β_{RTR}	0.4	0.4	0.4	0.4	Section 10.2 (good)
β_{DR}, β_{TD}, β_{MDL}	0.2	0.2	0.2	0.2	Section 10.2 (good)
β_{tot}	0.529	0.529	0.529	0.529	Eq. 2.6
$ACMR_{20\%}$ (β_{tot})	1.56	1.56	1.56	1.56	FEMA P695 (Table 7-3)
$ACMR_{10\%}$ (β_{tot})	1.96	1.96	1.96	1.96	
$Status_i$	**Pass**	**Pass**	**Pass**	**Pass**	Pass if $ACMR_{20\%}$< AMCR
$AMCR_{ave}$		8.07		7.99	Average in a performance group
$Status_{PG}$		**Pass**		**Pass**	Pass if $ACMR_{10\%}$< $AMCR_{ave}$
5. Final Results					
R	8	8	8	8	
Ω	2.55	2.31	2.38	1.89	
μ_T	5.29	5.94	7.9	6.47	
C_d	5.5	5.5	5.5	5.5	

10.4.6 Evaluation of Seismic Performance Factors

Results from the collapse performance evaluations of the 8-, 12-, 18- and 22-Story archetypes presented above indicate that the initial R factor of 8 used to design the archetypes considered is adequate. Results also indicate that the system over-strength factor (Ω_o) could be specified as 2.34 (which is the largest average value of the calculated archetype overstrength in all performance groups (2.19 for PG-1, 2.26 for PG-2, 2.34 for PG-3, and 2.06 for PG-4) (see Section 2.3.3)) and that the deflection amplification factor (C_d) equal to 5.5, which is the value for which all archetypes were designed.

Note that this C_d value of 5.5 recommended and used in the design of the archetypes compares well with maximum displacements obtained from the seismic response of the archetypes. For example, the Table below shows the C_d values calculated for the 8-story and 12-story archetype structures based on the results obtained from the nonlinear inelastic time history analysis models in OpenSees. These C_d values were calculated as the ratio of DR_{DBE} with respect to DR_{ELF}, where DR_{DBE} is the roof drift ratio for the design basis earthquake level, and DR_{ELF} is the roof drift ratio at equivalent lateral force level. The average value of C_d calculated is 5.25, which is close to the value of 5.5 recommended and used for design.

Table 10-9. C_d values calculated from maximum displacements obtained from non-linear time history analysis of 8 and 12 story archetypes (Units: kips, in, sec., g)

Archetype	DR_{DBE}	DR_{ELF}	C_d-calc
1A	0.81%	0.13%	6.3
1B	0.85%	0.14%	6.2
1C	0.85%	0.17%	5.1
2B	0.45%	0.11%	4.0
1D	0.70%	0.12%	5.6
1E	0.80%	0.12%	6.4
1F	0.59%	0.14%	4.2
2E	0.44%	0.11%	4.0
		Average C_d	**5.25**

It is important to note that the $DR_{ELF,}$ and therefore the value of C_d, depends on the stiffness of the models used for the elastic analysis of the structure subjected to the calculated equivalent lateral force. The draft code provisions (Chapters 3 and 4) include recommendations for estimating the stiffness of the composite walls and coupling beams. These stiffness recommendations are based on the fundamental moment-curvature behavior of the composite cross-section, and explicitly account for the contributions of

the structural steel and the cracked concrete components. The stiffness values are relatively accurate, and the resulting values of C_d (lower than the values of R=8) are reported above.

10.4.7 Results of extra 3-Story Archetype Results

In the initial design of archetypes, these type of wall systems were thought to be more likely to be used in tall structures. It was believed that practicing engineers would likely use other lateral-load-resisting systems (e.g., concentrically or eccentrically braced frames, moment-resisting frames or buckling-restrained braced frames) in low-rise construction. Hence, the archetypes were designed to be 8 story or taller – expecting implementations to be more likely for the taller ones, but relying on the 8 and 12 story archetypes to ensure consideration of archetypes for which design would not be governed by drift limits (which could potentially introduce over-strength and thus bias the results of the study with more favorable ACMR). However, acting on recommendations from members of the project peer-review panel (and of members of the Building Seismic Safety Council's 2020 NEHRP Provisions Update Committee), it was decided to investigate, using the FEMA P695 procedure, whether three-story archetype would also achieve satisfactory ACMR. For this purpose, five 3-story archetypes with planar walls and various coupling ratios were designed (see Table 5-8) and the same FEMA P695 analyses were performed for these extra archetypes.

Figure 10-15 shows the resulting fragility and IDA curves for each of the 3-story archetypes with various coupling ratios, and Table 10-10 shows the corresponding CMR and ACMR results. As indicated in Section 10.4.5, the acceptable ACMR for 10% and 20% collapse probability under MCE ground motions (i.e., $ACMR_{10\%}$ and $ACMR_{20\%}$) for β_{TOT} of 0.529 with "good" rating are 1.96 and 1.56 from Table 7-3 in the FEMA P695 document, respectively. Hence, all archetypes passed the performance requirement. The individual ACMR values of each 3-story archetype are considerably above the $ACMR_{20\%}$ threshold. Likewise, the average of ACMR value of 4.01 (calculated from the five values in the table) also passed $ACMR_{10\%}$ threshold.

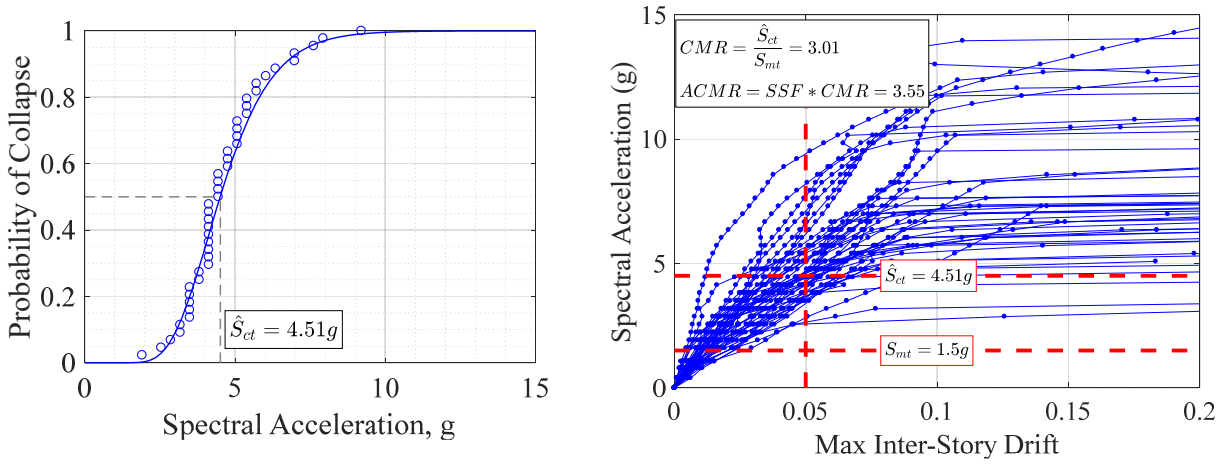

a)

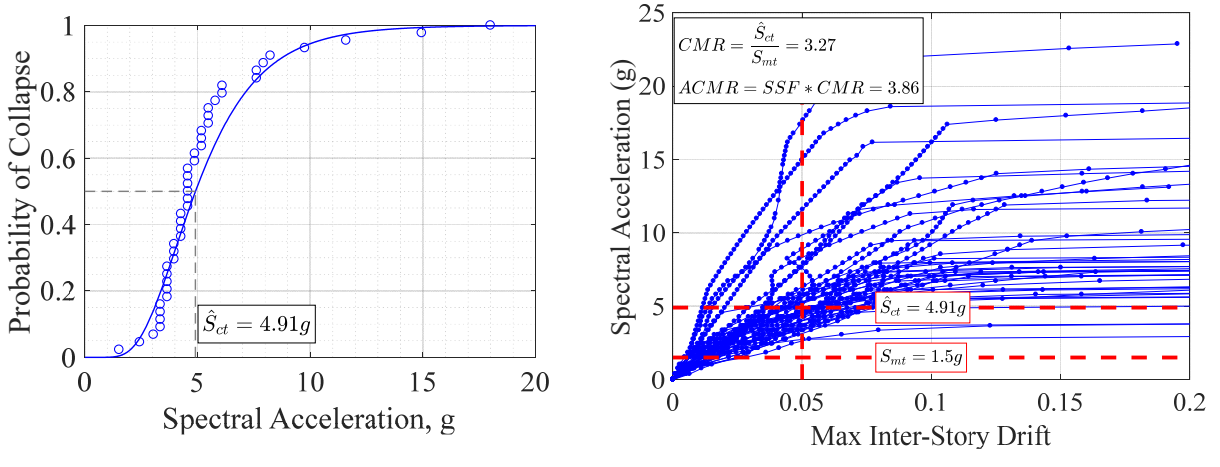

b)

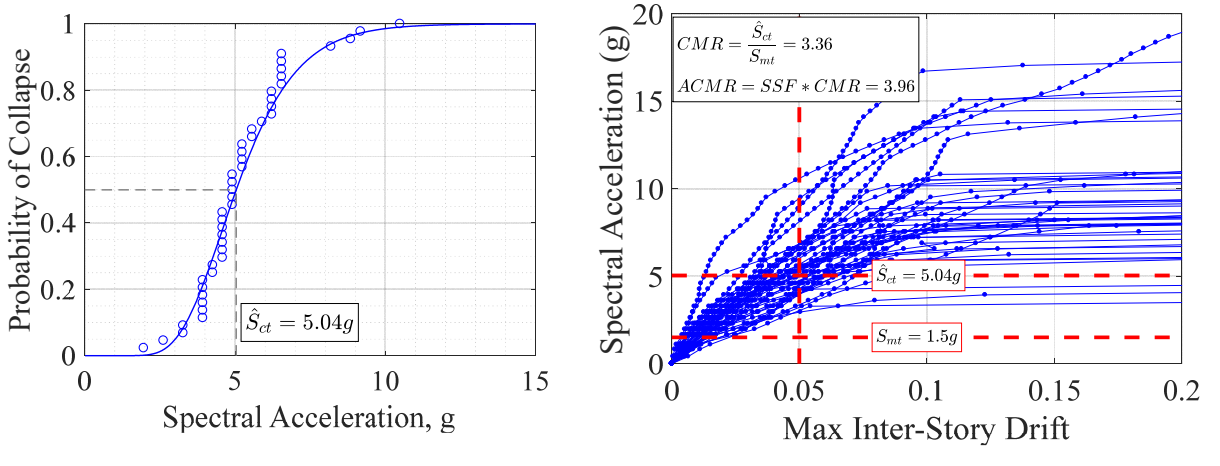

c)

Figure 10-15. Fragility Curve (left) and Incremental Dynamic Analysis (IDA) (right) results of 3 story archetypes designed with: a) 63% coupling ratio (CR), b) 48% CR, c) 54% CR, d) 48.5% CR and; e) 32% CR

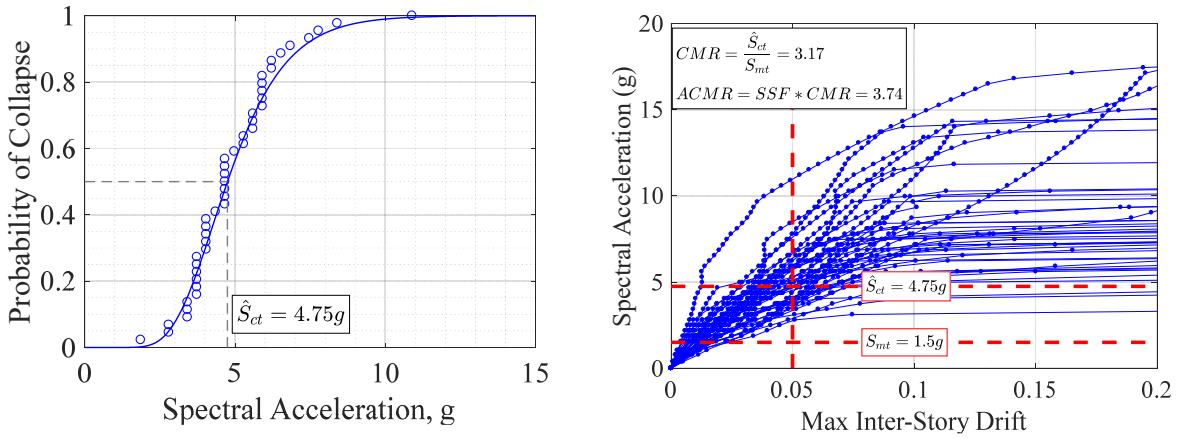

d)

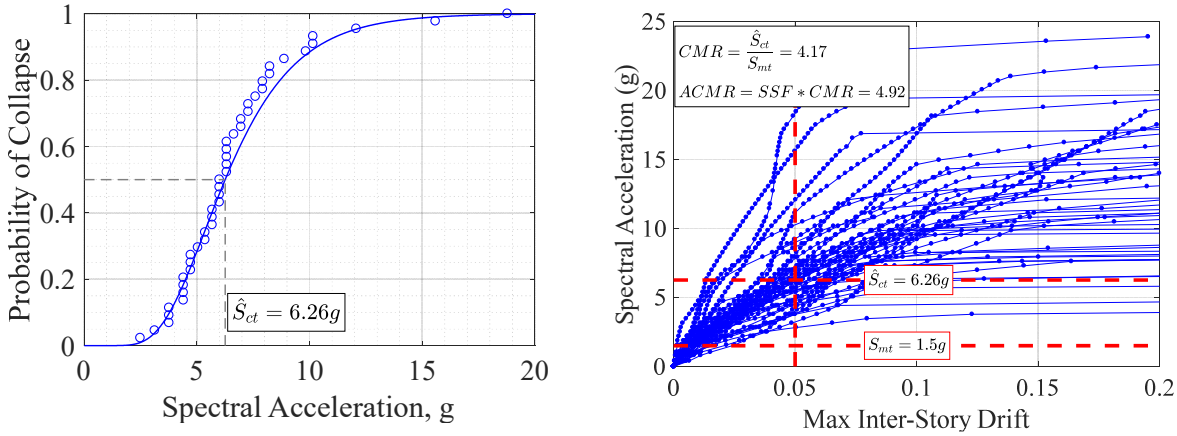

e)

Figure 10-15. (Continued)

Table 10-10. Incremental dynamic analysis (IDA) results of 3-Story archetypes (Units: kips, in, sec., g)

Parameter	63% CR	48% CR	54% CR	48.5% CR	32% CR
S_{CT}	4.51	4.91	5.04	4.75	6.26
S_{MT}	1.5	1.5	1.5	1.5	1.5
CMR = S_{CT}/S_{MT}	3.01	3.27	3.36	3.17	4.17
ACMR	3.55	3.86	3.96	3.74	4.92

10.4.8 Extra Studies

10.4.8.1 Plastic Hinge Length Study

It was mentioned in a previous section that the nonlinear beam-column elements were only assigned to the first floor of the walls to model the plastic hinging of the walls. However, the plastic hinge length is

physically defined by the distance from the point of maximum moment (at the base of the wall here) to the point along the height where the cross-section starts to yield. It was observed from pushover analysis of archetype models that this point of first yielding of the wall cross-sections can actually be up to the height of the third story. Therefore, a plastic hinge length study was performed for archetypes PG-1A, PG-1D, PG-3A, and PG-3D to investigate if IDA results were sensitive to the effect of using longer plastic hinge lengths. For this study, the region over which nonlinear elements were used was increased to 19ft. (2ft. above 1st floor), 31ft. (2nd floor), and 45ft. (3rd floor) in the models of the chosen archetypes and analyses were run with the N-S component of the Superstition Hills (BICC090) earthquake at their corresponding spectral acceleration levels at 5% maximum interstory drift. Figure 10-16 shows that increasing the plastic hinge length did not affect the IDA curve. For example, the maximum error observed in these plots is 6.4% in Figure 10-16c.

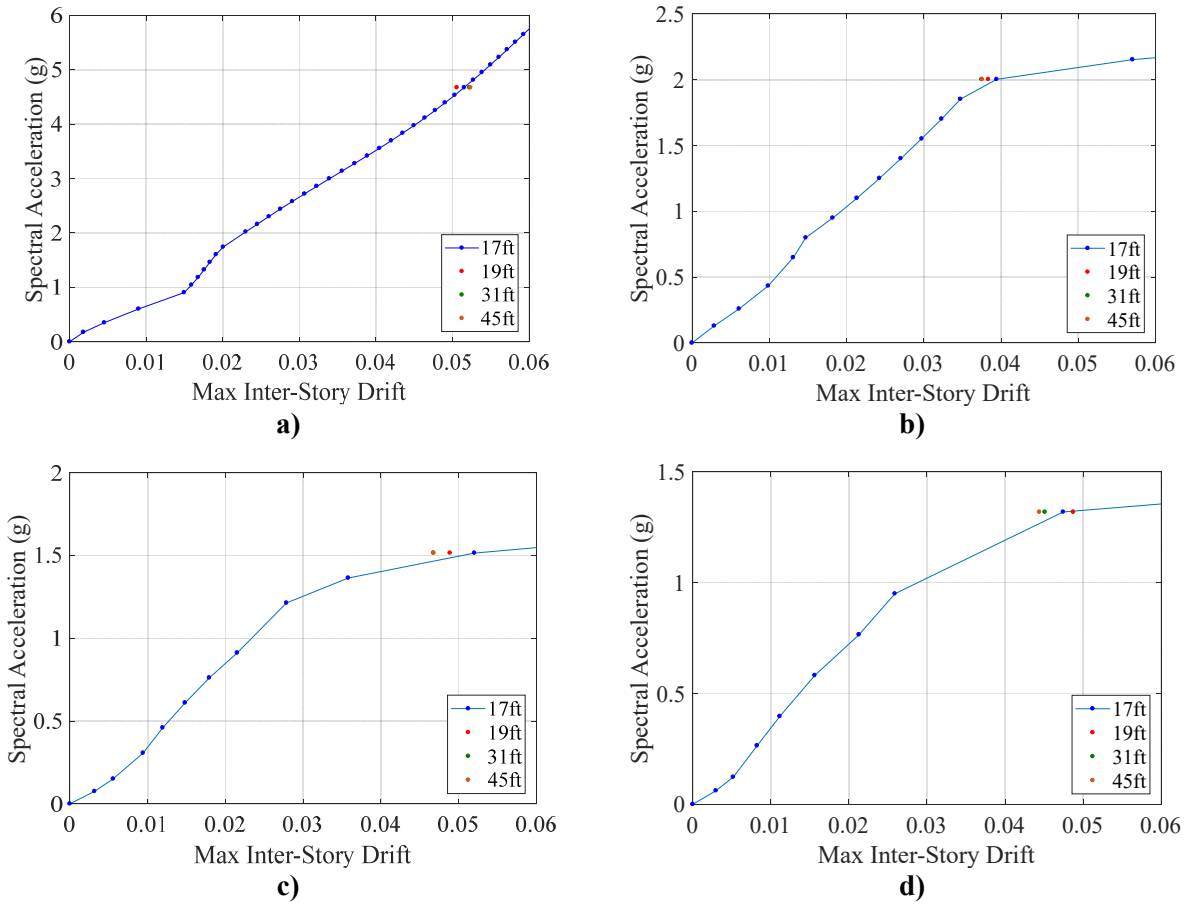

Figure 10-16. Hinge length study done for: a) PG-1A, b) PG-1D, c) PG-3A, and; d) PG-3D

10.4.8.2 Damping Ratio Study

In the nonlinear time history analyses of the archetypes, Rayleigh damping was used, with a value of 5% damping specified for the first and second periods of vibration. However, later, it was noticed that first and second modes of vibration contribute to only 80% of the total mass participation factor. It was further observed that in all of the archetypes, 90% of total mass participation factor contributing to the nonlinear analysis when the first four modes of vibration were considered, and additional analyses were therefore run with Rayleigh damping values of 5% anchored at the first and fourth periods of vibrations. In these subsequent analyses, the damping ratio was also reduced to a value based on the height of the structure, in accordance with the following equation from PEER TBI Section 4.2.7 (PEER 2010):

$$\xi_{critical} = \frac{0.36}{\sqrt{H}} \quad \textbf{(10.1)}$$

where H is the height of the structure in feet.

Therefore, for this study of sensitivity of results to damping values, the PG-1D archetype was selected. Figure 10-17a shows the IDA results obtained for the PG-1D archetype with a 5% damping ratio anchored at the first and second periods of vibration. Then, the same archetype was run with 2.75% damping ratio, obtained from Equation 10.1, anchored at the first and fourth periods of vibration. The resulting adjusted collapse margin ratio (ACMR) decreased by 8.6% (Figure 10-17b).

After further studying the behavior of these lateral loading resisting systems, it was observed that the composite walls are behaving individually at a much larger period of vibration after all coupling beams have fractured (the walls would also eventually develop a rocking behavior once fully fractured). As a result, the period of the system elongates significantly during that stage. In order to prevent overdamping of the structural system when it shifts to those higher periods of vibration, it was decided to also perform analyses with 2.75% damping ratio anchored at five times the first period and at the fourth period of vibration. With this significantly less damped model, the ACMR of PG-1D decreased by 27.2%, from 4.05 to 2.95, compared to the IDA results initially obtained from 5% damping (Figure 10-17c). However, note that even for these significantly less damped walls, the lower ACMR obtained were still sufficient to meet the FEMA P695 limits (refer to Section 10.4.5).

To ensure that other archetypes also meet the FEMA P695 ACMR limits when subjected to significantly lower damping, all the archetypes that were previously found to have the worst ACMR in their corresponding groups (i.e., PG-1C, PG-1D, PG-3C, and PG-3D) were re-analyzed with a lesser damping

ratio, as calculated from equation 10.1 and anchored at five times the first period and at the fourth period of vibration. It was believed that if the worst ACMR value in a performance group was found to have an acceptable ACMR when considering this reduced damping, then the others would also be adequate. Figure 10-18 shows the results of these additional IDA analyses for the selected archetypes. Table 10-11 summarizes these results for these selected archetypes for the various damping ratios considered. Among all selected archetypes, only PG-1C, with a 1.93 ACMR value, did not satisfy the $ACMR_{20\%}$ limit of 1.96 (refer to Section 10.4.5). However, the difference between ACMR and $ACMR_{20\%}$ limit is marginal (namely, a 0.03 difference), and negligible considering that the anchored period (chosen to capture the period elongation after all coupling beam fracture) was taken as the extreme case of being at five times the first period of vibration. Using such an extreme anchoring period resulted in a damping ratio of less than 1% at the first period of vibration which contributes to 80% of the total modal participation factor (as listed in Table 10-11). Therefore, all ACMR of the archetypes considered are considered to be satisfactory for this lower damping.

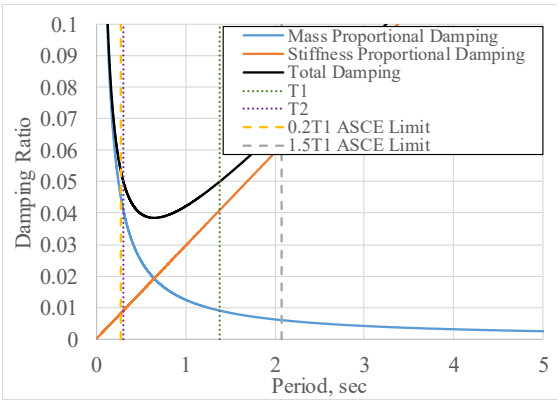

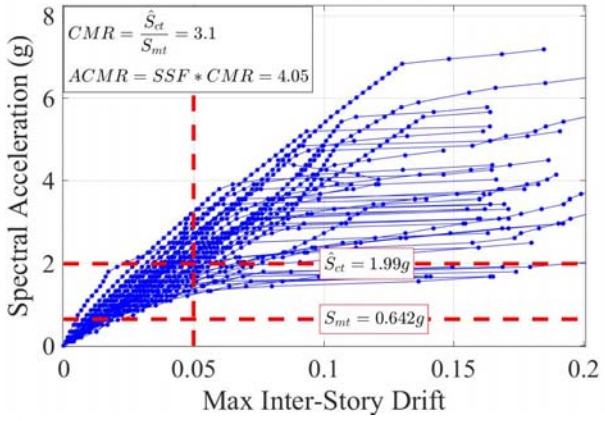

a)

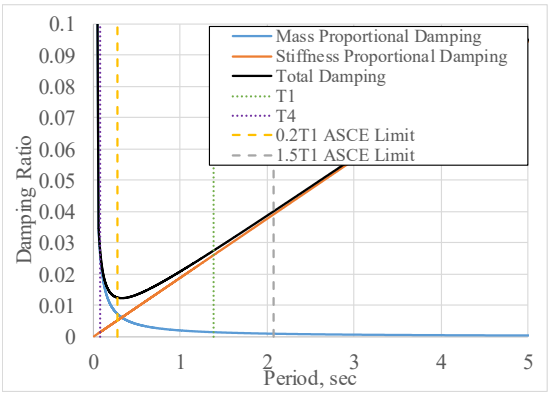

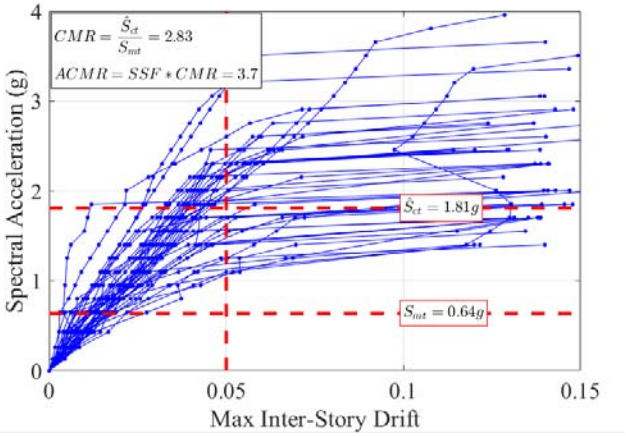

b)

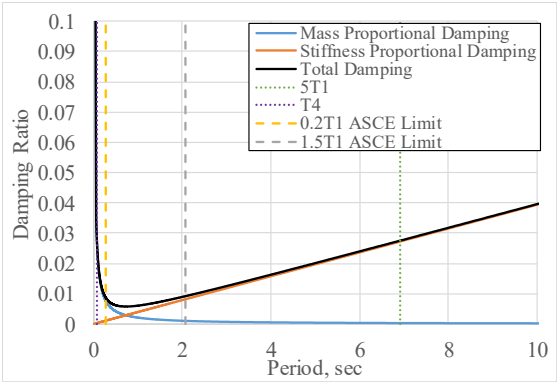

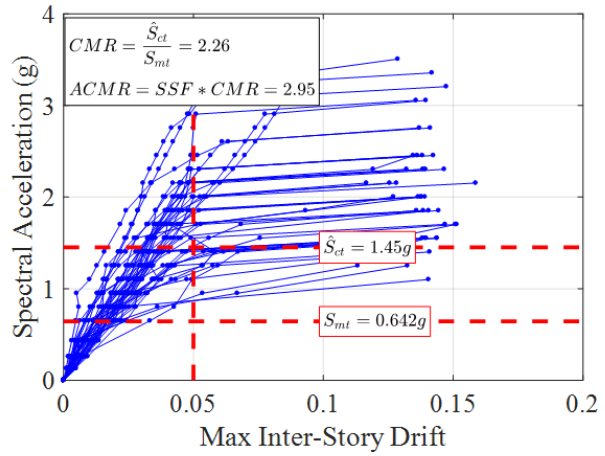

c)

Figure 10-17. Results for PG-1D with Rayleigh Damping ratio set to: a) 5% at the 1st and 2nd periods, b) 2.75% at the 1st and 4th periods, and; c) 2.75% at 5 time the 1st period and 4th period

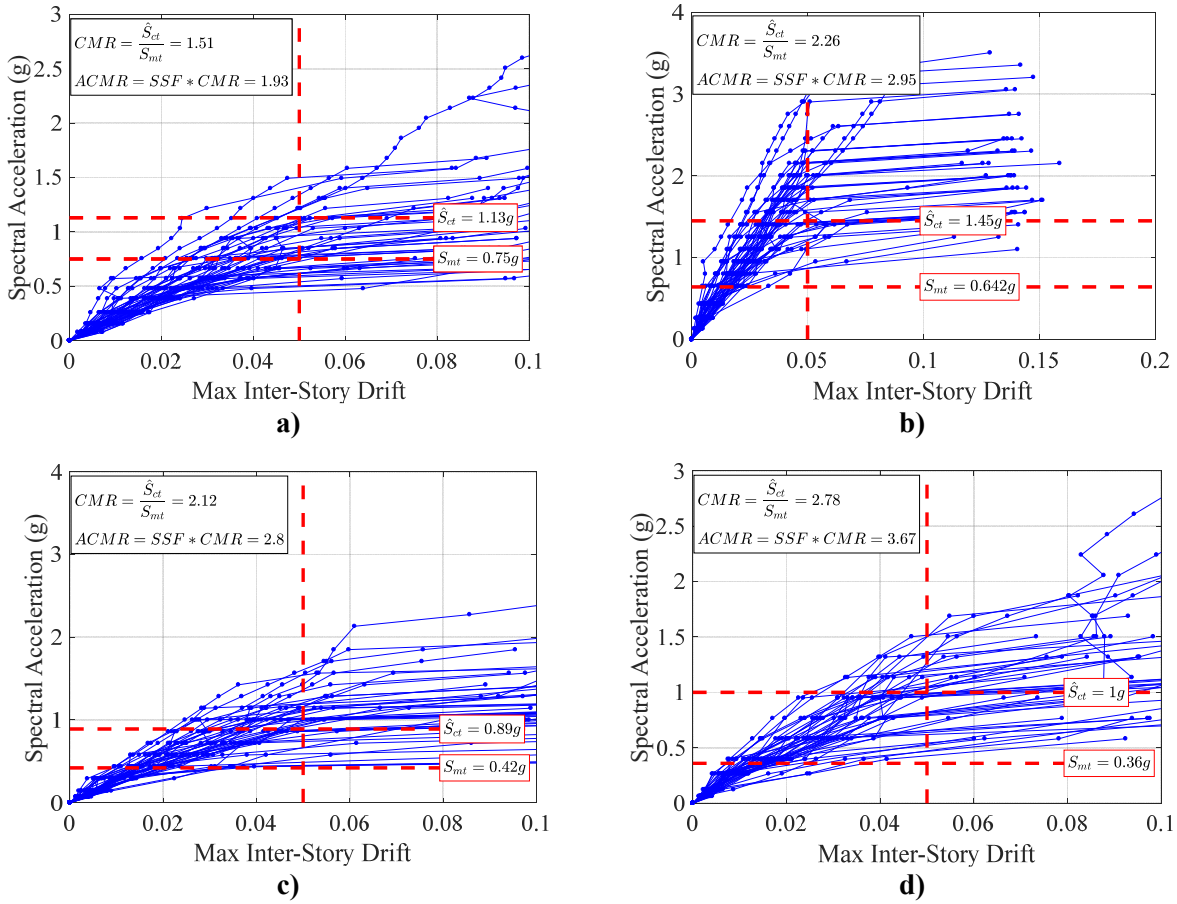

Figure 10-18. Reduced damping study done for: a) PG-1C, b) PG-1D, c) PG-3C, and; d) PG-3D

Table 10-11. Incremental dynamic analysis (IDA) results of PG-1C, PG-1D, PG-3C, and; PG-3D archetypes with reduced damping ratio
(Units: kips, in, sec., g)

Parameter	PG-1C	PG-1D	PG-3C	PG-3D
S_{CT}	1.13	1.45	0.89	1.0
S_{MT}	0.75	0.642	0.42	0.36
First Period	1.192	1.382	2.14	2.49
Damping Ratios at First Period	0.88%	0.7%	0.596%	0.511%
CMR = S_{CT}/S_{MT}	1.51	2.26	2.12	2.78
ACMR	1.93	2.95	2.8	3.67

10.5 Incremental Dynamic Analysis Abaqus Models

Incremental Dynamic Analysis was performed in Abaqus to establish a baseline performance for 8 and 12 story structures. These models were particularly instructive as these models included shell elements and the post-processing and visualization capabilities of Abaqus are much more advanced than OpenSees. 18 and 22 story structures were not analyzed as

10.5.1 Finite element modeling of CC-PSW/CF

A 2D multi-story finite element model of CC-PSW/CF was modeled using the proposed phenomenological effective stress-strain curves. In the 2D model, shear walls and coupling beams are modeled using four-node composite shell elements with reduced integration (S4R). Steel flange plates of shear walls and coupling beams are modeled using three-dimensional two-node truss elements (T3D2). Additionally, in order to consider P-Δ effects, the gravity frames are modeled with truss elements (T3D2). A typical 2D multi-story finite element model of CC-PSW/CF is shown in Figure 10-19.

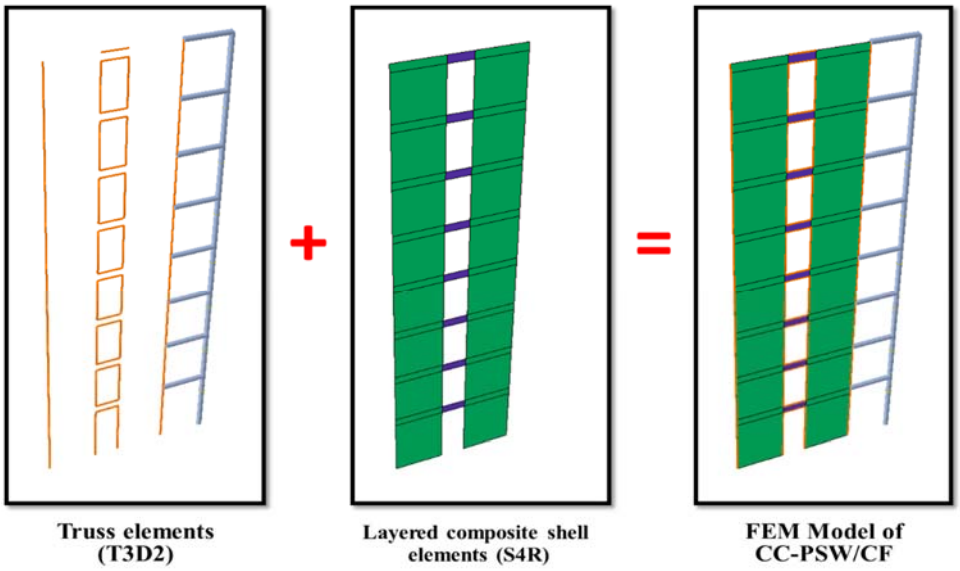

Figure 10-19. A typical 2D multi-story finite element model of CC-PSW/CF.

Mesh sensitivity analysis was conducted in order to understand the effect of mesh size on the lateral stiffness and response of multi-story CC-PSW/CF. Figure 10-20 and Figure 10-21 show the results of a typical 8-story CC-PSW/CF subjected to equivalent lateral force (ELF). According to the figures, the mesh size of 12 in. is able to model the behavior of multi-story CC-PSW/CF with efficient computational run time. Using

a fine mesh considerably increases the computational run time, so conducting nonlinear static pushover or dynamic time-history analysis with a more refined mesh would take too much time.

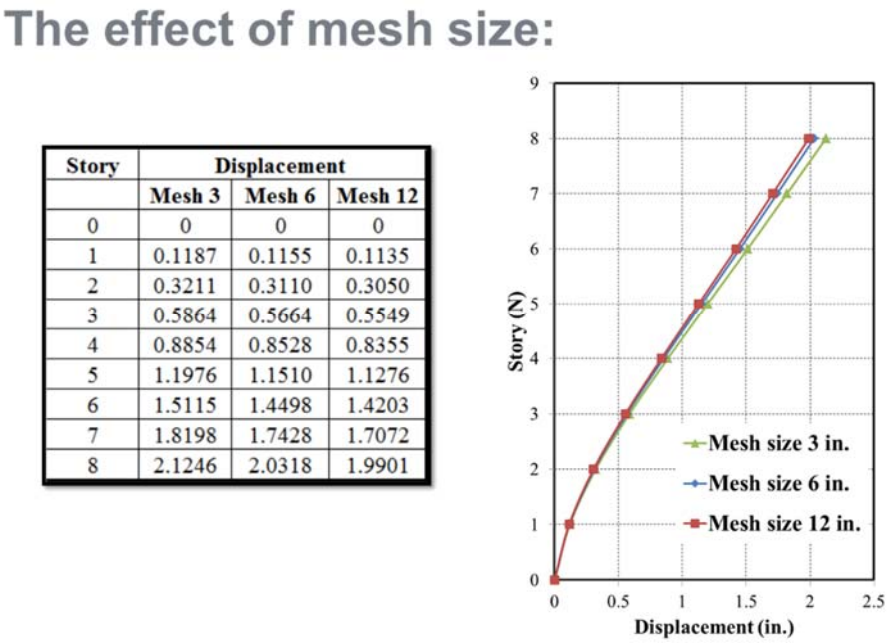

Figure 10-20. The effect of mesh size on the lateral displacement of an 8-story CC-PSW/CF.

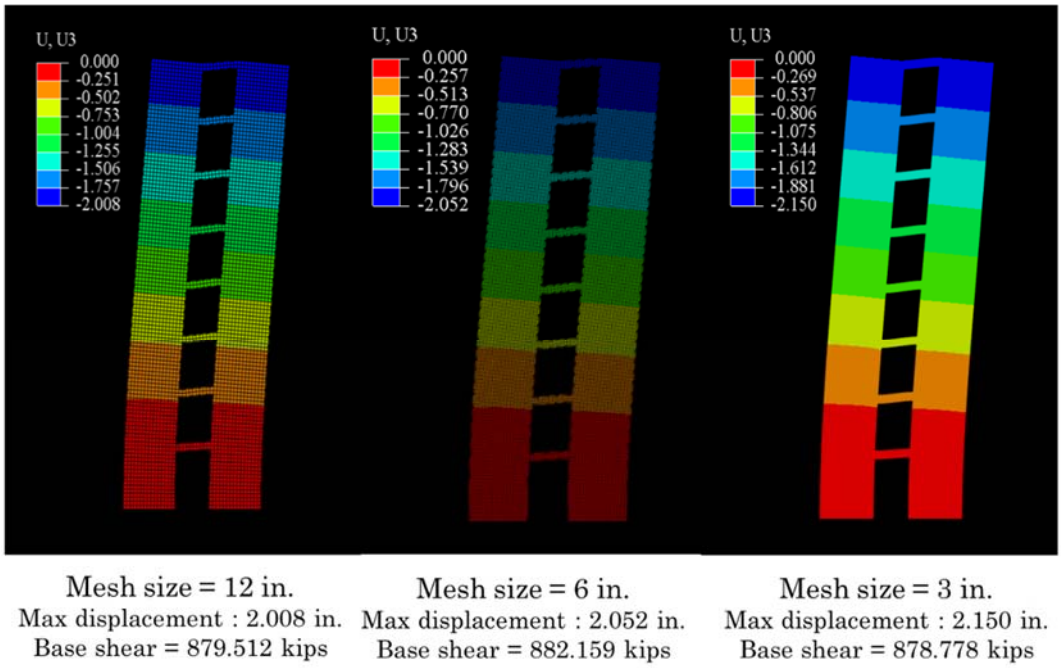

Figure 10-21. The effect of mesh size on the deformation of an 8-story CC-PSW/CF.

10.5.2 Modal analysis of CC-PSW/CF

Modal analyses of archetype CC-PSW/CF structures were conducted using the 2D finite element model discussed in the previous section. The period and natural frequency of CC-PSW/CF structures can also be calculated using modal analysis results. Figure 10-22 shows the natural frequencies and the first to fourth mode shapes of PG-1B structure. The first mode shapes of 8- and 12-story archetype structures are shown in Figure 10-23.

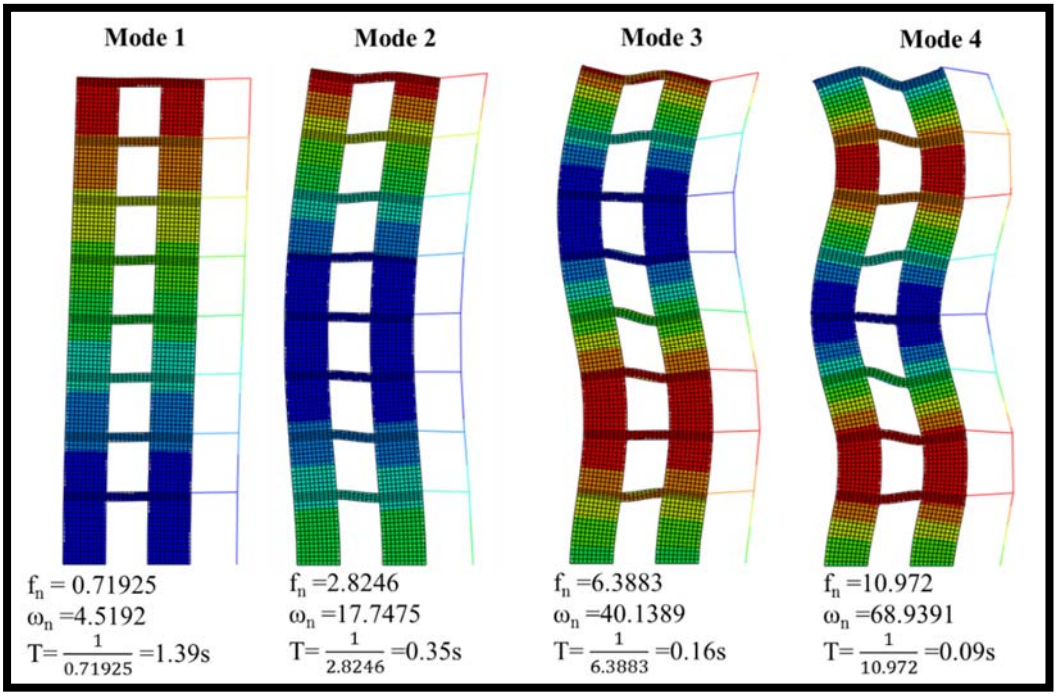

Figure 10-22. Mode shapes of PG-1B structure.

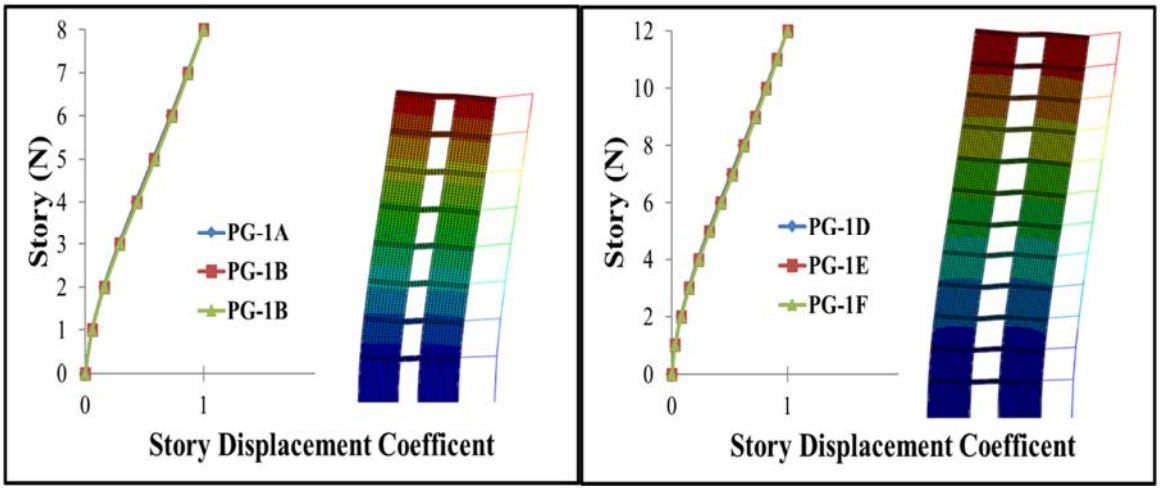

Figure 10-23. The first mode shapes of 8- and 12-story archetype structures.

10.5.3 Pushover analysis of CC-PSW/CF:

Pushover analyses of the 8- and 12-story archetype structures were completed to understand the response of CC-PSW/CFs. Composite shear walls and composite coupling beams were modeled using composite layered shell element. All steel flange plates of shear walls and coupling beams were modeled using truss elements. Additionally, a gravity frame was added to CC-PSW/CF to consider the effect of P-Δ on the lateral load behavior of the system.

At the first step, gravity loads were applied to gravity frame, as shown in Figure 10-24, and became constant. In the next step, lateral load (triangular loading) was applied according to the first mode.

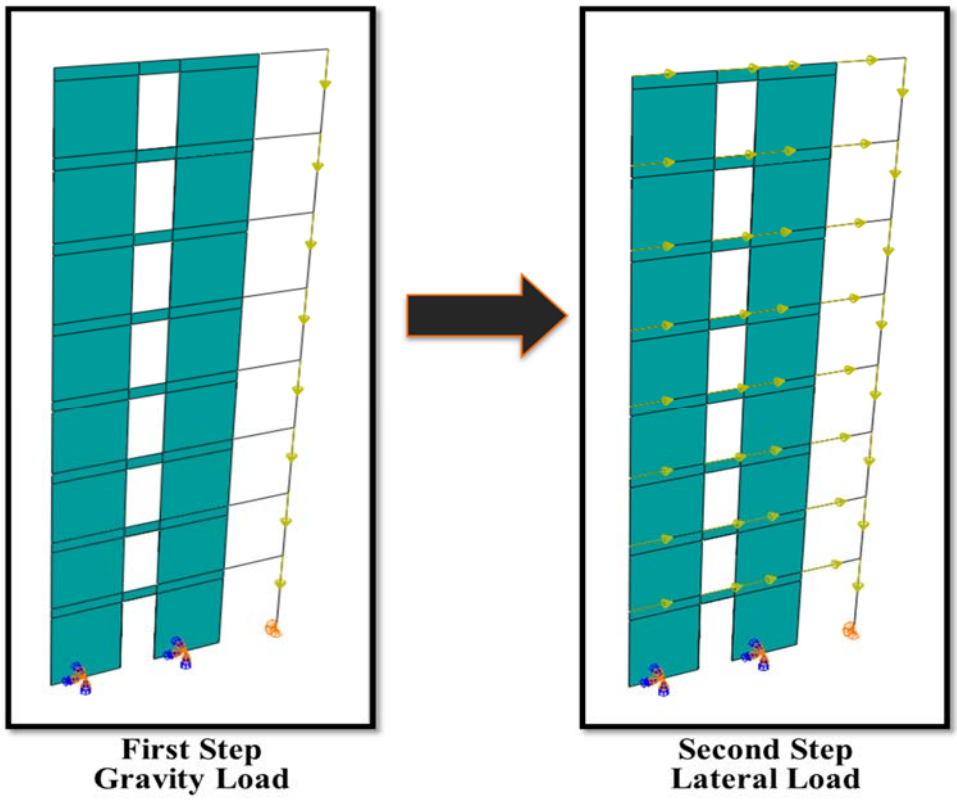

Figure 10-24. Loading of CC-PSW/CF in pushover analysis: (a) Gravity (b) Lateral.

A typical pushover response and the von Mises stress distribution of CC-PSW/CF are shown in Figure 10-25 and Figure 9-10-26. The elastic branch represents the initial lateral response of the CC-PSW/CF structure and the slope of this branch represents the effective structural stiffness.

On the base shear-roof displacement curve, Point A represents the lateral load level corresponding to the ELF distribution. The coupling beams are designed to have a flexural capacity adequate for this demand level. As the lateral load (and base shear force) increases, the coupling beams along the height of the structure undergo flexural plastic hinging at both ends. The response reaches the next milestone, Point B, where all of the coupling beams have developed flexural hinges. The composite walls are designed to have a flexural capacity adequate to resist this demand level. The next milestone on the response, Point C, corresponds to the overall inelastic mechanism with flexural plastic hinging in all of the coupling beams and the base of the composite walls. A final milestone, point D, represents fracture failure of the composite walls. The overstrength factor for this system, defined as the ratio of ultimate load capacity to capacity at ELF level loads, is approximately the ratio of base shear force at Point C to Point A.

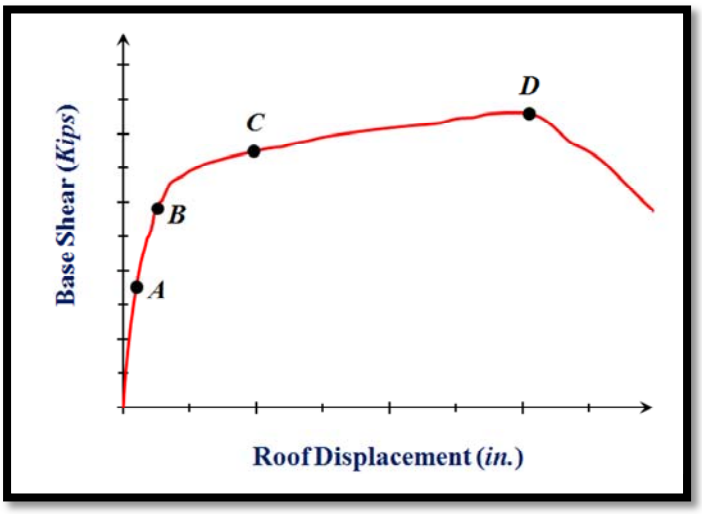

Figure 10-25. A typical pushover response of CC-PSW/CF.

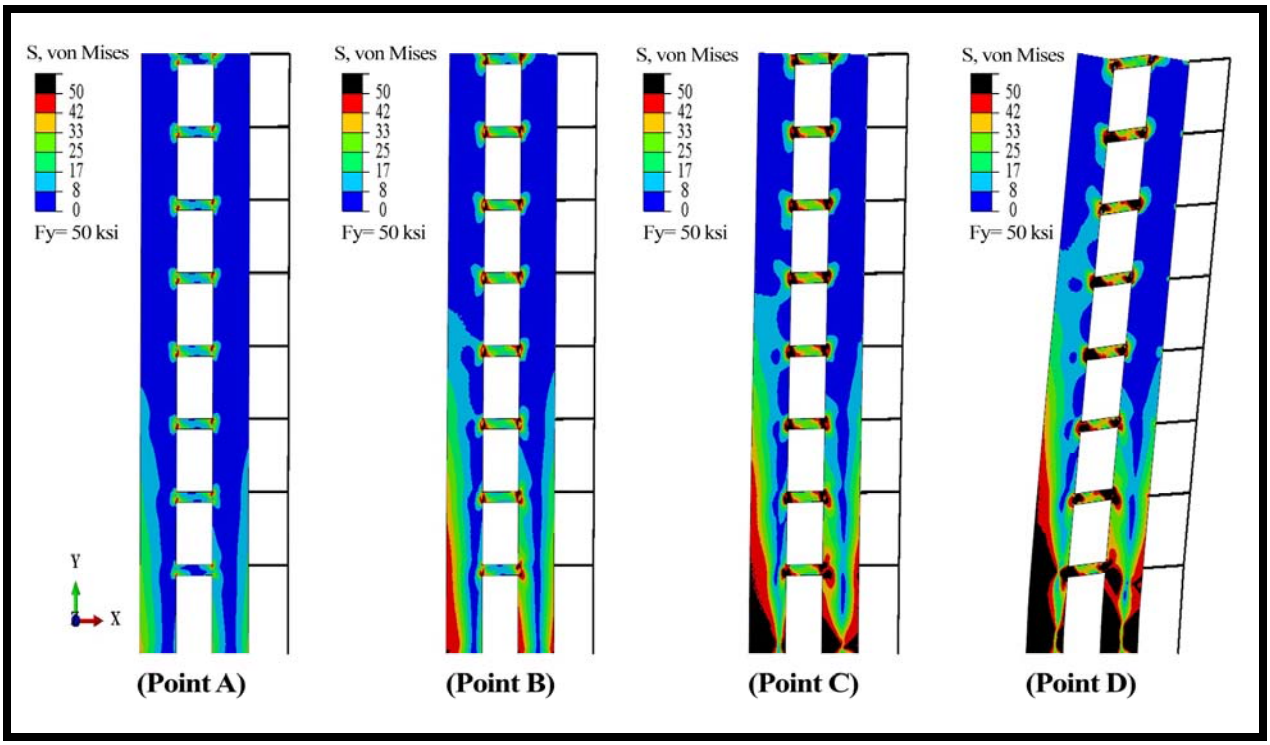

Figure 9-10-26. The von Mises stress distribution on the steel face plates for different points on pushover curve

10.5.4 Nonlinear time-history analysis of CC-PSW/CF:

Nonlinear dynamic time-history analyses of archetype CC-PSW/CF structures were conducted using the 2D finite element model and the phenomenological effective stress-strain curves. Figure 10-27 illustrates the roof displacement and interstory drift of the 12-story PG-1E structure subjected to a ground motion with scale factor of 7. The ground motion record is Superstition Hills earthquake occurred in 1987, as shown in Figure 9-10-28.

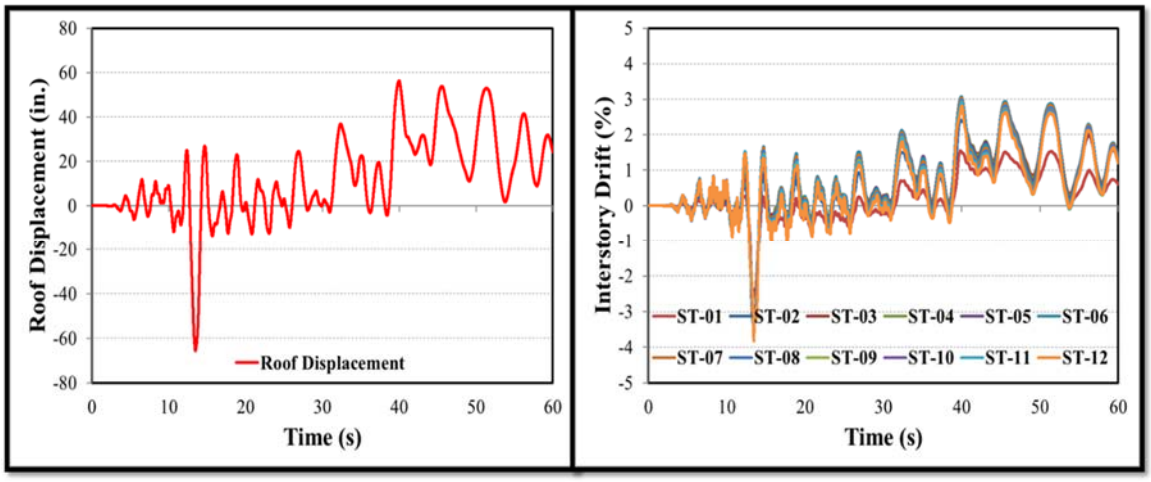

Figure 10-27. (a) Roof displacement of PG-1E at the scale factor of 7 (b) Interstory drift at the scale factor of 7.

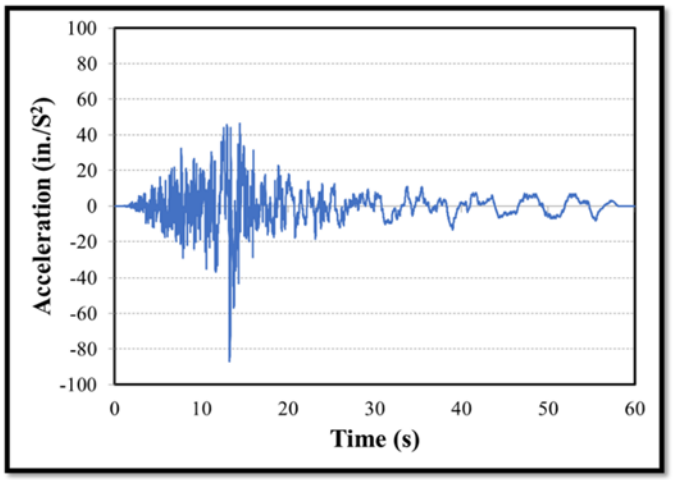

Figure 9-10-28. Ground motion (BICC090-16-2).

Figure 10-29 shows the collapse process of the 12-story PG-1E structure. The major events in the dynamic response are the following: (1) flexural yielding of composite coupling beams, (2) flexural yielding of C-PSW/CF, (3) propagation of yielding of coupling beam connections over C-PSW/CF height and plastic hinge formation, (4) fracture initiation of coupling beams and plastic hinge formation at the bottom of C-PSW/CFs, (5) fracture initiation of C-PSW/CFs, (6) total fracture of composite coupling beams, (7) the end of earthquake record.

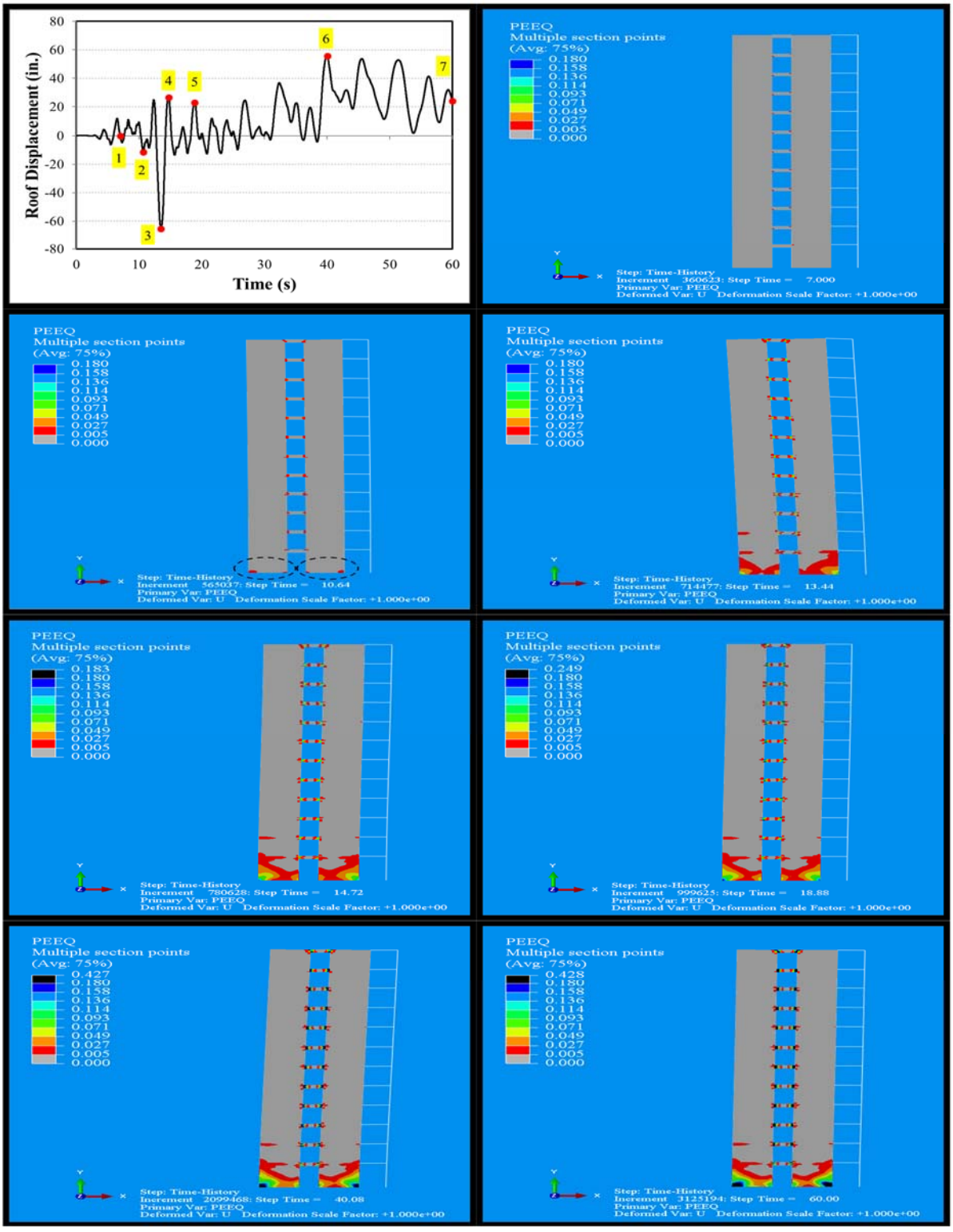

Figure 10-29. Nonlinear time history analysis of PG-1E.

10.5.5 Incremental dynamic analysis of CC-PSW/CF

Incremental dynamic analyses of 8- and 12-story archetype structures of CC-PSW/CF were conducted using 2D finite element model. Figure 10-30 depicts the results of incremental dynamic analyses of archetype structures of CC-PSW/CF.

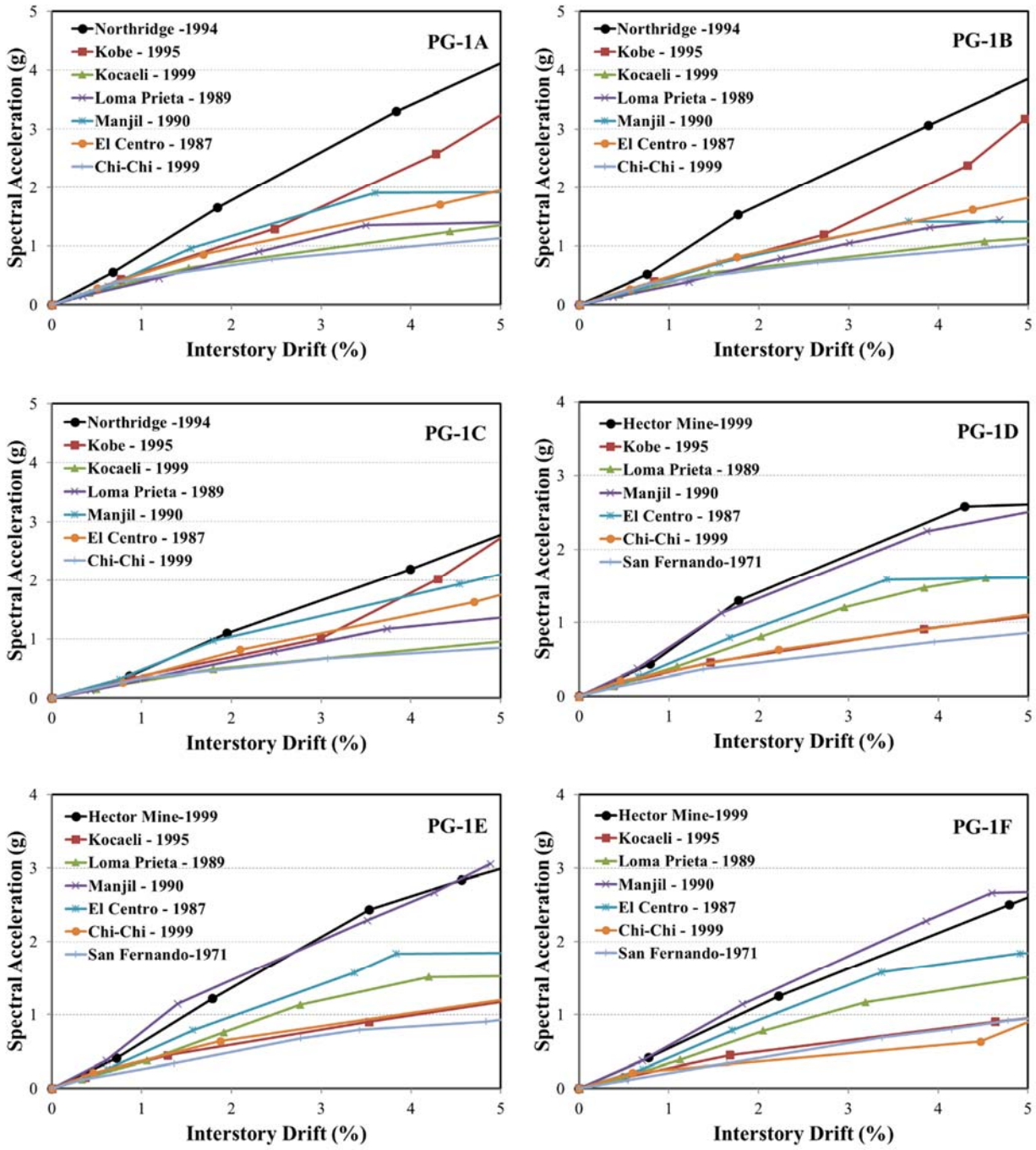

Figure 10-30. Incremental dynamic analysis (IND) of 8- and 12-story archetype structures.

10.6 Incremental Dynamic Analysis with Concentrated Plasticity Models

Incremental dynamic analysis (IDA) was performed on the concentrated plasticity archetype models for the 44 ground motions. These results were processed to yield the collapse margin ratios and other relevant data. The archetype modeling process, incremental dynamic analysis, collapse margin ratio, and adjusted collapse margin ratios are detailed in the following sections.

10.6.1 Models of the Archetypes

The concentrated plasticity models involved coupling walls defined with nonlinear fiber elements with representative concentrated plasticity rotational spring elements as coupling beams. A representation of this model is presented in Figure 10-31. Archetype dimensions are presented in Table 5-4, Table 5-5, Table 5-6, Table 5-7, and Table 5-8.

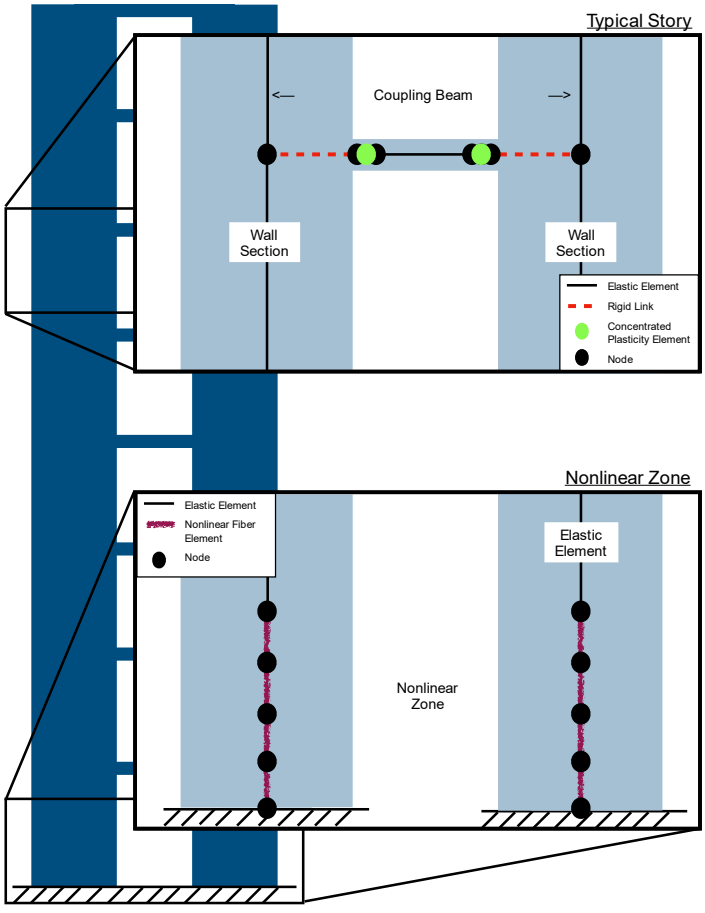

Figure 10-31. Depiction of element and node distribution in archetype models.

10.6.1.1 Archetype Walls

The wall behavior is based on the calibrated material model and element distribution presented before in Section 8.1. The parameters presented in Table 10-12 and Table 10-13 are used to model the material behavior.

Above the nonlinear wall section, elastic elements are used. For planar walls, these elements have an effective stiffness per the AISC 360 Eq. I2-12. For C-shape walls, the design procedure effective stiffness (Section 3.3.1) was used for the elastic elements.

Table 10-12. Concrete material parameters to fit assumed stress-strain curves.

Parameter	Value		Parameter	Value
f_{pc} (ksi)	6.0		f_t (ksi)	$0.1*f_{pc}$
e_{psc0}	0.0022		e_t	8e-5
f_{pcu} (ksi)	$0.6*f'_c$		λ	0.1
e_{psu}	0.008			

Table 10-13. Steel material parameters to fit assumed stress-strain curves.

Parameter	Value		Parameter	Value
E (ksi)	29000		L_{sr}	10.0
b	0.01		beta	1.0
E_{sh} (ksi)	E*b		r	0.65
F_y (ksi)	50		gamma	0.50
F_u (ksi)	65		C_f	0.60
e_{sh}	$2*F_y/E$		alpha	0.50
e_{ult}	0.1		C_d	0.35

10.6.1.2 Archetype Coupling Beams

The concentrated plasticity elements are calibrated to the performance of fiber elements in a similar configuration to the tests described in Nie et al. (2014). This process was very similar to the calibration of concentrated plasticity elements as described in Section 8.3; however, the elastic hinge previously used to

represent rotation through the wall elements was removed. The elastic elements connecting the plastic hinges remained with an effective stiffness defined by AISC Equation I2-12.

Initially, concentrated plasticity elements used the Modified Ibarra-Medina-Krawinkler Deterioration Model with Pinched Hysteretic Response ("IMK with pinching hinge") detailed in Figure 8-38. A comparison of the fiber based distributed plasticity coupling beam model to the concentrated plasticity coupling beam chosen for PG-1B is presented in Figure 10-32; other coupling beams concentrated plasticity models similarly mirrored the distributed plasticity model results. The concentrated plasticity model closely follows the distributed plasticity behavior with the initial stiffness, post yield slope, descending branch, and residual strength showing close correlation. Coupling beam parameters used for PG-1 and PG-2 structures are shown in Table 10-14 and Table 10-15, respectively. The yield moment was varied based on the section capacity while other parameters were kept constant including the initial stiffness, post-yield strength and rotation milestones. This hinge was used for 3, 8, and 12 story structures but proved unstable for the 18 and 22 story structures. Therefore, other concentrated plasticity elements were investigated. A Modified Ibarra-Medina-Krawinkler Deterioration Model with Bilinear Hysteretic Response ("IMK with bilinear hinge") was selected as this hinge proved more computationally stable and still could modeled the fiber-based coupling beam response well. This hinge was used for 8, 12, 18, and 22 story structures.

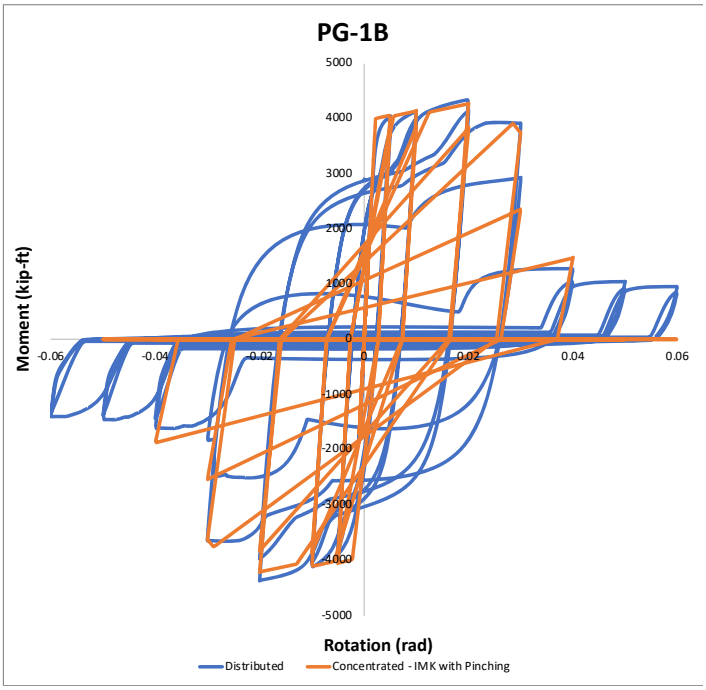

Figure 10-32. Moment versus rotation behavior for IMK with pinching hinge coupling beams of PG-1B.

Table 10-14. Parameters for IMK with pinching hinge coupling beams *See Table 10-15.

Parameter	Value	Parameter	Value	Parameter	Value
Stiffness, K_0	2.5e7	**λ_S**	1	**c_S**	**1**
Post yield stiffness coefficient, a_s	Varies*	**λ_C**	1	**c_C**	1
Yield Moment, My	Varies*	**λ_A**	0.5	**c_A**	0.5
Rotation at peak, Θ_p	0.025	**λ_K**	0.5	**c_K**	0.5
Rotation at post capping, Θ_{pc}	0.04	**Residual capacity ratio**	0.25	**F_{pr}**	1
Ultimate Rotation, Θ_u	0.05	**D**	1	**A_{Pinch}**	1

Table 10-15. Variable Parameters for IMK with pinching hinge coupling beams.

Structure	Post Yield Stiffness, a_s	Coupling Beam Yield Moment, M_y
PG-1A	0.005	18500
PG-1B	0.005	24000
PG-1C	0.005	23500
PG-1D	0.005	16000
PG-1E	0.005	20500
PG-1F	0.005	22500
PG-2B	0.0015	4700
PG-2E	0.0015	4150

The format of the IMK with bilinear hinge is similar to the IMK with pinching hinge with the envelope definition relying on the same backbone as shown in Figure 10-33 and Table 10-16. A comparison of the fiber based distributed plasticity coupling beam model to the IMK with bilinear hinge coupling beam for PG-1B is presented in Figure 10-34; other coupling beams concentrated plasticity models similarly mirrored the distributed plasticity model results. The IMK with bilinear hinge model closely follows the distributed plasticity behavior with the initial stiffness, post yield slope, and residual strength showing close correlation. However, this hinge does not have reloading behavior of the IMK with pinching hinge. The pinched reloading behavior is an important component of the hinge model because this response accounts for the concrete crack closure. To simulate this behavior, the reloading stiffness of the calibrated IMK with

bilinear hinge was compromised. The coupling beam parameters used are replicated in Table 10-17 and Table 10-18. The yield moment was varied based on the section capacity while other parameters including the initial stiffness, post-yield strength and rotation milestones were kept constant.

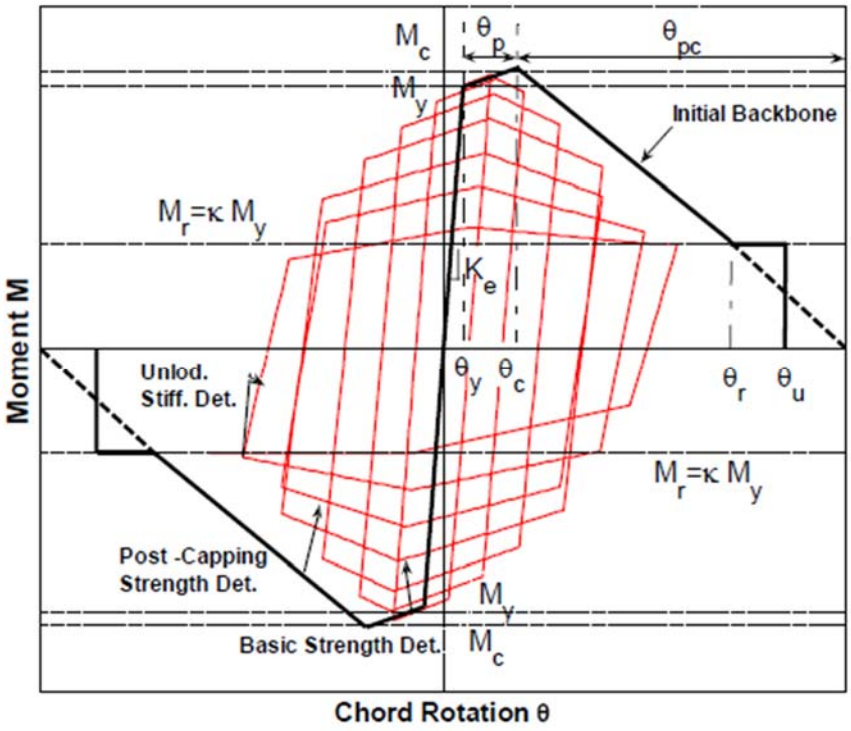

Figure 10-33. Modified Ibarra-Medina-Krawinkler Deterioration Model with Bilinear Hysteretic Response (OpenSees).

Table 10-16. Parameters for Modified Ibarra-Medina-Krawinkler Deterioration Model with Bilinear Hysteretic Response (OpenSees).

Parameter	Description		Parameter	Description
$\mathbf{K_0}$	Elastic stiffness		$\boldsymbol{\lambda_S}$	Cyclic deterioration parameter for strength deterioration
$\mathbf{a_s}$	Strain hardening ratio		$\boldsymbol{\lambda_C}$	Cyclic deterioration parameter for post-capping strength deterioration
$\mathbf{M_y}$	Yield Moment		$\boldsymbol{\lambda_A}$	Cyclic deterioration parameter for accelerated reloading stiffness deterioration
$\mathbf{A_{Pinch}}$	Ratio of reloading stiffness		$\boldsymbol{\lambda_K}$	Cyclic deterioration parameter for unloading stiffness deterioration
$\boldsymbol{\theta_p}$	Pre-capping rotation		$\mathbf{c_S}$	Rate of strength deterioration
$\boldsymbol{\theta_{pc}}$	Post-capping rotation		$\mathbf{c_C}$	Rate of post-capping strength deterioration
$\boldsymbol{\theta_u}$	Ultimate rotation capacity		$\mathbf{c_A}$	Rate of accelerated reloading deterioration
Res	Residual strength ratio		$\mathbf{c_K}$	Rate of unloading stiffness deterioration
D	Rate of cyclic deterioration		**nFactor**	Elastic stiffness amplification factor

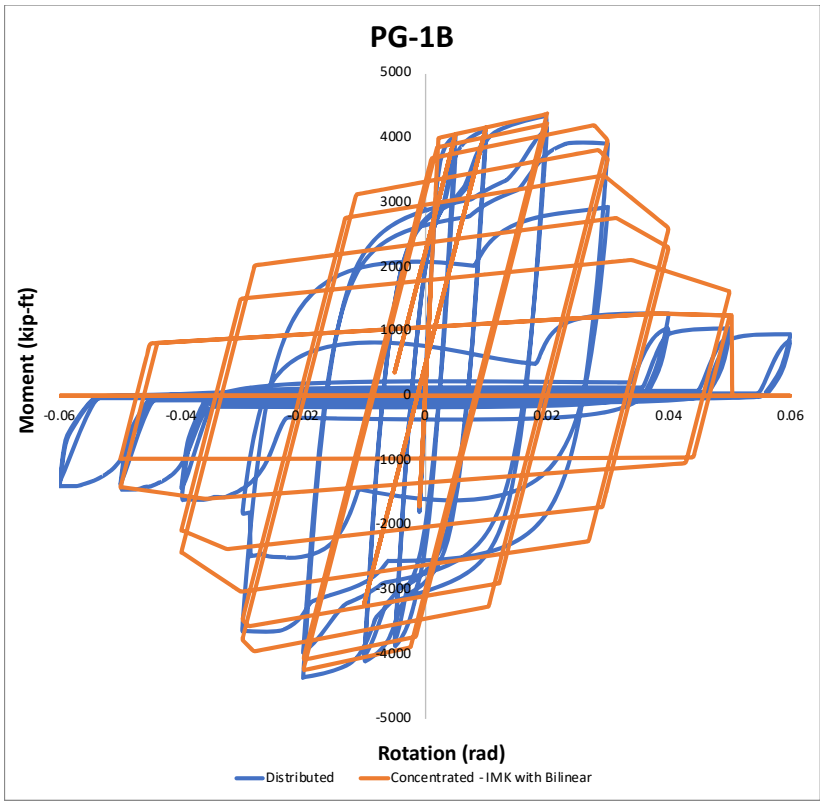

Figure 10-34. Moment versus rotation behavior for IMK Bilinear hinge coupling beams of PG-1B.

Table 10-17. Parameters for IMK with bilinear hinge coupling beams *See Table 10-18 .

Parameter	Value	Parameter	Value	Parameter	Value
Stiffness, K_0	Varies*	**λ_S**	0.5	**c_S**	1.0
Post yield stiffness coefficient, a_s	Varies*	**λ_C**	1.0	**c_C**	0.0
Yield Moment, My	Varies*	**λ_A**	1.0	**c_A**	1.0
Rotation at peak, Θ_p	0.025	**λ_K**	1.0	**c_K**	1.0
Rotation at post capping, Θ_{pc}	0.04	**Residual capacity ratio**	0.25	**nFactor**	0
Ultimate Rotation, Θ_u	0.05	**D**	1	**A_{Pinch}**	1

Table 10-18. Variable Parameters for IMK with pinching hinge coupling beams.

Structure	Stiffness, K_0	Post Yield Stiffness, a_s	Coupling Beam Yield Moment, M_y
PG-1A	2.5e7	0.005	18500
PG-1B	2.5e7	0.005	24000
PG-1C	2.5e7	0.005	23500
PG-1D	2.5e7	0.005	16000
PG-1E	2.5e7	0.005	20500
PG-1F	2.5e7	0.005	22500
PG-2B	2.5e7	0.0015	4700
PG-2E	2.5e7	0.0015	4150
PG-3A	5.0e7	0.005	31800
PG-3B	5.0e7	0.005	44100
PG-3C	5.0e7	0.005	49700
PG-3D	5.0e7	0.005	37200
PG-3E	5.0e7	0.005	44100
PG-3F	5.0e7	0.005	57000
PG-4B	5.0e7	0.0015	11950
PG-4 E	5.0e7	0.0015	13400

10.6.2 Incremental Dynamic Analysis of Archetypes

Incremental Dynamic Analysis (IDA) was performed to evaluate the Collapse Margin Ratio of each structure. Per the FEMA procedure, 44 ground motions (22 earthquakes with two components) at a variety of scale factors were run. The scale factor was increased until a drift of 5% was reached. Through comparing the performance, the median spectral acceleration value ($\hat{S}_{CT}$) can be determined.

This analysis was first performed with the IMK with pinching hinge for PG-1 and PG-2 structures as well as the 3 story structures. PG-1 structures results are shown in Figure 10-35 to Figure 10-40 for each archetype structure. PG-2 responses can be found in Figure 10-41 and Figure 10-42. 3-story structure results are in Figure 10-43 to Figure 10-45.

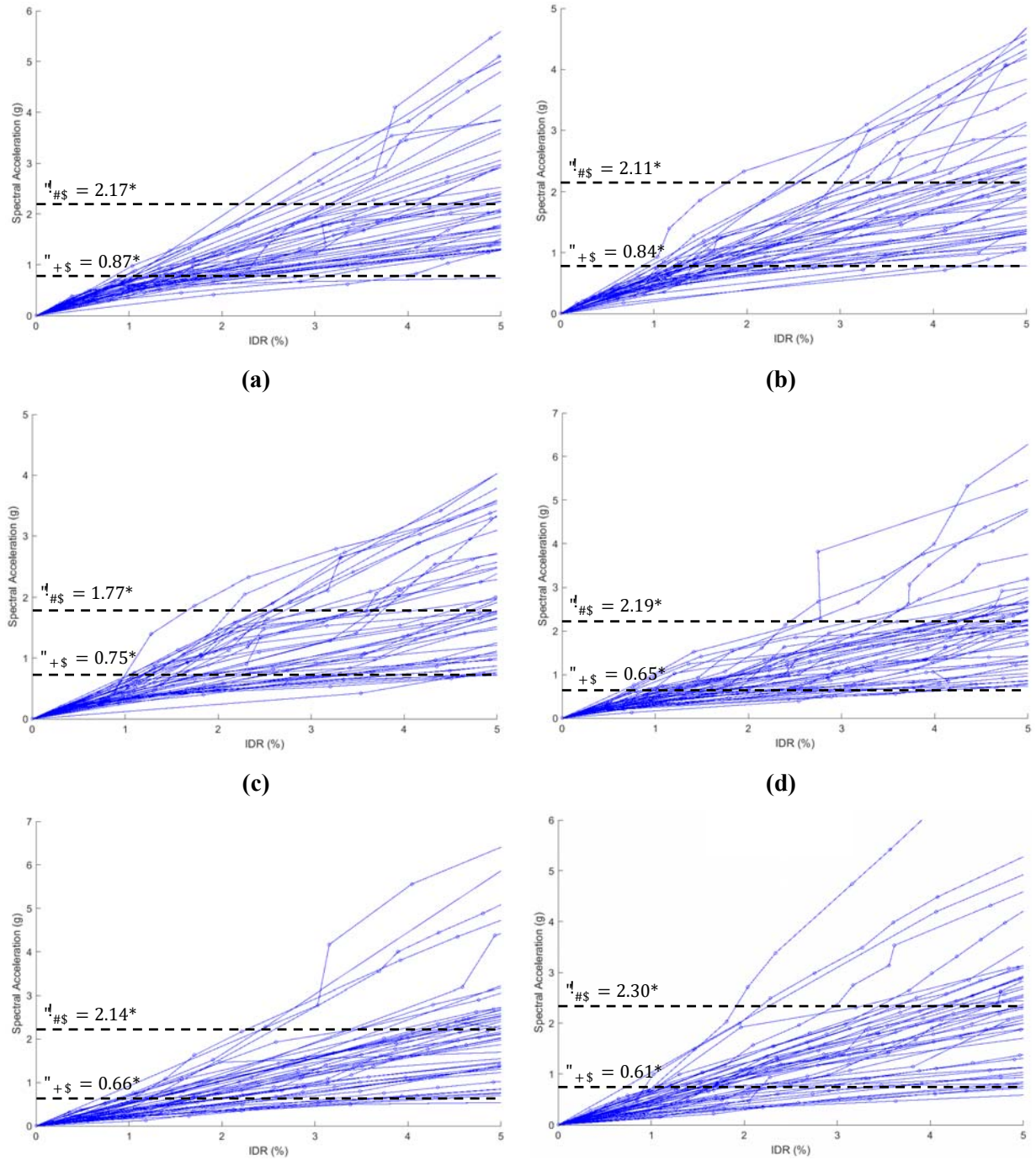

Figure 10-35. IDA curves for PG-1 structures – IMK with pinching hinge (a) PG-1A 8-story D_{max} structure with L/d=3, (b) PG-1B 8-story D_{max} structure with L/d=4, (c) PG-1C 8-story D_{max} structure with L/d=5, (d) PG-1D 12-story D_{max} structure with L/d=3, (e) PG-1E 12-story D_{max} structure with L/d=4, (e) PG-1F 12-story D_{max} structure with L/d=5.

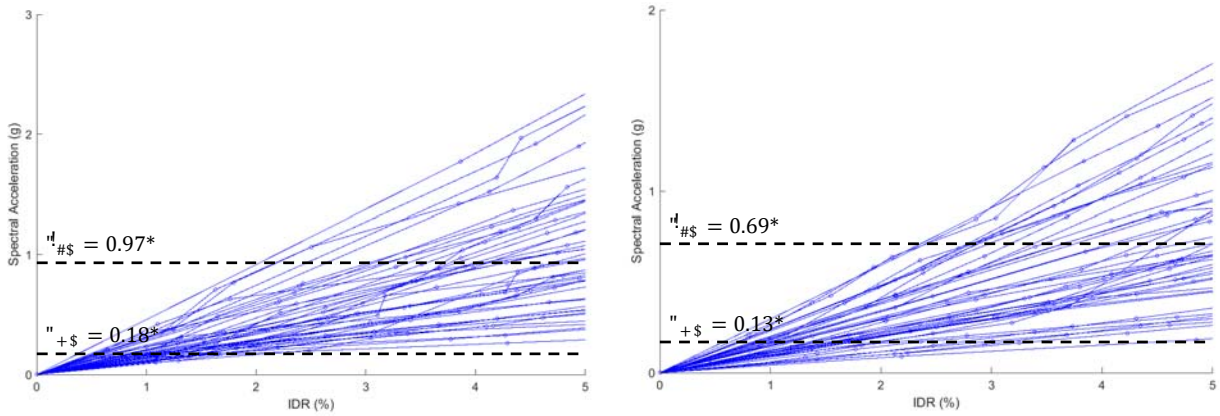

(a) **(b)**

Figure 10-36. IDA curves for PG-2 structures – IMK with pinching hinge (a) PG-2B 8-story D_{min} structure with L/d=4, (b) PG-2E 12-story D_{min} structure with L/d=4.

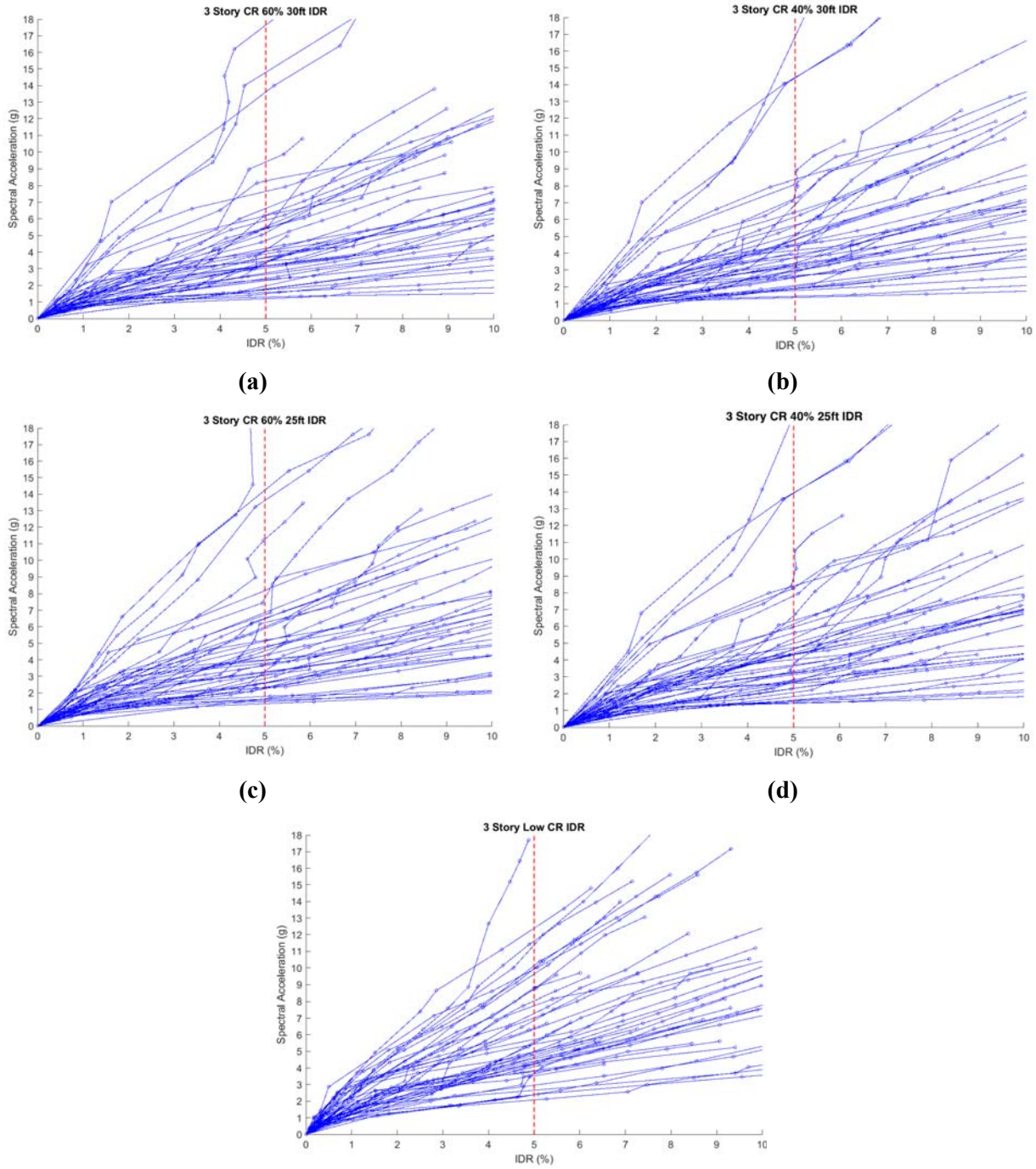

Figure 10-37. IDA curves for PG-2 structures – IMK with pinching hinge (a) Case 1 (3-story D_{max} 30ft structure with 60% CR target), (b) Case 2 (3-story D_{max} 30ft structure with 40% CR target), (c) Case 3 (3-story D_{max} 25ft structure with 60% CR target), (d) Case 4 (3-story D_{max} 25 ft structure with 40% CR target), (e) Case 5 (3-story D_{max} structure with low CR target)

After modifying the hinge to an IMK with bilinear hinge, analyses were run for PG-1, PG-2, PG-3, and PG-4 structures. PG-1 structures results are shown in Figure 10-38a to Figure 10-38f for each archetype structure. PG-2 responses can be found in Figure 10-39a and Figure 10-39b. PG-3 structure results are in Figure 10-40a to Figure 10-40f. PG-4 responses are in Figure 10-41a and Figure 10-41b.

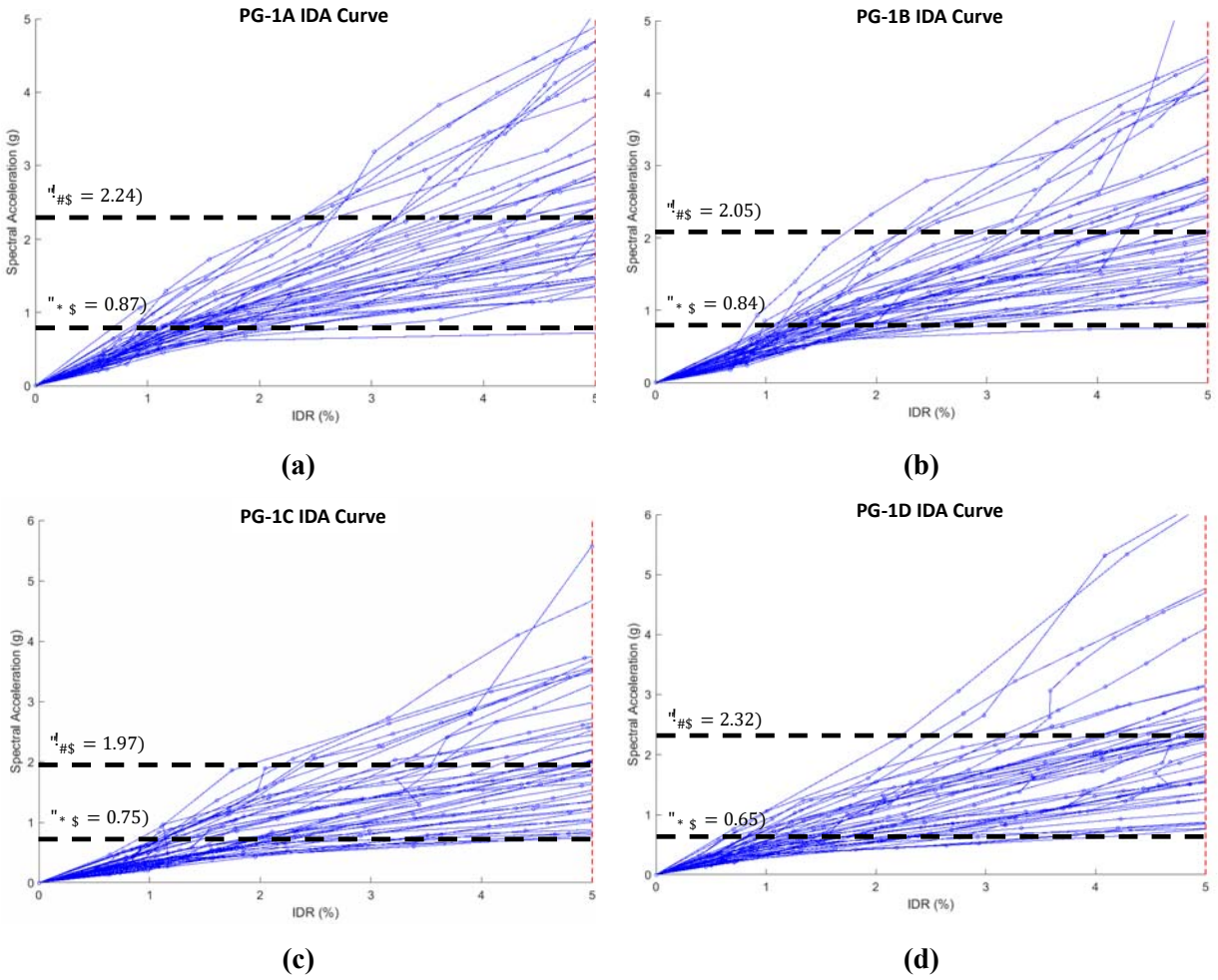

(a) **(b)** **(c)** **(d)**

Figure 10-38. IDA curves for PG-1 structures – IMK with bilinear hinge (a) PG-1A 8-story D_{max} structure with L/d=3, (b) PG-1B 8-story D_{max} structure with L/d=4, (c) PG-1C 8-story D_{max} structure with L/d=5, (d) PG-1D 12-story D_{max} structure with L/d=3, (e) PG-1E 12-story D_{max} structure with L/d=4, (e) PG-1F 12-story D_{max} structure with L/d=5.

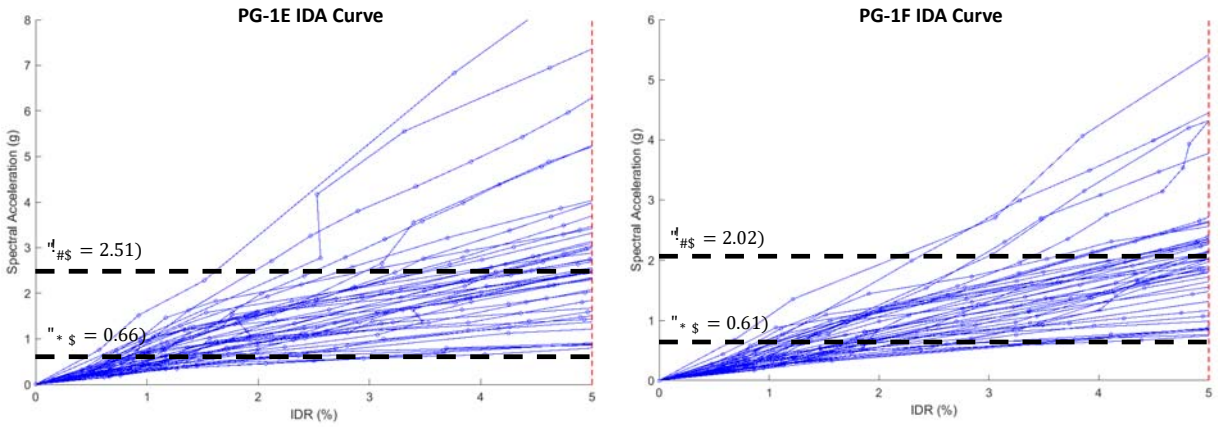

(e) **(f)**

Figure 10-38. (Continued)

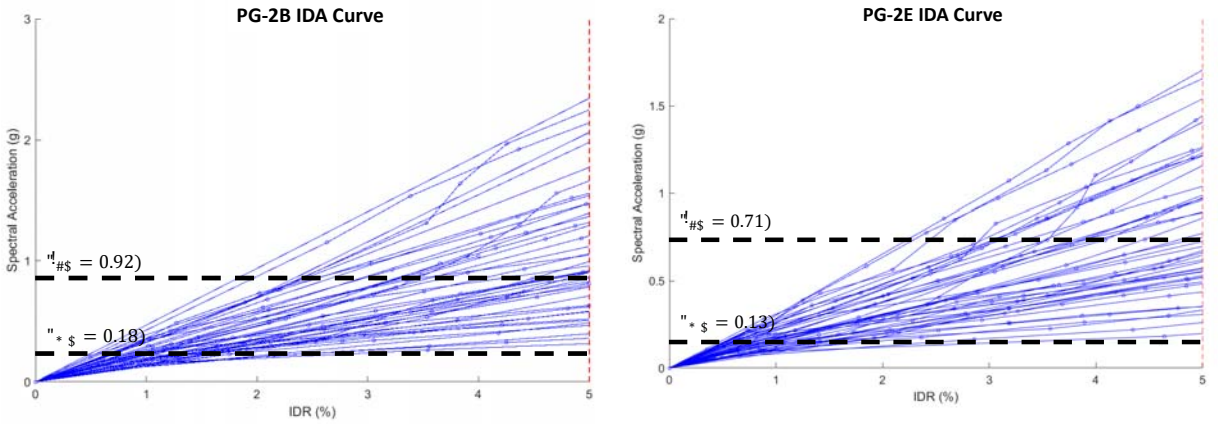

(a) **(b)**

Figure 10-39. IDA curves for PG-2 structures – IMK with bilinear hinge (a) PG-2B 8-story D_{min} structure with L/d=4, (b) PG-2E 12-story D_{min} structure with L/d=4.

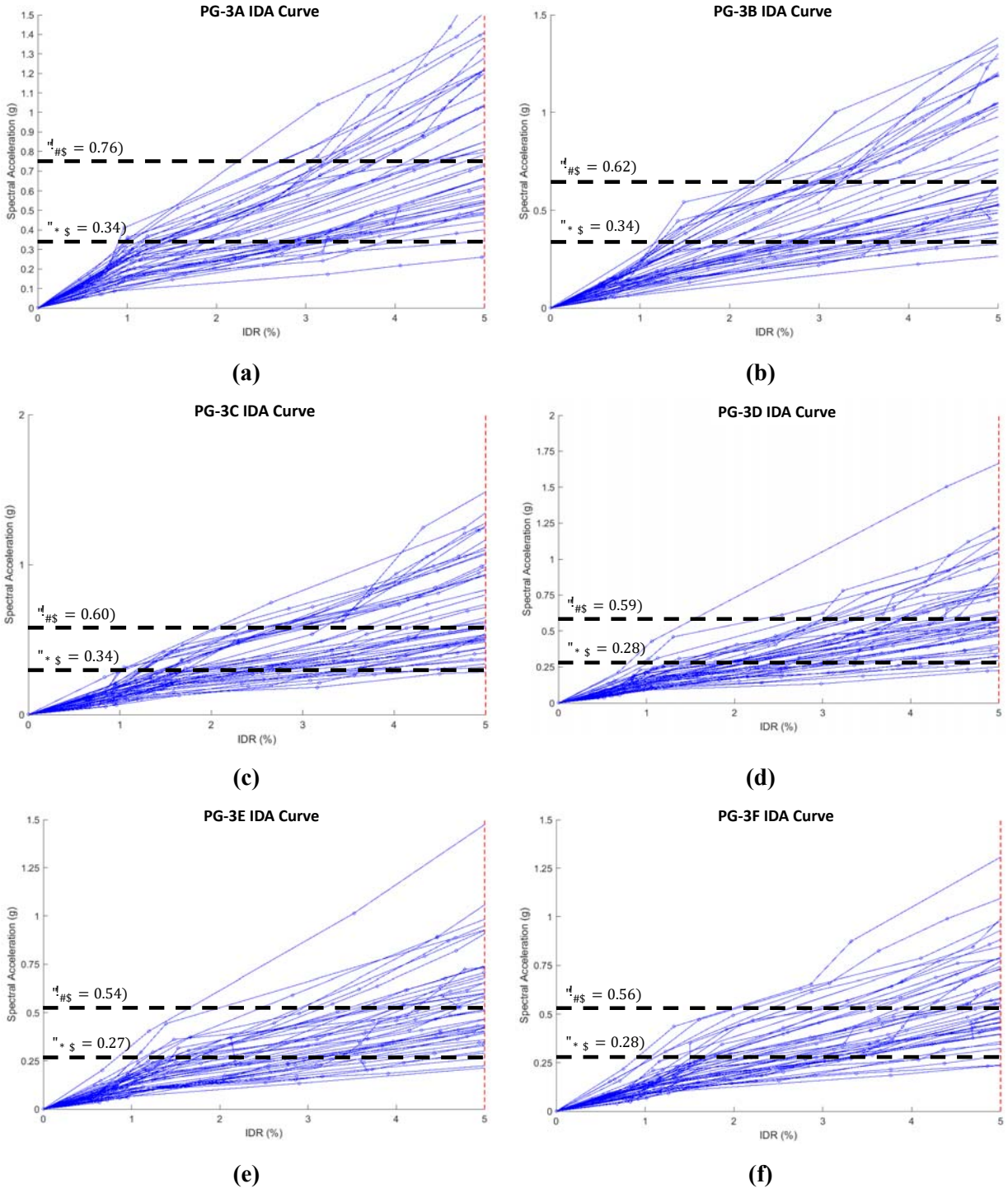

Figure 10-40. IDA curves for PG-3 structures – IMK with bilinear hinge (a) PG-3A 18-story D_{max} structure with L/d=3, (b) PG-3B 18-story D_{max} structure with L/d=4, (c) PG-3C 18-story D_{max} structure with L/d=5, (d) PG-3D 22-story D_{max} structure with L/d=3, (e) PG-3E 22-story D_{max} structure with L/d=4, (e) PG-3F 22-story D_{max} structure with L/d=5.

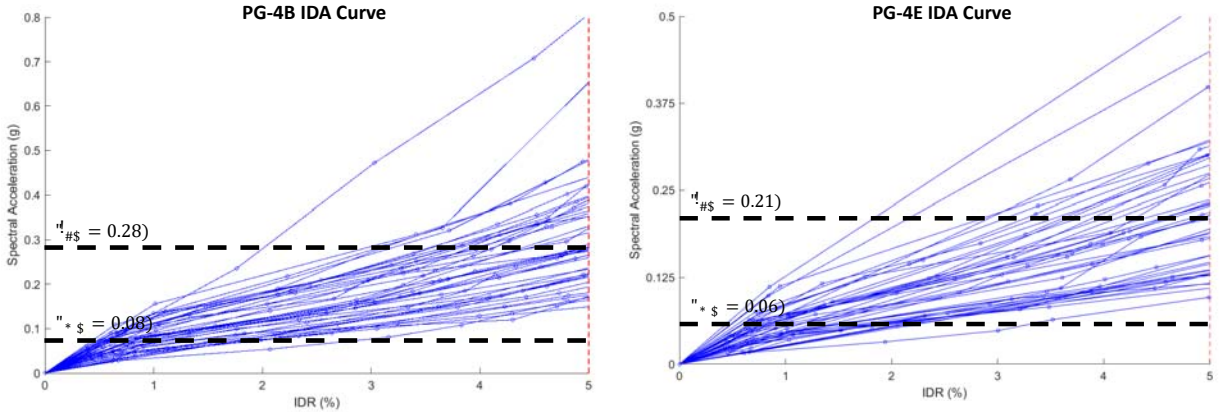

(a) **(b)**

Figure 10-41. IDA curves for PG-4 structures – IMK with bilinear hinge (a) PG-4B 18-story D_{min} structure with L/d=4, (b) PG-4E 22-story D_{min} structure with L/d=4.

10.6.3 Collapse Margin Ratios and Other Results

The collapse margin ratio (CMR) was calculated based on the failure spectral acceleration of the median response for a specific structure. The adjusted collapse margin ratio (ACMR) was then calculated by modifying the CMR by a factor correlated to the period-based ductility (μ_t) value and the structural period as specified in the FEMA P695 procedure. To determine μ_t and the overstrength factor (Ω) pushover analysis is performed. A sample pushover curve is presented in Figure 10-43 with relevant results for all archetype structure shown in Table 10-19.

Table 10-19. Overstrength and period based ductility factors IMK with pinching hinge.

Structure	Maximum Base Shear (V_{max})	Design Base Shear (V)	Overstrength Factor ($\Omega = \frac{V_{max}}{V}$)	Maximum Roof Displacement* (δ_{max})	Roof Displacement at yield (δ_y)	Period Based Ductility Factor ($\mu_t = \frac{\delta_{max}}{\delta_y}$)
PG-1A	1843 kip	879 kip	2.10	23.8 in	2.39 in	10.0
PG-1B	1802 kip	879 kip	2.05	29.2 in	2.49 in	11.7
PG-1C	1610 kip	879 kip	1.83	33.4 in	2.79 in	12.0
PG-2B	579 kip	273 kip	2.12	22.1 in	1.91 in	11.6
PG-1D	2244 kip	979 kip	2.29	26.3 in	3.53 in	7.5
PG-1E	2209 kip	979 kip	2.26	34.2 in	3.32 in	10.3
PG-1F	2025 kip	979 kip	2.07	40.0 in	3.56 in	11.2
PG-2E	717 kip	305 kip	2.36	24.2 in	3.09 in	7.8

Table 10-20. Overstrength and period-based ductility factors for concentrated plasticity model.

Structure	Maximum Base Shear (V_{max})	Design Base Shear (V)	Overstrength Factor ($\Omega = \frac{V_{max}}{V}$)	Maximum Roof Displacement (δ_{max})	Roof Displacement at yield (δ_y)	Period Based Ductility Factor ($\mu_t = \frac{\delta_{max}}{\delta_y}$)
Case 1	882 kip	506 kip	1.74	12.4 in	0.65 in	19.2
Case 2	1010 kip	506 kip	1.99	13.0 in	0.74 in	17.6
Case 3	1160 kip	506 kip	2.29	13.5 in	0.85 in	13.5
Case 4	1220 kip	506 kip	2.41	11.7 in	0.90 in	13.1
Case 5	1440 kip	506 kip	2.85	9.6 in	0.93 in	9.0

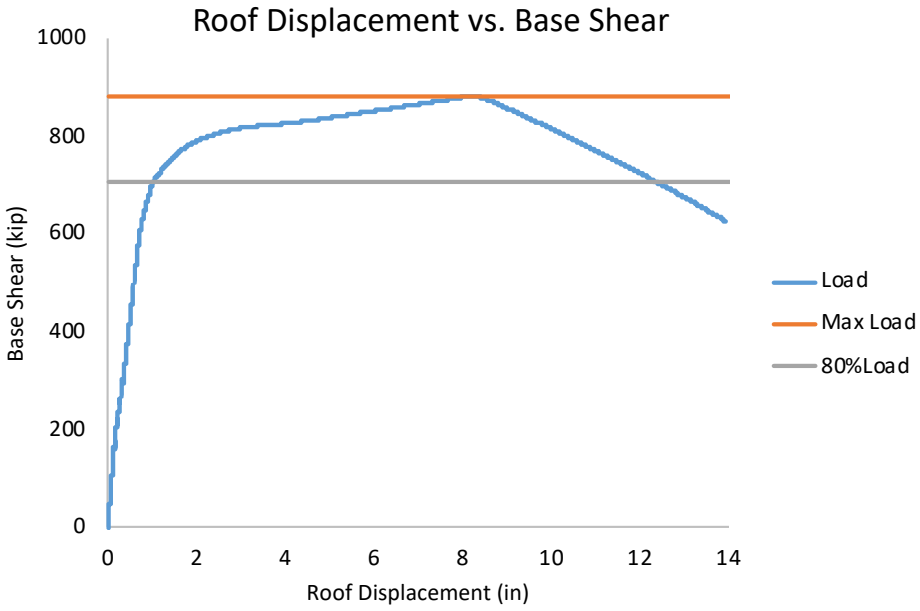

Figure 10-42. Base Shear versus Roof Displacement for Case 1.

Table 10-21. Overstrength and period based ductility factors for IMK with bilinear hinge.

Structure	Maximum Base Shear (V_{max})	Design Base Shear (V)	Overstrength Factor ($\Omega = \frac{V_{max}}{V}$)	Maximum Roof Displacement* (δ_{max})	Roof Displacement at yield (δ_y)	Period Based Ductility Factor ($\mu_t = \frac{\delta_{max}}{\delta_y}$)
PG-1A	1843 kip	879 kip	2.1	23.9 in	2.4 in	10.0
PG-1B	1797 kip	879 kip	2.0	29.9 in	2.5 in	12.0
PG-1C	1534 kip	879 kip	1.7	33.9 in	2.7 in	12.7
PG-2B	574 kip	273 kip	2.1	20.1 in	1.9 in	10.8
PG-1D	2244 kip	979 kip	2.3	26.3 in	3.5 in	7.5
PG-1E	2208 kip	979 kip	2.3	34.2 in	3.3 in	10.3
PG-1F	2023 kip	979 kip	2.1	40.2 in	3.6 in	11.3
PG-2E	711 kip	305 kip	2.3	23.7 in	3.1 in	7.7
PG-3A	4346 kip	2176 kip	2.0	32.0 in	7.8 in	4.1
PG-3B	4470 kip	2176 kip	2.1	43.2 in	8.8 in	4.9
PG-3C	4344 kip	2176 kip	2.0	48.0 in	8.6 in	5.6
PG-4B	1647 kip	725 kip	2.3	32.1 in	6.7 in	4.8
PG-3D	4889 kip	2291 kip	2.1	42.5 in	12.1 in	3.5
PG-3E	4691 kip	2291 kip	2.0	54.2 in	11.9 in	4.6
PG-3F	4923 kip	2291 kip	2.2	54.7 in	11.1 in	4.9
PG-4E	1858 kip	713 kip	2.6	40.2 in	11.7 in	3.4

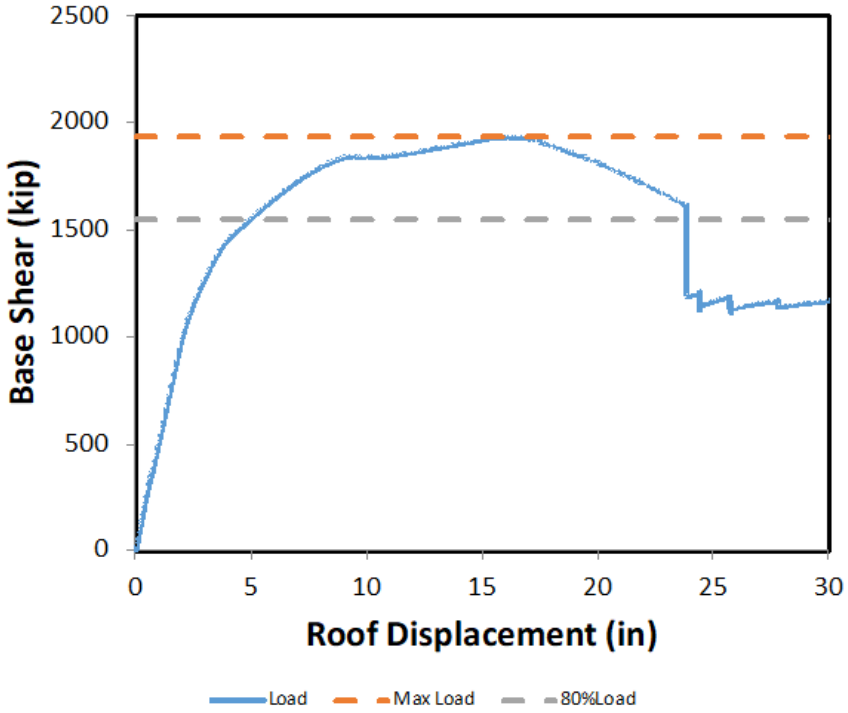

Figure 10-43. Base Shear versus Roof Displacement for PG-1A.

The calculated μ_t factor was large. Using the μ_t model is potentially unconservative, as the OpenSees model is not considered to model all failure modes; therefore, a conservative assumption of μ_t was also used. As shown in Table 10-22 and Table 10-23, by comparing the ACMR values and the FEMA ACMR threshold criteria for all 'good' ratings, all 8 and 12 story archetypes pass the for the calculated μ_t values and the assumed value of 3. As all of the PG-1 and PG-2 archetypes pass the FEMA defined limit, the design assumptions were adequate.

Table 10-22. CMR and ACMR values for PG-1 (IMK with pinching hinge)

	Period (s)	CMR	ACMR (calculated μ_t)	ACMR (assume $\mu_t = 3$)	FEMA ACMR Threshold Criteria
PG-1A	1.04	2.50	3.68	3.15	1.56
PG-1B	1.08	2.52	3.74	3.19	1.56
PG-1C	1.21	2.38	3.62	3.04	1.56
PG-1D	1.39	3.39	5.34	4.42	1.56
PG-1E	1.37	3.27	5.14	4.28	1.56
PG-1F	1.48	3.77	6.05	4.97	1.56
	Average	**2.97**	**4.60**	**3.84**	**1.96**

Table 10-23. CMR ACMR values for PG-2 (IMK with pinching hinge)

	Period (s)	CMR	ACMR (calculated μ_t)	ACMR (assume $\mu_t = 3$)	FEMA ACMR Threshold Criteria
PG-2B	1.66	5.38	7.37	6.51	1.56
PG-2E	2.31	5.32	7.28	6.44	1.56
	Average	**5.35**	**7.33**	**6.47**	**1.96**

The 3-story structures also pass as shown in Table 10-24. This set of structures indicates that the design assumptions are also adequate for shorter structure. These structures also were designed to explore the effects of coupling ratio. As all structures exceed the limit, the coupling ratio did not have an adverse effect on the performance enough to jeopardize passing the FEMA requirements. Meeting this limit, suggests that the design procedure is robust enough to eliminate structures, which would not meet the required performance.

Table 10-24. CMR and ACMR values for 3 story structures (IMK with pinching hinge)

	Period (s)	CMR	ACMR (calculated μ_t)	ACMR (assume $\mu_t = 3$)	FEMA ACMR Threshold Criteria
Case 1	0.468	2.45	3.25	2.89	1.56
Case 2	0.47	2.57	3.41	3.03	1.56
Case 3	0.442	2.58	3.44	3.05	1.56
Case 4	0.446	2.77	3.69	3.27	1.56
Case 5	0.2882	3.48	4.62	4.10	1.56
	Average	**2.77**	**3.68**	**3.26**	**1.96**

The ACMR values were also calculated for the IMK with bilinear hinge models. Table 10-25 to Table 10-28 detail these results. The PG-1 and PG 2 results for the IMK with bilinear hinge (Table 10-25 and Table 10-26) closely follow the results for the IMK with pinching hinge (Table 10-22 and Table 10-23). This correlation is encouraging because the hinges, the only modeling difference, were calibrated using the same process for both hinge models. Additionally, all ACMR values exceed the FEMA thresholds indicating the design assumptions are adequate for all archetype structures.

Table 10-25. CMR and ACMR values for PG-1 (IMK with bilinear hinge)

	Period (s)	CMR	ACMR (calculated μ_t)	ACMR (assume $\mu_t = 3$)	FEMA ACMR Threshold Criteria
PG-1A	1.04	2.58	3.80	3.25	1.56
PG-1B	1.08	2.45	3.64	3.10	1.56
PG-1C	1.21	2.64	4.02	3.38	1.56
PG-1D	1.39	3.58	5.65	4.69	1.56
PG-1E	1.37	3.83	6.01	5.01	1.56
PG-1F	1.48	3.32	5.32	4.38	1.56
	Average	**3.07**	**4.74**	**3.97**	**1.96**

Table 10-26. CMR ACMR values for PG-2 (IMK with bilinear hinge)

	Period (s)	CMR	ACMR (calculated μ_t)	ACMR (assume $\mu_t = 3$)	FEMA ACMR Threshold Criteria
PG-2B	1.66	5.08	6.96	6.15	1.56
PG-2E	2.31	5.48	7.50	6.63	1.56
	Average	**5.28**	**7.23**	**6.39**	**1.96**

Table 10-27. CMR and ACMR values for PG-3 (IMK with bilinear hinge)

	Period (s)	CMR	ACMR (calculated μ_t)	ACMR (assume $\mu_t = 3$)	FEMA ACMR Threshold Criteria
PG-3A	2.62	2.21	3.11	2.92	1.56
PG-3B	2.65	1.85	2.69	2.45	1.56
PG-3C	2.68	1.79	2.67	2.37	1.56
PG-3D	3.24	2.11	2.87	2.78	1.56
PG-3E	3.31	1.98	2.84	2.62	1.56
PG-3F	3.26	2.01	2.92	2.66	1.56
	Average	**1.99**	**2.85**	**2.63**	**1.96**

Table 10-28. CMR ACMR values for PG-4 (IMK with bilinear hinge)

	Period (s)	CMR	ACMR (calculated μ_t)	ACMR (assume $\mu_t = 3$)	FEMA ACMR Threshold Criteria
PG-4B	3.76	3.55	4.54	4.29	1.56
PG-4E	5.22	3.73	4.57	4.51	1.56
	Average	**3.64**	**4.56**	**4.40**	**1.96**

10.6.4 Comparison of time-history analysis results of Abaqus with OpenSees Concentrated Plasticity Results

OpenSees concentrated plasticity results and Abaqus results were compared for 8 and 12 story archetype structures (PG-1). As Abaqus models are able to directly account for more complex behavior, these comparisons are valuable as an additional validation check. A comparison for PG-1A is presented in Figure 10-44 to Figure 10-50. First, the IDA response from the 1994 Northridge earthquake is compared in Figure 10-44 for both scale factor and spectral acceleration. This comparison is then further broken down to compare the roof drift versus time response for a scale factor of 1 (Figure 10-45), 3 (Figure 10-46), 6 (Figure 10-47), and 9 (Figure 10-48). These plots show the effect of increasing the ground motion intensity on the comparisons. Finally, a comparison of the structure's response for seven selected ground motions is shown in Figure 10-49 and Figure 10-50. Together, these comparisons show high correlation between the models.

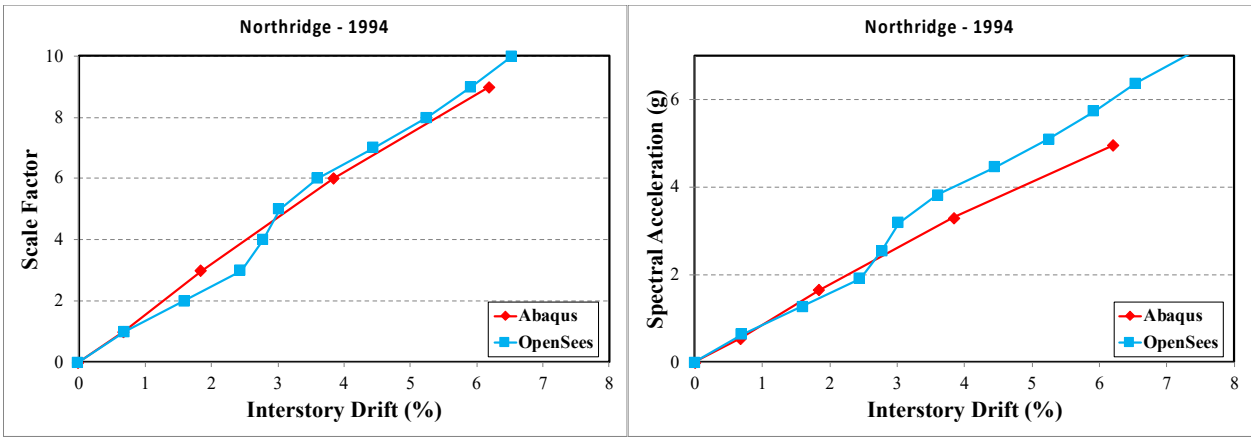

Figure 10-44. Comparison of IDA curves for PG-1A for Northridge ground motion (Record 1-1)

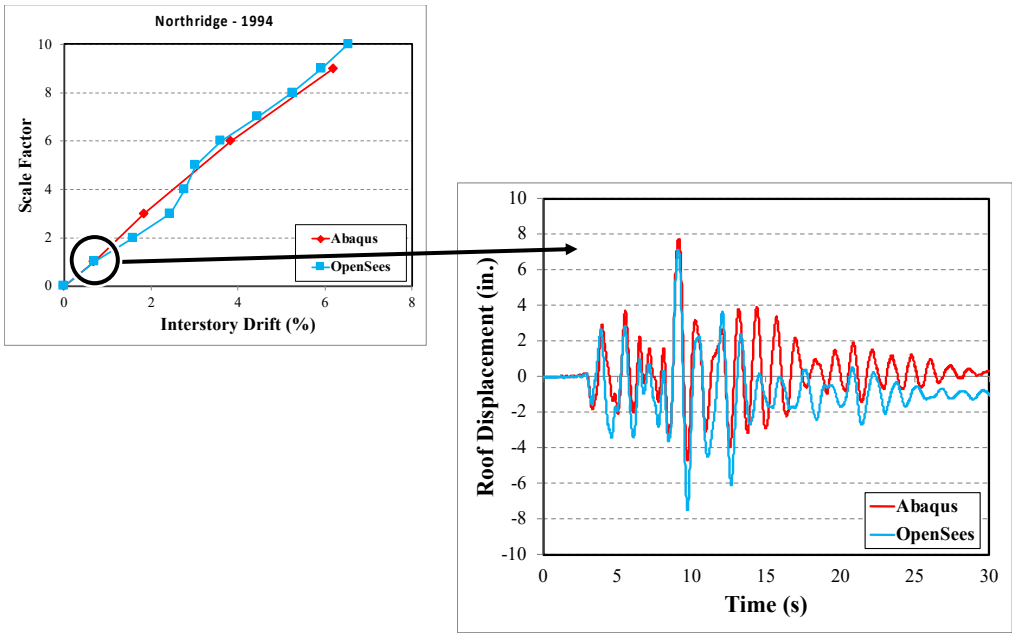

Figure 10-45. PG-1A – Comparison of roof drift at a scale factor of 1

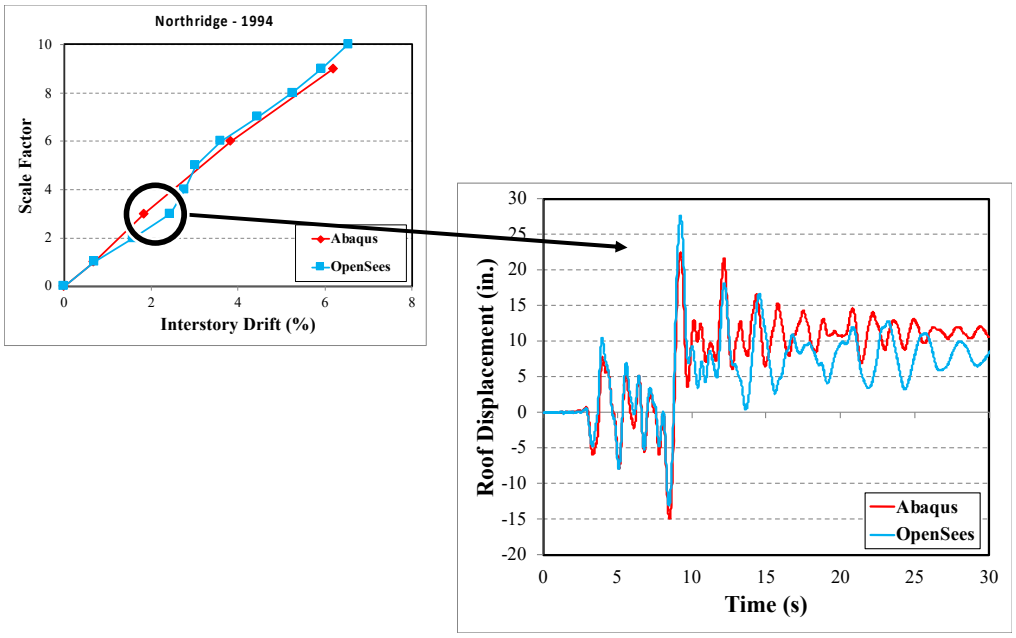

Figure 10-46. PG -1A – Comparison of roof drift at a scale factor of 3

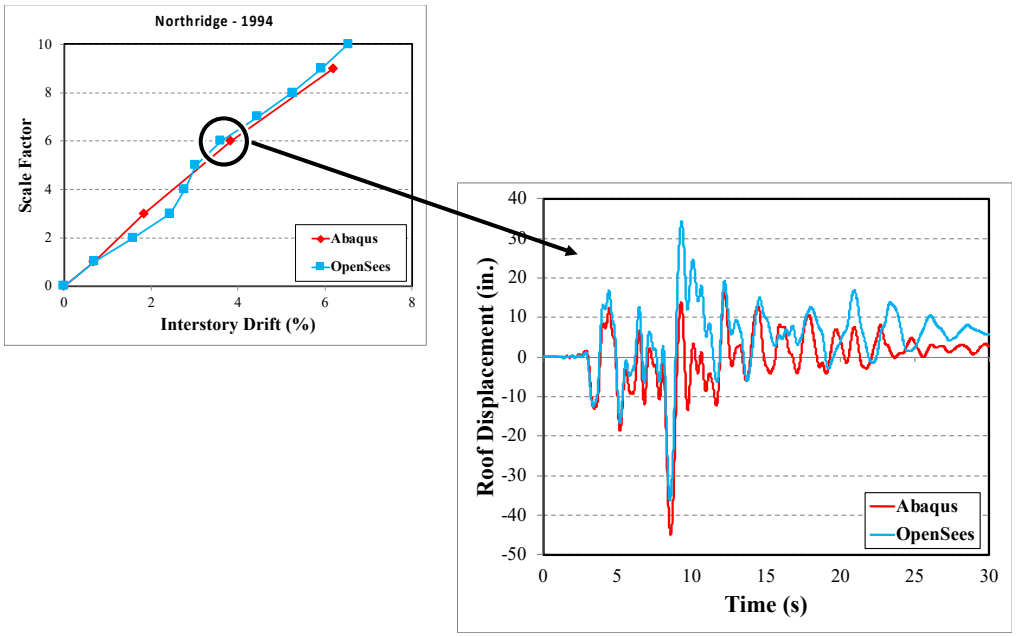

Figure 10-47. PG -1A – Comparison of roof drift at a scale factor of 6

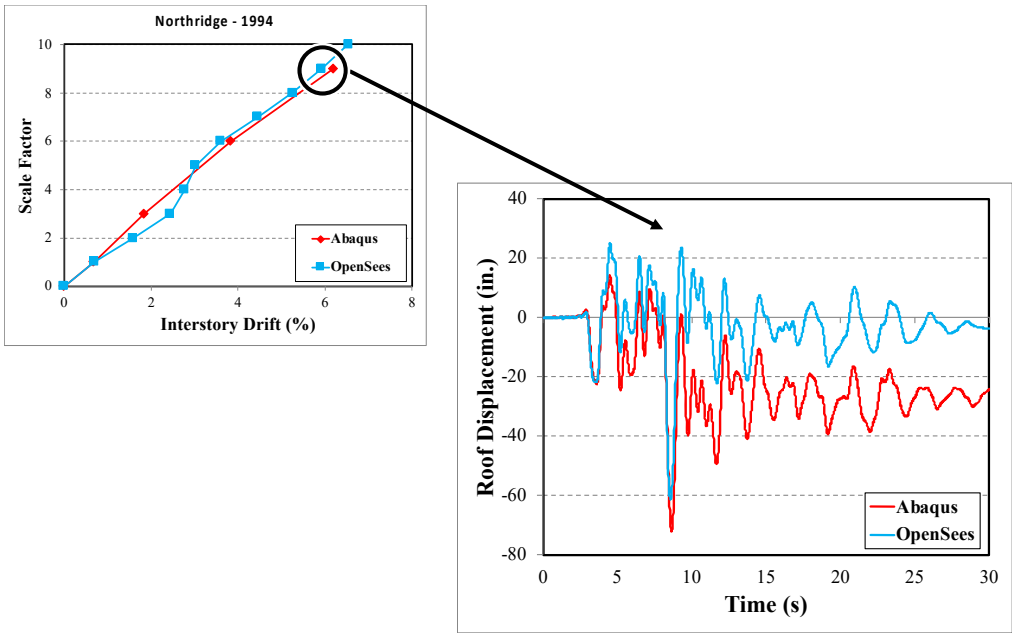

Figure 10-48. PG -1A – Comparison of roof drift at a scale factor of 9.

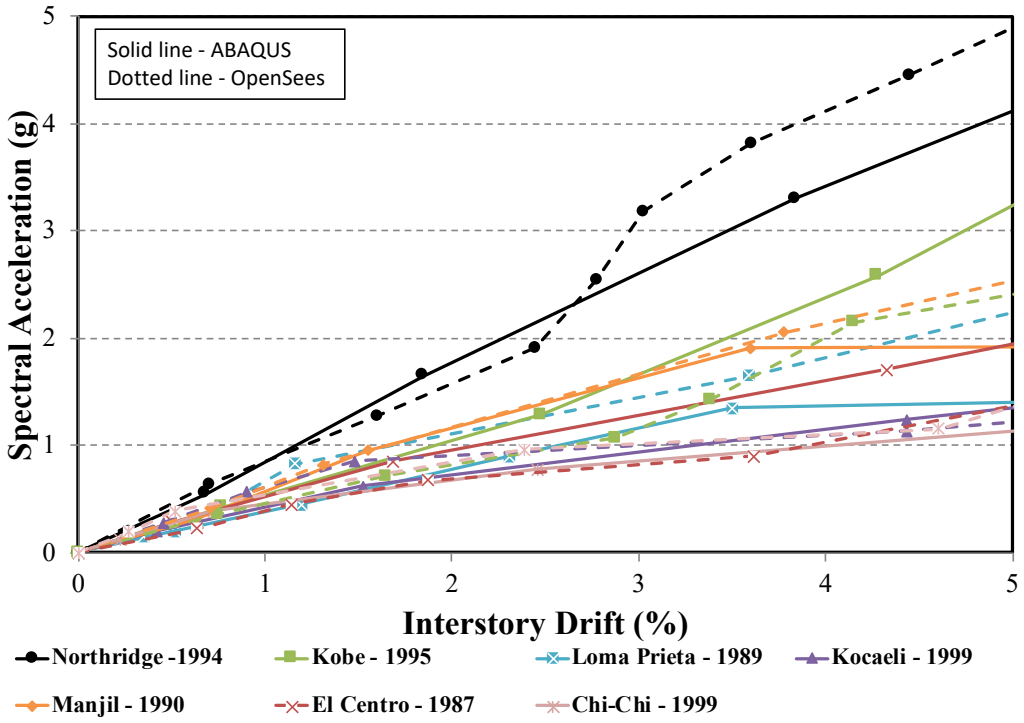

Figure 10-49. PG -1A – Comparison of OpenSees and Abaqus IDA curves for seven selected ground motions.

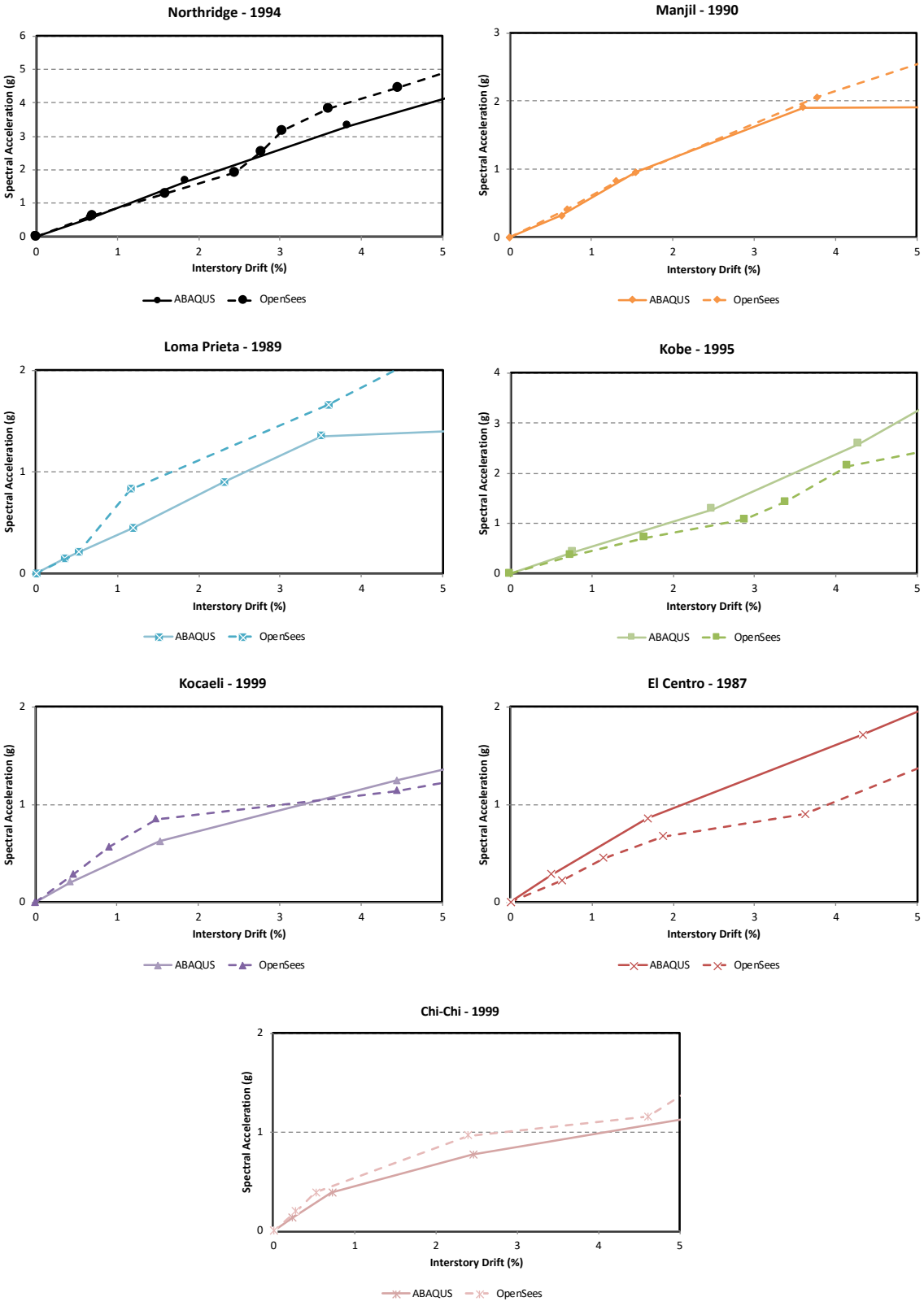

Figure 10-50. PG -1A – IDA curves for seven selected ground motions.

10.6.5 Comparison of Time-History Analysis Results for Different Non-Linear Models

Figure 10-51 shows the comparison between the OpenSees model with distributed plasticity, the OpenSees model with concentrated plasticity and the Abaqus model results for archetype PG-1A and for the scale factors considered for the BICC090 ground motion presented earlier in Section 10.4.3. Results obtained from the distributed plasticity model from the OpenSees and Abaqus results match well. Results of OpenSees model with the concentrated plasticity model has a slight mismatch with a maximum error of 18% at the scale factor of 9, which can be considered negligible.

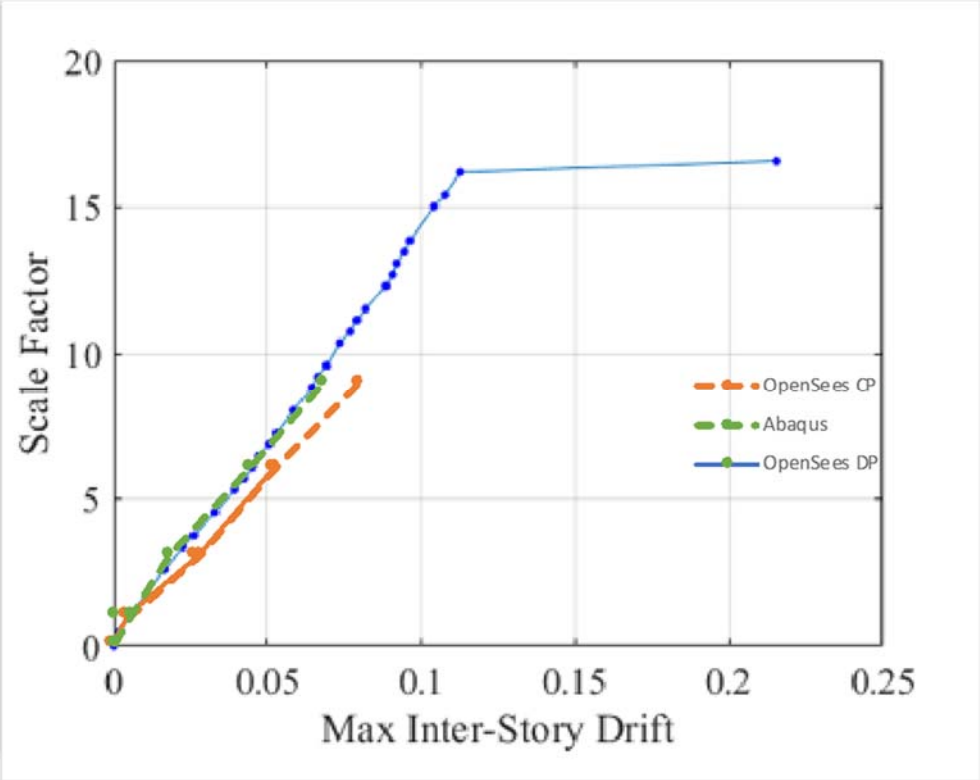

Figure 10-51. Comparison between distributed plasticity, concentrated plasticity and Abaqus models.

“This Page Intentionally Left Blank”

SECTION 11
SUMMARY AND CONCLUSION

Composite Plate Shear Wall—Concrete Filled (C-PSW/CF) is an efficient seismic force-resisting system for buildings and is already addressed by ASCE-7 2016. Coupled Composite Plate Shear Walls—Concrete Filled (CC-PSW/CF) are more ductile and have more redundancy than non-coupled composite plate shear walls, but ASCE 7-16 did not assign them seismic design coefficients and factors in Table 12.2-1. The FEMA P-695 study presented in this report was conducted to substantiate the design coefficients and factors that should be used for such CC-PSW/CF structures. Adding this as a separate category in ASCE 7 Table 12.2-1 is important because modern high-rise buildings often have core-wall systems; many of these core walls could utilize the CC-PSW/CF.

Chapters 3 and 4 above have outlined specific provisions for the definition and application of this CC-PSW/CF system, including details on the design philosophy and limits of applicability. The collapse assessment studies performed here using the FEMA P695 methodology have led to these proposed design provisions. This study consisted of the following steps:

1) Development of a thorough set of design requirements prescribed for CC-PSW/CF. These design requirements are presented in detail in Chapters 3 and 4. Key aspects of the design requirements include:
    a. Limiting coupling beam span-to-depth aspect ratios from 3 to 5 to ensure flexurally dominant behavior and plastic hinging, and requiring coupling beams with aspect ratio greater than or equal to 3 for all stories of the building, and less than or equal to 5 for at least 90% of the stories of the building.
    b. Calculation of design demands for the composite walls using a capacity-limited seismic load effect, E_{cl}, obtained considering all the coupling beams developing plastic hinges with capacities of 1.2 times their expected plastic moment;
    c. Limits on plate slenderness ratio for walls and coupling beam, to ensure development of plastic moment;
    d. Dimensional constraints, which when combined with the limits on plate slenderness ratio, contribute to ensuring substantial coupling beams sizes and coupling ratios;
    e. Minimum height-to-width ratio of 4 for each individual wall of the coupled-walls system, to develop flexurally-dominated wall deformations and therefore engage all coupling beams into the system's plastic mechanism;

f. Requirements for design of steel module under wet concrete condition, that govern the design of ties;
g. Amplification of calculated shear demand by a factor of 4, then compared against provided shear strength equations (note that the shear strength for these walls is large and rarely governs);
h. Specified minimum plastic rotation capacities for the coupling beams, with adequacy of coupling beam detailing to be based on experimental evidence or demonstrated by other approved methods;
i. Specified wall-to-foundation connection demands requirements;
j. Other requirements to achieve consistency with AISC-341 provisions, such as definition of protected zones, demand critical welds, and wall stiffness.

2) Design of 3-story, 8-story, 12-story, 18 story, and 22-story archetypes following the above design requirements, each considering 4 different coupled-walls, resulting in a total of 20 different archetypes. The archetypes were designed using an R value of 8 and C_d value of 5.5. The 3, 8 and 12-story archetype structures used planar composite walls, while the 18 and 22 story archetype structures used C-shaped walls.
3) Selection, validation, and calibration of the non-linear models used in that study. The numerical models for the structures accounted for the various complexities of flexural behavior of the coupling beams and composite walls. Two different set of non-linear models were considered and Incremental Dynamic Analyses (IDA) were performed in parallel, using these two different sets of non-linear models to assess sensitivity of the results. This contributed to enhance confidence in the results and provided a more robust validation of the proposed design provisions and seismic design coefficients and factors. For the first IDA, walls and coupling beams were both modeled using a fiber model able to capture the effects of concrete cracking, steel yielding, local buckling, concrete crushing, and steel inelastic behavior up to fracture due to cumulative plastic strains and low cycle fatigue. A thorough set of analyses was performed on example structures to ensure that the mechanics of the cross-section and member behavior was duly captured. For the second set of IDA, a discrete hinge model was used for the coupling beams, while the wall was modeled using a fiber model with effective stress-strain relationships assigned based on 3D finite element analysis results that implicitly accounted for the effects of steel local buckling, yielding and fracture and concrete cracking, crushing and confinement. For both sets of models, the numerical models were benchmarked using experimental data available in the literature and calibrated to match both the experimentally-obtained force-displacement and moment-rotation hysteretic curves, including full stiffness and strength degradation due to

buckling, fracture, and other non-linear behavior. Models calibrated on experimental results for planar walls were used for the 3, 8 and 12 story archetypes, and on experimental results for C-shaped walls for the 18 and 22 story archetypes. To further understand the mechanics of seismic response for the structural system, additional studies were performed to track the evolution of damage of selected archetype coupled-walls to identify the onset and full development of key limit states, such as yielding and fracture of coupling beams and walls. Non-linear finite element analyses were conducted in parallel for these selected archetypes to provide greater insights into the ultimate behavior of the structural system upon increasing severity of ground motion excitation.

4) Details of the parameters used in all non-linear time history dynamic analyses performed on the IDA for the two sets of non-linear models considered.
5) Findings from the Incremental Dynamic Analyses (IDA) performed and resulting Adjusted Collapse Margin Ratio (ACMR) values for all of the archetypes considered.

Results from the FEMA P-695 studies indicated that all archetypes reached collapse at drifts greater than 5%, but all collapse margin ratios established in this study were conservatively calculated based on results obtained at 5% drift (i.e., at less than actual collapse points). Results of the FEMA P695 studies indicated that collapse margin ratios increased for the taller buildings, which is consistent with the fact that code-specified drift limits governed the design of the 18 and 22 stories archetypes. For all the archetypes considered, the lowest obtained calculated Adjusted Collapse Margin Ratios were respectively 3.55, 3.54, 4.02, 4.75, and 6.5 for the 3, 8, 12, 18, and 22 story archetypes for the IDA conducted with the first set of non-linear models; corresponding values of 2.89, 3.04, 4.28, 2.37, and 2.62 were respectively obtained for the 3, 8, and 12, 18, and 22 story archetypes for the IDA conducted with the second set of non-linear models. All ACMR were calculated for a $\mu_T = 3.0$. These ACMR were compared with the acceptable adjusted collapse margin ratio values of 1.96 and 1.56 for $ACMR_{10\%}$ and $ACMR_{20\%}$. These values are obtained for a total system collapse uncertainty, β_{TOT}, calculated using a "good" rating for the design requrements related collapse uncertainity, test data related collapse uncertainity, and modelling related collapse uncertainity (incidentally, the ACMR would have been found acceptable even if the ratings had been "fair", or even mostly "poor"). Overstrength factor, Ω_o, for the archetypes were found to be on the order of 2.0 to 2.5, and the C_d for the archetypes were found to be the order of 5 to 6. Upon review of response time histories, the large ACMR obtained for overstrenth factors of this magnitude were found to be attributable to the considerable period elongation that developed as the coupled beams progressively failed, and the fact

that the walls hinged only at their base and had considerable shear strength along their height, precluding story-mechanisms.

Therefore, the findings from this study support the addition of items *B.27 and D.14* to ASCE 7-16 Table 12.2-1 in Building Frame Systems (Part B), and Dual Systems (Part D), respectively, as shown below.

Table 11-1. ASCE Table 12.2-1 Design Coefficients and Factors for Seismic Force-Resisting Systems

Seismic Force-Resisting System					Structural System Limitations Including Structural Height, h_n (ft) Limits[d]				
	ASCE 7 Section Where Detailing Requirements Are Specified	R	Ω_0	C_d	Seismic Design Category				
					B	C	D[e]	E[e]	F[f]
…									
B. BUILDING FRAME SYSTEMS									
…									
27. Steel and concrete coupled composite plate shear walls	14.3*	8	2½	5½	NL	NL	160	160	100
…									
D. DUAL SYSTEMS WITH SPECIAL MOMENT FRAMES CAPABLE OF RESISTING AT LEAST 25% OF PRESCRIBED SEISMIC FORCES	12.2.5.1								
…									
14. Steel and concrete coupled composite plate shear walls	14.3*	8	2½	5½	NL	NL	NL	NL	NL

* Section 14.3 is where the design provisions presented in Chapter 3 would be included in ASC 7-16.

Note that the height limits proposed in the above table are arbitrarily set to be similar to those of other structural systems assigned R=8 in the ASCE 7-16 Table 12.2-1, and that "Steel and concrete coupled composite plate shear walls" would correspondingly be added to the list of structural system for which a greater height limit of 240' is permitted when the requirements of ASCE 7-16 Section 12.2.5.4 are met.

“This Page Intentionally Left Blank”

SECTION 12
REFERENCES

AISC341 (2016). *"Seismic provisions for structural steel buildings."*, ANSI/AISC 341-16, American Institute of Steel Construction, Inc., Chicago, Illinois.

AISC (2013). "Steel Construction Manual." *American Institute of Steel Construction*, ANSI/AISC, American Institute of Steel Construction, Inc., Chicago, Illinois.

AISC (2019). "Speedcore." *Retrieved from https://www.aisc.org/why-steel/innovative-systems/SpeedCore/, 07/10/2019*.

Aly, N., AlHamaydeh, M., and Galal, K. (2018). "Quantification of the Impact of Detailing on the Performance and Cost of RC Shear Wall Buildings in Regions with High Uncertainty in Seismicity Hazards." *Journal of Earthquake Engineering*, 1-26.

Alzeni, Y., and Bruneau, M. (2014). "Cyclic Inelastic Behavior Of Concrete Filled Sandwich Panel Walls Subjected To In-Plane Flexure." *Technical Rep. MCEER 14-009*, MCEER The State University of New York at Buffalo.

Ang, A. H.-S., and Tang, W. H. (2007). *Probability concepts in engineering: emphasis on applications in civil & environmental engineering*, Wiley New York.

ASCE (2016). *Minimum design loads for buildings and other structures.*, American Society of Civil Engineers Inc., Chicago, Illinois.

ATC (1992). "ATC24, Guidelines for Cyclic Seismic Testing of Components of Steel Structures." *Applied Technology Council*, Redwood City, CA.

Basquin, O. (1910). "The exponential law of endurance tests." *Proc. American Society for Testing and Materials*, 10, 625-630.

Bezabeh, M., Tesfamariam, S., Popovski, M., Goda, K., and Stiemer, S. (2017). "Seismic base shear modification factors for timber-steel hybrid structure: collapse risk assessment approach." *Journal of Structural Engineering*, 143(10), 04017136.

Borello, D. J., and Fahnestock, L. A. (2012). "Seismic design and analysis of steel plate shear walls with coupling." *Journal of Structural Engineering*, 139(8), 1263-1273.

Brown, J., and Kunnath, S. K. (2000). "Low-cycle fatigue behavior of longitudinal reinforcement in reinforced concrete bridge columns." *Technical Rep. MCEER 00-0007*, MCEER The State University of New York at Buffalo.

Chang, G., and Mander, J. B. (1994). "Seismic energy based fatigue damage analysis of bridge columns: part 1-evaluation of seismic capacity." *Technical Rep. MCEER 94-0006*, MCEER The State University of New York at Buffalo.

Choi, K.-S., Park, J.-Y., and Kim, H.-J. (2017). "Numerical investigation on design requirements for steel ordinary braced frames." *Engineering Structures*, 137, 296-309.

CIS (2017). "SAP2000: integrated finite element analysis and design of structures." *Computers and Structures, Berkeley, California*.

Coffin, J. L. F. (1954). "A study of the effects of cyclic thermal stresses on a ductile metal." *trans. ASME*, 76, 931-950.

Coffin, L. (1971). "A note on low cycle fatigue laws(Plastic strain range-fatigue life behavior as two slope relationship, considering low cycle fatigue laws in terms of crack propagation mode change)." *Journal of Materials*, 6, 388-402.

Dhakal, R. P., and Maekawa, K. (2002). "Modeling for postyield buckling of reinforcement." *Journal of Structural Engineering*, 128(9), 1139-1147.

Donovan, L. T., and Memari, A. M. (2014). "Feasibility Study of Determination of Seismic Performance Factors for Structural Insulated Panels." *Journal of Architectural Engineering*, 21(2), B4014007.

Downing, S. D., and Socie, D. (1982). "Simple rainflow counting algorithms." *International journal of fatigue*, 4(1), 31-40.

El-Tawil, S., and Deierlein, G. G. (1999). "Strength and ductility of concrete encased composite columns." *Journal of Structural engineering*, 125(9), 1009-1019.

El-Tawil, S., Harries, K. A., Fortney, P. J., Shahrooz, B. M., and Kurama, Y. (2010). "Seismic design of hybrid coupled wall systems: state of the art." *Journal of structural engineering*, 136(7), 755-769.

Elkady, A., and Lignos, D. G. (2015). "Effect of gravity framing on the overstrength and collapse capacity of steel frame buildings with perimeter special moment frames." *Earthquake Engineering & Structural Dynamics*, 44(8), 1289-1307.

Ezzeldin, M., Wiebe, L., and El-Dakhakhni, W. (2016). "Seismic collapse risk assessment of reinforced masonry walls with boundary elements using the FEMA P695 methodology." *Journal of Structural Engineering*, 142(11), 04016108.

Farahi, M., and Mofid, M. (2013). "On the quantification of seismic performance factors of Chevron Knee Bracings, in steel structures." *Engineering Structures*, 46, 155-164.

FEMA (2009). "FEMA P695: Quantification of Building Seismic Performance Factors." *Applied Technology Council. Federal Emergency Management Agency*.

Filiatrault, A., and Christovasilis, I. "Example application of the FEMA P695 (ATC-63) Methodology for the collapse performance evaluation of wood light-frame systems." *Proc., 9th US National & 10th Canadian Conference on Earthquake Engineering, Toronto, Canada*.

Fiorino, L., Shakeel, S., Macillo, V., and Landolfo, R. (2017). "Behaviour factor (q) evaluation the CFS braced structures according to FEMA P695." *Journal of Constructional Steel Research*, 138, 324-339.

Gencturk, B., Kaymaz, I., and Hosseini, F. (2016). "Derivation of seismic design parameters for ECC and multi-material special moment-resisting frames." *Journal of Earthquake Engineering*, 20(7), 1054-1076.

Gogus, A., and Wallace, J. W. (2015). "Seismic safety evaluation of reinforced concrete walls through FEMA P695 methodology." *Journal of Structural Engineering*, 141(10), 04015002.

Gomes, A., and Appleton, J. (1997). "Nonlinear cyclic stress-strain relationship of reinforcing bars including buckling." *Engineering Structures*, 19(10), 822-826.

Hisham, M., and Yassin, M. (1994). "Nonlinear analysis of prestressed concrete structures under monotonic and cycling loads." *University of California, Berkeley*.

Ibarra, L. F., Medina, R. A., and Krawinkler, H. (2005). "Hysteretic models that incorporate strength and stiffness deterioration." *Earthquake engineering & structural dynamics*, 34(12), 1489-1511.

Jayamon, J., Line, P., and Charney, F. "An assessment of uncertainty in the performance evaluation of wood shear wall structures." *Proc., Structures Congress 2015*, 2749-2761.

Judd, J. P., and Charney, F. A. (2016). "Seismic collapse prevention system for steel-frame buildings." *Journal of Constructional Steel Research*, 118, 60-75.

Kanvinde, A. M. "Methods to evaluate the dynamic stability of structures-shake table tests and nonlinear dynamic analyses." *Proc., EERI Paper Competition 2003 Winner. Proceedings of the EERI Meeting, Portland*.

Kaufmann, E., Metrovich, B., and Pense, A. (2001). "Characterization of cyclic inelastic strain behavior on properties of A572 Gr. 50 and A913 Gr. 50 rolled sections." *ATLSS Report No. 01-13*.

Kechidi, S., Bourahla, N., and Castro, J. M. (2017). "Seismic design procedure for cold-formed steel sheathed shear wall frames: Proposal and evaluation." *Journal of Constructional Steel Research*, 128, 219-232.

Kircher, C., Deierlein, G., Hooper, J., Krawinkler, H., Mahin, S., Shing, B., and Wallace, J. (2010). "Evaluation of the FEMA P-695 Methodology for Quantification of Building Seismic Performance Factors| NIST." Grant/Contract Reports (NISTGCR) - 10-917-8.

Kizilarslan, E., Kenarangi, H., Klemencic, R., and Bruneau, M. (2019). "Cyclic Behavior of C-Shaped Composite Plate Shear Walls – Concrete Filled." *Journal of Structural Engineering, ASCE, In preparation*.

Koliou, M., Filiatrault, A., Kelly, D. J., and Lawson, J. (2015). "Buildings with rigid walls and flexible roof diaphragms. I: evaluation of current US seismic provisions." *Journal of Structural Engineering*, 142(3), 04015166.

Kunnath, S. K., Heo, Y., and Mohle, J. F. (2009). "Nonlinear uniaxial material model for reinforcing steel bars." *Journal of Structural Engineering*, 135(4), 335.

Kuşyılmaz, A., and Topkaya, C. (2016). "Evaluation of seismic response factors for eccentrically braced frames using FEMA P695 methodology." *Earthquake Spectra*, 32(1), 303-321.

Lee, J., and Kim, J. (2015). "Seismic response modification factors of reinforced concrete staggered wall structures." *Magazine of Concrete Research*, 67(20), 1070-1083.

Lignos, D. (2008). *Sidesway collapse of deteriorating structural systems under seismic excitations*, Doctoral dissertation, Stanford University.

Lu, X., Wu, H., and Zhou, Y. (2017). "Seismic collapse assessment of self‐centering hybrid precast walls and conventional reinforced concrete walls." *Structural Concrete*, 18(6), 938-949.

Manson, S. (1965). "Fatigue: a complex subject—some simple approximations." *Experimental mechanics*, 5(4), 193-226.

Masroor, A., and Mosqueda, G. (2015). "Assessing the collapse probability of base-isolated buildings considering pounding to moat walls using the FEMA P695 methodology." *Earthquake Spectra*, 31(4), 2069-2086.

Mathworks (1992). "Matlab, User's Guide." *Inc., Natick, MA*, 1992.

McKenna, F., Mazzoni, S., and Fenves, G. (2016). "Open System for Earthquake Engineering Simulation (OpenSees) Software Version 2.2. 5." *University of California, Berkeley, CA. Available from http://opensees.berkeley.edu*.

Menegotto, M. "Pinto,(1973), PE, Method of Analysis for Cyclically Loaded Reinforced Concrete Plane Frames Including Changes in Geometry and Non-elastic Behavior of Elements Under Combined Normal Force and Bending." *Proc., IABSE Symposium on the Resistance and Ultimate Deformability of Structures Acted on by Well-Defined Repeated Loads, Lisbon*.

Mindess, S., Young, J. F., and Darwin, D. (1981). *Concrete*, Prentice-Hall Englewood Cliffs, NJ.

Miner, M. A. (1945). "Cumulative damage in fatigue." *J. Appl. Mech.*, 12, A159–A164.

Neuenhofer, A., and Filippou, F. C. (1997). "Evaluation of nonlinear frame finite-element models." *Journal of structural engineering*, 123(7), 958-966.

Nicknam, A. (2015). *Seismic analysis and design of buildings equipped with propped rocking wall systems*, ProQuest Dissertations Publishing, 2015. 3683065, The State University of New York at Buffalo.

Nie, J.-G., Hu, H.-S., and Eatherton, M. R. (2014). "Concrete filled steel plate composite coupling beams: Experimental study." *Journal of Constructional Steel Research*, 94, 49-63.

Nobahar, E., Farahi, M., and Mofid, M. (2016). "Quantification of seismic performance factors of the buildings consisting of disposable knee bracing frames." *Journal of Constructional Steel Research*, 124, 132-141.

Panthaki, F. D. (1992). "Low cycle fatigue behavior of high strength and ordinary reinforcing steels." Doctoral dissertation, The State University of New York at Buffalo.

PEER (2005). "PEER NGA Database." *Pacific Earthquake Engineering Research Center (PEER), University of California, Berkeley, California <http://peer.berkeley.edu/nga/>*.

PEER, T. (2010). "Guidelines for performance-based seismic design of tall buildings." PEER Report No. 2010/05, University of California Berkeley, USA.

Post, N. M. (2019). "Erector Proves Speed Predictions for Radical Steel Frame of Seattle's Rainier Square Tower." *Engineering News-Records*, Retrieve from "https://www.enr.com/articles/46207-erector-proves-speed-predictions-for-radical-steel-frame-of-seattles-rainier-square-tower", 07/05/2019

Purba, R., and Bruneau, M. (2014). "Seismic performance of steel plate shear walls considering two different design philosophies of infill plates. I: Deterioration model development." *Journal of Structural Engineering*, 141(6), 04014160.

Restrepo-Posada, J., Dodd, L., Park, R., and Cooke, N. (1994). "Variables affecting cyclic behavior of reinforcing steel." *Journal of Structural Engineering*, 120(11), 3178-3196.

Richard, M., Albano, L., Kelly, D., and Liel, A. "Case study on the seismic performance of reinforced concrete intermediate moment frames using ACI design provisions." *Proc., Structures Congress 2010, Orlando, Florida*, 3523-3534.

Rodgers, J. E., and Mahin, S. A. (2006). "Effects of connection fractures on global behavior of steel moment frames subjected to earthquakes." *Journal of Structural Engineering*, 132(1), 78-88.

Sadeghi, S., and Rofooei, F. R. (2018). "Quantification of the seismic performance factors for steel diagrid structures." *Journal of Constructional Steel Research*, 146, 155-168.

Sarti, F., Palermo, A., Pampanin, S., and Berman, J. (2017). "Determination of the seismic performance factors for post‐tensioned rocking timber wall systems." *Earthquake Engineering & Structural Dynamics*, 46(2), 181-200.

Sato, A., and Uang, C.-M. (2010). "Seismic performance factors for cold-formed steel special bolted moment frames." *Journal of structural engineering*, 136(8), 961-967.

Sato, A., and Uang, C.-M. (2013). "A FEMA P695 study for the proposed seismic performance factors for cold-formed steel special bolted moment frames." *Earthquake Spectra*, 29(1), 259-282.

Shafaei, S., Varma, A. H., Broberg, M., and Seo, J. (2019). "An Introduction to Numerical Modeling of Composite Plate Shear Walls / Concrete Filled (CPSW/CF)." *Proceedings of the Annual Stability Conference Structural Stability Research Council St. Louis, Missouri, April 2-5, 2019*.

Shamim, I., and Rogers, C. (2015). "Numerical evaluation: AISI S400 steel-sheathed CFS framed shear wall seismic design method." *Thin-Walled Structures*, 95, 48-59.

Siyam, M. A., Konstantinidis, D., and El-Dakhakhni, W. (2016). "Collapse fragility evaluation of ductile reinforced concrete block wall systems for seismic risk assessment." *Journal of Performance of Constructed Facilities*, 30(6), 04016047.

Susantha, K., Ge, H., and Usami, T. (2001). "Uniaxial stress–strain relationship of concrete confined by various shaped steel tubes." *Engineering Structures*, 23(10), 1331-1347.

Tang, J., Hino, S.-i., Kuroda, I., and Ohta, T. (1996). "Modeling of stress-strain relationships for steel and concrete in concrete filled circular steel tubular columns." *Kou kouzou rombunshuu*, 3(11), 35-46.

Tao, Z., Wang, Z.-B., and Yu, Q. (2013). "Finite element modelling of concrete-filled steel stub columns under axial compression." *Journal of Constructional Steel Research*, 89, 121-131.

Usami, T., and Ge, H. (1998). "Cyclic behavior of thin-walled steel structures—numerical analysis." *Thin-walled structures*, 32(1-3), 41-80.

Vamvatsikos, D., and Cornell, C. A. (2002). "Incremental dynamic analysis." *Earthquake Engineering & Structural Dynamics*, 31(3), 491-514.

Vigh, L. G., Deierlein, G. G., Miranda, E., Liel, A. B., and Tipping, S. (2013). "Seismic performance assessment of steel corrugated shear wall system using non-linear analysis." *Journal of Constructional Steel Research*, 85, 48-59.

Zareian, F., Lignos, D., and Krawinkler, H. "Evaluation of seismic collapse performance of steel special moment resisting frames using FEMA P695 (ATC-63) methodology." *Proc., Structures Congress 2010*, 1275-1286.

Zhang, K., Varma, A. H., Malushte, S. R., and Gallocher, S. (2014). "Effect of shear connectors on local buckling and composite action in steel concrete composite walls." *Nuclear Engineering and Design*, 269, 231-239.

Zsarnóczay, Á., and Vigh, L. G. (2017). "Eurocode conforming design of BRBF–Part II: Design procedure evaluation." *Journal of Constructional Steel Research*, 135, 253-264.

“This Page Intentionally Left Blank”

APPENDIX A
Material Equations and Element Types

A.1 Steel Material in OpenSees

A.1.1 Backbone Curve

The *Reinforced Steel Material* model transforms the backbone curve of engineering stresses and strains to natural coordinates (Figure A-1) using the equations presented in this section.

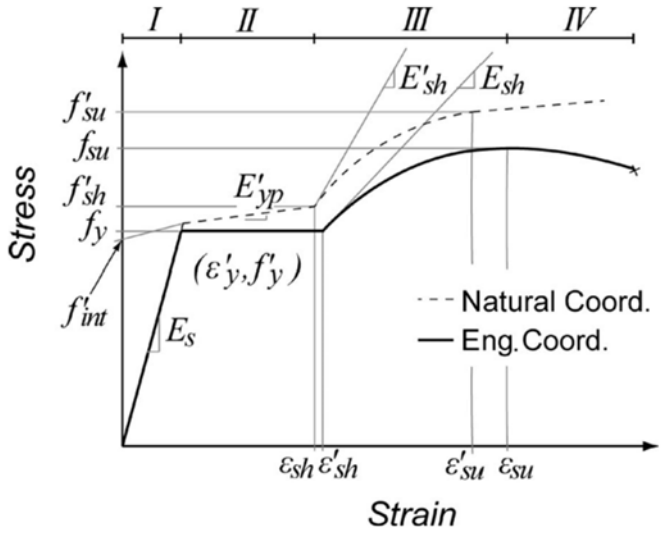

Figure A-1. Monotonic backbone curve (Kunnath et al. 2009).

Parameters with prime indicates the natural coordinates (a.k.a. as true stress and true strains). The conversion assumes conservation of steel volume.

$$\varepsilon'_s = \ln(1 + \varepsilon_s) \quad \textbf{(A.1)}$$

$$f'_s = f_s(1 + \varepsilon_s) \quad \textbf{(A.2)}$$

$$E'_s = \left(E_s + \frac{f_s}{\varepsilon_s + 1}\right)(\varepsilon_s + 1)^2 \quad \textbf{(A.3)}$$

At yield plateau:

$$E'_{yp} = \frac{f'_{sh} - f'_{y}}{\varepsilon'_{sh} - \varepsilon'_{y}} \quad \textbf{(A.4)}$$

$$f'_{int} = f'_{y} - E'_{yp} * \varepsilon'_{y} \quad \textbf{(A.5)}$$

For elastic and post-yield response up to hardening, the equivalent monotonic (bounding) curve in natural coordinate is:

$$f'_{s} = \varepsilon'_{s} * \left(E'_{yp} + \frac{E'_{s} - E'_{yp}}{\left(1 + \frac{\varepsilon'_{s}}{\varepsilon'_{y}}\right)^{R}} \right)^{\frac{1}{R}} \qquad \varepsilon'_{s} < \varepsilon'_{sh} \quad \textbf{(A.6)}$$

where R is curvature factor for controlling transition from elastic to yield plateau. The smaller the value of R, the smoother the transition.

The post hardening and the post peak response are defined by:

$$f'_{s} = f'_{su} + (f'_{sh} - f'_{su}) * \left(\frac{\varepsilon'_{su} - \varepsilon'_{s}}{\varepsilon'_{su} - \varepsilon'_{sh}} \right)^{p'} \qquad \varepsilon'_{sh} < \varepsilon'_{s} < \varepsilon'_{su} \quad \textbf{(A.7)}$$

$$f'_{s} = f'_{su} + E'_{su} * (\varepsilon'_{s} - \varepsilon'_{su}) \qquad \varepsilon'_{su} < \varepsilon'_{s} \quad \textbf{(A.8)}$$

where p' controls the shape of the curve and is given as:

$$p' = E'_{sh} * \left(\frac{\varepsilon'_{su} - \varepsilon'_{sh}}{f'_{su} - f'_{sh}} \right) \quad \textbf{(A.9)}$$

In order to define the backbone curve in OpenSees (McKenna et al. 2016), yield strength (f_y), ultimate strength (f_u), initial Young's modulus (E_s), Modulus at strain hardening (E_{sh}), strain at initial strain hardening (ε_{sh}) and ultimate strain at which stress is maximum (ε_u) must be entered.

A.1.2 Cyclic Buckling

A.1.2.1 Gomes and Appleton Model (Gomes and Appleton 1997)

The Gomes and Appleton buckling stress equation were derived from both the equilibrium of the buckled reinforcement in the deformed configuration; and compatibility between the transversal displacement, w, the longitudinal displacement, δ, and the rigid body rotation, θ, (Figure A-2). At the end, the following expressions were obtained:

$$\sigma_s = \frac{2\sqrt{2}}{A_s L} * \frac{4}{3} * r^3 \sin^3 \theta \, \sigma_{so} * \frac{1}{\sqrt{\varepsilon_s}} \qquad \textbf{(A.10)}$$

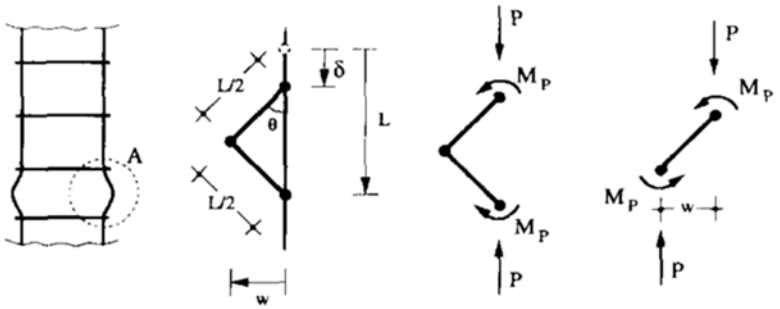

Figure A-2. Free body diagram in equilibrium of buckled state (Gomes and Appleton 1997).

To illustrate application of this model, the buckling parameters values recommended by Kunnath et al. (2009) listed in Table 6-1 were tried and the resulting backbone curve is shown in Figure A-3.

Table A-1. Inputs for Grade 50 steel with buckling properties.

F_y – ksi	F_u – ksi	E_s – ksi	E_{sh} – ksi	ε_{sh}	ε_u	Buckling Parameters
50	65	29000	967 (E_s/30)	10*ε_y	0.15	l_{SR} = 24.0 / β=1.0 / r = 0.6 / γ = 0.5

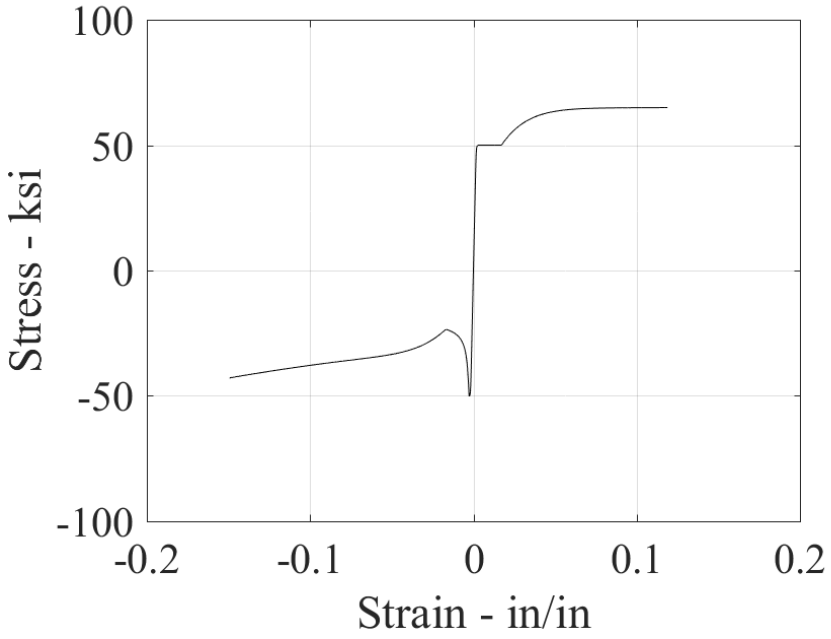

Figure A-3. Backbone curve with buckling included.

A series of analyses were conducted to illustrate to impact of each buckling parameters. For this study, a truss element having a 5/16"x5/16" cross-section and 8" in height (to replicate a fiber in any cross-section) was loaded with arbitrary cycles in the axial direction. Investigation of a parameter was done by keeping the rest of the parameters constant and giving different values for the parameter under investigation. The resulting stress versus strain diagrams are shown in Figures A-4 to A-8. Figure A-4 shows the slenderness ratio study (β=1; r=0; γ=1; and different l_{SR} values) and Figure A-4 indicates that this parameter controls the maximum peak compressive stress of the steel fibers in the hysteresis curve. Another study was performed for the beta factor (l_{SR}=24; r=0; γ=1; and different β values). Figure A-5 indicated that the behavior in the hysteresis loop does not change with different values of the beta factor. The study for the buckling curve factor, *r*, (l_{SR}=24; β =1; γ=1; and different r values) is shown in Figure A-6. Although the hysteretic curves remain full, the compression strength is shown to decrease with decreasing *r* values. For example, for r=0.4, the compression stress reaches at -0.055 radian is equal to 45% of the tension stress reached at 0.055 radian. To clarify the effect of the *r* factor, full buckling (r=0) and no buckling (r=1) is shown in Figure A-7.The last study done was for the gamma factor, γ, (l_{SR}=24; β =1; r=0; and different γ values). Figure A-8 shows that this parameter affects the tensile behavior of the hysteresis loops. The tensile strength is shown to decrease with decreasing γ factors. To illustrate, for γ=0.5, the tensile stress reaches 50 ksi at 0.055 radian but it is 65 ksi for γ=1.0.

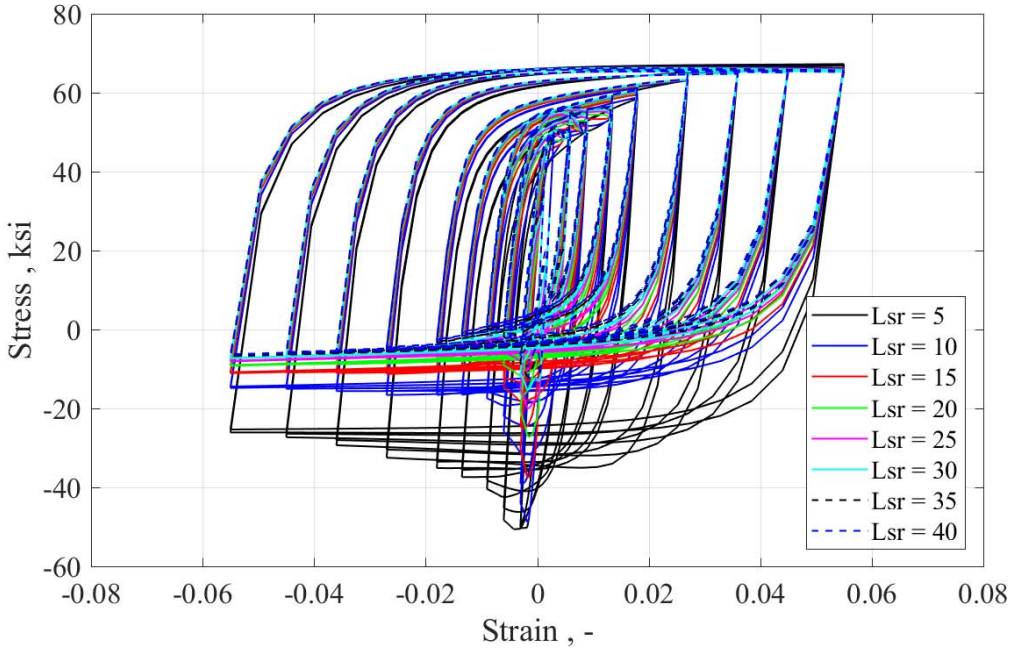

Figure A-4. Slenderness ratio factor, l_{SR}, study

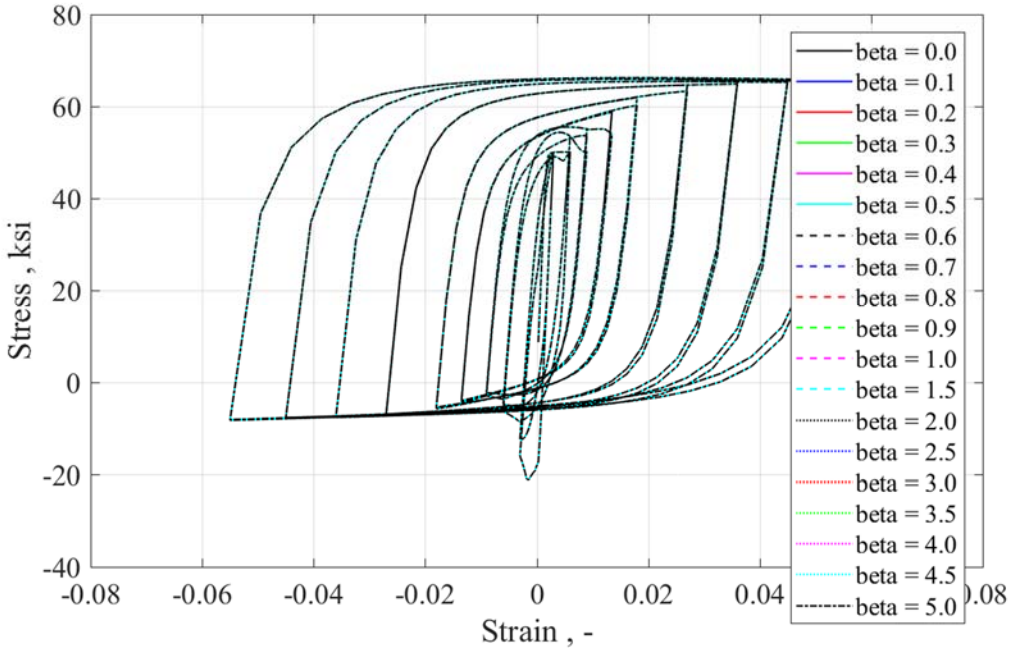

Figure A-5. Beta factor, β, study (lines are on top of each other)

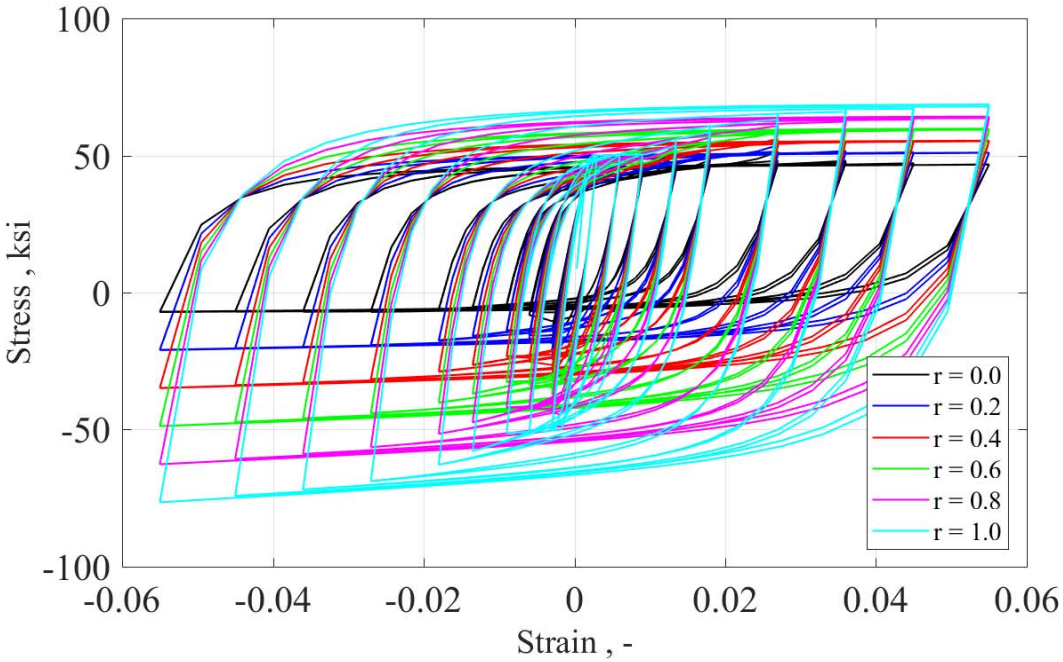

Figure A-6. Buckling curve factor, *r*, study

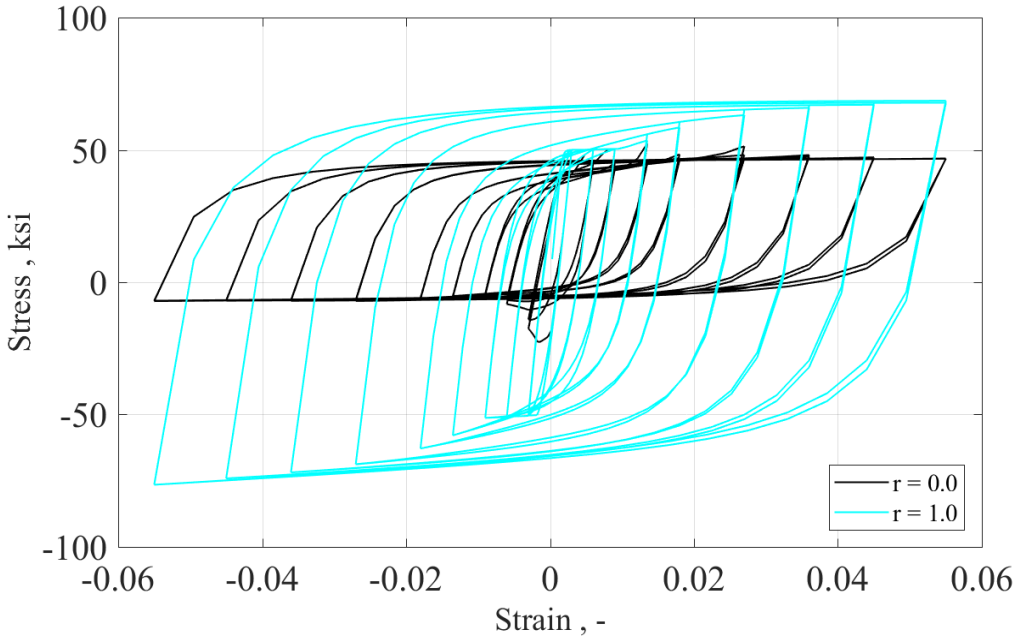

Figure A-7. Comparison of full buckling and no buckling curves for *r* study

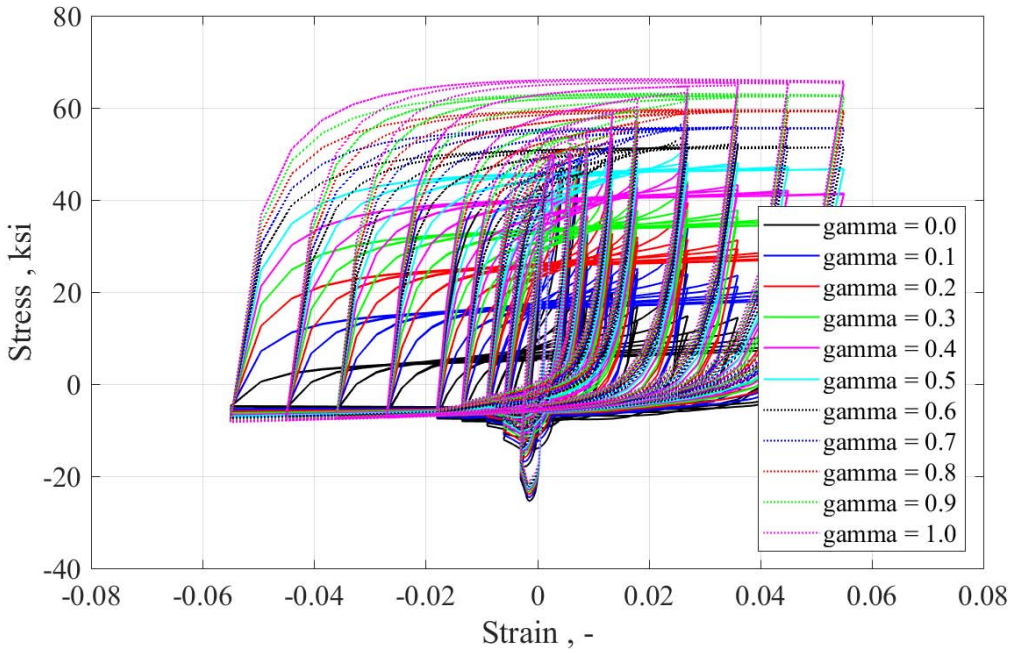

Figure A-8. Gama factor, γ, study

A.1.2.2 Dhakal and Maekawa Buckling Model (Dhakal and Maekawa 2002)

The same fiber described in Section A.1.2.1 was re-analyzed using the Dhakal and Maekawa buckling model (Dhakal and Maekawa 2002). The same slenderness ratio (l_{SR}=*6*) was given but various values of the modifier factor (α) were given to the material model. The resulting cyclic stress-strain relationships are shown in Figure A-9. This parameter affects the post peak behavior of the hysteresis loop. Another parametric study was performed for the slenderness ratio using the same the response modification factor (α=1) but different slenderness ratio as in Figure A-10. This parameter controls the peak strength of compressive side of the hysteresis curve.

However, in this model, as can be seen from Figures A-9 and A-10, the post buckling strength at large strains cannot be adjusted with just two parameters for other applications such as composite wall. Therefore, the Gomes and Appleton model was chosen for this project.

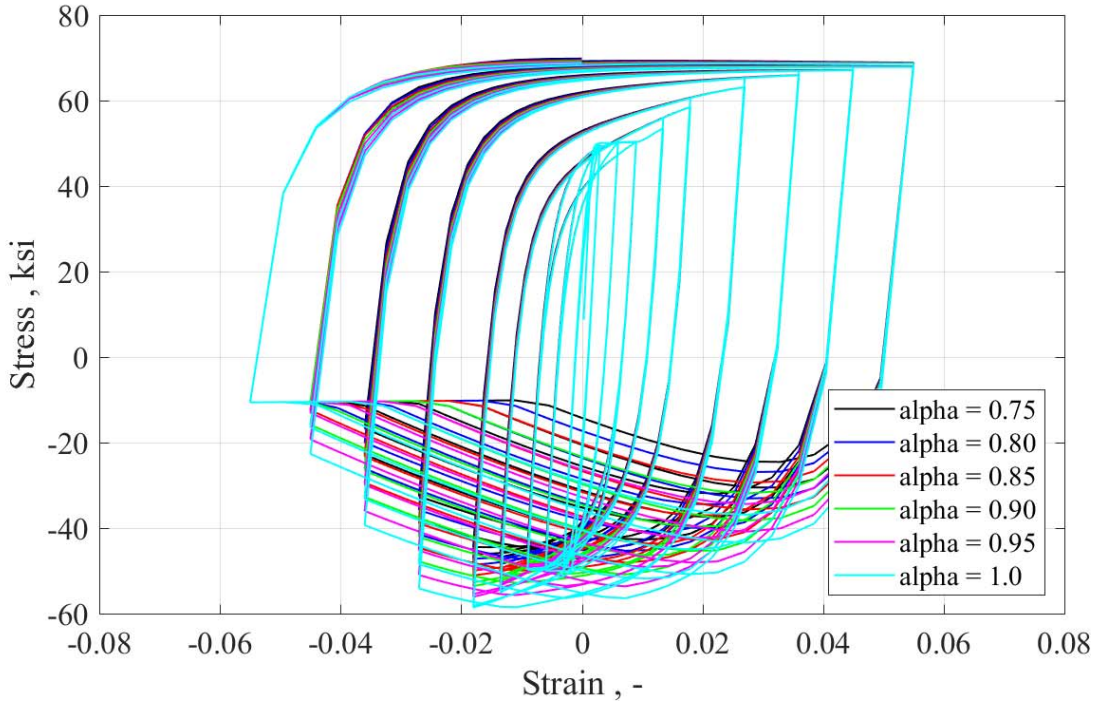

Figure A-9. The response modification factor, "α" study

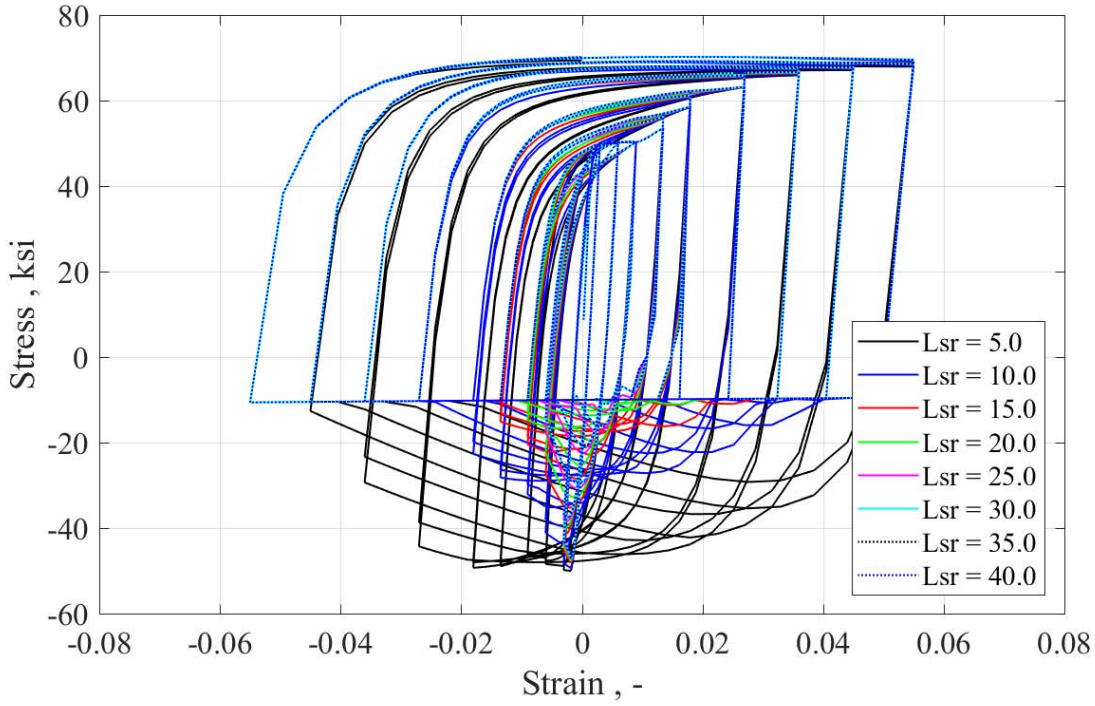

Figure A-10. The slenderness ratio, "L_{SR}" study.

A.1.3 Low-Cycle Fatigue

For the current application, it is important for the material model to capture the steel fracture as it leads to strength degradation of the walls' flexural strength. To account for fracture, the *Reinforced Steel Material* model utilizes the Coffin-Mansion relationship (Coffin(1954), Manson (1965)).

In this model, cyclic strain response is expressed as a function of elastic and plastic response by following expression.

$$\Delta\varepsilon = \Delta\varepsilon_e + \Delta\varepsilon_p \quad \textbf{(A.11)}$$

For the elastic response, Basquin's equation (Basquin 1910) is adopted to calculate fatigue life. The Coffin-Manson equations (Coffin 1954; Coffin 1971; Manson 1965) are used instead when response is in the plastic range. Combining the Basquin equation and Coffin-Manson equation provides the following equation for estimating fatigue life over the entire strain range (correspondingly illustrated in Figure A-11):

$$\Delta\varepsilon = \Delta\varepsilon_e + \Delta\varepsilon_p = \frac{\sigma_f'}{E} * (2 * N_f)^b + \varepsilon_f' * (2 * N_f)^c \quad \textbf{(A.12)}$$

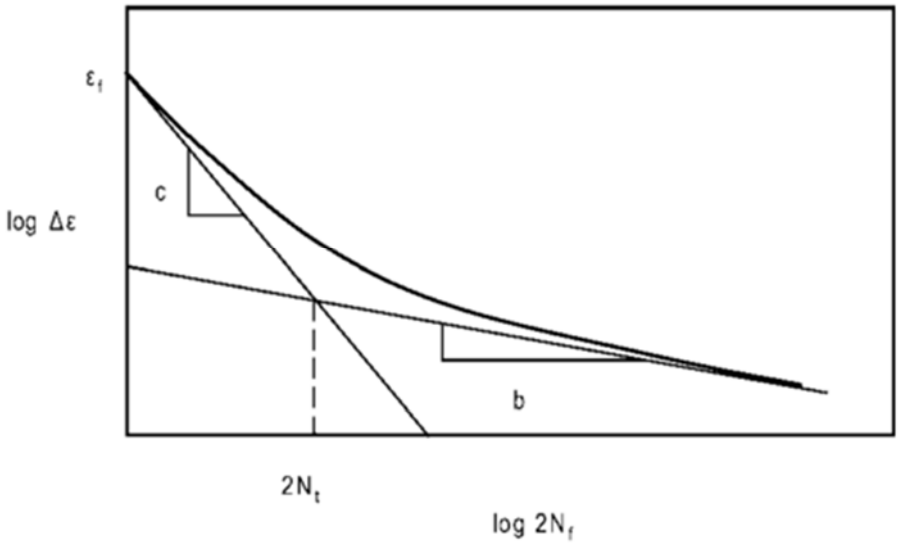

Figure A-11. Fatigue life in terms of total strain.

where $\Delta\varepsilon$ is total strain amplitude; σ'_f is the fatigue strength coefficient; *b* is the fatigue strength exponent; $2*N_f$: is the number of half cycles to failure (one cycle is two reversal); ε'_f is a fatigue ductility coefficient; *c* is a fatigue ductility exponent.

The constants in the above equations are obtained from engineering stress and strain curve. Therefore, the low-cycle fatigue calculations are done in engineering coordinates. If steel failure is predominantly due to low cycle fatigue (i.e., occurring under repeated plastic strain ranges), the fatigue equation can be simplified to:

$$\Delta\varepsilon_P = \varepsilon'_f * (2 * N_f)^c \quad \textbf{(A.13)}$$

The peak plastic strain amplitudes in tension and compression are measured during analysis and cumulative damage is calculated using the Palmgren-Miner rule (Miner 1945), expressed by the following equations (Note that Equation A.13 is redefined with parameters in Equation A.15 in the *Reinforcing Steel Material* model):

$$\Delta\varepsilon_P = \varepsilon_t - \frac{\sigma_t}{E_S} \quad \textbf{(A.14)}$$

$$2N_f = \left(\frac{\Delta\varepsilon_P}{C_f}\right)^{-\frac{1}{\alpha}} \quad \textbf{(A.15)}$$

$$D_i = \left(\frac{1}{2N_f}\right) \quad \textbf{(A.16)}$$

$$D_f = \Sigma D_i \quad \textbf{(A.17)}$$

where ε_p is the plastic strain amplitude; ε_t and σ_t are the total strain and stress amplitudes per cycle; C_f and α are the material constants; D_i is the fatigue damage per cycle; and D_f is the cumulative fatigue damage.

Once the cumulative damage "D" reaches to 1.0, the steel area fractures and the stress rapidly reduces to zero. Fatigue damage can also be modeled with progressive strength degradation. Kunnath et al. (2009) modeled the strength degradation by the following expression:

$$\varepsilon_P = C_d * (f_{SR})^\beta \quad \textbf{(A.18)}$$

where β and C_d are material constants and f_{SR} is a strength loss factor per cycle (Figure A-12) that can be obtained from a fatigue test at constant plastic strain amplitude of ε_p. For simplicity, a linear relationship was assumed by Kunnath et al. between f_{SR} and number of half cycles failure ($2N_f$). Then, the cumulative strength degradation (λ_{SR}) is obtained by summing the strength loss factor at each cycle; then, it was assumed to be related to cumulative fatigue damage (D_f) with a linear constant (Z_d).

$$\lambda_{SR} = \sum_{i=1}^{n} (f_{SR})_i \quad \textbf{(A.19)}$$

$$\lambda_{SR} = Z_d * D_f \quad \textbf{(A.20)}$$

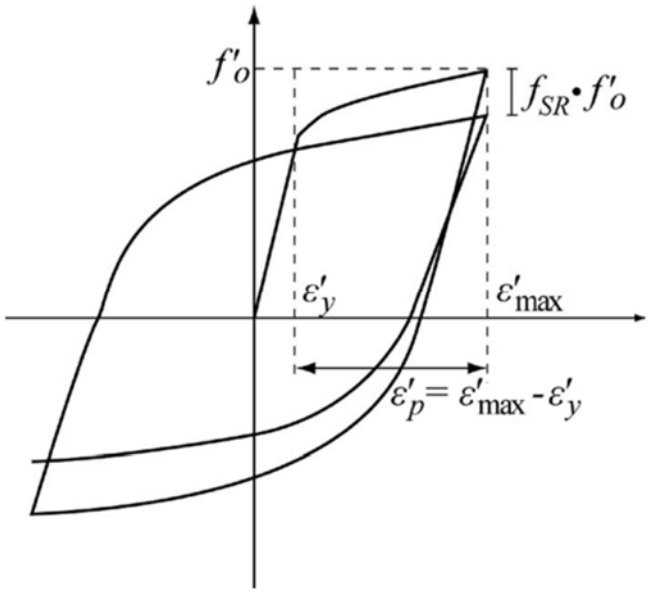

Figure A-12. Cyclic degradation (Kunnath et al. 2009).

In order to prove the assumption that cumulative fatigue damage and cumulative strength degradation are related by a constant, constant amplitude cyclic tests conducted by Brown and Kunnath (2009) were used by calibrating material constants, β, C_d and α and C_f separately using the method of least squares (Figure A-13) It was observed that the values of β and α are similar in these separate calibration, indicating that the strength reduction is related to fatigue damage. By equating cumulative strength degradation to cumulative fatigue damage, the following expression was formulated:

$$\frac{1}{(C_d)^{\frac{1}{\beta}}}\sum(\varepsilon_i^p)^{\frac{1}{\beta}} = Z_d\frac{1}{(C_f)^{\frac{1}{\alpha}}}\sum(\varepsilon_i^p)^{\frac{1}{\alpha}} \quad \textbf{(A.21)}$$

$$\beta = \alpha \quad \textbf{(A.22)}$$

$$Z_d = \left(\frac{C_f}{C_d}\right)^{1/\alpha} \quad \textbf{(A.23)}$$

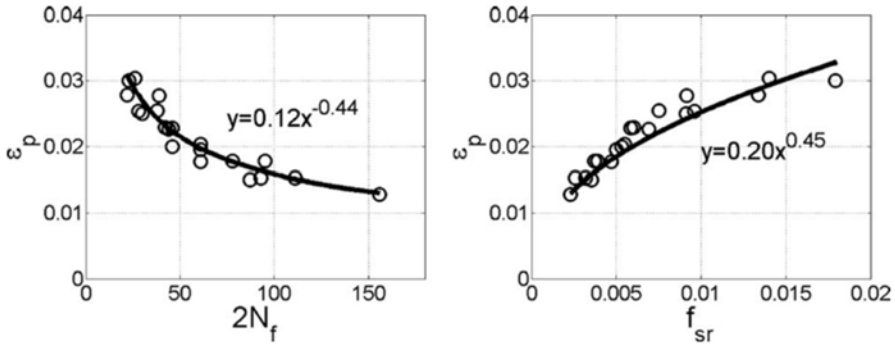

Figure A-13. Calibration of material coefficients: β, C_d and α and C_f (Kunnath et al. 2009).

To define the fatigue life of the steel in the *Steel Reinforcement Material* in OpenSees, users need to enter the ductility constant (ε'_f (or C_f in the *Reinforcing Steel Material* model)), the ductility exponent (*c* or *α* (or C_f in the *Reinforcing Steel Material* model)) and the strength degradation constant (C_d).

A.1.4 Menegotto-Pinto Curve Parameter

The Menegotto-Pinto (1973) equation is used for defining a curve connecting two tangents and having a variable radius of curvature at the intersection point of those two tangents (Figure A-14). The Menegotto Pinto equation can be expressed as:

$$f_s = f_o + E_o * (\varepsilon_s - \varepsilon_o)\left\{Q + \frac{1-Q}{\left[1 + \left|E_o * \frac{\varepsilon_s - \varepsilon_o}{f_{ch} - f_o}\right|\right]^{\frac{1}{R}}}\right\} \quad \textbf{(A.24)}$$

The tangent modulus, E_t, at any point along that curve is given by:

$$E_t = \frac{\partial f_s}{\partial \varepsilon_s} = E_{sec} - \frac{E_{sec} - Q * E_o}{1 + \left| E_o * \frac{\varepsilon_s - \varepsilon_o}{f_{ch} - f_o} \right|^{-R}} \quad \textbf{(A.25)}$$

where the secant modulus is defined by the curve connecting the origin coordinates (ε_o, f_o) and the coordinates of the point under consideration as, per the following equation:

$$E_{sec} = \frac{f_s - f_o}{\varepsilon_s - \varepsilon_o} \quad \textbf{(A.26)}$$

where ε_s is the steel strain at the secant point; f_s is the steel stress at the secant point, ε_o is the strain at initial point; f_o is the stress at initial point; E_o is the tangent modulus of elasticity at the initial point; and Q, R and f_{ch} are equation parameters to control the shape of the curve.

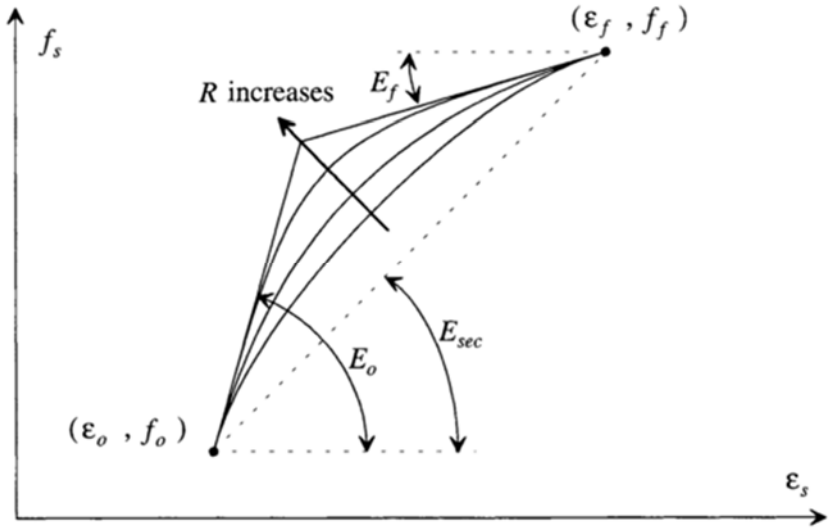

Figure A-14. Different curves having the same starting point (Chang and Mander 1994).

The equations that related the three control parameters (Q, f_{ch} and R factor) are:

$$Q = \frac{\frac{E_f}{E_o} - A^{-(R+1)}}{1 - A^{-(R+1)}} \quad \textbf{(A.27)}$$

where A is the denominator in Equation A.24.

$$\mathrm{A} = \left[1 + \left|E_o * \frac{\varepsilon_s - \varepsilon_o}{f_{ch} - f_o}\right|^R\right]^{\frac{1}{R}} \quad \textbf{(A.28)}$$

$$a = A^{-1} \quad \textbf{(A.29)}$$

$$\mathrm{f}_{ch} = f_o + \frac{E_o}{b} * \left(\varepsilon_f - \varepsilon_o\right) \quad \textbf{(A.30)}$$

where

$$\mathrm{b} = \frac{(1 - a^R)^{\frac{1}{R}}}{a} \quad \textbf{(A.31)}$$

and R is given by:

$$\mathrm{R} = \frac{E_f - E_{sec}}{E_{sec} - E_o} \quad \textbf{(A.32)}$$

With respect to modeling unloading and reloading with the Menegotto-Pinto equations, experiments by Panthaki (1992) on reinforcing bars showed that the initial Young's Modulus at the point of reversal from a tension envelope branch (unloading) and reversal from the compression envelope branch (loading) can be expressed by equations (A.33) and (A.34), respectively.

$$E_o^- = (1 - 3 * \Delta\varepsilon_a) * \mathrm{E}_s \quad \textbf{(A.33)}$$

$$E_o^+ = (1 - \Delta\varepsilon_a) * \mathrm{E}_s \quad \textbf{(A.34)}$$

Then, the R parameter was also found to be a function of the yield stress and was defined for corresponding branches as:

$$R^{-} = 16 * \left(\frac{f_y}{E_s}\right)^{\frac{1}{3}} * (1 - 10 * \Delta\varepsilon_a) \quad \textbf{(A.35)}$$

$$R^{+} = 20 * \left(\frac{f_y}{E_s}\right)^{\frac{1}{3}} * (1 - 20 * \Delta\varepsilon_a) \quad \textbf{(A.36)}$$

where $\Delta\varepsilon_a$ is strain amplitude for the cycle and E_o is the initial Young's Modulus for reversal branch as shown in Figure A-15.

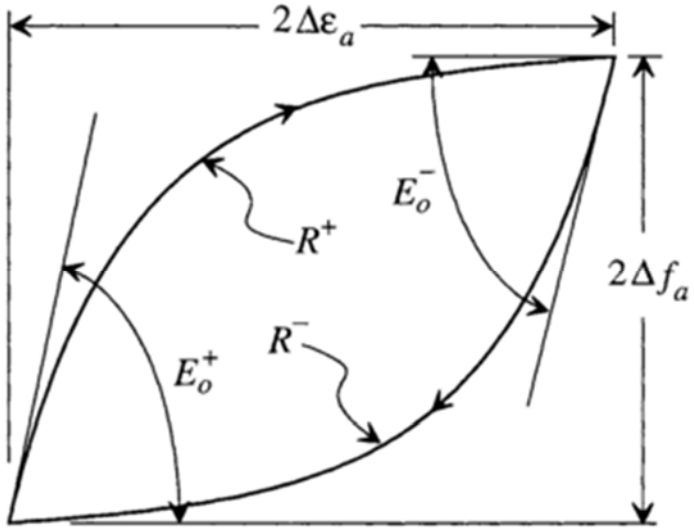

Figure A-15. Effect of the strain amplitude of the reversal on the equation parameter (Chang and Mander 1994).

The *Reinforcing Steel Material* model simplifies the equations (A.35) and (A.36), which are from different loading branches, into equation (A.37) and requires users to input these parameters, namely R1, R2, and R3. The default values are 0.333, 18.0, and 4.0, which are obtained by curve fitting of test results of reinforcing bars by Panthaki (1992).

$$R = \mathrm{R2} * \left(\frac{f_y}{E_s}\right)^{R1} * (1 - \mathrm{R3} * \Delta\varepsilon_a) \quad \textbf{(A.37)}$$

A.2 CONCRETE MODEL

A.2.1 Compressive Curve

The model utilizes the modified Kent and Park model [25] (Figure A-16). The monotonic compressive bounding curve is described by three regions (compression is positive):

$$\text{Region OA: } \varepsilon_c \le \varepsilon_0 \qquad \sigma_c = K * f'_c * \left[2 * \left(\frac{\varepsilon_c}{\varepsilon_0}\right) - \left(\frac{\varepsilon_c}{\varepsilon_0}\right)^2\right] \tag{A.38}$$

$$\text{Region AB: } \varepsilon_0 < \varepsilon_c \le \varepsilon_{20} \qquad \sigma_c = K * f'_c * [1 - Z * (\varepsilon_c - \varepsilon_0)] \tag{A.39}$$

$$\text{Region BC: } \varepsilon_c > \varepsilon_{20} \qquad \sigma_c = 0.2 * K * f'_c \tag{A.40}$$

The corresponding tangent moduli are:

$$\text{Region OA: } \varepsilon_c \le \varepsilon_0 \qquad E_t = \frac{2 * K * f'_c}{\varepsilon_0} * \left[1 - \left(\frac{\varepsilon_c}{\varepsilon_0}\right)\right] \tag{A.41}$$

$$\text{Region AB: } \varepsilon_0 < \varepsilon_c \le \varepsilon_{20} \qquad E_t = -Z * K * f'_c \tag{A.42}$$

$$\text{Region BC: } \varepsilon_c > \varepsilon_{20} \qquad E_t = 0 \tag{A.43}$$

where

$$\varepsilon_0 = 0.002 * K \tag{A.44}$$

$$K = 1 + \frac{\rho_s * f_{yh}}{f'_c} \tag{A.45}$$

$$Z = \frac{0.5}{\frac{3 + 0.29 * f'_c}{145 * f'_c - 1000} + 0.75 * \rho_s * \sqrt{\frac{h'}{s_h}} - 0.002 * K} \tag{A.46}$$

and where ε_0 is the concrete strain at maximum stress; ε_{20} is the concrete strain at 20 percent of maximum stress; K is the strength increase factor due to confinement; Z is the strain softening slope; f'_c is the concrete compressive cylinder strength; f_{yh} is the yield strength of stirrups; ρ_s is the ratio of the volume of hoop

reinforcement to the volume of the concrete core; h' is the width of concrete core measured to outside of stirrups; and s_h is the center to center spacing of stirrups.

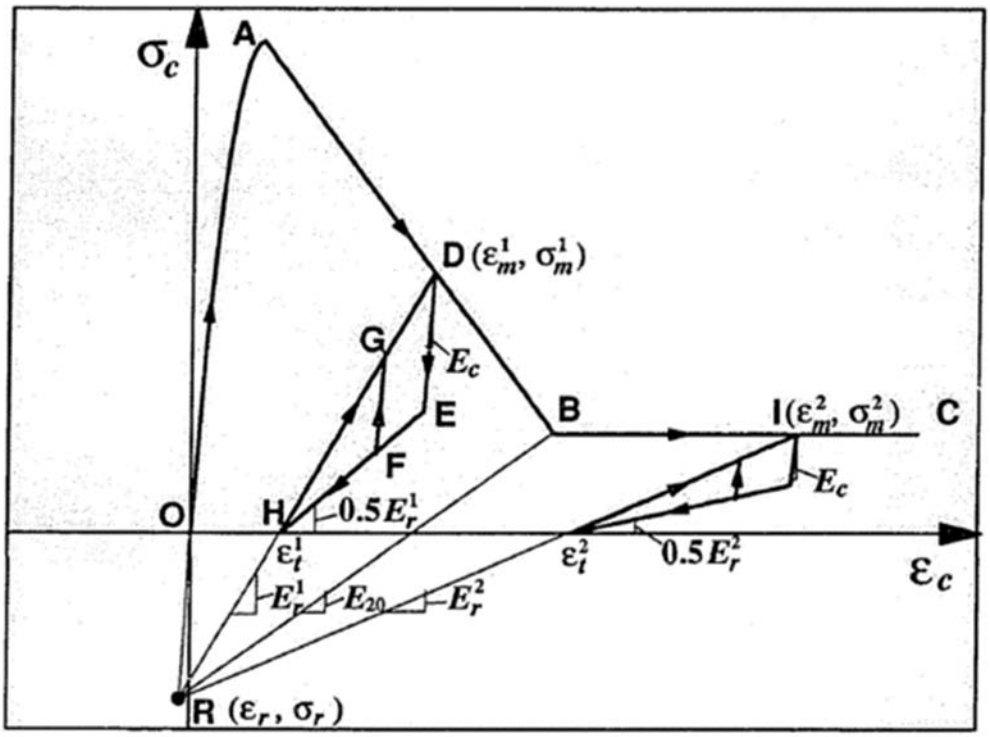

Figure A-16. Kent and Park concrete model (Hisham and Yassin 1994).

For cyclic loading in compression, the extension of all reloading lines intersect at a common point R to account for stiffness degradation (Figure A-17). The location of point R is defined by the intersection of the tangent line from the origin and the unloading line when concrete strength is 0.2*f'$_c$ (point B). The stress and strains along reloading line can be obtained by following expressions:

$$\varepsilon_r = \frac{0.2 * K * f'_c - E_{20} * \varepsilon_{20}}{E_c - E_{20}} \quad \textbf{(A.47)}$$

$$\sigma_r = E_c * \varepsilon_r \quad \textbf{(A.48)}$$

where E_c is the tangent modulus and E_{20} is the unloading modulus at point B.

If unloading occurs on the envelope curve before reaching zero stress (point H in Figure A-17), the model is defined by following expressions:

Maximum envelope (line HD): $$\sigma_{max} = \sigma_m + E_r * (\varepsilon_c - \varepsilon_m) \quad \textbf{(A.49)}$$

Minimum envelope (line HE): $$\sigma_{min} = 0.5 * E_r * (\varepsilon_c - \varepsilon_t) \quad \textbf{(A.50)}$$

where

$$E_r = \frac{\sigma_m - \sigma_r}{\varepsilon_m - \varepsilon_r} \quad \textbf{(A.51)}$$

$$\varepsilon_t = \varepsilon_m - \frac{\sigma_m}{E_r} \quad \textbf{(A.52)}$$

where σ_m and ε_m are the stress and strain at the unloading point in the monotonic envelope, respectively. For local loading/unloading, the model uses a straight line with Young's Modulus of E_c with following rules:

$$\sigma_c^T = \sigma_c' + E_c * \Delta\varepsilon_c \quad \textbf{(A.53)}$$

$$\text{if } \sigma_{min} \le \sigma_c^T \le \sigma_{max} \text{ then } \sigma_c = \sigma_c^T \text{ and } E_t = E_c \quad \textbf{(A.54)}$$

$$\text{if } \sigma_c^T < \sigma_{min} \text{ then } \sigma_c = \sigma_{min} \text{ and } E_t = 0.5 * E_t \quad \textbf{(A.55)}$$

$$\text{if } \sigma_c^T > \sigma_{max} \text{ then } \sigma_c = \sigma_{max} \text{ and } E_t = E_r \quad \textbf{(A.56)}$$

where σ^T_c is the new trial stress; σ'_c is the previous stress and $\Delta\varepsilon_c$ is the strain increment.
It should be noted that the reloading line will always reach to the point of unloading. Once the unloading passes the point H, tension rules govern for the hysteretic behavior.

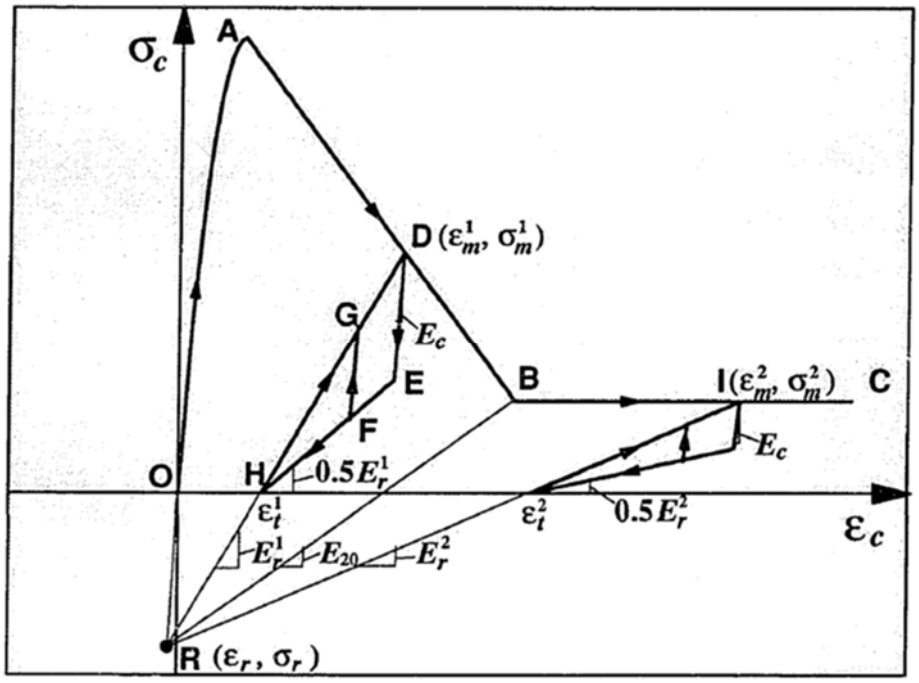

Figure A-17. Kent and Park concrete model under cyclic loading (Hisham and Yassin 1994).

A.3 Tension Curve

The tensile behavior of the model includes tension stiffening and stiffness degradation upon unloading and reloading for increasing values of tensile strain after initial crack. The maximum tensile strength of the concrete (modulus of rupture) is given by:

$$f_t' = 0.6228 * \sqrt{f_c'} \quad \text{in MPa} \tag{A.57}$$

The tensile hysteresis loops can occur anywhere along the strain axis due to either initial tensile loading or unloading from a compressive excursion. The tensile hysteresis curve is defined by three points, namely: points J, K, and M shown in Figure A-18. Point J is the strain when unloading a stress equal to zero. The value ε_t is calculated from equation (A.52). Point K is for peak tensile response and given by following equations:

$$\varepsilon_n = \varepsilon_t + \Delta\varepsilon_t \tag{A.58}$$

$$\sigma_n = f'_t * \left(1 + \frac{E_{ts}}{E_c}\right) - E_{ts} * \Delta\varepsilon_t \quad \textbf{(A.59)}$$

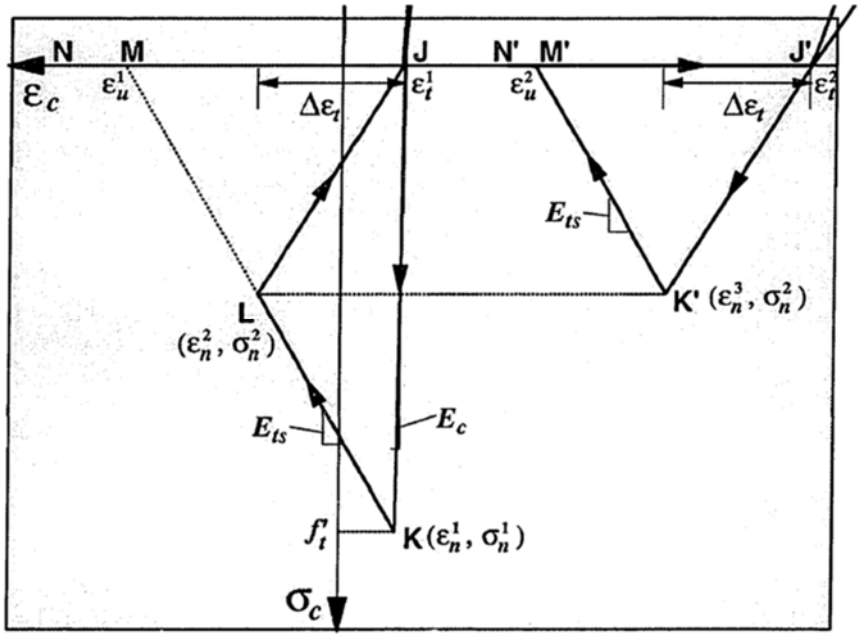

Figure A-18. Concrete model in tension (Hisham and Yassin 1994).

where $\Delta\varepsilon_t$ is the previous maximum differential between tensile strain and ε_t; E_{ts} is the tension stiffening modulus that is based on physical and numerical parameters. Lastly, point M (ε_u) is when the tensile stress is zero under more tensile strains and given by following equations:

$$\varepsilon_u = \varepsilon_t + f'_t * \left(\frac{1}{E_{ts}} + \frac{1}{E_c}\right) \quad \textbf{(A.60)}$$

In summary, stress-strain of the control points in tension and their corresponding tangent moduli are:

$$\text{Region JK: } \varepsilon_t < \varepsilon_c \leq \varepsilon_n \qquad \sigma_c = E_t * (\varepsilon_c - \varepsilon_t) \qquad E_t = \frac{\sigma_n}{\varepsilon_n - \varepsilon_t} \quad \textbf{(A.61)}$$

$$\text{Region KM: } \varepsilon_n < \varepsilon_c \leq \varepsilon_u \qquad \sigma_c = \sigma_n + E_t * (\varepsilon_c - \varepsilon_n) \qquad E_t = -E_{ts} \quad \textbf{(A.62)}$$

$$\text{Region MN: } \varepsilon_c > \varepsilon_u \qquad \sigma_c = 0 \qquad E_t = 0 \quad \textbf{(A.63)}$$

where E_{ts} controls tension stiffening, such that as the slope get stiffer, the effect of the tension stiffening becomes less. Also, the unloading/reloading lines are governed by Equation (A.61).

A.3.1 Concrete Confinement Model by Susantha et al. (2001)

The model is developed by Susantha et al. (2001) were used to identify the values of the concrete parameters that were provided in *Concrete02* to model the behavior of the confined concrete. These models focused on the confined concrete properties in concrete-filled steel tubes (CFT) with various shapes such as circular, box and octagonal sections. An analytical approach verified by existing experiments was taken to identify the uniaxial stress-strain relation for confined concrete for CFT columns. Then, a concrete-steel interaction was used to predict the lateral pressure, relating the maximum pressure to the strength of the confined concrete with an empirical formula.

The Susantha et al. stress-strain relationships are developed by modifying a prior model by Chang and Mander (1994):

$$f_c = f'_{cc} * \frac{x * r}{r - 1 + x^r} \quad \textbf{(A.64)}$$

$$x = \frac{\epsilon}{\epsilon_{cc}} \quad \textbf{(A.65)}$$

$$r = \frac{E_c}{(E_c - \frac{f'_{cc}}{\epsilon_{cc}})} \quad \textbf{(A.66)}$$

$$\epsilon_{cc} = \epsilon_c * \left[1 + 5 * \left(\frac{f'_{cc}}{f'_c} - 1\right)\right] \quad \textbf{(A.67)}$$

where f'_{cc} is the maximum confined concrete strength; and ε_{cc} is the strain at peak of confined concrete and $\alpha f'_c$ is the residual strength of the confined concrete.

In this model, the expression for maximum confined concrete strength is given by:

$$f'_{cc} = f'_c + m * f_{rp} \quad \textbf{(A.68)}$$

where f_{rp} is the maximum radial pressure on concrete and m is an empirical coefficient. Note that the equations for f_{rp} must recognize that in CFT, concrete and steel expand together. Also, for Equation A.68, Susantha et al. suggested to apply a 0.85 constant reduction for f'_c in the calculation for f'_{cc}. One of the reasons is that concrete strength of cylinder test could differ the actual strength of concrete in column.

Moreover, strength could vary along height of wall as aggregates tend to go down to the base making base stronger then top portion of walls (El-Tawil and Deierlein 1999). Based on experiments, *m* value was found to be in the range of 4-6. The authors recommended **4.0** as the *m* parameter. The radial pressure is given by:

$$f_r = \frac{2 * t}{D - 2 * t} * f_{sr} \quad \textbf{(A.69)}$$

where f_{sr} is circumference stress in steel, *D* is the diameter and *t* is the thickness.

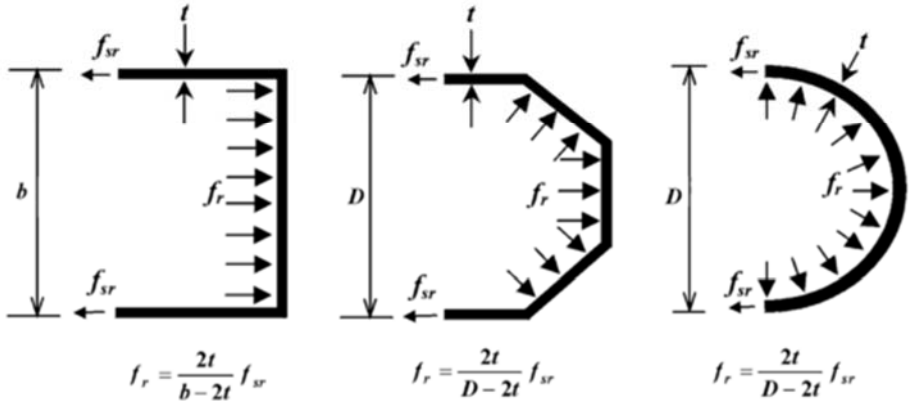

Figure A-19. Lateral pressure in various sections (Susantha et al. 2001).

The shape of the cross-section affects the confinement properties of the concrete. Even though the model is calibrated based on columns, the model could be applicable to C-PSW/CF walls as the behavior of the walls was observed to be flexurally dominated as in the case of most columns. In composite walls such as the one tested by Alzeni and Bruneau (2014), concrete confined by HSS steel is considered to be similar to confined concrete in circular column, and concrete confined by web steel was considered as unconfined concrete having the same ductility as concrete in HSS shape.

A.3.1.1 Circular Section

The equations for the confinement of concrete enclosed in a circular section were adopted from Tang et al. (1996), except that a "β" factor was introduced as shown in Equation (A.69):

$$f_{rp} = \beta * \frac{2 * t}{D - 2 * t} * f_{sr} \quad \textbf{(A.70)}$$

where

$$\beta = \nu_e - \nu_s \quad \textbf{(A.71)}$$

$$\nu_e = 0.2312 + 0.3582 * \nu'_e - 0.1524 * \frac{f'_c}{f_y} + 4.843 * \nu'_e * \frac{f'_c}{f_y} - 9.169 * \left[\frac{f'_c}{f_y}\right]^2 \quad \textbf{(A.72)}$$

$$\nu'_e = 0.881\text{x}10^{-6} * \left(\frac{D}{t}\right)^3 - 2.58\text{x}10^{-4} * \left(\frac{D}{t}\right)^2 + 1.953\text{x}10^{-2} * \left(\frac{D}{t}\right) + 0.4011 \quad \textbf{(A.73)}$$

where ν_e and ν_s is the Poisson ratios of a steel tube with and without filled-in concrete, and where ν_s is taken as **0.5** at the maximum strength point (0.5 being the Poisson's ratio of steel in a fully plastic state). Also, the equations (A.72) and (A.73) are valid only if f'_c/f_y is in the range of 0.04 to 0.2.

The ductility increases if steel restrains concrete in the lateral direction. The restrain action also depends on both the material properties and geometry of the column. Therefore, the post peak behavior should account for these factors. The local buckling effect could be included in the post peak calculation but according to the formula proposed by Usami and Ge (1998) (Equation (A.74)), the buckled stress to yield stress (f_b/f_y) was calculated to be larger than 1.0 so the local buckling effect was ignored in post peak behavior of the concrete.

$$\frac{f_b}{f_y} = 0.80 + \frac{0.025}{R_t} \leq 1.0 \quad \textbf{(A.74)}$$

where R_t is the radius-to-thickness ratio parameter is given by Equation (A.75).

$$R_t = \sqrt{3 * (1 - \nu^2)} * \frac{f_y}{E_s} * \frac{D}{2 * t} \leq 0.125 \quad \textbf{(A.75)}$$

Beyond the point of maximum strength, the model decreases strength using a linear relationship based on experimental curve fitting and given by:

$$\boldsymbol{Z}: \begin{cases} 0 & R_t * \frac{f'_{rc}}{f_{yst}} \leq 0.006 \\ \left[1x10^5 * \left(R_t * \frac{f'_{rc}}{f_{yst}}\right) - 600\right] MPa & R_t * \frac{f'_{rc}}{f_{yst}} \geq 0.006 \quad and\ f_y \leq 283\ MPa \\ \left[1x10^6 * \left(R_t * \frac{f'_{rc}}{f_{yst}}\right) - 6000\right] MPa & R_t * \frac{f'_{rc}}{f_{yst}} \geq 0.006 \quad and\ f_y \geq\ 336\ MPa \\ \left(\frac{f_y}{283}\right)^{13.4} \left[1x10^6 * \left(R_t * \frac{f'_{rc}}{f_{yst}}\right) - 600\right] MPa & R_t * \frac{f'_{rc}}{f_{yst}} \geq 0.006 \quad and\ 283 \leq\ f_y \leq 33 \end{cases} \quad \textbf{(A.76)}$$

Once the slope is determined, the coefficient for residual strength can be calculated from following expression:

$$\alpha = 1 - \frac{Z}{f'_{cc}}(\varepsilon_{cu} - \varepsilon_{cc}) \quad \textbf{(A.77)}$$

A constant value of **0.025** was given for ε_{cu} in circular cross-section based on a study of existing data.

A.3.1.2 Box Section

In box sections, the same equations are applicable except that, for the lateral pressure, the diameter in the above equations were changed to an equivalent diameter by the following expression:

$$D_{eq} = \frac{2 * b}{\sqrt{\pi}} \quad \textbf{(A.78)}$$

Also, for box sections, the falling branch slope, Z and ε_{cu} are expressed by different equations.

$$Z = \begin{cases} 0 & R_t * \frac{f'_{rc}}{f_{yst}} \leq 0.0039 \\ \left[23400 * R_t * \frac{f'_c}{f_y} - 91.26\right] MPa & R_t * \frac{f'_{rc}}{f_{yst}} > 0.0039 \end{cases} \quad \textbf{(A.79)}$$

$$\varepsilon_{cu} = \begin{cases} 0.04 & R_t * \frac{f'_{rc}}{f_{yst}} \leq 0.042 \\ 14.50\left(R_t * \frac{f'_c}{f_y}\right)^2 - 2.4 * R_t * \frac{f'_c}{f_y} + 0.116 & 0.042 < R_t * \frac{f'_{rc}}{f_{yst}} < 0.073 \\ 0.018 & R_t * \frac{f'_{rc}}{f_{yst}} \geq 0.073 \end{cases} \quad \textbf{(A.80)}$$

The slope of the descending branch increases as $R_t f'_c/f_{yst}$ increases.

A.4 Element Type

A.4.1 Theory of Element Types

The frame finite element models depend on Euler- Bernoulli beam theory and the torsional response was assumed elastic and uncoupled with axial and flexural responses. Therefore, torsional displacements and forces are neglected. With these assumptions, the governing variables for the displacement fields of the beam element and its deformation fields are (Figure A-20):

$$u(x) = [u(x) \quad w(x) \quad v(x)]^T \quad \textbf{(A.81)}$$

$$d(x) = \left[\varepsilon(x) \quad \kappa_y(x) \quad \kappa_z(x)\right]^T = \left[\frac{du(x)}{dx} \quad -\frac{d^2w(x)}{dx^2} \quad \frac{d^2v(x)}{dx^2}\right]^T \quad \textbf{(A.82)}$$

where $\varepsilon(x)$ is axial strain; $\kappa_y(x)$ and $\kappa_z(x)$ are the curvature about two orthogonal axes.

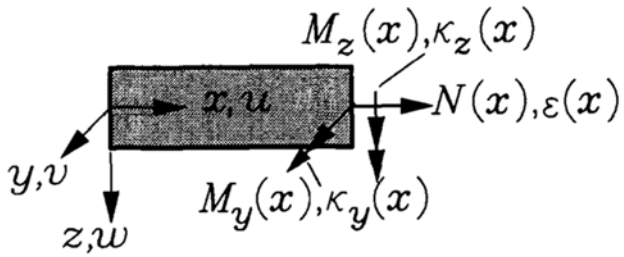

Figure A-20. Displacement, internal forces and deformations (Neuenhofer and Filippou 1997).

The corresponding stress resultants or internal force fields can be defined as:

$$\mathrm{D(x)} = \left[\mathrm{N(x)} \quad \mathrm{M_y(x)} \quad \mathrm{M_z(x)}\right]^{\mathrm{T}} \tag{A.83}$$

where N(x) is axial force; M_y(x) and M_z(x) are bending moments.
The assumed linearized relation is between deformation field and force field is:

$$\mathrm{D_{n+1}} = \mathrm{C} * [\mathrm{D_n}, \mathrm{d_n}, \mathrm{d_{n+1}}] \tag{A.84}$$

$$\Delta \mathrm{D} = \mathrm{k} * \Delta \mathrm{d} \tag{A.85}$$

(linearized constitutive relation)

$$\mathrm{k} = \frac{\partial \mathrm{D}}{\partial \mathrm{d}} = \begin{bmatrix} \frac{\partial \mathrm{N}}{\partial \varepsilon} & \frac{\partial \mathrm{N}}{\partial \kappa_y} & \frac{\partial \mathrm{N}}{\partial \kappa_z} \\ \frac{\partial \mathrm{M_y}}{\partial \varepsilon} & \frac{\partial \mathrm{M_y}}{\partial \kappa_y} & \frac{\partial \mathrm{M_y}}{\partial \kappa_z} \\ \frac{\partial \mathrm{M_z}}{\partial \varepsilon} & \frac{\partial \mathrm{M_z}}{\partial \kappa_y} & \frac{\partial \mathrm{M_z}}{\partial \kappa_z} \end{bmatrix} \tag{A.86}$$

A.4.1.1 Stiffness (Displacement Based) Method

In this method, the displacement field of the elements are discretized and interpolated in terms of elements' nodal displacements "q" as:

$$\mathrm{u(x)} = \mathrm{N(x)} * \mathrm{q} \tag{A.87}$$

where

$$N(x) = \begin{bmatrix} N_u(x) & 0 & 0 \\ 0 & N_w(x) & 0 \\ 0 & 0 & N_v(x) \end{bmatrix} \quad \textbf{(A.88)}$$

The matrix of shape functions, N(x) contains the shape functions for corresponding displacement fields, which are from Hermitian polynomials. Then, the deformation field, d(x) can be defined as:

$$d(x) = B(x) * q \quad \textbf{(A.89)}$$

where B(x) is the strain transformation matrix obtained by taking first and second derivative of the shape function of displacement fields. The force field increment can be obtain by:

$$\Delta D(x) = k(x) * \Delta d(x) = k(x) * B(x) * \Delta q \quad \textbf{(A.90)}$$

The element resisting forces, Q, can be obtained from the principle of virtual displacement leading to the equilibrium condition:

$$Q = \int_0^L B^T(x) * D(x) dx \quad \textbf{(A.91)}$$

The element stiffness matrix will be calculated from:

$$K = \frac{\partial Q}{\partial q} = \int_0^L B^T(x) * k(x) * B(x) dx \quad \textbf{(A.92)}$$

Then the residual forces are from:

$$R = K * \Delta q \quad \textbf{(A.93)}$$

A.4.1.2 Flexibility (Force Based) Method

In this method, the force field is defined as:

$$D(x) = b(x) * Q \tag{A.94}$$

where b(x) is the shape (interpolation) function and Q is generalized nodal forces. Then, from the linearized constitutive from (in equation (A.85)), the incremental deformation field is obtained:

$$\Delta d(x) = f(x) * \Delta D(x) = f(x) * b(x) * \Delta Q \tag{A.95}$$

where f is the inverse of stiffness matrix, which is referred to as flexibility matrix. The principle of virtual force leads to the compatibility condition and gives the element end displacement by:

$$q = \int_0^L b^T(x) * d(x)\, dx \tag{A.96}$$

Its linearization yields the residual displacement, r:

$$r = F * \Delta Q \tag{A.97}$$

The element flexibility matrix is:

$$F = \frac{\partial q}{\partial Q} = \int_0^L b^T(x) * f(x) * b(x) dx \tag{A.98}$$

Both types of elements require an iteration process. The difference is that stiffness (displacement based) method require initial displacements of nodes, on the other hand, the force based method starts iteration with initial nodal forces. For the solution of element quantities with integrals above, numerical integration is achieved using a number of integration points inside of the element to ease computation time. Depending intended application, OpenSees gives options for different types of numerical integrations such as Legendre (default), Lobotto, Radau, NewtonCotes, Trapezoidal, etc. for both element type. In accordance with the rules of each respective integration scheme, the values at the integration points for the element quantities

considered are multiplied by weight functions and summed up accordingly. Note that errors due to numerical integration can be mitigated by using more integration points. Displacement-based elements are also prone to additional discretization errors because they use constant strain ($\varepsilon = 1/L$) along the element irrespective of the number of integration points. Accuracy can be improved with improving the number of elements over the length of interest. However, this is not an issue for force-based method as the axial force shape function agrees with the exact solution (within numerical integration tolerance).

“This Page Intentionally Left Blank”

APPENDIX B Equivalent Lateral Force Calculations for the Trial Archetypes

B.1 Equivalent Lateral Force Calculation for Three Story Coupled Composite Walls

- USER NOTICES

Inpu -- Input

ImportantValu -- Strength of member or really important criteria

Check -- Means that there is comparison that is needed to be checked!

$NS := 3$ the number of stories $ORIGIN := 1$

- Weight of Each Story

$Weight_{Typical} := 1125 kip$

$$Weight := \left| \begin{array}{l} \text{for } q \in 1 .. (NS) \\ \quad Weight_q \leftarrow Weight_{Typical} \\ Weight \end{array} \right.$$

Total Weight of the structure:

$$W_T := \sum_{i=1}^{NS} Weight_i = 3375 \cdot kip$$

- Height of Each Story

$Height_1 := 10 ft$ $Ht_2 := 10 ft$

$$Height := \left| \begin{array}{l} \text{for } q \in 2 .. (NS) \\ \quad Height_q \leftarrow \left(Ht_2 + Height_{q-1}\right) \\ Height \end{array} \right.$$

$$Height = \begin{pmatrix} 10 \\ 20 \\ 30 \end{pmatrix} ft$$

Total height of the structure: $h_n := Height_{NS} = 30 \cdot ft$

Response Spectrum Site Class: D

Location: LA, Latitude 34.05224 and Longitude: -118.244

$S_s := 2.433g$ $S_1 := 0.853g$ $F_a := 1.2$ $F_v := 1.7$

$S_{DS} := 1.622g$ $S_{D1} := 0.853g$ $T_o := 0.11sec$ $T_S := 0.53sec$ $T_L := 8sec$

$I_e := 1.0$ $R_d := 8$ $\Omega_o := 2.5$ $C_d := 5.5$ Table 12.2-1 (ASCE 7-16)

$$S_a(T_a) := \begin{cases} S_{DS}\cdot\left(0.4 + 0.6\cdot\frac{T_a}{T_o}\right) & \text{if } 0 \le T_a < T_o \\ S_{DS} & \text{if } T_o \le T_a \le T_S \\ \frac{S_{D1}}{\frac{T_a}{sec}} & \text{if } T_S < T_a \le T_L \\ \left(S_{D1}\cdot\frac{T_L\cdot sec}{T_a^{\,2}}\right) & \text{otherwise} \end{cases}$$

Fundamental Period:

$C_t := 0.02$ ASCE7-16 Table 12.8-2 for all other structures

$x := 0.75$

$$T_a := C_t\cdot\left(\frac{h_n}{ft}\right)^x\cdot sec = 0.256\ s$$

The maximum period:

$$C_u := \begin{cases} 1.4 & \text{if } \frac{S_{D1}}{g} \geq 0.4 \\ 1.4 & \text{if } \frac{S_{D1}}{g} \geq 0.3 \wedge \frac{S_{D1}}{g} < 0.4 \\ 1.5 + \frac{\frac{S_{D1}}{g} - 0.2}{0.3 - 0.2} \cdot (1.4 - 1.5) & \text{if } \frac{S_{D1}}{g} \geq 0.2 \wedge \frac{S_{D1}}{g} < 0.3 \\ 1.6 + \frac{\frac{S_{D1}}{g} - 0.15}{0.2 - 0.15} \cdot (1.5 - 1.6) & \text{if } \frac{S_{D1}}{g} \geq 0.15 \wedge \frac{S_{D1}}{g} < 0.2 \\ 1.7 + \frac{\frac{S_{D1}}{g} - 0.1}{0.15 - 0.1} \cdot (1.6 - 1.7) & \text{if } \frac{S_{D1}}{g} \geq 0.1 \wedge \frac{S_{D1}}{g} < 0.15 \\ 1.7 & \text{otherwise} \end{cases}$$

$$C_u = 1.4$$

$$T_{max} := C_u \cdot T_a = 0.359\,s$$

Hence, the period and the response spectral acceleration is as follows:

$$T_{aw} := \begin{cases} T_a & \text{if } T_a < T_{max} \\ T_{max} & \text{otherwise} \end{cases}$$

$$T_a = 0.256\,s \qquad S_a(T_a) = 1.622\,g$$

$$T_{ad} := 0, 0.1\,sec .. 10\,sec$$

The plot of Response Spectrum

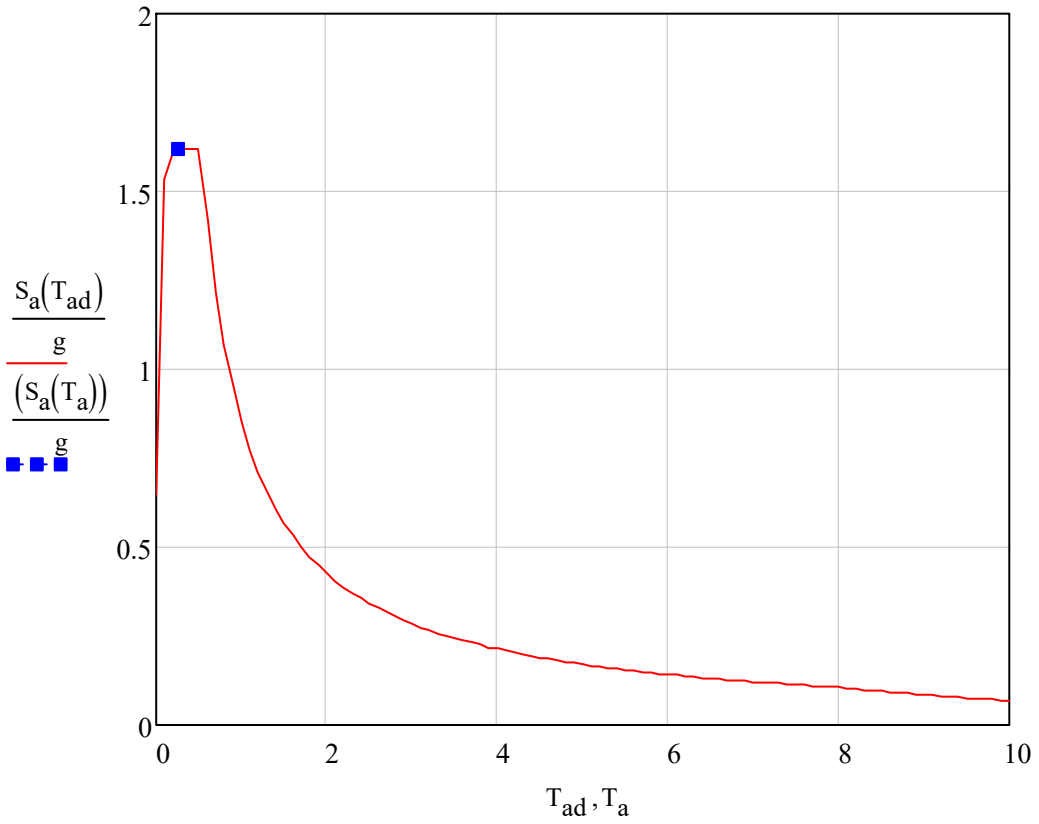

EQUIVALENT LATERAL FORCE PROCEDURE (ELF) ASCE 7-16 -Section 12.8

The seismic response coefficient

$$C_{s\_cal} := \frac{\frac{S_{DS}}{g}}{\frac{R_d}{I_e}} = 0.203 \quad I_e = 1$$

- Maximum and Minimum Limit for Cs:

$$C_{s\_max} := \begin{cases} \dfrac{S_{D1}}{T_{max}\cdot\dfrac{R_d}{I_e}}\cdot\dfrac{sec}{g} & \text{if } T_a \le T_L \quad \text{for constant velocity part} \\ \dfrac{S_{D1}\cdot T_L}{T_{max}^{2}\cdot\dfrac{R_d}{I_e}}\cdot\dfrac{sec}{g} & \text{otherwise} \quad \text{for constant displacement part} \end{cases}$$

$$C_{s\_max} = 0.297$$

$$C_{s\_min1} := \begin{cases} \left(0.044\cdot\dfrac{S_{DS}}{g}\cdot I_e\right) & \text{if } 0.044\cdot\dfrac{S_{DS}}{g}\cdot I_e \ge 0.01 \\ 0.01 & \text{otherwise} \end{cases}$$

$$C_{s\_min1} = 0.071$$

$$C_{s\_min} := \begin{cases} 0.5\cdot\dfrac{\dfrac{S_1}{g}}{\dfrac{R_d}{I_e}} & \text{if } S_1 \ge 0.6\cdot g \\ C_{s\_min1} & \text{otherwise} \end{cases}$$

$$C_{s\_min} = 0.053$$

$$C_s := \begin{cases} C_{s\_max} & \text{if } C_{s\_cal} > C_{s\_max} \\ C_{s\_min} & \text{if } C_{s\_cal} < C_{s\_min} \\ C_{s\_min} & \text{if } C_{s\_min} > C_{s\_max} \\ C_{s\_cal} & \text{otherwise} \end{cases}$$

$$C_s = 0.203$$

The base shear is:

$$V_{base} := C_s \cdot W_T = 684\,kip$$

Vertical Distribution of Seismic Forces:

An exponent related to the structural period

$$k := \begin{cases} 1 & \text{if } T_a \le 0.5\,sec \\ 2 & \text{if } T_a \ge 2.5\,sec \\ 1 + \frac{1}{2}\cdot\left(\frac{T_a}{sec} - 0.5\right) & \text{otherwise} \end{cases} \qquad k = 1$$

- The vertical distribution factor & Vertical Force Distribution:

$z := 1 .. NS$

$$Cv_z := \frac{Weight_z \cdot \left(\frac{Height_z}{ft}\right)^k}{\sum_{i=1}^{NS}\left[Weight_i \cdot \left(\frac{Height_i}{ft}\right)^k\right]} \qquad Cv = \begin{pmatrix} 0.167 \\ 0.333 \\ 0.5 \end{pmatrix}$$

The floor shear is:

$$F_x := Cv \cdot V_{base} \qquad F_x = \begin{pmatrix} 114.047 \\ 228.094 \\ 342.141 \end{pmatrix} \cdot kip$$

B.2 Equivalent Lateral Force Calculation for Eight Story Coupled Composite Walls

- USER NOTICES

Input -- Input

ImportantValue -- Strength of member or really important criteria

Check -- Means that there is comparison that is needed to be checked!

$NS := 8$ the number of stories $ORIGIN := 1$

- Weight of Each Story

$Weight_{Typical} := 1038kip$

$$Weight := \left| \begin{array}{l} \text{for } q \in 1..(NS) \\ \quad Weight_q \leftarrow Weight_{Typical} \\ Weight \end{array} \right.$$

Total Weight of the structure:

$$W_T := \sum_{i=1}^{NS} Weight_i = 8304 \cdot kip$$

- Height of Each Story

$Height_1 := 20ft$ $Ht_2 := 14ft$

$$Height := \left| \begin{array}{l} \text{for } q \in 2..(NS) \\ \quad Height_q \leftarrow (Ht_2 + Height_{q-1}) \\ Height \end{array} \right.$$

$$Height = \begin{pmatrix} 20 \\ 34 \\ 48 \\ 62 \\ 76 \\ 90 \\ 104 \\ 118 \end{pmatrix} ft$$

Total height of the structure:

$h_n := Height_{NS} = 118 \cdot ft$

Response Spectrum Site Class : D

Location: LA, Latitude 34.05224 and Longitude: -118.244

$S_s := 2.433 \cdot g$ $S_1 := 0.853 \cdot g$ $F_a := 1.2$ $F_v := 1.7$

$S_{DS} := 1.622g$ $S_{D1} := 0.853g$ $T_o := 0.11sec$ $T_S := 0.53sec$ $T_L := 8sec$

$I_e := 1.0$ $R_d := 8$ $\Omega_o := 2.5$ $C_d := 5.5$ Table 12.2-1 (ASCE 7-16)

$$S_a(T_a) := \begin{cases} S_{DS} \cdot \left(0.4 + 0.6 \cdot \frac{T_a}{T_o}\right) & \text{if } 0 \le T_a < T_o \\ S_{DS} & \text{if } T_o \le T_a \le T_S \\ \frac{S_{D1}}{\frac{T_a}{sec}} & \text{if } T_S < T_a \le T_L \\ \left(S_{D1} \cdot \frac{T_L \cdot sec}{T_a^{\,2}}\right) & \text{otherwise} \end{cases}$$

Fundamental Period:

$C_t := 0.02$ $x := 0.75$ ASCE7-16 Table 12.8-2

$$T_a := C_t \cdot \left(\frac{h_n}{ft}\right)^x \cdot sec = 0.716s$$

The maximum period:

$$C_u := \begin{cases} 1.4 \text{ if } \frac{S_{D1}}{g} \geq 0.4 \\ 1.4 \text{ if } \frac{S_{D1}}{g} \geq 0.3 \wedge \frac{S_{D1}}{g} < 0.4 \\ 1.5 + \frac{\frac{S_{D1}}{g} - 0.2}{0.3 - 0.2} \cdot (1.4 - 1.5) \text{ if } \frac{S_{D1}}{g} \geq 0.2 \wedge \frac{S_{D1}}{g} < 0.3 \\ 1.6 + \frac{\frac{S_{D1}}{g} - 0.15}{0.2 - 0.15} \cdot (1.5 - 1.6) \text{ if } \frac{S_{D1}}{g} \geq 0.15 \wedge \frac{S_{D1}}{g} < 0.2 \\ 1.7 + \frac{\frac{S_{D1}}{g} - 0.1}{0.15 - 0.1} \cdot (1.6 - 1.7) \text{ if } \frac{S_{D1}}{g} \geq 0.1 \wedge \frac{S_{D1}}{g} < 0.15 \\ 1.7 \text{ otherwise} \end{cases}$$

$$C_u = 1.4$$

$$T_{max} := C_u \cdot T_a = 1.002s$$

Hence, the period and the response spectral acceleration is as follows:

$$T_a := \begin{cases} T_a \text{ if } T_a < T_{max} \\ T_{max} \text{ otherwise} \end{cases}$$

$$T_a = 0.716s \qquad S_a\left(T_a\right) = 1.1913 \cdot g$$

$$T_{ad} := 0, 0.1sec .. 10sec$$

The plot of Response Spectrum

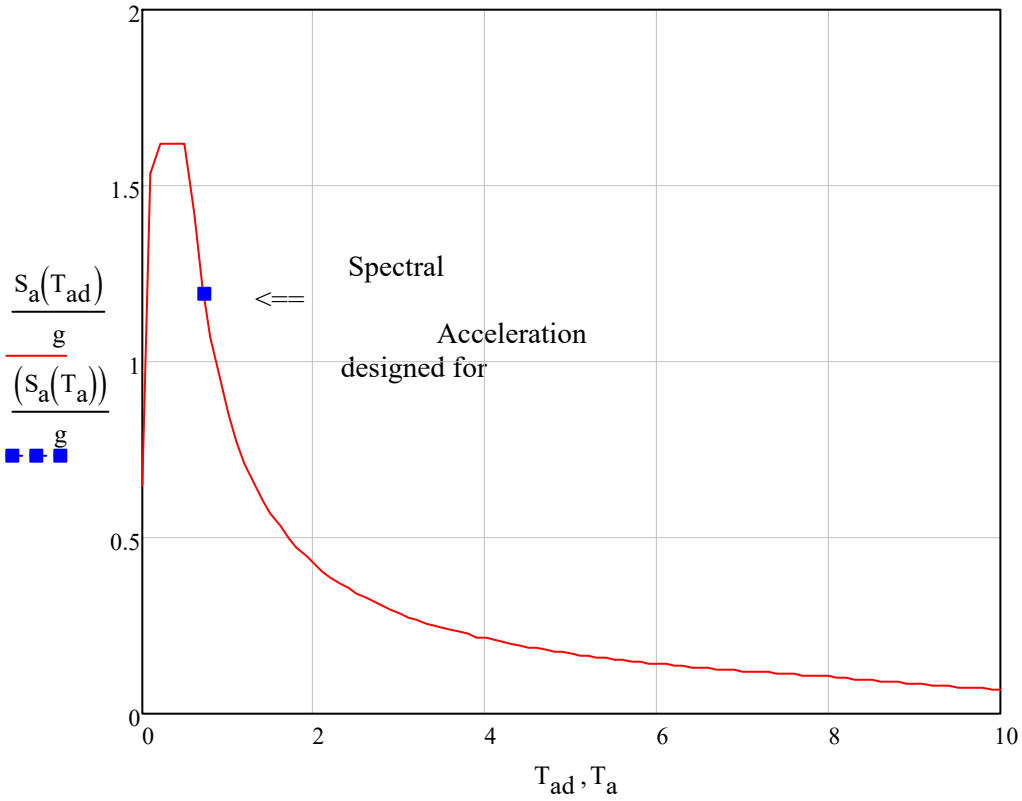

EQUIVALENT LATERAL FORCE PROCEDURE (ELF) ASCE 7-16 -Section 12.8

The seismic response coefficient

$$C_{s\_cal} := \frac{\frac{S_{DS}}{g}}{\frac{R_d}{I_e}} = 0.203 \qquad I_e = 1$$

- Maximum and Minimum Limit for Cs:

$$C_{s\_max} := \begin{cases} \dfrac{S_{D1}}{T_{max}\cdot\dfrac{R_d}{I_e}}\cdot\dfrac{sec}{g} & \text{if } T_a \le T_L \quad \text{for constant velocity part} \\ \dfrac{S_{D1}\cdot T_L}{T_{max}^{\,2}\cdot\dfrac{R_d}{I_e}}\cdot\dfrac{sec}{g} & \text{otherwise} \quad \text{for constant displacement part} \end{cases}$$

$$C_{s\_max} = 0.106$$

$$C_{s\_min1} := \begin{cases} \left(0.044\cdot\dfrac{S_{DS}}{g}\cdot I_e\right) & \text{if } 0.044\cdot\dfrac{S_{DS}}{g}\cdot I_e \ge 0.01 \\ 0.01 & \text{otherwise} \end{cases}$$

$$C_{s\_min1} = 0.071$$

$$C_{s\_min} := \begin{cases} 0.5\cdot\dfrac{\dfrac{S_1}{g}}{\dfrac{R_d}{I_e}} & \text{if } S_1 \ge 0.6\cdot g \\ C_{s\_min1} & \text{otherwise} \end{cases}$$

$$C_{s\_min} = 0.053$$

$$C_s := \begin{cases} C_{s\_max} & \text{if } C_{s\_cal} > C_{s\_max} \\ C_{s\_min} & \text{if } C_{s\_cal} < C_{s\_min} \\ C_{s\_min} & \text{if } C_{s\_min} > C_{s\_max} \\ C_{s\_cal} & \text{otherwise} \end{cases}$$

$$C_s = 0.106$$

The base shear is:

$V_{base} := C_s \cdot W_T = 883 \cdot kip$

Vertical Distribution of Seismic Forces:

An exponent related to the structural period

$$k := \begin{cases} 1 & \text{if } T_a \le 0.5\,sec \\ 2 & \text{if } T_a \ge 2.5\,sec \\ 1 + \frac{1}{2}\cdot\left(\frac{T_a}{sec} - 0.5\right) & \text{otherwise} \end{cases} \qquad k = 1.108$$

- The vertical distribution factor & Vertical Force Distribution:

$z := 1 .. NS$

$$Cv_z := \frac{Weight_z \cdot \left(\frac{Height_z}{ft}\right)^k}{\sum_{i=1}^{NS}\left[Weight_i \cdot \left(\frac{Height_i}{ft}\right)^k\right]} \qquad Cv = \begin{pmatrix} 0.031 \\ 0.056 \\ 0.082 \\ 0.11 \\ 0.137 \\ 0.166 \\ 0.194 \\ 0.223 \end{pmatrix}$$

The floor shear is:

$F_x := Cv \cdot V_{base}$

$$F_x = \begin{pmatrix} 27.614 \\ 49.713 \\ 72.846 \\ 96.731 \\ 121.21 \\ 146.184 \\ 171.583 \\ 197.355 \end{pmatrix} \cdot kip$$

“This Page Intentionally Left Blank”

APPENDIX C Design Procedure of Archetypes

This section presents the detailed design calculations of archetype structure PG-1B.

Step 1: Initial Parameters

Wall Configuration - Type I (Coupled and Uncoupled Walls)
SDC - Dmax

Floor Plan	Story Data	Material Properties	L/d ratio
$L_f := 200ft$	$n := 8$	$f_c := 6ksi$	$Ld := 4$
$W_f := 120ft$	$h_1 := 17ft$	$F_y := 50ksi$	$R := 8$
$DL := 0.12ksf$	$h_{typ} := 14ft$	$E_s := 29000ksi$	$I_e := 1$
$L_{wall} := 11ft$		$E_c := 57 \cdot ksi \cdot \sqrt{\frac{f_c}{psi}}$	$C_d := 5.5$

Coupling Beam

$CR := 0.60$

$L_{CB} := 8ft$

Shear Amplification Factor

$ShearAmpFactor := 4$

General Notes:
cw indicates coupled wall
uncw indicated uncoupled wall

Step 2: Equivalent Lateral Force Analysis

Step 2-1: Develop response spectra

From Dmax

$S_{DS} := 1.0$

$S_{D1} := 0.6$ $S_1 := 0.6$

Note: S_1 calculated from S_{D1} assuming stiff soil (site class D)

Step 2-2: Estimate Fundamental Period

$C_t := 0.02$

$x := 0.75$

$h_n := (n - 1) \cdot h_{typ} + h_1$

$T_a := C_t \cdot \left(\frac{h_n}{ft}\right)^x = 0.702$

$C_u := 1.4$

$C_u \cdot T_a = 0.983$

Actual period is greater than $C_U T_a$ so use this value for T

$T := C_u \cdot T_a = 0.983$

Step 2-3: Seismic Response Coefficient

$C_{scalc} := \frac{S_{DS}}{\frac{R}{I_e}} = 0.125$

$$C_{smax} := \frac{S_{D1}}{T \cdot \left(\frac{R}{I_e}\right)} = 0.076$$

$$C_{smin} := \max\left(0.044 \cdot S_{DS} \cdot I_e, 0.01\right) = 0.044$$

$$C_{smin2} := \frac{0.5 \cdot S_1}{\frac{R}{I_e}} = 0.038$$

$$C_s := C_{smax} = 0.076$$

Step 2-4: Distribute seismic forces vertically

$$W_{total} := n \cdot DL \cdot L_f \cdot W_f = 2.304 \times 10^4 \cdot kip$$

$$w_{floor} := DL \cdot L_f \cdot W_f = 2.88 \times 10^3 \cdot kip$$

$$StoryH := \begin{pmatrix} h_1 \\ h_{typ} \\ h_{typ} \\ h_{typ} \\ h_{typ} \\ h_{typ} \\ h_{typ} \\ h_{typ} \end{pmatrix}$$

$$i := 1 .. n$$

$$h_i := \sum_{j=1}^{i} StoryH_j$$

$$nn := i$$

$$V_t := C_s \cdot W_{total} = 1.757 \times 10^3 \cdot kip$$

$$k := 1.24$$

$$Cv_i := \frac{w_{floor} \cdot \left(\frac{h_i}{ft}\right)^k}{\sum_{nn} \left[w_{floor} \cdot \left(\frac{h_{nn}}{ft}\right)^k \right]}$$

$$F_i := Cv_i \cdot V_t$$

$$V_i := \sum_{k=i}^{n} F_k$$

Step 2-5: Compute base shear force and apply amplification factor

$$V_{base} := ShearAmpFactor \cdot V_1 = 7.029 \times 10^3 \cdot kip$$

Step 2-6: Compute overturning moment at base

$$OTM := \sum_i \left(F_i \cdot h_i\right) = 1.779 \times 10^6 \cdot kip \cdot in$$

Step 2-7: Compute sum of coupling beam forces

$L_{eff} := L_{CB} + L_{wall}$

Note: L is the distance between the centerlines of the coupled walls

$$SumV_{U\_CB} := \frac{CR \cdot OTM}{L_{eff}} = 4.682 \times 10^3 \cdot kip$$

Step 2-8: Compute shear force on coupling beam

$$V_{U\_CB} := \frac{SumV_{U\_CB}}{2n} = 292.628 \cdot kip$$

Note: the total lateral load is resisted by two coupled wall systems. Only one coupled wall is considered.

Step 3: Preliminary Design

Wall dimensions

$t_p := \frac{9}{16} in$ — Wall plate thickness

$t_{sc} := 24in$ — Wall thickness

$L_{wall} := 11 \cdot ft = 132 \cdot in$ — Wall length

Coupling Beam dimensions

$h_{CB} := 24in$ — Coupling beam depth

$b_{CB} := 24in$ — Coupling beam width

$t_{p.CB.f} := \frac{1}{2} in$ — Coupling beam flange plate thickness

$t_{p.CB.w} := \frac{3}{8} in$ — Coupling beam web plate thickness

Step 4: Design Checks

Steps 4-1 and 4-2 have been skipped since this calculation sheet focuses on wall and coupling beam design

Step 4-3: Coupling beam width-to-thickness ratio

$$\frac{b_{CB} - 2t_{p.CB.w}}{t_{p.CB.f}} = 46.5 \quad < \quad 2.26\cdot\left(\frac{29000}{50}\right)^{0.5} = 54.428$$ Compact flange

$$\frac{h_{CB} - 2t_{p.CB.f}}{t_{p.CB.w}} = 61.333 \quad < \quad 3\cdot\left(\frac{29000}{50}\right)^{0.5} = 72.25$$ Compact web

Step 4-4: Inter-story drift ratio

$Is := 1491101.8$ Sum of wall moment of inertia

$Itr := 6052697.8$ Wall moment of inertiaabout the centerline of structure from separate spreadsheet

$sumQn := 3766$ Sum of coupling beam shear corresponding to Mp from separate spreadsheet

$Cf := 8775$ Wall tensile strength from separate spreadsheet

$$I_{equiv} := Is + \sqrt{\frac{sumQn}{Cf}}\cdot(Itr - Is) = 4.479\times 10^{6}$$

Story displacement

$$Disp := \begin{pmatrix} 0.12817 \\ 0.40861 \\ 0.81246 \\ 1.31008 \\ 1.87427 \\ 2.48121 \\ 3.11147 \\ 3.75107 \end{pmatrix} = \begin{pmatrix} 0.128 \\ 0.409 \\ 0.812 \\ 1.31 \\ 1.874 \\ 2.481 \\ 3.111 \\ 3.751 \end{pmatrix}$$ Story displacement from separate spreadsheet

Inter-story drift ratio with Cd factor

$hl := 17\cdot 12$

$htyp := 14\cdot 12$

$$IDR := \begin{pmatrix} \frac{Disp_1}{hl}\cdot C_d \\ \frac{Disp_2 - Disp_1}{htyp}\cdot C_d \\ \frac{Disp_3 - Disp_2}{htyp}\cdot C_d \\ \frac{Disp_4 - Disp_3}{htyp}\cdot C_d \\ \frac{Disp_5 - Disp_4}{htyp}\cdot C_d \\ \frac{Disp_6 - Disp_5}{htyp}\cdot C_d \\ \frac{Disp_7 - Disp_6}{htyp}\cdot C_d \\ \frac{Disp_8 - Disp_7}{htyp}\cdot C_d \end{pmatrix} = \begin{pmatrix} 3.456\times 10^{-3} \\ 9.181\times 10^{-3} \\ 0.013 \\ 0.016 \\ 0.018 \\ 0.02 \\ 0.021 \\ 0.021 \end{pmatrix}$$ Inter-story drift ratio

$\max(IDR) = 0.021$

Max IDR = 2.1 %

Step 4-5: Coupling beam shear strength

Compute the exact CR

$EI_{wall} := 2 \cdot 21620975614$

Sum of wall EI using AISC equation from separate spreadsheet

$EI_{equiv} := I_{equiv} \cdot 29000 = 1.299 \times 10^{11}$

Equivalent flexural stiffness

$CR := \frac{EI_{equiv} - EI_{wall}}{EI_{equiv}} = 0.667$

Accurate CR

Required coupling beam shear strength

$L_{CB} := 8 \cdot 12 = 96$

$L_{wall} := 11 \cdot 12 = 132$

$L_{eff} := L_{CB} + L_{wall} = 228$

Effective wall distance (centroid to centroid)

$OTM := \frac{1.779 \cdot 10^{6}}{2} = 8.895 \times 10^{5}$

Overturning moment

$V_{U\_CB} := \frac{CR \cdot OTM}{L_{eff}^{n}} = 325.333$

Required coupling beam shear strength

Available coupling beam shear strength

$k_v := 5$

$1.1 \cdot \left(k_v \cdot \frac{29000}{50}\right)^{0.5} = 59.237 \quad < \quad \frac{h_{CB} - 2t_{p.CB.f}}{t_{p.CB.w}} = 61.333 \quad < \quad 1.37 \cdot \left(k_v \cdot \frac{29000}{50}\right)^{0.5} = 73.777$

$C_{v2} := \frac{1.1 \cdot \left(k_v \cdot \frac{29000}{50}\right)^{0.5}}{\frac{h_{CB} - 2t_{p.CB.f}}{t_{p.CB.w}}} = 0.966$

$F_y := 50$

$h_{CB} := 24$

Coupling beam depth

$t_{p.CB.f} := 0.5$

Coupling beam flange thickness

$t_{p.CB.w} := 0.375$

Coupling beam web thickness

$A_w := 2\left(h_{CB} - 2t_{p.CB.f}\right) \cdot t_{p.CB.w} = 17.25$

$\phi := 0.9$

$V_{n.CB} := 0.6 \cdot F_y \cdot A_w \cdot C_{v2} = 499.811$

$\phi \cdot V_{n.CB} = 449.83 \quad > \quad V_{U\_CB} = 325.333$

Available coupling beam shear strength

Step 4-6: Coupling beam flexural strength

Required coupling beam flexural strength

$M_{U\_CB} := V_{U\_CB} \cdot \frac{L_{CB}}{2} = 1.562 \times 10^4$

Available coupling beam flexural strength

$\phi := 0.9$

$M_p := 22596$ Mp from fiber analysis

$M_{n.CB} := M_p$

$\phi \cdot M_{n.CB} = 2.034 \times 10^4 \quad > \quad M_{U\_CB} = 1.562 \times 10^4$ Available coupling beam flexural strength

Step 4-7: Wall shear strength

Required wall shear strength

$V_{base} := 7.029 \cdot 10^3$

$V_{U\_wall} := \frac{V_{base}}{4} = 1.757 \times 10^3$ Required wall shear strength per wall

Available wall shear strength

$\phi := 0.9$

$t_{p.wall} := \frac{9}{16}$

$F_y = 50$

$A_w := 2 \cdot t_{p.wall} \cdot L_{wall} = 148.5$

$V_{n.wall} := F_y \cdot A_w = 7.425 \times 10^3$

$\phi \cdot V_{n.wall} = 6.683 \times 10^3 \quad > \quad V_{U\_wall} = 1.757 \times 10^3$ Available wall shear strength

Step 4-8: Wall flexural strength

Required wall flexural strength

$ExpMp := 27822$ 1.1RyMp of coupling beam from fiber analysis

$V_{n.ExpMp.CB} := 2 \cdot \frac{ExpMp}{L_{CB}} = 579.625$ Coupling beam shear corresponding to ExpMp

$V_f := V_{U\_CB} = 325.333$ Coupling beam shear demand

$\gamma_1 := \frac{n \cdot V_{n.ExpMp.CB}}{n \cdot V_f} = 1.782$ Overstrength factor

$EI_{wall.T} := 9692937457.03$ Flexural stiffness of wall under tension force

$EI_{wall.C} := 21620975613.55$ Flexural stiffness of wall under compression force from fiber analysis

$M_{U.wall.T} := \left(\frac{EI_{wall.T}}{EI_{wall.T} + EI_{wall.C}} \right) \cdot \gamma_1 \cdot OTM \cdot (1 - CR) = 1.633 \times 10^5$

$M_{U.wall.C} := \left(\frac{EI_{wall.C}}{EI_{wall.T} + EI_{wall.C}} \right) \cdot \gamma_1 \cdot OTM \cdot (1 - CR) = 3.642 \times 10^5$

Available wall flexural strength

$\phi := 0.9$

$P := n \cdot V_{n.ExpMp.CB} = 4.637 \times 10^{3}$ Axial force subjected to walls

$M_{n.wall.T} := 211508.3$

$M_{n.wall.C} := 529444.1$

Nominal wall flexural strength from fiber analysis

$\phi \cdot M_{n.wall.T} = 1.904 \times 10^{5} > M_{U.wall.T} = 1.633 \times 10^{5}$ Available wall flexural strength

$\phi \cdot M_{n.wall.C} = 4.765 \times 10^{5} > M_{U.wall.C} = 3.642 \times 10^{5}$ Available wall flexural strength

APPENDIX D
The Beta Factors

The material presented here was produced by Rahul Raman and Sai Chowdeswara Rao Korlapati and is provided here in support of information presented in Section 10.2.

D.1 The Beta Factor Study

This section is a review of the existing literature that has been carried out to determine if a correlation exists between the number of test data available and the choice of the uncertainty factors related to test data, β_{TD}, and modeling, β_{MDL}, as well as to assess if there exists a trend in the choice of beta factors for new structural systems.

As mentioned in Section 2.3, the FEMA P695 methodology requires creating nonlinear models to represent the actual behavior of the system over a range of time period and explicitly consider uncertainties in ground motions, modelling, design, and test data. In order to determine the seismic performance factors for the design of new seismic force resisting systems, it is necessary that the mentioned uncertainties be evaluated. Understanding the variations of these uncertainty factors can help in better estimation of the ACMR and hence the seismic performance factors of the lateral load resisting system. Furthermore, finding a correlation between the uncertainty factors selected in past FEMA P695 projects and the number of experimental studies conducted on the system can help minimize the number of tests required for a new system to determine appropriate performance factors. Hence, the existing literature was reviewed to determine if a correlation exists between the number of test data available and the choice of the uncertainty factors related to test data and modeling, as well as to assess if there exists a trend in the choice of beta factors for new structural systems.

A total of 173 publications were obtained from a search in Engineering Village, an information discovery platform, which was reduced to 150 after removing duplicates. When work from the same research project was presented at both a conference and in a referred journal, the journal paper, which had the more detailed information, was retained, further reducing the dataset, down to 123 individual publications. Out of the 123 publications, the full text was available only for 81 studies. These full texts were then read for further understanding of the procedure followed by the authors in the selection of uncertainty factors. In some papers, it was observed that the authors did not make decisions regarding the quality rating values but rather, reversed the problem by determining which trial values of the quality rating would be required to make an

assumed value of the response modification factor, "R" acceptable. Given that no engineering judgment is provided for the choice of quality rating in this approach, publications reporting these types of studies were also removed in establishing the final list of relevant publications. After all the above sorting was accomplished, a total of 31 individual research projects/publications were found to be relevant to the current objective of the current study. These are presented in Table D-2.

Table D-2. Quality Rating for 31 studies

TITLE	AUTHORS	MATERIAL USED	β_{TD}	β_{MDL}
Evaluation of seismic collapse performance of steel special moment resisting frames using FEMA P695 (ATC-63) methodology	Zareian et al. (2010)	Steel	Good	Good
Example application of the FEMA P695 (ATC-63) methodology for the collapse performance evaluation of wood light-frame systems	Filiatrault and Christovasilis (2010)	Wood	Good	Good/ Poor
Case study on the seismic performance of reinforced concrete intermediate moment frames using ACI design provisions	Richard et al. (2010)	Concrete	Good	Good
A FEMA P695 study for the proposed seismic performance factors for cold-formed steel special bolted moment frames	Sato and Uang (2010)	Steel	Superior	Good
Seismic performance assessment of steel corrugated shear wall system using non-linear analysis	Vigh et al. (2013)	Steel	Fair	Good
On the quantification of seismic performance factors of Chevron Knee Bracings, in steel structures	Farahi and Mofid (2013)	Steel	Fair	Good
Numerical evaluation: AISI S400 steel-sheathed CFS framed shear wall seismic design method	Shamim and Rogers (2015)	Steel	Good	Good
Seismic performance of steel plate shear walls considering two different design philosophies of infill plates. II: Assessment of collapse potential	Purba and Bruneau (2014)	Steel	Fair	Good
Seismic Safety Evaluation of Reinforced Concrete Walls through FEMA P695 Methodology	Gogus and Wallace (2015)	Concrete	Good	Good
Seismic response modification factors of reinforced concrete staggered wall structures	Lee and Kim (2015)	Concrete	Poor	Good
Feasibility study of determination of seismic performance factors for structural insulated panels	Donovan and Memari (2014)	Others*	Fair	Fair
Effect of gravity framing on the overstrength and collapse capacity of steel frame buildings with perimeter special moment frames	Elkady and Lignos (2015)	Steel	Good	Good
An assessment of uncertainty in the performance evaluation of wood shear wall structures	Jayamon et al. (2015)	Wood	Good	Poor
Assessing the collapse probability of base-isolated buildings considering pounding to moat walls using the FEMA P695 methodology	Masroor and Mosqueda (2015)	Steel	Good	Good

Seismic analysis and design of buildings equipped with propped rocking wall systems	Nicknam (2015)	Concrete	Fair	Fair
Collapse Fragility Evaluation of Ductile Reinforced Concrete Block Wall Systems for Seismic Risk Assessment	Siyam et al. (2016)	Concrete	Fair	Fair
Buildings with Rigid Walls and Flexible Roof Diaphragms. I: Evaluation of Current U.S. Seismic Provisions	Koliou et al. (2015)	Concrete	Fair	Fair
Evaluation of seismic response factors for eccentrically braced frames using FEMA P695 methodology	Kuşyılmaz and Topkaya (2016)	Steel	Superior	Superior
Seismic Collapse Risk Assessment of Reinforced Masonry Walls with Boundary Elements Using the FEMA P695 Methodology	Ezzeldin et al. (2016)	Masonry	Good	Good
Derivation of Seismic Design Parameters for ECC and Multi-Material Special Moment-Resisting Frames	Gencturk et al. (2016)	Others*	Good	Good
Seismic collapse prevention system for steel-frame buildings	Judd and Charney (2016)	Steel	Fair	Fair
Quantification of seismic performance factors of the buildings consisting of disposable knee bracing frames	Nobahar et al. (2016)	Steel	Fair	Good
Eurocode conforming design of BRBF – Part II: Design procedure evaluation	Zsarnóczay and Vigh (2017)	Steel	Good	Good
Seismic Base Shear Modification Factors for Timber-Steel Hybrid Structure: Collapse Risk Assessment Approach	Bezabeh et al. (2017)	Others*	Fair	Fair
Numerical investigation on design requirements for steel ordinary braced frames	Choi et al. (2017)	Steel	Fair	Fair
Seismic collapse assessment of self-centering hybrid precast walls and conventional reinforced concrete walls	Lu et al. (2017)	Concrete	Good	Good
Behavior factor (q) evaluation the CFS braced structures according to FEMA P695	Fiorino et al. (2017)	Steel	Good	Good
Seismic design procedure for cold-formed steel sheathed shear wall frames: Proposal and evaluation	Kechidi et al. (2017)	Steel	Good	Good
Determination of the seismic performance factors for post-tensioned rocking timber wall systems	Sarti et al. (2017)	Wood	Fair	Good
Quantification of the seismic performance factors for steel diagrid structures	Sadeghi and Rofooei (2018)	Steel	Superior	Good
Quantification of the Impact of Detailing on the Performance and Cost of RC Shear Wall Buildings in Regions with High Uncertainty in Seismicity Hazards	Aly et al. (2018)	Concrete	Good	Good

* Other materials namely, Engineered Cementitious Composite (ECC), Structural Insulated Panel (SIP), and hybrid systems

While reading the literature, it was observed that some studies only generically referred to the fact that some of the structural systems under consideration had been tested for decades, without any reference to the total number of prior tests, which made it difficult to quantitatively come up with a final number for the number of test data considered. Therefore, to overcome this hurdle, it was decided to use the number of test data specifically considered by researchers to validate the nonlinear inelastic model used in their specific

FEMA P695 studies as the key parameter to determine the quality ratings, instead of the total number of tests conducted in the literature at large for a specific structural system. This shift in logic, as a first compromise, is schematically illustrated in Figure D-21. However, it was further found that not all researchers specifically listed the number of test data used to validate the model used in their study. To further complicate matters, it was found that some of the researchers did not conduct experiments but rather referred to test data available in the literature and cited in their study. An attempt was made to obtain the total number of tests by reviewing the experimental studies conducted by the cited authors. However, even after such further refinement in tracking down the data, it turns out that the total number of tests used for the validation of models used in FEMA P695 studies could be obtained for only 11 such studies. The information obtained from these 11 studies is reported in Table D-3. This limited data set was then used to determine if there exists a correlation between the choice of uncertainty factors and the available number of experimental data used to validate the models considered as part of FEMA P695 studies.

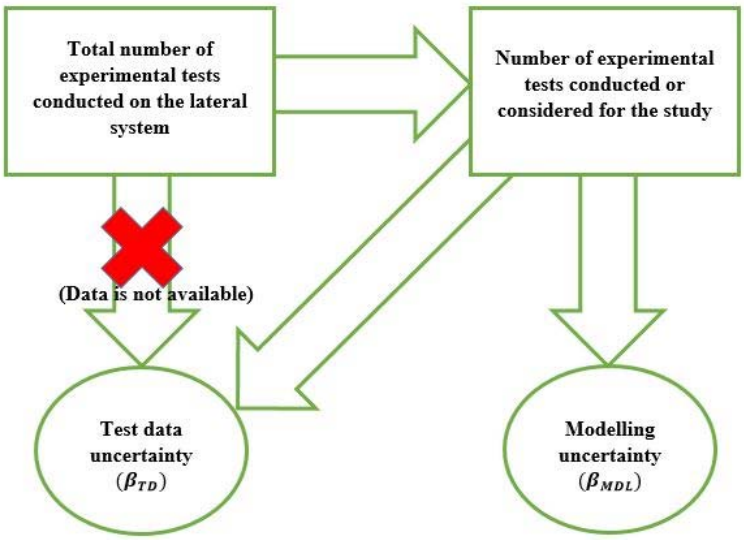

Figure D-21. Schematic representation of the study

Table D-3. Quality Rating and Number of Test Data for 11 studies

Authors	Number of Test data*	Quality rating of Test data	Quality rating of index archetype Models	Type of Seismic Force Resisting System
Zareian et al. (2010)	300	Good (0.2)	Good (0.2)	Steel Moment Frames
Sato and Uang (2010)	9	Superior (0.1)	Good (0.2)	Cold-Formed Steel Special Bolted Moment Frames
Vigh et al. (2013)	44	Fair (0.35)	Good (0.2)	Corrugated Steel Plate Shear Walls
Shamim and Rogers (2015)	10	Good (0.2)	Good (0.2)	Steel-Sheathed CFS Framed Shear Wall
Purba and Bruneau (2014)	36	Fair (0.35)	Good (0.2)	Steel Plate Shear Wall
Elkady and Lignos (2015)	7	Good (0.2)	Good (0.2)	Steel Special Moment Frames
Siyam et al. (2016)	6	Fair (0.35)	Fair (0.35)	Reinforced Concrete Block Wall
Ezzeldin et al. (2016)	4	Good (0.2)	Good (0.2)	Reinforced Masonry Walls
Fiorino et al. (2017)	12	Good (0.2)	Good (0.2)	CFS Strap Braced Stud Walls
Kechidi et al. (2017)	109	Good (0.2)	Good (0.2)	Steel Sheathed Shear Wall Frames
Sarti et al. (2017)	21	Fair (0.35)	Good (0.2)	Post-tensioned Rocking Timber Walls

*Number of test data used to validate the nonlinear inelastic model.

D.1.1 Correlation between Number of Test Data and Quality Rating of Test Data

It was expected that as the number of test data increased, the quality rating would shift towards superior, and vice versa. In order to verify this statement, the work of various researchers was reviewed.

As indicated in Table D-3, it was observed that out of these 11 studies, there was only one study for which the indices were given a “superior” quality rating, and that study referred to only nine test data for calibration of the numerical model (Sato and Uang 2013). The reason stated for the use of superior quality rating was that this study referred to cold formed steel special bolted moment frames and all the nine full-scale beam-column subassembly tests showed a consistent slip-bearing behavior and failure mode in the bolt group. Testing showed that the bolted moment connection could provide a reliable source of energy dissipation through bolt friction and bearing. Out of the remaining ten studies included in Table D-3, six used “good” quality ratings, and the rest used “fair” quality rating.

To establish what correlation existed (if any) between the total number of test data and the uncertainty factors, the data presented earlier in Table D-3 (consisting of the number of test data along with the assigned test data uncertainty) are plotted as shown in Figure D-22. The resulting linear regression provides a trend line that supports the initial assumption of "the number of test data increased, the quality rating would shift towards superior, and vice versa", but not strongly. However, one of the 11 studies (as one data point) somewhat slants the results, namely the study conducted by Zareian et al. (2010), which stated that the parameters of the deterioration model used in that study had been calibrated against 300 assembly tests. As this is the only study with a number of referenced test data above 150, it can be observed that this single data point plays a dominant role in defining the trend. In order to verify this statement, the resulting trend when calculating regression without this data point is shown in Figure D-22b. Comparing Figure D-22a and Figure D-22b, it can be seen that there is a reversal in the trend observed when the data point was removed. Therefore, in the absence of more data points, it is difficult to predict a definite trend here. However, what can be ascertained from the data in Table D-3 is that, even with few test data, some researchers were confident to assign a superior test data quality rating on the assertion that the tests conducted were able to effectively capture all failure modes. It is also shown that generally, in most studies, ratings were dominantly "good", often "fair", and never "poor".

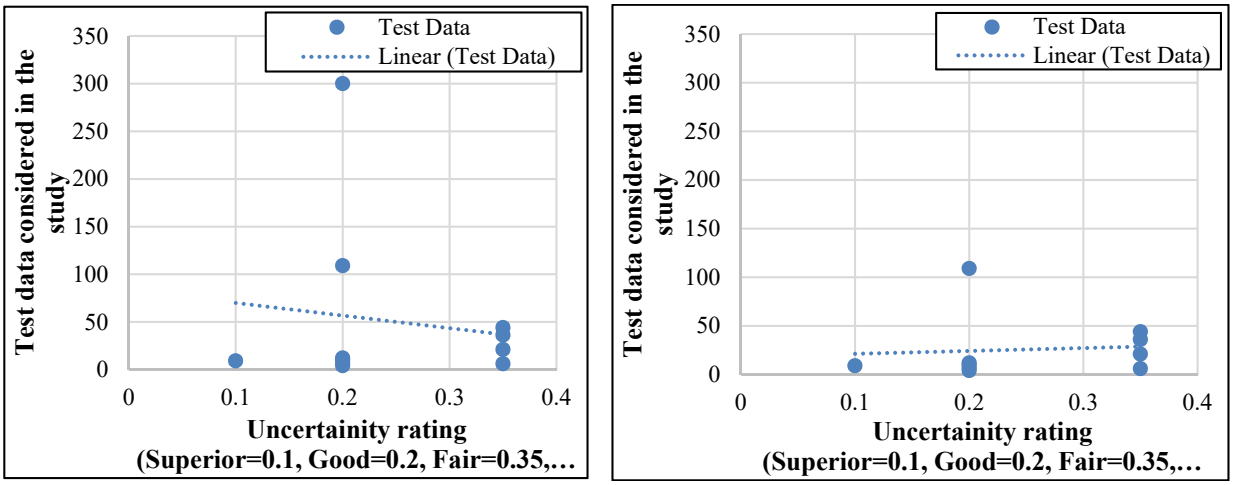

Figure D-22. Number of test data considered in the study versus test data uncertainty for: a) all 11 study, and; b) all except the study done by Zareian et al. (2010)

D.1.2 Correlation between Number of Test Data and Modeling Related Uncertainty

The quality rating of the index archetype is selected based on how well the structural behavioral effects that contribute to the collapse of the structure are captured in the model used in the non-linear inelastic analyses. This is typically verified by validating the model with the experimental data. Therefore, as shown previously in Figure D-21, the correlation between the test data used to validate the model with the modeling related uncertainty was also studied; it is shown in Figure D-23.

From Figure D-23a, it can be observed that all but one of the studies rated the modelling related uncertainty as "good" (the other one was labelled "fair"). This trend might be attributed to the fact that FEMA P695 recommends using the rating "good" if "the nonlinear models were able to capture most, but not all, nonlinear response mechanisms leading to collapse or the complete design space is not fully represented such that there is only a reasonable confidence that the range of response captured by the models is indicative of the primary structural behavior characteristics that affect collapse". This seems to suggest that most researchers share this restrained but generally positive confidence in the adequacy of non-linear hysteretic models in modern non-linear inelastic analysis. As discussed previously, to observe the change in trend without the study that referenced 300 tests, as this study may have biased the trends as it overwhelms all other data points, results were also plotted excluding the specific study having 300 test data, and the corresponding results are shown in Figure D-23b.

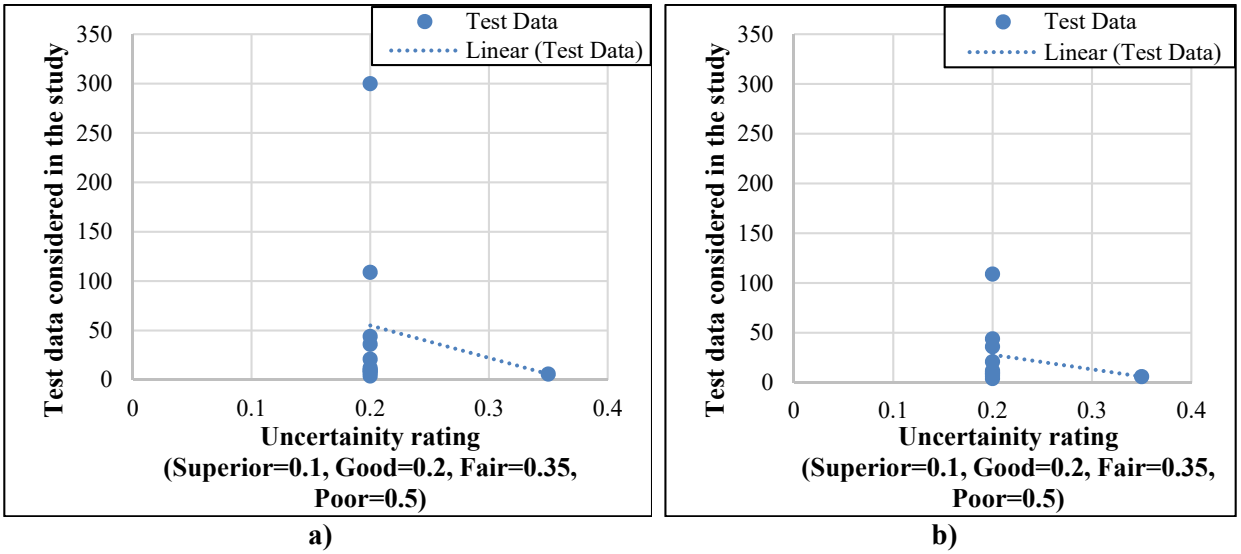

Figure D-23. Number of test data considered in the study versus modelling uncertainty for: a) all 11 study, and; b) all except the study done by Zareian et al. (2010)

D.1.3 Comparison of the Current Study with NIST GCR 10-917-8

In parallel with development of the FEMA P695 study, the National Institute of Standards and Technology (NIST) led a study to "test" the Methodology with a number of seismic structural systems that were already part of existing buildings codes and seismic design specifications. The results presented earlier in Table 3.1 for the 31 studies representing different lateral systems were compared with the data obtained from Section 8.4.2 of NIST GCR 10-917-8 document by Kircher et al. (2010). It was observed that out of the twelve types of system mentioned in the NIST document, six of them have been included in the above data set of 31 studies. Though the sources consulted here (i.e. research publications) for these data were different than the NIST report, the reported Beta factors were evidently the same, as shown in Table D-4 below. Most importantly, the studies reported in the NIST document do not explicitly refer to the number of test data used for validation. Hence, the trend presented in this study could not be verified against any other data set. Note that the NIST report indicated: "Many trial applications noted the subjective nature of the quality ratings used to define uncertainty associated with design requirements, test data, and nonlinear modeling." It also expressed the concern that "there is a need for a consistent and reliable method for selection of quality ratings, and a fair assessment of the quality of design requirements, test data, and nonlinear modeling capabilities across all systems. The Methodology recognizes this need, and control occurs through review and concurrence in the peer review process." This is consistent with the observations made as part of the current study.

Table D-4. Comparison of Data obtained from NIST GCR 10-917-8 with the results from this study

S.No	TYPE	DETAILING	NIST Data		Current Study Data	
			β_{TD}	β_{MDL}	β_{TD}	β_{MDL}
1	RMSW	SPECIAL	Good	Good	Good	Good
2	RMSW	ORDINARY	Fair	Good	-	-
3	RCSW	SPECIAL	Good	Good	Good	Good
4	RCSW	ORDINARY	Good	Good	Good	Good
5	SCBF	SPECIAL	Good	Good	-	-
6	BRBF	N/A	Good	Good	Good	Good
7	SMF	SPECIAL	Good	Good	Good	Good
8	SMF	SPECIAL	Good	Good	-	-
9	RCMF	SPECIAL	Good	Good	-	-
10	RCMF	ORDINARY	Good	Fair	-	-
11	SMF	SPECIAL	Good	Good	-	-
12	WLFSW	N/A	Good	Good/Poor	Good	Good/Poor

D.1.4 Quality Rating and Type of Material Used

In order to understand whether the type of material used for construction has any influence on the choice of quality rating of a lateral load resisting system, the number of time each quality rating has been used for structural systems having specific material types are presented in Figure D-24a and Figure D-24b, for the 31 studies mentioned in Table D-2, respectively. It can be observed that lateral systems made of steel have been the subject of more FEMA P695 studies, followed by concrete, wood, masonry and other materials (namely, Engineered Cementitious Composite (ECC), Structural Insulated Panel (SIP), and hybrid systems). This data also illustrates that the uncertainty factor associated with the studies done on steel structures is typically less than for the other building materials. As shown in Figure D-24a, three studies used the "superior" index for steel structures, while no studies did when other materials were used. It is speculated that this is attributed to a belief across the research community that the non-linear inelastic behavior and properties of steel lateral systems, and their failure modes, are better understood than for other materials. Nonetheless, it remains that, across all studies, "good" was the most frequently used index, particularly for steel and concrete.

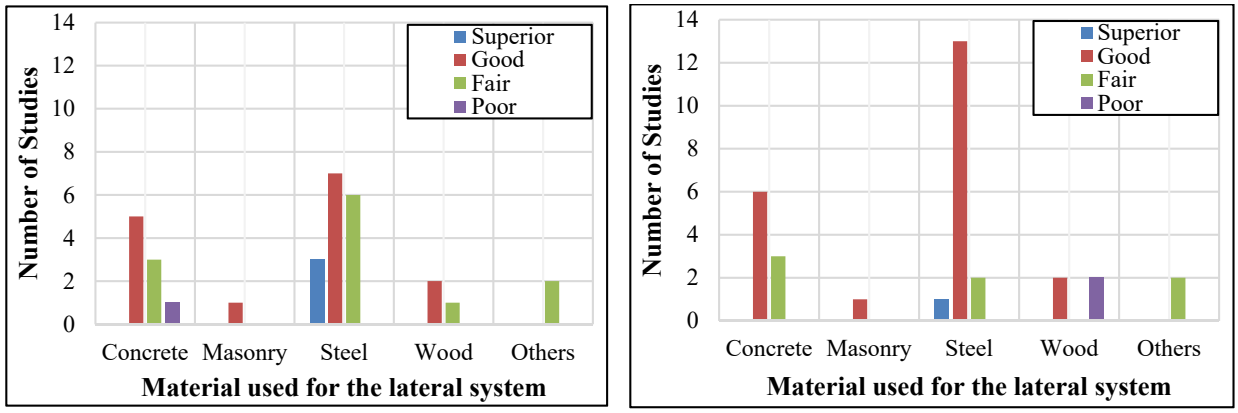

Figure D-24. Number of studies versus material used in 31 studies for: a) β_{TD}, and; β_{MDL}

D.1.5 Conclusion

The prior studies conducted by researchers who used the FEMA P695 methodology with various lateral load-resisting systems were reviewed in order to find a correlation between the choice of uncertainty factors and the number of test data used to validate the model. The initial list of 123 research publications related to FEMA P695 methodology were reviewed and the list was curtailed down to 31 publications based on (1)

the availability of full text for the study, and (2) whether the study specifically provided a justification for the choice of uncertainty factors. These 31 studies were then further reviewed to single out those that referred to a total number of tests used to validate the models used in the study. This reduced the data set to only 11 studies out of the earlier 31 studies**.** Based on this data set, a correlation was established between the choice of uncertainty factor and the number of tests used to validate the model. It was found that studies with higher number of test data often (but not always) had a better uncertainty factor, but no strong correlation could be established given the limited number of data in the set. A similar observation was made in case of the correlation between the number of tests and the modelling uncertainty. It was also observed, based on the 31 studies, that the uncertainty factor associated with test data and modeling are typically less for steel structural systems compared to the other building materials. Therefore, in this study, "good" rating was chosen for β_{TD} and β_{MDL} uncertainty factors.